STEM CELL SYSTEMS BIOENGINEERING

EDITED BY: Tiago G. Fernandes, Stephanie Michelle Willerth and Yuguo Lei
PUBLISHED IN: Frontiers in Bioengineering and Biotechnology

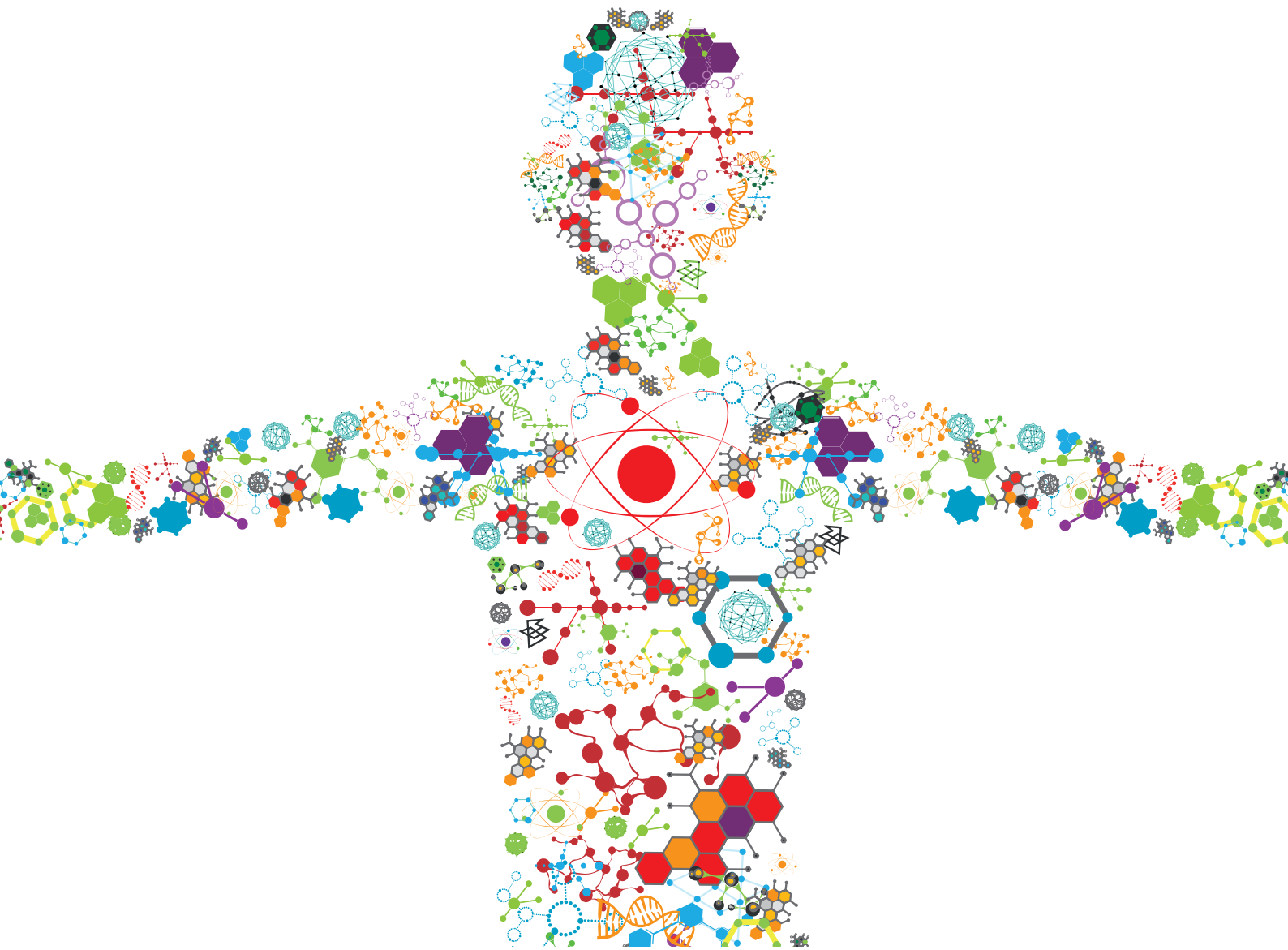

frontiers Research Topics

ISSN 1664-8714
ISBN 978-2-88966-895-3
DOI 10.3389/978-2-88966-895-3

About Frontiers

Frontiers is more than just an open-access publisher of scholarly articles: it is a pioneering approach to the world of academia, radically improving the way scholarly research is managed. The grand vision of Frontiers is a world where all people have an equal opportunity to seek, share and generate knowledge. Frontiers provides immediate and permanent online open access to all its publications, but this alone is not enough to realize our grand goals.

Frontiers Journal Series

The Frontiers Journal Series is a multi-tier and interdisciplinary set of open-access, online journals, promising a paradigm shift from the current review, selection and dissemination processes in academic publishing. All Frontiers journals are driven by researchers for researchers; therefore, they constitute a service to the scholarly community. At the same time, the Frontiers Journal Series operates on a revolutionary invention, the tiered publishing system, initially addressing specific communities of scholars, and gradually climbing up to broader public understanding, thus serving the interests of the lay society, too.

Dedication to Quality

Each Frontiers article is a landmark of the highest quality, thanks to genuinely collaborative interactions between authors and review editors, who include some of the world's best academicians. Research must be certified by peers before entering a stream of knowledge that may eventually reach the public - and shape society; therefore, Frontiers only applies the most rigorous and unbiased reviews.
Frontiers revolutionizes research publishing by freely delivering the most outstanding research, evaluated with no bias from both the academic and social point of view. By applying the most advanced information technologies, Frontiers is catapulting scholarly publishing into a new generation.

What are Frontiers Research Topics?

Frontiers Research Topics are very popular trademarks of the Frontiers Journals Series: they are collections of at least ten articles, all centered on a particular subject. With their unique mix of varied contributions from Original Research to Review Articles, Frontiers Research Topics unify the most influential researchers, the latest key findings and historical advances in a hot research area! Find out more on how to host your own Frontiers Research Topic or contribute to one as an author by contacting the Frontiers Editorial Office: frontiersin.org/about/contact

STEM CELL SYSTEMS BIOENGINEERING

Topic Editors:
Tiago G. Fernandes, University of Lisbon, Portugal
Stephanie Michelle Willerth, University of Victoria, Canada
Yuguo Lei, University of Nebraska-Lincoln, United States

Dr. Stephanie Willerth has a commercialization agreement with Aspect Biosystems with regards to bioprinting stem cell derived tissues. Dr. Yuguo Lei is a co-founder of CellGro Technologies, LLC, a company focusing on cell expansion technologies. Dr. Tiago Fernandes has no competing interests with regards to this Research Topic.

Citation: Fernandes, T. G., Willerth, S. M., Lei, Y., eds. (2021). Stem Cell Systems Bioengineering. Lausanne: Frontiers Media SA. doi: 10.3389/978-2-88966-895-3

Table of Contents

frontiers in Bioengineering and Biotechnology

EDITORIAL
published: 07 May 2021
doi: 10.3389/fbioe.2021.693107

Editorial: Stem Cell Systems Bioengineering

Yuguo Lei[1†], *Stephanie Michelle Willerth*[2†] *and Tiago G. Fernandes*[3,4*†]

[1] Department of Biomedical Engineering, Huck Life Science Institute, Pennsylvania State University, University Park, PA, United States, [2] Division of Medical Sciences, Department of Mechanical Engineering, University of Victoria, Victoria, BC, Canada, [3] Department of Bioengineering and iBB–Institute for Bioengineering and Biosciences, Instituto Superior Técnico, Universidade de Lisboa, Lisbon, Portugal, [4] Associate Laboratory i4HB–Institute for Health and Bioeconomy, Instituto Superior Técnico, Universidade de Lisboa, Lisbon, Portugal

Keywords: engineering cell systems, stem cells, cell fate specification, bioprocessing, regenerative medicine

Editorial on the Research Topic

Stem Cell Systems Bioengineering

Stem cells hold tremendous promise for advancing the field of regenerative medicine. Stem Cell Systems Bioengineering uses engineering principles to advance the knowledge of biological systems, which ultimately contribute to the translation of new therapeutic approaches to clinical practice. The key technologies associated with this field include novel bioprocesses for the maintenance and expansion of human stem cells, as well as their differentiated progeny, and micro/nanofabrication to produce tissue-like substitutes. Other emergent topics include the development of cellular products using innovative three-dimensional (3D) cultivation systems, e.g., organoids, functional human tissue-like substitutes, controlled-release particles for programming cellular responses, novel bioprinting to generate tissues, and using artificial intelligence to model these systems. Furthermore, the development of *in vitro* tests for toxicity, cell differentiation, genomic stability of expanded cells, and biocompatibility can benefit from these scientific and technological advancements. Finally, these technologies should be compatible with Good Manufacturing Practice (GMP) conditions for eventual translation to clinical application. Accordingly, this Research Topic contains a number of contributions related to these aspects of stem cell bioengineering, including original research articles, short reviews, and reviews that cover a variety of model systems, including embryonic and induced pluripotent stem cells (iPSCs), hematopoietic stem/progenitor cells (HSPCs), mesenchymal stem cells (MSCs), and neural stem cells (NSCs).

Recent progress in the bioengineering field has allowed the manipulation of singular aspects of the cellular microenvironment. This Research Topic focused on outstanding examples of bioengineering approaches used to promote the self-organization of human cells and the production of tissue-like structure formation. Also crucial to this endeavor is the understanding of the biological system in hand, and special attention was also given to methodologies that advance our understanding of the mechanisms that control stem cell activity. Moreover, such advancements should eventually be translated to the clinic to maximize their impact. Clinical translation will require scalable processes for the maintenance and expansion of transplantable human cells, particularly novel 3D organoid systems and devices for the production of functional tissue-like substitutes.

As mentioned above, 3D cell culture has been widely used to recreate the cellular microenvironment *in vitro* and control important cell signaling cues. Consequently, this Research Topic focused on diverse aspects of 3D cell culture. Gopal et al. explored the possible combination of CRISPR Cas9 and 3D cell culture methods to enhance our understanding of the molecular

OPEN ACCESS

Edited and reviewed by:
Hasan Uludag,
University of Alberta, Canada

***Correspondence:**
Tiago G. Fernandes
tfernandes@tecnico.ulisboa.pt

[†] These authors have contributed equally to this work

Specialty section:
This article was submitted to Biomaterials, a section of the journal Frontiers in Bioengineering and Biotechnology

Received: *09 April 2021*
Accepted: *16 April 2021*
Published: *07 May 2021*

Citation:
Lei Y, Willerth SM and Fernandes TG (2021) Editorial: Stem Cell Systems Bioengineering. Front. Bioeng. Biotechnol. 9:693107. doi: 10.3389/fbioe.2021.693107

mechanisms underpinning several disease phenotypes. This review outlines the possibility of bridging CRISPR Cas9 genome editing with 3D spheroid and organoid cell culture to better understand disease progression and address potential gaps to enable widespread use of these systems. Developmental biology and reproductive medicine would benefit significantly from these advancements. Artificial gametes and embryos represent a new tool for understanding human development. Zhang et al. reviewed the most recent efforts to achieve the reconstitution of the entire cycle of gametogenesis and embryo development *in vitro*. These efforts require the development of 3D culture systems capable of promoting self-organization and production of functional tissue. Silva et al. introduced a novel differentiation strategy that uses a defined medium to generate cerebellar tissue from human iPSCs. In particular, Purkinje cells, granule cells, interneurons, and deep cerebellar nuclei projection neurons were differentiated from human iPSCs and self-formed into electrically active neuronal networks *in vitro* without the need for co-culturing with rodent cells.

The examples mentioned above highlight the wide range of stimuli that can be used to guide tissue self-formation *in vitro*. NSCs are particularly responsive to biomaterial scaffolds providing appropriate mechanical and physicochemical cues that contribute to cell organization (e.g., cell alignment). Amores de Sousa et al. reported the impact of combining nanofiber alignment with functionalization of electrospun poly-ε-caprolactone nanofibers with biological adhesion motifs on the culture of NSCs. Aligned nanofibers directed NSC distribution and, in the presence of laminin and RGD-containing peptides, promoted higher cell elongation, a higher percentage of differentiated neurons, as well as significantly longer neurite development. Fang et al. also demonstrated the impact of 3D culture using graphene foams to support NSC growth and maintenance of an active proliferative state, which resulted from a reconfiguration of cell metabolism. Interestingly, recent evidence also shows that electrical stimulation improves neuronal differentiation of NSCs. Sordini et al. validated this by using electroconductive biocompatible materials for NSC culture and differentiation. Furthermore, electrical stimulation may also prove effective in promoting the differentiation of other stem cell types, like MSCs. Dawson et al. presented a theoretical framework to evaluate the influence of the applied electric field on osteogenic differentiation of MSCs. Their results showed that the differentiation rate depended on the applied electrical field, confirming other experimental findings reported in the literature.

Abecasis et al. explored another approach, based on alginate microencapsulation and suspension culture, to develop 3D human cardiac microtissues. Cell encapsulation allowed the co-culture of cardiac derivatives, including aggregates composed of cardiomyocytes, endothelial cells, and mesenchymal cells. Detailed characterization of the 3D cardiac microtissues revealed that crosstalk between different cell types and the extracellular matrix induced the maturation of iPSC–derived cardiomyocytes. Similarly, the study of the liver microenvironment has demonstrated the important roles of biochemical and biomechanical signals in regulating the progenitor cell functions that underlie liver morphogenesis and regeneration. Gentile et al. proposed an *in vitro* 3D liver spheroid model with integrated polyethylene glycol hydrogel microparticles for the local delivery of microenvironmental cues. This study demonstrated that treatment with the growth factor TGFβ1 directs differentiation of the spheroidal liver progenitor cells toward a biliary phenotype. These findings have direct implications in tissue engineering, drug testing, and our understanding of cellular metabolism. This work has critical implications in the context of the pancreas, which is of paramount importance for proper insulin secretion and maintenance of normal glycemia. In fact, it is now well-established that malfunction or destruction of β cells in the human pancreas causes diabetes. Velazco-Cruz et al. focused on this issue and reviewed recent advances in the engineering of β cells to understand and improve pancreatic cell differentiation and functional maturation. The authors summarized new differentiation strategies capable of producing advanced cellular systems with the ability to respond to glucose levels, secrete insulin, and rapidly achieve normal glycemia when transplanted into diabetic mouse models.

Scalable processes for the production of transplantable human cells and functional tissue-like substitutes are of special interest since they can significantly accelerate the translation of these products to the clinic, as these applications require significant numbers of cells. Human MSCs are a promising candidate for cell therapies given their tropism to the site of injury and secretion of trophic factors that facilitate tissue healing and/or modulate the immune response. Tsai et al. proficiently summarized the fundamental principles and concepts guiding future design of biomanufacturing systems for MSC-based therapy. Furthermore, Elanzew et al. also proposed the StemCellFactory, a modular platform that automates cell reprogramming and enables parallel derivation and expansion of human iPSC lines. This setting employs state-of-the-art cell culture techniques for optimal automated reprogramming of fibroblasts, clonal isolation, and parallel expansion of the emerging iPSCs colonies in multi-well-plates over ten passages to generate stocks of human iPSC lines.

Finally, the use of artificial intelligence and modeling to better understand differentiation and improve the production of a specific cell type was also covered in this Special Research Topic. Williams et al. examined the ability of data-driven modeling using machine learning for identifying critical experimental conditions and predicting cardiomyocyte content. The authors used data collected during human iPSC-cardiac differentiation in advanced stirred tank bioreactors to build their predictive models. Similarly, Branco et al. used a methodology based on experimental design and factorial modeling to optimize the cytokine cocktail, maximizing HSPC expansion *in vitro*. This tailored approach successfully led to an increase in HSPC productivity while enhancing our knowledge on the impact of cytokine supplementation on the HSPC yield.

In conclusion, we are proud to present our Research Topic "Stem Cell Systems Bioengineering" in Frontiers in Bioengineering and Biotechnology. We believe that all readers should experience the essence and possibilities surrounding engineering cell systems as covered in our topic. We are also optimistic that this Research Topic provides outstanding

insights into the important issues of stem cell research and regenerative medicine.

AUTHOR CONTRIBUTIONS

All authors listed have made a substantial, direct and intellectual contribution to the work, and approved it for publication.

Conflict of Interest: SW has a commercialization agreement with Aspect Biosystems with regards to bioprinting stem cell derived tissues. YL is a co-founder of CellGro Technologies, LLC, a company focusing on cell expansion technologies. The remaining author declares that the research was conducted in the absence of any commercial or financial relationships that could be construed as a potential conflict of interest.

frontiers in Bioengineering and Biotechnology

ORIGINAL RESEARCH
published: 08 January 2020
doi: 10.3389/fbioe.2019.00436

Three-Dimensional Graphene Enhances Neural Stem Cell Proliferation Through Metabolic Regulation

Qiaojun Fang[1], Yuhua Zhang[1†], Xiangbo Chen[2,3†], He Li[4†], Liya Cheng[5], Wenjuan Zhu[6], Zhong Zhang[1], Mingliang Tang[1], Wei Liu[7], Hui Wang[8], Tian Wang[4*], Tie Shen[9*] and Renjie Chai[1,10,11,12*]*

[1] MOE Key Laboratory for Developmental Genes and Human Disease, Jiangsu Province High-Tech Key Laboratory for Bio-Medical Research, Institute of Life Sciences, Southeast University, Nanjing, China, [2] Key Laboratory of Molecular Epigenetics of the Ministry of Education, Northeast Normal University, Changchun, China, [3] Hangzhou Rongze Biotechnology Co., Ltd. Hangzhou, China, [4] Department of Otolaryngology-Head and Neck Surgery, First Affiliated Hospital of Wenzhou Medical University, Wenzhou, China, [5] Institute of Life Sciences, Anhui Agricultural University, Hefei, China, [6] Zhangjiagang City First People's Hospital, The Affiliated Zhangjiagang Hospital of Suzhou University, Zhangjiagang, China, [7] Department of Otolaryngology-Head and Neck Surgery, The Second Xiangya Hospital, Central South University, Changsha, China, [8] Department of Otolaryngology Head and Neck Surgery, Shanghai Jiao Tong University Affiliated Sixth People's Hospital, Shanghai, China, [9] Key Laboratory of Information and Computing Science Guizhou Province, Guizhou Normal University, Guiyang, China, [10] Co-Innovation Center of Neuroregeneration, Nantong University, Nantong, China, [11] Institute for Stem Cell and Regeneration, Chinese Academy of Science, Beijing, China, [12] Beijing Key Laboratory of Neural Regeneration and Repair, Capital Medical University, Beijing, China

Edited by:
Stephanie Michelle Willerth, University of Victoria, Canada

Reviewed by:
Carlos Vicario-Abejón, Spanish National Research Council (CSIC), Spain
Banani Kundu, University of Minho, Portugal

***Correspondence:**
Renjie Chai
renjiec@seu.edu.cn
Tie Shen
shentie@mail.ustc.edu.cn
Tian Wang
wangtian1222@gmail.com
Hui Wang
wangh2005@alumni.sjtu.edu.cn

[†] These authors share first authorship

Specialty section:
This article was submitted to Biomaterials, a section of the journal Frontiers in Bioengineering and Biotechnology

Received: 08 October 2019
Accepted: 06 December 2019
Published: 08 January 2020

Citation:
Fang Q, Zhang Y, Chen X, Li H, Cheng L, Zhu W, Zhang Z, Tang M, Liu W, Wang H, Wang T, Shen T and Chai R (2020) Three-Dimensional Graphene Enhances Neural Stem Cell Proliferation Through Metabolic Regulation. Front. Bioeng. Biotechnol. 7:436. doi: 10.3389/fbioe.2019.00436

Graphene consists of two-dimensional sp2-bonded carbon sheets, a single or a few layers thick, which has attracted considerable interest in recent years due to its good conductivity and biocompatibility. Three-dimensional graphene foam (3DG) has been demonstrated to be a robust scaffold for culturing neural stem cells (NSCs) *in vitro* that not only supports NSCs growth, but also maintains cells in a more active proliferative state than 2D graphene films and ordinary glass. In addition, 3DG can enhance NSCs differentiation into astrocytes and especially neurons. However, the underlying mechanisms behind 3DG's effects are still poorly understood. Metabolism is the fundamental characteristic of life and provides substances for building and powering the cell. Metabolic activity is tightly tied with the proliferation, differentiation, and self-renewal of stem cells. This study focused on the metabolic reconfiguration of stem cells induced by culturing on 3DG. This study established the correlation between metabolic reconfiguration metabolomics with NSCs cell proliferation rate on different scaffold. Several metabolic processes have been uncovered in association with the proliferation change of NSCs. Especially, culturing on 3DG triggered pathways that increased amino acid incorporation and enhanced glucose metabolism. These data suggested a potential association between graphene and pathways involved in Parkinson's disease. Our work provides a very useful starting point for further studies of NSC fate determination on 3DG.

Keywords: three dimensional graphene, neural stem cell (NSC), metabolic pathway, proliferation, metabolites

INTRODUCTION

Neural stem cells (NSCs) have received much attention in recent years as a therapeutic candidate for many neurodegenerative diseases such as Parkinson's disease (PD) and Alzheimer's disease (AD) (Soldner et al., 2009; Swistowski et al., 2010; Kang et al., 2016), and much research has focused on uncovering the detailed mechanisms behind NSCs fate determination. NSCs have two main properties, first, they have unlimited self-renewal capacity throughout the lifespan of the organism (Akesson et al., 2008; Campbell et al., 2014), and secondly they are multipotent and can differentiate into all types of cells within the neuro-ectodermal lineages of central nervous system, for example, glia cells and a variety of neurons (Chiasson et al., 1999). NSC fate is affected by extracellular and intracellular factors, especially the particular microenvironment in which the NSC is located as well as metabolic state of the cell (Kim et al., 2014). Several studies have reported that metabolic pathways are regulators of NSC proliferation and differentiation fate decisions, but the detailed mechanisms behind this regulation are still not fully understood.

Graphene has been studied as an useful nanomaterial in biomedical applications, stem cell research, cell imaging, drug delivery, and photo-thermal therapy due to it's excellent conductivity, stability, and biocompatibility (Geim, 2009; Kim et al., 2010; Zhu et al., 2010). The monolayer of carbon atoms in graphene can be arranged in two-dimensional lattices, fibers, and three-dimensional graphene (3DG) foams (Guo et al., 2016; Ma et al., 2016). Some publications have reported that graphene can enhance the neuronal differentiation of NSCs, and 3DG has been shown to provide suitable microenvironments for NSC growth and influence NSC behaviors (Li et al., 2013). Taken together, 3DG might have therapeutic potential for treating neurodegenerative diseases and neuronal disorders (Yang et al., 2016).

The proliferation of NSCs was promoted when cultured on 3DG (Li et al., 2013). NSC metabolism plays an important role in cell fate decisions, especially proliferation. Numerous studies have reported that the cross-talk between metabolic pathways and signaling pathways impacts the fate decision of NSCs (Kim et al., 2014). For example, the glycolysis pathway is regulated by FoxO3 to promote adult stem cell proliferation and differentiation (Yeo et al., 2013). The pentose phosphate pathway is regulated by FoxO3 and p53, which are necessary for proliferation, growth, the maintenance of the reduced glutathione level and the suppression of cellular oxidative stress by generating NADPH (Bensaad et al., 2006, 2009; Zhao et al., 2009). In addition, glutamine metabolism is affected by FoxO3, TSC/mTOR, HIF-1, and Sirtuin (Nicklin et al., 2009; Hensley et al., 2013; Son et al., 2013), and single-carbon metabolism and lipid metabolism are regulated by mTOR, HIF-1 and MYC during proliferation and neurogenesis (Metallo et al., 2011; Knobloch et al., 2013; Sun and Denko, 2014). ABC transporters and aminoacyl-tRNA synthesis are also involved in the metabolic activities of NSCs (Ibba and Soll, 2004; Lin et al., 2006). In turn, glutamine metabolism provides carbon for lipids and glutathione biosynthesis and nitrogen for nucleotide biosynthesis and thus regulates oxidative stress and promotes tumor proliferation (Wise and Thompson, 2010; Le et al., 2012). Proliferation of skeletal stem cells can be regulated through glutamine metabolism (Yu et al., 2019), and the proliferation of intestinal stem cells can be regulated by mitochondrial pyruvate metabolism (Schell et al., 2017).

Despite these previous studies, the underlying mechanism of how graphene systems influence the metabolism of NSCs is still poorly understood and requires more careful study, especially for 3DG. Understanding the interplay between metabolism, related metabolites, and enzymes has proven to be a critical task. In this study, the influence of 3DG on NSC proliferation and cell fate decision has beenexplored using gas chromatography-mass spectrometry (GC-MS)-based metabolomics techniques.

RESULTS

Synthesis and Characterization of 3DG

The 3DG used in this study was synthesized as previously reported (Li et al., 2013). A typical Raman spectrum of 3DG was shown in **Figure 1A**, and the absence of a D band indicated that the 3DG was of high quality with few defects, while the intensity ratio between 2D and G bands and the shape of 2D band showed that the 3DG was made of only a few layers of graphene sheets (Ferrari et al., 2006). The I-V curve for 3DG is shown in **Figure 1B** and indicated excellent electrical conductivity (**Figure 1B**). The morphology of the 3DG was observed via scanning electron microscopy and showed a continuous and interconnected network with pores which can provide a three-dimensional scaffold to support NSCs attachment and growth, even it looked like a thin membrane. The porosity of 2DG and 3DG were determined to be 99.5 ± 0.2% and pore size of 3DG approximately 100–300 μm (**Figure 1C**).

NSC Proliferation on 3DG

In order to purify and confirm NSCs, immunostaining with Nestin and Ki67 antibodies were performed (**Figure 2A**), neurospheres were collected and digested into single cells, after four generations, NSCs were seeded and cultured on tissue culture polystyrene (TCPS), 2D graphene film (2DG), and 3DG which coated with laminin. As a widely used biomolecule for NSC culture, laminin can produce a NSC-favorable surface to enhance cell adhesion. The proliferation ability of the NSCs on the different scaffolds was measured by immunostaining with Ki67, a cellular marker of proliferation (Sun and Kaufman, 2018) (**Figures 2B,C**). The number of cells and Ki67 positive cells were smaller in TCPS than 2DG[$F_{(2,14)} = 35.06$, $p < 0.001$], this might because graphene enhances neural stem cell proliferation ability. 3DG surface provided sufficient area for the attachment and growth of NSCs, and most NSCs on the surface of 3DG were Ki67 positive [$F_{(2,14)} = 35.06$, $p < 0.05$], which was consistency with previous reports (Kenry et al., 2016; Liu et al., 2016).

Overall Metabolic Profiles of the NSCs

Using the GC-MS metabolomics approach, we found obvious differences between mouse NSCs grown on TCPS, 2DG, and 3DG for 5 days. We identified a total of 263 metabolites, including carboxylic acids, organic acids and

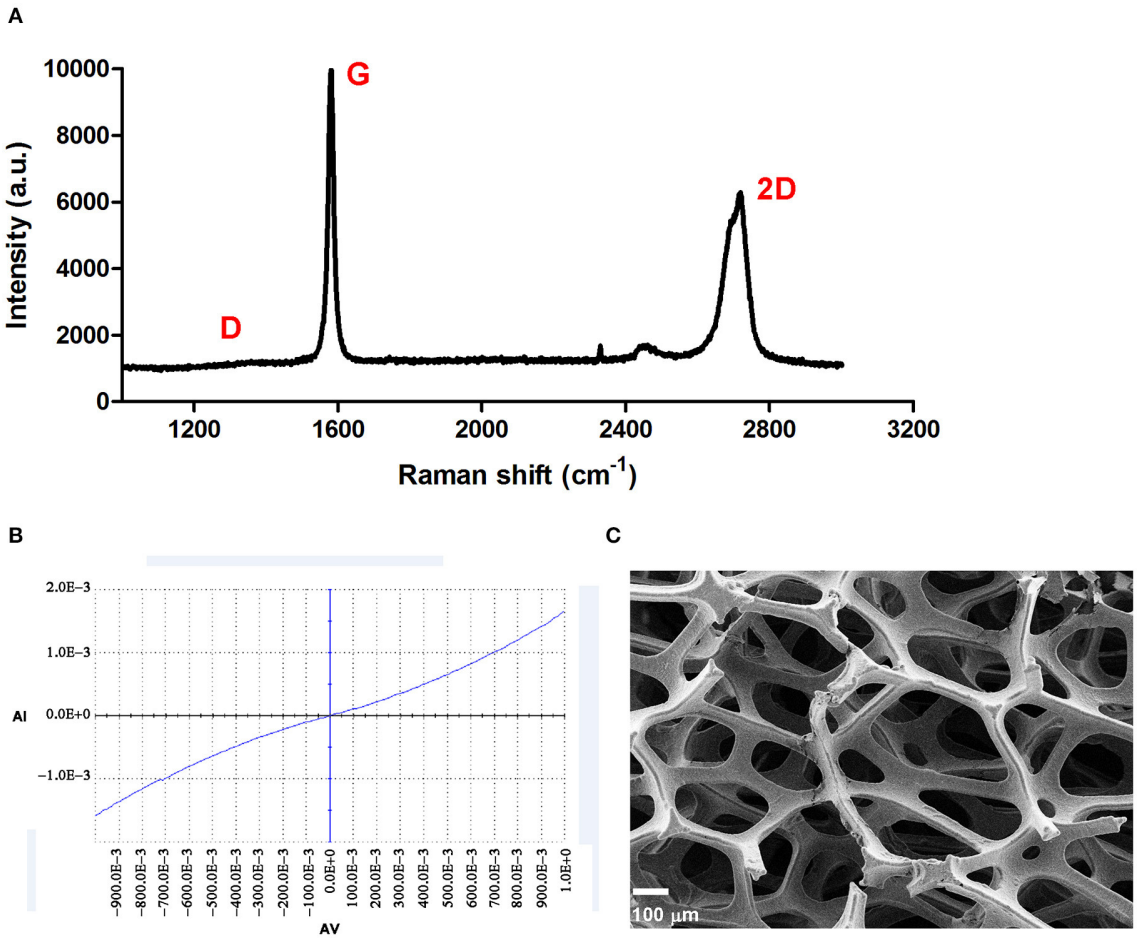

FIGURE 1 | Characterization of 3DG. **(A)** Typical Raman spectrum of 3DG. **(B)** Current curve of 3DG. **(C)** SEM micrograph of 3DG. Scale bar = 100 μm.

their derivatives, amino acids and their derivatives, lipids, cofactors, prosthetic groups, and electron carriers as well as nucleotides and secondary metabolites (**Supplementary Figure 1** and **Data Sheet 1**). These metabolites cover most of central metabolism and reflect the physiological status of NSCs.

An unsupervised principal component analysis (PCA) was used to observe the overall distribution of the samples and the stability of the overall analysis process. The PCA score plots showed classification trends between the 3DG, 2DG, and TCPS groups, with all of the observations falling within the Hoteling T^2 (0.95) ellipse (2DG-TCPS: $R^2X = 0.43$; $Q^2Y = 0.0498$; 3DG-TCPS: $R^2X = 0.507$; $Q^2Y = 0.176$; 3DG-2DG: $R^2X = 0.549$; $Q^2Y = 0.265$). Subsequently, a supervised partial least-squares discriminant analysis (PLS-DA) model was used to identify the differences among NSCs culturing under the three conditions (2DG-TCPS: $R^2X = 0.5$; $R^2Y = 0.991$; $Q^2 = 0.857$; $N = 12$), (3DG-TCPS: $R^2X = 0.498$; $R^2Y = 0.996$; $Q^2 = 0.966$; $N = 12$), and (3DG-2DG: $R^2X = 0.339$; $R^2Y = 0.936$; $Q^2 = 0.969$; $N = 12$). The PLS-DA model was also validated and passed the permutation test, which showed no observable over-fitting. In addition, we conducted an orthogonal partial least-squares discriminant analysis (OPLS-DA) on these data (**Figure 3** and **Supplementary Figure 2**).

These results demonstrate that different growth conditions indeed induce significant reconfigurations among a large number of metabolic pathways. These changes in turn reflect differences in the NSCs' growth parameters, and thus it would be useful to understand the metabolic mechanism behind this phenotype variation. This is especially the case for the 3DG-2DG comparison, which has a larger difference compared to the 2DG-TCPS comparison, because this might indicate the importance of spatial contacts between cells, which are closer to the *in vivo* state in 3DG compared to 2DG.

Distinctive Metabolomes of NSCs Cultured on 3DG, 2DG, and TCPS

NSCs produce different sets of metabolites when they are cultured on different materials. The levels of metabolites were considered significantly different if the variable influence on

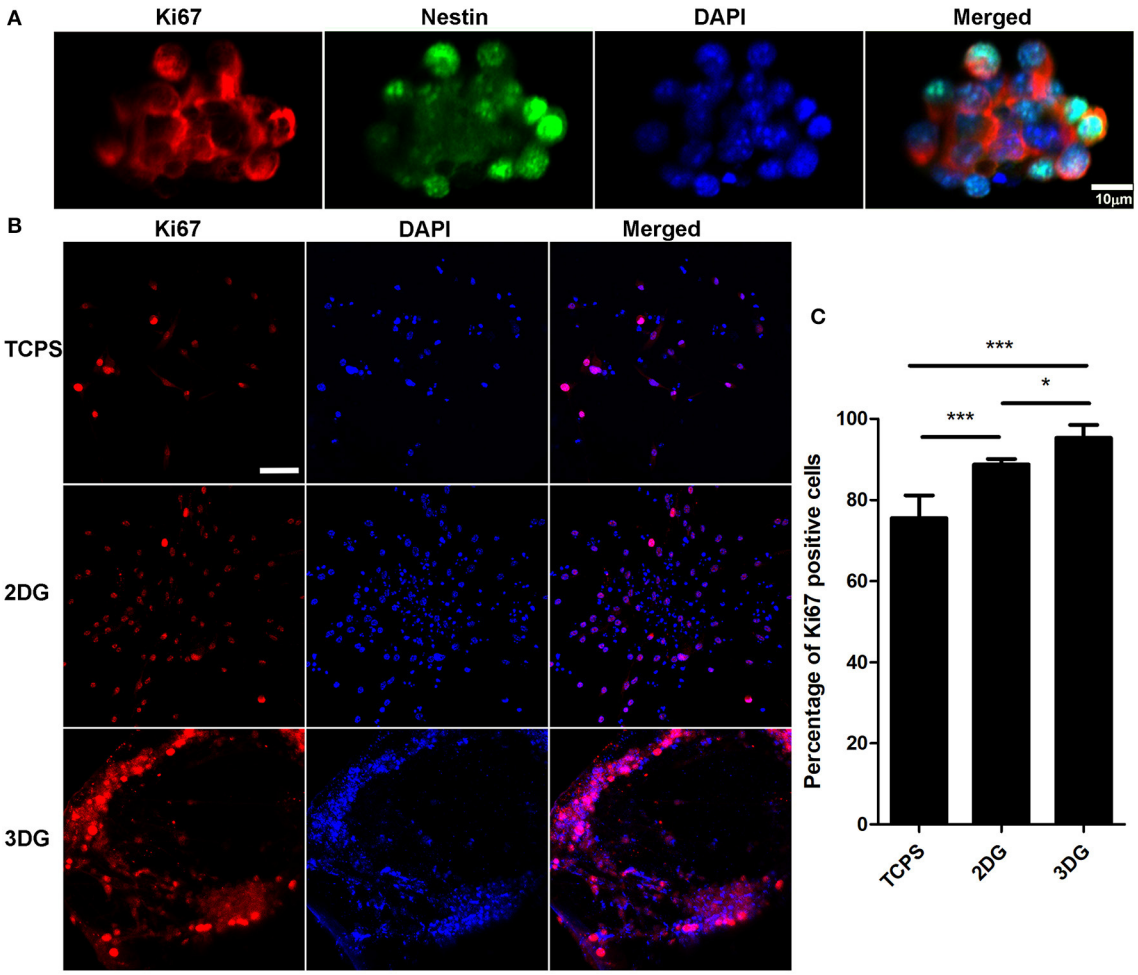

FIGURE 2 | Proliferation of NSC. **(A)** Immunostaining image of NSC spheres, scale bar = 10 μm. **(B)** Proliferation detected after 5 days culture using Ki-67 immunolabeling, nuclei were labeled using DAPI. Scale bar = 50 μm. **(C)** Quantification data of **(B)** shows percentage of Ki-67 positive cells among three groups. $n = 5$, data were shown as mean ± SD, $^{*}p < 0.05$, $^{***}p < 0.001$.

projection (VIP) value of the first principal component of the OPLS-DA was >1 and the *p*-value of the *t*-test was < 0.05. The relative abundance of 36 metabolites exhibited statistically significant differences between NSCs grown on 2DG and TCPS, with 8 metabolites higher in 2DG and 26 higher in TCPS. There were 93 differentially abundant metabolites between NSCs grown on 3DG and 2DG, with 37 metabolites being higher and 42 metabolites being lower in 3DG (**Data Sheet 1**). Among them, the most significantly up-regulated metabolites annotated in **Table 1** were from the glucose degradation pathway (glucose-6-phosphate, gluconic acid, and D-glyceric acid) or essential amino acids (isoleucine, valine, phenylalanine, tyrosine, and lysine). All of these are needed for rapid cell growth and cell proliferation.

Different metabolites were compared among the three groups in volcano plots (**Supplementary Figure 3**), and the results indicated higher metabolic activities in NSCs grown on 3DG compared to those grown on 2DG and TCPS.

Correlation Analysis Among Metabolites

The matrix of correlation values provided more detailed information and a better overview of the relationships among related metabolites (**Figure 4** and **Data Sheet 2**). A high positive correlation co-efficient means the enzymes producing the two metabolites likely function in the same pathway or have shared regulators in common. For instance, most of the highly correlated metabolites were between amino acids or between amino acids and carbohydrates, such as between tyrosine and valine or between serine and α-glucose-β-glucoside. Similarly, some lipids have very high correlations such as arachidonic acid and linoleic acid. High positive correlations between glucose and glucose-1-phosphate, glucose-1-phosphate and glucose-6-phosphate, asparagine and aspartic acid, and glutamic acid and glutamine are due to having the same substrates, enzymes, and pathways in their biosynthesis. A high negative correlation coefficient might reflect a competitive pathway or a pathway responsible for a different function.

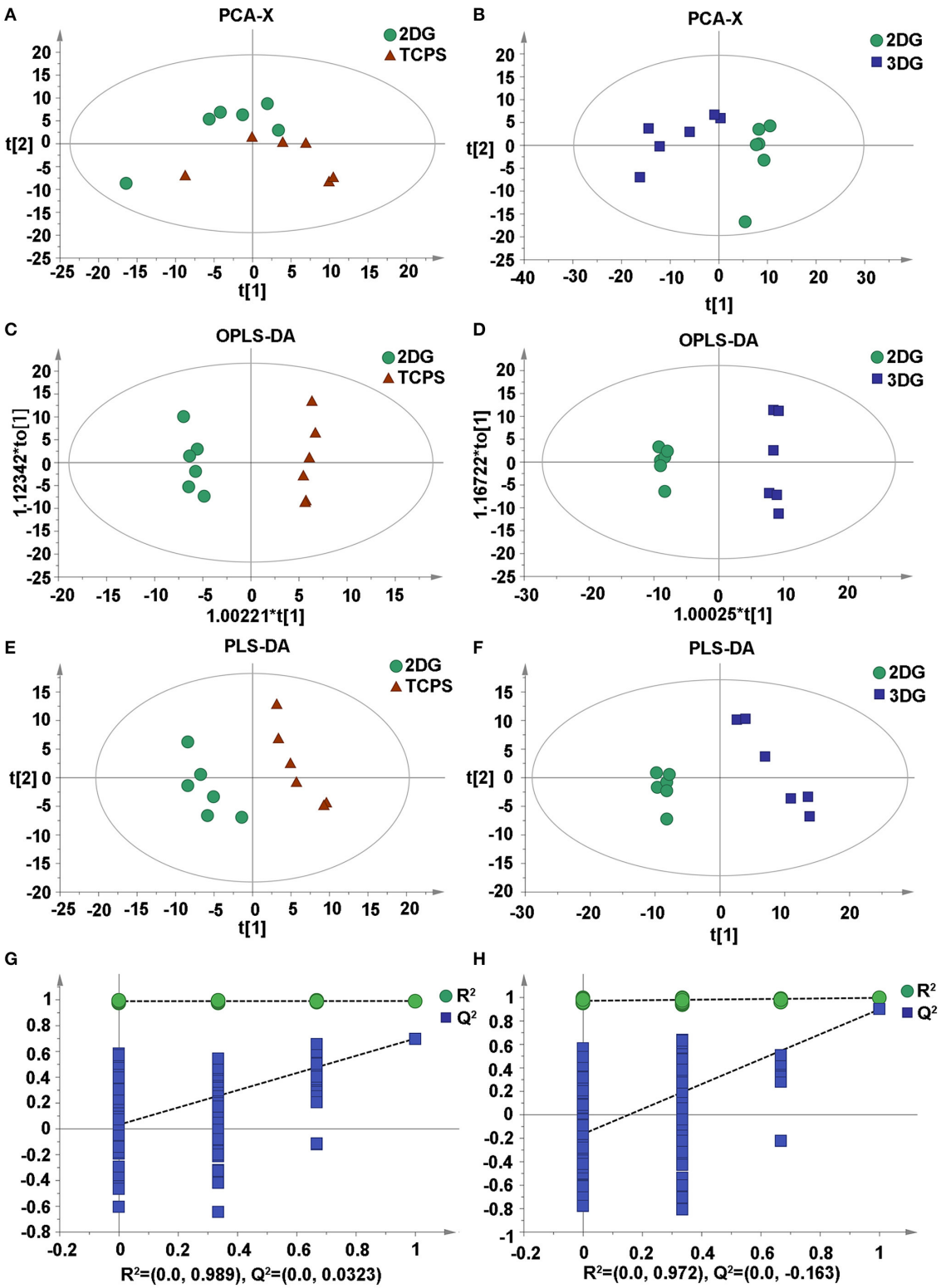

FIGURE 3 | Multivariate statistical score graph among three groups. **(A)** PCA score plot of 2DG and TCPS. **(B)** PCA score plot of 3DG and 2DG. **(C)** OPLS-DA score plot of 2DG and TCPS. **(D)** OPLS-DA score plot of 3DG and 2DG. **(E)** PLS-DA score plot of 2DG and TCPS. **(F)** PLS-DA score plot of 3DG and 2DG. **(G)** Statistical validation with permutation analysis (200 times) of the corresponding PLS-DA model of 2DG and TCPS, R^2 is the explained variance, and Q^2 is the predictive ability of the model. **(H)** Statistical validation with permutation analysis (200 times) of the corresponding PLS-DA model of 3DG and 2DG, R^2 is the explained variance, and Q^2 is the predictive ability of the model.

TABLE 1 | The top 30 metabolites contributing significantly to discriminating cells grown on 2DG from those grown on TCPS and discriminating cells grown on 3DG from those grown on 2DG.

Metabolites	*p*-value	FC(2DG/TCPS)	Metabolites	*p*-value	FC(3DG/2DG)
Aconitic acid	1.07324E-06	***	Noradrenaline	2.57505E-09	***
Methyl-beta-D-galactopyranoside	4.56232E-05	0.317870954	Methyl phosphate	8.61821E-09	***
Gly-pro	0.000373616	3.45951521	Isoleucine	8.14022E-08	3.518754687
Phosphate	0.000813695	3.446777793	Valine	1.38383E-07	2.227047157
Adenosine 5-monophosphate	0.002511806	0.311194121	Serine	3.24336E-07	2.896413697
Beta-glycerophosphoric acid	0.004631138	0.663134866	Maleamate	3.73766E-07	2.062659789
Zymosterol	0.005497805	0.645471315	Glycerol	1.10385E-06	0.185467901
Threonine	0.005498206	0.788136334	D-glyceric acid	1.35641E-06	6.838118979
Glutamic acid	0.006031692	0.875420839	Glucose	1.94841E-06	0
5-Hydroxyindole-3-acetic acid	0.006584791	0.390133763	Hippuric acid	2.56832E-06	0
D-(glycerol 1-phosphate)	0.007013536	0.639306064	Tagatose	2.62655E-06	0.366839581
Asparagine	0.007221201	0.863352541	Phenylalanine	1.33697E-05	2.262626572
Glutamine	0.008681747	0.829487685	Fumaric acid	1.58222E-05	0.355499536
p-Anisic acid	0.010866232	2.610415225	Methionine	3.25786E-05	2.536990702
Hypoxanthine	0.012409871	0.786350146	Zymosterol	3.79166E-05	0.04548959
Lysine	0.01344286	0.830148494	Myo-inositol	4.79027E-05	0.097851995
Pyridoxine	0.015190631	0.850717833	D-(glycerol 1-phosphate)	5.27231E-05	0.123170735
4-Hydroxybenzyl cyanide	0.01574558	0.408363696	Melatonin	6.63317E-05	***
Methyl phosphate	0.016445895	0	Tyrosine	8.27556E-05	2.30350299
Arachidonic acid	0.016462751	0.494956435	Pyridoxine	0.000101939	1.901166986
Saccharopine	0.016550748	1.527539438	L-cysteine	0.000114856	0.123003722
Tartronic acid	0.017334697	0.4177656	Allose	0.000143555	2.421915203
Tyrosine	0.017829593	0.854202113	Tryptophan	0.000153858	3.055253667
3-Aminopropionitrile	0.01918978	12.84284424	Cholesterol	0.000160539	0.169891796
Phenylalanine	0.022176113	0.889029039	Lysine	0.000223344	3.370009385
Tryptophan	0.025824103	0.76103943	Gluconic acid	0.000239199	2.90495105
O-phosphonothreonine	0.026995702	0.327946302	O-methylthreonine	0.000344787	1.879317736
D-fructose 1,6-bisphosphate	0.029010308	0.687092159	Glucose-6-phosphate	0.000523658	2.397178129
Histidine	0.030446806	0.234203095	3-Cyanoalanine	0.000749964	1.444802925
Valine	0.032441598	0.914732445	O-phosphorylethanolamine	0.000770173	0.241073435

****Indicates that the metabolite was only found in cells grown on 2DG or 3DG.*

Differential Metabolite-Related Enzyme Changes

The metabolite concentration can be considered as a reflection of the integration of the *in vivo* enzyme activity along the growth time. A high abundance metabolite is probably associated with a high activity of the enzymes producing it as well as a low activity of enzyme consuming it. Therefore, here we define an enzyme activity score, which is obtained by normalizing the value of (substrate concentration—product concentration). The value of the score is associated with the direction and probability of the enzyme activity's response induced by change of micro-environment. The reaction ID is the Kyoto Encyclopedia of Genes and Genomes (KEGG) term. Compared to TCPS, 2DG induced changes in the activities of the following enzymes: α-aminoadipate semialdehyde synthase, dihydropyrimidine dehydrogenase, phenylalanine-4-hydroxylase, tyrosine 3-monooxygenase, thyroid peroxidase, pyrimidine-5′-phosphate oxidase, ornithine carbamoyl transferase, nitric oxide synthase, argininosuccinate synthase, pyridoxine kinase, L-amino acid oxidase, tyrosinase, and dihydropyrimidinase (**Supplementary Table 1**). Relative to 2DG, 3DG changed the activities of the following enzymes: ornithine carbamoyltransferase, indoleamine 2,3-dioxygenase, tryptophan 5-monooxygen enzyme, L-serine/L-threonine ammonia lyase, phosphoserine phosphatase, alanine-glyoxylate aminotransferase/serine-glyoxylate aminotransferase/serine-pyruvate transaminase, betaine-homocysteine S-methyltransferase, phenylalanine-4-hydroxylase, thyroid peroxidase, fatty acid synthase, pyridoxamine 5′-phosphate oxidase, tyrosine 3-monooxygenase, fatty acid synthase, pyridoxine kinase, long chain acyl-CoA synthetase, L-amino acid oxidase, inositol-1-phosphate synthase, glycine hydroxymethyltransferase, L-amino acid oxidase, S-adenosylmethionine synthetase, serine palmitoyltransferase, cystathionine β-synthase, serine racemase, tyrosinase, L-amino acid oxidase, aromatic-L-amino acid/L-tryptophan decarboxylase, mono-oxidation nitrogen synthase, and arginine succinate synthetase (**Supplementary Table 2**). In comparing

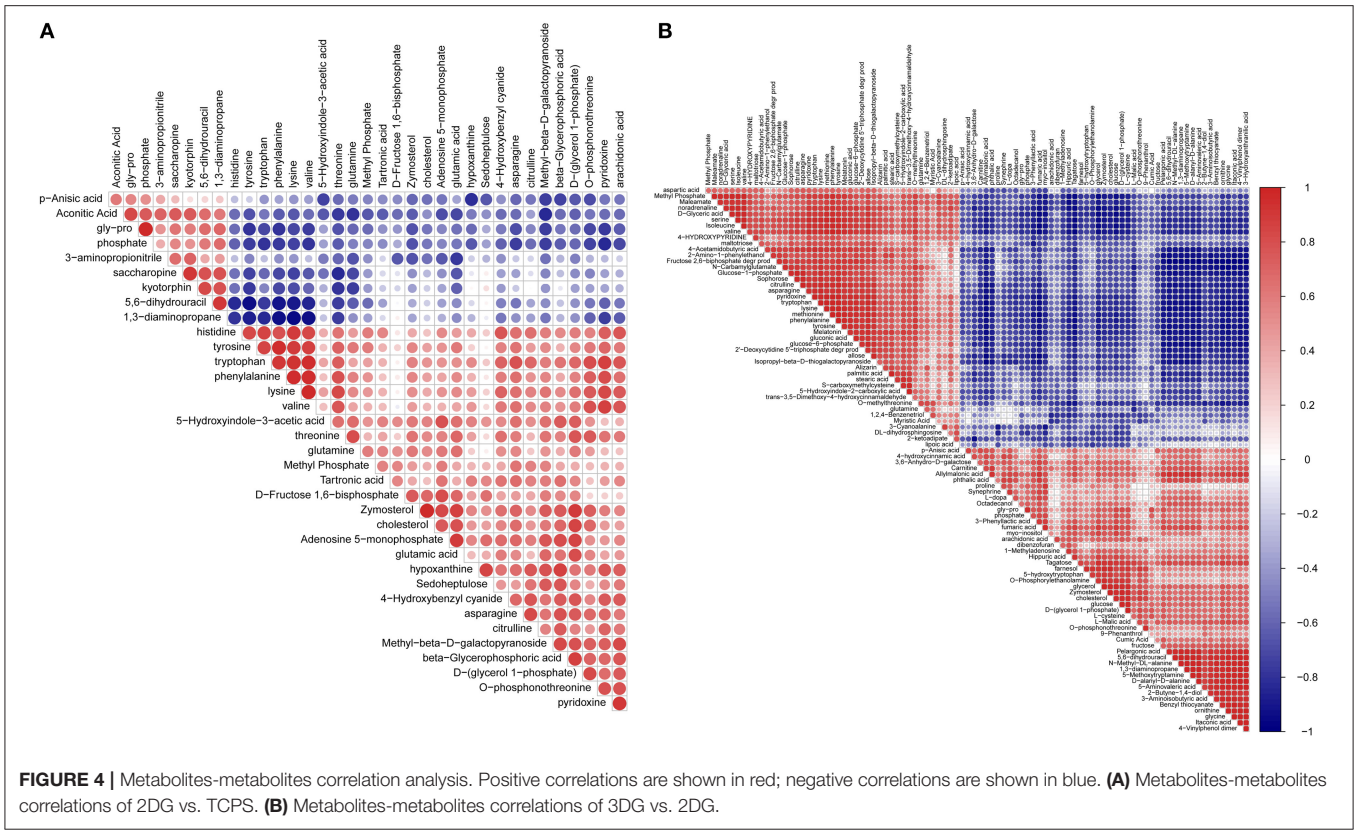

FIGURE 4 | Metabolites-metabolites correlation analysis. Positive correlations are shown in red; negative correlations are shown in blue. **(A)** Metabolites-metabolites correlations of 2DG vs. TCPS. **(B)** Metabolites-metabolites correlations of 3DG vs. 2DG.

the 2DG and TCPS groups, 32 enzymes had scores >0 and 37 enzymes had scores <0. In comparing the 3DG and 2DG groups, 58 enzymes had scores >0 and 56 enzymes had scores lower than 0. This suggested that more enzyme activities were changed in the 3DG group. In addition, when comparing **Supplementary Table 1** with **Supplementary Table 2**, it can be seen that many enzymes had increased activity in NSCs grown on 3DG. These results indicate increased metabolic activity in cells grown on 3DG, which is consistent with increased NSC proliferation when grown on 3DG.

Metabolic Pathway Analysis

By concatenating the differentially regulated enzymes and metabolites, we identified the altered metabolic pathways in cells grown on the different substrates. The identified metabolites were mapped as defined by KEGG. The top 20 KEGG metabolic pathways and the pathway IDs were listed in **Supplementary Table 3**. Between the NSCs grown on 2DG and those grown on TCPS, some significantly altered metabolites belong to Phenylalanine, tyrosine, and tryptophan biosynthesis (mmu00400), central carbon metabolism in cancer (mmu05230), Biosynthesis of amino acids (mmu01230), Parkinson disease (mmu05012), Aldosterone synthesis and secretion (mmu04925), Ovarian steroidogenesis (mmu04913), Basal cell carcinoma (mmu05217), Mineral absorption (mmu04978), Beta-alanine metabolism (mmu00410), Serotonergic synapse (mmu04726), Protein digestion and absorption (mmu04974), Glycine, serine, and threonine metabolism (mmu00260), Steroid biosynthesis (mmu00100), and Aminoacyl-tRNA biosynthesis (mmu00970) (**Figure 5A**).

However, a smaller number of metabolic pathways were altered when comparing NSCs grown on 2DG to those grown on TCPS than when comparing NSCs grown on 3DG to those grown on 2DG. **Figure 5** shows that the rich factor of the 3DG/2DG comparison is much higher than that of the 2DG/TCPS comparison. This is also the case for *p*-value. The shift from 2DG to 3DG induced regulation of a large number of pathways, including Central carbon metabolism in cancer (mmu05230), Mineral absorption (mmu04978), ABC transporters (mmu02010), Protein digestion and absorption (mmu04974), Aminoacyl-tRNA biosynthesis (mmu00970), Glycine, serine, and threonine metabolism (mmu00260), Biosynthesis of amino acids (mmu01230), and Tyrosine metabolism (mmu00350) (**Figure 5B**). The ABC transporter pathway might be responsible for increased levels of essential amino acids seen in NSCs grown on 3DG, and increased activity of the aminoacyl-tRNA biosynthesis pathway is consistent with the elevated protein synthesis needed due to the high growth rate of these cells.

DISCUSSION

As a carbon-based nanomaterial, graphene has excellent physical and chemical properties. Since its discovery in 2004 (Geim and Novoselov, 2007), it has not only been a hot topic in materials

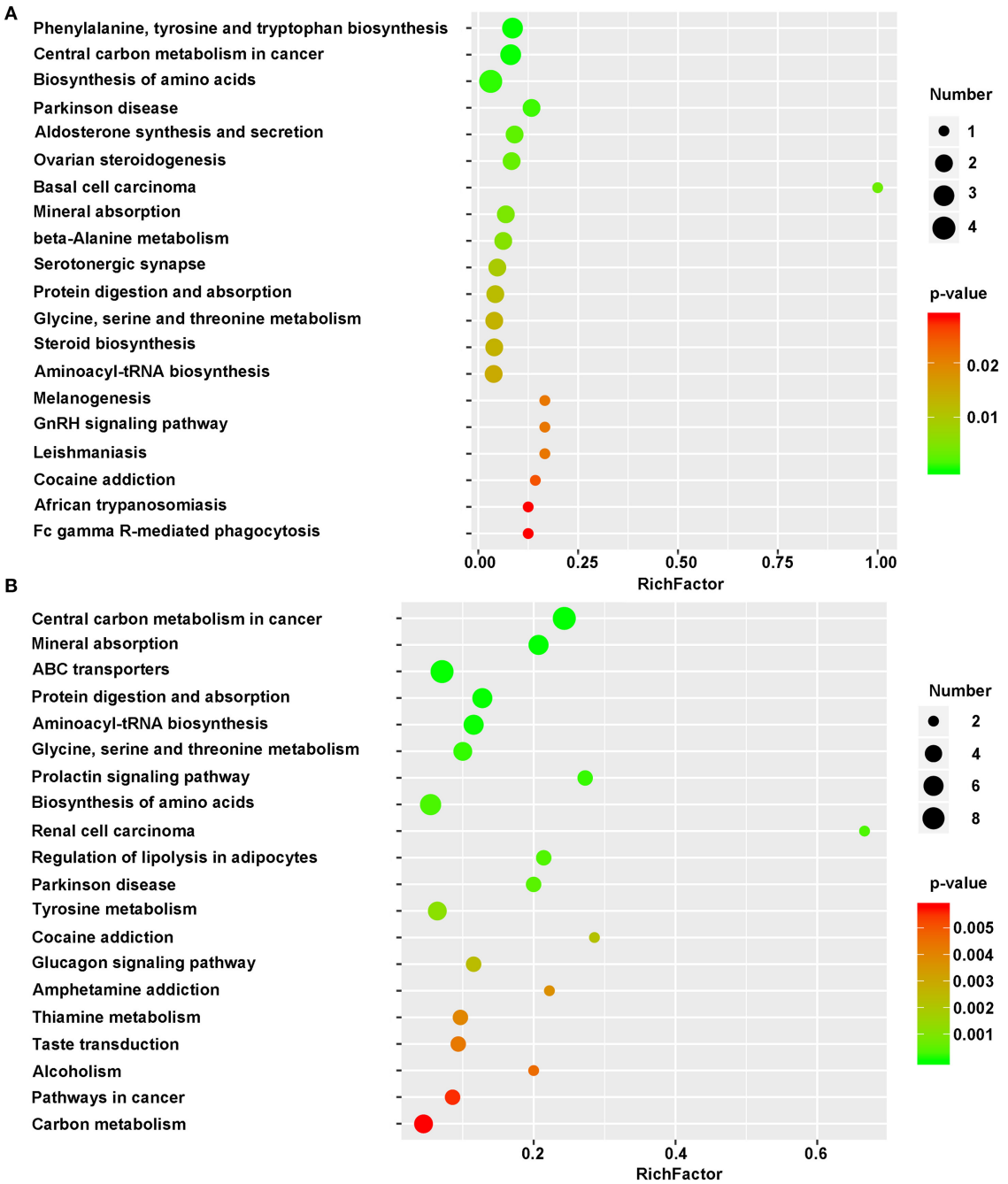

FIGURE 5 | Bubble diagram of differential metabolic pathways. One bubble represent one metabolic pathway. Top 20 pathways were list in left side. Numbers of involved metabolites and the *p*-value were list on right side. **(A)** Bubble diagram of 2DG vs. TCPS. **(B)** Bubble diagram of 3DG vs. 2DG. X-axis represent rich factor. This figure was drawn using R language.

science and condensed matter physics, but has also evoked interest in the biomedical field. For example, graphene has been used for drug transport, stem cell engineering, cell imaging, and tumor therapy (Zhu et al., 2010). Graphene oxide attracted much attention due to the larger surface and oxygen groups, It has been demonstrated that graphene oxide can be used in drug delivery of cancer therapy (Liu et al., 2018). In addition, study has reported that graphene oxide can be used in cell imaging without any additional fluorescent protein (Cheng et al., 2018).

The main function of NSCs is to serve as a cellular reserve to participate in the repair of nervous system damage or to replace dead cells (Forsberg et al., 2017). The hippocampus is the part of the brain involved in bodily sensations, learning, memory, and homeostasis, and hippocampal NSCs have been used for

decades as a typical model of the nervous system (Hattiangady and Shetty, 2012). Hippocampal NSCs hold the potential to treat or cure many neurological diseases and injuries. Particularly neurodegenerative diseases, like AD, PD, spinal cord injuries, and cerebral strokes (Taupin, 2011). Uncovering the underlying mechanism of the proliferation and differentiation of NSCs, especially regulated by metabolomics of the cells.

Metabolomics plays an increasingly prominent role in biomarker identification in various neurodegenerative disorders such as Parkinson's disease, Huntington disease, schizophrenia, and Batten disease (Pears et al., 2010; Oresic et al., 2011; Hatano et al., 2016; Skene et al., 2017). Parkinson's disease is characterized by the gradually develop of resting tremor, bradykinesia, and postural etc. Even the exact mechanism is not known, the abnormal metabolites may be underlined with several proteins expression. For example, the change of amino acids expression has been reported in past decades. Reduction of alanine, arginine, lysine and methionine, increasing of glycine, valine, and aspartate are related with the Parkinson's disease progression (Iwasaki et al., 1992; Jimenez-Jimenez et al., 1996; Mally et al., 1997).

The methodology of this study included a standardized non-targeted GC-MS-based metabolic profiling approach combined with statistical analysis. We found significant differences in the metabolomes between cells grown on TCPS, 2DG, and 3DG, and differential enrichment analysis showed significant changes in metabolic pathways between NSCs grown on 2DG and 3DG, such as the ABC transporter system, mineral uptake, protein digestion and absorption, and aminoacyl-tRNA biosynthesis. Protein digestion and absorption are highly relevant for the biosynthesis of amino acids, and ATP-binding (ABC) transporters form one of the largest known families of proteins that combine ATP hydrolysis with active transport of multiple substrates such as ions, sugars, amino acids lipids, sterols, peptides, proteins, and drugs. Together, protein digestion and absorption, amino acid biosynthesis, and the ABC transporter pathway provide both the non-essential and essential amino acids needed for cell proliferation and differentiation (Besingi and Clark, 2015; Price et al., 2018).

The correlation of metabolomics reconfiguration with cell proliferation is very interesting. For example, zymosterol, which is essential for cholesterol synthesis shown lower expression in TCPS group when compared with 2DG and 3DG groups. The proliferation of cells was inhibited when zymosterol and cholesterol were reduced (Urbina et al., 1997; Wang et al., 2019). T cell proliferation was inhibited by macrophage Tryptophan catabolism, therefore, the reduction of Tryptophan in 2DG when compared with TCPS consistent with our finding. Liver cancer development can be attenuated by inhibiting glycerol synthesis (Capiglioni et al., 2018), The reduction of glycerol also match with graphene enhancing NSCs proliferation. Glucose-6-phosphate promotes the proliferation of fibroblast-like synoviocytes (Zong et al., 2015). It is reasonable since high glucose-6-phosphate is associating with high activity glucose metabolism, which provides more energy during proliferation. The proliferation-related metabolites show more significant change when NSCs are grown on 3DG compared to 2DG or TCPS (**Table 1**).

Minerals are one of the five essential nutrients needed to sustain life (Ali et al., 2014). For example, calcium plays many roles in the body, and it is the main component of bones and is an intracellular messenger of muscle contraction/relaxation, neural networks, the immune system, and secretory cells. In addition to this, iron, copper, and other metal ions are required as cofactors in redox reactions and for the formation of hemoglobin and myoglobin for oxygen binding/transport (Novak Kujundzic et al., 2014). Many enzymes also require specific metal atoms in order to perform their catalytic functions (Copley, 2003).

It is also worth noting that 3DG and 2DG induce the metabolic pathways involved in Parkinson's disease in cultured NSCs. Abnormal amino-acid metabolism include Phenylalanine, tyrosine, tryptophan, Glycine, Serine and Threonine metabolism are involved in Parkinson's disease development, biosynthesis of amino-acid as well (Zhao et al., 2018). In general, the primary metabolic pathways enriched in Parkinson's disease were, tyrosine biosynthesis, glycerol phospholipid metabolism and bile acid biosynthesis. Recent study also shows abnormal cholesterol level in the Parkinson's patients (Luan et al., 2015). As primary energy resources, lipid and glucose metabolism provide most of energy in physiological condition. ABC transporters mediate the export of numerous substances, for example drugs and hydrophobic molecules. The relationship between ANC transporter and Parkinson's disease was based on the function of ABC transporter, the abnormal ABC transporter expression in PD has been reported. In this study, ABC transporter enriched when compared 2DG with 3DG. Further study also need to investigate if ABC transporter can be a candidate therapy.

In addition, many metabolite changes here show relevance to Parkinson' disease (**Table 1**). the reduction of tyrosine which involved in Parkinson's disease was found in 2DG group, when compared to TCPS group. The increasing of L-DOPA also found in 3DG group when compared to 2DG group. In recent years, researchers found that the reduction of tyrosine or the increasing of L-DOPA might be the candidate therapy of Parkinson's disease (Jankovic, 2005; Tanabe et al., 2014). The pathologic activities in Parkinson' disease can be mediated by asparagine endopeptidase (Zhang et al., 2017). The reduction of the glutamate metabolizing enzyme glutamine synthase activity may lead to redundant glutamate in Parkinson's patients (Zipp et al., 1998). arachidonic acid, which upregulated in Parkinson's disease mice, may contribute to the symptoms and pathology (Lee et al., 2010). Phenylalanine hydroxylase as a biomarker of Parkinson's disease also play important role in pathology development, even the detail mechanism is not well-known (Steventon and Mitchell, 2018). High level of serum cholesterol reduce the Parkinson's disease risk (Rozani et al., 2018). The data suggested a potential association between graphene and pathways involved in Parkinson's disease, and more research is required to get a better understanding.

In addition to understanding the function of an enzyme group, the roles of individual enzymes can be discussed in detail. Ornithine transcarbamylase is an aminotransferase and is mainly involved in the urea cycle (Nagasaka et al., 2013). Deficiency in the enzyme results in hypotonia, seizures, mental retardation, and hyperammonemia, which refers to elevated

levels of ammonia in the blood that can cause irreversible brain damage if not treated early. The high expression of ornithine transcarbamylase in NSCs grown on 3DG might be useful in recycling the ammonia produced as a by-product of rapid proliferation. As such, 3DG can become a good drug carrier for those diseases due to its extra capacity to induce this enzyme's expression. Nitric oxide synthase is an oxidoreductase involved in various biological processes such as neurotransmission, amino acid metabolism, environmental signaling pathways, catabolism (Li et al., 2007; Naglah et al., 2016), the endocrine system, and smooth muscle motor control (Adams and Bronner-Fraser, 2009; Hillard, 2015), neuronal damages, neurodegeneration, and NSCs proliferation (Chong et al., 2018). L-amino acid oxidase is involved in the biosynthesis and metabolism of amino acids (Niedermann and Lerch, 1991), and we found that 3DG causes down-regulation of this enzyme in NSCs. Phenylalanine-4-hydroxylase is involved in phenylalanine metabolism and in the phenylalanine, tyrosine, tryptophan, and folate biosynthesis pathways (Lin et al., 2014). Tyrosine 3-monooxygenase is an oxidoreductase that is involved in the metabolism of amino acids, cofactors, and vitamins and in the biosynthesis of other secondary metabolites, as well as the redundant dopamine in the nervous system (Otten et al., 1974). Tyrosinase is involved in amino acid metabolism and in the biosynthesis of other secondary metabolites that affect signaling pathways and cell growth and development (Wu, 2010). Thyroid peroxidase is involved in the regulation of amino acid metabolism and cellular proliferation in thyroid follicular tumors (Garcia et al., 1998). Indole amine 2, 3-dioxygenase is mainly involved in the metabolism of tryptophan which is a factor to inhibit cellular proliferation of T-lymphocyte (Menta et al., 2014). Aromatic-L-amino acid/L-tryptophan decarboxylase is a lytic enzyme that cleaves carbon-carbon groups, participates in the synthesis of amino acids and other secondary metabolites, and plays a role in dopamine synapses in the nervous system and in the processes of cell development and growth (Murali et al., 2003; Kalb et al., 2016). Tryptophan 5-monooxygenase is involved in the metabolism of amino acids, co-factors, and vitamins and plays a role in the physiological activities of serotonin synapses in the nervous system (Fujisawa and Nakata, 1987). Arginine succinate synthetase is a ligase that is involved in amino acid metabolism, signaling pathways, and cell growth processes in cardiovascular diseases (Valeev et al., 2016). Several reactions in vitamin B_6 metabolic pathway were catalyzed by Pyridoxamine 5'-phosphate oxidase and pyridoxine kinase which contribute to neurotransmitter and amino acid metabolism (Pandey et al., 2014; Huang et al., 2016; Ramos et al., 2017; Kim et al., 2018). In this study, the above enzyme scores in the 3DG-2DG comparison were higher than in the 2DG-TCPS comparison which also indicate the 3DG can enhance the proliferation of NSCs.

In summary, our results show that 3DG induces greater NSC proliferation compared to 2DG and TCPS. 3DG can not only mimic the *in vivo* environment very well, but can promote mineral absorption, protein digestion and absorption, biosynthesis of amino acids, and ABC transporter activity. Together, these properties allow for greater amino acid incorporation and enhanced glucose metabolism, which is likely the driving force for faster NSC growth on 3DG. In addition, our data show some correlation between the Parkinson's pathway and graphene, which need further study. Our findings suggest the possibility to regulate NSC cell fate through the regulation of metabolism and that 3DG might provide a powerful platform for investigating NSC proliferation and differentiation.

MATERIALS AND METHODS

Chemicals

All chemicals and solvents were analytical or HPLC grade. Water, methanol, acetonitrile, pyridine, n-hexane, methoxylamine hydrochloride (97%), and N, O-bis (trimethylsilyl) trifluoroacetamide (BSTFA) with 1% trimethylchlorosilane (TMCS) were purchased from CNW Technologies GmbH (Düsseldorf, Germany). Trichloromethane was from Shanghai Chemical Reagent Co., Ltd. (Shanghai, China). L-2-chlorophenylalanine was from Shanghai Hengchuang Bio-technology Co., Ltd. (Shanghai, China).

Characterization of 2DG and 3DG

The crystallinity and the number of the layers present within the graphene were determined using lamRAM (HR800, HORIBA, France). The surface chemistry was examined using XPS (Axis Ultra DLD, Kratos, UK) with an Al K α X-ray source operated at 40 eV.

Graphene Synthesis and NSC Culture

For 2DGs, Cu foils were heated to 950°C, then annealed under H_2 and Ar gases for 5 min, followed by exposure to CH_4 and H_2 for 5 min. Finally, substrates were cooled down to room temperature under H_2 and Ar gases. The 3DGs were synthesized by similar method with Ni foam as template. 2DG and 3DG were firstly soaked in $FeCl_3$ (1 M) solution for 72 h at room temperature. Then 3DG and 2DG were rinsed sequentially with 1 M, 0.1 M, and 0.01 M HCl solutions, followed by rinsing with running water for 72 h to remove the etching agents. Before using, 2DG and 3DG were sterilized with UV light and 70% alcohol and then clean with phosphate-buffered saline three times. NSCs were isolated and purified from the hippocampus of embryonic day 18.5 FVB mice. The hippocampus was dissected out and cells were dissociated with Accutase (Gibco, A11105) for 20 min at 37°C and then washed twice with 1 × PBS and then suspended in proliferation culture medium containing DMEM-F12 with EGF (20 ng/mL, R&D Systems, USA), 2% B27 supplement (Life Technologies, USA), FGF (20 ng/mL, R&D Systems, USA) and 1% penicillin-streptomycin (P/S, Sigma). Tissues were gently triturated using a pipette, and single cells were purified with a 40 μm filter (Corning). Then cells were transferred into sterile cell culture flask, cultured with 2 ml proliferation medium at 37°C with 5%CO_2. After four generations, neuron spheres were collected and then digested into single cells. Before seeding NSCs, the graphene substrates and TCPS was coated with laminin (20 μg/mL, 37°C, 4 h) in six well plate (Greiner Bio-One, 657160). Three times wash was performed using 1x PBS to remove redundant laminin. NSCs were seeded at around 4×10^4 cells/ml, 2 ml proliferation medium in total, then cultured for 5 days. All animal procedures were performed according to protocols approved by the Animal Care and Use Committee

of Southeast University and were consistent with the National Institutes of Health Guide for the Care and Use of Laboratory Animals. All efforts were made to minimize the number of animals used and to prevent their suffering.

Immunostaining for NSCs

After culturing for 5 days, NSCs were fixed with 4% paraformaldehyde for 30 min at room temperature and permeabilized with 0.5% Triton X-100 for 1 h. NSC spheres were stained with Nestin antibody (Beyotime Biotechnology, AN205), proliferation of NSCs was detected using the anti-Ki67 (Abcam, ab15580) antibody, which was incubated with the cells overnight at 4°C. DAPI was used to label NSC nuclei after the sample was washed three times with PBST (1× PBS, pH 7.2, with 0.1% Triton X-100). Secondary antibody (Abcam, ab150075) was incubated for 1 h at room temperature. Finally, the NSCs were mounted on glass slides with Fluoromount-G mounting medium, and images were acquired on a Zeiss LSM 700 confocal microscope.

Sample Preparation for GC-MS Metabolomics Analysis

NSCs were washed twice with 1× PBS before being frozen in liquid nitrogen. The culture dishes were filled with 80% methanol, and the cells were collected into 2 mL Eppendorf tubes. A total volume of 20 μL of 2-chloro-l-phenylalanine (0.3 mg/mL) dissolved in methanol was added as the internal standard, and 200 μL of methanol was added to each sample, which were then transferred to a 2 mL glass vial. A total volume of 200 μL chloroform was added to each sample and mixed with a pipette. The cells were lysed in an ultrasonic homogenizer for 6 min at 500 W. Each sample was transferred to a 1.5 mL Eppendorf tube then dispersed by ultrasonication for 20 min in an ice water bath. The sample was centrifuged for 10 min, 12,000 g, 4°C. Over a 0.22 μm organic phase film, 800 μL of supernatant in a glass vial was freeze dried in a concentrating centrifugal dryer. A total volume of 80 μL of 15 mg/mL methoxylamine hydrochloride in pyridine was added, and the mixture was vortexed vigorously for 2 min and incubated at 37°C for 90 min. Finally, 80 μL of BSTFA (with 1% TMCS) and 20 μL n-hexane were added to the mixture, which was vortexed vigorously for 2 min and then derivatized at 70°C for 60 min. The samples were equilibrated to ambient temperature for 30 min before GC-MS analysis.

GC-MS Analysis

The derivatized samples were analyzed on an Agilent 7890B gas chromatography system coupled to an Agilent 5977A MSD system (Agilent J & W Scientific, Folsom, CA, USA). A DB-5MS fused-silica capillary column (30 m × 0.25 mm × 0.25 μm, Agilent) was used to separate the derivatives. Helium (>99.999% purity) was used as the carrier gas at a constant flow rate of 1 mL/min through the column. The injector temperature was maintained at 260°C, and the injection volume was 2 μL by splitless mode. The initial oven temperature was 90°C, and this was ramped to 180°C at a rate of 10°C/min, to 240°C at a rate of 5°C/min, to 290°C at a rate of 25°C/min, and finally held at 290°C for 11 min. The temperature of the MS quadrupole was set to 150°C, and the ion source (electron impact) was set to 230°C. The collision energy was 70 eV. Mass data were acquired in full-scan mode (m/z 50–450), and the solvent delay time was set to 5 min.

The quality controls (QCs) were injected at regular intervals (every 9 samples) throughout the analytical run to provide a set of data from which repeatability could be assessed.

Data Preprocessing and Statistical Analysis

The acquired MS data from GC-MS were analyzed with Chroma TOF software (v 4.34, LECO, St. Joseph, MI). The metabolites were identified using the NIST and Fiehn database, which is linked to the Chroma TOF software. Briefly, after alignment with the Statistic Compare component of the software, a CSV file was obtained with three-dimensional data sets including sample information, peak names, retention times-m/z, and peak intensities. There were a total of 552 detectable peaks in the GC-MS data from the samples, and the internal standard was used for data quality control (reproducibility). After internal standards and any known false-positive peaks—such as peaks caused by noise, column bleed, and the BSTFA derivatization procedure—were removed from the data set and the peaks from the same metabolites were combined, there were 263 detectable metabolites.

The resulting data were normalized to the total peak area of each sample, multiplied by 10,000, transformed by log2 in Excel 2007 (Microsoft, USA), and imported into SIMCA (version 14.0, Umetrics, Umeå, Sweden), where PCA, PLS-DA, and OPLS-DA were performed. The Hotelling's T^2 region, shown as an ellipse in the score plots of the models, defines the 95% confidence interval of the modeled variation. The quality of the models is described by the R^2X or R^2Y and Q^2 values. R^2X and R^2Y are defined as the proportions of variance in the data explained by the models and indicate the goodness of fit. Q^2 is defined as the proportion of variance in the data predicted by the model and indicates predictability as calculated by a cross-validation procedure. A default seven-round cross-validation in SIMCA was performed throughout to determine the optimal number of principal components and to avoid model overfitting. The OPLS-DA models were also validated by a permutation analysis (200 times). The Ki67 positive cells among these groups were quantified and statistic analyzed, *p*-values from One Way ANOVA with *post-hoc* test.

Identification of Differential Metabolites

The differential metabolites were selected on the basis of the combination of a statistically significant threshold of VIP values obtained from the OPLS-DA model and *p*-values from a two-tailed Student's *t*-test on the normalized peak areas, where metabolites with VIP values larger than 1.0 and $p < 0.05$ were included.

KEGG Pathway Analysis of Identified Differential Metabolites

The identified differential metabolites were mapped onto the KEGG database with the Omics Bean software (http://www.geneforhealth.com) for KEGG pathways analysis.

DATA AVAILABILITY STATEMENT

All datasets generated for this study are included in the article/**Supplementary Material**.

ETHICS STATEMENT

The animal study was reviewed and approved by the Animal Care and Use Committee of Southeast University.

AUTHOR CONTRIBUTIONS

QF, YZ, and RC conceived and designed the experiments. QF, YZ, XC, HL, and WZ performed the experiments. LC, ZZ, MT, WL, TS, HW, and TW analysis data. QF, TS, YZ, TW, and RC wrote the manuscript.

FUNDING

This work was supported by grants from the National Key R&D Program of China 2017(YFA0103900), the Strategic Priority Research Program of the Chinese Academy of Science (XDA16010303), the National Natural Science Foundation of China (81570908, 81622013, 81670938, 81970882, 81900941, 81970883, and 31571530), the Fundamental Research Funds for the Central Universities, Boehringer Ingelheim Pharma GmbH, and the Open Research Fund of State Key Laboratory of Genetic Engineering, Fudan University (No. SKLGE1809), Jiangsu Province Natural Science Foundation (BK20190121), Postgraduate Research & Practice Innovation Program of Jiangsu Province (KYCX17_0051, KYCX19_0057), Zhejiang Provincial Natural Science Foundation of China (LY19H130003, LY19H130004), K. C. Wong Education Foundation.

ACKNOWLEDGMENTS

We thank Shanghai Lu-Ming Biotech Co., Ltd. (Shanghai, China) for assistance with Metabonomics analysis.

SUPPLEMENTARY MATERIAL

The Supplementary Material for this article can be found online at: https://www.frontiersin.org/articles/10.3389/fbioe.2019.00436/full#supplementary-material

Supplementary Figure 1 | Total ion chromatogram from neural stem cells cultured within different systems using GC-MS. **(A)** total ion chromatogram from NSC cultured on TCPS. **(B)** Total ion chromatogram from NSC cultured on 2D graphene system. **(C)** Total ion chromatogram from NSC cultured in 3D graphene system. **(D)** Total ion chromatogram from QC sample.

Supplementary Figure 2 | Multivariate statistical score graph among three groups. **(A)** PCA score plot of 3DG and TCPS. **(B)** OPLS-DA score plot of 3DG and TCPS. **(C)** PLS-DA score plot of 3DG and TCPS. **(D)** Statistical validation with permutation analysis (200 times) of the corresponding PLS-DA model of 3DG and TCPS, R^2 is the explained variance, and Q^2 is the predictive ability of the model.

Supplementary Figure 3 | volcano map of 3D graphene, 2D graphene and TCPS. **(A)** 2DG vs. TCPS. **(B)** 3DG vs. 2DG. **(C)** 3DG vs. TCPS. up regulation (red), down regulation (green). The horizontal axis is log2 (Fold change), and the vertical axis is –log10 (*P*-value), each dot represents a gene, and the two lines parallel to the Y axis are $X = 1$ and $X = -1$, respectively. The point on the right side of $X = 1$ is a gene that is up-regulated by a factor of two or more, and the point on the left side of $X = -1$ is a gene that is down-regulated by a factor of two or more. At the same time, there is a dotted line $Y =$ –log10 (0.05) parallel to the X axis, and a point above the dotted line indicates a gene with a significance $P < 0.05$. Significantly differentially expressed genes with >2-fold up-regulated genes are marked in red and down-regulated genes are marked in blue. In addition, the difference significance is <2 times and is marked with gray. Moreover, the farther away from the distance between the two axes of $X = 1$ and $X = -1$, the greater the variation of the gene represented by this point between the two groups. Through the volcano map, we can clearly see the difference in metabolites of neural stem cells cultured from three different materials. Compared with the 3DG and 2DG groups and the 3DG and TCPS groups, the significant metabolites were significantly better than the 2DG and more than TCPS groups.

Supplementary Figure 4 | (A) Metabolites-metabolites correlations of 3DG vs. TCPS. **(B)** Bubble diagram of differential metabolic pathways in 3DG vs. TCPS group.

Supplementary Table 1 | Changes in metabolite-related enzymes in two-dimensional graphene and ordinary slides.

Supplementary Table 2 | Changes in differential metabolite-related enzymes in three-dimensional graphene and two-dimensional graphene groups.

Supplementary Table 3 | Metabolic pathways and the KEGG ID in this study.

Datasheet 1 | Metabolites change in three comparable groups.

Datasheet 2 | Metabolites-metabolites correlations in three comparable groups.

REFERENCES

Adams, M. S., and Bronner-Fraser, M. (2009). Review: the role of neural crest cells in the endocrine system. *Endocr. Pathol.* 20, 92–100. doi: 10.1007/s12022-009-9070-6

Akesson, E., Sandelin, M., Kanaykina, N., Aldskogius, H., and Kozlova, E. N. (2008). Long-term survival, robust neuronal differentiation, and extensive migration of human forebrain stem/progenitor cells transplanted to the adult rat dorsal root ganglion cavity. *Cell Transplant.* 17, 1115–1123. doi: 10.3727/096368908787236585

Ali, L., Idrees, M., Ali, M., Hussain, A., Ur Rehman, I., Ali, A., et al. (2014). Inhibitory effect of kaolin minerals compound against hepatitis C virus in Huh-7 cell lines. *BMC Res. Notes* 7:247. doi: 10.1186/1756-0500-7-247

Bensaad, K., Cheung, E. C., and Vousden, K. H. (2009). Modulation of intracellular ROS levels by TIGAR controls autophagy. *EMBO J.* 28, 3015–3026. doi: 10.1038/emboj.2009.242

Bensaad, K., Tsuruta, A., Selak, M. A., Vidal, M. N., Nakano, K., Bartrons, R., et al. (2006). TIGAR, a p53-inducible regulator of glycolysis and apoptosis. *Cell* 126, 107–120. doi: 10.1016/j.cell.2006.05.036

Besingi, R. N., and Clark, P. L. (2015). Extracellular protease digestion to evaluate membrane protein cell surface localization. *Nat. Protoc.* 10, 2074–2080. doi: 10.1038/nprot.2015.131

Campbell, J. C., Stipcevic, T., Flores, R. E., Perry, C., and Kippin, T. E. (2014). Alcohol exposure inhibits adult neural stem cell proliferation. *Exp. Brain Res.* 232, 2775–2784. doi: 10.1007/s00221-014-3958-1

Capiglioni, A. M., Lorenzetti, F., Quiroga, A. D., Parody, J. P., Ronco, M. T., Pisani, G. B., et al. (2018). Attenuation of liver cancer development by oral glycerol supplementation in the rat. *Eur. J. Nutr.* 57, 1215–1224. doi: 10.1007/s00394-017-1404-4

Cheng, S. J., Chiu, H. Y., Kumar, P. V., Hsieh, K. Y., Yang, J. W., Lin, Y. R., et al. (2018). Simultaneous drug delivery and cellular imaging using graphene oxide. *Biomater. Sci.* 6, 813–819. doi: 10.1039/C7BM01192J

Chiasson, B. J., Tropepe, V., Morshead, C. M., and Van Der Kooy, D. (1999). Adult mammalian forebrain ependymal and subependymal cells demonstrate proliferative potential, but only subependymal cells have neural stem cell characteristics. *J. Neurosci.* 19, 4462–4471. doi: 10.1523/JNEUROSCI.19-11-04462.1999

Chong, C. M., Ai, N., Ke, M., Tan, Y., Huang, Z., Li, Y., et al. (2018). Roles of nitric oxide synthase isoforms in neurogenesis. *Mol. Neurobiol.* 55, 2645–2652. doi: 10.1007/s12035-017-0513-7

Copley, S. D. (2003). Enzymes with extra talents: moonlighting functions and catalytic promiscuity. *Curr. Opin. Chem. Biol.* 7, 265–272. doi: 10.1016/S1367-5931(03)00032-2

Ferrari, A. C., Meyer, J. C., Scardaci, V., Casiraghi, C., Lazzeri, M., Mauri, F., et al. (2006). Raman spectrum of graphene and graphene layers. *Phys. Rev. Lett.* 97:187401. doi: 10.1103/PhysRevLett.97.187401

Forsberg, D., Thonabulsombat, C., Jaderstad, J., Jaderstad, L. M., Olivius, P., and Herlenius, E. (2017). Functional stem cell integration into neural networks assessed by organotypic slice cultures. *Curr. Protoc. Stem Cell Biol.* 42, 1–30. doi: 10.1002/cpsc.34

Fujisawa, H., and Nakata, H. (1987). Tryptophan 5-monooxygenase from rat brain stem. *Meth. Enzymol.* 142, 83–87. doi: 10.1016/S0076-6879(87)42012-0

Garcia, S., Vassko, V., Henry, J. F., and De Micco, C. (1998). Comparison of thyroid peroxidase expression with cellular proliferation in thyroid follicular tumors. *Thyroid* 8, 745–749. doi: 10.1089/thy.1998.8.745

Geim, A. K. (2009). Graphene: status and prospects. *Science* 324, 1530–1534. doi: 10.1126/science.1158877

Geim, A. K., and Novoselov, K. S. (2007). The rise of graphene. *Nat. Mater.* 6, 183–191. doi: 10.1038/nmat1849

Guo, R., Zhang, S., Xiao, M., Qian, F., He, Z., Li, D., et al. (2016). Accelerating bioelectric functional development of neural stem cells by graphene coupling: implications for neural interfacing with conductive materials. *Biomaterials* 106, 193–204. doi: 10.1016/j.biomaterials.2016.08.019

Hatano, T., Saiki, S., Okuzumi, A., Mohney, R. P., and Hattori, N. (2016). Identification of novel biomarkers for Parkinson's disease by metabolomic technologies. *J. Neurol. Neurosurg. Psychiatr.* 87, 295–301. doi: 10.1136/jnnp-2014-309676

Hattiangady, B., and Shetty, A. K. (2012). Neural stem cell grafting counteracts hippocampal injury-mediated impairments in mood, memory, and neurogenesis. *Stem Cells Transl. Med.* 1, 696–708. doi: 10.5966/sctm.2012-0050

Hensley, C. T., Wasti, A. T., and Deberardinis, R. J. (2013). Glutamine and cancer: cell biology, physiology, and clinical opportunities. *J. Clin. Invest.* 123, 3678–3684. doi: 10.1172/JCI69600

Hillard, C. J. (2015). Endocannabinoids and the endocrine system in health and disease. *Handb. Exp. Pharmacol.* 231, 317–339. doi: 10.1007/978-3-319-20825-1_11

Huang, S., Yao, L., Zhang, J., and Huang, L. (2016). Direct and indirect effects of RNA interference against pyridoxal kinase and pyridoxine 5'-phosphate oxidase genes in *Bombyx mori*. *Gene* 587, 48–52. doi: 10.1016/j.gene.2016.04.035

Ibba, M., and Soll, D. (2004). Aminoacyl-tRNAs: setting the limits of the genetic code. *Genes Dev.* 18, 731–738. doi: 10.1101/gad.1187404

Iwasaki, Y., Ikeda, K., Shiojima, T., and Kinoshita, M. (1992). Increased plasma concentrations of aspartate, glutamate and glycine in Parkinson's disease. *Neurosci. Lett.* 145, 175–177. doi: 10.1016/0304-3940(92)90015-Y

Jankovic, J. (2005). Motor fluctuations and dyskinesias in Parkinson's disease: clinical manifestations. *Mov. Disord.* 20(Suppl. 11), S11–S16. doi: 10.1002/mds.20458

Jimenez-Jimenez, F. J., Molina, J. A., Vargas, C., Gomez, P., Navarro, J. A., Benito-Leon, J., et al. (1996). Neurotransmitter amino acids in cerebrospinal fluid of patients with Parkinson's disease. *J. Neurol. Sci.* 141, 39–44. doi: 10.1016/0022-510X(96)00115-3

Kalb, D., Gressler, J., and Hoffmeister, D. (2016). Active-site engineering expands the substrate profile of the basidiomycete l-tryptophan decarboxylase CsTDC. *Chembiochem* 17, 132–136. doi: 10.1002/cbic.201500438

Kang, J. M., Yeon, B. K., Cho, S. J., and Suh, Y. H. (2016). Stem cell therapy for Alzheimer's disease: a review of recent clinical trials. *J. Alzheimers. Dis.* 54, 879–889. doi: 10.3233/JAD-160406

Kenry, Chaudhuri, P. K., Loh, K. P., and Lim, C. T. (2016). Selective accelerated proliferation of malignant breast cancer cells on planar graphene oxide films. *ACS Nano* 10, 3424–3434. doi: 10.1021/acsnano.5b07409

Kim, D. Y., Rhee, I., and Paik, J. (2014). Metabolic circuits in neural stem cells. *Cell. Mol. Life Sci.* 71, 4221–4241. doi: 10.1007/s00018-014-1686-0

Kim, G., Jang, S., Yoon, E. K., Lee, S. A., Dhar, S., Kim, J., et al. (2018). Involvement of pyridoxine/pyridoxamine 5'-phosphate oxidase (PDX3) in ethylene-induced auxin biosynthesis in the arabidopsis root. *Mol. Cells* 41, 1033–1044. doi: 10.14348/molcells.2018.0363

Kim, J., Cote, L. J., Kim, F., Yuan, W., Shull, K. R., and Huang, J. (2010). Graphene oxide sheets at interfaces. *J. Am. Chem. Soc.* 132, 8180–8186. doi: 10.1021/ja102777p

Knobloch, M., Braun, S. M., Zurkirchen, L., Von Schoultz, C., Zamboni, N., Arauzo-Bravo, M. J., et al. (2013). Metabolic control of adult neural stem cell activity by Fasn-dependent lipogenesis. *Nature* 493, 226–230. doi: 10.1038/nature11689

Le, A., Lane, A. N., Hamaker, M., Bose, S., Gouw, A., Barbi, J., et al. (2012). Glucose-independent glutamine metabolism via TCA cycling for proliferation and survival in B cells. *Cell Metab.* 15, 110–121. doi: 10.1016/j.cmet.2011.12.009

Lee, H. J., Bazinet, R. P., Rapoport, S. I., and Bhattacharjee, A. K. (2010). Brain arachidonic acid cascade enzymes are upregulated in a rat model of unilateral Parkinson disease. *Neurochem. Res.* 35, 613–619. doi: 10.1007/s11064-009-0106-6

Li, D., Wang, L., Lee, C. W., Dawson, T. A., and Paterson, D. J. (2007). Noradrenergic cell specific gene transfer with neuronal nitric oxide synthase reduces cardiac sympathetic neurotransmission in hypertensive rats. *Hypertension* 50, 69–74. doi: 10.1161/HYPERTENSIONAHA.107.088591

Li, N., Zhang, Q., Gao, S., Song, Q., Huang, R., Wang, L., et al. (2013). Three-dimensional graphene foam as a biocompatible and conductive scaffold for neural stem cells. *Sci. Rep.* 3:1604. doi: 10.1038/srep01604

Lin, T., Islam, O., and Heese, K. (2006). ABC transporters, neural stem cells and neurogenesis–a different perspective. *Cell Res.* 16, 857–871. doi: 10.1038/sj.cr.7310107

Lin, Y., Sun, X., Yuan, Q., and Yan, Y. (2014). Engineering bacterial phenylalanine 4-hydroxylase for microbial synthesis of human neurotransmitter precursor 5-hydroxytryptophan. *ACS Synth. Biol.* 3, 497–505. doi: 10.1021/sb5002505

Liu, J., Dong, J., Zhang, T., and Peng, Q. (2018). Graphene-based nanomaterials and their potentials in advanced drug delivery and cancer therapy. *J. Control. Release* 286, 64–73. doi: 10.1016/j.jconrel.2018.07.034

Liu, W., Sun, C., Liao, C., Cui, L., Li, H., Qu, G., et al. (2016). Graphene enhances cellular proliferation through activating the epidermal growth factor receptor. *J. Agric. Food Chem.* 64, 5909–5918. doi: 10.1021/acs.jafc.5b05923

Luan, H., Liu, L. F., Meng, N., Tang, Z., Chua, K. K., Chen, L. L., et al. (2015). LC-MS-based urinary metabolite signatures in idiopathic Parkinson's disease. *J. Proteome Res.* 14, 467–478. doi: 10.1021/pr500807t

Ma, Q., Yang, L., Jiang, Z., Song, Q., Xiao, M., Zhang, D., et al. (2016). Three-dimensional stiff graphene scaffold on neural stem cells behavior. *ACS Appl. Mater. Interfaces* 8, 34227–34233. doi: 10.1021/acsami.6b12305

Mally, J., Szalai, G., and Stone, T. W. (1997). Changes in the concentration of amino acids in serum and cerebrospinal fluid of patients with Parkinson's disease. *J. Neurol. Sci.* 151, 159–162. doi: 10.1016/S0022-510X(97)00119-6

Menta, R., Mancheno-Corvo, P., Del Rio, B., Ramirez, C., Delarosa, O., Dalemans, W., et al. (2014). Tryptophan concentration is the main mediator of the capacity of adipose mesenchymal stromal cells to inhibit T-lymphocyte proliferation *in vitro*. *Cytotherapy* 16, 1679–1691. doi: 10.1016/j.jcyt.2014.07.004

Metallo, C. M., Gameiro, P. A., Bell, E. L., Mattaini, K. R., Yang, J., Hiller, K., et al. (2011). Reductive glutamine metabolism By IDH1 mediates lipogenesis under hypoxia. *Nature* 481, 380–384. doi: 10.1038/nature10602

Murali, D., Flores, L. G., Roberts, A. D., Nickles, R. J., and Dejesus, O. T. (2003). Aromatic L-amino acid decarboxylase (AAAD) inhibitors as carcinoid tumor-imaging agents: synthesis of 18F-labeled alpha-fluoromethyl-6-fluoro-m-tyrosine (FM-6-FmT). *Appl. Radiat. Isot.* 59, 237–243. doi: 10.1016/S0969-8043(03)00197-0

Nagasaka, H., Yorifuji, T., Egawa, H., Inui, A., Fujisawa, T., Komatsu, H., et al. (2013). Characteristics of NO cycle coupling with urea cycle in non-hyperammonemic carriers of ornithine transcarbamylase deficiency. *Mol. Genet. Metab.* 109, 251–254. doi: 10.1016/j.ymgme.2013.04.013

Naglah, A. M., Ahmed, A. F., Wen, Z. H., Al-Omar, M. A., Amr Ael, G., and Kalmouch, A. (2016). New inducible nitric oxide synthase and cyclooxygenase-2 inhibitors, nalidixic acid linked to isatin schiff bases via certain l-amino acid bridges. *Molecules* 21:498. doi: 10.3390/molecules21040498

Nicklin, P., Bergman, P., Zhang, B., Triantafellow, E., Wang, H., Nyfeler, B., et al. (2009). Bidirectional transport of amino acids regulates mtor and autophagy. *Cell* 136, 521–534. doi: 10.1016/j.cell.2008.11.044

Niedermann, D. M., and Lerch, K. (1991). Regulation of biosynthesis of L-amino acid oxidase by *Neurospora crassa*. *FEMS Microbiol. Lett.* 63, 309–313. doi: 10.1016/0378-1097(91)90104-I

Novak Kujundzic, R., Zarkovic, N., and Gall Troselj, K. (2014). Pyridine nucleotides in regulation of cell death and survival by redox and non-redox reactions. *Crit. Rev. Eukaryot. Gene Exp.* 24, 287–309. doi: 10.1615/CritRevEukaryotGeneExpr.2014011828

Oresic, M., Tang, J., Seppanen-Laakso, T., Mattila, I., Saarni, S. E., Saarni, S. I., et al. (2011). metabolome in schizophrenia and other psychotic disorders: a general population-based study. *Genome Med.* 3:19. doi: 10.1186/gm233

Otten, U., Mueller, R. A., Oesch, F., and Thoenen, H. (1974). Location of an isoproterenol-responsive cyclic AMP pool in adrenergic nerve cell bodies and its relationship to tyrosine 3-monooxygenase induction. *Proc. Natl. Acad. Sci. U.S.A.* 71, 2217–2221. doi: 10.1073/pnas.71.6.2217

Pandey, S., Garg, P., Lee, S., Choung, H. W., Choung, Y. H., Choung, P. H., et al. (2014). Nucleotide biosynthesis arrest by silencing SHMT1 function via vitamin B6-coupled vector and effects on tumor growth inhibition. *Biomaterials* 35, 9332–9342. doi: 10.1016/j.biomaterials.2014.07.045

Pears, M. R., Codlin, S., Haines, R. L., White, I. J., Mortishire-Smith, R. J., Mole, S. E., et al. (2010). Deletion of btn1, an orthologue of CLN3, increases glycolysis and perturbs amino acid metabolism in the fission yeast model of batten disease. *Mol. Biosyst.* 6, 1093–1102. doi: 10.1039/b915670d

Price, M. N., Zane, G. M., Kuehl, J. V., Melnyk, R. A., Wall, J. D., Deutschbauer, A. M., et al. (2018). Filling gaps in bacterial amino acid biosynthesis pathways with high-throughput genetics. *PLoS Genet.* 14:e1007147. doi: 10.1371/journal.pgen.1007147

Ramos, R. J., Pras-Raves, M. L., Gerrits, J., Van Der Ham, M., Willemsen, M., Prinsen, H., et al. (2017). Vitamin B6 is essential for serine de novo biosynthesis. *J. Inherit. Metab. Dis.* 40, 883–891. doi: 10.1007/s10545-017-0061-3

Rozani, V., Gurevich, T., Giladi, N., El-Ad, B., Tsamir, J., Hemo, B., et al. (2018). Higher serum cholesterol and decreased Parkinson's disease risk: a statin-free cohort study. *Mov. Disord.* 33, 1298–1305. doi: 10.1002/mds.27413

Schell, J. C., Wisidagama, D. R., Bensard, C., Zhao, H., Wei, P., Tanner, J., et al. (2017). Control of intestinal stem cell function and proliferation by mitochondrial pyruvate metabolism. *Nat. Cell Biol.* 19, 1027–1036. doi: 10.1038/ncb3593

Skene, D. J., Middleton, B., Fraser, C. K., Pennings, J. L., Kuchel, T. R., Rudiger, S. R., et al. (2017). Metabolic profiling of presymptomatic Huntington's disease sheep reveals novel biomarkers. *Sci. Rep.* 7:43030. doi: 10.1038/srep43030

Soldner, F., Hockemeyer, D., Beard, C., Gao, Q., Bell, G. W., Cook, E. G., et al. (2009). Parkinson's disease patient-derived induced pluripotent stem cells free of viral reprogramming factors. *Cell* 136, 964–977. doi: 10.1016/j.cell.2009.02.013

Son, J., Lyssiotis, C. A., Ying, H., Wang, X., Hua, S., Ligorio, M., et al. (2013). Glutamine supports pancreatic cancer growth through a KRAS-regulated metabolic pathway. *Nature* 496, 101–105. doi: 10.1038/nature12040

Steventon, G. B., and Mitchell, S. C. (2018). Corrigendum To "Phenylalanine hydroxylase: a biomarker of disease susceptibility in Parkinson's disease and amyotrophic lateral sclerosis" [Med. Hypotheses 118 (2018) 29-33]. *Med Hypotheses* 121:88. doi: 10.1016/j.mehy.2018.09.030

Sun, R. C., and Denko, N. C. (2014). Hypoxic regulation of glutamine metabolism through HIF1 and SIAH2 supports lipid synthesis that is necessary for tumor growth. *Cell Metab.* 19, 285–292. doi: 10.1016/j.cmet.2013.11.022

Sun, X., and Kaufman, P. D. (2018). Ki-67: more than a proliferation marker. *Chromosoma* 127, 175–186. doi: 10.1007/s00412-018-0659-8

Swistowski, A., Peng, J., Liu, Q., Mali, P., Rao, M. S., Cheng, L., et al. (2010). Efficient generation of functional dopaminergic neurons from human induced pluripotent stem cells under defined conditions. *Stem Cells* 28, 1893–1904. doi: 10.1002/stem.499

Tanabe, A., Yamamura, Y., Kasahara, J., Morigaki, R., Kaji, R., and Goto, S. (2014). A novel tyrosine kinase inhibitor AMN107 (nilotinib) normalizes striatal motor behaviors in a mouse model of Parkinson's disease. *Front. Cell. Neurosci.* 8:50. doi: 10.3389/fncel.2014.00050

Taupin, P. (2011). Neurogenesis, NSCs, pathogenesis and therapies for Alzheimer's disease. *Front. Biosci.* 3, 178–190. doi: 10.2741/s143

Urbina, J. A., Visbal, G., Contreras, L. M., Mclaughlin, G., and Docampo, R. (1997). Inhibitors of delta24(25) sterol methyltransferase block sterol synthesis and cell proliferation in *Pneumocystis carinii*. *Antimicrob. Agents Chemother.* 41, 1428–1432. doi: 10.1128/AAC.41.7.1428

Valeev, V. V., Trashkov, A. P., Kovaleko, A. L., Petrov, A. U., and Vasiliev, A. G. (2016). Sodium-L-arginine succinate—a new vasodilating medicine for the treatment and prophylaxis of doxorubicin-induced cardiotoxicity. *Patol. Fiziol. Eksp. Ter.* 60, 52–57.

Wang, Y., Liu, C., and Hu, L. (2019). Cholesterol regulates cell proliferation and apoptosis of colorectal cancer by modulating miR-33a-PIM3 pathway. *Biochem. Biophys. Res. Commun.* 511, 685–692. doi: 10.1016/j.bbrc.2019.02.123

Wise, D. R., and Thompson, C. B. (2010). Glutamine addiction: a new therapeutic target in cancer. *Trends Biochem. Sci.* 35, 427–433. doi: 10.1016/j.tibs.2010.05.003

Wu, G. (2010). Functional amino acids in growth, reproduction, and health. *Adv. Nutr.* 1, 31–37. doi: 10.3945/an.110.1008

Yang, K., Lee, J., Lee, J. S., Kim, D., Chang, G. E., Seo, J., et al. (2016). Graphene oxide hierarchical patterns for the derivation of electrophysiologically functional neuron-like cells from human neural stem cells. *ACS Appl. Mater. Interfaces* 8, 17763–17774. doi: 10.1021/acsami.6b01804

Yeo, H., Lyssiotis, C. A., Zhang, Y., Ying, H., Asara, J. M., Cantley, L. C., et al. (2013). FoxO3 coordinates metabolic pathways to maintain redox balance in neural stem cells. *EMBO J.* 32, 2589–2602. doi: 10.1038/emboj.2013.186

Yu, Y., Newman, H., Shen, L., Sharma, D., Hu, G., Mirando, A. J., et al. (2019). Glutamine metabolism regulates proliferation and lineage allocation in skeletal stem cells. *Cell Metab.* 29, 966–978 E4. doi: 10.1016/j.cmet.2019.01.016

Zhang, Z., Kang, S. S., Liu, X., Ahn, E. H., Zhang, Z., He, L., et al. (2017). Asparagine endopeptidase cleaves α-synuclein and mediates pathologic activities in Parkinson's disease. *Nat. Struct. Mol. Biol.* 24, 632–642. doi: 10.1038/nsmb.3433

Zhao, H., Wang, C., Zhao, N., Li, W., Yang, Z., Liu, X., et al. (2018). Potential biomarkers of Parkinson's disease revealed by plasma metabolic profiling. *J. Chromatogr. B Analyt. Technol. Biomed. Life Sci.* 1081–1082, 101–108. doi: 10.1016/j.jchromb.2018.01.025

Zhao, Y., Pan, X., Zhao, J., Wang, Y., Peng, Y., and Zhong, C. (2009). Decreased transketolase activity contributes to impaired hippocampal neurogenesis induced by thiamine deficiency. *J. Neurochem.* 111, 537–546. doi: 10.1111/j.1471-4159.2009.06341.x

Zhu, Y., Murali, S., Cai, W., Li, X., Suk, J. W., Potts, J. R., et al. (2010). Graphene and graphene oxide: synthesis, properties, and applications. *Adv. Mater.* 22, 3906–3924. doi: 10.1002/adma.201001068

Zipp, F., Demisch, L., Derouiche, A., and Fischer, P. A. (1998). Glutamine synthetase activity in patients with Parkinson's disease. *Acta Neurol. Scand.* 97, 300–302. doi: 10.1111/j.1600-0404.1998.tb05956.x

Zong, M., Lu, T., Fan, S., Zhang, H., Gong, R., Sun, L., et al. (2015). Glucose-6-phosphate isomerase promotes the proliferation and inhibits the apoptosis in fibroblast-like synoviocytes in rheumatoid arthritis. *Arthritis Res. Ther.* 17:100. doi: 10.1186/s13075-015-0619-0

Conflict of Interest: XC was employed by company Hangzhou Rongze Biotechnology Co. Ltd.

The remaining authors declare that the research was conducted in the absence of any commercial or financial relationships that could be construed as a potential conflict of interest.

frontiers in Bioengineering and Biotechnology

ORIGINAL RESEARCH
published: 14 February 2020
doi: 10.3389/fbioe.2020.00070

Maturation of Human Pluripotent Stem Cell-Derived Cerebellar Neurons in the Absence of Co-culture

*Teresa P. Silva[1,2], Evguenia P. Bekman[1,2,3], Tiago G. Fernandes[2], Sandra H. Vaz[1,4], Carlos A. V. Rodrigues[2], Maria Margarida Diogo[2], Joaquim M. S. Cabral[2] and Maria Carmo-Fonseca[1]**

[1] Instituto de Medicina Molecular João Lobo Antunes, Faculdade de Medicina, Universidade de Lisboa, Lisbon, Portugal, [2] Department of Bioengineering and Institute for Bioengineering and Biosciences, Instituto Superior Técnico, Universidade de Lisboa, Lisbon, Portugal, [3] The Discoveries Centre for Regenerative and Precision Medicine, Universidade de Lisboa, Lisbon, Portugal, [4] Instituto de Farmacologia e Neurociências, Faculdade de Medicina da Universidade de Lisboa, Lisbon, Portugal

OPEN ACCESS

Edited by:
Eduardo Jacob-Lopes, Universidade Federal de Santa Maria, Brazil

Reviewed by:
Martin L. Doughty, Uniformed Services University, United States
Noha M. Mesbah, Suez Canal University, Egypt

***Correspondence:**
Maria Carmo-Fonseca
carmo.fonseca@medicina.ulisboa.pt

Specialty section:
This article was submitted to Bioprocess Engineering, a section of the journal Frontiers in Bioengineering and Biotechnology

Received: *23 October 2019*
Accepted: *27 January 2020*
Published: *14 February 2020*

Citation:
Silva TP, Bekman EP, Fernandes TG, Vaz SH, Rodrigues CAV, Diogo MM, Cabral JMS and Carmo-Fonseca M (2020) Maturation of Human Pluripotent Stem Cell-Derived Cerebellar Neurons in the Absence of Co-culture. Front. Bioeng. Biotechnol. 8:70. doi: 10.3389/fbioe.2020.00070

The cerebellum plays a critical role in all vertebrates, and many neurological disorders are associated with cerebellum dysfunction. A major limitation in cerebellar research has been the lack of adequate disease models. As an alternative to animal models, cerebellar neurons differentiated from pluripotent stem cells have been used. However, previous studies only produced limited amounts of Purkinje cells. Moreover, *in vitro* generation of Purkinje cells required co-culture systems, which may introduce unknown components to the system. Here we describe a novel differentiation strategy that uses defined medium to generate Purkinje cells, granule cells, interneurons, and deep cerebellar nuclei projection neurons, that self-formed and differentiated into electrically active cells. Using a defined basal medium optimized for neuronal cell culture, we successfully promoted the differentiation of cerebellar precursors without the need for co-culturing. We anticipate that our findings may help developing better models for the study of cerebellar dysfunctions, while providing an advance toward the development of autologous replacement strategies for treating cerebellar degenerative diseases.

Keywords: human induced pluripotent stem cells, cerebellar differentiation, cerebellar neurons, defined culture condition, co-culture free

INTRODUCTION

The cerebellum plays a critical role in maintaining balance and posture, coordination of voluntary movements, and motor learning in all vertebrates (for a recent review see McLachlan and Wilson, 2017). Recent evidence has indicated that this brain structure also plays a role in auditory processing tasks, reward expectation (Wagner et al., 2017), and other forms of emotional processing (Adamaszek et al., 2017). Therefore, it is not surprising that many neurological disorders are associated with abnormalities in the cerebellum (Schöls et al., 2004; Taroni and DiDonato, 2004).

A major limitation in cerebellar research has been the lack of adequate experimental models that could help identify essential molecular and cellular pathways involved in cerebellum dysfunction. Indeed, much of the current knowledge about the mechanisms of cerebellar diseases has been

based on human postmortem studies, which do not inform on disease development or progression. Alternatively, animal models and immortalized human cell lines have been used (Manto and Marmolino, 2009). While these models permit in-depth investigation, they do not fully reflect the physiology and metabolism of human tissues. Thus, there is a great need for better models for the study of the human cerebellum.

The generation of cerebellar neurons using human induced pluripotent stem cells (iPSCs) aims to recapitulate early cerebellar development during human embryogenesis (Andreu et al., 2014; Butts et al., 2014; Leto et al., 2016). Pioneer studies were based on the formation of embryoid body-like structures derived from human or mouse embryonic stem cells that did differentiate into cerebellar-like cells (Su et al., 2006; Salero and Hatten, 2007; Erceg et al., 2010, 2012) but yielded a small number of immature Purkinje cells. Considering that most cerebellar disorders, namely ataxias, are associated with a loss of Purkinje cells, this technical limitation compromises the use of such embryoid bodies as a model for studying cerebellar biology and pathology.

Recent studies have generated bona fide Purkinje cells from mouse embryonic stem cells (Muguruma et al., 2010), human pluripotent stem cells (Muguruma et al., 2015), or spinocerebellar ataxia patient-derived iPSCs (Ishida et al., 2016). The maturation into functional Purkinje neurons has so far been achieved by co-culturing cells with either cerebellar granule cell precursors isolated from mouse embryos (Muguruma et al., 2015; Ishida et al., 2016) or fetal cerebellar slices (Wang et al., 2015). A co-culture system using postnatal cerebellum has produced cells with morphological and synaptogenesis features similar to mature Purkinje cells (Tao et al., 2010). However, significant variability in the efficiency to obtain functional Purkinje cells using different feeder cell sources was later reported by Wang et al. (2015). For instance, feeder-free and co-culturing with rat granular progenitors failed to sustain Purkinje cell maturation and survival, while co-culture with rat cerebellar slices did yield Purkinje cells that nevertheless were devoid of any action potential or spontaneous post-synaptic currents. In contrast, co-culture with human fetal cerebellar slices resulted in electrophysiologically active Purkinje neurons (Wang et al., 2015). Despite these important developments, the use of co-culture systems has limitations because feeder cells introduce inherent variability to the procedure, which may in turn affect its reproducibility and experimental outcomes (Akopian et al., 2010; Wang et al., 2015). Moreover, co-culture systems must be avoided when generating iPSC-derived cerebellar neurons for autologous transplantation. Thus, establishing long-term culture systems that sustain maturation of human cerebellar neurons without co-culturing is highly needed.

Here we present a novel strategy to generate distinct types of cerebellar cells that self-formed and differentiated into electrically active neurons in a defined medium. The possibility of efficiently generating cerebellar neurons from patient-derived iPSCs will facilitate drug screening and the study of specific pathways involved in disease development and progression.

MATERIALS AND METHODS

Maintenance of Human iPSCs

We used three distinct human induced pluripotent stem cell (iPSC) lines. A cell line, termed F002.1A.13, was derived from a healthy female donor using a standard protocol (Takahashi et al., 2007). Karyotyping of these cells revealed no abnormalities, and upon subcutaneous injection into immune-deficient mice they induced the formation of tumoral masses reminiscent of teratomas (Hentze et al., 2009), thus confirming their *in vivo* differentiation potential (**Supplementary Figure S1**). Besides the F002.1A.13, the Gibco® Human Episomal iPSC line (iPSC6.2, Burridge et al., 2011) and iPS-DF6-9-9T.B, provided by WiCell Bank, were also used. All iPSCs were cultured on Matrigel™ (Corning)-coated plates with mTeSR™1 Medium (StemCell Technologies). Medium was changed daily. Cells were passaged every 3–4 days (when the colonies covered approximately 85% of the surface area of the culture dish) using 0.5 mM EDTA dissociation buffer (Life Technologies). Before each differentiation process, frozen cells were thawed and cultured for 2–3 passages.

Teratoma Assay

Animal experimentation at Instituto de Medicina Molecular was conducted strictly within the rules of the Portuguese official veterinary directorate, which complies with the European Guideline 86/609/EC concerning laboratory animal welfare, according to a protocol approved by the Institute's Animal Ethics Committee. To assess the capacity of the F002.1A.13 cells to form teratomas, cells were collected using 0.5 mM EDTA dissociation buffer and 2×10^6 cells were resuspended in mTeSR™1/Matrigel 1:1 and subcutaneously injected into the flanks of 8-week-old immunocompromised mice (NGS). Animals were sacrificed with anesthetic overdose and necropsy was performed. Subcutaneous tumor and ipsilateral inguinal lymph node were harvested, fixed in 10% neutral-buffered formalin, embedded in paraffin, and 3 μm sections were stained with hematoxylin and eosin (**Supplementary Figure S1A**). Tissue sections were examined by a pathologist blinded to experimental groups in a Leica DM2500 microscope coupled to a Leica MC170 HD microscope camera.

Karyotyping and Flow Cytometry of Human iPSCs

F002.1A.13 cells were incubated with colcemid (10 μg/ml; Life Technologies) for 4 h to arrest cells in metaphase. Next, cells were collected and incubated with hypotonic potassium chloride solution for 15 min at 37°C. Finally, cells were resuspended and fixed in glacial acetic acid and methanol (1:3). Karyotype analysis was performed by Genomed SA (Lisbon, Portugal) (**Supplementary Figure S1B**). Flow cytometry analysis for five different pluripotency markers was performed on day zero of differentiation (**Supplementary Figure S1C**).

3D Culture of Cerebellar Progenitors

To promote human iPSC aggregation into embryoid body-like floating structures, the three iPSC lines used in this

study were incubated with ROCK inhibitor (ROCKi, Y-27632, 10 μM, StemCell Technologies) for 1 h at 37°C and then treated with accutase (Sigma) for 5 min at 37°C. After dissociation, cells were quickly re-aggregated using microwell plates (AggreWell^{TM}800, StemCell Technologies) according to the manufacturer's instructions. Cells were plated at a density of 1.8×10^6 cells/well (6,000 cells/microwell) in 1.5 mL/well of mTeSR^{TM}1 supplemented with 10 μM ROCKi. Twenty-four hours later the entire medium was replaced and cells were maintained in mTeSR^{TM}1 without ROCKi for another 24 h.

Day 0 was when the aggregate culture was started. The basal differentiation medium used during days 2–21 was growth-factor-free chemically defined medium (gfCDM) (Muguruma et al., 2015), consisting of Isocove's modified Dulbecco's medium (Life Technologies)/Ham's F-12 (Life Technologies) 1:1, chemically defined lipid concentrate (1% v/v, Life Technologies), monothioglycerol (450 μM, Sigma), apo-transferrin (15 μg/ml, Sigma), crystallization-purified BSA (5 mg/ml, >99%, Sigma), and 50 U/ml penicillin/50 μg/ml streptomycin (PS, Life Technologies). The medium was also supplemented with insulin (7 μg/ml, Sigma).

Recombinant human basic FGF (FGF2, 50 ng/ml, PeproTech) and SB431542 (SB, 10 μM, Sigma) were added to culture on day 2. The entire medium was replaced by gfCDM (supplemented with insulin, FGF2 and SB) on day 5. On day 7, the floating aggregates were transferred from microwell plates to ultra-low attachment 6-well plates (Costar, Corning) and cultured at a density of 1×10^6 cells/mL in 1.8 mL/well. Medium was replaced and 2/3 of the initial amount of FGF2 and SB was added. Recombinant human FGF19 was added to culture on day 14, and the entire medium was replaced by gfCDM (supplemented with insulin and FGF19) on day 18. From day 21 onward, the aggregates were cultured in Neurobasal medium (Life Technologies) supplemented with GlutaMax I (Life Technologies), N2 supplement (Life Technologies), and PS. The entire medium was then replaced weekly. Recombinant human SDF1 (300 ng/ml, PeproTech) was added to culture on day 28 (**Figure 1A**).

Maturation of Cerebellar Neurons in 2D Culture

On day 35 of differentiation, aggregates were dissociated using accutase (Sigma) and cells were plated on wells coated with poly-L-ornithine (15 μg/mL, Sigma) and Laminin (20 μg/mL, Sigma), at a seeding density between 80,000 cells/cm^2. Cells were cultured in BrainPhys^{TM} Neuronal Medium (STEMCELL Technologies), supplemented with NeuroCult^{TM} SM1 Neuronal Supplement (STEMCELL Technologies), N2 Supplement-A (StemCell Technologies), recombinant Human Brain Derived Neurotrophic Factor (BDNF, PeproTech, 20 ng/mL), recombinant Human Glial-Derived Neurotrophic Factor (GDNF, PeproTech, 20 ng/mL), dibutyryl cAMP (1 mM, Sigma), and ascorbic acid (200 nM, Sigma). One-third of the total volume was replaced at every 2–3 days.

Aggregate Size Analysis

To monitor the size of aggregates, images were acquired at different time-points using a Leica DMI 3000B microscope with a Nikon DXM 1200F digital camera. The aggregate diameter was estimated using the Mathworks computer tool (MATLAB), as described (Miranda et al., 2015).

Immunostaining

Aggregates were fixed in 4% paraformaldehyde (PFA, Sigma) for 20 min at 4°C followed by washing in Phosphate buffered saline (PBS, 0.1M) and overnight incubation in 15% sucrose at 4°C. Next, aggregates were embedded in 7.5% v/v gelatin/15% v/v sucrose and frozen in isopenthane at −80°C. Sections with approximately 12 μm in thickness were cut on a cryostat-microtome (Leica CM3050S, Leica Microsystems), collected on Superfrost^{TM} Microscope Slides (Thermo Scientific), and stored at −20°C. Finally, sections were de-gelatinized for 45 min in PBS at 37°C before being processed for immunohistochemistry.

Immunostaining was performed on either sections of 3D aggregates or on cells plated on coverslips (2D cultures). Cells in 2D cultures were fixed in 4% PFA for 20 min at 4°C. Samples were then incubated in 0.1 M Glycine (Millipore) for 10 min at room temperature (RT), permeabilized with 0.1% Triton X-100 (Sigma) for 10 min at RT, and blocked with 10% v/v fetal goat serum (FGS, Life Technologies) in TBST (20 mM Tris-HCl pH 8.0, 150 mM NaCl, 0.05% v/v Tween-20, Sigma) for 30 min at RT. Next, samples were incubated overnight at 4°C with the primary antibodies (**Supplementary Table S1**) diluted in blocking solution. Secondary antibodies (goat anti-mouse or goat anti-rabbit IgG, Alexa Fluor®–488 or –546, 1:500 v/v dilution, Molecular Probes) were incubated for 30 min at RT. Nuclei were stained with 4′,6-diamidino-2-phenylindole (DAPI, 1.5 μg/mL; Sigma). For phalloidin staining, cells were incubated with Alexa Fluor® 488 Phalloidin (1:40 in PBS, Life Technologies). Finally, samples were mounted in Mowiol (Sigma). Fluorescence images were acquired with Zeiss LSM 710 or Zeiss LSM 880 Confocal Laser Point-Scanning Microscopes.

Quantitative Real Time (qRT)-PCR

Total RNA was extracted using High Pure RNA Isolation Kit (Roche), according the instructions provided by the manufacturer. Total RNA was converted into complementary cDNA with Transcriptor High Fidelity cDNA Synthesis Kit (Roche) using 500 ng of RNA. RNA levels were measured using 10 ng of cDNA and 250 μM of each primer. Taqman® Gene Expression Assays (20X, Applied Biosystems) were selected for mRNAs from the following genes: *NANOG* (HS02387400-g1), *OCT4* (HS00999634-sh), *PAX6* (HS00240871-m1), *SOX1* (HS01057642-s1), *EN2* (Hs00171321_m1), *KIRREL2* (Hs00375638_m1), and *GAPDH* (HS02758991-g1). SYBR® green chemistry was used to analyze mRNAs from the following genes: *ALDOC, ATOH1, BARHL1, CBLN1, CORL2, EN2, FGF8, GAD65, GRID2, L7/PCP2, LHX5, NESTIN, NEUROGRANIN, OLIG2, OTX2, PARVALBUMIN, PAX2, TBR1, TBR2* and *VGLUT1* (**Supplementary Table S2**). All PCR reactions were done in duplicate or triplicate, using the StepOne^{TM} or ViiA^{TM} 7 RT-PCR

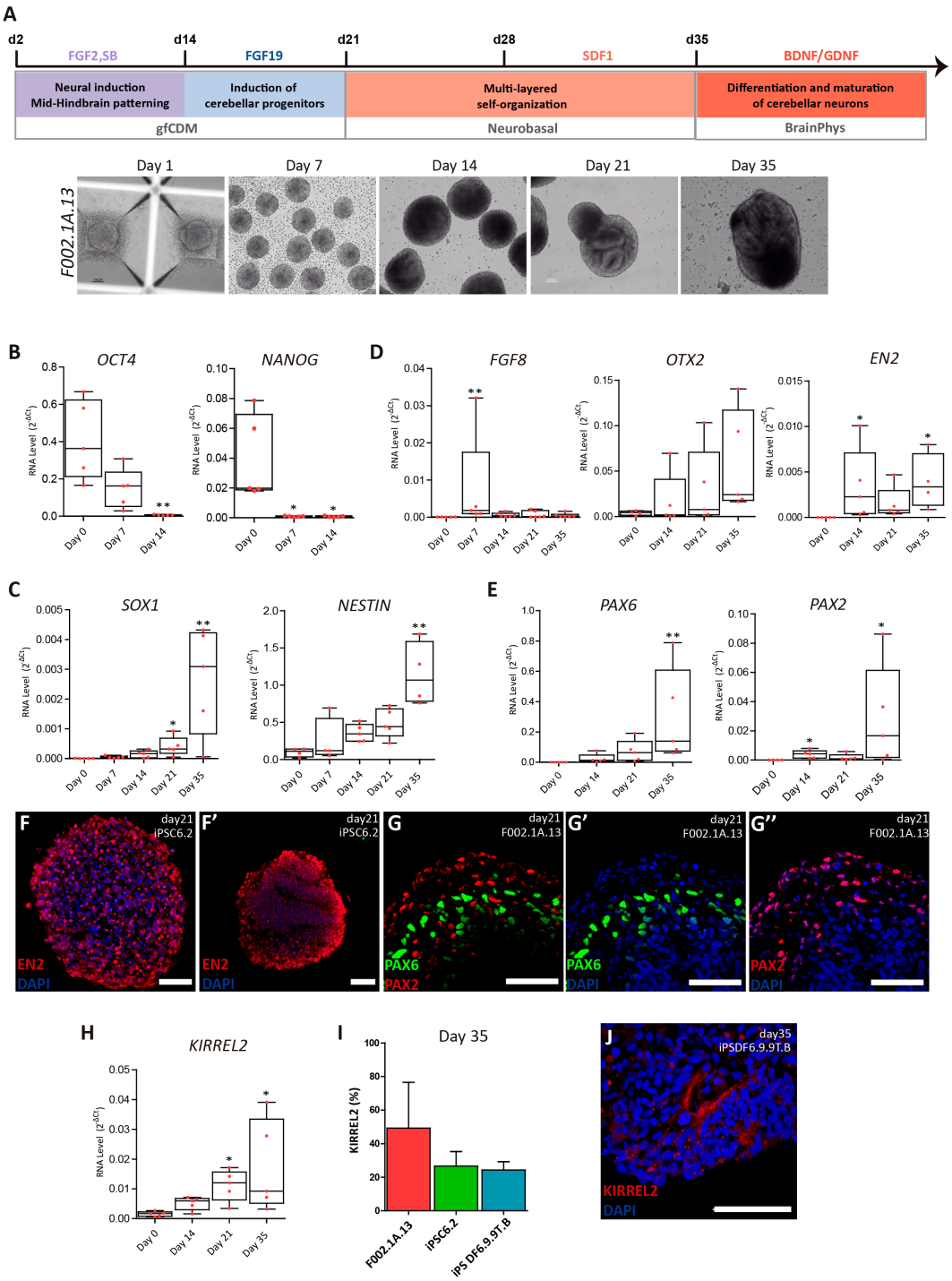

FIGURE 1 | Differentiation of cerebellar progenitors in 3D culture. **(A)** Schematics illustrating the 3D culture conditions used to induce differentiation of iPSCs to cerebellar neurons. Representative bright field images of cell aggregates taken at the indicated time points. Scale bar, 100 μm. **(B–E)** qRT-PCR analysis of cultures derived from F002.1A.13 cells for the indicated mRNAs. The graphs depict mRNA expression levels ($2^{-\Delta Ct}$) relative to GAPDH. Each dot represents data from an independent experiment ($n = 5$). One-way ANOVA (Dunn's Multiple Comparison Test), $^{*}p < 0.05$, $^{**}p < 0.01$; error bars represent SEM. **(F,G)** Immunofluorescence of cultures derived from the indicated iPSC lines for EN2 **(F,F')**, PAX6 **(G,G')**, and PAX2 **(G,G")** on day 21 of differentiation (scale bar, 50 μm). **(H)** qRT-PCR analysis of cultures derived from F002.1A.13 cells for mRNA encoding the KIRREL2 protein. The graph depicts mRNA expression levels ($2^{-\Delta Ct}$) relative to GAPDH. Each dot represents data from an independent experiment ($n = 5$). One-way ANOVA (Dunn's Multiple Comparison Test), $^{*}p < 0.05$; error bars represent SEM. **(I)** Flow cytometry analysis of KIRREL2^{+} cells on day 35. The graph depicts the proportion of KIRREL2^{+} cells in cultures derived from the indicated iPSC lines. Two independent experiments were performed for each cell line; error bars represent SEM. **(J)** Immunofluorescence for KIRREL2 in a culture derived from DF6.9.9T.B cells on day 35 (scale bar, 50 μm).

Systems (Applied BioSystems). Quantification was performed by calculating the ΔCt value using GAPDH as a reference and results are shown as mRNA expression levels ($2^{-\Delta Ct}$) relative to GAPDH.

Flow Cytometry

Aggregates were dissociated to single cells with accutase for 7 min at 37°C. Adherent cells in 2D cultures were detached by incubation with accutase at 37°C for 5 min. The enzyme was inactivated by addition of serum-containing medium. After centrifugation, the cell pellet was washed with PBS, fixed in 2% v/v PFA, and stored at 4°C. For Ki67 analysis, cells were fixed drop by drop with 70% v/v ethanol (previously stored at −20°C) and stored at −20°C. For cell staining, eppendorf tubes were coated with 1% v/v bovine serum albumin (BSA; Life Technologies) solution in PBS for 15 min. Samples stored in 2% v/v PFA were placed in the coated eppendorf tubes and centrifuged at 1000 rpm for 5 min. Samples stored in 70% v/v ethanol were also placed in coated eppendorf tubes and centrifuged at 1000 rpm for 10 min. Then, cells were washed twice with PBS. Surface staining: for each experiment, approximately 500,000 cells were resuspended in primary antibody diluted in 3% v/v BSA solution in PBS and incubated for 30 min at RT. Then, cells were washed with PBS, resuspended in 3% v/v BSA solution in PBS and incubated with secondary antibodies for 15 min at RT. Finally, cells were washed twice with PBS, resuspended in PBS and analyzed in a FACSCalibur™ flow cytometer (Becton Dickinson). Intracellular staining: for each experiment, approximately 500,000 cells were resuspended in 3% v/v normal goat serum (NGS, Sigma). The cell suspension was centrifuged at 1000 rpm for 3 min. Next, cells were permeabilized with 1% saponin (Sigma) diluted in a solution of 3% NGS in PBS for 15 min at RT. After washing three times with 1% NGS, cells were resuspended in primary antibody solution (in 3% NGS) and incubated for 1h at RT (**Supplementary Table S3**). Cells were then washed three times with 1% NGS, and incubated for 45 min in the dark with the secondary antibody (in 3% NGS). Secondary antibodies included goat anti-mouse and anti-rabbit IgG Alexa Fluor – 488 (Invitrogen, 1:500), and anti-mouse IgG-PE (1:500, Miltenyi Biotec). After washing, cells were resuspended in PBS and analyzed in a FACSCalibur™ flow cytometer (Becton Dickinson). As a negative control, cells were incubated with secondary antibody only. For each experimental sample, 10 000 events were collected within the defined gate, based on side scatter (SSC) and forward scatter (FSC). Results were analyzed using FlowJo.

Single Cell Calcium Imaging

For single cell calcium imaging (SCCI), aggregates were dissociated using accutase and cells were plated on glass bottom micro-well chambers previously coated with poly-D-lysine (MatTek) and Laminin (20 μg/mL, Sigma), at a seeding density of 80 000 cells/cm^2. At different time-points of differentiation, cells were loaded with 5 μM Fura-2 AM (Invitrogen) in Krebs solution (132 mM NaCl, 4 mM KCl, 1.4 mM MgCl2, 2.5 mM $CaCl_2$, 6 mM glucose, 10mM HEPES, pH 7.4) for 45 min at 37°C in an incubator with 5% CO_2 and 95% atmospheric air. Dishes were washed in Krebs solution and observed with an inverted microscope with epifluorescence optics (Axiovert 135TV, Zeiss). Cells were continuously perfused with Krebs solution and stimulated by applying high-potassium Krebs solution (containing 10–100 mM KCl, isosmotic substitution with NaCl), 2 μM ionomycin, or 100 μM histamine. Ratio images were obtained from image pairs acquired every 200 ms by exciting the cells at 340 and 380 nm. Excitation wavelengths were changed through a high-speed switcher (Lambda DG4, Sutter Instrument, Novato, CA, United States). The emission fluorescence was recorded at 510 nm by a cooled CDD camera (Photometrics CoolSNAP fx). Images were processed and analyzed using the software MetaFluor (Universal Imaging, West Chester, PA, United States). Regions of interest were defined manually.

Dendritic Spine Classification

After phalloidin-staining, dendritic spines were imaged with either a Zeiss LSM 710 or a Zeiss LSM 880 Confocal Laser Point-Scanning Microscope, using the 63x Plan-Apochromat oil objective. Regions with low density of neurons were selected to allow visualization of individual dendrites and spines. Three representative images were analyzed per experiment. For each dendritic spine, the head width and the neck length were measured manually using ImageJ software.

Patch-Clamp Recordings

Whole-cell patch-clamp recordings were obtained from cerebellar neurons visualized with an upright microscope (Zeiss Axioskop 2FS) equipped with differential interference contrast optics using a Zeiss AxioCam MRm camera and an x40 IR-Achroplan objective. During recordings, cells were continuously superfused with artificial cerebrospinal fluid (aCSF) containing 124 mM NaCl, 3 mM KCl, 1.2 mM NaH2PO$_4$, 25 mM $NaHCO_3$, 2 mM $CaCl_2$, 1 mM $MgSO_4$, and 10 mM glucose, which was continuously gassed with 95%O_2/5% CO_2. Recordings were performed at room temperature in current-clamp or voltage-clamp mode [holding potential (Vh) = -70 mV] with an Axopatch 200B (Axon Instruments) amplifier, as performed elsewhere (Felix-Oliveira et al., 2014). In the current-clamp mode, the step-and-hold stimulation protocol included 11 steps of 500 ms long depolarization pulses. The first injection current was −25 pA and the subsequent ones increased progressively until 225 pA. Synaptic currents and action potential activity were recorded using patch pipettes with 4–7 MΩ resistance filled with an internal solution containing 125 mM K-gluconate, 11 mM KCl, 0.1 mM $CaCl_2$, 2 mM $MgCl_2$, 1 mM EGTA, 10 mM HEPES, 2 mM MgATP, 0.3 mM NaGTP, and 10 mM phosphocreatine, pH 7.3, adjusted with 1 M NaOH, 280-290 mOsm. Acquired signals were filtered using an in-built, 2-kHz, three-pole Bessel filter, and data were digitized at 5 kHz under control of the pCLAMP 10 software program. The junction potential was not compensated for, and offset potentials were nulled before gigaseal formation. The resting membrane potential was measured immediately upon establishing whole-cell configuration. In the voltage-clamp mode, spontaneous miniature postsynaptic currents were recorded in aCSF solution for 5 min. After this period, the sCSF solution was supplemented with 500 nM TTX (tetrodotoxin,

a voltage-dependent sodium channel blocker), 5 μM CNQX (6-cano-7-nitroquinoxaline-2, 3-dione, a glutamate AMPA receptor antagonist), and 50 μM DL-APV (DL-(-)-2-amino-5-phosphonopentanoic acid, a glutamate NMDA receptor antagonist), for the specific recording of miniature post-synaptic inhibitory currents, miPSCs (Rombo et al., 2016). To silence miPSCs and confirm their GABAergic nature, 10 μM bicuculline (a $GABA_A$ receptor antagonist) was used at the end of the recording. The same protocol was performed but first inhibiting miPSCs and then Glutamatergic responses at the end of the recording. Analysis was performed offline using the spontaneous event detection parameters of the Synaptosoft Minianalysis software, the amplitude threshold for event detection being set at 3x the average root-mean-square noise.

RESULTS

Induction of Cerebellar Differentiation in a 3D Culture System

Three distinct lines of human iPSCs (F002.1A.13; iPSC6.2; and iPSDF6.9.9T.B) were induced to differentiate into cerebellar neurons. A total of 10 independent differentiation experiments were carried out using the F002.1A.13 cells, 8 using the iPSC6.2 cells, and 4 using the iPSDF6.9.9T.B cells. Initially, cells self-assembled spontaneously in suspension culture in mTESR1 medium. On day 2, the medium was replaced by gfCDM, on day 21 by neurobasal medium, and on day 35 by BrainPhys medium (**Figure 1A**). On day 2, fibroblast growth factor 2 (FGF2), insulin, and transforming growth factor β-receptor blocker SB431542 were added. Fibroblast growth factor 19 (FGF19) was then added between days 14 and 21, followed by stromal cell-derived factor 1 (SDF1) between days 28 and 35, as previously described (Muguruma et al., 2015). To maximize neural commitment, the sizes of 3D cell aggregates were controlled using V-shaped microwell plates. On day zero of differentiation, approximately 6,000 cells were plated per microwell and aggregation was induced by centrifugation. On day 7, the floating aggregates were transferred to ultra-low attachment 6-well culture plates. As shown in **Figure 1A** and **Supplementary Figure S2A**, on day 7 the three iPSC lines formed 3D aggregates that were homogeneous in size and shape. After day 7, the aggregates started to grow and vary in size and morphology (**Figure 1A** and **Supplementary Figures S2A,B**).

As expected, on day zero of differentiation the iPSCs expressed the pluripotency and self-renewal genes *OCT4* and *NANOG* (**Figure 1B**). On day 7, *OCT4* and *NANOG* mRNA levels were significantly reduced and on day 14 they were almost undetectable, indicating that cells were committed to differentiate. Starting on day 7 and going onward until day 35, aggregates progressively expressed higher mRNA levels encoding the neural stem cell markers SOX1 and NESTIN (**Figure 1C**). Immunofluorescence analysis further revealed that most cells within the aggregates expressed NESTIN and PAX6 (**Supplementary Figure S2C**). Altogether, these results support the iPSC-derived neural commitment.

As shown in **Figure 1D**, the level of RNA transcribed from *FGF8*, a gene encoding a signaling protein required for early cerebellum development (Chi et al., 2003), was at its highest on day 7 of differentiation and dropped thereafter. **Figure 1D** also shows that *OTX2* mRNA levels were higher on day 35. *OTX2* is a homeobox gene required for cerebellum development that is inhibited by FGF8 (Frantz et al., 1994; Larsen et al., 2010). As expected, *OTX2* levels increased only after *FGF8* mRNA levels dropped. On days 14 through 35, we also detected the expression of *EN2* (**Figure 1D**), another homeobox gene required to generate a fully functional cerebellum (Zec et al., 1997). These findings indicate that our iPSC-derived 3D aggregates expressed critical genes required for early cerebellum morphogenesis.

We next focused on detecting specific cerebellar progenitors. Starting on day 14, we detected increasing levels of *PAX6* mRNA (**Figure 1E**), which encodes a transcription factor required for the development of all cerebellar glutamatergic neurons (Yeung et al., 2016). We further found significant expression of *PAX2* (**Figure 1E**), which is a gene that encodes a transcription factor involved in normal functioning of mid-hindbrain junction and further cerebellar commitment (Urbánek et al., 1997). The expression of proteins encoded by the *EN2*, *PAX6,* and *PAX2* genes was also detected by immunostaining (**Figures 1F',G',G"**), confirming the efficient mid-hindbrain patterning and further cerebellar commitment within the aggregates.

As **Figure 1H** shows, on day 35 we detected a significant expression of *KIRREL2* mRNA, which encodes a cell adhesion molecule found on the surface of cerebellar GABAergic progenitors, including Purkinje cell precursors (Mizuhara et al., 2010). The results of flow cytometry analysis show that the proportion of KIRREL2 positive cells on day 35 was approximately 50% in F002.1A.13-derived cell aggregates, and about 30% in iPSC6.2 and iPSDF6.9.9T.B-derived cell aggregates (**Figure 1I**). KIRREL2 protein expression was further confirmed by immunofluorescence (**Figure 1J** and **Supplementary Figure S2D**), indicating that after 35 days of differentiation aggregates derived from the three iPSC lines had cerebellar GABAergic progenitors.

Cerebellar Progenitors in 3D Culture Self-Organize Into Polarized Neuroepithelium

On day 21, aggregates derived from the three iPSC lines displayed characteristic hollow structures with a radial organization (neural rosettes) reminiscent of the neural tube. These structures showed apical-basal polarity, with the apical side marked by a strong signal of *N*-cadherin (NCAD, **Figure 2A**). Polarized neuroepithelial structures were more prominent on day 35 (**Figures 2B–J**). Dividing cells stained by the proliferation marker KI67 were enriched on the apical (luminal) side of the neuroepithelium (**Figure 2C** and **Supplementary Figure S3A**). Immunostaining for SOX2 (**Figures 2D,D',E**) and PAX6 (**Figure 2F**) further showed that the proliferating apical cell layer was mainly composed of cerebellar progenitors. In contrast, cells expressing neuron-specific class III beta-tubulin (TUJ1) formed a separate, more basally

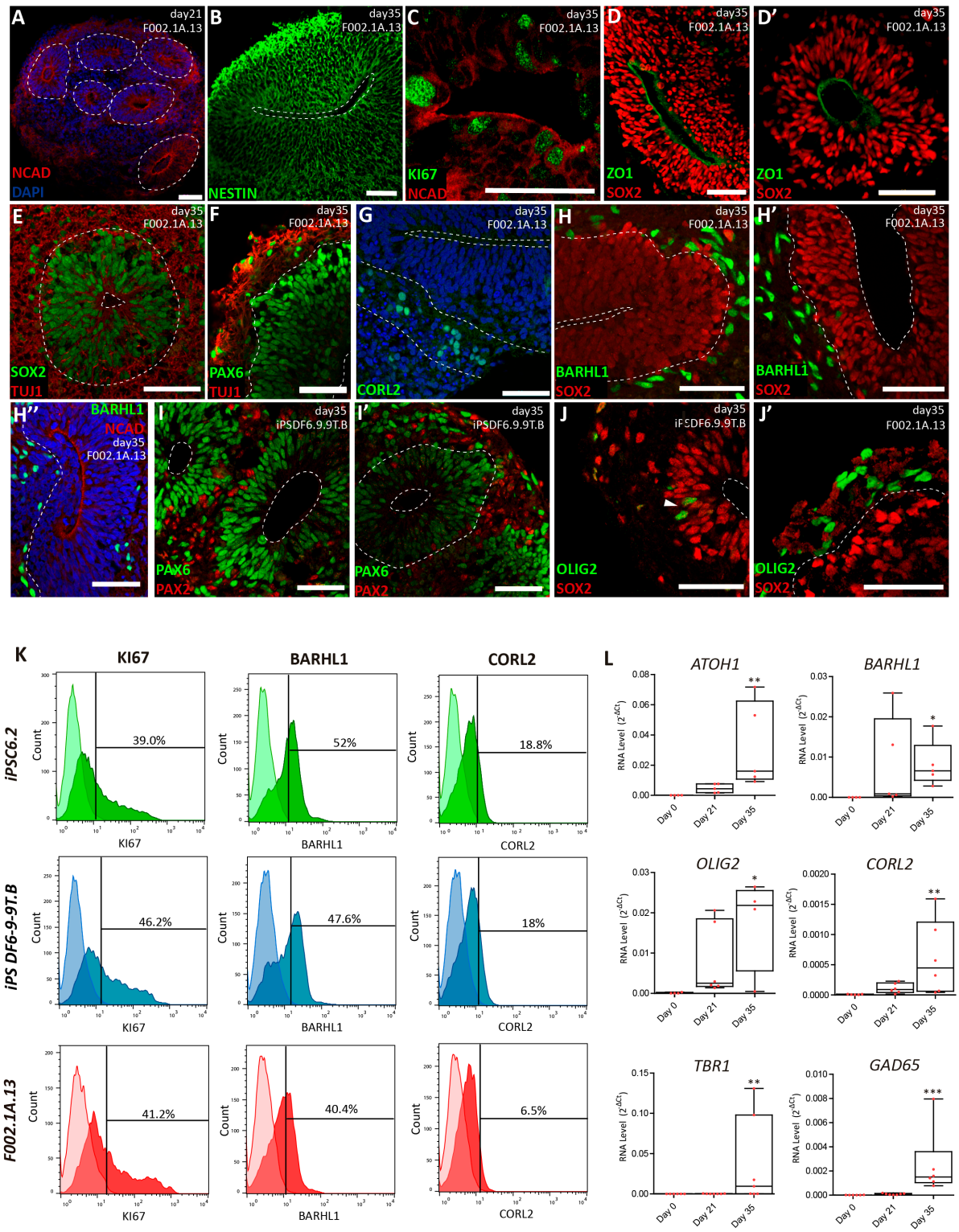

FIGURE 2 | Cerebellar progenitors self-organize into structures reminiscent of the neural tube. **(A–J)** Immunofluorescence analysis on days 21 and 35 of differentiation of the indicated iPSC lines. Blue staining corresponds to nuclei labeled with DAPI. **(A)** Dashed lines delineate neural rosettes containing a lumen-like center marked by N-Cadherin (NCAD). **(B)** Neuro-epithelial rosette stained for Nestin. **(C)** Proliferating cells positive for KI67 located close to the lumen marked by NCAD. **(D,D')** Apical layer of SOX2 positive cells surrounding the lumen marked by ZO1, a tight junction protein. **(E)** Dashed lines delineate the lumen and the boundary between the apical layer of SOX2 positive cells and the basal layer containing cells expressing neuron-specific class III beta-tubulin (TUJ1). **(F)** Dashed line

(Continued)

FIGURE 2 | Continued
delineates the boundary between the apical layer of PAX6 positive cells and the basal layer containing cells expressing TUJ1. **(G)** Dashed lines delineate the lumen and the boundary between the apical and basal layers; cells stained green express CORL2, a marker of Purkinje cell precursors. **(H,H')** Dashed lines delineate the lumen and the boundary between the apical layer of SOX2 positive cells and the basal layer containing cells expressing BARHL1, a marker for granule cell precursors. **(H")** Dashed line delineates the boundary between the apical layer (lumen marked by NCAD) and the basal layer containing cells expressing BARHL1. **(I,I')** Dashed lines delineate the lumen and the boundary between the apical layer of PAX6 positive cells and the basal layer containing cells expressing PAX2, a marker for GABAergic interneurons. **(J)** Dashed line delineates the lumen; arrowhead indicates cells expressing OLIG2 (a marker for newly formed Purkinje cells) interspersed among SOX2 positive cells. **(J')** Dashed line delineates the boundary between the apical layer of SOX2 positive cells and the basal layer containing cells expressing OLIG2. Scale bars, 50 μm. **(K)** Flow cytometry analysis of cells expressing KI67, BARHL1 and CORL2 on day 35 of differentiation of the indicated iPSC lines ($n = 3$ per marker). **(L)** qRT-PCR analysis of cultures derived from F002.1A.13 cells at the indicated time points. The graphs depict mRNA expression levels ($2^{-\Delta Ct}$) relative to GAPDH. Each dot represents data from an independent experiment ($n = 5$). One-way ANOVA (Dunn's Multiple Comparison Test), $^{*}p < 0.05$, $^{**}p < 0.01$, $^{***}p < 0.001$; error bars represent SEM.

located layer (**Figures 2E,F** and **Supplementary Figure S3C**). Cells located in the basal compartment expressed markers for precursors of Purkinje and granule cells, respectively CORL2 (**Figure 2G**) and BARHL1 (**Figures 2H,H',H"** and **Supplementary Figure S3D**), and the marker for maturing GABAergic neurons GAD65 (**Supplementary Figure S3E**). Basally located cells further expressed PAX2 (**Figures 2I,I'** and **Supplementary Figure S3F**), which is a marker of GABAergic interneurons and their precursors in the developing cerebellum (Zhang and Goldman, 1996; Maricich and Herrup, 1999). Cells positive for OLIG2, a transcription factor expressed in neurogenic progenitors and nascent Purkinje cells (Seto et al., 2014; Ju et al., 2016), were also predominantly located in the basal layer (**Figures 2J,J'** and **Supplementary Figures S3G,G'**).

The proportion of different cell populations within the aggregates was quantified by flow cytometry (**Figure 2K**). At day 35, 3D aggregates were composed by 42.1 ± 2.1% of $KI67^+$ proliferating cells, 46.7 ± 3.4% of $BARHL1^+$ granule cell precursors, and 14.4 ± 3.9% of $CORL2^+$ Purkinje cell precursors (Means ± SEM of the three iPSC lines). Significant levels of mRNAs encoding specific markers for different types of cerebellar neurons were also detected by qRT-PCR on day 35 (**Figure 2L**). These markers included, in addition to BARHL1, OLIG2, CORL2, and GAD65, the transcription factor ATOH1 (required for differentiation of cerebellar granule neurons) and TBR1 (expressed in deep cerebellar nuclei).

Maturation of Cerebellar Neurons in 2D Culture

To promote further maturation of cerebellar neurons, aggregates were dissociated on day 35. Cells were then transferred to laminin-coated plates and cultured in serum-free BrainPhys™ medium (Bardy et al., 2015) supplemented with BDNF and GDNF (**Figure 1A**). After 15 days in 2D culture, i.e., on day 50 and onward, cells were analyzed by immunofluorescence, flow cytometry and qRT-PCR (**Figure 3**). Immunofluorescence was performed using antibodies to microtubule-associated protein 2 (MAP2), a neuron-specific protein that stabilizes microtubules in the dendrites of postmitotic neurons. The results revealed $MAP2^+$ neurons with the nuclei stained for PAX6 and BARHL1 (**Figures 3A,B** and **Supplementary Figures S4A,B**), suggesting that these were granule cells. The quantification of $BARHL1^+$ cells by flow cytometry (**Figure 3C**) revealed a value of 46.2 ± 1.9% (Mean ± SEM of the three iPSC lines) on day 50, which is similar to the proportion of $BARHL1^+$ cells found in 3D aggregates on day 35 (**Figure 2K**). The 2D cultures further showed distinct types of $MAP2^+$ neurons with the nuclei stained for either TBR1 (**Figure 3D** and **Supplementary Figure S4C**), which identifies precursors of deep cerebellar nuclei projection neurons (Fink, 2006), or TBR2 (**Figure 3E** and **Supplementary Figure S4D**), which identifies precursors of unipolar brunch cells. Additional neurons expressed neurogranin in the cytoplasm (NRGN, **Figures 3F,G** and **Supplementary Figures S4E,F**) and PAX2 in the nucleus (**Figure 3G** and **Supplementary Figure S4F**), which are markers of Golgi cells (Singec et al., 2004; Leto and Rossi, 2012). Furthermore, immunostaining analysis using an antibody to calbindin (CALB), a calcium-binding protein highly expressed in Purkinje cells, revealed multiple positive cells (**Figure 3H**). In other neurons, immunostaining did not detect CALB but these cells were recognized by anti-parvalbumin antibodies (PVALB, **Figure 3H** and **Supplementary Figure S4G**, red staining), indicating that they were likely the precursors of GABAergic interneurons. Consistent with these immunofluorescence results, significant levels of mRNAs encoding the transcription factors PAX2, BARHL1, TBR1, and TBR2, as well as hallmark proteins of differentiated neurons, including the calmodulin-binding protein NRGN and the calcium-binding protein PVALB were detected by qRT-PCR analysis on days 56 and 80 (**Figure 3I**). Additionally, mRNAs encoding the GABAergic marker GAD65 and the glutamatergic marker VGLUT1 were significantly increased by day 80 of differentiation (**Supplementary Figure S4H**).

Immunofluorescence analysis further revealed that 2D cultures derived from the three iPSC lines differentiated for 56, 80, or 145 days had neurons expressing markers of Purkinje cells, including the calcium-binding protein calbindin (CALB, **Figures 4A–A""**), the Purkinje cell protein 2 (PCP2/L7, **Figure 4B**), aldolase C (ALDOC, also known as "zebrin II", **Figures 4C–C"**), a brain type isozyme of a glycolysis enzyme, and the LIM-homeodomain transcription factor LHX5 (**Figure 4D** and **Supplementary Figure S5**). In agreement with these results, significant levels of mRNA encoding L7, ALDOC and LHX5 were detected by qRT-PCR analysis of cultures

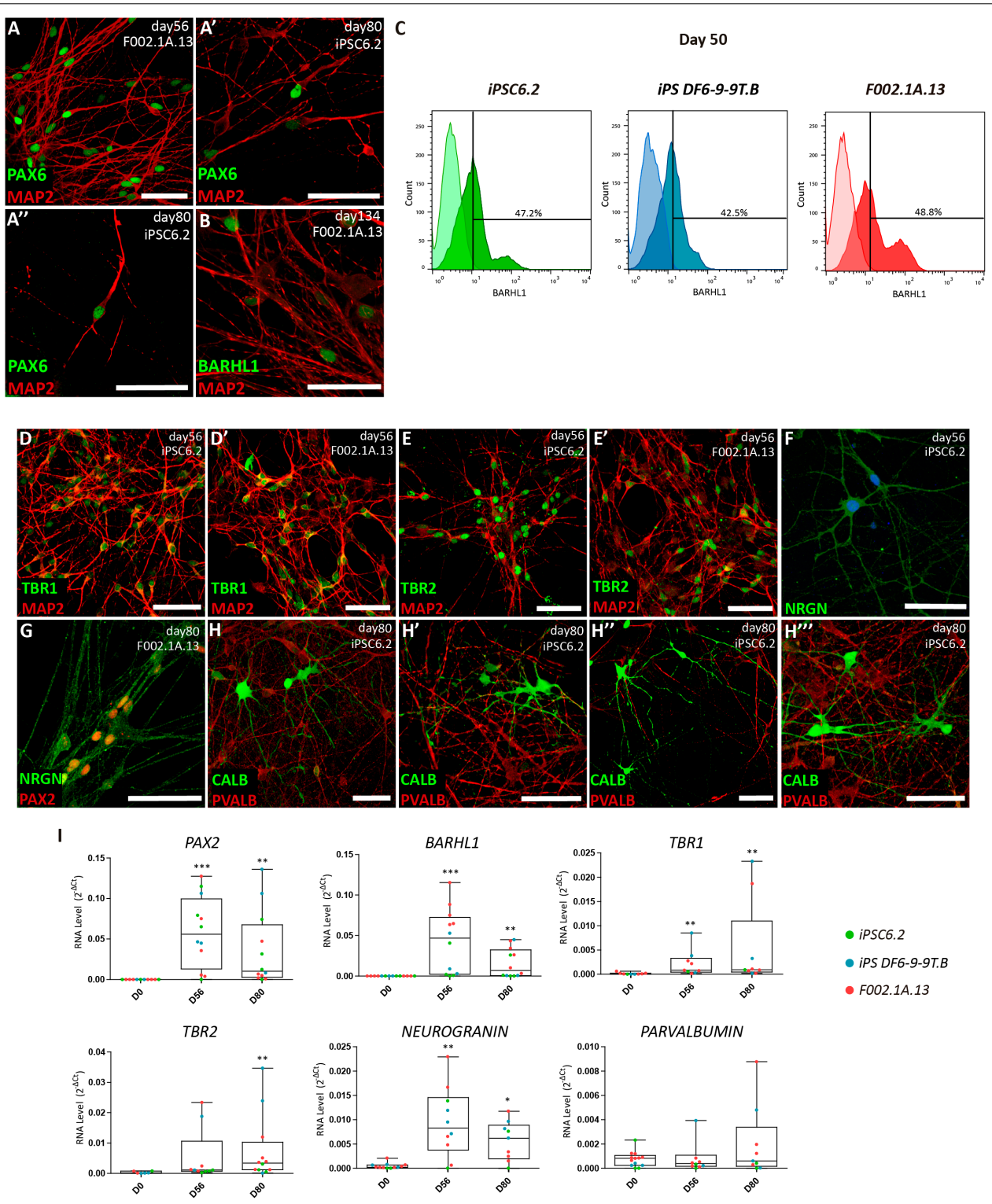

FIGURE 3 | Maturation of distinct types of cerebellar neurons in 2D culture. **(A,B)** Immunofluorescence analysis on days 56, 80, and 134 of differentiation of the indicated iPSC lines. The depicted MAP2^{+} neurons have the nuclei stained for PAX6 and BARHL1. Scale bars, 50 μm. **(C)** Flow cytometry analysis of BARHL1^{+} cells on day 50 of differentiation of the indicated iPSC lines. **(D–H)** Immunofluorescence analysis on days 56 and 80 of differentiation of iPSC lines using the indicated antibodies. In panel F, nuclei are stained with DAPI (blue). Scale bars, 50 μm. **(A', A'', E', H'–H''')** are used for different captures using the same antibodies combinations, regardless of the iPSC line and differentiation day. **(I)** qRT-PCR analysis of cultures derived from each iPSC line at the indicated time-points. Box-plot diagrams depict mRNA expression levels ($2^{-\Delta Ct}$) relative to GAPDH. Each color-coded dot represents data from one differentiation experiment. One-way ANOVA (Dunn's Multiple Comparison Test), $^{*}p < 0.05$, $^{**}p < 0.01$, $^{***}p < 0.001$; error bars represent SEM.

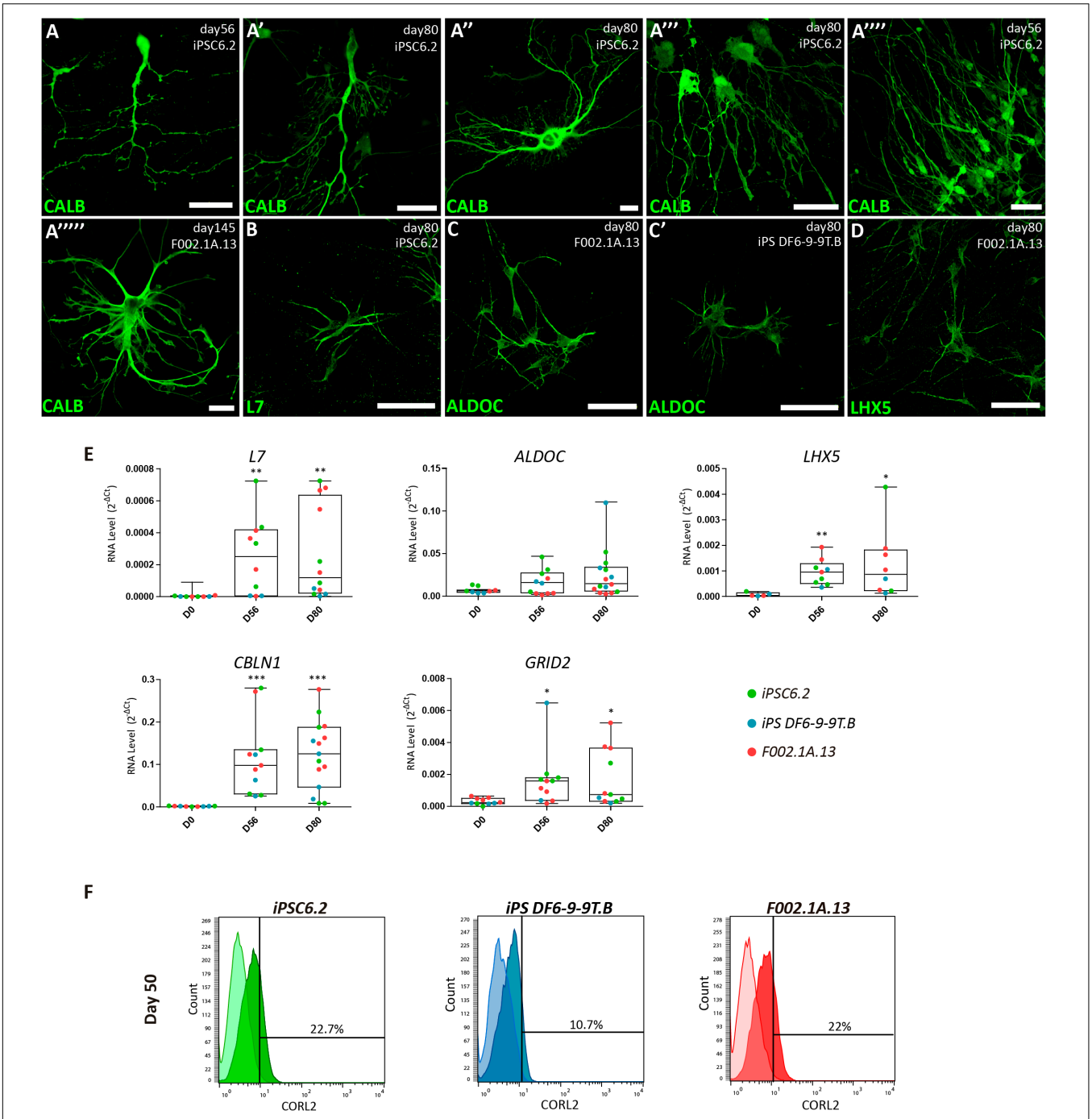

FIGURE 4 | Characterization of Purkinje cells in 2D culture. **(A–D)** Immunofluorescence analysis on days 56, 80, and 145 of differentiation of the indicated iPSC lines using specific markers for Purkinje cells. Scale bars, 50 μm. **(E)** qRT-PCR analysis of cultures derived from each iPSC line at the indicated time-points. Box-plot diagrams depict mRNA expression levels ($2^{-\Delta Ct}$) relative to GAPDH. Each color-coded dot represents data from one differentiation experiment. One-way ANOVA (Dunn's Multiple Comparison Test), $*p < 0.05$, $**p < 0.01$, $***p < 0.001$; error bars represent SEM. **(F)** Flow cytometry analysis of CORL2^{+} cells on day 50 of differentiation of the indicated iPSC lines.

derived from the three iPSC lines differentiated for 56 and 80 days (**Figure 4E**). Additionally, we detected expression of mRNAs encoding the Purkinje cell-specific glutamate receptor GRID2, and the glycoprotein CBLN1 that controls synaptic plasticity and synapse integrity of Purkinje cells (**Figure 4E**). To determine the proportion of Purkinje cells in 2D cultures, flow cytometry was used to quantify CORL2^{+} cells. The results show that depending on the iPSC line, the percentage of

post-mitotic Purkinje cells on day 50 ranged around 10 and 20% (**Figure 4F**).

Assessing the Maturity of Cerebellar Neurons in 2D Culture

In order to assess the maturation of the cerebellar neurons, we next performed SCCI. Cells were preloaded with the calcium indicator fluorescent dye Fura-2 that switches its excitation peak from 340 to 380 nm in response to calcium binding, allowing the concentration of intracellular calcium to be determined based on the ratio of fluorescence emission after sequential excitation at 340 and 380 nm (Grienberger and Konnerth, 2012). Cells were stimulated by exposure to KCl at different time-points. If cells were differentiated into excitable neurons, high KCl concentrations were expected to induce the opening of voltage sensitive calcium channels resulting in massive influx of calcium into the cytoplasm (Ambrósio et al., 2000; Macías et al., 2001). Elevations in cytosolic calcium concentration (visualized by increased fluorescence ratios) were indeed observed in cells cultured for 50 days (**Supplementary Figures S6A,B**). These results confirm that our iPSC-derived cultures produced excitable neurons.

In contrast to differentiated neurons, stem cells and neuronal progenitors express functional histamine receptors (Agasse et al., 2008; Molina-Hernández and Velasco, 2008; Rodríguez-Martínez et al., 2012). KCl depolarization causes an increase in calcium concentration in neurons, whereas stimulation with histamine leads to an increase in calcium concentration in stem/progenitor cells (Agasse et al., 2008; Rodrigues et al., 2017). We therefore measured variations in intracellular free calcium concentration following 50 mM KCl and 100 μM histamine stimulation to discriminate between progenitors and differentiated neurons in our cultures (**Supplementary Figure S6C**). Histamine/KCl ratios were calculated using the corresponding peak values given by the normalized ratios of fluorescence at 340/380 nm. Neurons typically depict ratios below 0.8 whereas progenitor cells have ratios between 1 and 1.3 (Agasse et al., 2008; Rodrigues et al., 2017). Quantification of the percentage of cells displaying a Histamine/KCl ratio below 0.8 showed that on day 42 of differentiation, approximately 80% of cells in iPS-DF6-9-9T.B and iPSC6.2-derived cultures exhibited properties of differentiated neurons while in the F002.1A.13-derived culture approximately half of the cells were still progenitors (**Figure 5A**). Remarkably, by day 80 the vast majority of cells in either culture behaved as differentiated neurons (**Figure 5A**), indicating that neuronal differentiation was a gradual and continuous time-dependent process in our 2D cultures.

Consistent with the results from SCCI analysis, immunofluorescence on day 50 revealed cells staining for PAX6 but not expressing MAP2 or the astrocyte marker glial fibrillary acidic protein (GFAP), revealing the presence of progenitor cells in these cultures (**Supplementary Figures S6D,E**). In contrast, on day 80, the cultures consisted predominantly of a dense $MAP2^+$ neuronal network with some scattered $GFAP^+$ astrocytes (**Supplementary Figures S6F,G**). This finding suggests that by day 80 the cultures were mainly composed of differentiated neurons and glial cells. Moreover, we used flow cytometry to quantify the proportion of cells expressing HuC/HuD (HuC/D), which are RNA-binding proteins expressed specifically in newborn neurons (Abranches et al., 2009). As expected, the proportion of HuC/D^+ newborn neurons in 2D cultures decreased from 72–76% on day 50 to 31–38% on day 80 (**Figure 5B**).

Because the morphology of dendritic spines changes during neuronal maturation (Hering and Sheng, 2001; Risher et al., 2014), we measured spine head width and neck length as shown in **Figure 5C**. Dendritic spines were classified as follows: Filopodia (length $>$ 2 μm); Long thin (length $<$ 2 μm); Thin (length $<$ 1 μm); Stubby (length/width ratio $<$ 1 μm); Mushroom (width $>$ 0.6 μm), and Branched (2 or more heads), as previously described (Risher et al., 2014). As shown in **Figure 5C**, from day 56 to day 81, the relative proportion of more mature branched spines increased, further confirming the progressive maturation of neurons over time in 2D culture.

Finally, we evaluated the electrophysiological properties of differentiated cells by using patch-clamp recordings. Cells analyzed on days 56 through 118 presented typical neuronal fire action potentials upon a current injection and were also able to depolarize, repolarize and recover, responding to a second current injection (**Figures 6A,B**). Most cells analyzed after 80 days of differentiation were spiking and showed high amplitude action potential (indicative of expression of voltage-dependent Na^+ channels) and reduced spike width (indicative of abundant K^+ channels), as expected for differentiated neurons. Furthermore, spontaneous currents were recorded, which indicates the presence of synaptic connections (**Figure 6C** and **Supplementary Figure S7A**). A subset of these currents remained in the presence of the sodium channel blocker TTX (indicative that they are independent of action potential generation) and of specific antagonists of ionotropic glutamate receptors, CNQX and DL-APV, suggestive of the existence of functional GABAergic synapses. Addition of the $GABA_A$ receptor antagonist bicuculline completely abolished all activity (**Figures 6C,D**), confirming that the previously recorded miniature events indeed resulted from the spontaneous activity of GABAergic synapses. To confirm these spontaneous inhibitory and excitatory outputs, GABAergic activity was first inhibited by using bicuculline (**Supplementary Figure S7B**). Indeed, a subset of spontaneous currents were maintained, suggesting the presence of Glutamatergic activity (**Supplementary Figure S7B**). Addition of CNQX and DL-APV completely blocked the synaptic activity (**Supplementary Figure S7B**), which confirmed the existence of Glutamatergic synapses. These data show first, that neurons in 2D culture established functional connections and second, that an active GABAergic and Glutamatergic neuronal network was created.

DISCUSSION

Using only a defined medium and without the need for co-culturing the cells, we successfully generated reproducible network-forming GABAergic and Glutamatergic cerebellar neurons derived from three distinct human iPSC lines.

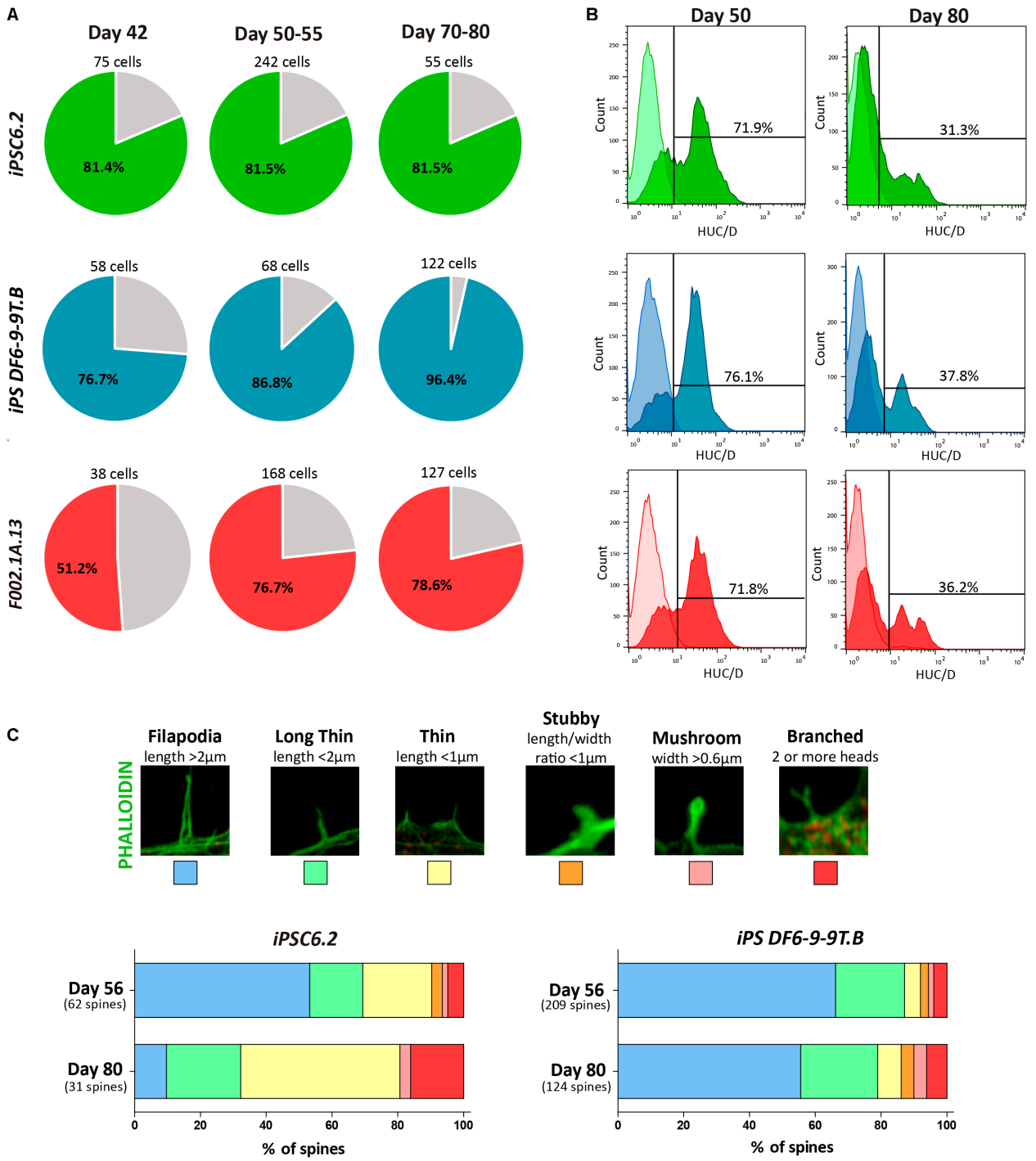

FIGURE 5 | Assessment of neuronal maturation. **(A)** The percentage of responsive cells displaying a Histamine/KCl ratio below 0.8 is shown in colored slices. For each iPSC line three independent differentiation experiments were performed. **(B)** Flow cytometry analysis of HuC/D^{+} cells on days 50 and 80 of differentiation of the indicated iPSC lines. **(C)** Representative images of dendritic spine morphologies. Bars depict the relative proportion of the distinct dendritic spine morphologies observed in cultures derived from the indicated iPSC lines on days 56 and 80.

We started with a 3D culture system and we controlled the sizes of cell aggregates as previously described (Ungrin et al., 2008), leading to an efficient neuronal commitment (Bauwens et al., 2008; Miranda et al., 2015). We produced hundreds of cell aggregates per cm^2, which is a significant increase over the 96-well plates used by most cerebellar

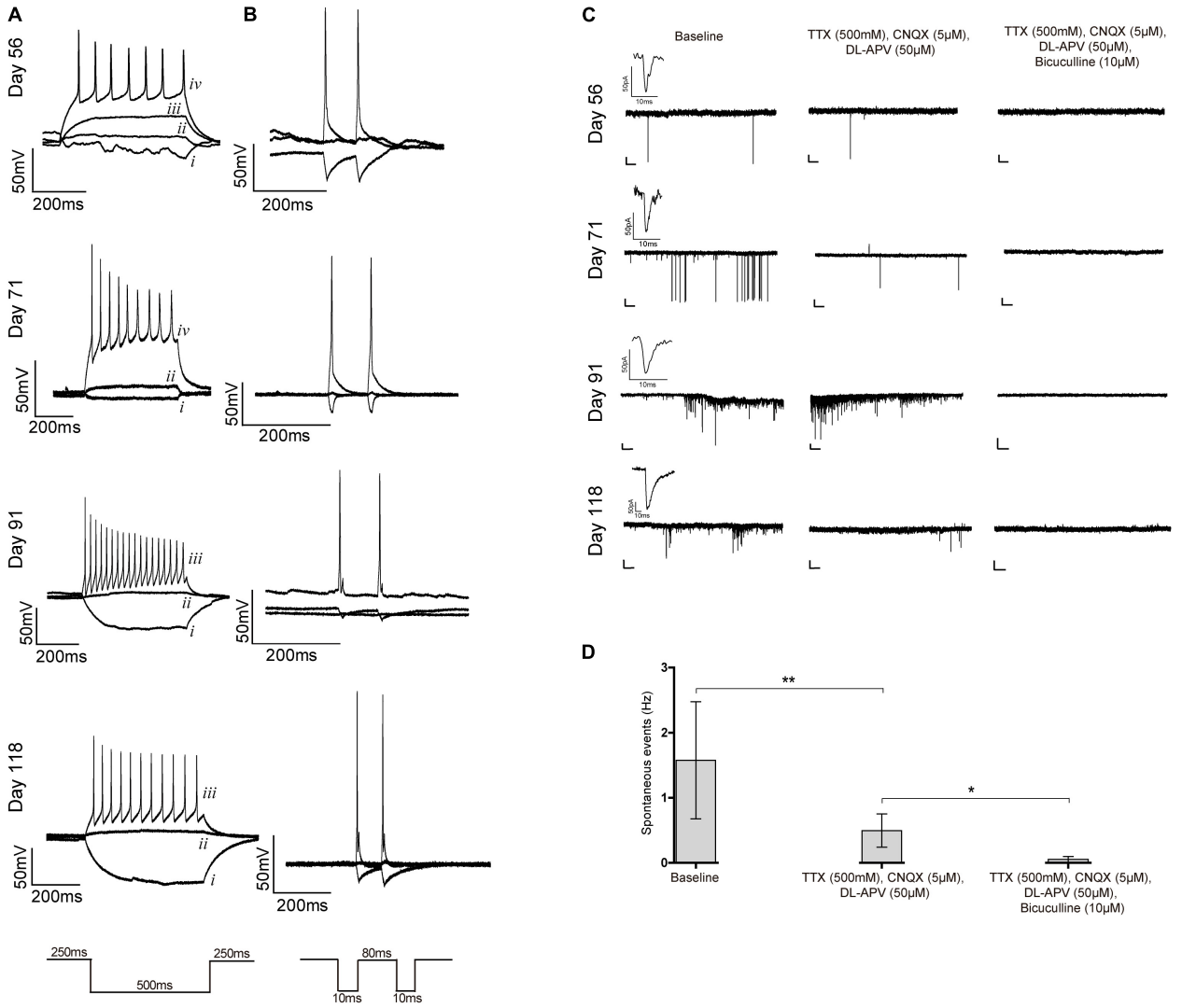

FIGURE 6 | Patch-clamp recordings. **(A–C)** Whole-cell patch clamp recordings for iPSC6.2-derived neurons on the indicated days of differentiation. **(A)** Representative traces of firing responses evoked by 500 ms current pulses. Each trace corresponds to a single injection current of –25 pA (*i*), 0 pA (*ii*), +25 pA (*iii*) or +50 pA (*iv*). **(B)** Firing responses to two independent current injections (10 ms) separated by 80 ms. **(C)** Representative traces of spontaneous postsynaptic currents recorded without any treatment (left), after blocking voltage dependent sodium channels using TTX and ionotropic glutamate receptors with CNQX and DL-APV (middle), and $GABA_A$ receptors with bicuculline (right); an example of a miniature postsynaptic current is also shown in each case. Recordings in each row are from the same cell on the indicated days in culture. Scale bars correspond to 50 pA and 2000 ms. **(D)** Frequency of spontaneous events recorded without any treatment (baseline) and after addition of the indicated blockers. Data from three independent differentiation experiments using iPCS6.2-derived cells. Student's *t*-test (two-tailed) statistics, $^{**}p < 0.05$, $^{**}p < 0.01$; error bars represent SEM.

differentiation protocols previously described (Ungrin et al., 2008; Bratt-Leal et al., 2009; Muguruma et al., 2015; Wang et al., 2015). We cultured cells in chemically defined medium with sequential addition of FGF2, SB, FGF19, and SDF1 to induce the spontaneous formation of a cerebellar plate neuroepithelium, which differentiated into a multilayered structure reminiscent of cerebellar ontogenesis *in vivo* (Muguruma et al., 2015; Ishida et al., 2016). The initial stage of cerebellar commitment in 3D aggregates was detected on day 7, when expression of *FGF8* mRNA was at its highest and dropped thereafter. This *in vitro* behavior recapitulates cerebellar ontogenesis *in vivo* (reviewed in Marzban et al., 2015). Indeed, previous *in vivo* studies have shown that at early embryonic stages FGF signaling is required to establish the cerebellar territory, however, its suppression afterward is essential for cerebellar development (Suzuki-Hirano et al., 2010; Butts et al., 2014).

In our study, cell aggregates formed neural tube-like structures organized in layers with apico-basal polarity. Most important, compared to findings from a previous study (Muguruma et al., 2015), the aggregates in our cultures exhibited an earlier neuronal differentiation pattern. On day 35, cells

were already positive for OLIG2, CORL2, and BARHL1. OLIG2 is the earliest marker for Purkinje cells, and is associated with cell cycle exit and differentiation into post-mitotic neurons (Takebayashi et al., 2002; Seto et al., 2014; Ju et al., 2016). CORL2 is specifically expressed in post-mitotic Purkinje cell precursors shortly after exiting the cell cycle (Minaki et al., 2008) and plays an essential role in Purkinje cell development (Wang et al., 2011; Nakatani et al., 2014). In contrast, BARHL1 is expressed in migrating granule cell precursors (Bulfone et al., 2000). These results indicate that Purkinje and granule cell precursors formed in our iPSC-derived cultures by day 35. Our cultures further had cells positive for GAD65, the protein glutamic acid decarboxylase isoform 65, which is a rate-limiting GABA synthesizing enzyme localized primarily on presynaptic boutons (Esclapez et al., 1994). Because the onset of GAD65 expression in the cerebellum occurs after synaptogenesis (Greif et al., 1991), we conclude that an interconnected neuronal network formed in our cultures by day 35.

Our differentiation strategy replaces co-culture by a defined basal medium optimized for neuronal cell culture (Bardy et al., 2015). Upon dissociation of cell aggregates on day 35 and re-plating on a laminin-coated surface, cerebellar precursors differentiated without the need for co-culturing. Remarkably, our 2D cultures remained viable for up to 145 days. On day 50, the percentage of post-mitotic Purkinje precursors ($CORL2^+$) in the 2D cultures ranged around 10 and 20%, depending on the iPSC line. The presence of cells expressing calbindin, a calcium-binding protein highly abundant in Purkinje cells (Nag and Wadhwa, 1999; Whitney et al., 2008), as well as additional late markers of Purkinje cells, including the Purkinje cell protein 2 (PCP2/L7, Oberdick et al., 1988; Zhang et al., 2002), the glycolysis enzyme aldolase C (ALDOC, Royds et al., 1987), the transcription factor LHX5 (Zhao et al., 2007), and the Purkinje cell-specific glutamate receptor GRID2 (Araki et al., 1993), strongly indicates that our culture conditions support the development of Purkinje cells by day 80 and onward.

Furthermore, our cultures had $MAP2^+$ neurons with distinctive morphology that stained for PAX6 in the nucleus, suggesting that these were granule cells. Another subset of neurons in our cultures were negative for calbindin but expressed parvalbumin, suggesting that they were GABAergic interneurons (Bastianelli, 2003). Others showed a strong positive signal for neurogranin and PAX2, which is highly expressed in Golgi cells in the mouse cerebellum (Singec et al., 2004; Leto and Rossi, 2012). Furthermore, $MAP2^+$ neurons expressing either TBR1 or TBR2 in the nucleus revealed the formation of deep cerebellar nuclei projection neurons (Fink, 2006) and unipolar brush cells (Englund, 2006), respectively.

Taken together, the results obtained with SCCI and patch-clamp recordings demonstrate that our culture conditions support the differentiation of iPSCs into electrophysiologically active cerebellar neurons. In particular, the presence of synaptic connections shows that a functional neuronal network has been generated.

Although we observed a progressive maturation of neurons over time in 2D culture, our cells did not reach the level of neuronal maturation equivalent to that occurring in post-natal human cerebellum. This is particularly evident for Purkinje cells, which in our cultures did not form the elaborated dendritic branches observed *in vivo*. Further studies should search for additional signaling molecules that are necessary, for *in vitro* differentiated cells to fully recapitulate the maturation processes that occur in the developing human cerebellum.

CONCLUSION

Here we show for the first time that is possible to generate different types of electrophysiologically active GABAergic and glutamatergic cerebellar neurons in long-term cultures without co-culturing with other cell types. Our findings represent an important contribution toward the development of autologous replacement strategies for the treatment of cerebellar degenerative diseases. Additionally, functional cerebellar neurons are an important cell source for drug screening and for the study of specific pathways involved with the development of cerebellar diseases such as ataxias, a group of disorders that affect many children and adults worldwide.

DATA AVAILABILITY STATEMENT

All datasets generated for this study are included in the article/**Supplementary Material**.

AUTHOR CONTRIBUTIONS

All authors contributed to design research. TS performed the culture cell differentiations and cell culture characterization. EB, TF, and CR assisted with cell culture maintenance and growth. TF assisted with flow cytometry experiments. EB and TF contributed with data analysis. TS and SV performed the single cell calcium imaging and patch clamp experiments. TS and MC-F wrote the manuscript.

FUNDING

This work was supported by the Fundação para a Ciência e a Tecnologia (FCT), Portugal (UID/BIO/04565/2013 and SFRH/BD/105773/2014 to TS, SFRH/BPD/81627/2011 to SV); projects co-funded by FEDER (POR Lisboa 2020—Programa Operacional Regional de Lisboa PORTUGAL 2020) and FCT through grant PAC-PRECISE LISBOA-01-0145-FEDER-016394 and CEREBEX Generation of Cerebellar Organoids for Ataxia Research grant LISBOA-01-0145-FEDER-029298. Funding was also received from the European Union's Horizon 2020 Research and Innovation programme, under the Grant Agreement number 739572—The Discoveries Centre for Regenerative and Precision Medicine H2020-WIDESPREAD-01-2016-2017.

ACKNOWLEDGMENTS

We thank Professor Giampietro Schiavo (UCL Institute of Neurology, United Kingdom) for insightful discussions and advice. We are grateful to our iMM colleagues Marcia Triunfol for her help in preparing the manuscript, Professor Ana Sebastião for her help in interpreting electrophysiology experiments, members of the bioimaging facility for helping with confocal microscopy, members of the rodent facility for helping with animal experiments, and Tânia Carvalho for doing the teratoma analysis. We are also grateful to Sónia Santos (GenoMed SA, Lisbon, Portugal) for karyotype analysis.

SUPPLEMENTARY MATERIAL

The Supplementary Material for this article can be found online at: https://www.frontiersin.org/articles/10.3389/fbioe.2020.00070/full#supplementary-material

REFERENCES

Abranches, E., Silva, M., Pradier, L., Schulz, H., Hummel, O., Henrique, D., et al. (2009). Neural differentiation of embryonic stem cells in vitro: a road map to neurogenesis in the embryo. *PLoS One* 4:e6286. doi: 10.1371/journal.pone.0006286

Adamaszek, M., D'Agata, F., Ferrucci, R., Habas, C., Keulen, S., Kirkby, K. C., et al. (2017). Consensus paper: cerebellum and emotion. *Cerebellum* 16, 552–576. doi: 10.1007/s12311-016-0815-818

Agasse, F., Bernardino, L., Silva, B., Ferreira, R., Grade, S., and Malva, J. O. (2008). Response to histamine allows the functional identification of neuronal progenitors, neurons, astrocytes, and immature cells in subventricular zone cell cultures. *Rejuvenation Res.* 11, 187–200. doi: 10.1089/rej.2007.0600

Akopian, V., Andrews, P. W., Beil, S., Benvenisty, N., Brehm, J., Christie, M., et al. (2010). Comparison of defined culture systems for feeder cell free propagation of human embryonic stem cells. *Vitro Cell. Dev. Biol. Anim.* 46, 247–258. doi: 10.1007/s11626-010-9297-z

Ambrósio, A. F., Silva, A. P., Malva, J. O., Mesquita, J. F., Carvalho, A. P., and Carvalho, C. M. (2000). Role of desensitization of AMPA receptors on the neuronal viability and an the [Ca2+](i) changes in cultured rat hippocampal neurons. *Eur. J. Neurosci.* 12, 2021–2031. doi: 10.1046/j.1460-9568.2000.00091.x

Andreu, A., Crespo-Enriquez, I., and Echevarria, D. (2014). Molecular events directing the patterning and specification of the cerebellum. *Eur. J. Anat.* 18, 245–252.

Araki, K., Meguro, H., Kushiya, E., Takayama, C., Inoue, Y., and Mishina, M. (1993). Selective expression of the glutamate receptor channel δ2 subunit in cerebellar Purkinje cells. *Biochem. Biophys. Res. Commun.* 197, 1267–1276. doi: 10.1006/bbrc.1993.2614

Bardy, C., van den Hurk, M., Eames, T., Marchand, C., Hernandez, R. V., Kellogg, M., et al. (2015). Neuronal medium that supports basic synaptic functions and activity of human neurons in vitro. *Proc. Natl. Acad. Sci. U.S.A.* 112, E2725–E2734. doi: 10.1073/pnas.1504393112

Bastianelli, E. (2003). Distribution of calcium-binding proteins in the cerebellum. *Cerebellum* 2, 242–262. doi: 10.1080/14734220310022289

Bauwens, C. L., Peerani, R., Niebruegge, S., Woodhouse, K., Kumacheva, E., Husain, M., et al. (2008). Control of human embryonic stem cell colony and aggregate size heterogeneity influences differentiation trajectories. *Stem Cells* 26, 2300–2310. doi: 10.1634/stemcells.2008-2183

Bratt-Leal, A. M., Carpenedo, R. L., and McDevitt, T. C. (2009). Engineering the embryoid body microenvironment to direct embryonic stem cell differentiation. *Biotechnol. Prog.* 25, 43–51. doi: 10.1002/btpr.139

Bulfone, A., Menguzzato, E., Broccoli, V., Marchitiello, A., Gattuso, C., Mariani, M., et al. (2000). Barhl1, a gene belonging to a new subfamily of mammalian homeobox genes, is expressed in migrating neurons of the CNS. *Hum. Mol. Genet.* 9, 1443–1452. doi: 10.1093/hmg/9.9.1443

Burridge, P. W., Thompson, S., Millrod, M. A., Weinberg, S., Yuan, X., Peters, A., et al. (2011). A universal system for highly efficient cardiac differentiation of human induced pluripotent stem cells that eliminates interline variability. *PLoS One* 6:e18293. doi: 10.1371/journal.pone.0018293

Butts, T., Green, M. J., and Wingate, R. J. T. (2014). Development of the cerebellum: simple steps to make a "little brain". *Development* 141, 4031–4041. doi: 10.1242/dev.106559

Chi, C. L., Martinez, S., Wurst, W., and Martin, G. R. (2003). The isthmic organizer signal FGF8 is required for cell survival in the prospective midbrain and cerebellum. *Development* 130, 2633–2644. doi: 10.1242/dev.00487

Englund, C. (2006). Unipolar brush cells of the cerebellum are produced in the rhombic lip and migrate through developing white matter. *J. Neurosci.* 26, 9184–9195. doi: 10.1523/JNEUROSCI.1610-06.2006

Erceg, S., Lukovic, D., Moreno-Manzano, V., Stojkovic, M., and Bhattacharya, S. S. (2012). Derivation of cerebellar neurons from human pluripotent stem cells. *Curr. Protoc. Stem Cell Biol.* 20, 1H.5.1–1H.5.10. doi: 10.1002/9780470151808.sc01h05s20

Erceg, S., Ronaghi, M., Zipancic, I., Lainez, S., Roselló, M. G., Xiong, C., et al. (2010). Efficient differentiation of human embryonic stem cells into functional cerebellar-like cells. *Stem Cells Dev.* 19, 1745–1756. doi: 10.1089/scd.2009.0498

Esclapez, M., Tillakaratne, N. J., Kaufman, D. L., Tobin, A. J., and Houser, C. R. (1994). Comparative localization of two forms of glutamic acid decarboxylase and their mRNAs in rat brain supports the concept of functional differences between the forms. *J. Neurosci.* 14, 1834–1855. doi: 10.1523/jneurosci.14-03-01834.1994

Felix-Oliveira, A., Dias, R. B., Colino-Oliveira, M., Rombo, D. M., and Sebastiao, A. M. (2014). Homeostatic plasticity induced by brief activity deprivation enhances long-term potentiation in the mature rat hippocampus. *J. Neurophysiol.* 112, 3012–3022. doi: 10.1152/jn.00058.2014

Fink, A. J. (2006). Development of the deep cerebellar nuclei: transcription factors and cell migration from the rhombic lip. *J. Neurosci.* 26, 3066–3076. doi: 10.1523/JNEUROSCI.5203-05.2006

Frantz, G. D., Weimann, J. M., Levin, M. E., and McConnell, S. K. (1994). Otx1 and Otx2 define layers and regions in developing cerebral cortex and cerebellum. *J. Neurosci.* 14, 5725–5740. doi: 10.1523/jneurosci.14-10-05725.1994

Greif, K. F., Erlander, M. G., Tillakaratne, N. J. K., and Tobin, A. J. (1991). Postnatal expression of glutamate decarboxylases in developing rat cerebellum. *Neurochem. Res.* 16, 235–242. doi: 10.1007/BF00966086

Grienberger, C., and Konnerth, A. (2012). Imaging calcium in neurons. *Neuron* 73, 862–885. doi: 10.1016/j.neuron.2012.02.011

Hentze, H., Soong, P. L., Wang, S. T., Phillips, B. W., Putti, T. C., and Dunn, N. R. (2009). Teratoma formation by human embryonic stem cells: evaluation of essential parameters for future safety studies. *Stem Cell Res.* 2, 198–210. doi: 10.1016/j.scr.2009.02.002

Hering, H., and Sheng, M. (2001). Dentritic spines: structure, dynamics and regulation. *Nat. Rev. Neurosci.* 2, 880–888. doi: 10.1038/35104061

Ishida, Y., Kawakami, H., Kitajima, H., Nishiyama, A., Sasai, Y., Inoue, H., et al. (2016). Vulnerability of purkinje cells generated from spinocerebellar ataxia type 6 patient-derived iPSCs. *Cell Rep.* 17, 1482–1490. doi: 10.1016/j.celrep.2016.10.026

Ju, J., Liu, Q., Zhang, Y., Liu, Y., Jiang, M., Zhang, L., et al. (2016). Olig2 regulates Purkinje cell generation in the early developing mouse cerebellum. *Sci. Rep.* 6:30711. doi: 10.1038/srep30711

Larsen, K. B., Lutterodt, M. C., Møllgård, K., and Møller, M. (2010). Expression of the homeobox genes OTX2 and OTX1 in the early developing human brain. *J. Histochem. Cytochem.* 58, 669–678. doi: 10.1369/jhc.2010.955757

Leto, K., Arancillo, M., Becker, E. B. E., Buffo, A., Chiang, C., Ding, B., et al. (2016). Consensus paper: cerebellar development. *Cerebellum* 15, 789–828. doi: 10.1007/s12311-015-0724-722

Leto, K., and Rossi, F. (2012). Specification and differentiation of cerebellar GABAergic neurons. *Cerebellum* 11, 434–435. doi: 10.1007/s12311-011-0324-328

Macías, W., Carlson, R., Rajadhyaksha, A., Barczak, A., and Konradi, C. (2001). Potassium chloride depolarization mediates CREB phosphorylation in striatal neurons in an NMDA receptor-dependent manner. *Brain Res.* 890, 222–232. doi: 10.1016/S0006-8993(00)03163-3162

Manto, M., and Marmolino, D. (2009). Animal models of human cerebellar ataxias: a cornerstone for the therapies of the twenty-first century. *Cerebellum* 8, 137–154. doi: 10.1007/s12311-009-0127-123

Maricich, S. M., and Herrup, K. (1999). Pax-2 expression defines a subset of GABAergic interneurons and their precursors in the developing murine cerebellum. *J. Neurobiol.* 41, 281–294. doi: 10.1002/(SICI)1097-4695(19991105)41

Marzban, H., Bigio, M. R., Del Alizadeh, J., Ghavami, S., Zachariah, R. M., and Rastegar, M. (2015). Cellular commitment in the developing cerebellum. *Front. Cell Neurosci.* 8:450. doi: 10.3389/fncel.2014.00450

McLachlan, N. M., and Wilson, S. J. (2017). The contribution of brainstem and cerebellar pathways to auditory recognition. *Front. Psychol.* 8:265. doi: 10.3389/fpsyg.2017.00265

Minaki, Y., Nakatani, T., Mizuhara, E., Inoue, T., and Ono, Y. (2008). Identification of a novel transcriptional corepressor, Corl2, as a cerebellar Purkinje cell-selective marker. *Gene Expr. Patterns* 8, 418–423. doi: 10.1016/j.gep.2008.04.004

Miranda, C. C., Fernandes, T. G., Pascoal, J. F., Haupt, S., Brüstle, O., Cabral, J. M. S., et al. (2015). Spatial and temporal control of cell aggregation efficiently directs human pluripotent stem cells towards neural commitment. *Biotechnol. J.* 10, 1612–1624. doi: 10.1002/biot.201400846

Mizuhara, E., Minaki, Y., Nakatani, T., Kumai, M., Inoue, T., Muguruma, K., et al. (2010). Purkinje cells originate from cerebellar ventricular zone progenitors positive for Neph3 and E-cadherin. *Dev. Biol.* 338, 202–214. doi: 10.1016/j.ydbio.2009.11.032

Molina-Hernández, A., and Velasco, I. (2008). Histamine induces neural stem cell proliferation and neuronal differentiation by activation of distinct histamine receptors. *J. Neurochem.* 106, 706–717. doi: 10.1111/j.1471-4159.2008.05424.x

Muguruma, K., Nishiyama, A., Kawakami, H., Hashimoto, K., and Sasai, Y. (2015). Self-organization of polarized cerebellar tissue in 3D culture of human pluripotent stem cells. *Cell Rep.* 10, 537–550. doi: 10.1016/j.celrep.2014.12.051

Muguruma, K., Nishiyama, A., Ono, Y., Miyawaki, H., Mizuhara, E., Hori, S., et al. (2010). Ontogeny-recapitulating generation and tissue integration of ES cell-derived Purkinje cells. *Nat. Neurosci.* 13, 1171–1180. doi: 10.1038/nn.2638

Nag, T. C., and Wadhwa, S. (1999). Calbindin immunoreactivity in the developing and adult human cerebellum. *J. Chem. Neuroanat.* 17, 1–12. doi: 10.1016/s0891-0618(99)00016-2

Nakatani, T., Minaki, Y., Kumai, M., Nitta, C., and Ono, Y. (2014). The c-Ski family member and transcriptional regulator Corl2/Skor2 promotes early differentiation of cerebellar Purkinje cells. *Dev. Biol.* 388, 68–80. doi: 10.1016/j.ydbio.2014.01.016

Oberdick, J., Levinthal, F., and Levinthal, C. (1988). A purkinje cell differentiation marker shows a partial DNA sequence homology to the cellular sis/PDGF2 gene. *Neuron* 1, 367–376. doi: 10.1016/0896-6273(88)90186-90189

Risher, W. C., Ustunkaya, T., Alvarado, J. S., and Eroglu, C. (2014). Rapid golgi analysis method for efficient and unbiased classification of dendritic spines. *PLoS One* 9:e107591. doi: 10.1371/journal.pone.0107591

Rodrigues, R. S., Ribeiro, F. F., Ferreira, F., Vaz, S. H., Sebastião, A. M., and Xapelli, S. (2017). Interaction between cannabinoid type 1 and type 2 receptors in the modulation of subventricular zone and dentate gyrus neurogenesis. *Front. Pharmacol.* 8:516. doi: 10.3389/fphar.2017.00516

Rodríguez-Martínez, G., Velasco, I., García-López, G., Solís, K. H., Flores-Herrera, H., Díaz, N. F., et al. (2012). Histamine is required during neural stem cell proliferation to increase neuron differentiation. *Neuroscience* 216, 10–17. doi: 10.1016/j.neuroscience.2012.04.049

Rombo, D. M., Dias, R. B., Duarte, S. T., Ribeiro, J. A., Lamsa, K. P., and Sebastião, A. M. (2016). Adenosine A1 receptor suppresses tonic GABAA receptor currents in hippocampal pyramidal cells and in a defined subpopulation of interneurons. *Cereb. Cortex* 26, 1081–1095. doi: 10.1093/cercor/bhu288

Royds, J. A., Ironside, J. W., Warnaar, S. O., Taylor, C. B., and Timperley, W. R. (1987). Monoclonal antibody to ALDOLASE C: a selective marker for Purkinje cells in the human cerebellum. *Neuropathol. Appl. Neurobiol.* 13, 11–21. doi: 10.1111/j.1365-2990.1987.tb00167.x

Salero, E., and Hatten, M. E. (2007). Differentiation of ES cells into cerebellar neurons. *Proc. Natl. Acad. Sci. U.S.A.* 104, 2997–3002. doi: 10.1073/pnas.0610879104

Schöls, L., Bauer, P., Schmidt, T., Schulte, T., and Riess, O. (2004). Autosomal dominant cerebellar ataxias: clinical features, genetics, and pathogenesis. *Lancet Neurol.* 3, 291–304. doi: 10.1016/S1474-4422(04)00737-739

Seto, Y., Ishiwata, S., and Hoshino, M. (2014). Characterization of Olig2 expression during cerebellar development. *Gene Expr. Patterns* 15, 1–7. doi: 10.1016/j.gep.2014.02.001

Singec, I., Knoth, R., Ditter, M., Volk, B., and Frotscher, M. (2004). Neurogranin is expressed by principal cells but not interneurons in the rodent and monkey neocortex and hippocampus. *J. Comp. Neurol.* 479, 30–42. doi: 10.1002/cne.20302

Su, H. L., Muguruma, K., Matsuo-Takasaki, M., Kengaku, M., Watanabe, K., and Sasai, Y. (2006). Generation of cerebellar neuron precursors from embryonic stem cells. *Dev. Biol.* 290, 287–296. doi: 10.1016/j.ydbio.2005.11.010

Suzuki-Hirano, A., Harada, H., Sato, T., and Nakamura, H. (2010). Activation of Ras-ERK pathway by Fgf8 and its downregulation by Sprouty2 for the isthmus organizing activity. *Dev. Biol.* 337, 284–293. doi: 10.1016/j.ydbio.2009.10.044

Takahashi, K., Tanabe, K., Ohnuki, M., Narita, M., Ichisaka, T., Tomoda, K., et al. (2007). Induction of pluripotent stem cells from adult human fibroblasts by defined factors. *Cell* 131, 861–872. doi: 10.1016/j.cell.2007.11.019

Takebayashi, H., Ohtsuki, T., Uchida, T., Kawamoto, S., Okubo, K., Ikenaka, K., et al. (2002). Non-overlapping expression of Olig3 and Olig2 in the embryonic neural tube. *Mech. Dev.* 113, 169–174. doi: 10.1016/S0925-4773(02)00021-27

Tao, O., Shimazaki, T., Okada, Y., Naka, H., Kohda, K., Yuzaki, M., et al. (2010). Efficient generation of mature cerebellar Purkinje cells from mouse embryonic stem cells. *J. Neurosci. Res.* 88, 234–247. doi: 10.1002/jnr.22208

Taroni, F., and DiDonato, S. (2004). Pathways to motor incoordination: the inherited ataxias. *Nat. Rev. Neurosci.* 5, 641–655. doi: 10.1038/nrn1474

Ungrin, M. D., Joshi, C., Nica, A., Bauwens, C., and Zandstra, P. W. (2008). Reproducible, ultra high-throughput formation of multicellular organization from single cell suspension-derived human embryonic stem cell aggregates. *PLoS One* 3:e1565. doi: 10.1371/journal.pone.0001565

Urbánek, P., Fetka, I., Meisler, M. H., and Busslinger, M. (1997). Cooperation of Pax2 and Pax5 in midbrain and cerebellum development. *Proc. Natl. Acad. Sci. U.S.A.* 94, 5703–5708. doi: 10.1073/pnas.94.11.5703

Wagner, M. J., Kim, T. H., Savall, J., Schnitzer, M. J., and Luo, L. (2017). Cerebellar granule cells encode the expectation of reward. *Nature* 544, 96–100. doi: 10.1038/nature21726

Wang, B., Harrison, W., Overbeek, P. A., and Zheng, H. (2011). Transposon mutagenesis with coat color genotyping identifies an essential role for Skor2 in sonic hedgehog signaling and cerebellum development. *Development* 138, 4487–4497. doi: 10.1242/dev.067264

Wang, S., Wang, B., Pan, N., Fu, L., Wang, C., Song, G., et al. (2015). Differentiation of human induced pluripotent stem cells to mature functional Purkinje neurons. *Sci. Rep.* 5:9232. doi: 10.1038/srep09232

Whitney, E. R., Kemper, T. L., Rosene, D. L., Bauman, M. L., and Blatt, G. J. (2008). Calbindin-D28k is a more reliable marker of human Purkinje cells than standard Nissl stains: a stereological experiment. *J. Neurosci. Methods* 168, 42–47. doi: 10.1016/j.jneumeth.2007.09.009

Yeung, J., Ha, T. J., Swanson, D. J., and Goldowitz, D. (2016). A novel and multivalent role of Pax6 in cerebellar development. *J. Neurosci.* 36, 9057–9069. doi: 10.1523/JNEUROSCI.4385-15.2016

Zec, N., Rowitch, D. H., Bitgood, M. J., and Kinney, H. C. (1997). Expression of the homeobox-containing genes EN1 and EN2 in human fetal midgestational medulla and cerebellum. *J. Neuropathol. Exp. Neurol.* 56, 236–242. doi: 10.1097/00005072-199703000-199703002

Zhang, L., and Goldman, J. E. (1996). Generation of cerebellar interneurons from dividing progenitors in white matter. *Neuron* 16, 47–54. doi: 10.1016/S0896-6273(00)80022-80027

Zhang, X., Zhang, H., and Oberdick, J. (2002). Conservation of the developmentally regulated dendritic localization of a Purkinje cell-specific mRNA that encodes a G-protein modulator: comparison of rodent and human Pcp2(L7) gene structure and expression. *Mol. Brain Res.* 105, 1–10. doi: 10.1016/S0169-328X(02)00379-370

Zhao, Y., Kwan, K. M., Mailloux, C. M., Lee, W. K., Grinberg, A., Wurst, W., et al. (2007). LIM-homeodomain proteins Lhx1 and Lhx5, and their cofactor Ldb1, control Purkinje cell differentiation in the developing cerebellum. *Proc. Natl. Acad. Sci. U.S.A.* 104, 13182–13186. doi: 10.1073/pnas.0705464104

Conflict of Interest: The authors declare that the research was conducted in the absence of any commercial or financial relationships that could be construed as a potential conflict of interest.

frontiers in Bioengineering and Biotechnology

REVIEW
published: 24 June 2020
doi: 10.3389/fbioe.2020.00692

Exploiting CRISPR Cas9 in Three-Dimensional Stem Cell Cultures to Model Disease

Sneha Gopal[1†], André Lopes Rodrigues[1,2†] and Jonathan S. Dordick[1,3,4]*

[1] Department of Chemical and Biological Engineering, Center for Biotechnology & Interdisciplinary Studies, Rensselaer Polytechnic Institute, Troy, NY, United States, [2] Department of Bioengineering and iBB-Institute for Bioengineering and Biosciences, Instituto Superior Técnico, University of Lisbon, Lisbon, Portugal, [3] Department of Biomedical Engineering, Rensselaer Polytechnic Institute, Troy, NY, United States, [4] Department of Biological Sciences, Rensselaer Polytechnic Institute, Troy, NY, United States

Three-dimensional (3D) cell culture methods have been widely used on a range of cell types, including stem cells to modulate precisely the cellular biophysical and biochemical microenvironment and control various cell signaling cues. As a result, more *in vivo*-like microenvironments are recapitulated, particularly through the formation of multicellular spheroids and organoids, which may yield more valid mechanisms of disease. Recently, genome-engineering tools such as CRISPR Cas9 have expanded the repertoire of techniques to control gene expression, which complements external signaling cues with intracellular control elements. As a result, the combination of CRISPR Cas9 and 3D cell culture methods enhance our understanding of the molecular mechanisms underpinning several disease phenotypes and may lead to developing new therapeutics that may advance more quickly and effectively into clinical candidates. In addition, using CRISPR Cas9 tools to rescue genes brings us one step closer to its use as a gene therapy tool for various degenerative diseases. Herein, we provide an overview of bridging of CRISPR Cas9 genome editing with 3D spheroid and organoid cell culture to better understand disease progression in both patient and non-patient derived cells, and we address potential remaining gaps that must be overcome to gain widespread use.

Keywords: pluripotent stem cell, 3D cell culture microsystem, organoids, microscale 3D printing, patient derived cells (PDCs)

OPEN ACCESS

Edited by:
Stephanie Michelle Willerth, University of Victoria, Canada

Reviewed by:
Jatin Roper, Koch Institute for Integrative Cancer Research at MIT, United States
Jennifer Patterson, KU Leuven, Belgium

***Correspondence:**
Jonathan S. Dordick
dordick@rpi.edu

[†] These authors have contributed equally to this work

Specialty section:
This article was submitted to Biomaterials, a section of the journal Frontiers in Bioengineering and Biotechnology

Received: *13 April 2020*
Accepted: *03 June 2020*
Published: *24 June 2020*

Citation:
Gopal S, Rodrigues AL and Dordick JS (2020) Exploiting CRISPR Cas9 in Three-Dimensional Stem Cell Cultures to Model Disease. Front. Bioeng. Biotechnol. 8:692. doi: 10.3389/fbioe.2020.00692

INTRODUCTION

Stem cells are defined by their long-term self-renewal and their ability to differentiate into specialized progeny (Reya et al., 2001). Pluripotent stem cells (PSCs) can adopt any cellular fate from the three germ layers (ecto-, meso-, and endoderm) (Shamblott et al., 1998). Based on their tissue of origin, stem cells can be classified as embryonic (ESC), which are collected from the inner cell mass of the blastocysts (Kim et al., 2020), or induced pluripotent (iPSC), which are somatic cells reprogrammed toward a more primitive state (Nakagawa et al., 2008). Multipotent stem cells, such as neural stem cells (NSC) and mesenchymal stem cells (MSC), have more limited differentiation capacity but can still generate multiple cell types (Zuk et al., 2002; Donato et al., 2007). Adult stem cells are found in various tissues in the body and serve to replace any tissue lost due to damage or injury (Young and Black, 2004).

The advent of genome engineering tools like Zinc Finger Nucleases (ZFNs), Transcription Activator-Like Effector Nucleases (TALENs) and most recently the Clustered Regularly Interspaced Short Palindromic Repeats Palindromic Repeats (CRISPR) Cas systems have vastly expanded our ability to modify gene expression (Mani et al., 2005; Xiao et al., 2013). In particular, the CRISPR Cas system has revolutionized our ability to perform gene knockout and gene regulation with a high degree of specificity with Cas9 (CRISPR associated protein 9) and dCas9 (deactivated Cas9), respectively (Doudna and Charpentier, 2014). The relative simplicity of this technique has facilitated the study of stem cells in a context dependent manner, particularly using more physiologically relevant 3D cell culture platforms.

Although, early embryonic development has been broadly studied using conventional two-dimensional, cell monolayer platforms (Chambers et al., 2009, 2016; Lian et al., 2012) these systems do not fully recapitulate *in vivo* behavior (Kwon et al., 2014; Duval et al., 2017; Nierode et al., 2019). Conversely, three-dimensional (3D) systems, such as spheroids and organoids, demonstrate a high degree of maturation and functionality. These structures are often generated by the formation of stem cell aggregates known as embryoid bodies (Rungarunlert et al., 2009). This is due to more *in vivo*-like signaling and biophysical gradients, as well as cell–cell contacts, that can impact the many transcriptional networks (Tekin et al., 2018; Branco et al., 2019) and metabolomic pathways inside the cell (Fong et al., 2016; Correia et al., 2018).

Herein, we focus on the application of CRISPR Cas9 tools to knockout/knock-in genes in pluripotent and adult stem cells for disease modeling. A broad overview is provided on the generation of 3D models and a mechanistic understanding of the CRISPR Cas9 technology, and this is followed by the use of gene knockouts to interrogate human diseases. Key to the latter is how CRISPR Cas9 has been used to develop physiologically relevant disease models that affect multiple organ systems. Finally, existing gaps are addressed leading to opportunities for future research.

ENGINEERING STRATEGIES FOR 3D ORGANOID MODELS FOR STEM CELLS

The current definition of an organoid is a self-organized, 3D multicellular structure that possesses functional attributes to its *in vivo* counterpart (Simian and Bissell, 2017). While organoids have been examined for decades in tumor-derived explants (Smith and Cochrane, 1946), more recently, organoids have been developed to include self-organized structures derived from pluripotent and adult stem cells. This self-organization is intrinsically dependent on biochemical factors like morphogens, small molecules and growth factors that are delivered in a spatiotemporal fashion as well as on biophysical stimuli provided by cell–cell and cell-extracellular matrix (ECM) interactions (extensively reviewed in Brassard and Lutolf, 2019; Silva et al., 2019).

Several protocols have been established to promote cellular assembly of 3D structures to recapitulate organ level functions *in vitro* with both scaffold-based and scaffold free approaches as shown in **Figure 1**. In scaffold-based approaches, the microenvironment of naive tissue is provided by matrices that replicate specific *in vivo* physical and biochemical stimuli. Early approaches relied on naturally derived matrices from decellularized tissue (Dye et al., 2015). For example, Sato et al. (2009) used laminin-rich Matrigel as an encapsulating matrix to support epithelial growth of mouse intestinal crypts. An alternative approach involved an air-liquid interface that provides better oxygenation to 3D intestinal cell cultures (Ootani et al., 2009). In this study, a collagen matrix was used to encapsulate primary intestinal cells in the presence of myofibroblast, which provided essential cues to recapitulate an intestinal stem cell niche allowing cell growth and differentiation with the additional external delivery of WNT and Notch signaling molecules. In the context of hPSC, Lancaster et al. (2013) and Lancaster and Knoblich (2014) have developed a widely used approach, in which cerebral organoids were prepared for modeling microcephaly via knockdown RNA interference (iRNA) on hiPSC lines with disease-associated Cyclin Dependent Kinase 5 Regulatory Subunit Associated Protein 2 (CDK5RAP2) mutations. By embedding embryoid bodies in Matrigel following neural commitment, the authors were able to achieve interdependent brain regions following formation of functional cortical neurons (Lancaster et al., 2013). Further in-depth transcriptomic analysis and DNA methylome sequencing demonstrated that these cerebral organoids share a similar expression profile and epigenetic signature with their fetal counterparts, namely similar gene expression patterns for neural progenitor self-renewal, differentiation, ECM production, adhesion and migration, and thus demonstrating how organoids could be used for neurodevelopmental studies (Camp et al., 2015; Luo et al., 2016).

Although Matrigel is widely used in stem cell organoid culture, its heterogenous composition poses a disadvantage to study specific spatial temporal cues that govern cell organization. As an alternative, hydrogels can be used to form 3D polymeric networks that support organoid culture under defined conditions. Lindborg et al. (2016) developed a hyaluronic acid (HA)-based hydrogel to grow cerebral organoids and avoid matrix variability. Hydrogels can also be functionalized with ECM proteins, such as collagen to mimic a defined cell microenvironment (Takezawa et al., 2004; Ootani et al., 2009; Lindborg et al., 2016). In addition, soft-lithography, including microcontact printing, has been used to promote cell aggregation in highly organized 3D structures (Rivron et al., 2012; Berger et al., 2015; Filipponi et al., 2016; Foncy et al., 2018).

Polysaccharides like alginate have also been shown to support growth of hiPSC-derived and patient-specific organoids, rendering similar phenotypic traits comparable to Matrigel-grown organoids (Lu et al., 2017; Wilkinson et al., 2017; Broguiere et al., 2018; Capeling et al., 2019). Osteogenesis and angiogenesis could be achieved in an artificial sphere-shaped organoid using mesenchymal stem cells (MSCs) and human umbilical vain endothelial cells (HUVECs) (Zhao et al., 2018). Such an approach may provide a functional delivery method of osteogenic factors for bone injury, which could be personalized

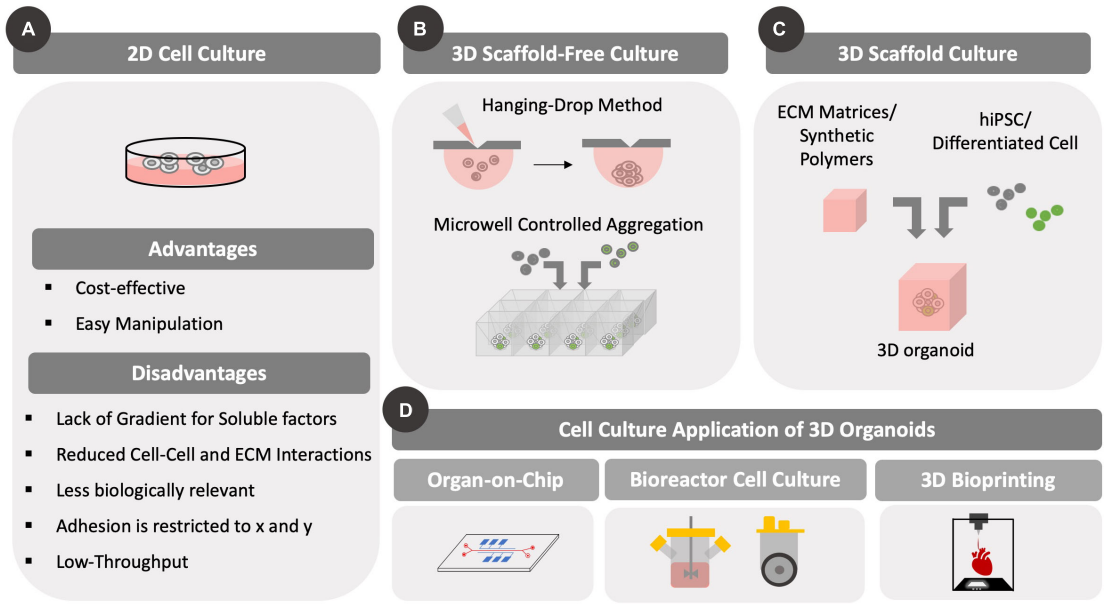

FIGURE 1 | Different types of cell culture formats. Differences between 2D and 3D cell culture methods are highlighted. Importantly, 3D cell culture formats have been developed to accommodate static and/or dynamic (with fluid flow/mixing) designs. The development of 3D culture methods has been prompted by scaffold-based and scaffold-free approaches that can be used for various culture methods, including microfluidic bioreactors and bioprinting. **(A)** Conventional 2D cell culture formats are illustrated along with advantages and disadvantages. Cells grow as a 2D monolayer with cell–cell contacts across a single surface. **(B)** Several scaffold-free approaches are highlighted including hanging drop and controlled aggregation methods that use gravity to assemble cells in 3D. **(C)** Scaffold based approaches include encapsulation of cells in synthetic or natural matrices that provide support to the cells and allow them to remain suspended. **(D)** The two methods of 3D cell culture have been adapted to both perfusion and static cultures in the form of microfluidic organ-on-chip platform/bioreactor platforms or as bioprinting on a surface, respectively.

by using patient-specific MSC or hiPSC. Other studies using alginate-based matrices include hiPSC-derived organoids such as to mimic a vascularized-myocardium on-chip (Zhang et al., 2016) as well as a 3D patient-specific lung organoid to study idiopathic pulmonary fibrosis (Wilkinson et al., 2017).

The same principle of tethering ECM components to biopolymers can also be applied to synthetic hydrogels like polyethylene glycol (PEG). Gjorevski et al. (2016) compared different designs of PEG-based defined matrices for intestinal stem cell organoid culture. PEGs were functionalized with HA, fibronectin, collagen or RGD peptide domain responsible for cellular adhesion to the ECM matrix, and examined resulting organoids *in vitro* (Gjorevski et al., 2016). Interestingly, there have been studies that do not include ECM components in matrix design. Cruz-Acuña et al. (2017) developed a four-armed PEG-macromer that was used to generate hPSC-dervied lung organoids with *in vivo*-like epithelial morphology. Likewise, Candiello et al. (2018) demonstrated that only PEG-crosslinked amikacin hydrogel was sufficient to induce a 3D self-organization of hESC-derived pancreatic cells, with further phenotypic maturation achieved upon addition HUVECs that promoted endocrine-like function.

Although the aforementioned studies do not introduce ECM components in matrix design, it should be noted that such components are still produced within the organoid. Indeed, this is the premise for scaffold-free methods. In such cases, cells can be cultured in small droplets of media (hanging drop method) and forced to aggregate based solely on gravitational force (Hsiao et al., 2012). This approach has been used widely to establish 3D models for cardiac diseases (Fennema et al., 2013; Beauchamp et al., 2015) and cancer (Amaral et al., 2017; Eder and Eder, 2017). Additional scaffold-free approaches include the formation of free-floating aggregates in exclusively non-adherent culture conditions (Eiraku et al., 2008; Paşca et al., 2015; Birey et al., 2017; Yoon et al., 2019), as well as the controlled aggregation of cells using microwells fabricated through soft-lithography techniques (Ungrin et al., 2008; Antonchuk, 2013; Dahlmann et al., 2013; Mitsunaga et al., 2017). Microfluidic devices have been employed to achieve physiologically relevant 3D organoid models. Herein, different groups have established protocols to study neural tube formation *in vitro* (Demers et al., 2016), perform drug screening using hepatic organoids (Novik et al., 2010; Au et al., 2014; Ortega-Prieto et al., 2018) and to develop 3D cardiac models (Shin et al., 2016; Devarasetty et al., 2017).

CRISPR Cas9 SYSTEMS

The CRISPR Cas9 system is made up of two components - a Cas9 nuclease and a short guide RNA (sgRNA) (Cho et al., 2013). Discovered as a part of the bacterial adaptive immune system, CRISPR Cas9 has been used widely to both knock out and regulate gene expression in now many cell types (Maeder et al., 2013; Qi et al., 2013; Ran et al., 2013b). A CRISPR knockout

can be accomplished by designing a 20-nucleotide (nt) sgRNA sequence that can bind to a specific gene of interest through complementary base pairing (Ran et al., 2013b; Shalem et al., 2014). Upon successful target identification, the Cas9 nuclease induces a double strand break (DSB) in the presence of a three-nucleotide protospacer adjacent motif (PAM).

The DSB causes the cells to repair the break by inserting and deleting random sequences at the site of the break through an error prone repair mechanism called Non-Homologous End Joining (NHEJ) (Shan et al., 2014). This process is often exploited when the CRISPR Cas9 system is used in stem cells to create different disease-specific models (Lin et al., 2018; Latour et al., 2019; Strikoudis et al., 2019). In addition, through homology dependent repair (HDR) a specific gene or sequence can be inserted at the site of the break if that sequence is simultaneously introduced to the cell with the CRISPR Cas9 system (Zhang et al., 2017). While this process occurs less frequently than NHEJ, HDR has been leveraged to generate multiple distinct reporter cell lines with applications in screening and cell modeling (Maruyama et al., 2015; Sluch et al., 2015; Wu et al., 2016; Zhou et al., 2016; Zhang et al., 2017). Two genomic editing tools were commonly used before CRISPR Cas9 - Zinc Finger Nucleases (ZFN) and Transcription Activator Like Effector Nucleases (Hai et al., 2014). These tools use complex nuclease design methods depending on the region to be targeted or they employ difficult cloning tools. Conversely, CRISPR Cas9 requires the design of just a 20-nt RNA sequence to ensure targeted genome editing (Hruscha et al., 2013). In addition, Cas9-mediated editing can introduce mutations at specific sites (Hwang et al., 2013; Ran et al., 2013a; Chiang et al., 2016).

Gene regulation with CRISPR Cas9 can be accomplished by using CRISPR interference (CRISPRi) and CRISPR activation (CRISPRa) (Charpentier and Marraffini, 2014; Du and Qi, 2016; Kampmann, 2017). In CRISPRi/a, several point mutations in the nuclease domain create a catalytically dead dCas9 (Larson et al., 2013; Guilinger et al., 2014). The dCas9 is still able complex with the sgRNA but no longer has any cleavage activity. The complex, therefore, binds to the DNA target without causing a DSB it at the specific site (Qi et al., 2013). In the case of CRISPRi, the sgRNA-dCas9 complex blocks the action of RNA polymerase and prevents transcription elongation (Mandegar et al., 2016). The efficiency of repression can be improved by further modification of the dCas9 to include a repressive domain, such as the Kruppel-associated box (KRAB) (Gilbert et al., 2013; Kearns et al., 2014; Genga et al., 2016). For gene upregulation, dCas9 can be fused to activator domains and targeted to promoter/enhancer regions of genes (Dominguez et al., 2015). Several systems have been generated, including direct dCas9 fusions (e.g., VPR, a tripartite fusion of VP64, p65, and Rta) (Chavez et al., 2015), utilizing a protein scaffold (e.g., SunTag system) (Papikian et al., 2019), and incorporating an RNA scaffold [e.g., Synergistic Activation Mediator complex (SAM)] (Konermann et al., 2015).

As a result of the growing success of genome regulation with CRISPRi and CRISPRa, the nuclease null version of Cas9 has been used in other applications including single nucleotide editing, chromatin modifications, imaging genomic sequences, evaluating regulatory sequences, among others (Chen et al., 2013; Anton et al., 2014; Thakore et al., 2015; Gaudelli et al., 2017; Takei et al., 2017) (**Figure 2**). The earliest example of single base editing was carried out with dCas9 coupled to an apolipoprotein B mRNA editing enzyme, a catalytic peptide where a cytosine group was converted to uracil or thymine (Komor et al., 2016). Other base editors that can carry out adenine–thymine base pair changes to cytosine-guanine base pairs have also been developed (Gaudelli et al., 2017). Such tools are useful from a therapeutic standpoint as they have the ability to be used to correct diseases that arise from single base pair changes in a gene therapy strategy. For a more thorough assessment of the different applications of dCas9-mediated control of cells, readers are referred to the review by Pickar-Oliver and Gersbach (2019).

In addition to these varied applications, CRISPR Cas9 has been adapted to genome wide screens like those carried out with RNA interference (RNAi) (Mohr and Perrimon, 2012; So et al., 2019). As a result, they have been adapted to identify genes involved in conferring cell viability, drug resistance and promoting differentiation or self-renewal in stem cells (Shalem et al., 2015; Ihry et al., 2019). Such screens are typically performed in a pooled or an array-based format (Tian et al., 2019). The former method delivers all of the sgRNAs simultaneously and requires a selection post-introduction to isolate the cells that take up a specific sgRNA, while the latter delivers one sgRNA to one group of cells, thereby removing the need for selection (So et al., 2019). While there have been several reports that have employed genome wide pooled screens in stem cells in 2D formats, more recent studies have used these tools to study 3D organoids that encapsulate adult stem cells (Michels et al., 2020; Ringel et al., 2020).

There are three ways to incorporate CRISPR Cas9 to study stem cells in 3D organoids. One method relies on genome modification of cells prior to their encapsulation in a matrix (Latour et al., 2019), while a second method involves introduction of a Cas9-sgRNA complex in organoids dissociated into single cells during infection and subsequent reformation of 3D structures (O'Rourke et al., 2017). The third method involves direction delivery of Cas9 and sgRNA to the organoids without generating single cells (Matano et al., 2015). Of the three methods, the first two have been employed more widely due to difficulties associated with efficient gene delivery through 3D matrices (Laperrousaz et al., 2018). Since hydrogel matrices can often pose diffusional limitations to highly charged, relatively large non-viral gene delivery vectors, limitations remain in using CRISPR Cas9 to study organoids. Nevertheless, viral vectors are being employed together with nucleofection and electroporation to deliver genes to spheroid and organoid cultures (Matano et al., 2015; Bian et al., 2018; Garita-Hernandez et al., 2020). The development of novel gene delivery tools can expand our ability to carry out direct genomic editing of organoids.

DEVELOPMENT OF DISEASE MODELS USING CRISPR Cas9 KNOCKOUT

The use of hiPSCs/hESCs for the development of human disease models is built on their ability to adopt essentially any

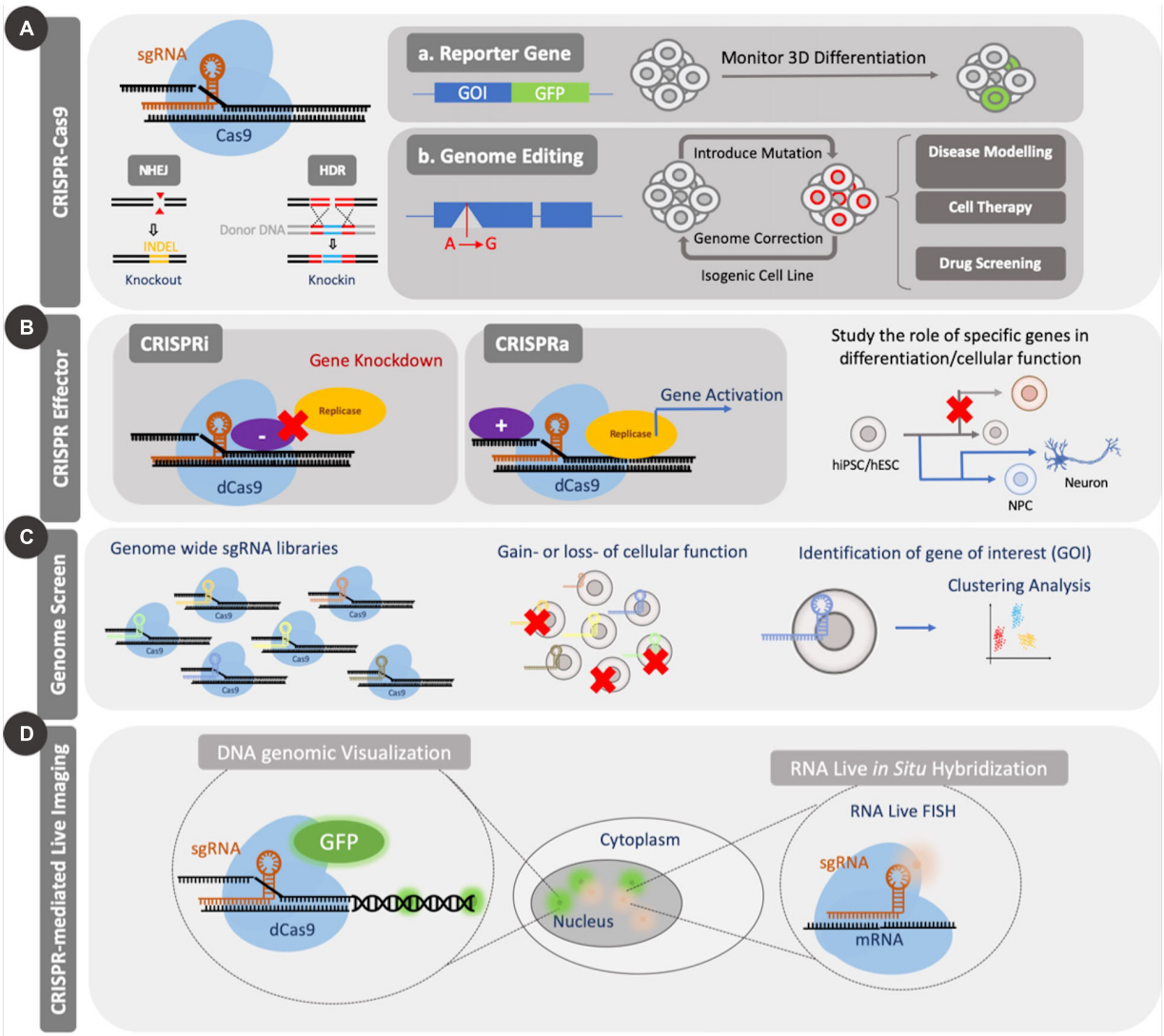

FIGURE 2 | Applications of CRISPR Cas9. CRISPR Cas9 can be used to introduce genetic mutations by causing a double strand break (DSB). The nuclease-null version, dCas9, can be coupled to effector domains to activate or repress gene expression or can be coupled to fluorescent proteins for imaging of genomic elements. CRISPR Cas9 knockout and effector tools have been used for screening applications. **(A)** Standard CRISPR Cas9 genome editing through introduction of mutations can be used to study the role of several genes during differentiation or to create disease models for enhanced mechanistic understanding or drug screening. **(B)** Application of dCas9 to genomic regulation in the form of CRISPRi/a can be used to study both differentiation and cellular function. **(C)** Large scale genomic screens using CRISPR Cas9/dCas9 can be used to identify essential genes for several cellular processes through gain or loss of function studies. Such screens enable identification of candidate genes from a pool for further investigation. **(D)** Coupling dCas9 to fluorescent domains, like GFP, enable facile visualization of specific regions of the genome and temporal tracking.

cellular fate through differentiation. Therefore, hiPSCs/hESCs may serve as an unlimited source of disease relevant cells. These cells can then be used to better understand pathologies associated with specific diseases, as well as to search for potential treatment options. Several diseases including Parkinson's disease, amyotrophic lateral sclerosis (ALS), cystic fibrosis, cardiac fibrosis, polycystic kidney disease, among others, have been studied using hiPSCs/hESCs and other cell types (Hofherr and Köttgen, 2013; Fujimori et al., 2018; Pollard and Pollard, 2018; Lee et al., 2019; Stoddard-Bennett and Reijo, 2019). Genome editing using CRISPR-Cas9 in 3D organoids has been used for such disease modeling, either by modifying a parental undifferentiated stem cell line or by rescuing a gene that is involved in causing the disease phenotype (**Figure 3**).

Generating Cells With Disease-Carrying Mutations

To introduce disease mutations and potentially mimic disease phenotypes, CRISPR Cas9 has been used to knock out various genes in healthy stem cells. Several types of organoids, including those consisting of brain (Kim et al., 2019), lung

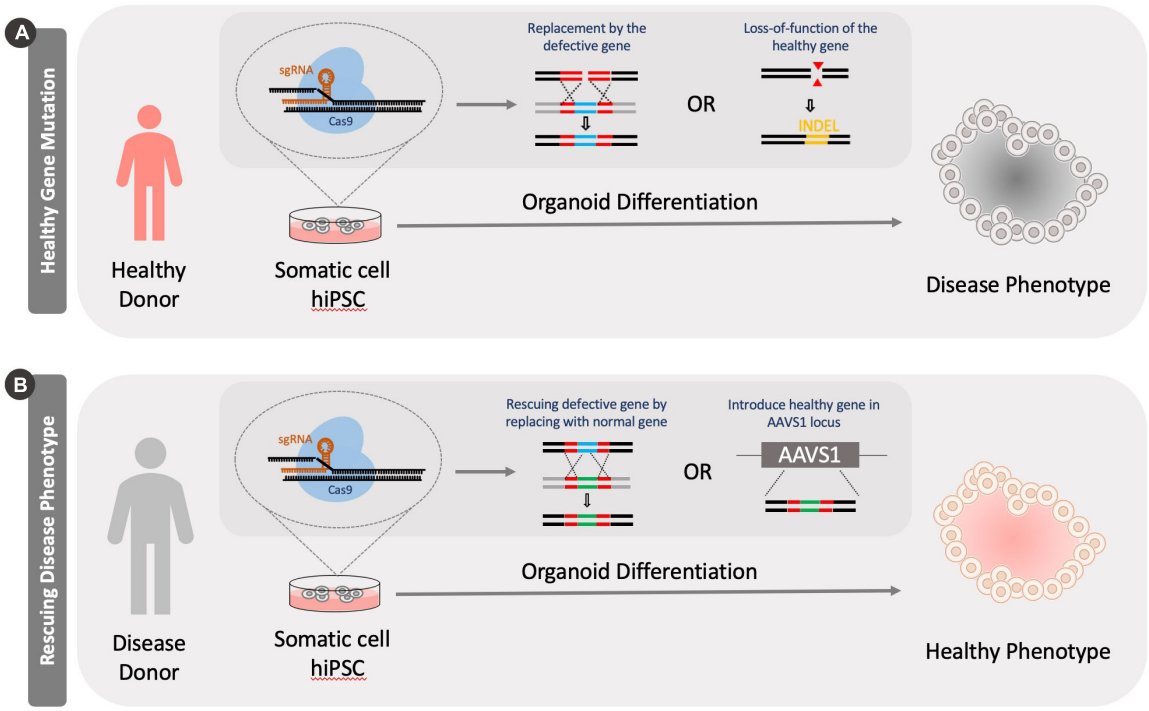

FIGURE 3 | Generation of disease models using CRISPR Cas9 knockout tools. Models can be generated by either knocking out a healthy version of a gene in cells or by rescuing a defective gene. **(A)** A healthy person's somatic cells are reprogrammed into a pluripotent stage. Specific disease causing mutations can be introduced to genes in these cells by either knocking in a defective genes or introducing INDELS through genome editing. **(B)** Alternatively, a diseased patient's cells can be isolated and reprogrammed into a pluripotent stage. These cells can be then fixed by correcting the mutation by knocking in a functional version of the gene or introducing healthy version at the adeno-associated virus integration site (AAVS1).

(Strikoudis et al., 2019), kidney (Freedman et al., 2015), intestinal (Jung et al., 2019), and other stem cells have been generated from these knockout stem cell types to better model *in vivo* environments. A majority of studies have focused on better understanding brain disorders with cerebral organoids and hence this is a major focus of this section.

A major advantage of genome engineering is the ability to study diseases in experimentally relevant human cell types. For example, patient-specific iPSCs were used to create a disease model of frontotemporal dementia (FTD), wherein CRISPR Cas9 was used to introduce mutations in the MAPT gene (Nakamura et al., 2019). There were several changes noted in generated neurons due to the mutation including lower phosphorylation levels in the tau protein, which resulted in structural reorganization of the microtubules as well as reduced numbers of mitochondria in the cells.

In addition, the specificity of gene targeting with CRISPR/Cas9 enabled the generation of similar mutations that are found in patients carrying a specific disease. This was shown with a cerebral organoid disease model for GM1 ganglioside storage disease that results in extensive buildup of a glycosphingolipid ganglioside due to a non-functional cellular β-galactosidase (Tonin et al., 2019). Human iPSCs were used to prepare isogenic cell lines with the disease carrying mutations in specific exons where most mutations for the disease were recorded in patients (Latour et al., 2019). Following gene editing, increased levels of GM1 were observed in mutated organoids over non-mutated controls leading to GM1 ganglioside storage disease phenotypes recapitulated in gene-edited organoids.

Phenotypes of major neurodegenerative diseases like Alzheimer's disease and Parkinson's disease can be recapitulated in a 3D organoid environment by CRISPR Cas9-mediated editing (Lin et al., 2018; Kim et al., 2019). For Alzheimer's disease, cerebral organoids were prepared from hiPSCs that harbored the disease causing variant of apolipoprotein E (APOE4), which was found to show ∼2 fold increase in the accumulation of amyloid β than control organoids that had the APOE3 gene variant (Lin et al., 2018). For Parkinson's disease, Kim et al. (2019) generated a single point base mutation to model a specific form of the disease, the LRRK2-associated sporadic disease. Cerebral organoids generated from mutated hiPSCs were then found to yield several different phenotypes that were observed with Parkinson's disease and also used to identify a disease relevant gene encoding for the thioredoxin interacting protein (TXNIP) (Kim et al., 2019). They further showed that the gene edited dopaminergic neurons showed enhanced cytotoxicity as indicated by a ∼20% increase in caspase-3 activity. These studies are especially relevant since CRISPR-edited iPSCs have the ability to generate a near limitless supply of cells for studying these diseases as opposed to patient derived adult cells, which are far more finite.

Structural conditions like macrocephaly, microcephaly and cell migration can be studied more accurately with 3D organoid models incorporating CRISPR induced mutations than with animal models. To this end, Li et al. (2017) generated a Phosphatase and Tensin Homolog (PTEN) gene knockout model to activate PTEN-AKT and cause 3D organoids to display a macrocephaly phenotype. The authors were thus able to address several interspecies differences in this pathway including stark differences in the expansion and folding mechanism of human organoids when compared to mice. Therefore, CRISPR Cas9 can be used to address some of the issues associated with translating results between multiple species by enabling study in the more relevant human cell lines.

Finally, genome modification to multipotent stem cell types, including neural stem cells (NSCs), have been used to model diseases like cancer in cerebral organoids (Bian et al., 2018). Direct introduction of CRISPR Cas9 for mutating several tumor suppressor genes in 3D embryoid bodies was performed at the NSC stage to identify key genes, which when mutated, resulted in abnormal growth associated with various cancers. Mutations in certain genes resulted in rapid proliferation of the organoids in culture. Further investigation revealed mRNA changes in the expression of several genes between mutated cancerous organoids and non-cancerous organoids. Such disease models have yielded a wealth of information on how cells change with tumorigenesis and how this information could be leveraged to generate better potential drug candidates to reduce tumorigenesis (Luo, 2016).

A cohort study conducted by van Rijn et al. (2018) is an interesting example of how CRISPR-engineered organoids are useful in determining genotypic-phenotypic associations. This study provided insights of the mechanism by which mutations in the diacylglycerol-acyltransferase 1 (DGAT1) gene is associated to congenital intestinal disorders. The authors used CRISPR-Cas9 to generate knockouts of the DGAT1 gene on cells obtained from duodenal biopsies of three healthy individuals and compared lipid production to patient-derived organoids that contain the mutations leading to similar results.

Kidney organoids have been studied in detail using CRISPR Cas9-edited hiPSCs to model renal diseases. A knockout of phosphoinositide dependent kinase 1 (PDK1) and phosphoinositide dependent kinase 2 (PDK2) used to model disease pathology of polycystic kidney disease showed enhanced cyst formation when cells were grown into kidney organoids (Freedman et al., 2015). Some of the lesser-studied organoid models with CRISPR Cas9 include lung organoid models where only one group has done major work to study a lung disease in 3D format using CRISPR Cas9 (Strikoudis et al., 2019). Nevertheless, this shows that Cas9 mediated knockout can be used to study multiple different organoid systems. A list of studies that have utilized CRISPR Cas9 to introduce disease causing mutations in stem cells for further study in 3D cell cultures are given in **Table 1**.

Genome wide pooled screening tools have only recently been employed to study stem cells in 3D organoid and spheroid cultures (Michels et al., 2020; Ringel et al., 2020). Michels et al. (2020) and Ringel et al. (2020) used adult intestinal stem cells and cancer stem cells to identify genes that prevent cells from responding to transforming growth factor-β (TGF-β) signaling. As a result, pooled CRISPR screens can effectively generate large amounts of data on the roles of several genes simultaneously. These experiments show the possibility of conducting screening experiments with stem cells and can now be expanded for use in studying pluripotent and multipotent stem cells. While a few experiments have been performed in 2D, to our knowledge there are no reported examples in 3D.

Animal models have been useful in helping us study disease progression as well to evaluate treatment options. Xenotransplantation of CRISPR engineered organoids are particularly useful as they do not require complex methods needed to generate mice carrying specific mutations (Roper et al., 2017). Modified tissue xenografts have been studied extensively with human and rodent adult intestinal stem cells (Drost et al., 2015; Matano et al., 2015; O'Rourke et al., 2017; Roper et al., 2017). These genome-edited organoids were used to evaluate tumor progression during cancer development (Drost et al., 2015; O'Rourke et al., 2017). In addition, such studies enable the development of gene expression profiles in tumors and essential mutations needed for cancer metastases (Matano et al., 2015; Roper et al., 2017).

Generating Healthy Cells With Gene Rescue

CRISPR Cas9 has been used to perform gene rescue and better understand disease pathologies. One of the earliest examples of using CRISPR Cas9 to repair a mutant gene was done using cystic fibrosis transmembrane conductor receptor (CFTR) (Schwank et al., 2013). Adult intestinal stem cells were transfected with Cas9, sgRNA, and wild type CFTR genes to allow for homologous recombination of the corrected gene following which a forskolin based swelling assay was carried out (Schwank et al., 2013). When these cells were grown into intestinal organoids, the corrected organoids displayed increased swelling in comparison to the diseased organoids (non-mutant) when they were subjected to a forskolin based assay. Forskolin swelling assay is commonly used to study cystic fibrosis since diseased cells carry a non-functional CFTR channel that prevents swelling of cells upon exposure to forskolin since the channel is unable to transport chloride ions into the cells (Boj et al., 2017).

Disease correction has also been carried out with CRISPR Cas9 in hiPSCs. This has important implications in regenerative medicine, as such genome editing tools may be used therapeutically. Diseased or mutant gene alleles can be modified into "healthy" versions in reprogrammed hiPSCs, which subsequently can be differentiated to any target cell type that can serve as a replacement to the diseased tissue. Some examples are summarized in **Table 2**. Gene rescue in hiPSCs has been used to generate multiple organoid types including cerebral (Allende et al., 2018), intestinal (Geurts et al., 2020), kidney (Forbes et al., 2018), and retinal (Deng et al., 2018) organoids.

In another example of gene rescue, a dyskeratosis congenital (DC) intestinal organoid model was used to identify the Wnt signaling pathway as a potential therapeutic target for the disease

TABLE 1 | Examples of CRISPR Cas9 to introduce disease causing mutations.

Edited cell type	Type of organoid	Gene knockout	Disease modeled	Patient derived (Y/N)	References
iPSC	Cerebral	MAPT	Frontotemporal dementia	Y	Nakamura et al., 2019
iPSC	Cerebral	GLB1	GM1 ganglioside storage disease	N	Latour et al., 2019
iPSC	Cerebral	RS1	X-linked juvenile retinoschisis	Y	Huang et al., 2019
iPSC	Cerebral	AXL	Zika virus	N	Wells et al., 2016
ESC	Cerebral	LIS1	Lissencephaly	N	Karzbrun et al., 2018
iPSC	Cerebral	APOE3	Alzheimer's disease	N	Lin et al., 2018
iPSC	Cerebral	LRRK2	Parkinson's disease	N	Kim et al., 2019
ESC	Cerebral	PTEN	Zika virus	N	Li et al., 2017
NSC derived from ESC	Cerebral	Multiple tumor suppressor genes	Brain tumor	N	Bian et al., 2018
iPSC	Cerebral	TSC1, TSC2	Tuberous sclerosis	N	Blair et al., 2018
Organoids from hESC	Cerebral	TP53	Glioblastoma	N	Ogawa et al., 2018
iPSC	Cerebral	DCHS1, FAT4	Neuronal heterotopia	Y	Klaus et al., 2019
iPSC	Cerebral	CLN3	Neuronal ceroid lipofuscinosis	N	Gomez-Giro et al., 2019
iPSC	Cerebral	CDH8	Schizoaffective disorder	Y	Wang et al., 2017
iPSC/ESC	Kidney	PODXL	Podocyte development	N	Freedman et al., 2015; Kim et al., 2017
ESC	Kidney	PKD1, PKD2	Polycystic kidney disease	N	Freedman et al., 2015
ESC	Intestinal	STAT3	Intestinal organoid maturation	N	Jung et al., 2019
ISC	Intestinal	APC, TP53, KRAS, SMAD4	Colorectal cancer	Y	Drost et al., 2015; Matano et al., 2015; O'Rourke et al., 2017; Roper et al., 2017
ISC	Intestinal	MLH1, NTLH1	Colorectal cancer	Y	Drost et al., 2017
ESC	Lung	HPS2, HPS4, HPS8	Hermansky-Pudlak syndrome interstitial pneumonia	N	Strikoudis et al., 2019
ISC	Intestinal	DGAT1	Congenital diarrheal disorder	Y	van Rijn et al., 2018

TABLE 2 | CRISPR Cas9 examples to rescue genes.

Cell type	Organoid	Gene rescued	Disease studied	Patient derived (Y/N)	References
ISC	Intestinal	CFTR	Cystic fibrosis	Y	Schwank et al., 2013
iPSC	Intestinal	DKC1	Dyskeratosis congenita	Y	Woo et al., 2016
ISC	Intestinal	CFTR	Cystic fibrosis	Y	Geurts et al., 2020
iPSC	Cerebral	HEXB	Sandhoff disease	Y	Allende et al., 2018
iPSC	Cerebral	CNTNAP2	Autism spectrum disorder	N	de Jong et al., 2019
iPSC	Kidney	IFT140	Nephronophthisis related ciliopathy	Y	Forbes et al., 2018
iPSC	Retinal	RPGR	Retinitis pigmentosa	Y	Deng et al., 2018
iPSC	Cerebral	LIS1, YWHAE (14.3.3e)	Miller-Dieker syndrome	N	Iefremova et al., 2017
Hepatocytes from fetal human livers	Hepatic	TP53	N/A	N	Artegiani et al., 2020

(Woo et al., 2016). CRISPR Cas9 corrected DC cells that were isolated from patients showed higher expression of several genes regulated by Wnt signaling. Specifically, Ascl2, a known regulator of intestinal stem cell development (Schuijers et al., 2015) showed differential expression between diseased and corrected organoids (Woo et al., 2016). The success in using intestinal organoids to model diseases has also resulted in newer CRISPR technologies including adenine base editing used to correct disease causing mutations with a large set of patient derived cells (Geurts et al., 2020). Four types of patient derived cells were corrected using a Cas9 base pair editor that allows for switching an adenine–thymine (A–T) base pair to cytidine–guanine base pair (C–G). This work is especially important since a large number disease causing mutations are due to a base pair substitution

event (C–G base pair change to A–T) (Gaudelli et al., 2017). Furthermore, the ability to utilize these base-editing tools with multiple different patient samples shows the versatility of CRISPR Cas9 for therapeutic purposes.

Normal cell function was restored in several other organoid models including cerebral (Allende et al., 2018), kidney (Forbes et al., 2018), and retinal (Deng et al., 2018) organoids using CRISPR Cas9. For example, CRISPR Cas9 was used to correct a mutation and rescue a gene involved in causing Sandhoff disease (a lysosomal storage disorder) from patient derived cells (Allende et al., 2018). Specifically, gene edited organoids showed reduced proliferation and did not show developmental abnormalities that were found with the diseased organoids. With kidney organoids, the intraflagellar transport 140 (IFT140) gene was rescued in cells derived from a patient who had nephronophthisis (NPHP)-related ciliopathy (NPHP-RC) (Forbes et al., 2018). There were several structural differences as well as gene expression differences in the organoids, especially in genes involved in the creation of apicobasal polarity, the formation of cell–cell junctions and in the assembly of dynein motor proteins. Finally, several phenotypic changes associated with retinitis pigmentosa were corrected with the use of CRISPR Cas9 mediated editing of retinitis pigmentosa 3 GTPase regulator (RPGR) in 3D retinal organoid model (Deng et al., 2018). The authors were able to reverse several disease-related symptoms including loss of photoreceptors and ciliopathy in the patient derived cells by correcting a frameshift mutation in the RPGR gene.

Alternatively, the safe harbor AAVS1 locus of patient-derived hiPSC cells can be used as a site to introduce the Cas9 encoding gene and a functional version of the gene to be rescued (Oceguera-Yanez et al., 2016; Iefremova et al., 2017). For example, Iefremova et al. (2017) transfected Miller-Dieker syndrome patient-derived hiPSCs with plasmids encoding Cas9 and two other proteins (LIS1 and 14.3.3e) to partially rescue the lissencephaly phenotype. They further showed that the neuroepithelial loops that were generated upon differentiation showed increased loop diameter and apical membrane length in organoids ($\sim$50 μm increase $\sim$200 μm increase, respectively, for LIS1 rescue and $\sim$75 and $\sim$100 μm increase, respectively, for 14.3.3e rescue).

Most of the aforementioned studies described in this section resort to HDR to introduce the gene mutation at a specific site, as this approach relies on homology arms present in the donor plasmid. Nevertheless, NHEJ-mediated mechanisms potentially could be used to generate knock-in functional genes (Artegiani et al., 2020). As a proof-of-concept, Artegiani et al. (2020) developed a CRISPR-Cas9-mediated homology-independent organoid transgenesis method, coined CRISPR-HOT, to mediate precise gene insertion in different types of organoids, namely liver-, and intestinal-derived tissues. When compared to HDR, a 10-fold higher efficiency was achieved with precise in-frame insertions of a gene encoding a fluorescent protein used for C-terminal tagging. Although this approach is a useful tool for reporter cell line generation and labeling cellular structures, it can also be multiplexed with gene knock-out studies, as demonstrated by the loss of TP53 gene in hepatic organoids, resulting in an aberrant mitotic spindle behavior and disorganization of microtubules. Thus, CRISPR-HOT may be useful in generating myriad disease models (Artegiani et al., 2020).

CONCLUSION AND FUTURE PERSPECTIVES

Although remarkable advancement in 3D model development has been achieved, there remain important questions to be answered. Recently, several vascularization processes have been incorporated into 3D models (Kang et al., 2009; Ovsianikov et al., 2011; Kook et al., 2018; Wörsdörfer et al., 2019). Two such methods include bioprinting encapsulated cells in synthetic hydrogels resulting in perfusable networks through two photon polymerization (Ovsianikov et al., 2011) or co-culturing organoids with endothelial cells (Kang et al., 2009; Kook et al., 2018). For a detailed summary of methods used to generate vascular tissue, readers are referred to the review by Grebenyuk and Ranga (2019). Despite progress made toward incorporating vascular structures in 3D organoid models, there are few studies on the use of such tools in understanding disease progression with CRISPR-modified organoids. Combining vascularization with specific disease-causing mutations in 3D may help yield more personalized patient models.

In addition, while the majority of this review has focused on using CRISPR Cas9 knockout tools for studying diseases, some groups have also started using CRISPRi/a for similar studies (Heman-Ackah et al., 2016). This is especially important because CRISPRi/a allows for temporary modifications to gene expression through inducible promoters as opposed to the more permanent gene knockout experiments. Such experiments can rapidly simplify the process of studying diseases in 3D organoids by removing the need for creating multiple different cell lines with and without mutations and also allows for dynamic control of disease phenotypes with a single population of cells. However, most such studies have been carried out in 2D cell formats. As an example, Heman-Ackah et al. (2017) demonstrated that the VPR (a tripartite fusion of VP64, p65, and Rta) domain coupled to dCas9 could be used to induce activation of endogenously expressed SCNA gene in healthy neurons, which led to an eightfold increase of the alpha-synuclein protein associated with Parkinson's disease (Heman-Ackah et al., 2017). In parallel, the KRAB domain was used to reduce the transcriptional expression of the same protein in diseased-phenotypic neurons that led to a 40% reduction relative to a non-edited Parkinsonian hiPSC-derived neuron (Heman-Ackah et al., 2016). Despite significant improvements in understanding the role of the SCNA gene, it is unclear how it would influence the 3D structure of the organoid, or how the specific microenvironmental cues could potentially influence epigenomic regulation of the edited gene (Lo and Qi, 2017). Modulating gene expression of SCNA or any other gene of interest in organoids and spheroids with CRISPRi/a tools can help address several of these unknowns.

Another important aspect that requires further study in this area is the use of artificial intelligence and machine learning tools coupled to CRISPR-engineered organoids. For

instance, groundbreaking work developed by Libby et al. (2019) demonstrate that machine learning algorithms could empirically determine and control the spatial self-organization of multicellular patterns without the need for micropatterning technique or other extrinsic patterning methods. Other studies demonstrated that trained machined learning models could be used to identify possible mutations (indels) generated by CRISPR genome editing and repair (Allen et al., 2018). This could be further used to improve disease models (Shen et al., 2019).

Finally, novel CRISPR Cas tools that utilize other Cas proteins including Cas12a and Cas13 and their catalytically dead counterparts, have been discovered specifically for nucleic acid detection and protein detection (Gootenberg et al., 2018; Bai et al., 2019; Dai et al., 2019). Of these two, Cas13 has the ability to target RNA sequences (Granados-Riveron and Aquino-Jarquin, 2018). Hence it has been used for several applications including detecting RNA viruses, downregulating genes by targeting RNA transcripts, imaging RNA sequences, etc. (Granados-Riveron and Aquino-Jarquin, 2018; Freije et al., 2019). RNA imaging is a powerful application because it potentially can be used as an alternative for fluorescence *in situ* hybridization (FISH) in live cells (Yang et al., 2019). Using this tool to study 3D organoids can allow for rapid real-time tracking of several genes that may not just be involved in causing diseases but also in elucidating healthy development and differentiation of stem cells.

In this review we addressed several examples in the use of CRISPR Cas9 tools to repair defective genes in diseased organoids. The ultimate goal of such studies is to aid in the development of emerging treatments that employ gene therapy, chimeric antigen receptor T cell therapy or cell therapy. This requires *in vivo* delivery of the Cas9-sgRNA complex, and examples of this have been shown for rodent disease models (Ding et al., 2014; Bakondi et al., 2016; Gao et al., 2018). While several therapeutic challenges remain, these animal models suggest that it may be possible to target defective genes in humans. Therefore, addressing these areas, particularly in patient-derived hiPSCs that are differentiated into specific adult stem cells and terminal progeny represents an opportunity to bring the "bedside" to the "bench" and advance therapeutic options for patients.

AUTHOR CONTRIBUTIONS

SG and AR wrote the manuscript along with JD. JD edited the manuscript. All authors contributed to the article and approved the submitted version.

FUNDING

This work was partly funded under a Project Award Agreement from the National Institute for Innovation in Manufacturing Biopharmaceuticals (NIIMBL) and financial assistance award 70NANB17H002 from the U.S. Department of Commerce, National Institute of Standards and Technology. The authors acknowledge financial support from Fundação para a Ciência e a Tecnologia (FCT), Portugal through iBB – Institute for Bioengineering and Biosciences (UID/BIO/04565/2013) and from Programa Operacional Regional de Lisboa 2020 (Project N. 007317). AR acknowledges FCT for financial support, for the scholarship with the reference (SFRH/BD/135524/2018).

REFERENCES

Allen, F., Crepaldi , L., Alsinet, C., Strong, A. J., Kleshchevnikov, V., De, A. P., et al. (2018). Predicting the mutations generated by repair of Cas9-induced double-strand breaks. *Nat. Biotechnol.* 37, 64–72. doi: 10.1038/nbt.4317

Allende, M. L., Cook, E. K., Larman, B. C., Nugent, A., Brady, J. M., Golebiowski, D., et al. (2018). Cerebral organoids derived from Sandhoff disease-induced pluripotent stem cells exhibit impaired neurodifferentiation. *J. Lipid Res.* 59, 550–563. doi: 10.1194/jlr.m081323

Amaral, R. L. F., Miranda, M., Marcato, P. D., and Swiech, K. (2017). Comparative analysis of 3D bladder tumor spheroids obtained by forced floating and hanging drop methods for drug screening. *Front. Physiol.* 8:605. doi: 10.3389/fphys.2017.00605

Anton, T., Bultmann, S., Leonhardt, H., and Markaki, Y. (2014). Visualization of specific DNA sequences in living mouse embryonic stem cells with a programmable fluorescent CRISPR/Cas system. *Nucleus* 5, 163–172. doi: 10.4161/nucl.28488

Antonchuk, J. (2013). Formation of embryoid bodies from human pluripotent stem cells using AggreWell^{TM} plates. *Methods Mol. Biol.* 946, 523–533. doi: 10.1007/978-1-62703-128-8_32

Artegiani, B., Hendriks, D., Beumer, J., Kok, R., and Zheng, X. (2020). Fast and efficient generation of knock-in human organoids using homology-independent CRISPR/Cas9 precision genome editing. *Nat. Cell Biol.* 22, 321–331. doi: 10.1038/s41556-020-0472-5

Au, S. H., Chamberlain, M. D., Mahesh, S., Sefton, M. V., and Wheeler, A. R. (2014). Hepatic organoids for microfluidic drug screening. *Lab Chip* 14, 3290–3299. doi: 10.1039/c4lc00531g

Bai, J., Lin, H., Li, H., Zhou, Y., Liu, J., Zhong, G., et al. (2019). Cas12a-based on-site and rapid nucleic acid detection of African Swine Fever. *Front. Microbiol.* 10:2830. doi: 10.3389/fmicb.2019.02830

Bakondi, B., Lv, W., Lu, B., Jones, M. K., Tsai, Y., Kim, K. J., et al. (2016). *In Vivo* CRISPR/Cas9 gene editing corrects retinal dystrophy in the S334ter-3 rat model of autosomal dominant retinitis pigmentosa. *Mol. Ther.* 24, 556–563. doi: 10.1038/mt.2015.220

Beauchamp, P., Moritz, W., Kelm, J. M., Ullrich, N. D., Agarkova, I., Anson, B. D., et al. (2015). Development and characterization of a scaffold-free 3D spheroid model of induced pluripotent stem cell-derived human cardiomyocytes. *Tissue Eng. Part C Methods* 21, 852–861. doi: 10.1089/ten.TEC.2014.0376

Berger, D. R., Ware, B. R., Davidson, M. D., Allsup, S. R., and Khetani, S. R. (2015). Enhancing the functional maturity of induced pluripotent stem cell-derived human hepatocytes by controlled presentation of cell-cell interactions *in vitro*. *Hepatology* 61, 1370–1381. doi: 10.1002/hep.27621

Bian, S., Repic, M., Guo, Z., Kavirayani, A., Burkard, T., Bagley, J. A., et al. (2018). Genetically engineered cerebral organoids model brain tumor formation. *Nat. Methods* 15, 631–639. doi: 10.1038/s41592-018-0070-7

Birey, F., Andersen, J., Makinson, C. D., Islam, S., Wei, W., Huber, N., et al. (2017). Assembly of functionally integrated human forebrain spheroids. *Nature* 545, 54–59. doi: 10.1038/nature22330

Blair, J. D., Hockemeyer, D., and Bateup, H. S. (2018). Genetically engineered human cortical spheroid models of tuberous sclerosis. *Nat. Med.* 24, 1568–1578. doi: 10.1038/s41591-018-0139-y

Boj, S. F., Vonk, A. M., Statia, M., Su, J., Dekkers, J. F., Vries, R. R. G., et al. (2017). Forskolin-induced swelling in intestinal organoids: an *in vitro* assay for assessing drug response in cystic fibrosis patients. *J. Vis. Exp*. 120:55159. doi: 10.3791/55159

Branco, M. A., Cotovio, J. P., Rodrigues, C. A. V., Vaz, S. H., Fernandes, T. G., Moreira, L. M., et al. (2019). Transcriptomic analysis of 3D cardiac differentiation of human induced pluripotent stem cells reveals faster cardiomyocyte maturation compared to 2D culture. *Sci. Rep.* 9:9229. doi: 10.1038/s41598-019-45047-9

Brassard, J. A., and Lutolf, M. P. (2019). Engineering stem cell self-organization to build better organoids. *Cell Stem Cell* 24, 860–876. doi: 10.1016/j.stem.2019.05.005

Broguiere, N., Isenmann, L., Hirt, C., Ringel, T., Placzek, S., Cavalli, E., et al. (2018). Growth of epithelial organoids in a defined hydrogel. *Adv. Mater.* 30:1801621. doi: 10.1002/adma.201801621

Camp, J. G., Badsha, F., Florio, M., Kanton, S., Gerber, T., Wilsch-Bräuninger, M., et al. (2015). Human cerebral organoids recapitulate gene expression programs of fetal neocortex development. *Proc. Natl. Acad. Sci. U.S.A.* 112, 15672–15677. doi: 10.1073/pnas.1520760112

Candiello, J., Grandhi, T. S. P., Goh, S. K., Vaidya, V., Lemmon-Kishi, M., Eliato, K. R., et al. (2018). 3D heterogeneous islet organoid generation from human embryonic stem cells using a novel engineered hydrogel platform. *Biomaterials* 177, 27–39. doi: 10.1016/j.biomaterials.2018.05.031

Capeling, M. M., Czerwinski, M., Huang, S., Tsai, Y.-H., Wu, A., Nagy, M. S., et al. (2019). Nonadhesive alginate hydrogels support growth of pluripotent stem cell-derived intestinal organoids. *Stem Cell Rep.* 12, 381–394. doi: 10.1016/j.stemcr.2018.12.001

Chambers, S. M., Fasano, C. A., Papapetrou, E. P., Tomishima, M., Sadelain, M., and Studer, L. (2009). Neural conversion of human ES and iPS cells by dual inhibition of SMAD signaling. *Nat. Biotechnol.* 27, 275–280. doi: 10.1038/nbt.1529

Chambers, S. M., Mica, Y., Lee, G., Studer, L., and Tomishima, M. J. (2016). Dual-SMAD inhibition/WNT activation-based methods to induce neural crest and derivatives from human pluripotent stem cells. *Methods Mol. Biol.* 1307, 329–343. doi: 10.1007/7651_2013_59

Charpentier, E., and Marraffini, L. A. (2014). Harnessing CRISPR-Cas9 immunity for genetic engineering. *Curr. Opin. Microbiol.* 19, 114–119. doi: 10.1016/j.mib.2014.07.001

Chavez, A., Scheiman, J., Vora, S., Pruitt, B. W., Tuttle, M., Iyer, E. P. R., et al. (2015). Highly efficient Cas9-mediated transcriptional programming. *Nat. Methods* 12, 326–328. doi: 10.1038/nmeth.3312

Chen, B., Gilbert, L. A., Cimini, B. A., Schnitzbauer, J., Zhang, W., Li, G.-W., et al. (2013). Dynamic imaging of genomic loci in living human cells by an optimized CRISPR/Cas system. *Cell* 155, 1479–1491. doi: 10.1016/j.cell.2013.12.001

Chiang, T.-W. W., le Sage, C., Larrieu, D., Demir, M., and Jackson, S. P. (2016). CRISPR-Cas9(D10A) nickase-based genotypic and phenotypic screening to enhance genome editing. *Sci. Rep.* 6:24356. doi: 10.1038/srep24356

Cho, S. W., Kim, S., Kim, J. M., and Kim, J.-S. (2013). Targeted genome engineering in human cells with the Cas9 RNA-guided endonuclease. *Nat. Biotechnol.* 31, 230–232. doi: 10.1038/nbt.2507

Correia, C., Koshkin, A., Duarte, P., Hu, D., Carido, M., Sebastião, M. J., et al. (2018). 3D aggregate culture improves metabolic maturation of human pluripotent stem cell derived cardiomyocytes. *Biotechnol. Bioeng.* 115, 630–644. doi: 10.1002/bit.26504

Cruz-Acuña, R., Quirós, M., Farkas, A. E., Dedhia, P. H., Huang, S., Siuda, D., et al. (2017). Synthetic hydrogels for human intestinal organoid generation and colonic wound repair. *Nat. Cell Biol.* 19, 1326–1335. doi: 10.1038/ncb3632

Dahlmann, J., Kensah, G., Kempf, H., Skvorc, D., Gawol, A., Elliott, D. A., et al. (2013). The use of agarose microwells for scalable embryoid body formation and cardiac differentiation of human and murine pluripotent stem cells. *Biomaterials* 34, 2463–2471. doi: 10.1016/j.biomaterials.2012.12.024

Dai, Y., Somoza, R. A., Wang, L., Welter, J. F., Li, Y., Caplan, A. I., et al. (2019). Exploring the trans-cleavage activity of CRISPR-Cas12a (cpf1) for the development of a universal electrochemical biosensor. *Angew. Chem. Int. Ed. Engl.* 58, 17399–17405. doi: 10.1002/anie.201910772

de Jong, J. O., Llapashtica, C., Strauss, K., Provenzano, F., Sun, Y., Cortese, G. P., et al. (2019). Cortical overgrowth in a preclinical forebrain organoid model of CNTNAP2-associated autism spectrum disorder. *bioRxiv* [Preprint]. doi: 10.1101/739391

Demers, C. J., Soundararajan, P., Chennampally, P., Cox, G. A., Briscoe, J., Collins, S. D., et al. (2016). Development-on-chip: *in vitro* neural tube patterning with a microfluidic device. *Development* 143, 1884–1892. doi: 10.1242/dev.126847

Deng, W. L., Gao, M. L., Lei, X. L., Lv, J. N., Zhao, H., He, K. W., et al. (2018). Gene correction reverses ciliopathy and photoreceptor loss in iPSC-derived retinal organoids from retinitis pigmentosa patients. *Stem Cell Rep.* 10, 1267–1281. doi: 10.1016/j.stemcr.2018.05.012

Devarasetty, M., Forsythe, S., Shupe, T. D., Soker, S., Bishop, C. E., Atala, A., et al. (2017). Optical tracking and digital quantification of beating behavior in bioengineered human cardiac organoids. *Biosensors* 7:24. doi: 10.3390/bios7030024

Ding, Q., Strong, A., Patel, K. M., Ng, S.-L., Gosis, B. S., Regan, S. N., et al. (2014). Permanent alteration of PCSK9 with *in vivo* CRISPR-Cas9 genome editing. *Circ. Res.* 115, 488–492. doi: 10.1161/CIRCRESAHA.115.304351

Dominguez, A. A., Lim, W. A., and Qi, L. S. (2015). Beyond editing: repurposing CRISPRCas9 for precision genome regulation and interrogation. *Nat. Rev. Mol. Cell Biol.* 17, 5–15. doi: 10.1038/nrm.2015.2

Donato, R., Miljan, E. A., Hines, S. J., Aouabdi, S., Pollock, K., Patel, S., et al. (2007). Differential development of neuronal physiological responsiveness in two human neural stem cell lines. *BMC Neurosci.* 8:36. doi: 10.1186/1471-2202-8-36

Doudna, J. A., and Charpentier, E. (2014). Genome editing. The new frontier of genome engineering with CRISPR-Cas9. *Science* 346:1258096. doi: 10.1126/science.1258096

Drost, J., van Boxtel, R., Blokzijl, F., Mizutani, T., Sasaki, N., Sasselli, V., et al. (2017). Use of CRISPR-modified human stem cell organoids to study the origin of mutational signatures in cancer. *Science* 358, 234–238. doi: 10.1126/science.aao3130

Drost, J., van Jaarsveld, R. H., Ponsioen, B., Zimberlin, C., van Boxtel, R., Buijs, A., et al. (2015). Sequential cancer mutations in cultured human intestinal stem cells. *Nature* 521, 43–47. doi: 10.1038/nature14415

Du, D., and Qi, L. S. (2016). CRISPR technology for genome activation and repression in mammalian cells. *Cold Spring Harb. Protoc.* 2016:pdb.prot090175. doi: 10.1101/pdb.prot090175

Duval, K., Grover, H., Han, L.-H., Mou, Y., Pegoraro, A. F., Fredberg, J., et al. (2017). Modeling physiological events in 2D vs. 3D cell culture. *Physiology* 32, 266–277. doi: 10.1152/physiol.00036.2016

Dye, B. R., Hill, D. R., Ferguson, M. A., Tsai, Y.-H., Nagy, M. S., Dyal, R., et al. (2015). *In vitro* generation of human pluripotent stem cell derived lung organoids. *eLife* 4:e05098. doi: 10.7554/eLife.05098

Eder, T., and Eder, I. E. (2017). 3D hanging drop culture to establish prostate cancer organoids. *Methods Mol. Biol.* 1612, 167–175. doi: 10.1007/978-1-4939-7021-6_12

Eiraku, M., Watanabe, K., Matsuo-Takasaki, M., Kawada, M., Yonemura, S., Matsumura, M., et al. (2008). Self-organized formation of polarized cortical tissues from ESCs and its active manipulation by extrinsic signals. *Cell Stem Cell* 3, 519–532. doi: 10.1016/j.stem.2008.09.002

Fennema, E., Rivron, N., Rouwkema, J., van, B. C., and de, B. J. (2013). Spheroid culture as a tool for creating 3D complex tissues. *Trends Biotechnol.* 31, 108–115. doi: 10.1016/j.tibtech.2012.12.003

Filipponi, L., Livingston, P., Kašpar, O., Tokárová, V., and Nicolau, D. V. (2016). Protein patterning by microcontact printing using pyramidal PDMS stamps. *Biomed. Microdevices* 18:9. doi: 10.1007/s10544-016-0036-4

Foncy, J., Estève, A., Degache, A., Colin, C., Dollat, X., Cau, J. C., et al. (2018). Dynamic inking of large-scale stamps for multiplexed microcontact printing and fabrication of cell microarrays. *PLoS One* 13:e0202531. doi: 10.1371/journal.pone.0202531

Fong, A. H., Romero-López, M., Heylman, C. M., Keating, M., Tran, D., Sobrino, A., et al. (2016). Three-dimensional adult cardiac extracellular matrix promotes maturation of human induced pluripotent stem cell-derived cardiomyocytes. *Tissue Eng. Part A* 22, 1016–1025. doi: 10.1089/ten.TEA.2016.0027

Forbes, T. A., Howden, S. E., Lawlor, K., Phipson, B., Maksimovic, J., Hale, L., et al. (2018). Patient-iPSC-derived kidney organoids show functional validation of a

ciliopathic renal phenotype and reveal underlying pathogenetic mechanisms. *Am. J. Hum. Genet.* 102, 816–831. doi: 10.1016/j.ajhg.2018.03.014

Freedman, B. S., Brooks, C. R., Lam, A. Q., Fu, H., Morizane, R., Agrawal, V., et al. (2015). Modelling kidney disease with CRISPR-mutant kidney organoids derived from human pluripotent epiblast spheroids. *Nat. Commun.* 6:8715. doi: 10.1038/ncomms9715

Freije, C. A., Myhrvold, C., Boehm, C. K., Lin, A. E., Welch, N. L., Carter, A., et al. (2019). Programmable inhibition and detection of RNA viruses using Cas13. *Mol. Cell* 76, 826–837.e11. doi: 10.1016/j.molcel.2019.09.013

Fujimori, K., Ishikawa, M., Otomo, A., Atsuta, N., Nakamura, R., Akiyama, T., et al. (2018). Modeling sporadic ALS in iPSC-derived motor neurons identifies a potential therapeutic agent. *Nat. Med.* 24, 1579–1589. doi: 10.1038/s41591-018-0140-5

Gao, X., Tao, Y., Lamas, V., Huang, M., Yeh, W.-H., Pan, B., et al. (2018). Treatment of autosomal dominant hearing loss by in vivo delivery of genome editing agents. *Nature* 553, 217–221. doi: 10.1038/nature25164

Garita-Hernandez, M., Routet, F., Guibbal, L., Khabou, H., Toualbi, L., Riancho, L., et al. (2020). AAV-mediated gene delivery to 3D retinal organoids derived from human induced pluripotent stem cells. *Int. J. Mol. Sci.* 21:994. doi: 10.3390/ijms21030994

Gaudelli, N. M., Komor, A. C., Rees, H. A., Packer, M. S., Badran, A. H., Bryson, D. I., et al. (2017). Programmable base editing of AT to GC in genomic DNA without DNA cleavage. *Nature* 551, 464–471. doi: 10.1038/nature24644

Genga, R. M., Kearns, N. A., and Maehr, R. (2016). Controlling transcription in human pluripotent stem cells using CRISPR-effectors. *Methods* 101, 36–42. doi: 10.1016/j.ymeth.2015.10.014

Geurts, M. H., de Poel, E., Amatngalim, G. D., Oka, R., Meijers, F. M., Kruisselbrink, E., et al. (2020). CRISPR-based adenine editors correct nonsense mutations in a cystic fibrosis organoid biobank. *Cell Stem Cell.* 26, 503–510.e7. doi: 10.1016/j.stem.2020.01.019

Gilbert, L. A., Larson, M. H., Morsut, L., Liu, Z., Brar, G. A., Torres, S. E., et al. (2013). CRISPR-mediated modular RNA-guided regulation of transcription in eukaryotes. *Cell* 154, 442–451. doi: 10.1016/j.cell.2013.06.044

Gjorevski, N., Sachs, N., Manfrin, A., Giger, S., Bragina, M. E., Ordóñez-Morán, P., et al. (2016). Designer matrices for intestinal stem cell and organoid culture. *Nature* 539, 560–564. doi: 10.1038/nature20168

Gomez-Giro, G., Arias-Fuenzalida, J., Jarazo, J., Zeuschner, D., Ali, M., Possemis, N., et al. (2019). Synapse alterations precede neuronal damage and storage pathology in a human cerebral organoid model of CLN3-juvenile neuronal ceroid lipofuscinosis. *Acta Neuropathol. Commun.* 7:222. doi: 10.1186/s40478-019-0871-7

Gootenberg, J. S., Abudayyeh, O. O., Kellner, M. J., Joung, J., Collins, J. J., and Zhang, F. (2018). Multiplexed and portable nucleic acid detection platform with Cas13, Cas12a, and Csm6. *Science* 360, 439–444. doi: 10.1126/science.aaq0179

Granados-Riveron, J. T., and Aquino-Jarquin, G. (2018). CRISPR–Cas13 precision transcriptome engineering in cancer. *Cancer Res.* 78, 4107–4113. doi: 10.1158/0008-5472.CAN-18-0785

Grebenyuk, S., and Ranga, A. (2019). Engineering organoid vascularization. *Front. Bioeng. Biotechnol.* 7:39. doi: 10.3389/fbioe.2019.00039

Guilinger, J. P., Thompson, D. B., and Liu, D. R. (2014). Fusion of catalytically inactive Cas9 to FokI nuclease improves the specificity of genome modification. *Nat. Biotechnol.* 32, 577–582. doi: 10.1038/nbt.2909

Hai, T., Teng, F., Guo, R., Li, W., and Zhou, Q. (2014). One-step generation of knockout pigs by zygote injection of CRISPR/Cas system. *Cell Res.* 24, 372–375. doi: 10.1038/cr.2014.11

Heman-Ackah, S. M., Bassett, A. R., and Wood, M. J. A. (2016). Precision modulation of neurodegenerative disease-related gene expression in human iPSC-derived neurons. *Sci. Rep.* 6:28420. doi: 10.1038/srep28420

Heman-Ackah, S. M., Manzano, R., Hoozemans, J. J., Scheper, W., Flynn, R., Haerty, W., et al. (2017). Alpha-synuclein induces the unfolded protein response in Parkinson's disease SNCA triplication iPSC-derived neurons. *Hum. Mol. Genet.* 26, 4441–4450. doi: 10.1093/hmg/ddx331

Hofherr, A., and Köttgen, M. (2013). Induced pluripotent stem cells from polycystic kidney disease patients: a novel tool to model the pathogenesis of cystic kidney disease. *J. Am. Soc. Nephrol.* 24, 1507–1509. doi: 10.1681/asn.2013070767

Hruscha, A., Krawitz, P., Rechenberg, A., Heinrich, V., Hecht, J., Haass, C., et al. (2013). Efficient CRISPR/Cas9 genome editing with low off-target effects in zebrafish. *Development* 140, 4982–4987. doi: 10.1242/dev.099085

Hsiao, A. Y., Tung, Y. C., Qu, X., Patel, L. R., Pienta, K. J., and Takayama, S. (2012). 384 hanging drop arrays give excellent Z-factors and allow versatile formation of co-culture spheroids. *Biotechnol. Bioeng.* 109, 1293–1304. doi: 10.1002/bit.24399

Huang, K.-C., Wang, M.-L., Chen, S.-J., Kuo, J.-C., Wang, W.-J., Nguyen, P. N. N., et al. (2019). Morphological and molecular defects in human three-dimensional retinal organoid model of X-linked juvenile retinoschisis. *Stem Cell Rep.* 13, 906–923. doi: 10.1016/j.stemcr.2019.09.010

Hwang, W. Y., Fu, Y., Reyon, D., Maeder, M. L., Tsai, S. Q., Sander, J. D., et al. (2013). Efficient genome editing in zebrafish using a CRISPR-Cas system. *Nat. Biotechnol.* 31, 227–229. doi: 10.1038/nbt.2501

Iefremova, V., Manikakis, G., Krefft, O., Jabali, A., Weynans, K., Wilkens, R., et al. (2017). An organoid-based model of cortical development identifies non-cell-autonomous defects in Wnt signaling contributing to Miller-Dieker Syndrome. *Cell Rep.* 19, 50–59. doi: 10.1016/j.celrep.2017.03.047

Ihry, R. J., Salick, M. R., Ho, D. J., Sondey, M., Kommineni, S., Paula, S., et al. (2019). Genome-scale CRISPR screens identify human pluripotency-specific genes. *Cell Rep.* 27, 616–630.e6. doi: 10.1016/j.celrep.2019.03.043

Jung, K. B., Kwon, O., Lee, M.-O., Lee, H., Son, Y. S., Habib, O., et al. (2019). Blockade of STAT3 causes severe *in vitro* and *in vivo* maturation defects in intestinal organoids derived from human embryonic stem cells. *J. Clin. Med.* 8:976. doi: 10.3390/jcm8070976

Kampmann, M. (2017). CRISPRi and CRISPRa screens in mammalian cells for precision biology and medicine. *ACS Chem. Biol.* 13, 406–416. doi: 10.1021/acschembio.7b00657

Kang, J. H., Gimble, J. M., and Kaplan, D. L. (2009). *In vitro* 3D model for human vascularized adipose tissue. *Tissue Eng. Part A* 15, 2227–2236. doi: 10.1089/ten.tea.2008.0469

Karzbrun, E., Kshirsagar, A., Cohen, S. R., Hanna, J. H., and Reiner, O. (2018). Human brain organoids on a chip reveal the physics of folding. *Nat. Phys.* 14, 515–522. doi: 10.1038/s41567-018-0046-7

Kearns, N. A., Genga, R. M., Enuameh, M. S., Garber, M., Wolfe, S. A., and Maehr, R. (2014). Cas9 effector-mediated regulation of transcription and differentiation in human pluripotent stem cells. *Development* 141, 219–223. doi: 10.1242/dev.103341

Kim, H., Park, H. J., Choi, H., Chang, Y., Park, H., Shin, J., et al. (2019). Modeling G2019S-LRRK2 sporadic Parkinson's disease in 3D midbrain organoids. *Stem Cell Rep.* 12, 518–531. doi: 10.1002/stem.2707

Kim, Y. K., Refaeli, I., Brooks, C. R., Jing, P., Gulieva, R. E., Hughes, M. R., et al. (2017). Gene-edited human kidney organoids reveal mechanisms of disease in podocyte development. *Stem Cells* 35, 2366–2378.

Kim, Y. Y., Kim, H., Suh, C. S., Liu, H.-C., Rosenwaks, Z., and Ku, S.-Y. (2020). Effects of natural progesterone and synthetic progestin on germ layer gene expression in a human embryoid body model. *Int. J. Mol. Sci.* 21:769. doi: 10.3390/ijms21030769

Klaus, J., Kanton, S., Kyrousi, C., Ayo-Martin, A. C., Giaimo, R. D., Riesenberg, S., et al. (2019). Altered neuronal migratory trajectories in human cerebral organoids derived from individuals with neuronal heterotopia. *Nat. Med.* 25, 561–568. doi: 10.1038/s41591-019-0371-0

Komor, A. C., Kim, Y. B., Packer, M. S., Zuris, J. A., and Liu, D. R. (2016). Programmable editing of a target base in genomic DNA without double-stranded DNA cleavage. *Nature* 533, 420–424. doi: 10.1038/nature17946

Konermann, S., Brigham, M. D., Trevino, A. E., Joung, J., Abudayyeh, O. O., Barcena, C., et al. (2015). Genome-scale transcriptional activation by an engineered CRISPR-Cas9 complex. *Nature* 517, 583–588. doi: 10.1038/nature14136

Kook, Y.-M., Kim, H., Kim, S., Lee, K., Heo, C. Y., Park, M. H., et al. (2018). Promotion of vascular morphogenesis of endothelial cells co-cultured with human adipose-derived mesenchymal stem cells using polycaprolactone/gelatin nanofibrous scaffolds. *Nanomaterials* 8:117. doi: 10.3390/nano8020117

Kwon, S. J., Lee, D. W., Shah, D. A., Ku, B., Jeon, S. Y., Solanki, K., et al. (2014). High-throughput and combinatorial gene expression on a chip for metabolism-induced toxicology screening. *Nat. Commun.* 5:3739. doi: 10.1038/ncomms4739

Lancaster, M. A., and Knoblich, J. A. (2014). Generation of cerebral organoids from human pluripotent stem cells. *Nat. Protoc.* 9, 2329–2340. doi: 10.1038/nprot.2014.158

Lancaster, M. A., Renner, M., Martin, C.-A., Wenzel, D., Bicknell, L. S., Hurles, M. E., et al. (2013). Cerebral organoids model human brain development and microcephaly. *Nature* 501, 373–379. doi: 10.1038/nature12517

Laperrousaz, B., Porte, S., Gerbaud, S., Härmä, V., Kermarrec, F., Hourtane, V., et al. (2018). Direct transfection of clonal organoids in Matrigel microbeads: a promising approach toward organoid-based genetic screens. *Nucleic Acids Res.* 46:e70. doi: 10.1093/nar/gky030

Larson, M. H., Gilbert, L. A., Wang, X., Lim, W. A., Weissman, J. S., and Qi, L. S. (2013). CRISPR interference (CRISPRi) for sequence-specific control of gene expression. *Nat. Protoc.* 8, 2180–2196. doi: 10.1038/nprot.2013.132

Latour, Y. L., Yoon, R., Thomas, S. E., Grant, C., Li, C., Sena-Esteves, M., et al. (2019). Human GLB1 knockout cerebral organoids: a model system for testing AAV9-mediated GLB1 gene therapy for reducing GM1 ganglioside storage in GM1 gangliosidosis. *Mol. Genet. Metab. Rep.* 21:100513. doi: 10.1016/j.ymgmr.2019.100513

Lee, M.-O., Jung, K. B., Jo, S.-J., Hyun, S.-A., Moon, K.-S., Seo, J.-W., et al. (2019). Modelling cardiac fibrosis using three-dimensional cardiac microtissues derived from human embryonic stem cells. *J. Biol. Eng.* 13:15. doi: 10.1186/s13036-019-0139-6

Li, Y., Muffat, J., Omer, A., Bosch, I., Lancaster, M. A., Sur, M., et al. (2017). Induction of expansion and folding in human cerebral organoids. *Cell Stem Cell* 20, 385–396.e3. doi: 10.1016/j.stem.2016.11.017

Lian, X., Hsiao, C., Wilson, G., Zhu, K., Hazeltine, L. B., Azarin, S. M., et al. (2012). Robust cardiomyocyte differentiation from human pluripotent stem cells via temporal modulation of canonical Wnt signaling. *Proc. Natl. Acad. Sci. U.S.A.* 109, E1848–E1857. doi: 10.1073/pnas.1200250109

Libby, A. R. G., Briers, D., Haghighi, I., Joy, D. A., Conklin, B. R., Belta, C., et al. (2019). Automated design of pluripotent stem cell self-organization. *Cell Syst.* 9, 483–495.e10. doi: 10.1016/j.cels.2019.10.008

Lin, Y.-T., Seo, J., Gao, F., Feldman, H. M., Wen, H.-L., Penney, J., et al. (2018). APOE4 causes widespread molecular and cellular alterations associated with Alzheimer's disease phenotypes in human iPSC-derived brain cell types. *Neuron* 98, 1141–1154.e7. doi: 10.1016/j.neuron.2018.05.008

Lindborg, B. A., Brekke, J. H., Vegoe, A. L., Ulrich, C. B., Haider, K. T., Subramaniam, S., et al. (2016). Rapid induction of cerebral organoids from human induced pluripotent stem cells using a chemically defined hydrogel and defined cell culture medium. *Stem Cells Transl. Med.* 5, 970–979. doi: 10.5966/sctm.2015-0305

Lo, A., and Qi, L. (2017). Genetic and epigenetic control of gene expression by CRISPR-Cas systems. *F1000Res.* 6:F1000. doi: 10.12688/f1000research.11113.1

Lu, Y.-C., Fu, D.-J., An, D., Chiu, A., Schwartz, R., Nikitin, A. Y., et al. (2017). Scalable production and cryostorage of organoids using core-shell decoupled hydrogel capsules. *Adv. Biosyst.* 1:1700165. doi: 10.1002/adbi.201700165

Luo, C., Lancaster, M. A., Castanon, R., Nery, J. R., Knoblich, J. A., and Ecker, J. R. (2016). Cerebral organoids recapitulate epigenomic signatures of the human fetal brain. *Cell Rep.* 17, 3369–3384. doi: 10.1016/j.celrep.2016.12.001

Luo, J. (2016). CRISPR/Cas9: from genome engineering to cancer drug discovery. *Trends Cancer* 2, 313–324. doi: 10.1016/j.trecan.2016.05.001

Maeder, M. L., Linder, S. J., Cascio, V. M., Fu, Y., Ho, Q. H., and Joung, J. K. (2013). CRISPR RNA-guided activation of endogenous human genes. *Nat. Methods* 10, 977–979. doi: 10.1038/nmeth.2598

Mandegar, M. A., Huebsch, N., Frolov, E. B., Shin, E., Truong, A., Olvera, M. P., et al. (2016). CRISPR interference efficiently induces specific and reversible gene silencing in human iPSCs. *Cell Stem Cell* 18, 541–553. doi: 10.1016/j.stem.2016.01.022

Mani, M., Smith, J., Kandavelou, K., Berg, J. M., and Chandrasegaran, S. (2005). Binding of two zinc finger nuclease monomers to two specific sites is required for effective double-strand DNA cleavage. *Biochem. Biophys. Res. Commun.* 334, 1191–1197. doi: 10.1016/j.bbrc.2005.07.021

Maruyama, T., Dougan, S. K., Truttmann, M. C., Bilate, A. M., Ingram, J. R., and Ploegh, H. L. (2015). Increasing the efficiency of precise genome editing with CRISPR-Cas9 by inhibition of nonhomologous end joining. *Nat. Biotechnol.* 33, 538–542. doi: 10.1038/nbt.3190

Matano, M., Date, S., Shimokawa, M., Takano, A., Fujii, M., Ohta, Y., et al. (2015). Modeling colorectal cancer using CRISPR-Cas9-mediated engineering of human intestinal organoids. *Nat. Med.* 21, 256–262. doi: 10.1038/nm.3802

Michels, B. E., Mosa, M. H., Streibl, B. I., Zhan, T., Menche, C., Abou-El-Ardat, K., et al. (2020). Pooled *in vitro* and *in vivo* CRISPR-Cas9 screening identifies tumor suppressors in human colon organoids. *Cell Stem Cell* 26, 782–792.e7. doi: 10.1016/j.stem.2020.04.003

Mitsunaga, S., Odajima, J., Yawata, S., Shioda, K., Owa, C., Isselbacher, K. J., et al. (2017). Relevance of iPSC-derived human PGC-like cells at the surface of embryoid bodies to prechemotaxis migrating PGCs. *Proc. Natl. Acad. Sci. U.S.A.* 114, E9913–E9922. doi: 10.1073/pnas.1707779114

Mohr, S. E., and Perrimon, N. (2012). RNAi screening: new approaches. Understandings and Organisms. *Wiley Interdiscip. Rev. RNA* 3, 145–158. doi: 10.1002/wrna.110

Nakagawa, M., Koyanagi, M., Tanabe, K., Takahashi, K., Ichisaka, T., Aoi, T., et al. (2008). Generation of induced pluripotent stem cells without Myc from mouse and human fibroblasts. *Nat. Biotechnol.* 26, 101–106. doi: 10.1038/nbt1374

Nakamura, M., Shiozawa, S., Tsuboi, D., Amano, M., Watanabe, H., Maeda, S., et al. (2019). Pathological progression induced by the frontotemporal dementia-associated R406W Tau mutation in patient-derived iPSCs. *Stem Cell Rep.* 13, 684–699. doi: 10.1016/j.stemcr.2019.08.011

Nierode, G. J., Gopal, S., Kwon, P., Clark, D. S., Schaffer, D. V., and Dordick, J. S. (2019). High-throughput identification of factors promoting neuronal differentiation of human neural progenitor cells in microscale 3D cell culture. *Biotechnol. Bioeng.* 116, 168–180. doi: 10.1002/bit.26839

Novik, E., Maguire, T. J., Chao, P., Cheng, K. C., and Yarmush, M. L. (2010). A microfluidic hepatic coculture platform for cell-based drug metabolism studies. *Biochem. Pharmacol.* 79, 1036–1044. doi: 10.1016/j.bcp.2009.11.010

Oceguera-Yanez, F., Kim, S. I., Matsumoto, T., Tan, G. W., Xiang, L., Hatani, T., et al. (2016). Engineering the AAVS1 locus for consistent and scalable transgene expression in human iPSCs and their differentiated derivatives. *Methods* 101, 43–55. doi: 10.1016/j.ymeth.2015.12.012

Ogawa, J., Pao, G. M., Shokhirev, M. N., and Verma, I. M. (2018). Glioblastoma model using human cerebral organoids. *Cell Rep.* 23, 1220–1229. doi: 10.1016/j.celrep.2018.03.105

Ootani, A., Li, X., Sangiorgi, E., Ho, Q. T., Ueno, H., Toda, S., et al. (2009). Sustained in vitro intestinal epithelial culture within a Wnt-dependent stem cell niche. *Nat. Med.* 15, 701–706. doi: 10.1038/nm.1951

O'Rourke, K. P., Loizou, E., Livshits, G., Schatoff, E. M., Baslan, T., Manchado, E., et al. (2017). Transplantation of engineered organoids enables rapid generation of metastatic mouse models of colorectal cancer. *Nat. Biotechnol.* 35, 577–582. doi: 10.1038/nbt.3837

Ortega-Prieto, A. M., Skelton, J. K., Wai, S. N., Large, E., Lussignol, M., Vizcay-Barrena, G., et al. (2018). 3D microfluidic liver cultures as a physiological preclinical tool for hepatitis B virus infection. *Nat. Commun.* 9:682. doi: 10.1038/s41467-018-02969-8

Ovsianikov, A., Deiwick, A., Van Vlierberghe, S., Pflaum, M., Wilhelmi, M., Dubruel, P., et al. (2011). Laser fabrication of 3D gelatin scaffolds for the generation of bioartificial tissues. *Materials*, 4, 288–299. doi: 10.3390/ma4010288

Papikian, A., Liu, W., Gallego-Bartolomé, J., and Jacobsen, S. E. (2019). Site-specific manipulation of Arabidopsis loci using CRISPR-Cas9 SunTag systems. *Nat. Commun.* 10:729. doi: 10.1038/s41467-019-08736-7

Paşca, A. M., Sloan, S. A., Clarke, L. E., Tian, Y., Makinson, C. D., Huber, N., et al. (2015). Functional cortical neurons and astrocytes from human pluripotent stem cells in 3D culture. *Nat. Methods* 12, 671–678. doi: 10.1038/nmeth.3415

Pickar-Oliver, A., and Gersbach, C. A. (2019). The next generation of CRISPRCas technologies and applications. *Nat. Rev. Mol. Cell Biol.* 20, 490–507. doi: 10.1038/s41580-019-0131-5

Pollard, B. S., and Pollard, H. B. (2018). Induced pluripotent stem cells for treating cystic fibrosis: state of the science. *Pediatr. Pulmonol.* 53, S12–S29. doi: 10.1002/ppul.24118

Qi, L. S., Larson, M. H., Gilbert, L. A., Doudna, J. A., Weissman, J. S., Arkin, A. P., et al. (2013). Repurposing CRISPR as an RNA-guided platform for sequence-specific control of gene expression. *Cell* 152, 1173–1183. doi: 10.1016/j.cell.2013.02.022

Ran, F. A., Hsu, P. D., Lin, C.-Y., Gootenberg, J. S., Konermann, S., Trevino, A., et al. (2013a). Double nicking by RNA-guided CRISPR Cas9 for enhanced genome editing specificity. *Cell* 154, 1380–1389. doi: 10.1016/j.cell.2013.08.021

Ran, F. A., Hsu, P. D., Wright, J., Agarwala, V., Scott, D. A., and Zhang, F. (2013b). Genome engineering using the CRISPR-Cas9 system. *Nat. Protoc.* 8, 2281–2308. doi: 10.1038/nprot.2013.143

Reya, T., Morrison, S. J., Clarke, M. F., and Weissman, I. L. (2001). Stem cells cancer, and cancer stem cells. *Nature* 414, 105–111. doi: 10.1038/35102167

Ringel, T., Frey, N., Ringnalda, F., Janjuha, S., Cherkaoui, S., Butz, S., et al. (2020). Genome-scale CRISPR screening in human intestinal organoids identifies drivers of TGF-β Resistance. *Cell Stem Cell* 26, 431–440.e8. doi: 10.1016/j.stem.2020.02.007

Rivron, N. C., Vrij, E. J., Rouwkema, J., Le, G. S., van den, B. A., Truckenmüller, R. K., et al. (2012). Tissue deformation spatially modulates VEGF signaling and angiogenesis. *Proc. Natl. Acad. Sci. U.S.A.* 109, 6886–6891. doi: 10.1073/pnas.1201626109

Roper, J., Tammela, T., Cetinbas, N. M., Akkad, A., Roghanian, A., Rickelt, S., et al. (2017). In vivo genome editing and organoid transplantation models of colorectal cancer and metastasis. *Nat. Biotechnol.* 35, 569–576. doi: 10.1038/nbt.3836

Rungarunlert, S., Techakumphu, M., Pirity, M. K., and Dinnyes, A. (2009). Embryoid body formation from embryonic and induced pluripotent stem cells: benefits of bioreactors. *World J. Stem Cells* 1, 11–21. doi: 10.4252/wjsc.v1.i1.11

Sato, T., Vries, R. G., Snippert, H. J., van de Wetering, M., Barker, N., Stange, D. E., et al. (2009). Single Lgr5 stem cells build crypt-villus structures in vitro without a mesenchymal niche. *Nature* 459, 262–265. doi: 10.1038/nature07935

Schuijers, J., Junker, J. P., Mokry, M., Hatzis, P., Koo, B.-K., Sasselli, V., et al. (2015). Ascl2 Acts as an R-spondin/Wnt-responsive switch to control stemness in intestinal crypts. *Cell Stem Cell* 16, 158–170. doi: 10.1016/j.stem.2014.12.006

Schwank, G., Koo, B.-K., Sasselli, V., Dekkers, J. F., Heo, I., Demircan, T., et al. (2013). Functional repair of CFTR by CRISPR/Cas9 in Intestinal Stem Cell Organoids of Cystic Fibrosis Patients. *Cell Stem Cell* 13, 653–658. doi: 10.1016/j.stem.2013.11.002

Shalem, O., Sanjana, N. E., Hartenian, E., Shi, X., Scott, D. A., Mikkelsen, T. S., et al. (2014). Genome-Scale CRISPR-Cas9 Knockout Screening in Human Cells. *Science* 343, 84–87. doi: 10.1126/science.1247005

Shalem, O., Sanjana, N. E., and Zhang, F. (2015). High-throughput functional genomics using CRISPR-Cas9. *Nat. Rev. Gen.* 16, 299–311. doi: 10.1038/nrg3899

Shamblott, M. J., Axelman, J., Wang, S., Bugg, E. M., Littlefield, J. W., Donovan, P. J., et al. (1998). Derivation of pluripotent stem cells from cultured human primordial germ cells. *Proc. Natl. Acad. Sci. U.S.A.* 95, 13726–13731. doi: 10.1073/pnas.95.23.13726

Shan, Q., Wang, Y., Li, J., and Gao, C. (2014). Genome editing in rice and wheat using the CRISPR/Cas system. *Nat. Protoc.* 9, 2395–2410. doi: 10.1038/nprot.2014.157

Shen, M. W., Arbab, M., Hsu, J. Y., Worstell, D., Culbertson, S. J., Krabbe, O., et al. (2019). Author correction: predictable and precise template-free CRISPR editing of pathogenic variants. *Nature* 567, E1–E2. doi: 10.1038/s41586-019-0938-4

Shin, S. R., Zhang, Y. S., Kim, D. J., Manbohi, A., Avci, H., Silvestri, A., et al. (2016). Aptamer-based microfluidic electrochemical biosensor for monitoring cell-secreted trace cardiac biomarkers. *Anal. Chem.* 88, 10019–10027. doi: 10.1021/acs.analchem.6b02028

Silva, T. P., Cotovio, J. P., Bekman, E., Carmo-Fonseca, M., Cabral, J. M. S., and Fernandes, T. G. (2019). Design principles for pluripotent stem cell-derived organoid engineering. *Stem Cells Int.* 2019:4508470. doi: 10.1155/2019/4508470

Simian, M., and Bissell, M. J. (2017). Organoids: a historical perspective of thinking in three dimensions. *J. Cell Biol.* 216, 31–40. doi: 10.1083/jcb.201610056

Sluch, V. M., Davis, C. O., Ranganathan, V., Kerr, J. M., Krick, K., Martin, R., et al. (2015). Differentiation of human ESCs to retinal ganglion cells using a CRISPR engineered reporter cell line. *Sci. Rep.* 5:16595. doi: 10.1038/srep16595

Smith, E., and Cochrane, W. J. (1946). CYSTIC ORGANOID TERATOMA: (Report of a Case). *Can. Med. Assoc. J.* 55, 151–152.

So, R. W. L., Chung, S. W., Lau, H. H. C., Watts, J. J., Gaudette, E., Al-Azzawi, Z. A. M., et al. (2019). Application of CRISPR genetic screens to investigate neurological diseases. *Mol. Neurodegener.* 14:41. doi: 10.1186/s13024-019-0343-3

Stoddard-Bennett, T., and Reijo, P. R. (2019). Treatment of Parkinson's disease through personalized medicine and induced pluripotent stem cells. *Cells* 8:26. doi: 10.3390/cells8010026

Strikoudis, A., Cieślak, A., Loffredo, L., Chen, Y.-W., Patel, N., Saqi, A., et al. (2019). Modeling of fibrotic lung disease using 3d organoids derived from human pluripotent stem cells. *Cell Rep.* 27, 3709–3723.e5. doi: 10.1016/j.celrep.2019.05.077

Takei, Y., Shah, S., Harvey, S., Qi, L. S., and Cai, L. (2017). Multiplexed dynamic imaging of genomic loci by combined CRISPR imaging and DNA Sequential FISH. *Biophys. J.* 112, 1773–1776. doi: 10.1016/j.bpj.2017.03.024

Takezawa, T., Ozaki, K., Nitani, A., Takabayashi, C., and Shimo-Oka, T. (2004). Collagen vitrigel: a novel scaffold that can facilitate a three-dimensional culture for reconstructing organoids. *Cell Transplant.* 13, 463–473. doi: 10.3727/000000004783983882

Tekin, H., Simmons, S., Cummings, B., Gao, L., Adiconis, X., Hession, C. C., et al. (2018). Effects of 3D culturing conditions on the transcriptomic profile of stem-cell-derived neurons. *Nat. Biomed. Eng.* 2, 540–554. doi: 10.1038/s41551-018-0219-9

Thakore, P. I., D'Ippolito, A. M., Song, L., Safi, A., Shivakumar, N. K., Kabadi, A. M., et al. (2015). Highly specific epigenome editing by CRISPR-Cas9 repressors for silencing of distal regulatory elements. *Nat. Methods* 12, 1143–1149. doi: 10.1038/nmeth.3630

Tian, R., Gachechiladze, M. A., Ludwig, C. H., Laurie, M. T., Hong, J. Y., Nathaniel, D., et al. (2019). CRISPR interference-based platform for multimodal genetic screens in human iPSC-derived neurons. *Neuron* 104, 239–255.e12. doi: 10.1016/j.neuron.2019.07.014

Tonin, R., Caciotti, A., Procopio, E., Fischetto, R., Deodato, F., Mancardi, M. M., et al. (2019). Pre-diagnosing and managing patients with GM1 gangliosidosis and related disorders by the evaluation of GM1 ganglioside content. *Sci. Rep.* 9:17684. doi: 10.1038/s41598-019-53995-5

Ungrin, M. D., Joshi, C., Nica, A., Bauwens, C., and Zandstra, P. W. (2008). Reproducible, ultra high-throughput formation of multicellular organization from single cell suspension-derived human embryonic stem cell aggregates. *PLoS One* 3:e1565. doi: 10.1371/journal.pone.0001565

van Rijn, J. M., Ardy, R. C., Kuloğlu, Z., Härter, B., van Haaften-Visser, D. Y., van der Doef, H. P. J., et al. (2018). Intestinal failure and aberrant lipid metabolism in patients with DGAT1 deficiency. *Gastroenterology* 155, 130–143.e15. doi: 10.1053/j.gastro.2018.03.040

Wang, P., Lin, M., Pedrosa, E., Hrabovsky, A., Zhang, Z., Guo, W., et al. (2017). CRISPR/Cas9-mediated heterozygous knockout of the autism gene CHD8 and characterization of its transcriptional networks in neurodevelopment. *Mol. Autism* 8:11. doi: 10.1186/s13229-017-0124-1

Wells, M. F., Salick, M. R., Wiskow, O., Ho, D. J., Worringer, K. A., Ihry, R. J., et al. (2016). Genetic ablation of AXL does not protect human neural progenitor cells and cerebral organoids from Zika Virus infection. *Cell Stem Cell* 19, 703–708. doi: 10.1016/j.stem.2016.11.011

Wilkinson, D. C., Alva-Ornelas, J. A., Sucre, J. M. S., Vijayaraj, P., Durra, A., Richardson, W., et al. (2017). Development of a three-dimensional bioengineering technology to generate lung tissue for personalized disease modeling. *Stem Cells Transl. Med.* 6, 622–633. doi: 10.5966/sctm.2016-0192

Woo, D.-H., Chen, Q., Yang, T.-L. B., Glineburg, M. R., Hoge, C., Leu, N. A., et al. (2016). Enhancing a Wnt-telomere feedback loop restores intestinal stem cell function in a human organotypic model of Dyskeratosis Congenita. *Cell Stem Cell* 19, 397–405. doi: 10.1016/j.stem.2016.05.024

Wörsdörfer, P., Dalda, N., Kern, A., Krüger, S., Wagner, N., Kwok, C. K., et al. (2019). Generation of complex human organoid models including vascular networks by incorporation of mesodermal progenitor cells. *Sci. Rep.* 9:15663. doi: 10.1038/s41598-019-52204-7

Wu, J., Hunt, S. D., Xue, H., Liu, Y., and Darabi, R. (2016). Generation and characterization of a MYF5 reporter human iPS cell line using CRISPR/Cas9 mediated homologous recombination. *Sci. Rep.* 6:18759. doi: 10.1038/srep18759

Xiao, A., Wang, Z., Hu, Y., Wu, Y., Luo, Z., Yang, Z., et al. (2013). Chromosomal deletions and inversions mediated by TALENs and CRISPR/Cas in zebrafish. *Nucleic Acids Res.* 41:e141. doi: 10.1093/nar/gkt464

Yang, L.-Z., Wang, Y., Li, S.-Q., Yao, R.-W., Luan, P.-F., Wu, H., et al. (2019). Dynamic imaging of RNA in living cells by CRISPR-Cas13 systems. *Mol. Cell* 76, 981–997.e987. doi: 10.1016/j.molcel.2019.10.024

Yoon, S. J., Elahi, L. S., Pașca, A. M., Marton, R. M., Gordon, A., Revah, O., et al. (2019). Reliability of human cortical organoid generation. *Nat. Methods* 16, 75–78. doi: 10.1038/s41592-018-0255-0

Young, H. E., and Black, A. C. (2004). Adult stem cells. *Anat. Rec. A Discov. Mol. Cell. Evol. Biol.* 276, 75–102. doi: 10.1002/ar.a.10134

Zhang, J.-P., Li, X.-L., Li, G.-H., Chen, W., Arakaki, C., and Botimer, G. D. (2017). Efficient precise knockin with a double cut HDR donor after CRISPR/Cas9-mediated double-stranded DNA cleavage. *Genome Biol.* 18:35. doi: 10.1186/s13059-017-1164-8

Zhang, Y. S., Arneri, A., Bersini, S., Shin, S.-R., Zhu, K., Goli-Malekabadi, Z., et al. (2016). Bioprinting 3D microfibrous scaffolds for engineering endothelialized myocardium and heart-on-a-chip. *Biomaterials* 110, 45–59. doi: 10.1016/j.biomaterials.2016.09.003

Zhao, H., Chen, Y., Shao, L., Xie, M., Nie, J., Qiu, J., et al. (2018). Airflow-assisted 3D bioprinting of human heterogeneous microspheroidal organoids with microfluidic nozzle. *Small* 14:1802630. doi: 10.1002/smll.201802630

Zhou, J., Wang, C., Zhang, K., Wang, Y., Gong, X., Wang, Y., et al. (2016). Generation of human embryonic stem cell line expressing zsgreen in cholinergic neurons using CRISPR/Cas9 system. *Neurochem. Res.* 41, 2065–2074. doi: 10.1007/s11064-016-1918-9

Zuk, P. A., Zhu, M., Ashjian, P., Ugarte, D. A. D., Huang, J. I., Mizuno, H., et al. (2002). Human adipose tissue is a source of multipotent stem cells. *Mol. Biol. Cell* 13, 4279–4295.

Conflict of Interest: The authors declare that the research was conducted in the absence of any commercial or financial relationships that could be construed as a potential conflict of interest.

frontiers in Bioengineering and Biotechnology

REVIEW
published: 24 June 2020
doi: 10.3389/fbioe.2020.00640

Influence of Microenvironment on Mesenchymal Stem Cell Therapeutic Potency: From Planar Culture to Microcarriers

Ang-Chen Tsai†, Richard Jeske, Xingchi Chen, Xuegang Yuan and Yan Li**

Department of Chemical and Biomedical Engineering, FAMU-FSU College of Engineering, Florida State University, Tallahassee, FL, United States

Human mesenchymal stem cells (hMSCs) are a promising candidate in cell therapy as they exhibit multilineage differentiation, homing to the site of injury, and secretion of trophic factors that facilitate tissue healing and/or modulate immune response. As a result, hMSC-derived products have attracted growing interests in preclinical and clinical studies. The development of hMSC culture platforms for large-scale biomanufacturing is necessary to meet the requirements for late-phase clinical trials and future commercialization. Microcarriers in stirred-tank bioreactors have been widely utilized in large-scale expansion of hMSCs for translational applications because of a high surface-to-volume ratio compared to conventional 2D planar culture. However, recent studies have demonstrated that microcarrier-expanded hMSCs differ from dish- or flask-expanded cells in size, morphology, proliferation, viability, surface markers, gene expression, differentiation potential, and secretome profile which may lead to altered therapeutic potency. Therefore, understanding the bioprocessing parameters that influence hMSC therapeutic efficacy is essential for the optimization of microcarrier-based bioreactor system to maximize hMSC quantity without sacrificing quality. In this review, biomanufacturing parameters encountered in planar culture and microcarrier-based bioreactor culture of hMSCs are compared and discussed with specific focus on cell-adhesion surface (e.g., discontinuous surface, underlying curvature, microcarrier stiffness, porosity, surface roughness, coating, and charge) and the dynamic microenvironment in bioreactor culture (e.g., oxygen and nutrients, shear stress, particle collision, and aggregation). The influence of dynamic culture in bioreactors on hMSC properties is also reviewed in order to establish connection between bioprocessing and stem cell function. This review addresses fundamental principles and concepts for future design of biomanufacturing systems for hMSC-based therapy.

Keywords: human mesenchymal stem cells, microcarriers, bioreactors, shear stress, microenvironment, expansion

OPEN ACCESS

Edited by:
Tiago G. Fernandes, University of Lisbon, Portugal

Reviewed by:
Denise Salzig, University of Applied Sciences Mittelhessen, Germany
Amanda Mizukami, Hemocentro Foundation of Ribeirão Preto, Brazil
Nohra E. Beltran, Metropolitan Autonomous University, Mexico

****Correspondence:***
Xuegang Yuan
xy13b@my.fsu.edu
Yan Li
yli4@fsu.edu

†Present address:
Ang-Chen Tsai, University of Florida, Gainesville, FL, United States

Specialty section:
This article was submitted to Bioprocess Engineering, a section of the journal Frontiers in Bioengineering and Biotechnology

Received: *18 March 2020*
Accepted: *26 May 2020*
Published: *24 June 2020*

Citation:
Tsai A-C, Jeske R, Chen X, Yuan X and Li Y (2020) Influence of Microenvironment on Mesenchymal Stem Cell Therapeutic Potency: From Planar Culture to Microcarriers. Front. Bioeng. Biotechnol. 8:640. doi: 10.3389/fbioe.2020.00640

INTRODUCTION

Human mesenchymal stem cells (hMSCs) are a rising candidate for cell therapy and have attracted growing interests due to their ability of immunomodulation and trophic effects beyond tri-lineage differentiation. With thousands of *in vitro* and *in vivo* studies and more than 1000 hMSC-based clinical trials completed or in progress on ClinicalTrials.gov, the potential of hMSCs in therapeutic applications is very promising (Atkinson et al., 2017; Tsuchiya et al., 2019). However, to confirm the effectiveness of hMSCs in cell therapy, late phases of clinical trials require a large amount of cells for transplantation and administration into patients (Yin et al., 2019). In addition, as an immunomodulator, hMSCs exhibit immunoprivileged/immunoevasive properties and can be used in allogeneic therapies, which also demand large-scale biomanufacturing because of the cost of goods (Rowley et al., 2012; Simaria et al., 2014; Zhang et al., 2015; Schnitzler et al., 2016). Due to the limited number of hMSCs acquired from a single donor, *in vitro* expansion under current Good Manufacturing Practices (cGMP) has to be performed to reach pratical cell numbers for dosage requirements in clinical applications (Rojewski et al., 2013; Barckhausen et al., 2016; McGrath et al., 2019). In addition, as an anchorage-dependent cell type, the number of harvested hMSCs should be proportional to the culture surface area in biomanufacturing. Thus, increasing culture surface without sacrificing spacial and labor costs is critical in designing culture vessels in hMSC biomanufacturing. One current technique uses multi-layer vessels designed for cell expansion by stacking layers into one chamber to increase the culture surface. However, these labor-extensive and semi-closed processes require clean room facilities and class-A laminar biosafety cabinets for each step of operation (dos Santos et al., 2013; Martin et al., 2017). Alternatively, automated well-controlled bioreactors provide efficient mixing in a closed system for large-scale expansion in lot size at reduced labor and time, but these automated bioreactors are not readily available (Grayson and Stephenson, 2018; Olsen et al., 2018; Moutsatsou et al., 2019). Among various types of bioreactors that are commercially available, stirred-tank bioreactors with microcarriers are the most commonly used system for scaling-up manufacturing of hMSCs as the microcarriers provide a high surface-to-volume ratio for high density cell culture with a cost of goods reduction ($0.044 per cm^2) compared to plate stacks ($0.061 per cm^2) (Simon, 2015). Moreover, microcarrier suspension culture allows real-time cell sampling and off-line analysis for monitoring culture parameters and evaluating critical stem cell properties during expansion. Different feeding strategies, such as batch, fed-batch, and perfusion (dos Santos et al., 2014; Fernandes-Platzgummer et al., 2016), with bead-to-bead transfer can support hMSC stable proliferation under short- and long-term expansion (Panchalingam et al., 2015).

The advantages of microcarrier culture in stirred-tank bioreactors include the scalable design, even cell distribution, homogeneous nutrition and oxygen access, and the timely assessment of medium composition and evaluation of cell properties. Nevertheless, recent studies have shown that microcarrier-expanded hMSCs differ from dish- or flask-expanded cells in size, morphology, proliferation, viability, surface marker, gene expression, differentiation capacity, and secretion of cytokines, which may lead to the alteration of their therapeutic potency (Goh et al., 2013; Hupfeld et al., 2014; Lin et al., 2016; Teixeira et al., 2016). Thus, hMSC properties exhibited in planar culture may not be consistent with microcarrier culture. As seen in our previous studies, these deviations likely result from the altered microenvironment between planar and microcarrier culture in seeding, attaching, expanding, and harvesting, as well as the change of adhesion surface geography and flow-induced dynamic environment (Ma et al., 2016). Therefore, it is important to understand how to optimize bioreactor conditions to maximize hMSC quantity without sacrificing quality and therapeutic potency (Castilla-Casadiego et al., 2020). In this review, influences on hMSC properties from manufacturing parameters in microcarrier bioreactor culture (e.g., discontinuous surface, curvature, microcarrier stiffness, porosity, roughness, coating, and charges) and flow dynamics (e.g., oxygen and nutrient diffusion, shear stress, particle collision, and aggregation) are discussed. Advanced techniques and processes to improve hMSC expansion in microcarrier-based bioreactors are also reviewed.

THE REQUIREMENT OF HMSCS FOR CLINICAL APPLICATIONS: QUANTITY AND QUALITY

Originally, hMSCs are isolated from bone marrows, and only occupy 0.001–0.01% of mononuclear cells for healthy adults (Pittenger et al., 1999). hMSCs isolated from other tissues, such as adipose tissues, dermal tissue, dental pump, placenta, and umbilical cords, contain a higher percentage of hMSCs (Fernandes-Platzgummer et al., 2016). For instance, human adipose tissue on average contains 1.2% hMSCs (Fraser et al., 2006), and umbilical cords have 0.3% hMSCs (Wegmeyer et al., 2013). Even though these numbers are 10 to 100 times higher than bone marrow, it is still far below the cell number requirement of one single therapeutic dose (35–350 million hMSCs per dose) in clinical applications (Jossen et al., 2016). Therefore, *in vitro* expansion is necessary to achieve sufficient cells for cell-based therapies. As the demand for hMSC-based therapeutics is increasing exponentially, development of noval biomanufacturing techniques for culture expansion is in urgent need (Olsen et al., 2018).

While most cell therapy products rely on autologous cells for immunologic compatibility (Duijvestein et al., 2010; Honmou et al., 2012), hMSCs provide a possibility in allogeneic therapies as an "off-the-shelf" product (Pittenger and Martin, 2004; Newman et al., 2009; Zhang et al., 2012). According to Robb et al.'s study, 44.05% of clinical trials were targeting allogenic therapies (Robb et al., 2019). Among the 13 commercialized hMSC products, 9 of them use allogeneic approaches (Jossen et al., 2018). In autologous therapies, a rapid expansion of patient-specific cells in a fully closed and automated bioreactor system is important to ensure the product free of cross-contamination with a reasonable yield in minimal production

time. The scale-out system can satisfy the need of autologous therapies to parallelly produce personalized products for specific patients (Hourd et al., 2014). In allogeneic therapies, hMSCs manufactured from one or several selective donors are used as a universal drug for multiple patients. The scale-up manufacturing system can reduce the cost of goods to meet the dosage requirement and "off-the-shelf" standard (Pigeau et al., 2018). The importance of the scale-up process is to obtain homogeneous cells from a single batch and eliminate the lot-to-lot variations to manufacture hMSCs as a standardized product. Therefore, the current hurdle for hMSC large-scale expansion in allogeneic therapies is to minimize donor-to-donor variations, reduce bioprocessing fluctuations, and eliminate the cell heterogeneity.

Due to the diversity of characteristics displayed by hMSCs from different sources with various isolation methods, the International Society for Cellular Therapy (ISCT) recommended minimal criteria to define hMSCs: (1) cell adhesion on the plastic surface, (2) specific positive and negative surface markers, and (3) *in vitro* tri-lineage differentiation (Dominici et al., 2006). Although these criteria are helpful to establish the baseline of hMSC characterizations, they cannot be used to evaluate hMSC therapeutic potentials as most of the hMSCs from different research groups satisfy ISCT's criteria while still exhibiting functional variance (Samsonraj et al., 2015; Yuan et al., 2019). For effective cell therapies, hMSC-based products have to be characterized for efficacy, function, and potency. For instance, ISCT reported the test for the levels of vascular endothelial growth factor (VEGF), chemokine (C-X-C motif) ligand 5 (CXCL5), and interleukin (IL)-8 of manufactured MultiStem® (a cellular therapy product of hMSCs) to assess the potency in angiogenesis (Bravery et al., 2013). Similarly, ISCT also required immunological characterization for hMSCs to treat immunological diseases with standardized approaches (Krampera et al., 2013; Galipeau et al., 2016). Although many research groups have reported donor-to-donor variations and tissue source comparisons (Alge et al., 2010; Al-Nbaheen et al., 2013; Menard et al., 2013; Marquez-Curtis et al., 2015; Billing et al., 2016; Isobe et al., 2016), only few studies explored the impact of bioprocessing parameters on hMSC therapeutic potency (Hupfeld et al., 2014; Teixeira et al., 2016; Cunha et al., 2017; Martin et al., 2017).

BIOPROCESSING FOR hMSC PRODUCTION

Distinct from typical bioprocesses for protein production using organisms, such as *E. coli*, yeast, and Chinese hamster ovary cells, hMSCs themselves are the final products for cell-based therapy. Thus, the focus is on the fold increase in cell number and population doublings rather than the extracellular factor production, although extracellular vesicles have attracted tremendous attentions recently (Phinney et al., 2015; Koniusz et al., 2016). Isolation from non-adherent hematopoietic cells and *in vitro* expansion of hMSCs in planar culture is the initial process, although the resulting cell number can not meet the clinical requirements (Chen et al., 2013; Siddiquee and Sha, 2014; Simaria et al., 2014). Thus, it is necessary to develop new platforms to efficiently expand functional hMSCs on a larger scale to reach sufficient cell number and dosages, which theoretically determines the success of clinical trials (Rowley et al., 2012; Olsen et al., 2018).

The manufacturing processes under cGMP regulations normally require complete defined serum-free or xeno-free media, effective feeding strategies, automated closed systems, efficient harvest process, cell purification, and cryopreservation methods (Sotiropoulou et al., 2006; Sensebé et al., 2013; Li et al., 2015). The expansion time and population doublings are commonly used as critical quality attributes of the products to evaluate these operational parameters. Knowledge of process control and the parameters acquired from static planar cultures may not be appropriate to directly translate into dynamic bioreactor culture systems without modifications due to the dramatic change in the microenvironment (Sart et al., 2014a; Ma et al., 2016). Therefore, the impacts of bioprocess parameters on hMSC phenotype, cell fate, and therapeutic potency should be investigated systematically. **Figure 1** illuminates the types of mass transfer in static culture and dynamic culture in biomanufacturing.

Multi-Layer Vessels

To manufacture adherent hMSCs, the producion depends on the accessible surface area. Large-scale production of hMSCs requires large surface area, to support efficient cell proliferation while preserving their innate biological properties. Ameliorating from T-flasks, multi-layer vessels, including Nunc™ Cell Factory™ (Thermo Fisher Scientific) and Corning® CellSTACK® (Corning), allow for cell expansion in one chamber by stacking the layers to save the space for incubation, and thus can produce >100 times of cells from a single T-flask. For example, a 40-layer vessel provides a surface of 25,280 cm^2 which is 144 times of a conventional T-175 flask. The challenge in multi-layer vessel production is the labor-intensive and time-consuming operation. Advanced equipment like automatic robot systems, such as Nunc™ Automatic Cell Factory™ Manipulator System (Thermo Fisher Scientific), are designed for more convenient operations and lowering the risk of contamination.

hMSCs are highly sensitive to biological, chemical, and physical cues in the culture microenvironment, and changes in gene expression and phenotypical markers were observed in planar culture (Bara et al., 2014). Thus, hMSCs cultured in multi-layer vessels exploiting the similar microenvironment to original T-flasks make the bioprocess transfer easier, such as coating surface, seeding density, feeding regimes, and cell harvesting (Ma et al., 2016). So far, multi-layer vessels are commonly used in commercial manufacturing but still with the limited lot size, ranging from 100 to 400 billion cells (Rowley et al., 2012). Furthermore, limitation in characterizations of cell growth and behaviors still exists. For example, real-time observation of cell morphological changes may not be applicable under a regular microscope.

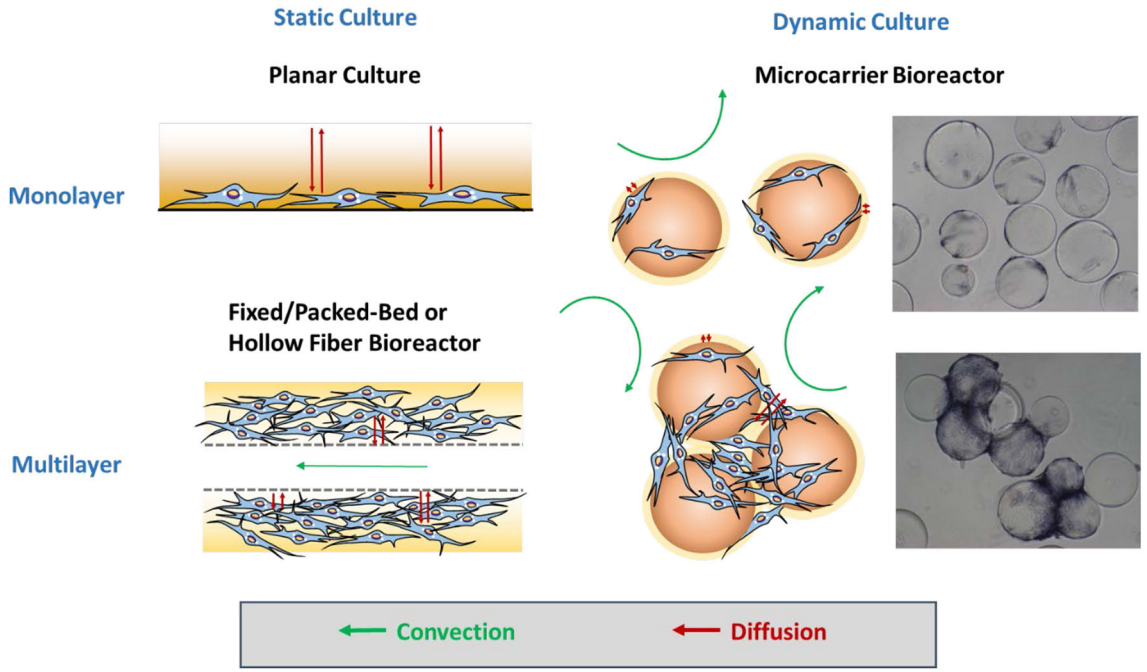

FIGURE 1 | Mass transfer for microcarrier-based culture. For static culture, hMSCs are expanded as monolayers in planar culture or multilayers in the fixed/packed or hollow fiber bioreactor. Mass transfer only relies on diffusion in planar culture, whereas additional convection enhances the mass transfer efficiency in the fixed/packed bed and hollow fiber bioreactor. For dynamic culture in the microcarrier-based bioreactor, hMSCs first attach and grow as monolayers on isolated microcarriers in which convection flows play a more important role in transport. Later, multiple microcarriers are aggregated into a cluster, the internal area of which requires further diffusion for mass transfer like multilayers.

Fixed/Packed-Bed Bioreactors and Hollow Fiber Bioreactors

Instead of providing a planar surface, fixed-bed/packed-bed bioreactors and hollow fiber bioreactors create a spatial microenvironment for cell growth. In fixed/packed-bed bioreactors, hMSCs are captured within the bed that can be filled with various scaffolds composed of biocompatible polystyrene pellets, glass beads, or fibrous materials to provide large surface area for cell expansion (Zhao et al., 2007; Weber et al., 2010; Osiecki et al., 2015; Tsai et al., 2016). Similarly, in hollow fiber bioreactors (Nold et al., 2013; Mizukami et al., 2018), hMSCs grow in the interstitial space between hollow fibers that were used to mimic blood capillaries (Hanley et al., 2014; Martin-Manso and Hanley, 2015). In these two types of bioreactors, the network of frame structures in hMSC microenvironment not only prevents cells from direct fluidic force, but also supports three-dimensional (3D) cell growth with retention of extracellular matrix (ECM). In addition, 3D architecture better mimics the *in vivo* physiological environment. In the absence of direct exposure to the flow, hMSCs still can benefit from perfused flow, mainly relying on diffusion for mass transfer of nutrients, waste, and oxygen. As a result, cells do not suffer damages from shear stress and physical collisions (**Figure 1**). Therefore, hMSCs can be cultured in a highly compact 3D system while still reaching a high cell number.

However, fixed/packed-bed bioreactors and hollow fiber bioreactors still have some challenges in the large scale of biomanufacturing: (1) the non-homogeneity of the culture systems; (2) the depletion of nutrition and accumulation of waste when the cell density is too high and the interstitial flow is insufficient to satisfy mass transfer needs; and (3) cell dissociation from a highly condensed 3D clusters (Meuwly et al., 2007; Barckhausen et al., 2016). Other crucial issues include limited potential in scaling-up and inability for continuous long-term culture without enzymatic treatment and passaging. To avoid the depletion of nutrients and accumulation of metabolic waste, perfusion mode can be applied to increase the flow rate according to the real time in culture. A real time analysis of cell state is also possible in fixed bed bioreactor, for example, via oxygen measurements at inlet and outlet and the calculation of cell numbers over oxygen consumption.

Microcarriers in Spinner Flasks and Stirred-Tank Bioreactors

Microcarriers, designed to replace T-flasks and petri dishes as the adhesion surface for cell growth, have been used for human cell culture since 1967 (Van Wezel, 1967). Most studies on hMSC expansion with microcarriers were conducted in spinner flasks or stirred-tank bioreactors (António et al., 2016), though some other dynamic systems, such as rotating wall vessels or wave motion bioreactors, have also been reported.

The apparent advantages for microcarrier suspension culture include the scalable design, homogeneous culture environment, real-time monitoring of cells and medium, and the feasibility to maintain long-term culture via bead-to-bead transfer without enzymatic treatment/passaging (Leber et al., 2017; Rafiq et al., 2018). Moreover, due to the high surface to volume ratio, less culture medium (a main cost driver) is used in hMSC-microcarrier bioprocessing. Therefore,the production cost is reduced. Although this platform has been widely exploited in academia and industry (Badenes et al., 2016a,b), recent studies have shown that cells cultured in spinner flasks or stirred-tank bioreactors are exposed to high and non-homogeneous fluid shear stresses due to the mixing agitation (Ismadi et al., 2014; van Eikenhorst et al., 2014), possibly resulting in reduced hMSC qualities and therapeutic potentials. For example, increasing fluid shear stress during hMSC culture can induce osteogenic and chondrogenic differentiation (Knippenberg et al., 2005; Zhao et al., 2007; Li et al., 2009; Yourek et al., 2010; Schatti et al., 2011). Therefore, application of the slowest agitation rate is always recommended to support both the required mixing of culture and the undifferentiated state of stem cells. Additionally, the fluid flow leads to frequent cell-cell collisions and may result in spontaneous aggregation and clustering, which should be cautiously considered at the late stage of stem cell culture (Caruso et al., 2014; Yuan et al., 2018).

Screening of Microcarriers for hMSC Expansion

To date, a wide variety of microcarriers are commercially available. These microcarriers are made of diverse materials, such as polystyrene, dextran, cellulose, gelatin, glass, or decellularized tissue, with different surface properties (Chen et al., 2013; Yu et al., 2017). The size of microcarriers ranges from 100 to 300 μm in diameter, which is large enough for cell adherence. The density of microcarriers is designed between 1.02 and 1.1 g/cm^3, not only for settling down the microcarriers when changing the medium, but also for reducing input energy of agitation for the submerged suspension. Therefore, screening and comparing these commercial microcarriers to assess hMSC expansion is the initial step.

In addition to the size and density, microcarriers should be evaluated for cell adhesion, expansion, and dissociation. Recently, some commercial microcarriers have been modified from traditional non-porous, uncoated, uncharged surfaces to porous, collagen- or fibronectin-coated, and/or surfaces with positive charge for enhancing cell attachment efficiency (Rafiq et al., 2013a). Based on literature, hMSC attachment on microcarriers can achieve 70% to 90% under the static or dynamic condition in serum-containing medium, whereas the efficiency significantly decreases to 22% to 23% in serum- and xeno-free medium (dos Santos et al., 2011; Timmins et al., 2012). But there is also evidence that hMSCs can grow fast and achieve the same cell density in a xeno-free serum compared to serum-containing culture despite the low adhesion efficiency (Moreira et al., 2020). Currently, most studies on screening microcarriers for bioprocessing only emphasize the seeding efficiency and expansion fold; however, the recovery efficiency or yield is equally critical for the large-scale production (Schnitzler et al., 2012; Timmins et al., 2012; Goh et al., 2013; Rafiq et al., 2016; Moloudi et al., 2019). The cell detachment from microcarriers is not considered as a key factor and has not been optimized in traditional bioprocessing of protein production. Nevertheless, as the final products in cell-based therapies, hMSCs have to be isolated and harvested from these bioreactors. Thus, the detachment efficiency and recovery rate can not be ignored. For example, hMSCs have high expansion fold using Cytodex I microcarriers, but the enzymatic detachment efficiency is low, and it eventually leads to the low cell yield after cell harvest (Weber et al., 2007; Sun et al., 2010; Schnitzler et al., 2012; Timmins et al., 2012; Loubière et al., 2019). Similarly, although macropores provide more surface area for cell expansion and protect cells from direct flows, i.e., shear stress resulted from the eddies at the Kolmogorov scale, the detachment efficiency is generally not applicable for hMSC expansion (Nienow et al., 2016).

In addition to commercial microcarriers, customized microcarriers can be developed to improve the bioprocessing for hMSC attachment, proliferation, and harvest as well as maintaining their phenotype and therapeutic potency. For example, hydrogel-based microcarriers can improve cell attachment and harvesting efficiency (Chui et al., 2019). Thermo-responsive surfaces on microcarriers have been developed to improve harvest efficiency without enzymatic treatment (Yang et al., 2010; Song et al., 2016; Yuan et al., 2018). Biodegradable, implantable, or enzyme-dissolvable microcarriers can avoid the dissociation or separation step during cell harvesting (Sart et al., 2009; Sun et al., 2010; Park et al., 2013; Shekaran et al., 2016; Confalonieri et al., 2017; Wang et al., 2017; Rodrigues et al., 2019). Microcarriers coated with chemically-defined polymers can better control culture systems and increase the reproducibility (Krutty et al., 2019). Hollow microcarriers provide inner surface for cells to grow and are able to protect hMSCs from direct flow damage (YekrangSafakar et al., 2018). Magnetic microcarriers can speedily settle down when changing medium, and are easily separated from cells after enzymatic treatment to improve cell yield (Lin et al., 2014). Modification of surface charge may be another approach to enhance hMSC attachment or detachment (Rafiq et al., 2016). However, each method should be carefully reviewed and modified for large-scale bioprocessing as most studies were conducted at the laboratory scale. For example, when using the microcarriers with a thermo-sensitive surface, the temperature should be well-controlled throughout bioprocessing. To simplify the harvesting process, novel dispersible and dissolvable porous microcarriers have also been reported recently (Yan et al., 2020).

Agitation

Agitation in stirred-tank bioreactors provides the driving force to generate convective flow, and proper agitation is needed for homogenization of culture microenvironment, dispersion of gas and nutrients, optimal mixing, reduction of the laminar boundary layer, and to increase the convective mass transfer coefficients, all of which are important in MSC bioprocessing. For bioreactors at different scales and with different microcarriers, the operation of agitation should be evaluated for hMSC adhesion, expansion, and dissociation.

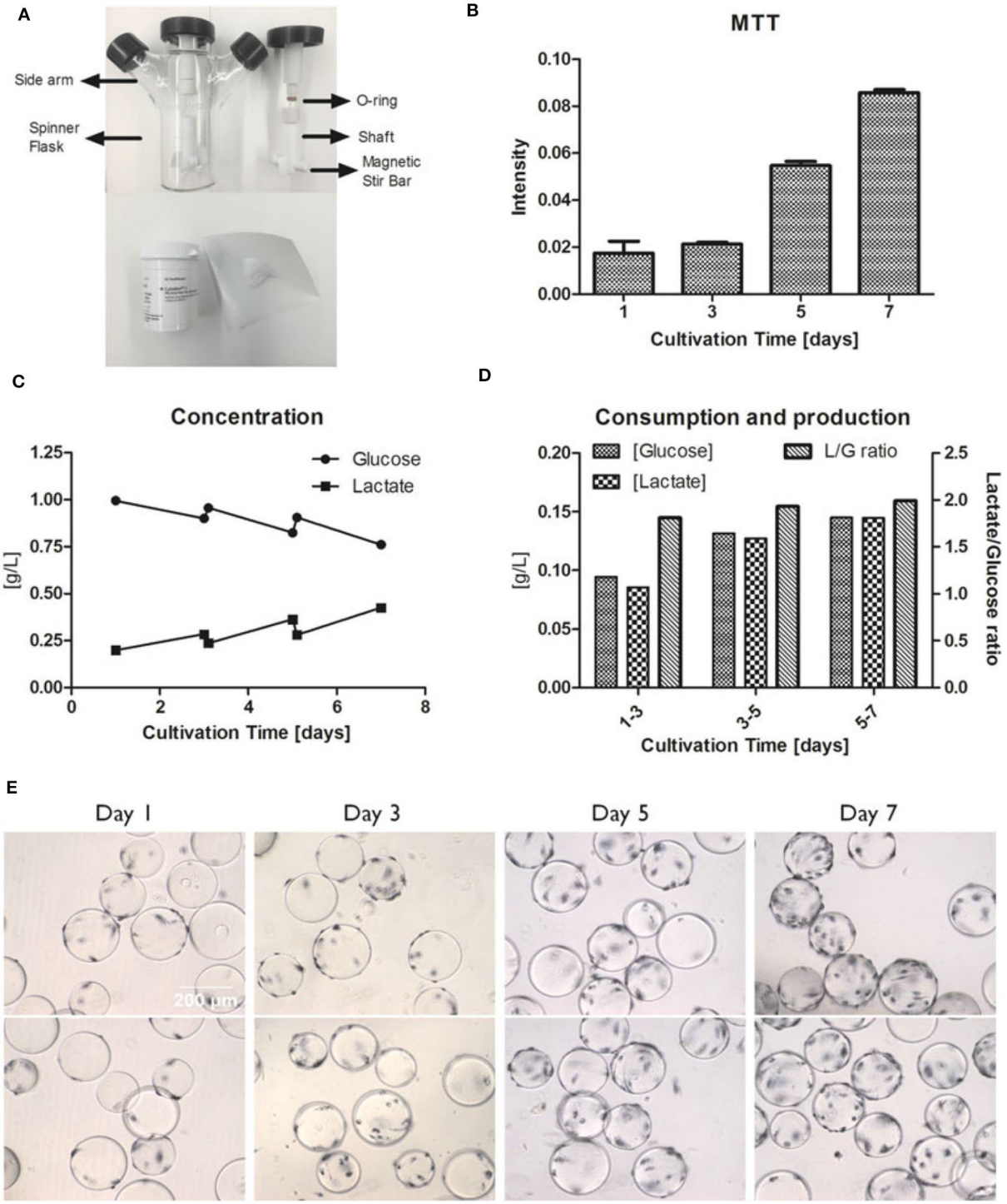

FIGURE 2 | Example of hMSC growth in microcarrier-based spinner flasks. **(A)** Spinner flask bioreactor and internal components (top). Cytodex I microcarriers (bottom). **(B)** hMSC proliferation measured by MTT intensities at day 1, 3, 5, and 7. **(C)** Concentration of glucose and lactate in the media over a 7-days culture period. **(D)** The glucose consumption and lactate production with the lactate/glucose ratio over a 7-days culture period. **(E)** MTT staining of hMSCs on Cytodex I at day 1, 3, 5, and 7. The spinner flask was operated at 30 rpm. Reference: Tsai and Ma (2016). Copyright was permitted.

To maximize seeding efficiency with an even cell distribution, it is recommended to utilize intermittent agitation and reduced initial working volume. For example, the use of intermittent agitation (3 min agitation at 60 rpm followed by no agitation for 27 min) showed 1.5 to 2-fold higher attachment efficiency than the continuous agitation (60

rpm) in the first 24 h for hMSC expansion on CultiSpher-S microcarriers (Yuan et al., 2014).

To determine the agitation speed for hMSC expansion, N_{S1} and N_{S1u} were introduced to represent the criteria of agitation for microcarrier suspension culture. N_{S1} stands for the minimum impeller speed that fully suspends the microcarriers, and N_{S1u} represents the agitation speed that merely allows microcarriers moving along the bottom of bioreactors (Schirmaier et al., 2014; Jossen et al., 2016). It is noted that N_{S1} and N_{S1u} are highly dependent on working volume, microcarrier type and concentration. For instance, Kaiser et al. found no significant difference in expansion when culturing adipose tissue-derived hMSCs at 49, 60, and 82 rpm on Hillex® II and ProNectin®-F-coated microcarriers, and it is possible that the agitation speed is still within the optimal N_{S1} range (Kaiser et al., 2013). A follow-up study tested a broader range of agitation speeds (25–120 rpm) in spinner flasks with 100 mL working volume, and the results showed that hMSCs reached the highest expansion (117-fold) at 49 rpm, and only 71-fold and 19-fold increase were observed at 25 and 120 rpm, respectively (Jossen et al., 2016). Another study showed that hMSCs cultured on CultiSpher-S microcarriers at 60 and 90 rpm had slightly higher expansion (5.5-fold) compared to the culture at 115 rpm (4.3-fold) after an 8-days culture (Yuan et al., 2014). Undoubtedly, optimized agitation speed is critical for hMSC expansion, because higher agitation speed may inhibit hMSC growth due to cell exposure to high shear stress, while low agitation speed cannot fully suspend microcarriers, leading to microcarrier clustering (Jossen et al., 2014; Takahashi et al., 2017). Furthermore, the agitation speed has a linear correlation to the average fluid shear stress in spinner flasks (Ismadi et al., 2014). Based on this observation, Nienow reported a method to detach hMSCs from Plastic P102-L microcarriers with a short time of exposure to the high agitation (220 rpm), which generates high shear stress and reduces Kolmogorov scale (Nienow et al., 2014). Our study also showed the hMSC expansion when cultured on Cytodex-1 microcarriers (Tsai and Ma, 2016). The 30 rpm agitation was observed to support active metabolic activity and glucose consumption, which is usually associated with high cell growth rate (**Figure 2**).

It needs to be noted that the agitation speed using rpm cannot be compared among different culture systems. It is better to use Reynolds number or tip speed [m/s], with the knowledge of the exact reactor set up and geometry. In particular, to transfer the knowledge from spinner flasks to large stirred tank bioreactors, a dimensionless number, such as Reynolds number should be used.

Considering the high and non-homogeneous shear stress in the spinner flasks or stirred-tanks, several bioreactor geometries have been designed to reduce the effects of shear stress. For example, an indentation on the bottom of the spinner flasks can prevent microcarriers from accumulation and clustering below the impeller where the lowest flow velocity occurs (Kaiser et al., 2013). Side baffles can convert the rotational flow to radial flow and axial flow to enhance the microcarrier suspension (Nienow, 2006; Rafiq et al., 2013a). The dimensions, shapes, locations, and orientations of impellers exhibit specific different hydrodynamics, in terms of microcarrier suspension and shear stress exposure (Nienow, 2006; Ismadi et al., 2014; Collignon et al., 2016). A pitched-blade impeller design has been commonly used in stirred-tank bioreactors for hMSC expansion (Goh et al., 2013; Rafiq et al., 2013a; dos Santos et al., 2014; Siddiquee and Sha, 2014; Fernandes-Platzgummer et al., 2016).

TABLE 1 | Comparison of spinner flask and stirred-tank bioreactor.

Parameters	Spinner flask	Stirred-tank bioreactor
Impeller type	Stir bar and impeller	Various types (Mirro and Voll, 2009)
Agitation mixing direction	Radial	Radial and/or axial
DO measurement	None for most cases; Some spinner flasks, e.g., from Presens can monitor DO level (Demuth et al., 2016)	DO probe
DO control	None	O_2 input and gas-sparging. Use a proportional–integral–derivative (PID) controller which switches on the aeration with air or pure oxygen, several aeration strategies can be performed, e.g., gas bubbles, membrane aeration etc. (Levinson et al., 2015)
pH monitor	None for most cases; Some spinner flasks, e.g., from PreSens can monitor pH level (Demuth et al., 2016)	pH probe
pH control	Incubator CO_2 concentration	Addition of acid and base; Or CO_2 gassing (Hoshan et al., 2019)
Scalability	Small	Medium to large
Closed system	No	Can be (Levinson et al., 2015)
Inner pressure	As ambient	Positive pressure (Wilson and Kowol, 1994)
Condenser	None	Equipped

Spinner Flasks vs. Stirred-Tank Bioreactors

Compared to stirred-tank bioreactors, spinner flasks (**Figure 2**) also create dynamic environment due to stirring and can be easily set up in a regular incubator for process optimization and characterization. The available volume for commercial spinner flasks are from 25 mL to 36 L, with 50–250 mL commonly selected for lab use (Eibes et al., 2010; dos Santos et al., 2011; Hewitt et al., 2011; Kaiser et al., 2013; Caruso et al., 2014; Hervy et al., 2014; Schirmaier et al., 2014; Heathman et al., 2015; Petry et al., 2016; Tsai and Ma, 2016). Although spinner flasks have comparable design to stirred-tank bioreactors, there still exist some differences (**Table 1**). Volumetric productivity and fold increase can be used to evaluate hMSC expansion. Rafiq et al. (2013a) demonstrated that 5 L stirred-tank bioreactors can support slightly higher expansion fold (6.02 and 7.02) of hMSCs than 100 mL spinner flasks (3.66 and 5). Similar trends were also reported by Goh et al. using 1 L stirred-tank bioreactors in comparison with

100 mL spinner flasks (Goh et al., 2013). Though, scaling-up normally deals with non-homogeneous quality and a lower yield because of extensive handling and mass transfer limitations (Hernandez, 2016), there are considerations in bioprocessing for choosing stirred-tank bioreactors rather than spinner flasks. As an open system, spinner flask is suitable for laboratory expansion and cannot be scale-up with processing control and automation. Moreover, hMSC products of clinical grade have requirements for product standardization and robustness, which can only be achieved through closed bioreactor systems. Due to a better control on culture environment (e.g., pH, oxygen), improved hMSC expansion can be observed in stirred-tank bioreactors compared to spinner flasks.

In spinner flasks, pH value is regulated by the ambient CO_2 concentration in the incubator and there is no control on dissolved oxygen (DO). Conversely, most large-scale stirred-tank bioreactors can balance the pH value by adding diluted acids or bases, and compensate the DO level by adjusting partial oxygen tension input or turning on the gas sparging. Another discrepancy is that large-scale stirred-tank bioreactors are usually equipped with a condenser to avoid medium evaporation, which is alleviated by the humidified ambiance in the incubator (95% relative humidity at 37°C) for spinner flasks. Positive pressure in the head space also prevents evaporation in bioreactors. Other differences, including the extra perfusion system to attenuate media variation, the baffles on the side wall to enhance vertical mixing, and the homogenization at different scales of working volume with different impeller geometry, may further promote hMSC production in stirred-tank bioreactors.

The challenges in large scale manufacturing of hMSCs lie in the mixing of circulation system and non-homogeneous cell quality. The process parameters from several studies for scale-up production of hMSCs are summarized in **Table 2**. Only a few cases achieved successful expansion of hMSCs in bioreactors at large scale. For example, Schirmaier et al. reported that production of 1×10^{10} hMSCs can be achieved at a harvest density of 3×10^5 cells/mL in a 50-L single-use stirred-tank bioreactor (CultiBag® STR 50 L, Sartorius Stedim Biotech) with 35 L working volume (Schirmaier et al., 2014). Similarly, Lawson et al. reported that 1.28×10^{10} hMSCs were harvested at the density of 2.56×10^5 cells/mL in a 50-L single-use stirred-tank bioreactor (Mobius® 50 L, MilliporeSigma) with 50 L working volume (Lawson et al., 2017). In spite of the lower harvest cell density in large scale bioreactors (**Table 2**), comparable volumetric productivity in UniVessel® SU 2 L bioreactors (Sartorius Stedim Biotech) and CultiBag® STR 50 L bioreactors was also reported (Schirmaier et al., 2014). The commonly used scale up criteria include similar power input per volume, gas flow rate per reactor volume (vvm), and oxygen transfer coefficients (Xu et al., 2017). The correspondingly adjusted operational parameters, such as the geometry of vessels and impellers, agitation speed, microcarrier concentration, working volume, aeration (type and vvm), feeding strategies, and seeding/harvesting procedures, all impact culture microenvironment and thus cell production (Castilla-Casadiego et al., 2020).

CHARACTERIZATION OF hMSCs IN MICROCARRIER SUSPENSION CULTURE

hMSCs cultured on microcarriers are exposed to a significantly different microenvironment from planar culture, therefore it is still unclear how much knowledge obtained from planar culture can be translated to microcarrier culture. Most studies mainly reported the increased folds in cell number, the expression of surface markers, colony formation ability, and differentiation capability of microcarrier-expanded hMSCs. However, these criteria only represent the minimal properties of hMSCs and do not indicate their therapeutic potency. In addition, bioprocessing parameters, such as type of microcarriers, controlled agitation, and culture scale, all may influence hMSC properties. Thus, understanding how the microcarrier culture acts on cellular behaviors and how these process parameters change therapeutic potency are beneficial for hMSC-based therapies and the associated biomanufacturing (**Table 3**).

Expansion and Proliferation

In microcarrier culture of hMSCs, a long lag phase in cell proliferation is commonly observed (Eibes et al., 2010; Sun et al., 2010; dos Santos et al., 2011; Hewitt et al., 2011; Goh et al., 2013), suggesting that the cells need longer time to adjust themselves to the culture environment in bioreactors compared to planar culture. The microcarrier culture systems have not been maturely developed for hMSC expansion yet, and may not have reached the maximum expansion potential. hMSCs grow faster in planar culture than microcarrier culture, showing higher proliferation rates and lower doubling times (Sun et al., 2010; Goh et al., 2013). However, when only considering the exponential phase, microcarrier culture can have comparable or increased growth rate after optimization (Sun et al., 2010). Moreover, long-term culture can be achieved by bead-to-bead transfer in microcarrier bioreactors. Hence, as long as the lag phase can be reduced, microcarrier bioreactors are suitable for the production of hMSCs within a comparable time to planar culture.

In planar culture, cell density is typically expressed as cells/cm^2. In microcarrier culture, cell density can also be described by cells/mL. Using vendor's information on the surface area per unit mass of microcarriers (cm^2/g), growth area at a certain microcarrier concentration in the vessel can be calculated. Loss of microcarriers may occur in each step of washing, transferring, medium changing, and harvesting. Extra microcarriers, about 5–10%, can be added for compensation if needed. With online systems, e.g., impedance spectroscopy, cell biomass on the microcarriers can be determined at real time with no loss due to sampling.

Phenotype Characterization and Colony-Forming Unit-Fibroblast (CFU-F)

Current studies on microcarrier expansion of hMSCs usually provide results for the expression of positive surface markers

TABLE 2 | Case studies of microcarrier-based bioreactor systems for human mesenchymal stem cell expansion.

Cell source	Working volume (mL)	Vessel model	Micro-carrier type	Medium	Agitation (rpm)	Tip speed (cm/s)	Fold increase	Time (day)	Seeding density (10^5/mL)	Harvest density (10^5/mL)	Glucose consu. (pmol/cell/day)	Lactate product. (pmol/cell/day)	Quality test (gene or protein)	Differentiation	References
hAD-MSC	100	Spinner flask; Single use	Hillex II; ProNectin-F (P)	EGM-2 MV	49 60 82	10.9 13.0 17.8	16.3–18.3 (Hillex) 26.4–31.4 (P)	6	0.15	–	–	–	–	–	(Kaiser et al., 2013)
hAD-MSC; hBM-MSC	80	Spinner flask	Cultispher-S; Non-porous plastic	MesenPRO RS; StemPro MSC Xeno-Free	40	–	14 ± 7 (AD) 18 ± 1 (BM)	14	0.1	1.4 ± 0.5 (AD) 2 ± 0.2 (BM)	12 ± 2 (AD) 10 ± 1 (BM)	19 ± 2 (AD) 15 ± 1 (BM)	CD31 CD73 CD80 CD90 CD105 HLA-DR	Tri-lineage differentiation	(dos Santos et al., 2011)
hPL-MSC	500	Culti-Bag; Single use	Cytodex-1; Cytodex-3; Cultispher-S; FACT; ProNectin Collagen	DMEM + 20% FBS	–	–	14.9 ± 1.2 (Cultispher-S) 15.7 and 16.3 (5% O_2)	7	–	–	–	–	CD44 CD45 CD73 CD90 CD105 CD146	Tri-lineage differentiation	(Timmins et al., 2012)
hPL-MSC	100	Spinner flask	Cytodex-3	DMEM + 10% FBS	50 (type 1) 30 (type 2)	11.7 (type 1) 8.6 (type 2)	2.0–11 (type 1) 3.0–20 (type 2)	8.0–10	0.15–0.75	0.6–3.8 (type 1) 0.7–3.8 (type 2)	–	–	–	–	(Hewitt et al., 2011)
hBM-MSC	50	Cell-Spin	Culti-spher S	MesenPRO; DMEM + 10% FBS	30	–	8.4 ± 0.8	8	0.5	4.2	5.4 ± 0.3	10.3 ± 0.9	CD73 CD90 CD105	Osteo-genesis; adipo-genesis	(Eibes et al., 2010)
hUC-MSC	100	Spinner flask	Plastic Plus (screen micro-carriers)	DMDM + 10% hPL	40	–	16.4 (Male) 13.8 (Female)	7 (Male) 6 (Female)	0.16 (Male) 0.38 (Female)	2.6 (Male) 5.3 (Female)	–	–	CD11b, CD19, CD34, CD45, CD73, CD90, CD105; HLA-DR; CFU-F	Tri-lineage differentiation	(Petry et al., 2016)
hAD-MSC	100 1,500	Spinner flask; Biostat Culti-Bag	Polystyrene with 2 different densities and sizes	Lonza medium + 5% FBS	25, 43, 49, 63, 90, 120	–	71.4, 79.6 117, 97.4 28.5, 19.4 6.59 (Cultibag)	7 (49 rpm) 9	0.108 (SF)	12.5 ± 0.05 (49 rpm)	1.08–5.07	2.43–8.82	CD14, CD20, CD34, CD45, CD73, CD90, CD105	–	(Jossen et al., 2016)
hBM-MSC	50	Spinner flask	Cytodex 3	αMDM + 15% FBS	50	–	3.9	7	1.25	4.82 ± 1.18	1.86	4.04	CD13, CD14, CD29, CD31, CD45, CD49e, CD90, CD105, CD146; HLA-DR	Osteo-genesis; adipo-genesis	(Caruso et al., 2014)

(Continued)

TABLE 2 | Continued

Cell source	Working volume (mL)	Vessel model	Micro-carrier type	Medium	Agitation (rpm)	Tip speed (cm/s)	Fold increase	Time (day)	Seeding density (10^5/mL)	Harvest density (10^5/mL)	Glucose consu. (pmol/cell/day)	Lactate product. (pmol/cell/day)	Quality test (gene or protein)	Differentiation	References
hF-MSC	100	Spinner flask; Biostat B-DCU	Cytodex 3	DMEM or αMEM + 10% FBS	30 (SF) 60–80 (Bio-stat)	–	10 (SF DMEM) 10 (SF αMEM)	8, SF DMEM 6–7, SF αMEM	0.5	5 (SF DMEM) 5.1 (SF αMEM) 10.8 (SF αMEM)	12 ± 1.2 (SF DMEM) 4.3 ± 1.4 (SF αMEM)	23.7 ± 5.3 (SF DMEM) 7.5 ± 0.2 (SF αMEM)	CD34 CD73 CD90 CD105	Tri-lineage differentiation	(Chen et al., 2015)
hBM-MSC	100	Spinner flask	Non-porous Plastic P-102L	DMEM + 10% FBS; PRIME-XV™ SFM		Paddle 50 mm in diameter							CD34 CD73 CD90 CD105 HLA-DR	Tri-lineage differentiation	(Heathman et al., 2015)
hBM-MSC	2,200 250	Verti-cal Wheel (PBS); Biostat Qplus stirred-tank	Corning Synthemax II	MesenCult™-XF	17 (PBS) 40–45 (Bio-stat)	–	12 (PBS) 11 (Biostat)	14	0.25	3 (PBS) 2.8 (Biostat)	6.72 ± 1.92	13.92 ± 1.68	CD34, CD44, CD73, CD90, CD105, CD166 HLA-DR	Tri-lineage differentiation	(Sousa et al., 2015)
hBM-MSC	35–45	Spinner flask; Single use	Corning Syn-themax II	Mesen-cult XF (M); Stempro hMSC (S)	30 rpm every 2 h for 15 min	–	5 (M) 7 (S) 3×10^7 (M) 10,000 (S)	5 42 (M) 26 (S)	0.21–0.29	–	–	–	CD14 CD45 CD73 CD105	Osteo-genesis; adipo-genesis; chondro-genesis	(Hervy et al., 2014)
hF-MSC	100 1,000	Spinner flask; Biostat B-DCU	Cytodex-1 Cytodex-3 Culti-spher GL HyQ-sphere P102-L	DMEM + 10% FBS	30 (SF) 50 (Bio-stat)	–	13.6 (SF) 12 (Biostat)	11 (SF) 8 (Biostat)	0.5	6.8 ± 0.1 (SF) 6 ± 0.2 (Biostat)	5.5 (Biostat) 12.5 (Planar)	10 (Biostat) 30.5 (planar)	CD34, CD73, CD90, CD105 STRO-1 CFU-F; ALP; Calcium deposition	Osteo-genesis	(Goh et al., 2013)
hBM-MSC	2,500	Biostat B Plus (Bio); Spinner flask	Nonporous Plastic P-102L	DMEM 10% FBS	75 (Bio) 30 (SF)	62.8 (Bio) 9.4 (SF)	7.02 and 6.02 (Bio) 3.66 and 5 (SF)	12 (Bio) 12 (SF)	0.24	1.68 and 1.44 (Bio) 1.1 and 1.5 (SF)	8.0–14 (Bio) 8.0–11 (SF)	22–28 (Bio) 23–28 (SF)	CD14, CD19, CD34, CD45, CD73, CD90, CD105 HLA-DR	Tri-lineage differentiation	(Rafiq et al., 2013b)
hBM-MSC	3,000	Mobius Cell-Ready Single use	Cytodex 1 Cytodex 3 collagen-Hillix; Culti-spher G, S	DMEM 10% FBS	25–35	–	40	12	0.05 by calculation	>2	–	–	CD11b, CD14, CD19, CD34, CD44, CD45, CD73, CD79α, CD90, CD105, CD106, CD146, CD274	Osteo-genesis; adipo-genesis	(Kehoe et al., 2013)

(Continued)

TABLE 2 | Continued

Cell source	Working volume (mL)	Vessel model	Micro-carrier type	Medium	Agitation (rpm)	Tip speed (cm/s)	Fold increase	Time (day)	Seeding density (10^5/mL)	Harvest density (10^5/mL)	Glucose consu. (pmol/cell/day)	Lactate product. (pmol/cell/day)	Quality test (gene or protein)	Differentiation	References
hBM-MSC	200 2,000	Spinner flask; Mobius Cell-Ready; Single use	Collagen-coated Solohill C102-1521	DMEM 10% FBS	30 (SF) 25 (1 L) 40 (2 L)	–	5.2	5	0.2 (125 mL) 0.3 (3 L)	0.75	2.7×10^{-9} g/cell/day	1.9×10^{-9} g/cell/day	CD105 CD14 CD19 CD44 CD90 (protein and gene)	Adipo-genesis	(Schnitzler et al., 2012)
hAD-MSC	100 2,000 35,000	Spinner flask; UniVessel SU; Culti-Bag	Pro-Nectin F-COATED	Specialmedium (Lonza, USA) 5% FBS	60 (100 mL) 100–140 (2 L) 50–66 (35 L)	13 (100 mL) 28.3–39.6 (2 L) 37.4 (35 L)	58.4 ± 12.4 (100 mL) 35.4 ± 0.4 (2 L)	7	0.05–0.1	6.1 ± 1.9 (100 mL) 2.7 ± 0.2 (2 L) 3.1 (35 L)	–	–	CD34 CD45 CD73 CD90 CD105	–	(Schirmaier et al., 2014)
hAD-MSC hBM-MSC	800	Spinner flask; to Bioflo 110	Nonporous plastic (SoloHill)	StemProMSC SFM Xeno-Free	40	–	3 (AD) 7 (BM)	(4) + 7	0.5	0.57 ± 0.2 (AD) 1.3 ± 0.1 (BM)	12.0–13	23–25	CD31, CD73, CD80, CD90, CD105 HLA-DR	Tri-lineage differentiation	(dos Santos et al., 2014)
hAD-MSC	3,750	Bio-BLU 5c; Single use	Polystyrene P-221-040 (PS); collagen C102-1521	ATCC basal medium	25 (PS) 35 (Collagen)	–	7 (PS) 14 (Collagen)	18 (PS) 16 (Collagen)	0.05 (PS) 0.175 (Collagen)	0.39 (PS) 2.4 (Collagen)	–	–	CD44 CD90 CD105 Oct3/4 Sox2	Osteo-genesis; adipo-genesis	(Siddiquee and Sha, 2014)
hBM-MSC	2,400 50,000	Mobiu; Single use	Pall collagen-coated MCs	αMDM 10% PL	For 50 L, 64 for 4 h 75–85 95–100	–	64 (3 L) 36 (50 L)	9 (3 L) 11 (50 L)	0.0625 (3 L) 0.05 (50 L)	4 (3 L) 1.9 (50 L)	–	–	CD11b, CD14, CD19, CD34, CD44, CD45, CD73, CD79a, CD90, CD105 HLA-DR	Tri-lineage differentiation	(Lawson et al., 2017)
hPDCs	80	Spinner flask	Cultispher-S	DMEM 10% FBS	30	–	3.2 ± 0.64	12	0.25	0.8	500–1,000	1,000–2,000	CD14, CD20, CD34, CD45, CD73, CD90, CD105	Tri-lineage differentiation	(Gupta et al., 2019)
hPDCs	80	Spinner flask	Cultispher-S	DMEM 10% hPL or 10% FBS	–	–	5.2 ± 0.61 (hPL) 2.7 ± 0.22 (FBS)	10	0.25	1.3 (hPL) 0.675 (FBS)	500–1,300	1,000–2,000	CD14, CD20, CD34, CD45, CD73, CD90, CD105	Tri-lineage differentiation	(Gupta et al., 2018)

MSC, mesenchymal stem cells; hAD-MSC, human adipose tissue-derived MSC; hBM-MSC, human bone marrow-derived MSC; hPL-MSC, human placenta-derived MSC; hUC-MSC, human umbilical cord-derived MSC; hF-MSC, human fetal bone marrow-derived MSC; hPDCs, human periosteum-derived MSC; FBS, fetal bovine serum; hPl, human platelet lysate; SF, spinner flask; CFU-F, colony-forming units-fibroblast; ALP, alkaline phosphatase.

TABLE 3 | Alteration of hMSC properties from planar culture to microcarrier-based bioreactor culture.

hMSC Characteristics	Microcarrier-base bioreactor vs. planer	Therapeutic perspective	References
Expansion	Extended lag phase; Comparable/lower proliferation rate; Longer doubling times; Stable chromosome	Support long-term culture and large-scale expansion; satisfy clinical cell dosage requirements	Schatti et al., 2011; Hanley et al., 2014; Hupfeld et al., 2014; Martin-Manso and Hanley, 2015; Yu et al., 2017
Phenotype	Stable ISCT criteria; Negative for CD349 in UC, AM, Placenta; CD146 ↓ in UC, AM and BM; HLA-DR↑ in BM	Meet ISCT's minimal criteria, while certain markers have variations	Timmins et al., 2012; Hupfeld et al., 2014; Collignon et al., 2016; Petry et al., 2016; Lawson et al., 2017
Differentiation potential	Osteogenic differentiation ↑; Adipogenic differentiation ↓; Chondrogenic differentiation ↑	Lineage commitment via modification of microcarrier surface properties.	Aggarwal and Pittenger, 2005; Sun et al., 2010; Hervy et al., 2014; Hupfeld et al., 2014; Kang et al., 2015; Panchalingam et al., 2015
Migration ability	Cell size ↓; CXCR4 ↑	Improve MSC homing after transplantation	Levato et al., 2015; Yu et al., 2017
Secretory function (Immunomodulation, Angiogenesis and neuroprotection)	IL-6 ↑; IL-8 ↑; CXCL5 ↑; Cystatin C ↑; GDN ↑; Galectin-1 ↑; PEDF ↑; BDNF ↑; IGF-1 ↑; VEGF ↑; IL-1ra ↑; SDF-1a ↑; bFGF ↑; M-CSF ↑; NGF ↑; MCP-1 ↑; HGF ↑	Maintain or improve anti-inflammation and immunomodulation for T cells and macrophages after transplantation, enhance therapeutic effects in neurological disease.	Fernandes-Platzgummer et al., 2016; Lin et al., 2016; Petry et al., 2016; Teixeira et al., 2017

UC, umbilical cords; AM, amniotic membrane; BM, bone marrow; CXCR4, C-X-C chemokine receptor type 4; BDNF, brain-derived neurotrophic factor; CXCL5, C-X-C motif chemokine 5; GDN, glia-derived nexin; HGF, hepatocyte growth factor; IGF-1, insulin-like growth factor 1; IL-1ra, interleukin 1 receptor antagonist; IL-6, interleukin 6; IL-8, interleukin 8; MCP-1, monocyte chemotactic protein-1; M-CSF, macrophage colony-stimulating factor; NGF, nerve growth factor; PEDF, pigment epithelium-derived factor; SDF-1a, stromal-derived-factor-1; VEGF, vascular endothelial growth factor.

(CD73, CD90, and CD105) and negative surface markers (CD45, CD34, CD14 or CD11b, CD79α or CD19, and HLA-DR) along with *in vitro* tri-lineage differentiation capacity (dos Santos et al., 2011; Goh et al., 2013; Kehoe et al., 2013; Rafiq et al., 2013a; Caruso et al., 2014; Siddiquee and Sha, 2014; Jossen et al., 2016; Petry et al., 2016). It is well-known that surface marker expression can be different for hMSCs due to various donors and tissue sources. Hupfeld et al. (2014) manifested that the bioprocessing (planar vs. microcarrier) may affect the expression of hMSC phenotypic marker CD349 (frizzled 9) in three different donors. In particular, flask-expanded hMSCs derived from amniotic membrane and umbilical cord positively expressed CD349, whereas microcarrier-expanded hMSCs did not. And $CD349^{-}$ hMSCs derived from placenta can effectively recover blood flow after vascular occlusion in a mouse model rather than $CD349^{+}$ hMSCs (Tran et al., 2011), suggesting that microcarrier-expanded hMSCs may have higher capacity of arteriogenesis and angiogenesis (Hupfeld et al., 2014). Other surface markers, including CD136, CD143, CD146, and CD200, were expressed inconsistently in Hupfeld's study. Interestingly, Shekaran et al. reported that a significant decrease of CD146 expression, known as a pericyte- and endothelial-specific marker (Shi and Gronthos, 2003) or a marker of hMSC multi-potency (Russell et al., 2010), in microcarrier-expanded fetal hMSCs compared to planar culture (Shekaran et al., 2015). Moreover, the expression of CD105 was reported to decrease from more than 90% to 85.9 ± 7.9 and 86.7 ± 2.4 for Cultispher-S and plastic microcarriers, respectively (dos Santos et al., 2011; Mizukami et al., 2018).

In addition, microcarrier-expanded hMSCs were reported to have higher expression of early osteogenic gene markers, such as RUNX2, ALPL, and Osterix/SP7, and late osteogenic marker IBSP during osteogenic differentiation, indicating that hMSCs from microcarrier culture may favor osteogenic lineage commitment (Shekaran et al., 2016). Similarly, microcarrier culture was reported to up-regulate RUNX2, ALP, COL1, and SOX9 gene expression of placenta-derived hMSCs compared to planar culture (Tseng et al., 2012). Microcarrier-expanded hMSCs were also reported to have higher gene expression of crucial chondrogenic transcriptional regulators, such as SOX9, SOX5, and SOX6, as well as the chondrogenic ECM marker COL2A1, suggesting that microcarrier culture may augment chondrogenic commitment (Lin et al., 2016). In addition, hMSCs harvested from microcarriers were found to have slightly lower CFU-F number in comparison with hMSCs from monolayers (Goh et al., 2013). Altogether, hMSCs manufactured from microcarrier culture systems still meet the release criteria defined by ISCT, although the cells exhibit differences in surface markers, CFU-F, and lineage-specific gene expression.

Therapeutic Potency: Differentiation Potential, Migration Ability, and Secretory Function

To date, more than 1000 completed or ongoing hMSC-based clinical trials have been reported (Tsuchiya et al., 2019), including bone and cartilage regeneration, graft-vs.-host disease, kidney injury, liver disease, myocardial infarction, and type I and II diabetes (Chen et al., 2013; Simaria et al., 2014).

These clinical applications of hMSCs are attributed to unique stem cell properties: renewability of regeneration, capacity for multi-lineage differentiation, migration ability to inflammatory tissue, and secretion of anti-inflammatory and pro-angiogenic trophic factors (Aggarwal and Pittenger, 2005; Prockop et al., 2010; Wang et al., 2012; Bianco et al., 2013; Stroncek et al., 2014). However, most therapeutic characterizations are based on hMSCs expanded from planar culture system. Thus, it is necessary to characterize hMSCs manufactured from microcarrier culture, particularly in therapeutic efficacy which is generally indicated by differentiation potential, migratory ability, and secretory function.

Differentiation Potential

It is well-acknowledged that hMSCs are able to differentiate into osteoblasts, adipocytes, and chondrocytes *in vitro* using inducing factors in the medium (Pittenger et al., 1999). The tri-lineage differentiation capability is included in the release criteria of hMSCs by ISCT (Dominici et al., 2006). Beyond biochemical signaling, physical cues including gravity, adhesion geometry, surface elasticity, adhesion force, and fluid shear stress all contribute to lineage commitment and differentiation (Zayzafoon et al., 2004; Engler et al., 2006; Kilian et al., 2010; Yourek et al., 2010; Mathieu and Loboa, 2012). For bone and cartilage regeneration, high yield of differentiated cells from hMSCs within a short time frame is preferred. Many groups have reported that microcarrier culture improves hMSC osteogenic and chondrogenic differentiation potential *in vitro* or *in vivo* (Tseng et al., 2012; Goh et al., 2013; Shekaran et al., 2015, 2016; Lin et al., 2016; Gupta et al., 2018, 2019). For example, microcarrier-expanded hMSCs were reported to have considerably increased pellet size and DNA content, as well as higher production of glycosaminoglycan and collagen II per pellet, after 28-days chondrogenic differentiation, compared to those from planar culture (Lin et al., 2016). The microcarrier-expanded hMSCs were also found to have increased osteogenic gene expression, alkaline phosphatase activity, calcium deposition, and collagen I secretion compared to the planar control (Tseng et al., 2012). The enhancement of osteogenesis may arise from increased cytoskeletal tension and actomyosin contraction of hMSCs on microcarriers, which can be inhibited by latrunculin B and blebbistatin (Tseng et al., 2012). By contrast, lower gene expression of adipocyte markers, such as PPARγ2 was observed in microcarrier culture, which demonstrates that microcarrier culture may down-regulate adipogenic differentiation potential (Tseng et al., 2012). Indeed, dynamic microcarrier culture system could alter hMSC commitment and differentiation compared to planar culture.

Migration Ability

hMSCs demonstrate homing and migration ability to the injured or disordered tissues *in vivo* after administration. Thus, migratory capacity is an important indicator for hMSC-based therapies. While not many studies examined hMSC migratory ability after microcarrier expansion, some evidence of migratory ability changes can be found. It has been reported that microcarrier-expanded hMSCs have smaller size, and display higher CXCR4 expression in comparison with planer culture (Sun et al., 2010; Levato et al., 2015), suggesting that microcarrier-culture possibly enhanced hMSCs' migration ability. Further *in vitro* and *in vivo* examinations should be performed to elucidate this possibility.

Secretory Function

hMSCs also play an important role in secreting growth factors, chemokines, and cytokines to maintain the physiological environment and attenuate immunogenicity in their original niche (Aggarwal and Pittenger, 2005; Ren et al., 2008; Liang et al., 2014). It has been reported that microcarrier-expanded fetal hMSCs secreted higher levels of IL-6 (an immunomodulatory cytokine), IL-8 (a pro-angiogenic chemokine), and CXCL5 (a chemokine) than planar culture-expanded cells (Shekaran et al., 2015). Also, changes in secretome of hMSCs cultured on microcarriers facilitated neuroregulatory function and differentiation of neural progenitor cells *in vitro* and *in vivo* as compared to those from planar culture (Teixeira et al., 2016). Specific proteins involved in the central nervous system, such as cystatin C, glia-derived nexin, galectin-1, and pigment epithelium-derived factor, were upregulated in microcarrier systems as well. Similarly, after tumor necrosis factor-α and interferon γ stimulation, microcarrier-expanded umbilical cord-derived hMSCs exhibited higher secretion of VEGF, interleukin 1 receptor antagonist (IL-1ra), and stromal cell-derived factor 1-alpha (SDF-1α) compared with flask-expanded hMSCs. Likewise, amniotic membrane-derived hMSCs cultured in microcarrier bioreactors secreted more VEGF, basic fibroblast growth factor, macrophage colony-stimulating factor (M-CSF), nerve growth factor, monocyte chemotactic protein-1 (MCP-1), and hepatocyte growth factor than flask-cultured hMSCs (Hupfeld et al., 2014). Upregulated secretion of brain-derived neurotrophic factor and insulin-like growth factor 1 was also reported in microcarrier systems (Teixeira et al., 2016). Furthermore, functional studies with immune cells under inflammation indicated that MSCs cultured on microcarrier exhibited improved IDO activity and thus maintained their immunomodulatory potentials characterized by inhibition of T cell proliferation (Lawson et al., 2017; Das et al., 2019). Taken together, microcarrier culture likely promotes hMSC's therapeutic potency in immunomodulation and angiogenesis by altering their secretome profiles.

THE MICROENVIRONMENT CHANGE IN MICROCARRIER-BASED BIOREACTORS

The alteration of hMSC properties is most likely associated with the discernible differences in culture microenvironment between planar and microcarrier culture (Sart et al., 2013; Ma et al., 2016). This part is to elucidate the possible relationship between hMSC properties and bioprocessing parameters/microenvironment based on two factors: the adhesion surface and the hydrodynamics.

Adhesion Surface: Discontinuous Surface, Convex Curvature, and Microcarrier Rigidity

The primary adhesion surface change is the substrate topography which means cells colonize on individual disconnected microcarriers with a convex curvature. Other properties of adhesion substrate including rigidity, roughness, porousness, coating, charge, hydrophilicity, and wettability may also influence cellular microenvironment.

Discontinuous Surface

Upon inoculation, the microenvironment in microcarrier culture immediately changes compared to planar culture. Microcarriers provide abundant accessible surface per unit volume while lack of a bridge between individual microcarriers impedes cell migration from bead to bead. In planar culture, however, migration can compensate non-homogeneous cell distribution at a certain level. Migration on microcarriers is completely different as cells can only migrate within the single bead under dynamic environment. Thus, simply counting cell attachment efficiency is not informative without considering the percentage of microcarriers with attached cells. Generally, inoculation cell density is determined by the cell-to-bead ratio which needs to reach the threshold of critical cell number per microcarrier (Hu et al., 1985). In literature, a seeding density of 5 cells per microcarrier is commonly used for hMSCs (Rafiq et al., 2013a). Initial colonization of microcarriers by cells theoretically can be estimated by Poisson distribution (Frauenschuh et al., 2007), and the expected percentage of occupied microcarriers at a cell-to-bead ratio of 5 is 99.3%. Due to discontinuous surfaces, the homogeneous cell attachment on microcarriers and initial percentage of colonized microcarriers are critical for maintaining culture microenvironment and preventing uneven distribution of cells and mass transfer limitations.

Even if perfect homogeneous cell attachment on microcarriers can be achieved, the natural heterogeneity of hMSC populations still exists (Phinney, 2007). These heterogeneous characteristics including proliferation rate, metabolic activity, and contact limit would result in different confluence on each microcarrier at harvesting. Some cells on microcarriers may reach the stationary phase, while other cells are still in the lag phase or exponential phase. In addition, the heterogeneity of microcarriers also contributes to the heterogeneity of hMSCs. For example, SoloHill® plastic microcarriers formed by cross-linked polystyrene have the size range of 125–212 μm in diameter, and 1.7 times of difference in diameter would result in 2.9 times of difference in surface area. Also, therapeutic potency may vary for cells harvested at different confluency (Lam et al., 2019). Thus, the right timing for harvest should ensure that a majority of microcarriers are ready.

Convex Curvature

Geometric cues can regulate cell fate and differentiation commitment in planar culture via the changes of mechanical microenvironment, leading to a reorganization of cytoskeletons and formation of myosin-generated contractility (Chen et al., 2003; Discher et al., 2005; Kilian et al., 2010). These geometric cues include the dimension, shape, and curvature of the culture surface. In microcarrier culture, the accessible surface area provided by a single microcarrier with a diameter of 100–300 μm is in the range of 0.03–0.28 mm^2, which is much larger than the area for a spreading single cell (**Figure 3**). Therefore, the curvature would be the dominant factor in topographic cues. The curvature of a surface is defined as the reciprocal of the radius of the sphere fitting to the camber (Xu et al., 2011; Ueki and Kidoaki, 2015). The curvature of a microcarrier is ranged from 1/50 to 1/150 μm^{-1}, and the level of the curvature is inverse to the microcarrier size.

To investigate the role of curvature, both microcarriers and planar surfaces should be made of the same materials with the same biophysical characteristics, and with cells cultured under the same flow condition. Indeed, it is difficult to isolate the effect of curvature during microcarrier suspension culture. Researchers have tried to use microprinting techniques to generate different geometric cues to address the influence of dimension and geometric shape on cytoskeleton distribution and mechanical contractility (Théry et al., 2006; James et al., 2008; Kilian et al., 2010; Théry, 2010), though it is still not the optimized model to mimic the underlying curvature on microcarriers. Recently, Werner et al. (2017) cultured hMSCs on the stereolithographic convex spherical structures with the curvature of 1/125, 1/175, 1/250, and 1/375 μm^{-1}, which have

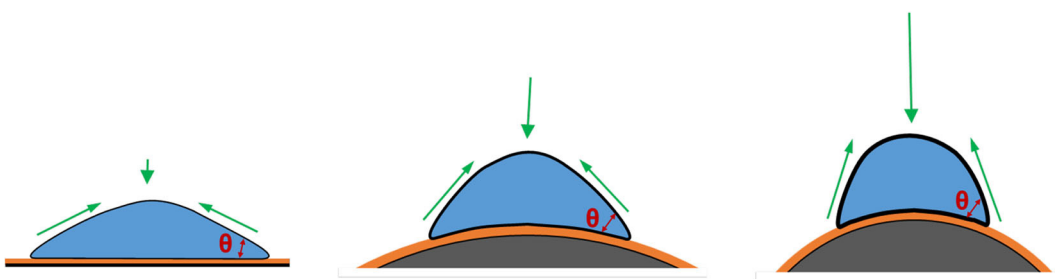

FIGURE 3 | Effects of substrate curvature. Compared to cells cultured on the planar surface (Left), cells cultured on the convex surface (Middle and Right), like microcarriers, have a higher contact angle and thus under a higher mechanical force, against which cells develop more actin stress fibers, as a result of increased cytoskeletal tension. This trend shows more significant when the microcarriers are smaller.

the similar topography to semi-spheres, partially mimicking the curvature on microcarriers. The results reveal that cells on convex spherical structures have higher F-actin intensity and higher osteocalcin levels compared to cells on flat surfaces after 10-days expansion or osteogenic induction, and the enhancement becomes more significant when decreasing the convex diameters (Werner et al., 2017). The enhanced mechanical stress may be attributed to the push-force by the perinuclear actin cap to deform the nucleus (Werner et al., 2017). Based on the tensegrity theory, a numerical model was used by Vassaux to investigate the influence of biophysical environment on adherent cells on concave hemispheres (Ingber, 2003a). The results indicate that cells can experience higher mechanical microenvironment and become stiffer if the underlying substrate becomes more convex (Vassaux and Milan, 2017). Thus, higher underlying curvature from the smaller microcarrier size may contribute to higher mechanical stress and improved osteogenic differentiation. Another study was performed by culturing hMSCs on 4, 3, 2, 1.1 mm-, 900, 750, and 500 μm-diameter glass balls, which were half-embedded in polyacrylamide gels. hMSCs exhibited the increased gene expression of adipogenesis when cultured on the beads with the size in diameter equal or below 1.1 mm (Lee and Yang, 2017).

To measure cell contractility, cells were seeded on a microprinted surface covered by crowded micropillars. Through the direction and the level of localized deformation of the micropillar top, the contractile force can be calculated (Du Roure et al., 2005; Ghassemi et al., 2012; Trichet et al., 2012). To further understand the effect of the biophysical microenvironment in microcarrier culture, similar techniques should be developed and applied to the microcarrier-like curvature.

Microcarrier Rigidity

The biophysical cues, such as substrate elasticity, have been reported to influence hMSC lineage specification (Discher et al., 2005; Engler et al., 2006). hMSCs can be induced into osteogenic differentiation on a surface with the elasticity of 25–40 kPa, but into myogenic differentiation on a softer surface (8–17 kPa) and neurogenic differentiation on the softest surface (0.1–1 kPa). Consequent studies demonstrated that cells sense the stiffness of ECM via heterodimeric integrin receptors of α and β subunits through focal adhesions with involved proteins, including talin, paxillin, and vinculin (Liu et al., 2000). Followed by actin polymerization and elongation, the stress fibers are formed, which are induced by the RhoA-Rho-associated coiled-coil containing protein kinase (ROCK)-myosin light chain phosphatase (MLCP) signaling pathway responsible for cell skeletal tension along the edges (Galbraith et al., 2007). The integrin-mediated mechanotransducers, e.g., ROCK, activated by RhoA activity and influenced by cell adhesion and actin-myosin tension regulate hMSC lineage commitment through the mitogen activated protein kinase (MAPK)/the extracellular-signal-regulated kinase (ERK) and Yes-associated protein/transcriptional coactivator with PDZ-binding motif (TAZ) signaling pathways (McBeath et al., 2004; Bhadriraju et al., 2007; Dupont et al., 2011; Shih et al., 2011; Kim et al., 2014). The surface stiffness with the capacity of regulating hMSC differentiation is identified in planar culture, but whether the surface stiffness still has the same effects in microcarrier system, and whether it is possible to use the particular microcarrier stiffness to produce a specific lineage of hMSCs have not been well-investigated.

To date, the characteristics of microcarriers provided by the vendors usually only contain the information of size, composition, density, porosity, surface area, coating, and surface charge, but not the elasticity, rigidity, or stiffness. Most microcarriers are composed of a mixture of peptides or polymers, and the elasticity of these materials differs with the combination and concentration of molecules (i.e., degree of crosslinking) and the average length of polymers (i.e., degree of polymerization). For example, Lück et al. (2016) proposed a fabrication method of synthetic hydrogel microcarriers by telechelic poly(2-oxazoline) crosslinkers and methacrylate monomers, and the microcarrier rigidity can be regulated from 2 to 20 kPa in Young's modulus. Microcarrier rigidity can be measured by the high-resolution elasticity microscope (Cohn et al., 2000) with colloidal probe spectroscopy, an atomic force microscopy modified by gluing a micron-sized spherical force sensor to the end of cantilever (Kappl and Butt, 2002; Butt et al., 2005; Lück et al., 2016). To date, the influence of microcarrier rigidity on hMSC properties has not been well-investigated, possibly due to the confounded curvature effect on mechanical stress from the substrate. Hence, cells on microcarriers may not be as sensitive to the stiffness as they are on the flat surface.

Hydrodynamics: Shear Stress and Collision and Aggregation

The flow in microcarrier culture provides dynamic environment capable of resuspending microcarriers for homogeneous mixing and induces non-homogeneous shear stress and microcarrier-microcarrier collisions, all of which have critical impacts on the extracellular microenvironment of hMSCs.

Shear Stress

In microcarrier culture, fluid flow plays a critical role in maintaining microcarriers in suspension and induces shear stress in culture microenvironment. Flush-mounted film probes (Dantec Dynamics, Germany) can be used to measure flow-induced shear stress, but have to be stuck on the wall (Kalmbach et al., 2011). Particle image velocimetry is able to generate comprehensive profiles of fluid shear stress and velocity in the spinner flasks (Ismadi et al., 2014). Computational fluid dynamics also offers an alternative approach to predict fluid shear stress (Jossen et al., 2016; Tsai et al., 2017). From these results, the maximum shear stress is 0.07–0.1 Pa at 25 rpm and 0.22–0.31 Pa at 60 rpm. Although only a small population of cells are exposed to the localized high shear stress and the volume-weighted mean of shear stress is very low (e.g., 0.0032 Pa at 25 rpm and 0.0067 Pa at 60 rpm), accumulated influence induced by shear stress is still significant on cell growth (Yuan et al., 2014; Jossen et al., 2016). Accordingly, alternative bioreactor designs have been developed to provide a low-shear stress environment, such as WAVE Bioreactor™ (GE Healthcare), BIOSTAT® CultiBag RM bioreactor (Sartorius), and Vertical-Wheel™ bioreactor (PBS Biotech) (Timmins et al., 2012; Sousa et al., 2015; Jossen et al., 2016; da Silva et al., 2019).

When flow-induced physical force directly acts on the cells, the cells may respond in several possible ways. For example, Ingber proposed a theory of tensegrity that a cell is structured by a hierarchical framework of cytoskeletons (Ingber, 2003a,b). Thus, the external forces acting at any point of the cell would be translated into the whole internal cell structure to revoke the force effect by cytoskeletal reorganization. Another possibility is that shear stress mechanically influences the integrins that connect ECM and cytoskeletons through the focal adhesion and the anchorage proteins to mechanotransduce the biomechanical stress into biochemical signals (Ingber, 2003b). Moreover, the cell membrane become more fluidized to change membrane composition and ion channels for the mechanotransduction pathways under elevated fluid shear stress (Barakat et al., 2006). These responses expedite hMSCs' commitment to osteogenic lineage by regulating opening and closing of membrane ion channels to increase intracellular Ca^{2+} concentration, and reorganizing cytoskeleton which activates focal adhesion kinase (FAK)/ERK1/2 pathways to trigger Runx2 and AP-1 and initiate the transcripted osteogenic differentiation (Liu et al., 2010). In addition to osteogenic differentiation, microcarrier culture has also been reported to improve chondrogenic differentiation (Lin et al., 2016). hMSCs undergo chondrogenic differentiation normally requiring cells clustering into spheroids that provide the unique mechanical microenvironment (Sart et al., 2014b; Tsai et al., 2015). Thus, shear stress in microcarrier culture reshapes the microenvironment for hMSCs to exhibit lineage specificity.

Collision and Aggregation

In bioreactors, microcarrier-impeller and microcarrier-microcarrier collisions occur frequently when mixing microcarriers in suspension. Microcarrier concentration and agitation speed determine the collision frequency and microcarrier kinetic energy, respectively.

Increased microcarrier concentration can increase the volumetric production at a lower cost, and higher cell culture density can induce more concentrated autocrine and paracrine factors which accelerate cell growth and facilitate cell function. However, high microcarrier concentration may promote collision frequency and damage cell growth. For example, addition of Sephadex G-50 beads (Pharmacia) was used to change the collision frequency. Severely decreased cell growth was observed at high collision frequency, which may detach cells from microcarriers (Croughan et al., 1988). Furthermore, increased microcarrier concentration normally requires frequent medium change and results in nutrient limitations or toxic by-product accumulation due to high cell density (Chen et al., 2015), which can be overcome by a perfusion culture system.

Agitation speed associated with microcarrier kinetic energy has been reported to influence hMSC expansion, and the optimal cell growth was observed at 49 rpm in a 100 mL spinner flask (Yuan et al., 2014; Jossen et al., 2016). Jossen et al. demonstrated that hMSC expansion significantly decreased when the agitation speed reached above 90 rpm (Jossen et al., 2016). Besides the shear stress effect, another possible explanation is the increased physical collisions due to the elevated kinetic energy and collision frequency (Yuan et al., 2014). The agitation speed of above 90 rpm may reach the threshold of microcarrier kinetic energy for initiating cell death (Jossen et al., 2016). The highest velocity at the tips of impeller can be calculated by agitation speed and impeller diameter (Ismadi et al., 2014; Odeleye et al., 2014). For example, in a 100 mL spinner flask with a standard impeller of 4 cm in diameter, the tip speed is 0.19 m/s at 90 rpm.

The accumulated collision impact likely leads to cell death and phenotypic alteration. Although the damage from collisions depends on the frequency and the intensity, it is difficult to isolate the shear stress effect. Moreover, cell concentration or cell coverage on microcarriers can also impact collision damage at the late stage of cultivation. Clusters bridged by cells may form due to the microcarrier-microcarrier collisions and non-proper mixing, especially when cells are confluent (Cherry and Papoutsakis, 1988; Caruso et al., 2014). Once multiple-microcarrier clusters are formed, cells tend to migrate to interstitial space between microcarriers, and multi-cellular aggregation has been well-known to promote cell differentiation, migration, and secretion (Sart et al., 2014b; Cesarz and Tamama, 2016; Zhang et al., 2016). Nevertheless, cells in the clusters may endure the limitation of mass transfer since diffusion is dominant over convection. Besides, shear stress randomly tears apart bridged microcarriers and may further provoke cell death (Cherry and Papoutsakis, 1988; Takahashi et al., 2017). Therefore, the microcarrier concentration and the agitation speed along with culture time need to be optimized to avoid severe collision damage and oversized clusters (Chen et al., 2015).

CONCLUSION

To expand hMSCs under cGMP compliant regulations, advanced biotechnologies have been developed, such as multi-layer vessels, fixed/packed bed bioreactors, hollow fiber bioreactors, and microcarrier suspension bioreactors. However, there is no guarantee that hMSC therapeutic potency is well-preserved, owing to the fundamental change in culture microenvironment. As a result, standardized characterization of manufactured hMSCs from different bioprocesses is necessary to certify their therapeutic potency for specific disease models. This article focuses on the microcarrier bioreactor systems and discusses the influences of bioprocessing parameters (e.g., agitation speed, heterogeneous shear stress exposure, microcarrier size, rigidity, adhesive force, coating charge, and cell-cell collision and aggregation) on the differentiation, migratory ability, and secretory function of manufactured hMSCs. Based on literature, microcarrier culture has been reported to enhance hMSC osteogenic and chondrogenic differentiation but impair their adipogenic differentiation compared to planar culture. Moreover, the improved migration and secretion abilities suggest microcarrier culture may augment hMSC therapeutic potency in immunomodulation, angiogenesis, and neural differentiation. Overall, microcarrier culture in bioreactors provides the possibility to scale up hMSC production and regulates hMSC therapeutic properties for clinical applications. Future studies should focus on improving the robustness of

hMSC biomanufacturing system as well as engineering hMSCs with desired stem cell properties.

AUTHOR CONTRIBUTIONS

A-CT wrote the majority of the manuscript. RJ and XC revised the manuscript. XY and YL conceived the whole study, revised, and finalized the manuscript.

FUNDING

This work was supported by National Science Foundation of USA (CBET-1743426 and 1917618). This work was also partially supported by the National Institutes of Health (NIH; R01 NS102395). The content is solely the responsibility of the authors and does not necessarily represent the official views of the NIH.

REFERENCES

Aggarwal, S., and Pittenger, M. F. (2005). Human mesenchymal stem cells modulate allogeneic immune cell responses. *Blood* 105, 1815–1822. doi: 10.1182/blood-2004-04-1559

Alge, D. L., Zhou, D., Adams, L. L., Wyss, B. K., Shadday, M. D., Woods, E. J., et al. (2010). Donor-matched comparison of dental pulp stem cells and bone marrow-derived mesenchymal stem cells in a rat model. *J. Tissue Eng. Regen. Med.* 4, 73–81. doi: 10.1002/term.220

Al-Nbaheen, M., Ali, D., Bouslimi, A., Al-Jassir, F., Megges, M., Prigione, A., et al. (2013). Human stromal (mesenchymal) stem cells from bone marrow, adipose tissue and skin exhibit differences in molecular phenotype and differentiation potential. *Stem Cell Rev. Rep.* 9, 32–43. doi: 10.1007/s12015-012-9365-8

António, M., Fernandes-Platzgummer, A., da Silva, C. L., and Cabral, J. M. (2016). Scalable microcarrier-based manufacturing of mesenchymal stem/stromal cells. *J. Biotechnol.* 236, 88–109. doi: 10.1016/j.jbiotec.2016.08.007

Atkinson, K., Timmins, N., Kiel, G., Heazlewood, C., Doran, M., and Brooke, G. (2017). Closed automated large-scale bioreactors for manufacturing mesenchymal stromal cells for clinical use. *Biol. Ther. Appl. Mesenchymal Cells* 2017, 616–618. doi: 10.1002/9781118907474.ch42

Badenes, S. M., Fernandes, T. G., Cordeiro, C. S., Boucher, S., Kuninger, D., Vemuri, M. C., et al. (2016b). Defined essential 8^{TM} medium and vitronectin efficiently support scalable xeno-free expansion of human induced pluripotent stem cells in stirred microcarrier culture systems. *PLoS ONE* 11:e0151264. doi: 10.1371/journal.pone.0151264

Badenes, S. M., Fernandes, T. G., Rodrigues, C. A., Diogo, M. M., and Cabral, J. M. (2016a). Microcarrier-based platforms for in vitro expansion and differentiation of human pluripotent stem cells in bioreactor culture systems. *J. Biotechnol.* 234, 71–82. doi: 10.1016/j.jbiotec.2016.07.023

Bara, J. J., Richards, R. G., Alini, M., and Stoddart, M. J. (2014). Concise Review: Bone marrow-derived mesenchymal stem cells change phenotype following *in vitro* culture: implications for basic research and the clinic. *Stem Cells* 32, 1713–1723. doi: 10.1002/stem.1649

Barakat, A. I., Lieu, D. K., and Gojova, A. (2006). Secrets of the code: do vascular endothelial cells use ion channels to decipher complex flow signals? *Biomaterials* 27, 671–678. doi: 10.1016/j.biomaterials.2005.07.036

Barckhausen, C., Rice, B., Baila, S., Sensebé, L., Schrezenmeier, H., Nold, P., et al. (2016). GMP-compliant expansion of clinical-grade human mesenchymal stromal/stem cells using a closed hollow fiber bioreactor. *Methods Mol. Biol.* 416, 389–412. doi: 10.1007/978-1-4939-3584-0_23

Bhadriraju, K., Yang, M., Ruiz, S. A., Pirone, D., Tan, J., and Chen, C. S. (2007). Activation of ROCK by RhoA is regulated by cell adhesion, shape, and cytoskeletal tension. *Exp. Cell Res.* 313, 3616–3623. doi: 10.1016/j.yexcr.2007.07.002

Bianco, P., Cao, X., Frenette, P. S., Mao, J. J., Robey, P. G., Simmons, P. J., et al. (2013). The meaning, the sense and the significance: translating the science of mesenchymal stem cells into medicine. *Nat. Med.* 19, 35–42. doi: 10.1038/nm.3028

Billing, A. M., Hamidane, H. B., Dib, S. S., Cotton, R. J., Bhagwat, A. M., Kumar, P., et al. (2016). Comprehensive transcriptomic and proteomic characterization of human mesenchymal stem cells reveals source specific cellular markers. *Sci. Rep.* 6:21507. doi: 10.1038/srep21507

Bravery, C. A., Carmen, J., Fong, T., Oprea, W., Hoogendoorn, K. H., Woda, J., et al. (2013). Potency assay development for cellular therapy products: an ISCT review of the requirements and experiences in the industry. *Cytotherapy* 15, 9–19. doi: 10.1016/j.jcyt.2012.10.008

Butt, H. J., Cappella, B., and Kappl, M. (2005). Force measurements with the atomic force microscope: technique, interpretation and applications. *Surf. Sci. Rep.* 59, 1–152. doi: 10.1016/j.surfrep.2005.08.003

Caruso, S. R., Orellana, M. D., Mizukami, A., Fernandes, T. R., Fontes, A. M., Suazo, C. A., et al. (2014). Growth and functional harvesting of human mesenchymal stromal cells cultured on a microcarrier-based system. *Biotechnol. Prog.* 30, 889–895. doi: 10.1002/btpr.1886

Castilla-Casadiego, D. A., Reyes-Ramos, A. M., Domenech, M., and Almodovar, J. (2020). Effects of physical, chemical, and biological stimulus on h-MSC expansion and their functional characteristics. *Ann. Biomed. Eng.* 48, 519–535. doi: 10.1007/s10439-019-02400-3

Cesarz, Z., and Tamama, K. (2016). Spheroid culture of mesenchymal stem cells. *Stem Cells Int.* 2016:9176357. doi: 10.1155/2016/9176357

Chen, A. K. L., Chew, Y. K., Tan, H. Y., Reuveny, S., and Oh, S. K. W. (2015). Increasing efficiency of human mesenchymal stromal cell culture by optimization of microcarrier concentration and design of medium feed. *Cytotherapy* 17, 163–173. doi: 10.1016/j.jcyt.2014.08.011

Chen, A. K. L., Reuveny, S., and Oh, S. K. W. (2013). Application of human mesenchymal and pluripotent stem cell microcarrier cultures in cellular therapy: achievements and future direction. *Biotechnol. Adv.* 31, 1032–1046. doi: 10.1016/j.biotechadv.2013.03.006

Chen, C. S., Alonso, J. L., Ostuni, E., Whitesides, G. M., and Ingber, D. E. (2003). Cell shape provides global control of focal adhesion assembly. *Biochem. Biophys. Res. Commun.* 307, 355–361. doi: 10.1016/S0006-291X(03)01165-3

Cherry, R. S., and Papoutsakis, E. T. (1988). Physical mechanisms of cell damage in microcarrier cell culture bioreactors. *Biotechnol. Bioeng.* 32, 1001–1014. doi: 10.1002/bit.260320808

Chui, C. Y., Odeleye, A., Nguyen, L., Kasoju, N., Soliman, E., and Ye, H. (2019). Electrosprayed genipin cross-linked alginate–chitosan microcarriers for *ex vivo* expansion of mesenchymal stem cells. *J. Biomed. Mater. Res. Part A* 107, 122–133. doi: 10.1002/jbm.a.36539

Cohn, N. A., Kim, B. S., Erkamp, R. Q., Mooney, D. J., Emelianov, S. Y., Skovoroda, A. R., et al. (2000). High-resolution elasticity imaging for tissue engineering. *IEEE Trans. Ultrason. Ferroelectr. Freq. Control* 47, 956–966. doi: 10.1109/58.852079

Collignon, M. L., Delafosse, A., Calvo, S., Martin, C., Marc, A., Toye, D., et al. (2016). Large-Eddy simulations of microcarrier exposure to potentially damaging eddies inside mini-bioreactors. *Biochem. Eng. J.* 108, 30–43. doi: 10.1016/j.bej.2015.10.020

Confalonieri, D., La Marca, M., van Dongen, E. M. W. M., Walles, H., and Ehlicke, F. (2017). An injectable recombinant collagen I peptide–based macroporous microcarrier allows superior expansion of C2C12 and human bone marrow-derived mesenchymal stromal cells and supports deposition of mineralized matrix. *Tissue Eng. Part A* 23, 946–957. doi: 10.1089/ten.tea.2016.0436

Croughan, M. S., Hamel, J. F. P., and Wang, D. I. (1988). Effects of microcarrier concentration in animal cell culture. *Biotechnol. Bioeng.* 32, 975–982. doi: 10.1002/bit.260320805

Cunha, B., Aguiar, T., Carvalho, S. B., Silva, M. M., Gomes, R. A., Carrondo, M. J., et al. (2017). Bioprocess integration for human mesenchymal stem cells: from up to downstream processing scale-up to cell proteome characterization. *J. Biotechnol.* 248, 87–98. doi: 10.1016/j.jbiotec.2017.01.014

da Silva, J. D. S., Mizukami, A., Gil, L. V. G., de Campos, J. V., Assis, O. B., Covas, D. T., et al. (2019). Improving wave-induced motion bioreactor performance

for human mesenchymal stromal cell expansion. *Process Biochem.* 84, 143–152. doi: 10.1016/j.procbio.2019.06.004

Das, R., Roosloot, R., van Pel, M., Schepers, K., Driessen, M., Fibbe, W. E., et al. (2019). Preparing for cell culture scale-out: establishing parity of bioreactor- and flask-expanded mesenchymal stromal cell cultures. *J. Transl. Med.* 17:241. doi: 10.1186/s12967-019-1989-x

Demuth, C., Varonier, J., Jossen, V., Eibl, R., and Eibl, D. (2016). Novel probes for pH and dissolved oxygen measurements in cultivations from millilitre to benchtop scale. *Appl. Microbiol. Biotechnol.* 100, 3853–3863. doi: 10.1007/s00253-016-7412-0

Discher, D. E., Janmey, P., and Wang, Y. (2005). Tissue cells feel and respond to the stiffness of their substrate. *Science* 310, 1139–1143. doi: 10.1126/science.1116995

Dominici, M., Le Blanc, K., Mueller, I., Slaper-Cortenbach, I., Marini, F., Krause, D., et al. (2006). Minimal criteria for defining multipotent mesenchymal stromal cells. The International Society for Cellular Therapy position statement. *Cytotherapy* 8, 315–317. doi: 10.1080/14653240600855905

dos Santos, F., Andrade, P. Z., Abecasis, M. M., Gimble, J. M., Chase, L. G., Campbell, A. M., et al. (2011). Toward a clinical-grade expansion of mesenchymal stem cells from human sources: a microcarrier-based culture system under xeno-free conditions. *Tissue Eng. Part C Methods* 17, 1201–1210. doi: 10.1089/ten.tec.2011.0255

dos Santos, F., Andrade, P. Z., da Silva, C. L., and Cabral, J. M. (2013). Bioreactor design for clinical-grade expansion of stem cells. *Biotechnol. J.* 8, 644–654. doi: 10.1002/biot.201200373

dos Santos, F., Campbell, A., Fernandes-Platzgummer, A., Andrade, P. Z., Gimble, J. M., Wen, Y., et al. (2014). A xenogeneic-free bioreactor system for the clinical-scale expansion of human mesenchymal stem/stromal cells. *Biotechnol. Bioeng.* 111, 1116–1127. doi: 10.1002/bit.25187

Du Roure, O., Saez, A., Buguin, A., Austin, R. H., Chavrier, P., Siberzan, P., et al. (2005). Force mapping in epithelial cell migration. *Proc. Natl. Acad. Sci. U.S.A.* 102, 2390–2395. doi: 10.1073/pnas.0408482102

Duijvestein, M., Vos, A. C. W., Roelofs, H., Wildenberg, M. E., Wendrich, B. B., Verspaget, H. W., et al. (2010). Autologous bone marrow-derived mesenchymal stromal cell treatment for refractory luminal Crohn's disease: results of a phase I study. *Gut* 59, 1662–1669. doi: 10.1136/gut.2010.215152

Dupont, S., Morsut, L., Aragona, M., Enzo, E., Giulitti, S., Cordenonsi, M., et al. (2011). Role of YAP/TAZ in mechanotransduction. *Nature* 474, 179–183. doi: 10.1038/nature10137

Eibes, G., dos Santos, F., Andrade, P. Z., Boura, J. S., Abecasis, M. M., da Silva, C. L., et al. (2010). Maximizing the *ex vivo* expansion of human mesenchymal stem cells using a microcarrier-based stirred culture system. *J. Biotechnol.* 146, 194–197. doi: 10.1016/j.jbiotec.2010.02.015

Engler, A. J., Sen, S., Sweeney, H. L., and Discher, D. E. (2006). Matrix elasticity directs stem cell lineage specification. *Cell* 126, 677–689. doi: 10.1016/j.cell.2006.06.044

Fernandes-Platzgummer, A., Carmelo, J. G., da Silva, C. L., and Cabral, J. M. (2016). Clinical-grade manufacturing of therapeutic human mesenchymal stem/stromal cells in microcarrier-based culture systems. *Methods Mol. Biol.* 1416, 375–388. doi: 10.1007/978-1-4939-3584-0_22

Fraser, J. K., Schreiber, R., Strem, B., Zhu, M., Alfonso, Z., Wulur, I., et al. (2006). Plasticity of human adipose stem cells toward endothelial cells and cardiomyocytes. *Nat. Clin. Pract. Cardiovasc. Med.* 3, S33–S37. doi: 10.1038/ncpcardio0444

Frauenschuh, S., Reichmann, E., Ibold, Y., Goetz, P. M., Sittinger, M., and Ringe, J. (2007). A microcarrier-based cultivation system for expansion of primary mesenchymal stem cells. *Biotechnol. Prog.* 23, 187–193. doi: 10.1021/bp060155w

Galbraith, C. G., Yamada, K. M., and Galbraith, J. A. (2007). Polymerizing actin fibers position integrins primed to probe for adhesion sites. *Science* 315, 992–995. doi: 10.1126/science.1137904

Galipeau, J., Krampera, M., Barrett, J., Dazzi, F., Deans, R. J., DeBruijn, J., et al. (2016). International Society for Cellular Therapy perspective on immune functional assays for mesenchymal stromal cells as potency release criterion for advanced phase clinical trials. *Cytotherapy* 18, 151–159. doi: 10.1016/j.jcyt.2015.11.008

Ghassemi, S., Meacci, G., Liu, S., Gondarenko, A. A., Mathur, A., Roca-Cusachs, P., et al. (2012). Cells test substrate rigidity by local contractions on submicrometer pillars. *Proc. Natl. Acad. Sci. U.S.A.* 109, 5328–5333. doi: 10.1073/pnas.1119886109

Goh, T. K. P., Zhang, Z. Y., Chen, A. K. L., Reuveny, S., Choolani, M., Chan, J. K. Y., et al. (2013). Microcarrier culture for efficient expansion and osteogenic differentiation of human fetal mesenchymal stem cells. *BioRes. Open Access* 2, 84–97. doi: 10.1089/biores.2013.0001

Grayson, W. L., and Stephenson, M. (2018). Recent advances in bioreactors for cell-based therapies. *F1000Res.* 7:517. doi: 10.12688/f1000research.12533.1

Gupta, P., Geris, L., Luyten, F. P., and Papantoniou, I. (2018). An integrated bioprocess for the expansion and chondrogenic priming of human periosteum-derived progenitor cells in suspension bioreactors. *Biotechnol. J.* 13:e1700087. doi: 10.1002/biot.201700087

Gupta, P., Hall, G. N., Geris, L., Luyten, F. P., and Papantoniou, I. (2019). Human platelet lysate improves bone forming potential of human progenitor cells expanded in microcarrier-based dynamic culture. *Stem Cells Transl. Med.* 8, 810–821. doi: 10.1002/sctm.18-0216

Hanley, P. J., Mei, Z., Durett, A. G., M., da Graca Cabreira-Harrison, Klis, M., Li, W., et al. (2014). Efficient manufacturing of therapeutic mesenchymal stromal cells with the use of the Quantum Cell Expansion System. *Cytotherapy* 16, 1048–1058. doi: 10.1016/j.jcyt.2014.01.417

Heathman, T. R., Glyn, V. A., Picken, A., Rafiq, Q. A., Coopman, K., Nienow, A. W., et al. (2015). Expansion, harvest and cryopreservation of human mesenchymal stem cells in a serum-free microcarrier process. *Biotechnol. Bioeng.* 112, 1696–1707. doi: 10.1002/bit.25582

Hernandez, R. (2016). Scale-up of complex biologics. *BioPharm. Int.* 29, 26–30. doi: 10.1111/tri.12886

Hervy, M., Weber, J. L., Pecheul, M., Dolley-Sonneville, P., Henry, D., Zhou, Y., et al. (2014). Long term expansion of bone marrow-derived hMSCs on novel synthetic microcarriers in xeno-free, defined conditions. *PLoS ONE* 9:e92120. doi: 10.1371/journal.pone.0092120

Hewitt, C. J., Lee, K., Nienow, A. W., Thomas, R. J., Smith, M., and Thomas, C. R. (2011). Expansion of human mesenchymal stem cells on microcarriers. *Biotechnol. Lett.* 33, 2325–2335. doi: 10.1007/s10529-011-0695-4

Honmou, O., Onodera, R., Sasaki, M., Waxman, S. G., and Kocsis, J. D. (2012). Mesenchymal stem cells: therapeutic outlook for stroke. *Trends Mol. Med.* 18, 292–297. doi: 10.1016/j.molmed.2012.02.003

Hoshan, L., Jiang, R., Moroney, J., Bui, A., Zhang, X., Hang, T. C., et al. (2019). Effective bioreactor pH control using only sparging gases. *Biotechnol. Prog.* 35:e2743. doi: 10.1002/btpr.2743

Hourd, P., Chandra, A., Medcalf, N., and Williams, D. J. (2014). *Regulatory Challenges for the Manufacture and Scale-Out of Autologous Cell Therapies, StemBook*. Cambridge, MA: Harvard Stem Cell Institute.

Hu, W., Meier, J., and Wang, D. (1985). A mechanistic analysis of the inoculum requirement for the cultivation of mammalian cells on microcarriers. *Biotechnol. Bioeng.* 27, 585–595. doi: 10.1002/bit.260270507

Hupfeld, J., Gorr, I. H., Schwald, C., Beaucamp, N., Wiechmann, K., Kuentzer, K., et al. (2014). Modulation of mesenchymal stromal cell characteristics by microcarrier culture in bioreactors. *Biotechnol. Bioeng.* 111, 2290–2302. doi: 10.1002/bit.25281

Ingber, D. E. (2003a). Tensegrity I. Cell structure and hierarchical systems biology. *J. Cell Sci.* 116, 1157–1173. doi: 10.1242/jcs.00359

Ingber, D. E. (2003b). Tensegrity II. How structural networks influence cellular information processing networks. *J. Cell Sci.* 116, 1397–1408. doi: 10.1242/jcs.00360

Ismadi, M. Z., Hourigan, K., and Fouras, A. (2014). Experimental characterisation of fluid mechanics in a spinner flask bioreactor. *Processes* 2, 753–772. doi: 10.3390/pr2040753

Isobe, Y., Koyama, N., Nakao, K., Osawa, K., Ikeno, M., Yamanaka, S., et al. (2016). Comparison of human mesenchymal stem cells derived from bone marrow, synovial fluid, adult dental pulp, and exfoliated deciduous tooth pulp. *Int. J. Oral Maxillofac. Surg.* 45, 124–131. doi: 10.1016/j.ijom.2015.06.022

James, J., Goluch, E. D., Hu, H., Liu, C., and Mrksich, M. (2008). Subcellular curvature at the perimeter of micropatterned cells influences lamellipodial distribution and cell polarity. *Cell Motil. Cytoskeleton* 65, 841–852. doi: 10.1002/cm.20305

Jossen, V., C., van den Bos, Eibl, R., and Eibl, D. (2018). Manufacturing human mesenchymal stem cells at clinical scale: process and regulatory challenges. *Appl. Microbiol. Biotechnol.* 102, 3981–3994. doi: 10.1007/s00253-018-8912-x

Jossen, V., Eibl, R., Kaiser, S. C., Kraume, M., Pörtner, R., and Eibl, D. (2014). Mass production of mesenchymal stem cells: impact of bioreactor design and flow conditions on proliferation and differentiation. *Cells Biomater. Regen. Med.* 2014, 119–172. doi: 10.5772/59385

Jossen, V., Schirmer, C., Mostafa Sindi, D., Eibl, R., Kraume, M., Pörtner, R., et al. (2016). Theoretical and practical issues that are relevant when scaling up hMSC microcarrier production processes. *Stem Cells Intl.* 2016:4760414. doi: 10.1155/2016/4760414

Kaiser, S., Jossen, V., Schirmaier, C., Eibl, D., Brill, S., C., et al. (2013). Fluid Flow and Cell Proliferation of mesenchymal adipose-derived stem cells in small-scale, stirred, single-use bioreactors. *Chem. Ingen. Tech.* 85, 95–102. doi: 10.1002/cite.201200180

Kalmbach, A., Bordás, R., Öncül, A. A., Thévenin, D., and Genzel, Y., Reichl, U. (2011). Experimental characterization of flow conditions in 2-and 20-l bioreactors with wave-induced motion. *Biotechnol. Prog.* 27, 402–409. doi: 10.1002/btpr.516

Kang, H., Lu, S., Peng, J., Yang, Q., Liu, S., Zhang, L., et al. (2015). Chondrogenic differentiation of human adipose-derived stem cells using microcarrier and bioreactor combination technique. *Mol. Med. Rep.* 11, 1195–1199. doi: 10.3892/mmr.2014.2820

Kappl, M., and Butt, H. J. (2002). The colloidal probe technique and its application to adhesion force measurements. *Part Part Syst. Charact.* 19, 129–143. doi: 10.1002/1521-4117(200207)19:3<129::AID-PPSC129>3.0.CO;2-G

Kehoe, D., Niss, K., Rook, M., Punreddy, S., Murrel, J., Sunil, N., et al. (2013). Growth kinetics of human mesenchymal stem cells in a 3-L single-use, stirred-tank bioreactor. *BioPharm. Int.* 26, 28–38.

Kilian, K. A., Bugarija, B., Lahn, B. T., and Mrksich, M. (2010). Geometric cues for directing the differentiation of mesenchymal stem cells. *Proc. Natl. Acad. Sci. U.S.A.* 107, 4872–4877. doi: 10.1073/pnas.0903269107

Kim, K. M., Choi, Y. J., Hwang, J. H., Kim, A. R., Cho, H. J., Hwang, E. S., et al. (2014). Shear stress induced by an interstitial level of slow flow increases the osteogenic differentiation of mesenchymal stem cells through TAZ activation. *PLoS ONE* 9:e92427. doi: 10.1371/journal.pone.0092427

Knippenberg, M., Helder, M. N., Zandieh Doulabi, B., Semeins, C. M., Wuisman, P. I., and Klein-Nulend, J. (2005). Adipose tissue-derived mesenchymal stem cells acquire bone cell-like responsiveness to fluid shear stress on osteogenic stimulation. *Tissue Eng.* 11, 1780–1788. doi: 10.1089/ten.2005.11.1780

Koniusz, S., Andrzejewska, A., Muraca, M., Srivastava, A. K., Janowski, M., and Lukomska, B. (2016). Extracellular vesicles in physiology, pathology, and therapy of the immune and central nervous system, with focus on extracellular vesicles derived from mesenchymal stem cells as therapeutic tools. *Front. Cell Neurosci.* 10:109. doi: 10.3389/fncel.2016.00109

Krampera, M., Galipeau, J., Shi, Y., Tarte, K., and Sensebe, L. (2013). Immunological characterization of multipotent mesenchymal stromal cells—The International Society for Cellular Therapy (ISCT) working proposal. *Cytotherapy* 15, 1054–1061. doi: 10.1016/j.jcyt.2013.02.010

Krutty, J. D., Dias, A. D., Yun, J., Murphy, W. L., and Gopalan, P. (2019). Synthetic, chemically defined polymer-coated microcarriers for the expansion of human mesenchymal stem cells. *Macromol. Biosci.* 19:1800299. doi: 10.1002/mabi.201800299

Lam, A. T. L., Sim, E. J. H., Shekaran, A., Li, J., Teo, K. L., Goggi, J. L., et al. (2019). Sub-confluent culture of human mesenchymal stromal cells on biodegradable polycaprolactone microcarriers enhances bone healing of rat calvarial defect. *Cytotherapy* 21, 631–642. doi: 10.1016/j.jcyt.2019.03.004

Lawson, T., Kehoe, D. E., Schnitzler, A. C., Rapiejko, P. J., Der, K. A., Philbrick, K., et al. (2017). Process development for expansion of human mesenchymal stromal cells in a 50L single-use stirred tank bioreactor. *Biochem. Eng. J.* 120, 49–62. doi: 10.1016/j.bej.2016.11.020

Leber, J., Barekzai, J., Blumenstock, M., Pospisil, B., Salzig, D., and Czermak, P. (2017). Microcarrier choice and bead-to-bead transfer for human mesenchymal stem cells in serum-containing and chemically defined media. *Process Biochem.* 59, 255–265. doi: 10.1016/j.procbio.2017.03.017

Lee, S. J., and Yang, S. (2017). Substrate curvature restricts spreading and induces differentiation of human mesenchymal stem cells. *Biotechnol. J.* 12:1700360. doi: 10.1002/biot.201700360

Levato, R., Planell, J. A., Mateos-Timoneda, M. A., and Engel, E. (2015). Role of ECM/peptide coatings on SDF-1α triggered mesenchymal stromal cell migration from microcarriers for cell therapy. *Acta Biomater.* 18, 59–67. doi: 10.1016/j.actbio.2015.02.008

Levinson, Y., Eylon, Y., Heymann, A., and Zaretsky-Rits, A. (2015). Foundation elements for cell therapy smart scaling. *Bioprocess. Int.* 13, 10–19.

Li, C., Wu, X., Tong, J., Yang, X., Zhao, J., Zheng, Q., et al. (2015). Comparative analysis of human mesenchymal stem cells from bone marrow and adipose tissue under xeno-free conditions for cell therapy. *Stem Cell Res. Ther.* 6:55. doi: 10.1186/s13287-015-0066-5

Li, Z., Yao, S. J., Alini, M., and Stoddart, M. J. (2009). Chondrogenesis of human bone marrow mesenchymal stem cells in fibrin–polyurethane composites is modulated by frequency and amplitude of dynamic compression and shear stress. *Tissue Eng. Part A* 16, 575–584. doi: 10.1089/ten.tea.2009.0262

Liang, X., Ding, Y., Zhang, Y., Tse, H. F., and Lian, Q. (2014). Paracrine mechanisms of mesenchymal stem cell-based therapy: current status and perspectives. *Cell Transplant.* 23, 1045–1059. doi: 10.3727/096368913X667709

Lin, C. Y., Huang, C. H., Wu, Y. K., Cheng, N. C., and Yu, J. (2014). Maintenance of human adipose derived stem cell (hASC) differentiation capabilities using a 3D culture. *Biotechnol. Lett.* 36, 1529–1537. doi: 10.1007/s10529-014-1500-y

Lin, Y. M., Lim, J. F. Y., Lee, J., Choolani, M., Chan, J. K. Y., Reuveny, S., et al. (2016). Expansion in microcarrier-spinner cultures improves the chondrogenic potential of human early mesenchymal stromal cells. *Cytotherapy* 18, 740–753. doi: 10.1016/j.jcyt.2016.03.293

Liu, L., Yuan, W., and Wang, J. (2010). Mechanisms for osteogenic differentiation of human mesenchymal stem cells induced by fluid shear stress. *Biomech. Model. Mechanobiol.* 9, 659–670. doi: 10.1007/s10237-010-0206-x

Liu, S., Calderwood, D. A., and Ginsberg, M. H. (2000). Integrin cytoplasmic domain-binding proteins. *J. Cell Sci.* 113, 3563–3571.

Loubière, C., Sion, C., De Isla, N., Reppel, L., Guedon, E., Chevalot, I., et al. (2019). Impact of the type of microcarrier and agitation modes on the expansion performances of mesenchymal stem cells derived from umbilical cord. *Biotechnol. Prog.* 35:e2887. doi: 10.1002/btpr.2887

Lück, S., Schubel, R., Rüb, J., Hahn, D., Mathieu, E., Zimmermann, H., et al. (2016). Tailored and biodegradable poly (2-oxazoline) microbeads as 3D matrices for stem cell culture in regenerative therapies. *Biomaterials* 79, 1–14. doi: 10.1016/j.biomaterials.2015.11.045

Ma, T., Tsai, A. C., and Liu, Y. (2016). Biomanufacturing of human mesenchymal stem cells in cell therapy: influence of microenvironment on scalable expansion in bioreactors. *Biochem. Eng. J.* 108, 44–50. doi: 10.1016/j.bej.2015.07.014

Marquez-Curtis, L. A., Janowska-Wieczorek, A., McGann, L. E., and Elliott, J. A. (2015). Mesenchymal stromal cells derived from various tissues: biological, clinical and cryopreservation aspects. *Cryobiology* 71, 181–197. doi: 10.1016/j.cryobiol.2015.07.003

Martin, C., Olmos, É., Collignon, M. L., De Isla, N., Blanchard, F., Chevalot, I., et al. (2017). Revisiting MSC expansion from critical quality attributes to critical culture process parameters. *Process Biochem.* 59, 231–243. doi: 10.1016/j.procbio.2016.04.017

Martin-Manso, G., and Hanley, P. J. (2015). Using the quantum cell expansion system for the automated expansion of clinical-grade bone marrow-derived human mesenchymal stromal cells, *Methods Mol. Biol.* 1283, 53–63. doi: 10.1007/7651_2014_164

Mathieu, P. S., and Loboa, E. G. (2012). Cytoskeletal and focal adhesion influences on mesenchymal stem cell shape, mechanical properties, and differentiation down osteogenic, adipogenic, and chondrogenic pathways. *Tissue Eng. Part B Rev.* 18, 436–444. doi: 10.1089/ten.teb.2012.0014

McBeath, R., Pirone, D. M., Nelson, C. M., Bhadriraju, K., and Chen, C. S. (2004). Cell shape, cytoskeletal tension, and RhoA regulate stem cell lineage commitment. *Dev. Cell* 6, 483–495. doi: 10.1016/S1534-5807(04)00075-9

McGrath, M., Tam, E., Sladkova, M., AlManaie, A., Zimmer, M., and de Peppo, G. M. (2019). GMP-compatible and xeno-free cultivation of mesenchymal progenitors derived from human-induced pluripotent stem cells. *Stem Cell Res. Ther.* 10, 1–13. doi: 10.1186/s13287-018-1119-3

Menard, C., Pacelli, L., Bassi, G., Dulong, J., Bifari, F., Bezier, I., et al. (2013). Clinical-grade mesenchymal stromal cells produced under various good manufacturing practice processes differ in their immunomodulatory properties: standardization of immune quality controls. *Stem Cells Dev.* 22, 1789–1801. doi: 10.1089/scd.2012.0594

Meuwly, F., Ruffieux, P. A., Kadouri, A., and Von Stockar, U. (2007). Packed-bed bioreactors for mammalian cell culture: bioprocess and biomedical applications. *Biotechnol. Adv.* 25, 45–56. doi: 10.1016/j.biotechadv.2006.08.004

Mirro, R., and Voll, K. (2009). Which impeller is right for your cell line. *BioProcess. Int.* 7, 52–57.

Mizukami, A., Chilima, T. D. P., Orellana, M. D., Neto, M. A., Covas, D. T., Farid, S. S., et al. (2018). Technologies for large-scale umbilical cord-derived MSC expansion: experimental performance and cost of goods analysis. *Biochem. Eng. J.* 135, 36–48. doi: 10.1016/j.bej.2018.02.018

Moloudi, R., Oh, S., Yang, C., Teo, K. L., Lam, A. T. L., Ebrahimi Warkiani, M., et al. (2019). Scaled-up inertial microfluidics: retention system for microcarrier-based suspension cultures. *Biotechnol. J.* 14:e1800674. doi: 10.1002/biot.201800674

Moreira, F., Mizukami, A., de Souza, L. E. B., Cabral, J. M., da Silva, C. L., Covas, D. T., et al. (2020). Successful use of human AB serum to support the expansion of adipose tissue-derived mesenchymal sem/stromal cell in a microcarrier-based platform. *Front. Bioeng. Biotechnol.* 8:307. doi: 10.3389/fbioe.2020.00307

Moutsatsou, P., Ochs, J., Schmitt, R., Hewitt, C., and Hanga, M. (2019). Automation in cell and gene therapy manufacturing: from past to future. *Biotechnol. Lett.* 41, 1245–1253. doi: 10.1007/s10529-019-02732-z

Newman, R. E., Yoo, D., LeRoux, M. A., and Danilkovitch-Miagkova, A. (2009). Treatment of inflammatory diseases with mesenchymal stem cells. *Inflamm. Allergy Drug Targets* 8, 110–123. doi: 10.2174/187152809788462635

Nienow, A. W. (2006). Reactor engineering in large scale animal cell culture. *Cytotechnology* 50, 9–33. doi: 10.1007/s10616-006-9005-8

Nienow, A. W., Hewitt, C. J., Heathman, T. R., Glyn, V. A., Fonte, G. N., Hanga, M. P., et al. (2016). Agitation conditions for the culture and detachment of hMSCs from microcarriers in multiple bioreactor platforms. *Biochem. Eng. J.* 108, 24–29. doi: 10.1016/j.bej.2015.08.003

Nienow, A. W., Rafiq, Q. A., Coopman, K., and Hewitt, C. J. (2014). A potentially scalable method for the harvesting of hMSCs from microcarriers. *Biochem. Eng. J.* 85, 79–88. doi: 10.1016/j.bej.2014.02.005

Nold, P., Brendel, C., Neubauer, A., Bein, G., and Hackstein, H. (2013). Good manufacturing practice-compliant animal-free expansion of human bone marrow derived mesenchymal stroma cells in a closed hollow-fiber-based bioreactor. *Biochem. Biophys. Res. Commun.* 430, 325–330. doi: 10.1016/j.bbrc.2012.11.001

Odeleye, A., Marsh, D., Osborne, M., Lye, G., and Micheletti, M. (2014). On the fluid dynamics of a laboratory scale single-use stirred bioreactor. *Chem. Eng. Sci.* 111, 299–312. doi: 10.1016/j.ces.2014.02.032

Olsen, T. R., Ng, K. S., Lock, L. T., Ahsan, T., and Rowley, J. A. (2018). Peak MSC—are we there yet? *Front. Med.* 5:178. doi: 10.3389/fmed.2018.00178

Osiecki, M. J., Michl, T. D., Babur, B. K., Kabiri, M., Atkinson, K., Lott, W. B., et al. (2015). Packed bed bioreactor for the isolation and expansion of placental-derived mesenchymal sromal cells. *PLoS ONE* 10:e0144941. doi: 10.1371/journal.pone.0144941

Panchalingam, K. M., Jung, S., Rosenberg, L., and Behie, L. A. (2015). Bioprocessing strategies for the large-scale production of human mesenchymal stem cells: a review. *Stem Cell Res. Ther.* 6:225. doi: 10.1186/s13287-015-0228-5

Park, J. H., Pérez, R. A., Jin, G. Z., Choi, S. J., Kim, H. W., and Wall, I. B. (2013). Microcarriers designed for cell culture and tissue engineering of bone. *Tissue Eng. Part B Rev.* 19, 172–190. doi: 10.1089/ten.teb.2012.0432

Petry, F., Smith, J. R., Leber, J., Salzig, D., Czermak, P., and Weiss, M. L. (2016). Manufacturing of human umbilical cord mesenchymal stromal cells on microcarriers in a dynamic system for clinical use. *Stem Cells Int.* 2016:4834616. doi: 10.1155/2016/4834616

Phinney, D. G. (2007). Biochemical heterogeneity of mesenchymal stem cell populations: clues to their therapeutic efficacy. *Cell Cycle* 6, 2884–2889. doi: 10.4161/cc.6.23.5095

Phinney, D. G., Di Giuseppe, M., Njah, J., Sala, E., Shiva, S., St. Croix, C. M., et al. (2015). Mesenchymal stem cells use extracellular vesicles to outsource mitophagy and shuttle microRNAs. *Nat Commun.* 6:8472. doi: 10.1038/ncomms9472

Pigeau, G. M., Csaszar, E., and Dulgar-Tulloch, A. (2018). Commercial scale manufacturing of allogeneic cell therapy. *Front. Med.* 5:233. doi: 10.3389/fmed.2018.00233

Pittenger, M. F., Mackay, A. M., Beck, S. C., Jaiswal, R. K., Douglas, R., Mosca, J. D., et al. (1999). Multilineage potential of adult human mesenchymal stem cells. *Science* 284, 143–147. doi: 10.1126/science.284.5411.143

Pittenger, M. F., and Martin, B. J. (2004). Mesenchymal stem cells and their potential as cardiac therapeutics. *Circ. Res.* 95, 9–20. doi: 10.1161/01.RES.0000135902.99383.6f

Prockop, D. J., Kota, D. J., Bazhanov, N., and Reger, R. L. (2010). Evolving paradigms for repair of tissues by adult stem/progenitor cells (MSCs). *J. Cell. Mol. Med.* 14, 2190–2199. doi: 10.1111/j.1582-4934.2010.01151.x

Rafiq, Q. A., Brosnan, K. M., Coopman, K., Nienow, A. W., and Hewitt, C. J. (2013a). Culture of human mesenchymal stem cells on microcarriers in a 5l stirred-tank bioreactor. *Biotechnol. Lett.* 35, 1233–1245. doi: 10.1007/s10529-013-1211-9

Rafiq, Q. A., Coopman, K., and Hewitt, C. J. (2013b). Scale-up of human mesenchymal stem cell culture: current technologies and future challenges. *Curr. Opin. Chem. Eng.* 2, 8–16. doi: 10.1016/j.coche.2013.01.005

Rafiq, Q. A., Coopman, K., Nienow, A. W., and Hewitt, C. J. (2016). Systematic microcarrier screening and agitated culture conditions improves human mesenchymal stem cell yield in bioreactors. *Biotechnol. J.* 11, 473–486. doi: 10.1002/biot.201400862

Rafiq, Q. A., Ruck, S., Hanga, M. P., Heathman, T. R., Coopman, K., Nienow, A. W., et al. (2018). Qualitative and quantitative demonstration of bead-to-bead transfer with bone marrow-derived human mesenchymal stem cells on microcarriers: utilising the phenomenon to improve culture performance. *Biochem. Eng. J.* 135, 11–21. doi: 10.1016/j.bej.2017.11.005

Ren, G., Zhang, L., Zhao, X., Xu, G., Zhang, Y., Roberts, A. I., et al. (2008). Mesenchymal stem cell-mediated immunosuppression occurs via concerted action of chemokines and nitric oxide. *Cell Stem Cell* 2, 141–150. doi: 10.1016/j.stem.2007.11.014

Robb, K. P., Fitzgerald, J. C., Barry, F., and Viswanathan, S. (2019). Mesenchymal stromal cell therapy: progress in manufacturing and assessments of potency. *Cytotherapy* 21, 289–306. doi: 10.1016/j.jcyt.2018.10.014

Rodrigues, A. L., Rodrigues, C. A., Gomes, A. R., Vieira, S. F., Badenes, S. M., Diogo, M. M., et al. (2019). Dissolvable microcarriers allow scalable expansion and harvesting of human induced pluripotent stem cells under xeno-free conditions. *Biotechnol. J.* 14:e1800461. doi: 10.1002/biot.201800461

Rojewski, M. T., Fekete, N., Baila, S., Nguyen, K., Fürst, D., Antwiler, D., et al. (2013). GMP-compliant isolation and expansion of bone marrow-derived MSCs in the closed, automated device quantum cell expansion system. *Cell Transplant.* 22, 1981–2000. doi: 10.3727/096368912X657990

Rowley, J., Abraham, E., Campbell, A., Brandwein, H., and Oh, S. (2012). Meeting lot-size challenges of manufacturing adherent cells for therapy. *BioProcess. Int.* 10:7.

Russell, K. C., Phinney, D. G., Lacey, M. R., Barrilleaux, B. L., Meyertholen, K. E., and O'Connor, K. C. (2010). *In vitro* high-capacity assay to quantify the clonal heterogeneity in trilineage potential of mesenchymal stem cells reveals a complex hierarchy of lineage commitment. *Stem Cells* 28, 788–798. doi: 10.1002/stem.312

Samsonraj, R. M., Rai, B., Sathiyanathan, P., Puan, K. J., Rötzschke, O., Hui, J. H., et al. (2015). Establishing criteria for human mesenchymal stem cell potency. *Stem Cells* 33, 1878–1891. doi: 10.1002/stem.1982

Sart, S., Agathos, S. N., and Li, Y. (2013). Engineering stem cell fate with biochemical and biomechanical properties of microcarriers. *Biotechnol. Prog.* 29, 1354–1366. doi: 10.1002/btpr.1825

Sart, S., Schneider, Y. J., and Agathos, S. N. (2009). Ear mesenchymal stem cells: an efficient adult multipotent cell population fit for rapid and scalable expansion. *J. Biotechnol.* 139, 291–299. doi: 10.1016/j.jbiotec.2008.12.011

Sart, S., Schneider, Y. J., Li, Y., and Agathos, S. N. (2014a). Stem cell bioprocess engineering towards cGMP production and clinical applications. *Cytotechnology* 66, 709–722. doi: 10.1007/s10616-013-9687-7

Sart, S., Tsai, A. C., Li, Y., and Ma, T. (2014b). Three-dimensional aggregates of mesenchymal stem cells: cellular mechanisms, biological properties, and applications. *Tissue Eng. Part B Rev.* 20, 365–380. doi: 10.1089/ten.teb.2013.0537

Schatti, O., Grad, S., Goldhahn, J., Salzmann, G., Li, Z., Alini, M., et al. (2011). A combination of shear and dynamic compression leads to mechanically induced chondrogenesis of human mesenchymal stem cells. *Eur. Cell Mater.* 22:b97. doi: 10.22203/eCM.v022a17

Schirmaier, C., Jossen, V., Kaiser, S. C., Jüngerkes, F., Brill, S., Safavi-Nab, A., et al. (2014). Scale-up of adipose tissue-derived mesenchymal stem cell production in stirred single-use bioreactors under low-serum conditions. *Eng. Life Sci.* 14, 292–303. doi: 10.1002/elsc.201300134

Schnitzler, A., Kehoe, D., Simler, J., DiLeo, A., and Ball, A. (2012). Scale-up of human mesenchymal stem cells on microcarriers in suspension in a single-use bioreactor. *BioPharm. Int.* 25, 28–38.

Schnitzler, A. C., Verma, A., Kehoe, D. E., Jing, D., Murrell, J. R., Der, K. A., et al. (2016). Bioprocessing of human mesenchymal stem/stromal cells for therapeutic use: current technologies and challenges. *Biochem. Eng. J.* 108, 3–13. doi: 10.1016/j.bej.2015.08.014

Sensebé, L., Gadelorge, M., and Fleury-Cappellesso, S. (2013). Production of mesenchymal stromal/stem cells according to good manufacturing practices: a review. *Stem Cell Res. Ther.* 4:1. doi: 10.1155/2013/678063

Shekaran, A., Lam, A., Sim, E., Jialing, L., Jian, L., Wen, J. T. P., et al. (2016). Biodegradable ECM-coated PCL microcarriers support scalable human early MSC expansion and *in vivo* bone formation. *Cytotherapy* 18, 1332–1344. doi: 10.1016/j.jcyt.2016.06.016

Shekaran, A., Sim, E., Tan, K. Y., Chan, J. K., Choolani, M., Reuveny, S., et al. (2015). Enhanced *in vitro* osteogenic differentiation of human fetal MSCs attached to 3D microcarriers versus harvested from 2D monolayers. *BMC Biotechnol.* 15:102. doi: 10.1186/s12896-015-0219-8

Shi, S., and Gronthos, S. (2003). Perivascular niche of postnatal mesenchymal stem cells in human bone marrow and dental pulp. *J. Bone Miner. Res.* 18, 696–704. doi: 10.1359/jbmr.2003.18.4.696

Shih, Y. R. V., Tseng, K. F., Lai, H. Y., Lin, C. H., and Lee, O. K. (2011). Matrix stiffness regulation of integrin-mediated mechanotransduction during osteogenic differentiation of human mesenchymal stem cells. *J. Bone Miner. Res.* 26, 730–738. doi: 10.1002/jbmr.278

Siddiquee, K., and Sha, M. (2014). Large-scale production of human mesenchymal stem cells in BioBLU® 5c single-use vessels. *Appl. Note* 334, 1–10.

Simaria, A. S., Hassan, S., Varadaraju, H., Rowley, J., Warren, K., Vanek, P., et al. (2014). Allogeneic cell therapy bioprocess economics and optimization: single-use cell expansion technologies. *Biotechnol. Bioeng.* 111, 69–83. doi: 10.1002/bit.25008

Simon, M. (2015). Bioreactor design for adherent cell culture: the bolt-on bioreactor project, part 1—volumetric productivity. *BioProcess Int.* 13.

Song, K., Yang, Y., Wu, S., Zhang, Y., Feng, S., Wang, H., et al. (2016). In vitro culture and harvest of BMMSCs on the surface of a novel thermosensitive glass microcarrier. *Mater. Sci. Eng. C* 58, 324–330. doi: 10.1016/j.msec.2015.08.033

Sotiropoulou, P. A., Perez, S. A., Salagianni, M., Baxevanis, C. N., and Papamichail, M. (2006). Characterization of the optimal culture conditions for clinical scale production of human mesenchymal stem cells. *Stem Cells* 24, 462–471. doi: 10.1634/stemcells.2004-0331

Sousa, M. F., Silva, M. M., Giroux, D., Hashimura, Y., Wesselschmidt, R., Lee, B., et al. (2015). Production of oncolytic adenovirus and human mesenchymal stem cells in a single-use, vertical-wheel bioreactor system: impact of bioreactor design on performance of microcarrier-based cell culture processes. *Biotechnol. Prog.* 31, 1600–1612. doi: 10.1002/btpr.2158

Stroncek, D. F., Sabatino, M., Ren, J., England, L., Kuznetsov, S. A., Klein, H. G., et al. (2014). Establishing a bone marrow stromal cell transplant program at the National Institutes of Health Clinical Center. *Tissue Eng. Part B Rev.* 20, 200–205. doi: 10.1089/ten.teb.2013.0529

Sun, L. Y., Hsieh, D. K., Syu, W. S., Li, Y. S., Chiu, H. T., and Chiou, T. W. (2010). Cell proliferation of human bone marrow mesenchymal stem cells on degradable microcarriers enhances *in vitro* differentiation potential. *Cell Prolif.* 43, 445–456. doi: 10.1111/j.1365-2184.2010.00694.x

Takahashi, I., Sato, K., Mera, H., Wakitani, S., and Takagi, M. (2017). Effects of agitation rate on aggregation during beads-to-beads subcultivation of microcarrier culture of human mesenchymal stem cells. *Cytotechnology* 69, 503–509. doi: 10.1007/s10616-016-9999-5

Teixeira, F. G., Carvalho, M. M., Panchalingam, K. M., Rodrigues, A. J., Mendes-Pinheiro, B., Anjo, S., et al. (2017). Impact of the secretome of human mesenchymal stem cells on brain structure and animal behavior in a rat model of Parkinson's disease. *Stem Cells Transl. Med.* 6, 634–646. doi: 10.5966/sctm.2016-0071

Teixeira, F. G., Panchalingam, K. M., Assunção-Silva, R., Serra, S. C., Mendes-Pinheiro, B., Patrício, P., et al. (2016). Modulation of the mesenchymal stem cell secretome using computer-controlled bioreactors: impact on neuronal cell proliferation, survival and differentiation. *Sci. Rep.* 6:27791. doi: 10.1038/srep27791

Théry, M. (2010). Micropatterning as a tool to decipher cell morphogenesis and functions. *J. Cell Sci.* 123, 4201–4213. doi: 10.1242/jcs.075150

Théry, M., Pépin, A., Dressaire, E., Chen, Y., and Bornens, M. (2006). Cell distribution of stress fibres in response to the geometry of the adhesive environment. *Cell Motil. Cytoskeleton* 63, 341–355. doi: 10.1002/cm.20126

Timmins, N., Kiel, M., Günther, M., Heazlewood, C., Doran, M., Brooke, G., et al. (2012). Closed system isolation and scalable expansion of human placental mesenchymal stem cells. *Biotechnol. Bioeng.* 109, 1817–1826. doi: 10.1002/bit.24425

Tran, T. C., Kimura, K., Nagano, M., Yamashita, T., Ohneda, K., Sugimori, H., et al. (2011). Identification of human placenta-derived mesenchymal stem cells involved in re-endothelialization. *J. Cell Physiol.* 226, 224–235. doi: 10.1002/jcp.22329

Trichet, L., Le Digabel, J., Hawkins, R. J., Vedula, S. R. K., Gupta, M., Ribrault, C., et al. (2012). Evidence of a large-scale mechanosensing mechanism for cellular adaptation to substrate stiffness. *Proc. Natl. Acad. Sci. U.S.A.* 109, 6933–6938. doi: 10.1073/pnas.1117810109

Tsai, A. C., Liu, Y., and Ma, T. (2016). Expansion of human mesenchymal stem cells in fibrous bed bioreactor. *Biochem. Eng. J.* 108, 51–57. doi: 10.1016/j.bej.2015.09.002

Tsai, A. C., Liu, Y., Yuan, X., Chella, R., and Ma, T. (2017). Aggregation kinetics of human mesenchymal stem cells under wave motion. *Biotechnol. J.* 12:1600448. doi: 10.1002/biot.201600448

Tsai, A. C., Liu, Y., Yuan, X., and Ma, T. (2015). Compaction, fusion, and functional activation of three-dimensional human mesenchymal stem cell aggregate. *Tissue Eng. Part A* 21, 1705–1719. doi: 10.1089/ten.tea.2014.0314

Tsai, A. C., and Ma, T. (2016). Expansion of human mesenchymal stem cells in a microcarrier bioreactor. *Methods Mol. Biol.* 1502, 77–86. doi: 10.1007/7651_2016_338

Tseng, P. C., Young, T. H., Wang, T. M., Peng, H. W., Hou, S. M., and Yen, M. L. (2012). Spontaneous osteogenesis of MSCs cultured on 3D microcarriers through alteration of cytoskeletal tension. *Biomaterials* 33, 556–564. doi: 10.1016/j.biomaterials.2011.09.090

Tsuchiya, A., Takeuchi, S., Watanabe, T., Yoshida, T., Nojiri, S., Ogawa, M., et al. (2019). Mesenchymal stem cell therapies for liver cirrhosis: MSCs as "conducting cells" for improvement of liver fibrosis and regeneration. *Inflamm. Regen.* 39, 1–6. doi: 10.1186/s41232-019-0107-z

Ueki, A., and Kidoaki, S. (2015). Manipulation of cell mechanotaxis by designing curvature of the elasticity boundary on hydrogel matrix. *Biomaterials* 41, 45–52. doi: 10.1016/j.biomaterials.2014.11.030

van Eikenhorst, G., Thomassen, Y. E., L. A., and van der Pol, Bakker, W. A. (2014). Assessment of mass transfer and mixing in rigid lab-scale disposable bioreactors at low power input levels. *Biotechnol. Prog.* 301269–1276. doi: 10.1002/btpr.1981

Van Wezel, A. (1967). Growth of cell-strains and primary cells on micro-carriers in homogeneous culture. *Nature* 216, 64–65. doi: 10.1038/216064a0

Vassaux, M., and Milan, J. (2017). Stem cell mechanical behaviour modelling: substrate's curvature influence during adhesion. *Biomech. Model. Mechanobiol.* 16, 1295–1308. doi: 10.1007/s10237-017-0888-4

Wang, S., Qu, X., and Zhao, R. C. (2012). Clinical applications of mesenchymal stem cells. *J. Hematol. Oncol.* 5:19. doi: 10.1186/1756-8722-5-19

Wang, Z., Wu, D., Zou, J., Zhou, Q., Liu, W., Zhang, W., et al. (2017). Development of demineralized bone matrix-based implantable and biomimetic microcarrier for stem cell expansion and single-step tissue-engineered bone graft construction. *J. Mater. Chem. B* 5, 62–73. doi: 10.1039/C6TB02414A

Weber, C., Freimark, D., Pörtner, R., Pino-Grace, P., Pohl, S., Wallrapp, C., et al. (2010). Expansion of human mesenchymal stem cells in a fixed-bed bioreactor system based on non-porous glass carrier—part A: inoculation, cultivation, and cell harvest procedures. *Int. J. Artif. Organs* 33:512. doi: 10.1177/039139881003300802

Weber, C., Pohl, S., Pörtner, R., Wallrapp, C., Kassem, M., Geigle, P., et al. (2007). Expansion and harvesting of hMSC-TERT. *Open Biomed. Eng. J.* 1, 38–46. doi: 10.2174/1874120700701010038

Wegmeyer, H., Bröske, A. M., Leddin, M., Kuentzer, K., Nisslbeck, A. K., Hupfeld, J., et al. (2013). Mesenchymal stromal cell characteristics vary depending on their origin. *Stem Cells Dev.* 22, 2606–2618. doi: 10.1089/scd.2013.0016

Werner, M., Blanquer, S. B., Haimi, S. P., Korus, G., Dunlop, J. W., Duda, G. N., et al. (2017). Surface curvature differentially regulates stem cell migration and differentiation via altered attachment morphology and nuclear deformation. *Adv. Sci.* 4:1600347. doi: 10.1002/advs.201600347

Wilson, J. R., and Kowol, E. (1994). *Pressure Control System for a Bioreactor*. U.S. Patent No 5,330,915. Alexandria, VA: United States Patent and Trademark Office.

Xu, J., Chen, C., Jiang, X., Xu, R., Tambe, D., Zhang, X., et al. (2011). Effects of micropatterned curvature on the motility and mechanical properties of airway smooth muscle cells. *Biochem. Biophys. Res. Commun.* 415, 591–596. doi: 10.1016/j.bbrc.2011.10.111

Xu, S., Hoshan, L., Jiang, R., Gupta, B., Brodean, E., O'Neill, K., et al. (2017). A practical approach in bioreactor scale-up and process transfer using a combination of constant P/V and vvm as the criterion. *Biotechnol. Prog.* 33, 1146–1159. doi: 10.1002/btpr.2489

Yan, X., Zhang, K., Yang, Y., Deng, D., Lyu, C., Xu, H., et al. (2020). Dispersible and dissolvable porous microcarrier tablets enable efficient large scale hMSC expansion. *Tissue Eng. Part C Methods*. 26, 263–275. doi: 10.1089/ten.tec.2020.0039

Yang, H. S., Jeon, O., Bhang, S. H., Lee, S. H., and Kim, B. S. (2010). Suspension culture of mammalian cells using thermosensitive microcarrier that allows cell detachment without proteolytic enzyme treatment. *Cell Transplant.* 19, 1123–1132. doi: 10.3727/096368910X516664

YekrangSafakar, A., Acun, A., Choi, J. W., Song, E., Zorlutuna, P., and Park, K. (2018). Hollow microcarriers for large-scale expansion of anchorage-dependent cells in a stirred bioreactor. *Biotechnol. Bioeng.* 115, 1717–1728. doi: 10.1002/bit.26601

Yin, J. Q., Zhu, J., and Ankrum, J. A. (2019). Manufacturing of primed mesenchymal stromal cells for therapy. *Nat. Biomed. Eng.* 3, 90–104. doi: 10.1038/s41551-018-0325-8

Yourek, G., McCormick, S. M., Mao, J. J., and Reilly, G. C. (2010). Shear stress induces osteogenic differentiation of human mesenchymal stem cells. *Regen. Med.* 5, 713–724. doi: 10.2217/rme.10.60

Yu, C., Kornmuller, A., Brown, C., Hoare, T., and Flynn, L. E. (2017). Decellularized adipose tissue microcarriers as a dynamic culture platform for human adipose-derived stem/stromal cell expansion. *Biomaterials* 120, 66–80. doi: 10.1016/j.biomaterials.2016.12.017

Yuan, X., Logan, T. M., and Ma, T. (2019). Metabolism in human mesenchymal stromal cells: a missing link between hMSC biomanufacturing and therapy? *Front. Immunol.* 10:977. doi: 10.3389/fimmu.2019.00977

Yuan, X., Tsai, A. C., Farrance, I., Rowley, J. A., and Ma, T. (2018). Aggregation of culture expanded human mesenchymal stem cells in microcarrier-based bioreactor. *Biochem. Eng. J.* 131, 39–46. doi: 10.1016/j.bej.2017.12.011

Yuan, Y., Kallos, M. S., Hunter, C., and Sen, A. (2014). Improved expansion of human bone marrow-derived mesenchymal stem cells in microcarrier-based suspension culture. *J. Tissue Eng. Regen. Med.* 8, 210–225. doi: 10.1002/term.1515

Zayzafoon, M., Gathings, W. E., and McDonald, J. M. (2004). Modeled microgravity inhibits osteogenic differentiation of human mesenchymal stem cells and increases adipogenesis. *Endocrinology* 145, 2421–2432. doi: 10.1210/en.2003-1156

Zhang, J., Huang, X., Wang, H., Liu, X., Zhang, T., Wang, Y., et al. (2015). The challenges and promises of allogeneic mesenchymal stem cells for use as a cell-based therapy. *Stem Cell Res. Ther.* 6:234. doi: 10.1186/s13287-015-0240-9

Zhang, Y., Mao, H., Gao, C., Li, S., Shuai, Q., Xu, J., et al. (2016). Enhanced biological functions of human mesenchymal stem-cell aggregates incorporating E-cadherin-modified PLGA microparticles. *Adv. Healthc. Mater.* 5, 1949–1959. doi: 10.1002/adhm.201600114

Zhang, Z. Y., Teoh, S. H., Hui, J. H., Fisk, N. M., Choolani, M., and Chan, J. K. (2012). The potential of human fetal mesenchymal stem cells for off-the-shelf bone tissue engineering application. *Biomaterials* 33, 2656–2672. doi: 10.1016/j.biomaterials.2011.12.025

Zhao, F., Chella, R., and Ma, T. (2007). Effects of shear stress on 3-D human mesenchymal stem cell construct development in a perfusion bioreactor system: experiments and hydrodynamic modeling. *Biotechnol. Bioeng.* 96, 584–595. doi: 10.1002/bit.21184

Conflict of Interest: The authors declare that the research was conducted in the absence of any commercial or financial relationships that could be construed as a potential conflict of interest.

frontiers in Bioengineering and Biotechnology

MINI REVIEW
published: 09 July 2020
doi: 10.3389/fbioe.2020.00786

Advances Toward Engineering Functionally Mature Human Pluripotent Stem Cell-Derived β Cells

*Leonardo Velazco-Cruz[1], Madeleine M. Goedegebuure[1,2] and Jeffrey R. Millman[1,2]**

[1] Division of Endocrinology, Metabolism and Lipid Research, Washington University School of Medicine, St. Louis, MO, United States, [2] Department of Biomedical Engineering, Washington University in St. Louis, St. Louis, MO, United States

Human stem cell-derived β (SC-β) cells have the potential to revolutionize diabetes treatment through disease modeling, drug screening, and cellular therapy. SC-β cells are likely to represent an early clinical translation of differentiated human pluripotent stem cells (hPSC). In 2014, two groups generated the first *in vitro*-differentiated glucose-responsive SC-β cells, but their functional maturation at the time was low. This review will discuss recent advances in the engineering of SC-β cells to understand and improve SC-β cell differentiation and functional maturation, particularly new differentiation strategies achieving dynamic glucose-responsive insulin secretion with rapid correction to normoglycemia when transplanted into diabetic mice.

Keywords: stem cells, diabetes, differentiation, pluripotent, transplantation

OPEN ACCESS

Edited by:
Tiago G. Fernandes, University of Lisbon, Portugal

Reviewed by:
Xiaojun Lian, Pennsylvania State University (PSU), United States
Maria Cristina Nostro, University Health Network (UHN), Canada

***Correspondence:**
Jeffrey R. Millman
jmillman@wustl.edu

Specialty section:
This article was submitted to Biomaterials, a section of the journal Frontiers in Bioengineering and Biotechnology

Received: *30 April 2020*
Accepted: *22 June 2020*
Published: *09 July 2020*

Citation:
Velazco-Cruz L, Goedegebuure MM and Millman JR (2020) Advances Toward Engineering Functionally Mature Human Pluripotent Stem Cell-Derived β Cells. Front. Bioeng. Biotechnol. 8:786. doi: 10.3389/fbioe.2020.00786

INTRODUCTION

Diabetes mellitus can be characterized as a disease of the β cell, which results in improper insulin secretion and failure to maintain normal glycemia. Type 1 diabetes (T1D) is the result of the dysregulated autoimmune destruction of β cells (Gillespie, 2006). Type 2 diabetes (T2D) is characterized by β cell malfunction and depletion due to high stress caused by chronic hyperglycemia. Currently T1D and many T2D patients are reliant on exogenous insulin treatment. Exogenous insulin treatment requires constant monitoring and injections throughout the day, reducing quality of life and failing to accurately maintain normal glycemia leading to secondary complications (Caro et al., 2002; Powers and D'Alessio, 2011). Transplantation of whole pancreas or purified islets of Langerhans have been shown to result in exogenous insulin independence with accurate glycemic regulation in T1D and T2D patients (Posselt et al., 2010; Gruessner and Gruessner, 2016; Kandaswamy et al., 2018). Widespread application of islet transplantation is limited by replacement tissue availability and the need for immunosuppression (Millman and Pagliuca, 2017).

Human SC-β cells are a promising alternative cell source for diabetes cell replacement therapy as well as disease modeling and drug screening (Millman and Pagliuca, 2017). *In vitro* differentiated SC-β cells were first produced in 2014 (Pagliuca et al., 2014; Rezania et al., 2014). These early SC-β cells presented β cell hallmarks, such as insulin secretion in response to glucose, expression of β cell transcription factors, and *in vivo* function in weeks after transplantation in mice. However, critical differences remained between SC-β cells and primary adult β cells, including inferior insulin secretion per cell, dysregulated glucose-stimulated insulin secretion (GSIS) dynamics, and lower expression of key β cell transcription factors. Recent studies, discussed here, have significantly advanced the functional maturity of SC-β cells resulting in functionally enhanced SC-β cells. These

enhanced SC-β cells have improved function, with some achieving dynamic insulin secretion marked by the presence of first and second phase insulin secretion. Despite the enhancement of these SC-β cells, they fail to match the glucose responsiveness and transcriptomic profile of primary cadaveric islets (Baron et al., 2016; Nair et al., 2019; Velazco-Cruz et al., 2019; Hogrebe et al., 2020; Mahaddalkar et al., 2020). In this review we describe the advancements made for achieving enhanced SC-β cells and the path toward differentiating fully functional SC-β cells resembling cadaveric islets in terms of their function and transcriptomic profile.

THE PATH TOWARD SC-β CELLS

The path toward differentiating SC-β cells has proved challenging, having already spanned over two decades. Progress has occurred in waives as hard-fought milestones are achieved. Early pioneering work established methodologies for differentiating hPSCs toward definitive endoderm (D'Amour et al., 2005), the first developmental stage in the path toward making β cells. Further sequential treatments of growth factors and small molecules continued to mimic pancreatic organogenesis guiding hPSCs through stages resembling definitive endoderm, gut-tube endoderm, pancreatic endoderm, and ultimately hormone expressing endoderm. The resulting insulin producing cells were polyhormonal, failed to maintain PDX1 and NKX6.1 expression, and were not glucose responsive (D'Amour et al., 2006). However, transplantation of hPSC-derived pancreatic progenitors into immunocompromised mice allowed for their differentiation into monohormonal glucose-stimulated insulin-secreting cells after several months *in vivo* (Kroon et al., 2008; Rezania et al., 2012). Since then, other groups have demonstrated that PDX1 and NKX6.1 expressing pancreatic progenitors have the potential of differentiating toward β cells (Rezania et al., 2013; Schaffer et al., 2013; Nostro et al., 2015; Millman et al., 2016).

In 2014, two protocols were published for the efficient generation of glucose-responsive monohormonal *in vitro*-differentiated SC-β cells (Pagliuca et al., 2014; Rezania et al., 2014). These protocols generated pancreatic progenitors with high PDX1, NKX6.1 and low NGN3 expression. Low NGN3 expression through Vitamin C treatment distinguishes these pancreatic progenitors from earlier protocols (Kroon et al., 2008; Rezania et al., 2012). These pancreatic progenitors where then differentiated to hormone expressing endocrine cells through transient NGN3 upregulation by treatment with TGFβR1 inhibitor ALK5i Type II (ALK5i) and thyroid hormone (T3). Air-liquid interface culture was observed to increase NGN3 expression relative to planar culture (Rezania et al., 2014) while the other protocol was completed in suspension culture (Pagliuca et al., 2014). The continued treatment of endocrine CHGA+ cells with ALK5i, T3, and γ-secretase (XXI or XX) drives the endocrine population toward monohormonal INS+ cells. The final stage of these protocols cultured the cells with ALK5i and T3 resulting in glucose responsive SC-β cells making up ∼40% of the population. In addition to ALK5i and T3, Rezania includes compounds R428, an AXL inhibitor, with N-acetyl cysteine, claiming them to drive expression of β cell maturation gene MAFA. The Rezania et al. air-liquid interface culture format can be more easily replicated by laboratories with standard culture experience and equipment, however it is less scalable than the suspension culture format described in Pagliuca et al. which requires more specialized equipment and knowledge of 3D cell culture. These original SC-β cells represented a monumental accomplishment being scalable, glucose responsive, transcriptionally similar to primary islets, and capable of regulating mouse blood glucose in weeks post transplantation. Despite these accomplishments the resulting SC-β cells were functionally immature, secreting low levels of insulin, no dynamic insulin secretion, immature calcium response, and transcriptional differences remained relative to cadaveric islets with measurable differences in MAFA, UCN3, and GCK gene expression (Pagliuca et al., 2014; Rezania et al., 2014).

ADVANCING SC-β CELLS

Early SC-β cells are functionally immature lacking dynamic insulin secretion and observable functional maturation occurring after transplantation *in vivo*, marked by an increase in secreted insulin with time post transplantation (Pagliuca et al., 2014; Rezania et al., 2014; Russ et al., 2015). More functional SC-β cells are needed to improve cell replacement outcomes and facilitate more robust disease modeling studies. Recent publications have demonstrated improved differentiation efficiency, higher glucose stimulated insulin secretion, first and second phase insulin secretion, response to multiple secretagogues, and fast *in vivo* glucose regulation upon transplantation (**Table 1**; Nair et al., 2019; Velazco-Cruz et al., 2019; Veres et al., 2019; Hogrebe et al., 2020; Mahaddalkar et al., 2020).

Velazco-Cruz et al. was first to report robust dynamic insulin secretion of SC-β cells (Velazco-Cruz et al., 2019) with both first and second phase kinetics using a suspension differentiation protocol with temporal TGFβ modulation, cellular cluster size control, serum free media, endocrine enrichment without cell selection, and a simplified final stage media lacking notable prior factors (T3, N-acetyl cysteine, Trolox, and R428). The authors show that treatment with TGFβR1 inhibitor, ALK5 inhibitor type II (ALK5i), is necessary for specification of the β cell fate. However, upon β cell specification permittance of TGFβ signaling is critical for SC-β cell functional maturation. However, ALK5i is widely used in the final stage of many β cell differentiation protocols (Pagliuca et al., 2014). The authors show that by re-sizing cellular clusters during the last stage of the differentiation, a process which involves partial dissociation of clusters as previously reported (Song and Millman, 2017), enhances static GSIS and nearly doubles the C-Peptide+ NKX6.1+ co-expressing SC-β cell population. In dynamic secretion assays, robust dynamic function with a clear first phase, stable second phase, and

TABLE 1 | Characteristics of Enhanced SC-β cell protocols.

Article	Format	Reaggregation	Sorting	Endocrine	SC-β Cell	1st Phase stimulation	2nd Phase stimulation	Return to baseline insulin secretion at low glucose	Insulin content μ IU insulin/1,000 cells
Velazco-Cruz et al., 2019	S	Yes	n/a	>95%	52%	7.6	2.1	Yes	321
Veres et al., 2019	S	Yes	CD49A + S6	>95%	80%	3.2	1.5	No	N.R.
Nair et al., 2019	S	Yes	INS:GFP S6	>99%	80%	3.5	1	n/a	N.R.
Hogrebe et al., 2020	P	Yes	n/a	>95%	31%	9.4	1.9	Yes	150
Mahaddalkar et al., 2020	S	Yes	CD177 + S1	N.R.	62%	5	1.15	n/a	317

Quantitative values estimated from graphs when not reported in text. N.R., not reported; S, suspension; P, planar; S#, stage #.

a return to basal levels after high glucose treatment ends was shown. However, a weakness of the study was that insulin secretion per cell and the degree insulin secretion was increased in response to high glucose varied across different hPSC lines. Transplantation of these cells improved glucose tolerance in mice.

Veres et al. employed some of the same changes as Velazco-Cruz et al., including cellular cluster size control, serum free media, endocrine enrichment without cell selection, and a final stage media lacking T3, N-acetyl cysteine, Trolox, and R428 (Veres et al., 2019). Additionally, Veres et al. employs β cell enrichment using cell sorting. Through a similar cellular reaggregation method, Veres et al. sees strong endocrine enrichment and an increase in the frequency of the C-Peptide+ /NKX6.1+ SC-β cell population along with improved static GSIS. The authors further show that enrichment of the β cell population through CD49a+ cell sorting improved static GSIS relative to unsorted and reaggregated SC-β cells. CD49a+ sorted cells demonstrated first and second phase insulin secretion, however a return to basal levels did not occur when high glucose was removed. The authors did not show if reaggregated cells could undergo dynamic GSIS. The authors identify enterochromaffin-like cells in their SC-β cell preps and CD49+ sorting removes these cell types. Enterochromaffin cells, marked by TPH1 expression, secrete serotonin in the gut and are absent from the human pancreas. This study indicates β cells and enterochromaffin cells share a similar developmental path resulting in their presence in β cell differentiation protocols. It is unclear if the functional benefits observed by CD49+ sorting are due to the removal of off target cell types, such as enterochromaffin-like cells, or other mechanisms. Transplantation into mice was not investigated in this study.

In a separate study, Nair et al. achieved first phase insulin secretion using an insulin-driven GFP tag cell sorting approach and a reaggregation process (Nair et al., 2019). The authors achieved a high β cell population with 80% C-Peptide/NKX6.1 co-expression. In functional studies the authors compare reaggregated GFP enriched cells to un-reaggregated unsorted β cell clusters, with limited functional studies using reaggregated and unsorted clusters as a control. The authors see no first phase response in the immature clusters or the reaggregated and unsorted clusters while there GFP sorted reaggregated clusters have a first phase stimulation index of ∼3 and no second phase response. However, the study design did not allow for distinguishing functional improvements related to endocrine enrichment by reaggregation or β cell enrichment by sorting, like done with CD49a enrichment (Veres et al., 2019). This study was performed using only one insulin-driven GFP reporter cell line, making it unclear how well this approach would apply to other cell lines and whether the low levels of insulin secretion are due to the genetic engineering or genetic background of this cell line relative to other protocols. It is important to note that this differentiation protocol retains ALK5i and T3 during the final stage of differentiation, while other enhanced SC-β cell protocols have removed them (Rosado-Olivieri et al., 2019; Velazco-Cruz et al., 2019; Veres et al., 2019;

Hogrebe et al., 2020; Maxwell et al., 2020). Therefore, it is possible that removal of these compound will allow for more robust dynamic secretion including the missing second phase observed by this protocol. Transplantation of these cells improved glucose tolerance in mice.

Hogrebe et al. (2020) used a different differentiation strategy for generating SC-β cells, demonstrating that regulation of actin cytoskeleton polymerization controls differentiation to endocrine and other endodermal lineages. This insight led to development of a planar β cell differentiation protocol. Other protocols use suspension (Pagliuca et al., 2014; Russ et al., 2015; Rosado-Olivieri et al., 2019; Velazco-Cruz et al., 2019; Veres et al., 2019) or pseudo-suspension air-liquid interface (Rezania et al., 2014) culture methodologies for endocrine specification, increasing the technical expertise required for SC-β cell differentiations. Using a novel planar differentiation protocol with actin depolymerizer latrunculin A driving endocrine specification, through neurogenin three upregulation, the authors generate SC-β cells which undergo dynamic GSIS. When these SC-β cells are transplanted into mice, they rapidly reversed severe preexisting diabetes at a rate resembling that achieved by cadaveric islets.

In a controlled and parallel fashion, Hogrebe et al. compared his planar differentiated β cells to suspension differentiated β cells using the Velazco-Cruz et al. protocol. Using the HUES8 cell line, for which the two protocols were optimized, the suspension protocols had higher percent yields of CP+ NKX6.1+ SC-β cells. Functionally, planar and suspension derived SC-β cells were similar when assayed by static and dynamic GSIS as well as insulin content. When assayed by real-time PCR, the planar and suspension derived SC-β cells were similar. An equal number of planar and suspension derived SC-β cells were transplanted into diabetic mice. Diabetes reversal with planar differentiated β cells occurred in two weeks, while the suspension protocol took 5 weeks. This discrepancy in diabetes cure speed is interesting, as *in vitro* functional and transcriptomic assays did not show evident differences between the two protocols and based on reported differentiation efficiencies the suspension protocol generates a higher proportion of SC-β cells. Single-cell RNA sequencing, comparing transcriptomes of planar and suspension derived SC-β cells could reveal further insights into the source of this discrepancy. Importantly, the Hogrebe et al. planar protocol was able to successfully differentiate SC-β cells from multiple pluripotent stem cell lines, with some cell lines matching cadaveric islets in function when assayed with dynamic perfusion assays. While the HUES8 suspension and planar derived SC-β cells were functionally similar, the planar protocol yielded higher functioning cells when applied to different cell lines. The robustness of the planar Hogrebe et al. differentiation protocol facilitates studies using more than one cell line (Maxwell et al., 2020; Velazco-Cruz et al., 2020).

Using a sorting approach for CD177/NB1 glycoprotein, Mahaddalkar et al. isolated anterior definitive endoderm cells with increased pancreatic and β cell potential (Mahaddalkar et al., 2020). The authors characterize CD177+ cells to have increase PDX1 and NKX6.1 pancreatic progenitor potential when compared to unsorted and CD275+ definitive endoderm populations. Additionally, this work shows canonical WNT inhibition by IWP2 treatment to increase pancreatic progenitor differentiation efficiency, a finding supported by previous publications (Loh et al., 2014; Davenport et al., 2016; Zhu et al., 2016). Differentiation of CD177+ cells toward β cells resulted in improved differentiation efficiency and function relative to unsorted cells. CD177+ cells presented a first phase insulin response with no second phase, while unsorted cells did not present a first or second phase insulin secretion (Mahaddalkar et al., 2020). The cells were not transplanted into mice.

Direct comparison of these studies is difficult, as assays evaluating function are variable, including technical methodologies, normalization strategies, and *in vivo* models differ. Normalizing SC-β cells to cadaveric human islet insulin secretion is imperfect, as cadaveric islet function is highly variable within and between studies (Pagliuca et al., 2014; Nair et al., 2019; Velazco-Cruz et al., 2019; Veres et al., 2019). Standardized static and dynamic GSIS assays, normalized to DNA, can greatly facilitate comparison of differentiation protocols while imposing minimal burden on investigators. Standardization of *in vivo* assays are more challenging, as many mouse and diabetic models exist with variable severity of diabetes. By providing standardized *in vitro* GSIS results, individual researchers can better compare protocols and guide the differentiation protocols employed in their studies.

FORGING A PATH FORWARD

Despite advances, current SC-β cells lack the functional maturity of cadaveric islets. In the continuing quest to functionally mature SC-β cells, teams are employing novel technologies and approaches, such as single-cell sequencing, genetic engineering, cell sorting, and drug screening, to identify factors which contribute to β cell differentiation and function. Recent publications have compared gene expression between adult and fetal or juvenile islets, with many adult genes having potential roles in the functional maturation of SC-β cells. ERRγ has been characterized to be enriched in adult vs neonatal mouse β cells and mice deficient of β cell ERRγ fail to properly regulate their blood glucose (Yoshihara et al., 2016). Yoshira et al. differentiates hPSCs toward an immature β-like state in which many β cells genes are expressed but are incapable of undergoing *in vitro* GSIS. The authors overexpress ERRγ in these β-like cells and observed improvements to mitochondrial respiration and the β-like cells gain the ability to undergo *in vitro* GSIS. Upregulation of ERRγ can potentially be used to further mature SC-β cells. However, since its effects were only observed in immature insulin-expressing endocrine cells incapable of undergoing *in vitro* GSIS with immature mitochondrial respiration, it may not translate to more advanced protocols which are more metabolically mature (Nair et al., 2019). In a separate study, Arda et al. shows islet function increases in adult vs juvenile human islets identifying several genes associated

with age in β cells including ONECUT2, MAFA, TSHZ3, SIX2, and SIX3 (Arda et al., 2016). It remains to be investigated whether upregulation of these genes in SC-β cells can drive their functional maturation.

Inhibition of YAP signaling has been shown to drive endocrine induction through neurogenin three upregulation and when incorporated into differentiation protocols during endocrine induction, using verteporfin, β differentiation efficiency and function is enhanced (Rosado-Olivieri et al., 2019). Dynamic function is not assayed in this work. This work is supported by a previous study showing pancreatic progenitor endocrinogenesis is stimulated by YAP inhibition (Mamidi et al., 2018). Incorporation of YAP inhibitors during endocrine specification and YAP agonist during β cell maturation may drive improvements to β cell generation.

Recent work (Ameri et al., 2017; Cogger et al., 2017; Nair et al., 2019; Veres et al., 2019; Mahaddalkar et al., 2020) has shown that enrichment of certain cell populations can ultimately improve β cell differentiation efficiency and function. Transcriptomic (Ameri et al., 2017) and proteomic (Cogger et al., 2017) approaches have revealed glycoprotein two as a cell surface marker beneficial for sorting PDX1+/NKX6.1+ pancreatic progenitors improving β cell differentiation efficiency. Although functional improvements were not seen, this strategy may increase the proportion of β cells generated using enhanced differentiation protocols. Enrichment of the β cell population through sorting may enhance the functional maturation of SC-β cells (Nair et al., 2019; Veres et al., 2019). Whether this improvement is through cell-cell contact, paracrine signaling, or the removal of inhibitory cell types, such as enterochromaffin cells (Veres et al., 2019), remains to be determined with more robust studies necessary. Cell enrichment using cell sorting limits large scale production of SC-β cells. However, the scale of production necessary for SC-β cells may be compatible with magnetic-activated cell sorting approaches, particularly as they have proven beneficial. Additionally, identification of markers such as glycoprotein two can guide the search for small molecules to increase the population of cells expressing the desired markers. High throughput screening for small molecules affecting differentiation has been successful, with the identification of Rho-kinase inhibitor H1152, capable of increasing MAFA and UCN3 expression (Ghazizadeh et al., 2017).

Single-cell sequencing technologies are rapidly advancing our understanding of β cell fate, differentiation, and functional maturation. Several studies have increasingly elucidated the β cell transcriptome (Baron et al., 2016; Segerstolpe et al., 2016; Wang et al., 2016; Xin et al., 2016; Veres et al., 2019), revealing novel β cell enriched genes which may be used as markers for driving β cell functional maturation. Recently, single-cell patch-clamp sequencing was used linking β cell gene expression to functional phenotypes revealing sets of genes correlating with β cell function (Camunas-Soler et al., 2020). Veres et al. (2019) performed single-cell sequencing at multiple stages during SC-β cell differentiations revealing transcriptomic profiles of each stage and genes whose expression is correlated to the acquisition of function by SC-β cells. Epigenome analysis of SC-β cell differentiation reveal LMX1B as a regulator of endocrine specification and circadian rhythms as a component toward SC-β cell functional maturation (Alvarez-Dominguez et al., 2020). These studies give researchers a more accurate β cell transcriptomic model to guide differentiation protocol development. To further advance SC-β cell technology, researchers must continue efforts to build our understanding of β cell development which guides development of β cell differentiation protocols.

DISCUSSION

SC-β cells are a promising cell source for diabetes cell therapy, disease modeling, and understanding human development. The use of small molecules and growth factors to drive stem cell differentiation toward β cells, mimicking *in vivo* development, has proven a reliable strategy amenable to scale-up and genetic perturbations. Since the first fully *in vitro* differentiation protocols (Pagliuca et al., 2014; Rezania et al., 2014) capable of generating glucose responsive β cells, the field has significantly advanced. Through the optimization of differentiation protocols, including the removal of ALK5i during the final stage of differentiation and reaggregation driven endocrine enrichment, enhanced SC-β cells have greater glucose responsiveness undergoing dynamic GSIS. Currently, SC-β cells are still less functional than cadaveric islets secreting lower amounts of insulin and a stable but lower in magnitude second phase insulin secretion (Nair et al., 2019; Velazco-Cruz et al., 2019; Veres et al., 2019). Transcriptionally, SC-β cells resemble cadaveric islets more so than fetal islets, however critical differences remain, such as reduced expression of maturation factors MAFA and SIX3 (Veres et al., 2019). Using recently published technologies and approaches our understanding of β cell development is improving, guiding the development of novel protocols capable of generating SC-β cells with function matching that of primary islets. Generation of fully functionally mature SC-β cells may be possible in the next few years and will drive diabetes cell therapies forward while providing a robust model for development and disease modeling.

AUTHOR CONTRIBUTIONS

LV-C and JM conceived the manuscript. All authors contributed to the article and approved the submitted version.

FUNDING

Support by the NIH (R01DK114233) and JDRF (5-CDA-2017-391-A-N and 1-SRA-2020-928-S-B) was provided.

REFERENCES

Alvarez-Dominguez, J. R., Donaghey, J., Rasouli, N., Kenty, J. H. R., Helman, A., Charlton, J., et al. (2020). Circadian entrainment triggers maturation of human in vitro islets. *Cell Stem Cell* 26, 108–122. doi: 10.1016/j.stem.2019.11.011

Ameri, J., Borup, R., Prawiro, C., Ramond, C., Schachter, K. A., Scharfmann, R., et al. (2017). Efficient generation of glucose-responsive beta cells from isolated GP2+ human pancreatic progenitors. *Cell Rep.* 19, 36–49. doi: 10.1016/j.celrep.2017.03.032

Arda, H. E., Li, L., Tsai, J., Torre, E. A., Rosli, Y., Peiris, H., et al. (2016). Age-dependent pancreatic gene regulation reveals mechanisms governing human β cell function. *Cell Metab.* 23, 909–920. doi: 10.1016/j.cmet.2016.04.002

Baron, M., Veres, A., Wolock, S. L., Faust, A. L., Gaujoux, R., Vetere, A., et al. (2016). A single-cell transcriptomic map of the human and mouse pancreas reveals inter- and intra-cell population structure. *Cell Syst.* 3, 346–360. doi: 10.1016/j.cels.2016.08.011

Camunas-Soler, J., Dai, X.-Q., Hang, Y., Bautista, A., Lyon, J., Suzuki, K., et al. (2020). Patch-seq links single-cell transcriptomes to human islet dysfunction in diabetes. *Cell Metab.* 31, 1017–1031. doi: 10.1016/j.cmet.2020.04.005

Caro, J. J., Ward, A. J., and O'Brien, J. A. (2002). Lifetime costs of complications resulting from type 2 diabetes in the U.S. *Diabetes Care* 25, 476–481. doi: 10.2337/diacare.25.3.476

Cogger, K. F., Sinha, A., Sarangi, F., McGaugh, E. C., Saunders, D., Dorrell, C., et al. (2017). Glycoprotein 2 is a specific cell surface marker of human pancreatic progenitors. *Nat. Commun.* 8:331. doi: 10.1038/s41467-017-00561-0

D'Amour, K. A., Agulnick, A. D., Eliazer, S., Kelly, O. G., Kroon, E., and Baetge, E. E. (2005). Efficient differentiation of human embryonic stem cells to definitive endoderm. *Cell* 23, 1534–1541. doi: 10.1038/nbt1163

D'Amour, K. A., Bang, A. G., Eliazer, S., Kelly, O. G., Agulnick, A. D., Smart, N. G., et al. (2006). Production of pancreatic hormone-expressing endocrine cells from human embryonic stem cells. *Nat. Biotechnol.* 24, 1392–1401. doi: 10.1038/nbt1259

Davenport, C., Diekmann, U., Budde, I., Detering, N., and Naujok, O. (2016). Anterior-posterior patterning of definitive endoderm generated from human embryonic stem cells depends on the differential signaling of retinoic acid, Wnt-, and BMP-signaling. *Stem Cells* 34, 2635–2647. doi: 10.1002/stem.2428

Ghazizadeh, Z., Kao, D.-I., Amin, S., Cook, B., Rao, S., Zhou, T., et al. (2017). ROCKII inhibition promotes the maturation of human pancreatic beta-like cells. *Nat. Commun.* 8:298. doi: 10.1038/s41467-017-00129-y

Gillespie, K. M. (2006). Type 1 diabetes: pathogenesis and prevention. *Can. Med. Assoc. J.* 175, 165–170. doi: 10.1503/cmaj.060244

Gruessner, A. C., and Gruessner, R. W. G. (2016). Long-term outcome after pancreas transplantation: a registry analysis. *Curr. Opin. Organ Transplant.* 21, 377–385. doi: 10.1097/MOT.0000000000000331

Hogrebe, N. J., Augsornworawat, P., Maxwell, K. G., Velazco-Cruz, L., and Millman, J. R. (2020). Targeting the cytoskeleton to direct pancreatic differentiation of human pluripotent stem cells. *Nat. Biotechnol.* 38, 460–470. doi: 10.1038/s41587-020-0430-6

Kandaswamy, R., Stock, P. G., Gustafson, S. K., Skeans, M. A., Curry, M. A., Prentice, M. A., et al. (2018). OPTN/SRTR 2016 annual data report: pancreas. *Am. J. Transplant* 18(Suppl. 1), 114–171. doi: 10.1111/ajt.14558

Kroon, E., Martinson, L. A., Kadoya, K., Bang, A. G., Kelly, O. G., Eliazer, S., et al. (2008). Pancreatic endoderm derived from human embryonic stem cells generates glucose-responsive insulin-secreting cells in vivo. *Nat. Biotechnol.* 26, 443–452. doi: 10.1038/nbt1393

Loh, K. M., Ang, L. T., Zhang, J., Kumar, V., Ang, J., Auyeong, J. Q., et al. (2014). Efficient endoderm induction from human pluripotent stem cells by logically directing signals controlling lineage bifurcations. *Cell Stem Cell* 14, 237–252. doi: 10.1016/j.stem.2013.12.007

Mahaddalkar, P. U., Scheibner, K., Pfluger, S., Ansarullah, L., Sterr, M., Beckenbauer, J., et al. (2020). Generation of pancreatic β cells from CD177+ anterior definitive endoderm. *Nat. Biotechnol.* doi: 10.1038/s41587-020-0492-5

Mamidi, A., Prawiro, C., Seymour, P. A., de Lichtenberg, K. H., Jackson, A., Serup, P., et al. (2018). Mechanosignalling via integrins directs fate decisions of pancreatic progenitors. *Nature* 564, 114–118. doi: 10.1038/s41586-018-0762-2

Maxwell, K. G., Augsornworawat, P., Velazco-Cruz, L., Kim, M. H., Asada, R., Hogrebe, N. J., et al. (2020). Gene-edited human stem cell-derived β cells from a patient with monogenic diabetes reverse preexisting diabetes in mice. *Sci. Transl. Med.* 12:106. doi: 10.1126/scitranslmed.aax9106

Millman, J. R., and Pagliuca, F. W. (2017). Autologous pluripotent stem cell-derived β-Like cells for diabetes cellular therapy. *Diabetes* 66, 1111–1120. doi: 10.2337/db16-1406

Millman, J. R., Xie, C., Van Dervort, A., Gürtler, M., Pagliuca, F. W., and Melton, D. A. (2016). Generation of stem cell-derived β-cells from patients with type 1 diabetes. *Nat. Commun.* 7:11463. doi: 10.1038/ncomms11463

Nair, G. G., Liu, J. S., Russ, H. A., Tran, S., Saxton, M. S., Chen, R., et al. (2019). Recapitulating endocrine cell clustering in culture promotes maturation of human stem-cell-derived β cells. *Nat. Cell Biol.* 21, 263–274. doi: 10.1038/s41556-018-0271-4

Nostro, M. C., Sarangi, F., Yang, C., Holland, A., Elefanty, A. G., Stanley, E. G., et al. (2015). Efficient generation of NKX6-1+ pancreatic progenitors from multiple human pluripotent stem cell lines. *Stem Cell Rep.* 4, 591–604. doi: 10.1016/j.stemcr.2015.02.017

Pagliuca, F. W., Millman, J. R., Gürtler, M., Segel, M., Van Dervort, A., Ryu, J. H., et al. (2014). Generation of functional human pancreatic β cells in vitro. *Cell* 159, 428–439. doi: 10.1016/j.cell.2014.09.040

Posselt, A. M., Szot, G. L., Frassetto, L. A., Masharani, U., Tavakol, M., Amin, R., et al. (2010). Islet transplantation in type 1 diabetic patients using calcineurin inhibitor-free immunosuppressive protocols based on T-cell adhesion or costimulation blockade. *Transplantation* 90, 1595–1601. doi: 10.1097/TP.0b013e3181fe1377

Powers, A., and D'Alessio, D. (2011). "Endocrine pancreas and pharmacotherapy of diabetes mellitus and hypoglycemia," in *Goodman & Gilman's The Pharmacological Basis of Therapeutics*, eds L. L. Brunton, B. A. Chabner, and B. C. Knollmann (New York, NY: McGraw-Hill).

Rezania, A., Bruin, J. E., Arora, P., Rubin, A., Batushansky, I., Asadi, A., et al. (2014). Reversal of diabetes with insulin-producing cells derived in vitro from human pluripotent stem cells. *Nat. Biotechnol.* 32, 1121–1133. doi: 10.1038/nbt.3033

Rezania, A., Bruin, J. E., Riedel, M. J., Mojibian, M., Asadi, A., Xu, J., et al. (2012). Maturation of human embryonic stem cell-derived pancreatic progenitors into functional islets capable of treating pre-existing diabetes in mice. *Diabetes* 61, 2016–2029. doi: 10.2337/db11-1711

Rezania, A., Bruin, J. E., Xu, J., Narayan, K., Fox, J. K., O'Neil, J. J., et al. (2013). Enrichment of human embryonic stem cell-derived NKX6.1-expressing pancreatic progenitor cells accelerates the maturation of insulin-secreting cells in vivo. *Stem Cells* 31, 2432–2442. doi: 10.1002/stem.1489

Rosado-Olivieri, E. A., Anderson, K., Kenty, J. H., and Melton, D. A. (2019). YAP inhibition enhances the differentiation of functional stem cell-derived insulin-producing beta cells. *Nat. Commun.* 10:1464. doi: 10.1038/s41467-019-09404-6

Russ, H. A., Parent, A. V., Ringler, J. J., Hennings, T. G., Nair, G. G., Shveygert, M., et al. (2015). Controlled induction of human pancreatic progenitors produces functional beta-like cells in vitro. *EMBO J.* 34, 1759–1772. doi: 10.15252/embj.201591058

Schaffer, A. E., Taylor, B. L., Benthuysen, J. R., Liu, J., Thorel, F., Yuan, W., et al. (2013). Nkx6.1 controls a gene regulatory network required for establishing and maintaining pancreatic beta cell identity. *PLoS Genet.* 9:e1003274. doi: 10.1371/journal.pgen.1003274

Segerstolpe, A., Palasantza, A., Eliasson, P., Andersson, E.-M., Andréasson, A.-C., Sun, X., et al. (2016). Single-cell transcriptome profiling of human pancreatic islets in health and type 2 diabetes. *Cell Metab.* 24, 593–607. doi: 10.1016/j.cmet.2016.08.020

Song, J., and Millman, J. R. (2017). Economic 3D-printing approach for transplantation of human stem cell-derived β-like cells. *Biofabrication.* 9:015002. doi: 10.1088/1758-5090/9/1/015002

Velazco-Cruz, L., Goedegebuure, M. M., Maxwell, K. G., Augsornworawat, P., Hogrebe, N. J., and Millman, J. R. (2020). SIX2 regulates human β cell differentiation from stem cells and functional maturation in vitro. *Cell Rep.* 31:107687. doi: 10.1016/j.celrep.2020.107687

Velazco-Cruz, L., Song, J., Maxwell, K. G., Goedegebuure, M. M., Augsornworawat, P., Hogrebe, N. J., et al. (2019). Acquisition of dynamic function in human stem cell-derived β cells. *Stem Cell Rep.* 12, 351–365. doi: 10.1016/j.stemcr.2018.12.012

Veres, A., Faust, A. L., Bushnell, H. L., Engquist, E. N., Kenty, J. H.-R., Harb, G., et al. (2019). Charting cellular identity during human in vitro β-cell differentiation. *Nature* 569, 368–373. doi: 10.1038/s41586-019-1168-5

Wang, Y. J., Schug, J., Won, K.-J., Liu, C., Naji, A., Avrahami, D., et al. (2016). Single-cell transcriptomics of the human endocrine pancreas. *Diabetes* 65, 3028–3038. doi: 10.2337/db16-0405

Xin, Y., Kim, J., Okamoto, H., Ni, M., Wei, Y., Adler, C., et al. (2016). RNA sequencing of single human islet cells reveals type 2 diabetes genes. *Cell Metab.* 24, 608–615. doi: 10.1016/j.cmet.2016.08.018

Yoshihara, E., Wei, Z., Lin, C. S., Fang, S., Ahmadian, M., Kida, Y., et al. (2016). ERRγ is required for the metabolic maturation of therapeutically functional glucose-responsive β cells. *Cell Metab.* 23, 622–634. doi: 10.1016/j.cmet.2016.03.005

Zhu, Z., Li, Q. V., Lee, K., Rosen, B. P., González, F., Soh, C. L., et al. (2016). Genome editing of lineage determinants in human pluripotent stem cells reveals mechanisms of pancreatic development and diabetes. *Cell Stem Cell* 18, 755–768. doi: 10.1016/j.stem.2016.03.015

Conflict of Interest: LV-C and JM are inventors in patents and patent applications relating to the differentiation of stem cell-derived β cells.

The remaining author declares that the research was conducted in the absence of any commercial or financial relationships that could be construed as a potential conflict of interest.

frontiers in Bioengineering and Biotechnology

ORIGINAL RESEARCH
published: 21 July 2020
doi: 10.3389/fbioe.2020.00792

Integration of Hydrogel Microparticles With Three-Dimensional Liver Progenitor Cell Spheroids

*Stefan D. Gentile†, Andreas P. Kourouklis†, Hyeon Ryoo and Gregory H. Underhill**

Department of Bioengineering, University of Illinois at Urbana-Champaign, Champaign, IL, United States

The study of the liver progenitor cell microenvironment has demonstrated the important roles of both biochemical and biomechanical signals in regulating the progenitor cell functions that underlie liver morphogenesis and regeneration. While controllable two-dimensional *in vitro* culture systems have provided key insights into the effects of growth factors and extracellular matrix composition and mechanics on liver differentiation, it remains unclear how microenvironmental signals may differentially affect liver progenitor cell responses in a three-dimensional (3D) culture context. In addition, there have only been limited efforts to engineer 3D culture models of liver progenitor cells through the tunable presentation of microenvironmental stimuli. We present an *in vitro* model of 3D liver progenitor spheroidal cultures with integrated polyethylene glycol hydrogel microparticles for the internal presentation of modular microenvironmental cues and the examination of the combinatorial effects with an exogenous soluble factor. In particular, treatment with the growth factor TGFβ1 directs differentiation of the spheroidal liver progenitor cells toward a biliary phenotype, a behavior which is further enhanced in the presence of hydrogel microparticles. We further demonstrate that surface modification of the hydrogel microparticles with heparin influences the behavior of liver progenitor cells toward biliary differentiation. Taken together, this liver progenitor cell culture system represents an approach for controlling the presentation of microenvironmental cues internalized within 3D spheroidal aggregate cultures. Overall, this strategy could be applied toward the engineering of instructive microenvironments that control stem and progenitor cell differentiation within a 3D context for studies in tissue engineering, drug testing, and cellular metabolism.

Keywords: tissue engineering, microenvironment, liver, spheroid, microparticles, polyethylene glycol (PEG)

OPEN ACCESS

Edited by:
Yuguo Lei,
University of Nebraska-Lincoln, United States

Reviewed by:
Hon Fai Chan,
The Chinese University of Hong Kong, China
Nathaniel Huebsch,
Washington University in St. Louis, United States

****Correspondence:***
Gregory H. Underhill
gunderhi@illinois.edu

† These authors have contributed equally to this work

Specialty section:
This article was submitted to Biomaterials, a section of the journal Frontiers in Bioengineering and Biotechnology

Received: *24 April 2020*
Accepted: *22 June 2020*
Published: *21 July 2020*

Citation:
Gentile SD, Kourouklis AP, Ryoo H and Underhill GH (2020) Integration of Hydrogel Microparticles With Three-Dimensional Liver Progenitor Cell Spheroids. Front. Bioeng. Biotechnol. 8:792. doi: 10.3389/fbioe.2020.00792

INTRODUCTION

During liver development, liver progenitor cells, termed hepatoblasts, differentiate into hepatocytes, which comprise the majority of the liver tissue and biliary epithelial cells (cholangiocytes) that line the bile ducts (Strick-Marchand and Weiss, 2002; Strick-Marchand et al., 2004). These bipotential liver progenitor cells play an important role in adult liver regeneration

and the progression of liver diseases including fibrosis (Hanley et al., 2008; Carpentier et al., 2011). The complex architecture of the liver microenvironment exposes these cells to various physical and chemical stimuli that can influence their differentiation trajectories. It has been shown that the growth factor TGFβ1 can push these progenitor cells toward the cholangiocytic fate and that substrate stiffness and other biochemical signals can further influence liver progenitor differentiation (Clotman et al., 2005; Lemaigre and Clotman, 2005; Gyorfi et al., 2018). To date, many techniques have been used to approximate the liver microenvironment. Recently, there has been extensive work with cellular microarrays to create a high-throughput system of microenvironments independently tunable for extracellular matrix proteins linked to other chemical signals (Kaylan et al., 2016). This can also be paired with substrates of various stiffnesses to investigate combinatorial physical and chemical effects (Kourouklis et al., 2016).

Much of the previous work dissecting the liver microenvironment has been done in two-dimensional (2D) systems that allow for a great degree of control. However, utilizing a three-dimensional (3D) culture configuration allows for more complexity and *in vivo*-like conditions (Legant et al., 2009; Underhill et al., 2012). Namely, this allows for differential cell–cell interactions, cellular organization, and environmental cues that may be missing in a simple 2D monolayer system. Toward the development of suitable 3D culture models, one approach consists of cells encapsulated within a hydrogel in order to control for aggregate shape, size, and surrounding chemistry. Cells can also be forced to self-aggregate into spheroids ranging in size from a few cells to millions (Goude et al., 2014).

Three-dimensional spheroids can be further modified by the addition of artificial micro- or nanoparticles to control the internal structure, act as carriers for various factors, or to present different functional groups to the aggregating cells (Bratt-Leal et al., 2011). Previous experiments have used a wide variety of materials to construct microparticles, including simple metallic and ceramic microparticles (Palombella et al., 2017), mineral coated plastics (Khalil et al., 2017), and particles manufactured with agarose, gelatin (Fan et al., 2008; Bratt-Leal et al., 2011; Tabata and Tajima, 2017), or extracellular matrix (ECM) proteins such as collagen. Polymers such as poly(lactic-co-glycolic acid) (PLGA; Solorio et al., 2010; Bratt-Leal et al., 2011) or polyethylene glycol (PEG; Ravindran et al., 2011; Parlato et al., 2013) have been used to create hydrogel microparticles via photo- or chemical crosslinking (Parlato et al., 2013; Ahmed, 2015). These particles were further modified to express surface ligands or proteins to present different chemical signals.

The method of microparticle-imbued spheroids has been used extensively to study tumor formation and to model *in vivo* cancer conditions (Weiswald et al., 2015; Song et al., 2016; Ishiguro et al., 2017; Ferreira et al., 2018). Three-dimensional spheroids have also advanced the study of stem cell microenvironments (Bratt-Leal et al., 2009; Rivron et al., 2018). Poly(lactic-co-glycolic acid), PEG, and hyaluronic acid based microparticles have all been used to induce or modulate differentiation (Bratt-Leal et al., 2011; Ravindran et al., 2011; Ansboro et al., 2014). It has been shown that simply the physical presence of microparticles within a pluripotent stem cell aggregate can change the differentiation phenotype (Bratt-Leal et al., 2011; Baraniak et al., 2012). Coupling the physical effects of microparticles with growth factors in human mesenchymal stem cell spheroids can tune chondrogenesis (Ravindran et al., 2011; Ansboro et al., 2014; Goude et al., 2014). Further surface functionalization of the hydrogel can also be used to sequester proteins within the spheroid (Rinker et al., 2018).

In this report, we demonstrate an approach to integrate PEG microparticles into liver progenitor spheroids to create 3D models of liver microtissues with controllable physical and biochemical cues. In the absence of a supporting scaffold, we incorporated hydrogel particles in liver progenitor spheroids, with control over their presentation density and surface chemistry. Despite the lack of control over the particles position within the spheroids, our studies revealed the combinatorial effects of TGFβ1 and hydrogel particles on cell behavior. In summary, our studies showed that the addition of a sufficient number of particles among the liver progenitor cells during spheroidal aggregation leads to an enhancement in biliary differentiation. Specifically, we demonstrate that the combined presentation of hydrogel particles and TGFβ1 significantly increased the expression of biliary markers. Further, we found that the surface modification of the hydrogel particles with heparin and their subsequent incorporation in 3D spheroids provided another route to control the extent of biliary differentiation in the presence of TGFβ1.

MATERIALS AND METHODS

Formulation of Microscale PEG Hydrogels

Biotinylated PEG hydrogel microparticles were fabricated through acrylamide crosslinking between PEGDA (3.4 kDa, Laysan Bio, ACRL-PEG-ACRL-3400-1GR) and Acry-PEG-biotin (5 kDa, Nanocs, Cat.#: PG2-ARBN-5k). The reaction performed within an emulsified mixture of water-separated PEG and Dextran phases that are rich in their corresponding components. Specifically, 1 volume part of PEGDA (24%w/v) was mixed with 7.2 parts of Dextran (40%w/v, 40 kDa, Sigma Aldrich, 31389), 4.8 parts of magnesium sulfate anhydrous reagent (40%w/v, SCS Storeroom, 34533000) and 1.4 parts of Acrylate-PEG-Biotin (3.5%w/v). Irgacure 2959 (0.25%w/v, BASF, 55047962) was added to the polymer mixture with a volume percentage of 10%v/v volume. All the components were dissolved in PBS (pH 8) with 0.22 M potassium chloride and were subject to vortex for 1min following their initial mixing. The resulted emulsion was allowed to equilibrate for 20min before it became subject to UV light via an OmniCure S1500 Spot UV Curing System (Excelitas Technologies) with Fiber Light Guide (320–309 nm filter) at 13% (approx. 560 mW/cm^2). The crosslinked particle suspension was diluted 40 times in dH_2O and placed for centrifugation at 4,000 × *g* for 4 min. Subsequently, the supernatant was exchanged with dH_2O (2×) to complete particles cleaning. The average size of the formed hydrogels was monitored through bright field microscopy.

Toward heparin presentation, particles were incubated with streptavidin (50 ug/ml, VWR, 97062-810) and trace amounts of Alexa Fluor 647-conjugated streptavidin (Invitrogen, Cat.#: S-21374) to support fluorescent microscopy studies. Following streptavidin conjugation on the microscopic hydrogels, the latter were further incubated with biotin-heparin (1 mg/ml, Sigma Aldrich, B9806-10MG). The various hydrogel particles were rinsed through a 5 μm cut-off filter (PluriSelect, 43-50005) combined with further PBS rinsing. The collected hydrogels were counted and added to cell suspensions at selected cells to particle ratios.

Formation of Liver Progenitor Cell Spheroids

We utilized bipotential mouse embryonic liver (BMEL) 9A1 cells between passages 30 and 33 that were cultured as previously described (Strick-Marchand and Weiss, 2002). Collagen I (0.5 mg/ml) solution was prepared and used to coat a T-150 tissue culture plastic flask over before seeding cells under controlled environmental conditions (37°C and 5% CO_2). Cells were treated with trypsin-EDTA (0.25% [v/v] for ≤10 min) and then subjected to centrifugation (800 × *g* for 5 min) for pellet formation and counting. Basal media for expansion consisted of Roswell Park Memorial Institute (RPMI) 1640 + Glutamine (Life Technologies, 61870-127) and fetal bovine serum (10% [v/v], FBS), penicillin/streptomycin (1% [v/v], P/S), human recombinant insulin (10 μg/ml, Life Technologies, 12585-014), IGF-2 (30 ng/ml, PeproTech, 100-12), and epidermal growth factor (EGF) (50 ng/ml, PeproTech, AF-100-15). Differentiation media consisted of Advanced RPMI 1640 (Life Technologies, 12633-012) with FBS (2% [v/v]), P/S (0.5% [v/v]), L-glutamine (1% [v/v]), and minimum non-essential amino acids (1% [v/v], Life Technologies, 11140-050). For spheroid culture, the cells were seeded in 96-well ultra-low-attachment (ULA) plates at a density of 20E3 cells/well and with the corresponding differentiation media. Smaller spheroids were created using AggreWell^{TM}400 plates (Stemcell Technologies, 24 well variant, 34411). The cell mixtures were added to the plates at a seeding density such that the individual spheroids would initially have 1E3 cells/spheroid. In this process, cells were concentrated at 6E5 cells/ml of growth media and 2 ml of cell suspension was added to each well of the AggreWell plate (1.2E6 cells/well). Using a balance plate, the AggreWell plate was spun at 100 × *g* for 3 min, forcing cells into the smaller microwells that were incorporated in the bottom plate to form cell aggregates.

Co-culture of Liver Progenitor Cell Spheroids With Microscale Hydrogels

For the fabrication of cell spheroids with microscopic hydrogels, the latter were mixed with BMEL 9A1 cells at certain cell-to-particle ratio (no particles, 2:1 5:1, 20:1, and 100:1) and then applied within the corresponding 96-well ULA plates or AggreWell^{TM}400 plates. During all the different conditions of cell-particle co-culture, 20E3 cells/well was used as seeding density in ULA plates and 1E3 cells/microwell was used in the AggreWell plates, unless otherwise specified.

Immunostaining of Spheroid Cultures

Cell spheroids were treated with brefeldin A (10 μg/ml, R&D Systems, 1231/5), an inhibitor of protein translocation to the Golgi that facilitates intracellular immunostaining of secreted factors such as OPN, for 2 h and subsequently fixed in paraformaldehyde (4% [v/v] in 1 × PBS) for 1 h. Fixed samples were permeabilized with Triton X-100 (1% [v/v] in 1 × PBS) for overnight incubation under 4°C and then washed with PBS three times for 5 min each before they got incubated in blocking buffer (5% [v/v] donkey serum in 1 × PBS, with 0.25% [v/v] Triton X-100) for 1 h at room temperature. We incubated samples for 24 h at 4°C and with continuous rocking with one or more of the following primary antibodies diluted in blocking buffer: mouse anti-ALB (1/50 from stock, R&D Systems, MAB 1455) and goat anti-OPN (1/60 from stock, R&D Systems, AF808). We next incubated samples for 24 h at room temperature with one or more of the following secondary antibodies diluted in blocking buffer: DyLight 550-conjugated donkey anti-mouse IgG (1/50 from stock, Abcam, ab98767) and DyLight 488-conjugated donkey anti-goat IgG (1/50 from stock, Abcam, ab96935). Samples were immersed in DAPI solution for 24 h at 4°C and then mounted in Fluoromount G with DAPI (Southern Biotech, 0100-20) and imaged the next day using a Zeiss LSM 700 confocal microscope (Carl Zeiss, Inc.) and associated Zen Pro software. In order to stain the smaller, AggreWell spheroids, the staining times were reduced to 25% to avoid oversaturation and nonspecific attachment. In order to capture entire spheroid volumes, we got sections of cell spheroid for determined intervals of 1–5 μm in the *z*-axis. Intensity was measured in ImageJ with at least 3 spheroids imaged for each condition with at least three biological replicates. Data was represented as a mean ± SEM, unless otherwise noted.

RNA Isolation and qRT-PCR Analysis

Trizol solution (Life Technologies 15596-026) was used to collect RNA from cell spheroids that were cultured for the referred periods. For larger, ULA spheroids, 16–24 spheroids were pooled for RNA collection, while several hundred of the smaller, AggreWell-formed spheroids were used. The collected RNA was later isolated through phenol-chloroform extraction following manufacturer's instructions. Samples were digested through DNAse (New England Biolabs, M0303S) at 37°C for 30 min and cleaned using an RNeasy Mini Kit (Qiagen, 74104). RNA concentration was measured by UV spectroscopy and only samples with a ratio >1.8 were used for cDNA preparation. cDNA from isolated RNA was generated using the Supermix iScript cDNA synthesis kit (BioRad, 1708841) and mixed with pre-added primer pairs at a final concentration of 100 nM/primer, again per manufacturer's instructions. Primer pairs for each gene were designed as previously shown using the NCBI's Primer-BLAST with a target Tm of 60°C (see **Supplementary Table 1** for primer pair sequences). Thermal cycling and measurement of amplification curves were executed through the CFX Connect Real-Time PCR Detection System (Bio-Rad) and mRNA expression was calculated relative to Hprt1 and control samples as indicated, with $n \geq 3$ biological replicates, unless otherwise noted.

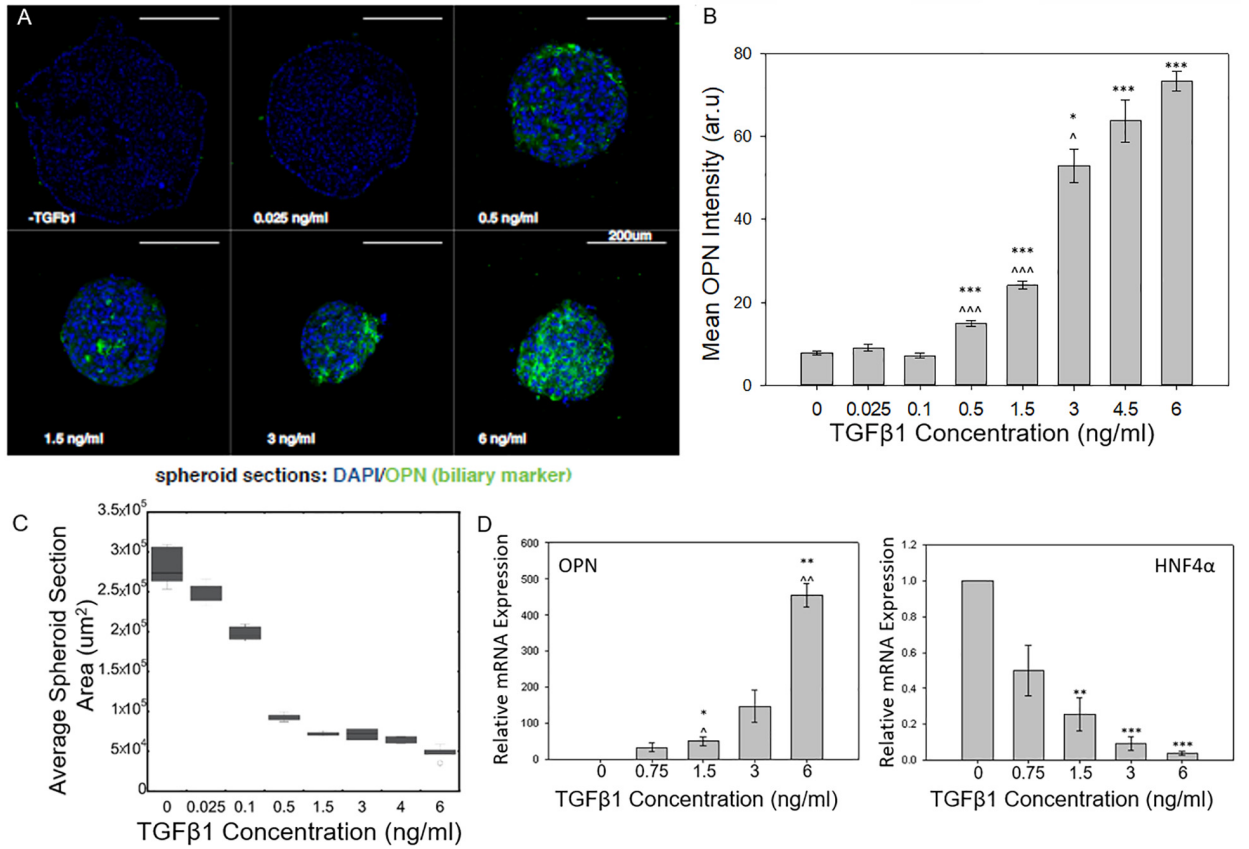

FIGURE 1 | TGFβ1-mediated differentiation of liver progenitor cell spheroids. **(A)** Cross sections of BMEL spheroids immunostained for OPN with increasing TGFβ1 dosage. **(B)** Mean OPN intensity of BMEL spheroids increased as TGFβ1 concentration is increased. Student *t*-tests were performed both against 0 ng/ml TGFβ1 (*$P < 0.05$; ***$P < 0.001$) and against the next lowest TGFβ1 concentration (^$P < 0.05$; ^^$P < 0.001$). **(C)** An increase in TGFβ1 concentration leads to a decrease in spheroid cross-sectional area **(D)** Relative mRNA expression of OPN and HNF4a against TGFβ1 concentration. (*$P < 0.05$; ***$P < 0.001$ compared to 0 ng/ml TGFβ1 and ^$P < 0.05$; ^^$P < 0.01$ compared to next lowest TGFβ1 concentration).

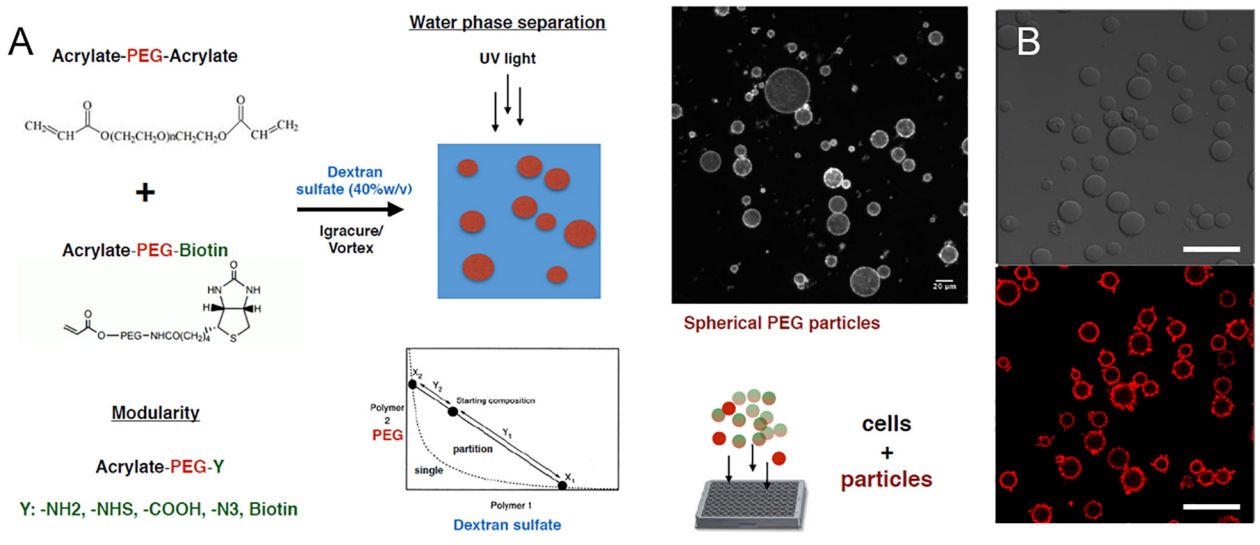

FIGURE 2 | PEG hydrogel microparticle fabrication. **(A)** Fabrication of PEG hydrogel microparticles via photopolymerization of Acrylate-PEG-Acrylate with Acrylate-PEG-Biotin. **(B)** 0.7% Biotin-PEG particles with surface conjugated streptavidin-Alexa Fluor 647 as a visual marker. Scale bar: 50 μm.

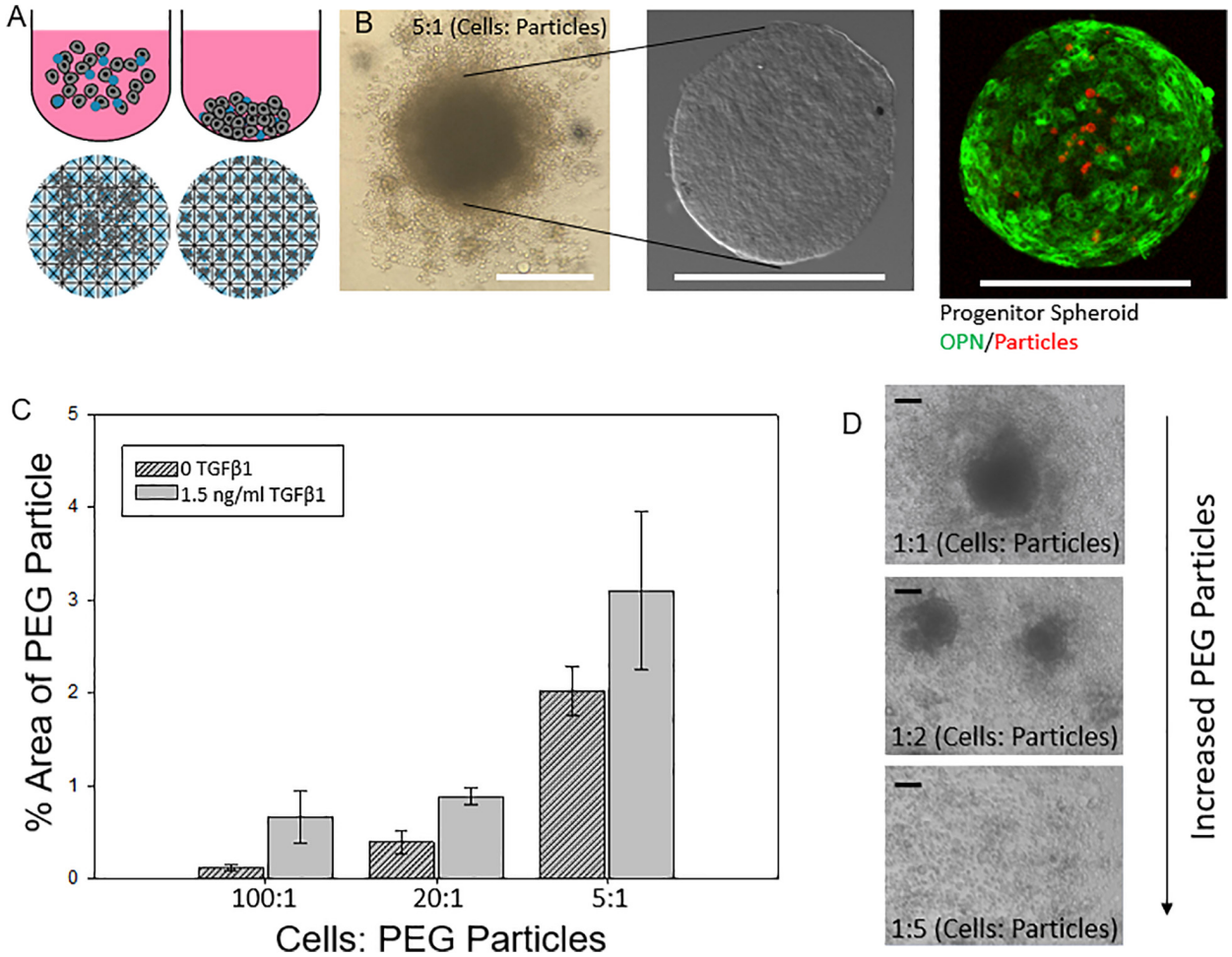

FIGURE 3 | Engineering liver differentiation through hydrogel microparticles. **(A)** Spheroids made by one of two methods. **(Top)** Cells added to the wells of an Ultra Low Attachment (ULA) plate and allowed to settle and self-organize. **(Bottom)** Cells added to the wells of an AggreWell 400 plate (STEMCELL Tech, Cat.# 34421) and centrifuged to form spheroids in the microwells. Scale bars: 200 μm **(B)** ULA spheroids with PEG particles during formation- many of the PEG particles are not incorporated into the fully formed spheroid, after being removed from the well, cleaned and fixed, and after staining for differentiation markers. **(C)** Percent area of a confocal image z slice that is occupied by a PEG particle vs a cell for increasing concentrations of initial added particles with and without TGFβ1. **(D)** Integration of PEG particle into the spheroid based on initial ratio of cells: particles for spheroids with and without soluble TGFβ1. **(D)** As the relative amount of particles increases past a 2:1 cell: particle ratio, the spheroids become smaller as less cells form the initial aggregate and past a 5:1 particle to cell ratio spheroids no longer form. Scale bar: 100 μm.

RESULTS AND DISCUSSION

TGFβ1-Mediated Differentiation of Liver Progenitor Cell Spheroids

To examine the broad effects of TGFβ1, which plays an important role in cholangiocytic fate, on 3D progenitor cell aggregates, we formed BMEL cell spheroids in ULA plates and AggreWells with multiple concentrations of TGFβ1 ranging from 0 to 6 ng/ml. Broadly, stem and progenitor cell differentiation is modulated by a variety of important factors such as growth factors and cell-cell interactions. At the beginning of the culture, BMEL cells were subjected to different concentrations of TGFβ1 in order to assess the effects of the latter on self-organization and differentiation of the cells.

As the concentration of TGFβ1 was increased, the BMEL spheroids underwent increasing levels of cholangiocytic differentiation as shown by the higher expression of the biliary marker osteopontin (OPN; **Figures 1A,B**). The mean expression of OPN measured from the different cross sections of each spheroid observed in the ULA spheroid cross sections increased during the transition from low TGFβ1 (in the range of 0 to 0.1 ng/ml) to medium TGFβ1 concentration (0.5 to 1.5 ng/ml) and again from the medium to the high concentration (3 to 6 ng/ml). This differentiation trajectory was also seen in the smaller diameter AggreWell spheroids that showed an upregulation of OPN and a corresponding reduced expression HNF4a (a hepatocytic transcription factor) with the addition of TGFβ1 (**Supplementary Figure 1**). Both spheroid systems demonstrated

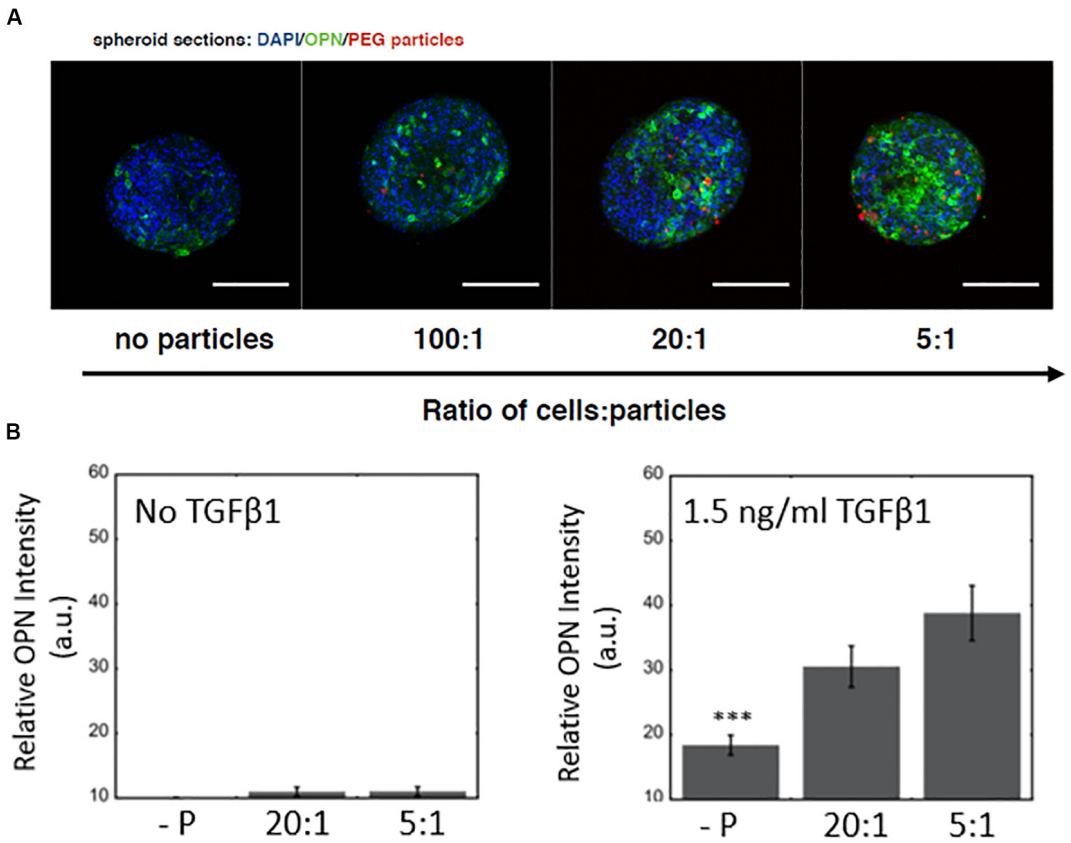

FIGURE 4 | Microparticle integration at a constant TGFβ1 dose and differentiation response for spheroids embedded with PEG hydrogel microparticles **(A)** Increased OPN expression with an increase in PEG microparticle concentration. No particle controls (-P). Scale bars: 150 μm. **(B)** Without TGFβ1, increasing microparticle density does not have any significant effect on OPN expression, while at a constant TGFβ1 concentration (1.5 ng/ml), there is a difference between spheroids with and without microparticles.

the role of TGFβ1 in driving the 3D systems toward the cholangiocytic fate while in turn depressing the hepatocytic. Additionally, TGFβ1 treatment was observed to influence spheroid size and morphology. At higher concentrations of TGFβ1, by t = 72 h post-spheroid. BMEL spheroids demonstrated a more compact morphology with decreasing cross-sectional area against increasing amounts of TGFβ1 (**Figures 1A,C**).

Using qRT-PCR, we further examined the dose-responsive effect of TGFβ1 on spheroid differentiation. We found that an increase in OPN relative mRNA expression corresponded with increasing TGFβ1 concentration. At the highest concentration of TGFB1 (6 ng/ml), the OPN expression was several hundred times higher than the 0 ng/ml TGFβ1 control condition. A converse relationship was observed in regards to the mRNA expression of HNF4a; in particular, treatment with increased concentrations of TGFβ1 reduced the expression of this hepatocytic differentiation marker (**Figure 1D**).

With this 3D spheroidal culture approach, we have confirmed that increasing the concentration of exogenous TGFβ1 leads to an enhanced induction the BMEL cell aggregates toward the biliary fate. Earlier work by Kaylan et al. (2016) measured increasing levels of TGFβ1 on BMEL cells on 2D substrates. At low doses of TGFβ1, these previous studies observed an increase in the relative expression of OPN that corresponded with an increase in TGFβ1 concentration. At what can be considered an intermediate TGFβ1 concentration (1.5 ng/ml) for *in vitro* liver progenitor experiments, these previous studies showed that the relative OPN mRNA expression exhibited a saturation behavior, and even after increasing the concentration to 6 ng/ml TGFβ1, the concentration did not increase or pass a 64 fold increase in expression compared to a 0 ng/ml TGFβ1 control. In contrasting these previous findings with the current 3D spheroid system, we found the relative expression of OPN did not saturate at intermediate TGFβ1 concentrations but continued to increase at higher doses. This was confirmed via immunostaining for OPN, which showed a continued increase in mean OPN intensity with further elevated TGFβ1 concentrations (**Figure 1B**). These results suggest that progenitor cells in a 3D system are more susceptible to variations in growth factor availability especially at higher concentrations compared to monolayer culture. In addition, previous studies with these progenitor cells have demonstrated that in the presence of exogenous TGFβ1, the cells undergo both morphological alterations and cellular

contraction (Kaylan et al., 2016; Kourouklis et al., 2016) as they differentiate into biliary cells. Accordingly, the change in spheroid size with the addition of TGFβ1 is consistent with such cellular morphology changes. Further, our current and previous studies suggest that the *in vitro* treatment of BMEL cells with TGFβ1 can also lead to some reductions in cell numbers, likely in conjunction with the modest induction of cell apoptosis. In future work, there is potential to prevent impacts on cell survival during the biliary differentiation of progenitor cells by the replacement of TGFβ1 with alternative growth factors, or the optimization of additional co-delivered microenvironmental cues.

Engineering Liver Differentiation Through Hydrogel Microparticles: Formulation and Uptake of Hydrogel Microparticles

We next explored the manipulation of the spheroid microenvironment via the incorporation of the PEG hydrogel microparticles. The microparticle fabrication process is described in detail in the "Materials and Methods" section and is illustrated in **Figure 2**. The size distribution of the hydrogel microparticles is illustrated in **Supplementary Figure 2**. The median microparticle radius for these studies was determined to be approximately 7 μm. We examined the effect of the relative number of microparticles within the spheroids by increasing the ratio of cells to PEG particles at the beginning of the cell seeding into the ULA plates or the AggreWell culture platform. We observed that not all of the microparticles in the initial microparticle–cell mixture got incorporated into the spheroids as the spheroidal aggregates formed (**Figures 3A,B**). In addition, the distribution of the microparticles throughout the spheroid was random; due to the self-organization of cells, the uptake and distribution of microparticles among the cells remained random and it is was possible to precisely control the distribution and location of the microparticles within the spheroid. The size distribution of particles within the spheroids was also random as the current and presented method of particle generation created a distribution of particle sizes in the single cell size range (**Supplementary Figure 2**). A future study involving monodisperse microparticles, with more tightly controlled microparticle dimensions, could potentially illustrate a microparticle integration pattern that is not observed with the diverse particles created here. Nonetheless, we observed that final number of microparticles was increased in accordance with their differences in the initial seeding density and independent of the treatment with TGFβ1. Specifically, this increase in microparticle incorporation due to an increase in relative microparticle numbers was observed both for spheroids formed with and without the presence of TGFβ1 (**Figure 3C**). There was a modest increase in the number of microparticles incorporated into spheroids treated TGFβ1, which may have been a consequence of the enhanced compaction of TGFβ1-treated spheroids relative to untreated controls (**Figure 1**). Through manipulation of the cell to microparticle ratio, we also found that increasing the number of PEG microparticles interfered with spheroid formation; specifically, at a 1:1 cell to microparticle ratio, the resulting spheroids were smaller compared to lower particle ratios leaving a significant number of cells outside of the forming spheroid. At 1:2 cell to microparticles, there was no longer a single spheroid and distinct, and smaller spheroids were formed. At 1:5, there was no longer any spheroid formation (**Figure 3D**), as the PEG microparticles inhibited the aggregation of the progenitor cells at this ratio.

Hydrogel Microparticles Influence Progenitor Cell Differentiation in a TGFβ1-Dependent Manner

Next, we examined the effect of microparticle density on the differentiation of BMEL cells following microparticle integration into the spheroidal aggregate cultures. In these studies, the hydrogel microparticles were encased by the 3D cell clusters during formation and remained within the spheroids throughout the maturation of the cultures. We showed that an increased number of hydrogel microparticles relative to BMEL cells was sufficient to incorporate an increased number of microparticles within the differentiating spheroids (**Figure 4A**). In addition, exogenous treatment with the growth factor TGFβ1, together with the introduction of the microparticles, exhibited a synergistic effect on differentiation. Specifically, spheroids with an increased number of microparticles demonstrated an enhancement of biliary differentiation at the same concentration of TGFβ1, relative to the spheroidal aggregates formed without the PEG microparticles (**Figure 4B**). These results suggest that the addition of PEG hydrogel microparticles, without any additional active surface chemistry, was sufficient to modulate the differentiation trajectory. Possible mechanisms underlying this effect include the influence of integrated microparticles on the collective biomechanical stiffness of the spheroid, or the potential modulation of the diffusive characteristics of the spheroid in response to microparticle incorporation, therefore, enabling greater growth factor penetration. As previously discussed, these progenitor cells undergo a morphological change and contract in the presence of TGFβ1. Integrated particles could potentially modulate this contraction process. It is also possible that there is an underlying effect of the streptavidin used to coat the microparticles for subsequent labeling with fluorescent tags and other moieties. Previous work has demonstrated that RYDS motifs on streptavidin have been shown to bind cell surface integrins (Murray et al., 2002). Therefore, it is possible that the presence of streptavidin could support some adhesion-based signaling within the aggregate. Future studies utilizing a different variant of streptavidin, such as Neutravidin, or an overall distinct attachment scheme, may be used to investigate this possibility and any potential role for integrin engagement. Additionally, future efforts could be undertaken to modify the surface of these microparticles, with charged or other adhesive groups, to further enhance spheroidal integration. However, any alterations that lead to biochemical or mechanical interactions within the spheroidal culture could produce secondary effects on differentiation trajectories, that would need to be evaluated in parallel.

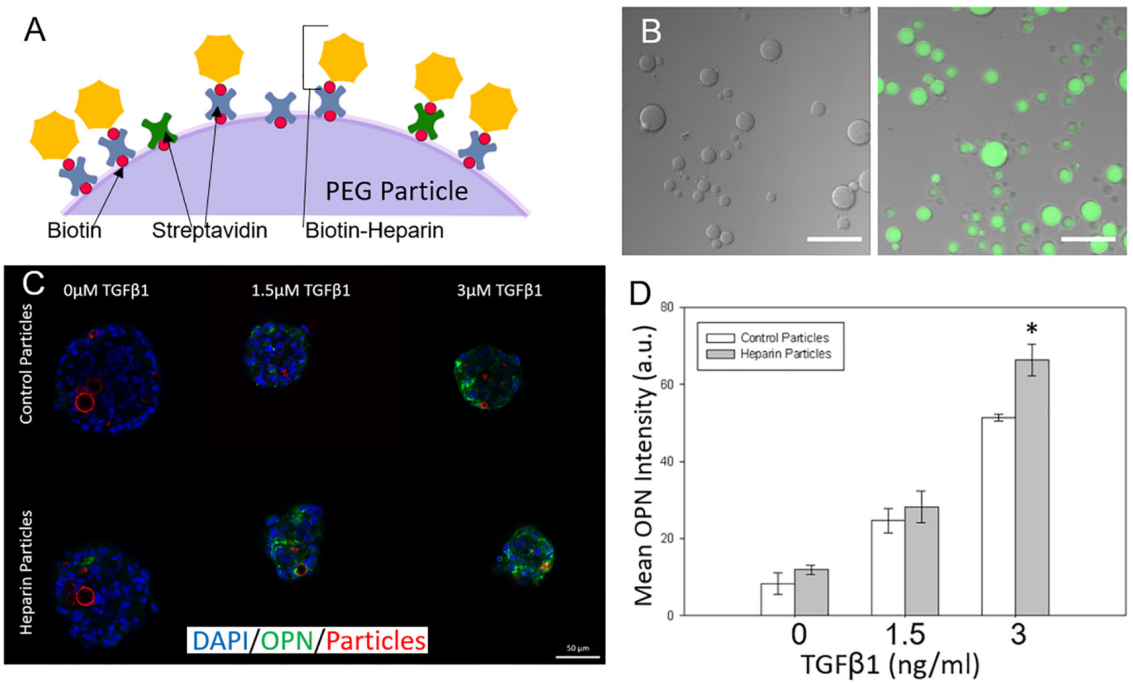

FIGURE 5 | Adding surface conjugated heparin to microparticles to tune liver differentiation. **(A)** Biotinylated heparin is conjugated to the PEG particle surface via a biotin-streptavidin-biotin bridge. **(B)** Heparin presence on PEG particles was verified by conjugating AF488 fluorescent heparin to particles and imaging. **(Left)** control particle without heparin addition. **(Right)** AF488-heparin conjugated to particle. Scale Bars: 50 μm **(C)** Heparin and control particles integrated into Aggrewell spheroids and exposed to different levels of TGFβ1 (Blue: DAPI; Green; OPN; and Red: AF647-PEG particles) **(D)** Mean OPN intensity for Aggrewell spheroids with the 2 particle types.

Adding Surface Conjugated Heparin to Microparticles to Tune Liver Differentiation

After examining the effects of unmodified hydrogel microparticles, we sought to investigate if the surface functionalization of the microparticles could further influence the differentiation process (Benoit et al., 2008; Lutolf et al., 2009). In particular, we conjugated the glycosaminoglycan heparin to the PEG microparticles due to its known ability to bind and sequester growth factors (Rinker et al., 2018). This was achieved by the addition of biotinylated heparin to the microparticles via the incorporation of acrylate-PEG-biotin into the PEG microparticles during fabrication, and the post-particle fabrication treatment with streptavidin, to establish a streptavidin bridge (**Figures 5A,B**). Heparin conjugation was verified by using Alexa Fluor 488-labeled heparin-biotin, and the assessment of microparticle fluorescence using microscopy (**Figure 5B**).

Modifying Particles With Heparin Alters Progenitor Differentiation

Differentiation studies demonstrated that spheroids with induced heparin-conjugated PEG microparticles expressed higher OPN than spheroids with unmodified microparticles, particularly at higher TGFβ1 concentrations (**Figures 5C,D**). At higher concentrations of TGFβ1 (3 ng/ml), smaller Aggrewell-formed spheroids with heparin particles expressed OPN at ∼1.25 fold over the spheroids with standard particles. Spheroids were further treated with SB-43154 (a TGFβ1 inhibitor) to show the continued importance, and specificity, of the effect of the growth factor TGFβ1 on differentiation within the combined growth factor and heparin coated particle system by eliminating the biliary differentiation (**Supplementary Figure 3**).

The effects of heparin-conjugated microparticles on differentiation behavior were mirrored in the analysis of OPN mRNA expression, using mRNA isolated from progenitor cells cultured within the larger ULA spheroids. In three separate experiments, we demonstrated that at the relatively high TGFβ1 concentrations, there was increased OPN expression in spheroids containing heparin-modified microparticles compared to those containing unmodified PEG microparticles (**Supplementary Figure 4**). In each replicate experiment, spheroids exposed to high concentrations of TGFβ1 (3 and 6 ng/ml) showed increased expression with statistically significant ($P < 0.5$) increases at the highest concentration (6 ng/ml). Although there was variation in the expression of OPN relative to the undifferentiated progenitor cells, the effect of heparin-conjugated microparticles on the relative enhancement of OPN expression at higher TGFβ1 concentrations, was consistently observed across replicate studies.

Overall, modifying the surface of our integrated PEG microparticles with heparin shifted the differentiation trajectory of the spheroids with increasing levels of TGFβ1. Heparin has been demonstrated to bind a broad range of growth factors,

and our results demonstrate that at higher concentrations of TGFβ1 there was an increase in the expression of a marker of biliary differentiation that has been previously established to be induced by TGFβ1 treatment. Consequently, we hypothesize that the heparin presented by the modified PEG microparticles may sequester TGFβ1 in the spheroid, and thereby facilitate an increased local concentration of TGFβ1, which subsequently leads to an enhancement of biliary differentiation (Rinker et al., 2018). In future efforts, to mitigate some of the variations observed across distinct microparticle culture experiments, a change in the particle formation to select for more narrow range of particle sizes, or the incorporation of defined microparticle surface modification that could enable a better standardization in regards to microparticle spheroidal integration, may help to control these variations. In addition, complementary studies incorporating techniques such as fluorescence resonance energy transfer (FRET) to directly evaluate the effect of microparticle-presented heparin on the molecular interaction with growth factors such as TGFβ1 within the spheroid, could provide insights into the mechanisms underlying the differentiation effects and provide a blueprint for further tuning the microparticle approach.

CONCLUSION

In conclusion, we have established a 3D culture system to study and subsequently modulate liver progenitor cell differentiation based on the concentration of TGFβ1 and the incorporation of cell-sized hydrogel microparticles. Liver progenitor cell fate was dependent on the concentration of the exogenous growth factor, but by modulating the amounts and surface chemistry of PEG microparticles within the spheroids, we demonstrated the potential to further tune this differentiation process, including a specific enhancement of liver progenitor differentiation toward the biliary lineage. Overall, these efforts demonstrate the utility of a microparticle integration approach for the systematic study of progenitor cell differentiation and represent an important building block toward the improved understanding of the nature of bipotential liver progenitor cells in the context of complex 3D microenvironments.

DATA AVAILABILITY STATEMENT

All datasets generated for this study are included in the article/**Supplementary Material**.

AUTHOR CONTRIBUTIONS

SG: overall experimental design and execution, data collection and analysis, and text and figure preparation. AK: experimental design and execution, data collection and analysis, and text and figure preparation. HR: experimental implementation and data collection and analysis (confocal imaging and PCR). GU: text and figure preparation. All authors contributed to the article and approved the submitted version.

FUNDING

This work was supported by the National Science Foundation (#1636175 to GU).

ACKNOWLEDGMENTS

We are grateful for Hélène Strick-Marchand and Mary C. Weiss (Institut Pasteur) for providing BMEL cells. We are grateful for the help of undergraduate student researchers Partha Ryali, Harris Nisar, and Sarah Warren (University of Illinois at Urbana-Champaign). We also acknowledge the Carl R. Woese Institute for Genomic Biology for assistance with confocal microscopy.

SUPPLEMENTARY MATERIAL

The Supplementary Material for this article can be found online at: https://www.frontiersin.org/articles/10.3389/fbioe.2020.00792/full#supplementary-material

REFERENCES

Ahmed, E. M. (2015). Hydrogel: preparation, characterization, and applications: a review. *J. Adv. Res.* 6, 105–121. doi: 10.1016/j.jare.2013.07.006

Ansboro, S., Hayes, J. S., Barron, V., Browne, S., Howard, L., Greiser, U., et al. (2014). A chondromimetic microsphere for in situ spatially controlled chondrogenic differentiation of human mesenchymal stem cells. *J. Control. Rel.* 179, 42–51. doi: 10.1016/j.jconrel.2014.01.023

Baraniak, P. R., Cooke, M. T., Saeed, R., Kinney, M. A., Fridley, K. M., and McDevitt, T. C. (2012). Stiffening of human mesenchymal stem cell spheroid microenvironments induced by incorporation of gelatin microparticles. *J. Mech. Behav. Biomed. Mater.* 11, 63–71. doi: 10.1016/j.jmbbm.2012.02.018

Benoit, D. S. W., Schwartz, M. P., Durney, A. R., and Anseth, K. S. (2008). Small molecule functional groups for the controlled differentiation of human mesenchymal stem cells encapsulated in poly(ethylene glycol) hydrogels. *Nat. Mater.* 7, 816–823. doi: 10.1038/nmat2269

Bratt-Leal, A. M., Carpenedo, R. L., and McDevitt, T. C. (2009). Engineering the embryoid body microenvironment to direct embryonic stem cell differentiation. *Biotechnol. Prog.* 25, 43–51. doi: 10.1002/btpr.139

Bratt-Leal, A. M., Carpenedo, R. L., Ungrin, M. D., Zandstra, P. W., and McDevitt, T. C. (2011). Incorporation of biomaterials in multicellular aggregates modulates pluripotent stem cell differentiation. *Biomaterials* 32, 48–56. doi: 10.1016/j.biomaterials.2010.08.113

Carpentier, R., Suner, R. E., van Hul, N., Kopp, J. L., Beaudry, H.-B., Cordi, S., et al. (2011). Embryonic ductal plate cells give rise to cholangiocytes, periportal hepatocytes, and adult liver progenitor cells. *Gastroenterology* 141, 1432–1438. doi: 10.1053/j.gastro.2011.06.049

Clotman, F., Jacquemin, P., Plumb-Rudewiez, N., Pierreux, C. E., Van der Smissen, P., Dietz, H. C., et al. (2005). Control of liver cell fate decision by a gradient of TGFβ signaling modulated by Onecut transcription factors. *Genes Dev.* 19, 1849–1854. doi: 10.1101/gad.340305

Fan, H., Hhang, C., Li, J., Bi, L., Qin, L., Wu, H., et al. (2008). Gelatin microspheres containing TGF-β3 enhance the chondrogenesis of mesenchymal

stem cells in modified pellet culture. *Biomacromolecules* 9, 927–934. doi: 10.1021/bm7013203

Ferreira, L. P., Gaspar, V. M., and Mano, J. F. (2018). Bioinstructive microparticles for self-assembly of mesenchymal stem cell-3dtumor spheroids. *Biomaterials* 185, 155–173. doi: 10.1016/j.biomaterials.2018.09.007

Goude, C. C., McDevitt, T. C., and Temenoff, J. S. (2014). Chondroitin sulfate microparticles modulate TGF-β1-induced chondrogenesis of human mesenchymal stem cell spheroids. *Cells Tissues Organ.* 199, 117–130. doi: 10.1159/000365966

Gyorfi, A. H., Matei, A.-E., and Distler, J. H. W. (2018). Targeting TGF-β signaling for the treatment of fibrosis. *Matrix Biol.* 69:8. doi: 10.1016/j.matbio.2017.12.016

Hanley, K. P., Oakley, F., Sugden, S., Wilson, D. I., Mann, D. A., and Hanley, N. A. (2008). Ectopic SOX9 mediates extracellular matrix deposition characteristic of organ fibrosis. *J. Biol. Chem.* 283, 14063–14071. doi: 10.1074/jbc.M707390200

Ishiguro, T., Ohata, H., Sato, A., Tamawaki, K., Enomoto, T., and Okamoto, K. (2017). Tumor-derived spheroids: relevance to cancer stem cells and clinical applications. *Cancer Sci.* 108, 283–289. doi: 10.1111/cas.13155

Kaylan, K. B., Ermilova, V., Yada, R. C., and Underhill, G. H. (2016). Combinatorial microenvironmental regulation of liver progenitor differentiation by Notch ligands, TGFβ, and extracellular matrix. *Sci. Rep.* 6:490. doi: 10.1038/srep23490

Khalil, A. S., Yu, X., Xie, A. W., Fortana, G., Umhoefer, J. M., Johnson, H. J., et al. (2017). Functionalization of microparticles with mineral coatings enhances non-viral transfection of primary human cells. *Sci. Rep.* 7:14211. doi: 10.1038/s41598-017-14153-x

Kourouklis, A. P., Kaylan, K. B., and Underhill, G. H. (2016). Substrate stiffness and matrix composition coordinately control the differentiation of liver progenitor cells. *Biomaterials* 99, 82–94. doi: 10.1016/j.biomaterials.2016.05.016

Legant, W. R., Pathak, A., Yang, M. T., Deshpande, V. S., McMeeking, R. M., and Chen, C. S. (2009). Microfabricated tissue gauges to measure and manipulate forces from 3D microtissues. *Proc. Natl. Acad. Sci. U.S.A.* 106, 10097–10102. doi: 10.1073/pnas.0900174106

Lemaigre, F. P., and Clotman, F. (2005). Control of hepatic differentiation by activin/TGFβ signaling. *Cell Cycle* 5, 168–171. doi: 10.4161/cc.5.2.2341

Lutolf, M. P., Gilbtert, P. M., and Blau, H. M. (2009). Designing materials to direct stem-cell fate. *Nature* 462, 433–441. doi: 10.1038/nature08602

Murray, S., Maraveyas, A., Dougan, T., and Chu, A. C. (2002). Reduction of streptavidin RYDS-mediated renal adhesion by site-directed mutagenesis. *Biochim. Biophys. Acta Gen. Subj.* 1570, 81–88. doi: 10.1016/S0304-4165(02)00157-5

Palombella, S., Pirrone, C., Rossi, F., Armenia, I., Cherubino, M., Valdatta, L., et al. (2017). Effects of metal micro and nano-particles on hascs: an in vitro model. *Nanomaterials* 7:212. doi: 10.3390/nano7080212

Parlato, M., Johnson, A., Hudalla, G. A., and Murphy, W. L. (2013). Adaptable poly(ethylene glycol) microspheres capable of mixed-mode degradation. *Acta Biomater.* 9, 9270–9280. doi: 10.1016/j.actbio.2013.08.011

Ravindran, S., Roam, J. L., Nguyen, P. K., Hering, T. M., Elbert, D. L., and McAlinden, A. (2011). Changes of chondrocyte expression profiles in human MSC aggregates in the presence of PEG microspheres and TGF-β3. *Biomaterials* 32, 8436–8445. doi: 10.1016/j.biomaterials.2011.07.056

Rinker, T. E., Philbrick, B. D., Hettiaratchi, M. H., Smalley, D. M., McDevitt, T. C., and Temenoff, J. S. (2018). Microparticle-mediated sequestration of cell-secreted proteins to modulate chondrocytic differentiation. *Acta Biomater.* 68, 125–136. doi: 10.1016/j.actbio.2017.12.038

Rivron, N. C., Frias-Aldeguer, J., Vrij, E. J., Boisset, J.-C., Korving, J., Vivie, J., et al. (2018). Blastocyst-like structures generated solely from stem cells. *Nature* 557, 106–111. doi: 10.1038/s41586-018-0051-0

Solorio, L. D., Fu, A. S., Hernandez-Irizarry, R., and Alsberg, E. (2010). Chondrogenic differentiation of human mesenchymal stem cell aggregates via controlled release of TGF-β1 from incorporated polymer microspheres. *J. Biomed. Mater. Res. A* 92, 1139–1144. doi: 10.1002/jbm.a.32440

Song, Y., Kim, S. H., Kim, K. M., Choi, E. K., Kim, J., and Seo, H. R. (2016). Activated hepatic stellate cells play pivotal roles in hepatocellular carcinoma cell chemoresistance and migration in multicellular tumor spheroids. *Sci. Rep.* 6:36750. doi: 10.1038/srep36750

Strick-Marchand, H., Morosan, S., Charneau, P., Kremsdorf, D., and Weiss, M. C. (2004). Bipotential mouse embryonic liver stem cell lines contribute to liver regeneration and differentiate as bile ducts and hepatocytes. *Proc. Natl. Acad. Sci. U.S.A.* 101, 8360–8365. doi: 10.1073/pnas.0401092101

Strick-Marchand, H., and Weiss, M. C. (2002). Inducible differentiation and morphogenesis of bipotential liver cell lines from wild-type mouse embryos. *Hepatology* 36, 794–804. doi: 10.1053/jhep.2002.36123

Tabata, Y., and Tajima, S. (2017). Preparation of EpH4 and 3T3L1 cells aggregates incorporating gelatin hydrogel microspheres for a cell condition improvement. *Regener. Ther.* 6, 90–99. doi: 10.1016/j.reth.2017.03.001

Underhill, G. H., Peter, G., Chen, C. S., and Bhatia, S. N. (2012). Bioengineering methods for analysis of cells in vitro. *Annu. Rev. Cell Dev. Biol.* 28, 385–410. doi: 10.1146/annurev-cellbio-101011-155709

Weiswald, L.-B., Bellet, D., and Dangles-Marie, V. (2015). Spherical cancer models in tumor biology. *Neoplasia* 17, 1–15. doi: 10.1016/j.neo.2014.12.004

Conflict of Interest: The authors declare that the research was conducted in the absence of any commercial or financial relationships that could be construed as a potential conflict of interest.

frontiers in Bioengineering and Biotechnology

REVIEW
published: 22 July 2020
doi: 10.3389/fbioe.2020.00781

Generation of Artificial Gamete and Embryo From Stem Cells in Reproductive Medicine

Pu-Yao Zhang[1,2], Yong Fan[3], Tao Tan[1,4] and Yang Yu[1,2]**

[1] Clinical Stem Cell Research Center, Peking University Third Hospital, Beijing, China, [2] Beijing Key Laboratory of Reproductive Endocrinology and Assisted Reproductive Technology and Key Laboratory of Assisted Reproduction, Ministry of Education, Center for Reproductive Medicine, Department of Obstetrics and Gynecology, Peking University Third Hospital, Beijing, China, [3] Key Laboratory for Major Obstetric Diseases of Guangdong Province, The Third Affiliated Hospital of Guangzhou Medical University, Guangzhou, China, [4] Yunnan Key Laboratory of Primate Biomedical Research, Institute of Primate Translational Medicine, Kunming University of Science and Technology, Kunming, China

OPEN ACCESS

Edited by:
Yuguo Lei,
University of Nebraska–Lincoln,
United States

Reviewed by:
Pradeep Reddy,
Salk Institute for Biological Studies,
United States
Guangdun Peng,
Guangzhou Institutes of Biomedicine and Health (CAS), China

***Correspondence:**
Tao Tan
tant@lpbr.cn
Yang Yu
yuyang5012@hotmail.com

Specialty section:
This article was submitted to Bioprocess Engineering, a section of the journal Frontiers in Bioengineering and Biotechnology

Received: 17 April 2020
Accepted: 19 June 2020
Published: 22 July 2020

Citation:
Zhang P-Y, Fan Y, Tan T and Yu Y (2020) Generation of Artificial Gamete and Embryo From Stem Cells in Reproductive Medicine. Front. Bioeng. Biotechnol. 8:781. doi: 10.3389/fbioe.2020.00781

In addition to the great growing need for assisted reproduction technologies (ART), additional solutions for patients without functional gametes are strongly needed. Due to ethical restrictions, limited studies can be performed on human gametes and embryos; however, artificial gametes and embryos represent a new hope for clinical application and basic research in the field of reproductive medicine. Here, we provide a review of the research progress and possible application of artificial gametes and embryos from different species, including mice, monkeys and humans. Gametes specification from adult stem cells and embryonic stem cells (ESCs) as well as propagation of stem cells from the reproductive system and from organized embryos, which are similar to blastocysts, have been realized in some nonhuman mammals, but not all achievements can be replicated in humans. This area of research remains noteworthy and requires further study and effort to achieve the reconstitution of the entire cycle of gametogenesis and embryo development *in vitro*.

Keywords: artificial gametes, artificial embryogenies, stem cell, reproductive medicine, gametogenesis, embryo development

INTRODUCTION

The number of infertile couples has increased from 10 to 15% in the past 10 years. The growing need for assisted reproduction technologies (ART) is a signal for progress in this field. With the development of reproductive medicine, the use of ART is expanding. However, current technologies cannot offer help for patients who lack healthy gametes of their own but yearn for genetically related offspring. Many different pathologies can cause the absence of available gametes. PCOS, ovarian cancer, premature ovarian insufficiency and other ovarian diseases in women and nonobstructive azoospermia (NOA) and chemoradiotherapy of cancer in men are common causes a lack of eggs and sperm. Donor gametes are used in patients for whom ART failed, patients without functional gametes, and homosexual couples who yearn for their genetic offspring. However, this is a passable solution that is not available in many regions and countries. Sperm banking can be a choice for

these patients, but it is useless for prepubertal cancer patients, so the cryopreservation of testicular tissues has been applied as a fertility preservation strategy (Goossens et al., 2013; Picton et al., 2015; Gassei and Orwig, 2016). Germ cells obtained from germ cell transplantation or *in vitro* maturation can be used to fertilize oocytes and achieve pregnancy through ART (Brinster and Zimmermann, 1994; Schlatt et al., 2002; Kim, 2006; Kim et al., 2008; Hermann et al., 2012; Saiz and Plusa, 2013). However, it is only helpful for patients who used to have healthy gametes. In addition, for many couples who are bothered with repeated implantation failures and other diseases leading to failed pregnancy, more exploration and specific treatment are needed. However, ethical restrictions are the main impediment for human embryo studies. Protocols for *in vitro* human embryo culture beyond the blastocyst stage remain suboptimal (Deglincerti et al., 2016; Shahbazi et al., 2016). Furthermore, bioethical guidelines prohibit *in vitro* culture of human embryos beyond 14 days post-fertilization or reach the onset of primitive streak (PS) development (Daley et al., 2016; Hyun et al., 2016). Therefore, more research is required in reproductive medicine, and artificial gametes and embryos might be a good platform both in the clinic and for research.

Artificial gametes and embryos can be defined as gametes and embryos generated by manipulation of progenitor cells or somatic cells and stem cells to derive gametes and embryos assemble to their natural state, which provides a new possible therapy for infertility, especially for those people who lack healthy gametes. The ideal goal of artificial gamete production involves gamete formation, fertilization and the birth of offspring, and for embryos, it also requires implantation and development as well as the birth of offspring; these endpoints have been fully achieved. Nevertheless, while this constitutes a barrier, artificial gametes and embryos still represent a promising direction in reproductive medicine. Hopefully, the complete germline will be able to be established *in vitro* in mammalian species, especially in humans.

The generation of artificial gametes and embryos will not only provide therapeutic advantages clinically but also will generate a terrific platform for studying developmental biology. Developmental studies on human germ cells and embryos are mostly based on animal models due to the lack of available human samples. However, gametogenesis and the process of embryo development are species-specific, and the knowledge acquired from animal models cannot be directly translated to humans (Irie et al., 2015; Sugawa et al., 2015). The main reason for interest in artificial gametes and embryos is the possibility of establishing a reproducible method so that ethical issues can be avoided, cellular and molecular events during the developmental process can be well studied, disease models can be established and possible treatment can be developed. The *in vitro* development of human eggs and sperm will pave the way for understanding the complex processes of gametogenesis and for treatment of infertility. In addition, if artificial gametes and embryos can be obtained from patients with diseases, the mechanisms underlying some infertilities could be unraveled, and potential treatment could be explored with this personal disease model. Dominguez et al. (2015) produced pluripotent stem cells from individuals with Turner syndrome, and then the cells were differentiated into germ cell-like cells (GCLCs) and were compared to GCLCs from control individuals. This study revealed that a correct dose of the X chromosome is critical for the maintenance and function of GSCs, which uncovered the mechanism of infertility for Turner syndrome. Patients with inherited genetic disease can obtain healthy progeny without carrying the gene causing the disease if gene editing technology is combined with artificial gamete and embryo technology.

GAMETES FROM STEM CELLS

Gametes transmit genetic and epigenetic information through generations (Johnson et al., 2011). Fusion of oocytes and spermatozoa leads to the formation of zygotes, and multistep cleavage gives rise to blastocysts. After implantation, germ layers appear, and the formation and specification of primordial germ cells (PGCs) in the endoderm initiates male and female-specific germ cell development. PGCs develop into germ cells that migrate and colonize before entering into programs of oogenesis or spermatogenesis after puberty. The whole process is generally summarized in **Figure 1**. This cycling *in vivo* reveals the fundamental stages of gamete formation, and most *in vitro* studies are focused on the establishment of specific cell stages, such as PGCs.

Reconstitution of PGCs *in vitro*

The key goal of artificial gametes is to produce a functional egg or sperm by reconstituting the process of gametogenesis in culture. Many studies have been focused on the differentiated state of the germ cell lineage.

Primordial germ cells are the precursors of sperm and egg cells, which generate the totipotent state. PGCs arise from the proximal epiblast, which is a region of the early mouse embryo that also contributes to the first blood lineages of the embryonic yolk sac (Lawson and Hage, 1994); PGCs are first observed at the base of the allantois in gastrulating embryos at E7.5 in mice. During gastrulation, a group of mesodermal cells escape from somatic fate; they maintain pluripotency and undergo epigenetic remodeling. In mouse models, PGCs are regulated by BMP4 and BMP8b (Ginsburg et al., 1990; Lawson et al., 1999; Ying et al., 2000), and they upregulate *Prdm1* and *Prdm14* through the mesodermal factor T (Irie et al., 2015; Sugawa et al., 2015). *Tcfap2c1* is downstream of *Prdm1*, which encodes AP2γ and represses somatic gene expression. PGCs are characterized by the expression pluripotent markers such as *Nanog*, *Sox2*, and *Oct4* (Weber et al., 2010) as well as other markers, such as *Fragilis* and *Stella*. PGCs also undergo epigenetic remodeling, including X chromosome activation and a global erasure of DNA methylation patterns. These developments return PGCs to a basal epigenetic state and prepare them or their further differentiation into gametes (Godin et al., 1990; Hackett et al., 2012). PGCs in humans go through a similar pathway of development, but it is not identical. *Prdm14 is* downregulated, and *Sox2* is not expressed.

Primordial germ cells are identified by several key transcription factors (TFs), such as SOX17, TFAP2C and

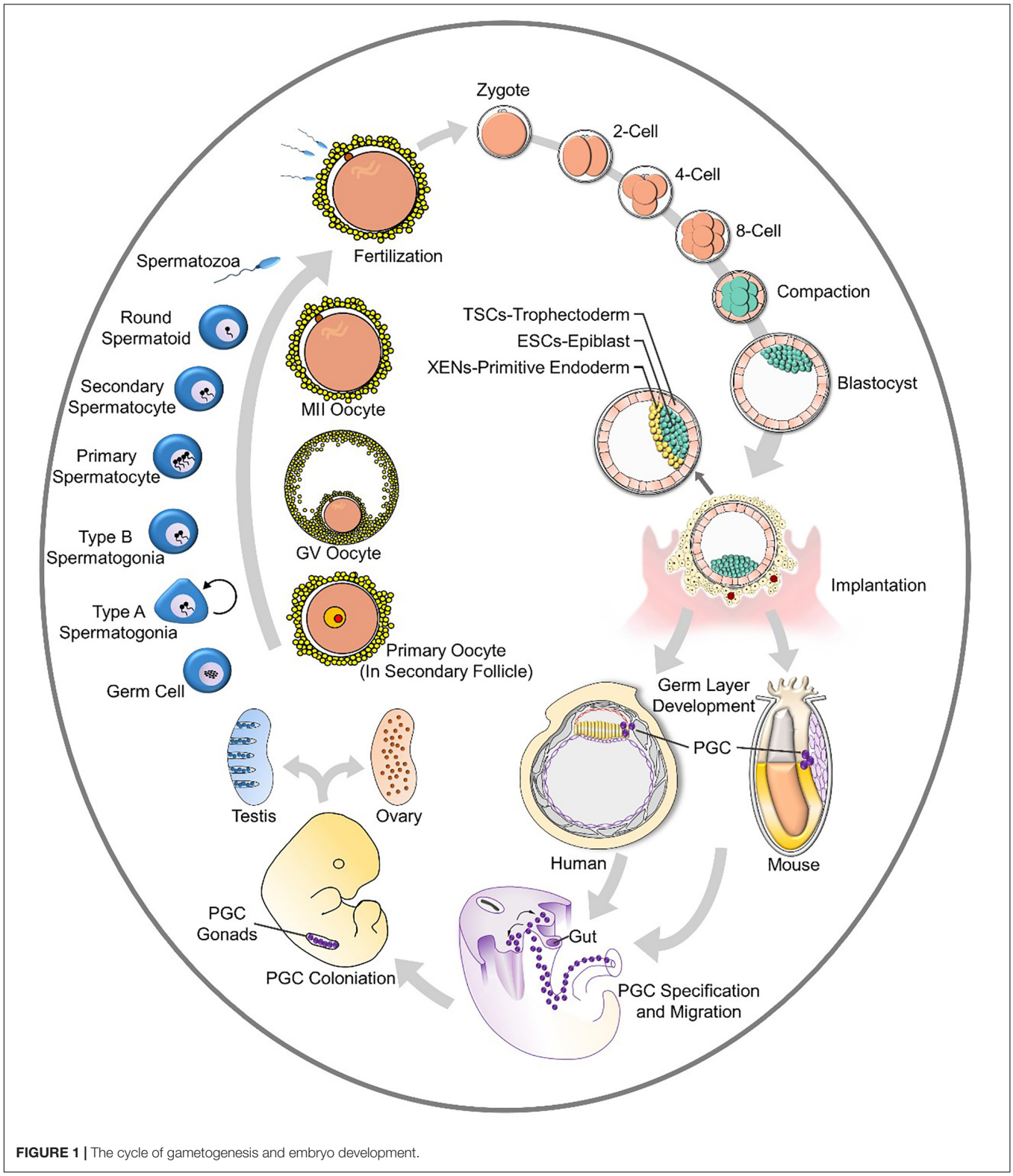

FIGURE 1 | The cycle of gametogenesis and embryo development.

BLIMP1 (also known as PRDM1). These markers are generally used for PGC specification *in vitro* among different species.

Two kinds of stem cells can be used as starting material for generating PGCs: adult stem cells from male and female gonads and pluripotent stem cells, which include embryonic stem cells (ESCs) (Aguilar-Gallardo et al., 2010) and induced pluripotent stem cells (iPSCs) (Takahashi and Yamanaka, 2006; Takahashi et al., 2007; Yu et al., 2007). The pluripotent state of ESCs can be

divided into two states: naïve and primed states. The former stage closely resembles the preimplantation epiblast of the blastocyst, while the latter stage resembles the post-implantation epiblast around gastrulation. iPSCs in different species are in different states. Mouse iPSCs mostly resemble the naïve state, and human iPSCs are typically in the primed state. Mouse ESCs are believed to be naïve, while human ESCs are primed (Nichols and Smith, 2009). The two states require different sets of growth factors for their self-renewal and are interchangeable under certain culture conditions. It is also believed that the cellular state that is between naïve and primed ESCs in mice contains the cells that are most easily transformed into PGC-like cells (PGCLCs) (Hayashi et al., 2011).

The derivation of most mouse PGCs from ESCs was accomplished through stepwise differentiation and enables expansion of the cells *in vitro*. Further differentiation is a pathway that stimulates the natural development process *in vivo*. Hayashi et al. reported that they derived mouse PGCLCs from ESCs and iPSCs as well as epiblast-like cells (EpiLCs), a cellular state highly similar to pregastrulating epiblasts but distinct from epiblast stem cells (EpiSCs). Then, further PGC specification was induced with BMP4, BMP8b, LIF, SCF, and EGF. BMP4 plays a vital role in PGC specification, Rolipram and forskolin work in the process of expansion, and RA and BMP2 induce meiosis (Ohta et al., 2017; Miyauchi et al., 2018). The reconstitution of PGCs has also been explored in primates. ESCs and iPSCs from cynomolgus monkeys (*Macaca fascicularis*, referred to as "cy") are efficiently induced to differentiate into PGCLCs bearing a transcriptome similar to that of early cyPGCs (Sakai et al., 2019). In humans, the specification of PGCLCs has not been achieved. Germline competency and the specification of PGCs are thought to occur in a restricted developmental window during early embryogenesis. Despite the importance of specifying the appropriate number of PGCs for human reproduction, the molecular mechanisms governing PGC formation remain largely unexplored. Studies have shown that the TFAP2C-regulated OCT4 naïve enhancer is involved in human germline formation, and TGFβ and WNT signaling pathways function in PGC formation (Chen et al., 2017, 2018). Improved protocols for producing human PGCLCs are required.

Studies have been undertaken to assess these pathways as they relate to PGCs in more advanced mammals; based on these findings, gametes can be derived.

Gametes From Adult Stem Cells

Gametes from adult stem cells require expansion and directional differentiation. Adult stem cells have specific pluripotency; these cells can self-renewal and differentiation into limited cell lineages. Adult stem cells rely on the niche *in vivo*. The stem cell niche offers a specific microenvironment containing different metabolic factors, molecular pathway factors, sex steroids, immunologic protection, nutrition and even topology.

In adult males, adult stem cells in testicles are named spermatogonial stem cells (SSCs), and their function has been proven by transplantation (Brinster and Avarbock, 1994; Brinster and Zimmermann, 1994) and lineage tracing of self-renewal and differentiation. SSCs are a population of diploid stem cells that undergo self-renewal, and the complex process of cellular differentiation results in spermatogenesis. In mouse models, the number of SSCs is very limited. It is estimated that SSC only accounts for 0.03% of the whole population of germ cells in testicles (Tagelenbosch and de Rooij, 1993).

The long-term *in vitro* propagation of mouse SSCs (mSSCs) was first published in 2003 (Kanatsu-Shinohara et al., 2003). This protocol was established with several factors secreted by somatic cells in mouse testes, including glial cell line-derived neurotrophic factor (GDNF), leukemia inhibitory factor (LIF), epidermal growth factor (EGF), and basic fibroblast growth factor (bFGF). Other substances were added to this culture medium to build a microenvironment similar to the niche in mouse testes. This work offered inspiration for many studies focusing on SSC *in vitro* propagation, and several kinds of modified media have been applied to different primate cells, including cells from humans (Tesarik et al., 2000; Izadyar et al., 2003; Lim et al., 2010; Kokkinaki and Djourabtchi, 2011; Zheng et al., 2014; Medrano et al., 2016; Gat et al., 2017). However, this medium cannot achieve the expectation of long-term proliferation of SSCs in every type of primate.

The testicular niche consists of two compartments: the interstitial tissue and the seminiferous tubules. Sertoli cells are present inside the tubules and serve as structural support for germ cells. The tubules are surrounded by peritubular myoid cells. Outside the tubules, the insterstitium consists of Leydig cells, macrophages, fibroblasts and blood vessels. The function and fate of SSCs are regulated by the niche, which refers to the microenvironment surrounding SSCs that is mostly constituted by Sertoli cells (SCs). The microenvironment of SSCs differs in different primates; several studies focused on the testicular niche, which is constituted by SCs, the extracellular matrix and the vasculature network (Shinohara et al., 1999; Yoshida et al., 2007; De Rooij, 2009), but subtle differences exist in different species. For example, the number of germ cells that SCs could support is limited and species-specific (Griswold, 1998; Johnson et al., 2008; Schlatt and Ehmcke, 2014; França et al., 2016). SCs are mostly described as being the main supporter for spermatogenesis. This evidence has been supported by *in vitro* experiences. Although spermatogenesis has not been fully achieved *in vitro*, the most successful attempts to this point have been based on co-culture of germ cells with SCs (Griswold, 1998; Nagano et al., 1998; Zanganeh et al., 2013; Rebourcet et al., 2014; Xie et al., 2015; França et al., 2016). Sertoli cells secrete factors that direct germ cell fate. In addition, the metabolic state supported by the Sertoli cell-generated microenvironment also matters. Stem cells, including SSCs, have a tendency to favor the Warburg effect. Therefore, SCs support a glycolytic environment for SSCs (Alves et al., 2014; Oliveira et al., 2015; Meneses et al., 2016; Helsel et al., 2017; Marco and Pedro, 2018). *In vitro* experiments with SSCs from non-human primates and humans cannot reach the standard mSSCs reached, which means establishing a testicular niche *in vitro* may require not only substances secreted by somatic cells but also the spatial structure. In addition, the number of somatic cells could be a large factor in the *in vitro* culture system because of their responsiveness to media additives and because they have shorter proliferation cycles (Gat et al., 2017). SSCs are mostly quiescent. Hereafter,

effectively controlling the number of somatic cells in the culture system may trigger the SSCs to proliferate.

For women, the presence of oogonial stem cells (OSCs) in postnatal mammalian ovaries is controversial, as it has long been held that the ovaries contain a fixed number of germ cells throughout a woman's lifetime (Zuckerman, 1951). However, recent studies have provided evidence of mitotically active OSCs in adult murine and human ovaries (Johnson et al., 2004; Zou et al., 2009; Parte et al., 2011; White et al., 2012). Based on the ability of stem cells, which is a function of the self-renewal and differentiation of the cells, OSCs are believed to be a potentially inexhaustible source of oocytes that can be exploited to achieve fertility in women who are infertile or have an exhausted ovarian reserve, as long as the genetic integrity of the OSCs is maintained (Virant-Klun et al., 2008; Woods and Tilly, 2012; Dunlop et al., 2013; Gheorghisan-Galateanu et al., 2014). Unlike OSCs (expressing nuclear OCT-4B), which are large, another population of small stem cells is believed to exist in the ovary. Very small embryonic-like cells (VSELs, expressing nuclear OCT-4A) are located in the ovary surface epithelium (OSE). There is a postulation that VSELs are the most primitive, pluripotent stem cells in the ovary and that they give rise to committed tissue-specific progenitors, including OSCs, expressing OCT-4 in the cytoplasm as well as other germ cell markers (Virant-Klun et al., 2008; Bhartiya et al., 2014).

Even though the existence of OSCs is in dispute, there have been studies that generated oocytes or oocyte-like cells from OSCs. Investigators found SSEA4+ cells on the human OSE that abundantly expressed markers of primordial and pluripotent germ cells. Tilly and coworkers observed that OSCs isolated by FACS (Virant-Klun et al., 2009, 2013; Stimpfel et al., 2013) differentiated *in vitro* into large mature oocytes that became progressively larger, reaching up to 30–50 μm in diameter; further, they expressed terminal markers such as zona pellucida (ZP) glycoproteins, GDF-9 (growth differentiation factor-9), NOBOX (newborn ovary homeobox), YBX2 (Y-box binding protein 2), SYCP3 (synaptonemal protein complex-3) and molecular modifications typical of a haploid karyotype (White et al., 2012; Zhang et al., 2015).

Similar to SSCs with Sertoli cells, somatic cells also play an important supporting role in oocyte specification. Oocyte-granulosa cell complexes (OGCs) are regarded as the stem cell niche in the female reproductive system. Extracellular matrix signaling activates the differentiation of OSCs in human ovaries, and the function is species-specific. Changes in the tissue microenvironment with age have been postulated to affect ovarian function and failure (Niikura et al., 2009; Massasa et al., 2010). Contact between mouse OSCs (mOSCs) and both type I and type IV collagens activates meiotic differentiation (Stra8 expression) and oogenesis (IVD oocyte formation) through a pathway that involves interaction between the collagens and RGD motif-binding integrin subunits. In comparison, human OSCs (hOSCs) express a pattern of integrin subunits that is different from that of mOSCs, and hOSCs were unresponsive to a collagen-based ECM; however, hOSCs exhibited increased differentiation into IVD oocytes when cultured on laminin (MacDonald et al., 2019).

The pool of stem cells is believed to be balanced. Thus, the expansion of adult stem cells and differentiation into gametes has great potential for clinical use. If SSCs can be expanded and differentiated into spermatids, men who suffer from a lack of efficient gametes, such as those with nonobstructive asthenia (NOA), may be enabled to produce genetically related offspring. If OSCs can be expanded and differentiated into oocytes, this technique can be applied clinically for women who lack oocytes for different reasons, such as PCOS. However, there are still obstacles to overcome before these methods can be applied in the clinic due to the related ethical problems. In addition, whether artificial gametes are healthy enough to produce offspring is still uncertain.

Gametes From Embryonic Stem Cells

Apart from adult stem cells, ESCs have always been a good platform for studying *in vitro* cell lineage differentiation (Nishikawa et al., 1998; Rathjen et al., 1998). Germ cell differentiation goes through several stages, and studies focus on different stages. The germ cell lineage arises from epiblasts, and they express specific genes that are absent from somatic cells such as *Dazl*, *Piwil2*, *Rnf17*, *Rnh2*, *Tdrd1*, and *Tex14* (Cooke et al., 1996; Seboun et al., 1997; Wang et al., 2001; Moore et al., 2003).

The testes or ovaries of infertile people still contain SSCs or OSCs, and these precursor cells can proliferate and differentiate *in vitro* and may serve a role in assisted reproductive technologies. However, for people lacking adult stem cells, the only remaining option is the transformation of patient-specific somatic cells into pluripotent stem cells, which is then followed by differentiation into genetically related haploid gametes. There are two ways to generate patient-specific PSCs. First, the nucleus of a somatic cell can be transferred into an enucleated oocyte, which is also known as somatic cell nuclear transfer (SCNT) (Tachibana et al., 2013). This oocyte will develop into an embryo at the blastocyst stage, and the ICM can be retrieved. With these cells, a patient-specific ESC line can be generated. Second, somatic cells can be reprogrammed into human induced pluripotent stem cells (hiPSCs) (Takahashi et al., 2007). In general, the iPSC is more commonly used in the initial steps of this process. It is believed that somatic cells constitute an important support system guiding differentiation, but most studies focus on either female or male *in vitro* gametogenesis. Many developed procedures use a stepwise differentiation that is based on the specification of PGCLCs.

The biologically active vitamin A metabolite all-trans RA has two important functions in human spermatogenesis. RA is a key regulator of the transition from undifferentiated spermatogonia into differentiating spermatogonia, and RA plays an important role by promoting the initiation of meiosis in germ cells. In the testis, Sertoli cells synthesize RA from retinol and tightly regulate its distribution to germ cells. All protocols established for *in vitro* spermatogenesis require RA (Hogarth and Griswold, 2010). Male haploid germ cells at the round spermatid stage have been derived from ESCs by spontaneous differentiation *in vitro*. This offers the possibility of investigating germ cell development, epigenetic reprogramming, and germline gene modification. ESC-derived PGCs can differentiate into sperm, as shown by

transplantation experiments wherein the form MVH-expressing spermatogenic cells. Injecting ESC-derived PGCs into oocytes can restore the somatic diploid chromosome complement and can enable development into blastocysts (Toyooka et al., 2003; Geijsen et al., 2004). Zhou et al. reported the generation of haploid male gametes from mouse ESCs that can produce viable and fertile offspring, demonstrating functional recapitulation of meiosis *in vitro*. Haploid spermatid-like cells (SLCs) were derived by stepwise differentiation of ESCs. Derived PGCLCs co-cultured with neonatal testicular somatic cells and factors including retinoic acid (RA), BMP4, BMP8a, Activin A, follicle stimulating hormone (FSH), bovine pituitary extract (BPE) and testosterone. This process completely recapitulated meiosis *in vitro*, as shown by the achievement of meiotic hallmarks, and intracytoplasmic injection of SLCs produced euploid and fertile offspring (Zhou et al., 2016). Additionally, due to the interspecies differences in spermatogenesis between rodents and humans, it is inappropriate to simply copy the protocols used in mouse studies and apply them to human cells. Full clarification of the *in vivo* regulators of human spermatogenesis has not yet been obtained. However, regulators such as Activin A, TGFβ, BMP4, GDNF, bFGF, LIF, SCF, EGF, RA, and testicular somatic cell support have been demonstrated to be important mediators of hPSC differentiation toward germ cells of different maturation stages.

For female gametes, appropriate conditions must be available for the three events necessary for *in vitro* reconstitution of oogenesis: the initial phase of meiosis, follicular assembly, and oocyte growth and complete maturation. Many *in vitro* oogenesis attempts have been made in mice using cells from ovaries. Morohaku et al. (2016) used an estrogen inhibitor, ICI182780, to inhibit estrogen-mediated signaling in their organ culture system to prevent the formation of multioocyte follicles (MOFs). Human oogonia can be derived from hiPSCs, which also starts with hPGCLC specification and the co-culture of xenogeneic reconstituted ovaries (xrOvaries) with mouse embryonic ovarian somatic cells. After almost 4 months of culture, cells exhibit characteristics similar to those of human oogonia. Transcriptional information indicates that these cells are undergoing processes such as epigenetic reprogramming, erasing the parental imprints and reactivating the inactive X chromosome (Xi) (Yamashiro et al., 2018). Studies focused on *in vitro* oogenesis and their culturing pathways are summarized in **Table 1**. We can tell that the culturing system of mouse oogenesis is fully developed, but a similar system cannot be replicated in humans. Obstacles exist, including the complicated events that occur during oogenesis.

Somatic cells in adult gonads are pivotal for germ cell maintenance and gamete differentiation. Many studies have proven their function and have established protocols for producing artificial gametes. The interaction between somatic cells and germ cells and the 3D structure that somatic cells maintain are crucial for the steady state in adult gonads, which might provide insights into the *in vitro* derivation and expansion of artificial gametes. In addition, these artificial models might explain the relationship between gametes and somatic cells and provide new insights into diseases that cause infertility.

Derivation of gametes from PSCs occurs from a more specific and fixed initial state than derivation of gametes from other sources. However, due to the differences between species, the protocols for mice cannot be directly applied to humans and any other more advanced mammals. Generating fertile offspring with the gametes produced from these procedures is a criterion of success. This is a feasible method for experimental animals but not for humans because of ethical restrictions. Therefore, more suitable protocols and practicable criteria for humans are required.

EMBRYOS FROM STEM CELLS

The blastocyst (the early mammalian embryo) forms all embryonic and extraembryonic tissues, including the placenta. This structure occurs at the 32-cell stage, which is shortly after the embryo loses its "ball of cells" shapes and forms a cavity. In this structure, the inner cell mass (ICM) will develop into the embryo proper (Nishioka et al., 2009; Stephenson et al., 2010; Hirate et al., 2015; Yu et al., 2016). Cells enveloped around the ICM are trophectoderm (TE) cells, which will later contribute to extraembryonic tissues (fetal placenta and membranes). The ICM further differentiates into the embryonic epiblast and primitive endoderm (PrE) while preparing for implantation (Plusa et al., 2008; Guo et al., 2010; Saiz and Plusa, 2013). Different kinds of stem cells develop from different locations in the blastocyst, as summarized in **Figure 1**.

Very little is known about the very first steps of human embryonic development due to the small size of the embryo and the limited accessibility in the womb. Several factors may affect implantation, and problems during implantation or shortly after implantation are the main reasons for pregnancy loss at early stages (Norwitz et al., 2001). Generating large numbers of isogenic, accessible embryos of the relevant stage is not possible through *in vivo* or IVF approaches, so an alternative approach would provide a valuable system for studying early pregnancy problems (Pour and Nachman, 2019). Thus, artificial embryos might be a solution for this problem. The goal of artificial embryos is to establish embryo-like structures without any germ cells; some researchers have focused on the differentiation of ESCs to make these structure, while others have found that assembling several types of stem cells might be feasible. The reorganized embryos can be identified through morphological and transcriptomic analysis. The cavity and expression important gene markers are required for successful embryo-like structure establishment. In addition, developmental potency is an important metric.

Many studies have focused on generating blastocyst-like structures by aggregating several kinds of stem cells. Rivron et al. aggregated mouse embryo stem (ES) cells for 24 h and covered these non-adherent aggregates with trophoblast stem (TS) cells to form blastoids that were similar to E3.5 mouse embryos; the formation frequency was low (0.3%). They also proved that cAMP and WNT pathway stimulation can increase TS cell cavitation and blastoid formation and that the ratio of different cell lines is important for the efficiency of blastoid

TABLE 1 | Pathways of oogenesis.

Species	Culturing system	Resource of ovary cells	Fertile offspring	References
Mouse	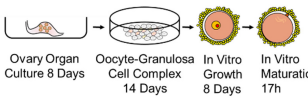	Ovaries From Newborn Mice	Yes	Eppig and O'Brien, 1996; O'Brien et al., 2003; Mochida et al., 2013
Mouse			Yes	Morohaku et al., 2016
Mouse	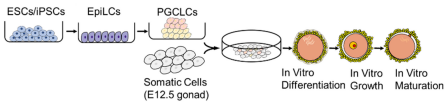	Mouse Embryo Gonads Completes the rOvary	Yes	Hayashi et al., 2011, 2012
Mouse	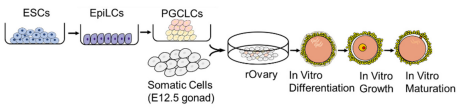		Yes	Hasegawa et al., 2006; Hikabe et al., 2016
Human			No	Jung et al., 2017
Human	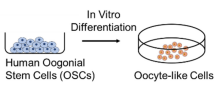		No	Silvestris et al., 2018
Human	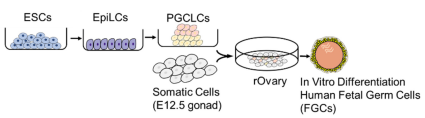	Mouse Embryo Gonads Completes the rOvary	No	Yamashiro et al., 2018

formation (Rivron et al., 2018). There are other studies that have used multiple stem cell types to assemble embryo-like structures. Aggregation of ESCs, TSCs, and/or XENs generated embryo-like structures that recapitulated several key morphogenetic events characteristic of early post-implantation development, including lumenogenesis, epithelialization, and symmetry breaking to specify mesoderm and primordial germ-cell-like cells (Harrison et al., 2017; Sozen et al., 2018; Zhang et al., 2019). Following the identification of EPS cells, which have bidevelopmental potential toward both Em and ExEm lineages (Yang Y. et al., 2017; Yang J. et al., 2017), a method was created that enabled the generation of blastocyst-like structures from mouse EPS cells arose. The embryos they generated resembled blastocysts in morphology and cell lineage allocation and had implantation ability (Li et al., 2019).

Embryonic stem cells are believed to have the property of totipotency. Naïve PSCs are described as cells in the preimplantation BC ICM-like state, and primed PSCs are cells in the post-implantation epiblast-like state. Early attempts to generate embryo-like structures relied on the spontaneous differentiation of ESCs in 3D culture, thereby producing embryoid bodies, which are structurally disorganized cell aggregates (Evans and Kaufman, 1981; Martin, 1981; Doetschman et al., 1985). Kime et al. (2016) converted primed PSCs from mice into a naïve state and then generated BC-like cysts (iBLCs) through sequential culturing (Kime et al., 2019). These iBLCs developed from a totipotent state and expressed important genes but lacked full BC potency. Transcriptome and proteome differences were found between iBLCs and BCs. The implantation and developmental potency of pseudopregnant mice were tested. Cotransferring iBLCs with BCs frequently yielded focal deciduae that were greater in total number than the number of BCs transferred. This might offer new insights for methods to use in cases of difficult embryo transfer in IVF (Mochida et al., 2014). Mouse and human ESCs could establish reorganized embryos resembling a gastrulating embryo when cultured in a soft fibrin matrix and micropatterned condition, respectively (Poh et al., 2014; Warmflash et al., 2014). Moreover, pulsing mouse ESC aggregates in a shaking 3D culture undergoing differentiation with a WNT-b-catenin pathway activator gave rise to elongated gastruloids (Beccari et al., 2018).

The construction of embryo-like structures *in vitro* can offer a model for studying fundamental biological questions in both preimplantation and early post-implantation mammalian embryogenesis and can enable the modeling of diseases related to early pregnancy, the performing of high-throughput pharmacological and toxicological screens, and possibly the bioengineering of mammalian embryos. The development of early mammalian embryos is plastic and is regulated by several evolutionarily conserved developmental processes that can be recapitulated *in vitro*. Artificial embryos are desired not only in mice but also in other mammalian species, including humans. However, the derived reorganized embryos exhibit features of different embryonic stages, but they are not equivalent

to totipotent blastomeres. A deeper understanding of these differences is required to build a better *in vitro* environment for natural embryos. In addition, to date, no artificial embryos derived from the organization of stem cells develop normally, and fertile offspring have not been reported. This indicates that artificial and reorganized embryos remain a substantial challenge in the field, and more investment and research are required.

RNA-seq OFFERS INSIGHTS INTO ARTIFICIAL GERM CELL AND EMBRYO DEVELOPMENT

Since RNA sequencing was developed a decade ago (Emrich et al., 2007; Lister et al., 2008), it has become a ubiquitous tool in molecular biology that is shaping nearly every aspect of our understanding of genomic function. Beyond bulk RNA analysis, single-cell analysis and spatially resolved RNA-seq offer deeper information for the answering of biologic questions (Tang et al., 2009; Montoro et al., 2018). Based on single-cell transcriptional profiling and characterization, cells can be utilized not only to determine an accurate picture of cellular stages but also for bulk studies of embryogenesis, maturation, and pathological conditions or regeneration. Single-cell RNA sequencing offers insights into building an *in vitro* culturing system for gametes and embryos. The identification of different stages of gamete differentiation and embryo development is crucial for artificial gametes and embryos. As we discussed above, the number of adult stem cells is very small in adult gonads, and the cells are difficult to evaluate and isolate. Single-cell analysis introduces the possibility of identifying this small cluster of cells.

A single-cell RNA sequencing (scRNA-seq) analysis of 2,854 human testicular cells provides insight into the possible development process of human spermatogenesis, and several pivotal signaling pathways, including the BMP and FGF pathways, have been found to be involved in human SSC self-renewal (von Kopylow et al., 2016; Wang et al., 2018). ScRNA-seq of various stages of oocyte maturation offers transcriptional proteomic and metabolic information of the stages, and comparison of oocytes in healthy women and patients with PCOS reveals that they are dysfunctional in meiotic maturation, gap junctions, hormone responses, DNA damage, and in the factors they secrete in the early GV phase. Thus, meiosis of oocytes at the GV stage is delayed by malfunctioning genes, which may also hinder fertilization and other processes (Liu et al., 2016; Virant-Klun et al., 2016). Comparison of blastocyst-like cysts and blastoids has mainly been performed at the transcriptional level. Markers for the three lineages of cells, trophectoderm, polarization, X inactivation, development potential and implantation, were all tested and compared between blastocysts and reorganized embryos. Instead of testing several genes in artificial gametes and embryos, scRNA-seq offers a complete picture of how similar they are to natural gametes and embryos (Li et al., 2019).

RNA-seq analysis offers researchers a powerful tool for gathering information to help portray the detailed environment and state of natural gametogenesis and embryo development. Differences between species can also be revealed by such methods, and modified procedures can be established based on animal models.

THE POSSIBLE USES OF ARTIFICIAL GAMETES AND EMBRYOS

Artificial gametes and embryos have scientific uses. Due to ethical restrictions, there are areas where little is known in human embryonic development. The processes of gametogenesis and embryonic development could be better understood. With isogenic gametes and embryos, further culture of human embryos might be achieved, and the processes of early embryo development might be described. Disease models could be established. iPSC technology has brought hope for disease model establishment *in vitro* and treatment for some diseases (Takahashi and Yamanaka, 2006; Takahashi et al., 2007; Han et al., 2016; Paquet et al., 2016; Qian et al., 2016), and we believe that artificial gametes and embryos have the same potential. The mechanisms behind causes of infertility, such as PCOS, endometriosis and gamete developmental disorders, might be explored with the construction of a patient disease model *in vitro*. Treatment could be well developed, and it might even be customized. Embryo resorption represents the failure of implantation (Cossée et al., 2000).

Apart from the research purpose, artificial gametes and embryos are expected to have clinical use; they might represent another available treatment for infertility. Instead of donated sperm or eggs, artificial gametes and embryos could bring hope for genetically related offspring. In addition, patients who lost their fertility because of cancer treatment, including pediatric cancer patients, might regain fertility. These tools also offers another choice of fertility preservation. The safety of artificial gametes and embryos is of special concern. Although fertile offspring can be derived in several rodent studies, these protocols cannot guarantee success in more advanced mammalian species, including humans.

Artificial embryos will become a powerful research platform for early embryo development, especially human embryonic development.

DISCUSSION

Genetic and epigenetic information is transmitted through the cycle of gametogenesis and embryo development. The reconstitution of the entire cycle of gametogenesis and embryo development *in vitro* is the goal behind the generation of artificial gametes and embryos. Gametogenesis can be initiated from ESCs or adult stem cells. The number of adult stem cells is very limited in both male and female gonads; therefore, expansion of adult stem cells is a critical step before gametogenesis. For ESCs, the limited number of cells is no longer a concern, but it always takes multiple steps to accomplish differentiation. Whether important information has been fully maintained is uncertain, and whether deriving artificial gametes directly from the PSC stage is feasible

and preferable is also unknown. The experience derived from mouse models can be inspiring for humans but cannot be translated directly. More experience is required on advanced mammalian species, such as nonhuman primates and humans. The significance of the stem cell niche in the testis and ovary is realized but not fully understood in humans; thus, reconstitution cannot be fully implemented. The field of artificial embryos has just started, and additional work is required.

The development of RNA sequencing started a revolution in biology and medicine, and with this powerful tool, researchers can elucidate the complex relationships between subtypes of cells in the context of sequential cell fate determination in gametogenesis and can pave the way for identifying molecules involved in embryo development. We believe that further investigation of reproduction-related disorders can be performed with RNA sequencing tools. The future of artificial gametes and embryos is profound and lasting. They have both possible scientific and clinical uses, and they might represent a powerful tool for reproductive medicine because they offer potential treatments for infertility and a model of embryo development without the concerns of ethical problems. Artificial gametes and embryos might also be a remarkable tool for rare disease model establishment. In summary, more investment and research are needed in this area.

AUTHOR CONTRIBUTIONS

P-YZ and YF designed the study and drafted the manuscript. TT and YY designed the study and supervised the project. All authors contributed to the discussion and approved the final version.

FUNDING

This work was supported in part by the National Key R&D Program of China (Nos. 2017YFC1001003 and 2016YFC1000601), the National Natural Science Funds (Grant Nos. 81671419, 81571400, 81771580, 81471427, 81570101, 81741006, and 81521002), the Science and Technology Project of Guangzhou (No. 201803010048), Major Science and Technology Projects of Yunnan Province (No. 2017ZF028), and Outstanding Overseas Returnees Fund of the Peking University Third Hospital (No. BYSYLXHG2019002).

REFERENCES

Aguilar-Gallardo, C., Poo, M., Gomez, E., Galan, A., Sanchez, E., Marques-Mari, A., et al. (2010). Derivation, characterization, differentiation, and registration of seven human embryonic stem cell lines (VAL-3, -4, -5, -6M, -7, -8, and -9) on human feeder. *In Vitro Cell. Dev. Biol. Anim*. 46, 317–326. doi: 10.1007/s11626-010-9285-3

Alves, M. G., Martins, A. D., Vaz, C. V., Correia, S., Moreira, P. I., Oliveira, P. F., et al. (2014). Metformin and male reproduction: effects on Sertoli cell metabolism. *Br. J. Pharmacol.* 171, 1033–1042. doi: 10.1111/bph.12522

Beccari, L., Moris, N., Girgin, M., Turner, D. A., Baillie-Johnson, P., Cossy, A., et al. (2018). Multi-axial self-organization properties of mouse embryonic stem cells into gastruloids. *Nature* 562, 272–276. doi: 10.1038/s41586-018-0578-0

Bhartiya, D., Parte, S., Patel, H., Anand, S., Sriraman, K., and Gunjal, P. (2014). "Pluripotent very small embryonic-like stem cells in adult mammalian gonads," in *Adult Stem Cell Therapies: Alternatives to Plasticity*. ed. M. Z. Ratajczak (New York, NY: Springer Science, Business Media), 191–209.

Brinster, R. L., and Avarbock, M. R. (1994). Germline transmission of donor haplotype following spermatogonial transplantation. *Proc. Natl. Acad. Sci. U.S.A.* 91, 11303–11307. doi: 10.1073/pnas.91.24.11303

Brinster, R. L., and Zimmermann, J. W. (1994). Spermatogenesis following male germ-cell transplantation. *Proc. Natl. Acad. Sci. U.S.A.* 91, 11298–11302. doi: 10.1073/pnas.91.24.11298

Chen, D., Liu, W., Lukianchikov, A., Hancock, G. V., Zimmerman, J., Lowe, M. G., et al. (2017). Germline competency of human embryonic stem cells depends on eomesodermin. *Biol. Reprod.* 97, 850–861. doi: 10.1093/biolre/iox138

Chen, D., Liu, W., Zimmerman, J., Pastor, W. A., Kim, R., Hosohama, L., et al. (2018). The TFAP2C-regulated OCT4 naive enhancer is involved in human germline formation. *Cell Rep.* 25, 3591–3602. doi: 10.1016/j.celrep

Cooke, H. J., Lee, M., Kerr, S., and Ruggiu, M. (1996). A murine homologue of the human DAZ gene is autosomal and expressed only in male and female gonads. *Hum. Mol. Genet.* 5, 513–516. doi: 10.1093/hmg/5.4.513

Cossée, M., Puccio, H., Gansmuller, A., Koutnikova, H., Dierich, A., LeMeur, M., et al. (2000). Inactivation of the Friedreich ataxia mouse gene leads to early embryonic lethality without iron accumulation. *Hum. Mol. Genet*. 9, 1219–1226. doi: 10.1093/hmg/9.8.1219

Daley, G. Q., Hyun, I., Apperley, J. F., Barker, R. A., Benvenisty, N., Bredenoord, A. L., et al. (2016). Setting global standards for stem cell research and clinical translation: the 2016 ISSCR guidelines. *Stem Cell Rep.* 6, 787–797. doi: 10.1016/j.stemcr

De Rooij, D. G. (2009). The spermatogonial stem cell niche. *Microsc. Res. Techniq.* 72, 580–585. doi: 10.1002/jemt.20699

Deglincerti, A., Croft, G. F., Pietila, L. N., Zernicka-Goetz, M., Siggia, E. D., and Brivanlou, A. H. (2016). Self-organization of the in vitro attached human embryo. *Nature* 533, 251–254. doi: 10.1038/nature17948

Doetschman, T. C., Eistetter, H., Katz, M., Schmidt, W., and Kemler, R. (1985). The in vitro development of blastocyst-derived embryonic stem cell lines: formation of visceral yolk sac, blood islands and myocardium. *J. Embryol. Exp. Morphol.* 87, 27–45.

Dominguez, A. A., Chiang, H. R., Sukhwani, M., Orwig, K. E., and Reijo Pera, R. A. (2015). Human germ cell formation in xenotransplants of induced pluripotent stem cells carrying X chromosome aneuploidies. *Sci. Rep.* 4:6432. doi: 10.1038/srep06432

Dunlop, C. E., Telfer, E. E., and Anderson, R. A. (2013). Ovarian stem cells–potential roles in infertility treatment and fertility preservation. *Maturitas* 76, 279–283. doi: 10.1016/j.maturitas.2013.04.017

Emrich, S. J., Barbazuk, W. B., Li, L., and Schnable, P. S. (2007). Gene discovery and annotation using LCM-454 transcriptome sequencing. *Genome Res.* 17, 69–73. doi: 10.1101/gr.5145806

Eppig, J. J., and O'Brien, M. J. (1996). Development in vitro of mouse oocytes from primordial follicles. *Biol. Reprod.* 54, 197–207. doi: 10.1095/biolreprod54.1.197

Evans, M. J., and Kaufman, M. H. (1981). Establishment in culture of pluripotential cells from mouse embryos. *Nature* 292, 154–156. doi: 10.1038/292154a0

França, L. R., Hess, R. A., Dufour, J. M., Hofmann, M. C., and Griswold, M. D. (2016). The Sertoli cell: one hundred fifty years of beauty and plasticity. *Andrology* 4, 189–212. doi: 10.1111/andr.12165

Gassei, K., and Orwig, K. E. (2016). Experimental methods to preserve male fertility and treat male factor infertility. *Fertil. Steril.* 105, 256–266. doi: 10.1016/j.fertnstert

Gat, I., Maghen, L., Filice, M., Wyse, B., Zohni, K., and Jarvi, K. (2017). Optimal culture conditions are critical for efficient expansion of human testicular somatic and germ cells in vitro. *Fertil. Steril.* 107, 595–605. doi: 10.1016/j.fertnstert

Geijsen, N., Horoschak, M., Kim, K., Gribnau, J., Eggan, K., and Daley, G. Q. (2004). Derivation of embryonic germ cells and male gametes from embryonic stem cells. *Nature* 427, 148–154. doi: 10.1038/nature02247

Gheorghisan-Galateanu, A. A., Hinescu, M. E., and Enciu, A. M. (2014). Ovarian adult stem cells: hope or pitfall? *J. Ovarian Res.* 7:71. doi: 10.1186/1757-2215-7-71

Ginsburg, M., Snow, M. H. L., and McLaren, A. (1990). Primordial germ cells in the mouse embryo during gastrulation. *Development* 110, 521–528.

Godin, I., Wylie, C., and Heasman, J. (1990). Genital ridges exert long-range effects on mouse primordial germ cell numbers and direction of migration in culture. *Development* 108, 357–363.

Goossens, E., Van Saen, D., and Tournaye, H. (2013). Spermatogonial stem cell preservation and transplantation: from research to clinic. *Hum. Reprod.* 28, 897–907. doi: 10.1093/humrep/det039

Griswold, M. D. (1998). The central role of Sertoli cells in spermatogenesis. *Semin. Cell Dev. Biol.* 9, 411–416. doi: 10.1006/scdb.1998.0203

Guo, G., Huss, M., Tong, G. Q., Wang, C., Li Sun, L., Clarke, N. D., et al. (2010). Resolution of cell fate decisions revealed by single-cell gene expression analysis from zygote to blastocyst. *Dev. Cell.* 18, 675–685. doi: 10.1016/j.devcel.2010.02.012

Hackett, J. A., Zylicz, J. J., and Surani, M. A. (2012). Parallel mechanisms of epigenetic reprogramming in the germline. *Trends Genet*. 28, 164–174. doi: 10.1016/j.tig.2012.01.005

Han, S., Lee, S., Kim, K. E., Lee, H. S., Oh, N., Park, I., et al. (2016). Amelioration of sepsis by TIE2 activation-induced vascular protection. *Sci. Transl. Med*. 8, 335r–355r. doi: 10.1126/scitranslmed.aad9260

Harrison, S. E., Sozen, B., Christodoulou, N., Kyprianou, C., and Zernicka-Goetz, M. (2017). Assembly of embryonic and extraembryonic stem cells to mimic embryogenesis in vitro. *Science* 356:l1810. doi: 10.1126/science.aal1810

Hasegawa, A., Mochida, N., Ogasawara, T., and And Koyama, K. (2006). Pup birth from mouse oocytes in preantral follicles derived from vitrified and warmed ovaries followed by in vitro growth, in vitro maturation, and in vitro fertilization. *Fertil. Steril*. 86, 1182–1192. doi: 10.1016/j.fertnstert.2005.12.082

Hayashi, K., Ogushi, S., Kurimoto, K., Shimamoto, S., Ohta, H., and Saitou, M. (2012). Offspring from oocytes derived from in vitro primordial germ cell-like cells in mice. *Science* 338, 971–975. doi: 10.1126/science.1226889

Hayashi, K., Ohta, H., Kurimoto, K., Aramaki, S., and Saitou, M. (2011). Reconstitution of the mouse germ cell specification pathway in culture by pluripotent stem cells. *Cell* 146, 519–532. doi: 10.1016/j.cell.2011.06.052

Helsel, A. R., Oatley, M. J., and Oatley, J. M. (2017). Glycolysis-optimized conditions enhance maintenance of regenerative integrity in mouse spermatogonial stem cells during long-term culture. *Stem Cell Rep*. 8, 1430–1441. doi: 10.1016/j.stemcr.2017.03.004

Hermann, B. P., Sukhwani, M., Winkler, F., Pascarella, J. N., Peters, K. A., Sheng, Y., et al. (2012). Spermatogonial stem cell transplantation into rhesus testes regenerates spermatogenesis producing functional sperm. *Cell Stem Cell* 11, 715–726. doi: 10.1016/j.stem.2012.07.017

Hikabe, O., Hamazaki, N., Nagamatsu, G., Obata, Y., Hirao, Y., Hamada, N., et al. (2016). Reconstitution in vitro of the entire cycle of the mouse female germ line. *Nature* 539, 299–303. doi: 10.1038/nature20104

Hirate, Y., Hirahara, S., Inoue, K., Kiyonari, H., Niwa, H., and Sasaki, H. (2015). Par-aPKC-dependent and -independent mechanisms cooperatively control cell polarity, Hippo signaling, and cell positioning in 16-cell stage mouse embryos. *Dev. Growth Diff.* 57, 544–556. doi: 10.1111/dgd.12235

Hogarth, C. A., and Griswold, M. D. (2010). The key role of vitamin A in spermatogenesis. *J. Clin. Invest.* 120, 956–962. doi: 10.1172/jci41303

Hyun, I., Wilkerson, A., and Johnston, J. (2016). Embryology policy: revisit the 14-day rule. *Nature* 533, 169–171. doi: 10.1038/533169a

Irie, N., Weinberger, L., Tang, W. W., Kobayashi, T., Viukov, S., and Manor, Y. S. (2015). SOX17 is a critical specifier of human primordial germ cell fate. *Cell* 160, 253–268. doi: 10.1016/j.cell.2014.12.013

Izadyar, F., den Ouden, K., Creemers, L. B., Posthuma, G., Parvinen, M., and de Rooij, D. G. (2003). Proliferation and differentiation of bovine type A spermatogonia during long-term culture. *Biol. Reprod*. 68, 272–281. doi: 10.1095/biolreprod.102.004986

Johnson, A. D., Richardson, E., Bachvarova, R. F., and Crother, B. I. (2011). Evolution of the germ line–soma relationship in vertebrate embryos. *Reproduction* 141, 291–300. doi: 10.1530/REP-10-0474

Johnson, J., Canning, J., Kaneko, T., Pru, J. K., and Tilly, J. L. (2004). Germline stem cells and follicular renewal in the postnatal mammalian ovary. *Nature* 428, 145–150. doi: 10.1038/nature02868

Johnson, L., Thompson, D. L., and Varner, D. D. (2008). Role of Sertoli cell number and function on regulation of spermatogenesis. *Anim. Reprod. Sci.* 105, 23–51. doi: 10.1016/j.anireprosci

Jung, D., Xiong, J., Ye, M., Qin, X., Li, L., Cheng, S., et al. (2017). In vitro differentiation of human embryonic stem cells into ovarian follicle-like cells. *Nat. Commun.* 8:15680. doi: 10.1038/ncomms15680

Kanatsu-Shinohara, M., Ogonuki, N., Inoue, K., Miki, H., Ogura, A., Toyokuni, S., et al. (2003). Long-term proliferation in culture and germline transmission of mouse male germline stem cells. *Biol. Reprod*. 69, 612–616. doi: 10.1095/biolreprod.103.017012

Kim, Y. (2006). Recipient preparation and mixed germ cell isolation for spermatogonial stem cell transplantation in domestic cats. *J. Androl.* 27, 248–256. doi: 10.2164/jandrol.05034

Kim, Y., Turner, D., Nelson, J., Dobrinski, I., McEntee, M., and Travis, A. J. (2008). Production of donor-derived sperm after spermatogonial stem cell transplantation in the dog. *Reproduction* 136, 823–831. doi: 10.1530/REP-08-0226

Kime, C., Kiyonari, H., Ohtsuka, S., Kohbayashi, E., Asahi, M., Yamanaka, S., et al. (2019). Induced 2C expression and implantation-competent blastocyst-like cysts from primed pluripotent stem cells. *Stem Cell Rep.* 13, 485–498. doi: 10.1016/j.stemcr.2019.07.011

Kime, C., Sakaki-Yumoto, M., Goodrich, L., Hayashi, Y., Sami, S., Derynck, R., et al. (2016). Autotaxin-mediated lipid signaling intersects with LIF and BMP signaling to promote the naive pluripotency transcription factor program. *Proc. Natl. Acad. Sci. U.S.A.* 113, 12478–12483. doi: 10.1073/pnas.1608564113

Kokkinaki, M., and Djourabtchi, A. (2011). Long-term culture of human SSEA-4 positive spermatogonial stem cells (SSCs). *J. Stem Cell Res. Ther.* 2:2488. doi: 10.4172/2157-7633.S2-003

Lawson, K. A., Dunn, N. R., Roelen, B. A., Zeinstra, L. M., Davis, A. M., Wright, C. V., et al. (1999). Bmp4 is required for the generation of primordial germ cells in the mouse embryo. *Genes Dev*. 13, 424–436. doi: 10.1101/gad.13.4.424

Lawson, K. A., and Hage, W. J. (1994). Clonal analysis of the origin of primordial germ cells in the mouse. *Ciba Found. Symp*. 182, 68–84; discussion 84–91. doi: 10.1002/9780470514573.ch5

Li, R., Zhong, C., Yu, Y., Liu, H., Sakurai, M., Yu, L., et al. (2019). Generation of blastocyst-like structures from mouse embryonic and adult cell cultures. *Cell* 179, 687–702. doi: 10.1016/j.cell.2019.09.029

Lim, J. J., Sung, S. Y., Kim, H. J., Song, S. H., Hong, J. Y., Yoon, T. K., et al. (2010). Long-term proliferation and characterization of human spermatogonial stem cells obtained from obstructive and non-obstructive azoospermia under exogenous feeder-free culture conditions. *Cell Proliferat.* 43, 405–417. doi: 10.1111/j.1365-2184.2010.00691.x

Lister, R., O'Malley, R. C., Tonti-Filippini, J., Gregory, B. D., Berry, C. C., Millar, A. H., et al. (2008). Highly integrated single-base resolution maps of the epigenome in *Arabidopsis*. *Cell* 133, 523–536. doi: 10.1016/j.cell.2008.03.029

Liu, Q., Li, Y., Feng, Y., Liu, C., Ma, J., Li, Y., et al. (2016). Single-cell analysis of differences in transcriptomic profiles of oocytes and cumulus cells at GV, MI, MII stages from PCOS patients. *Sci. Rep.* 6:39638. doi: 10.1038/srep39638

MacDonald, J. A., Takai, Y., Ishihara, O., Seki, H., Woods, D. C., and Tilly, J. L. (2019). Extracellular matrix signaling activates differentiation of adult ovary-derived oogonial stem cells in a species-specific manner. *Fertil. Steril.* 111, 794–805. doi: 10.1016/j.fertnstert.2018.12.015

Marco, G. A., and Pedro, F. O. (2018). Sertoli cells: methods and protocols. *Methods Mol. Biol.* 1748, 157–171. doi: 10.1007/978-1-4939-7698-0_12

Martin, G. R. (1981). Isolation of a pluripotent cell line from early mouse embryos cultured in medium conditioned by teratocarcinoma stem cells. *Proc. Natl. Acad. Sci. U.S.A.* 78, 7634–7638. doi: 10.1073/pnas.78.12.7634

Massasa, E., Costa, X. S., and Taylor, H. S. (2010). Failure of the stem cell niche rather than loss of oocyte stem cells in the aging ovary. *Aging* 2, 1–2. doi: 10.18632/aging.100119

Medrano, J. V., Rombaut, C., Simon, C., Pellicer, A., and Goossens, E. (2016). Human spermatogonial stem cells display limited proliferation in vitro under mouse spermatogonial stem cell culture conditions. *Fertil. Steril.* 106, 1539–1549. doi: 10.1016/j.fertnstert

Meneses, M. J., Bernardino, R. L., Sá, R., Silva, J., Barros, A., Sousa, M., et al. (2016). Pioglitazone increases the glycolytic efficiency of human Sertoli cells

with possible implications for spermatogenesis. *Int. J. Biochem. Cell Biol.* 79, 52–60. doi: 10.1016/j.biocel.2016.08.011

Miyauchi, H., Ohta, H., and Saitou, M. (2018). Mitosis and meiosis part A. *Methods Cell Biol.* 144, 409–429.

Mochida, K., Hasegawa, A., Otaka, N., Hama, D., Furuya, T., Yamaguchi, M., et al. (2014). Devising assisted reproductive technologies for wild-derived strains of mice: 37 strains from five subspecies of mus musculus. *PLoS One* 9:e114305. doi: 10.1371/journal.pone.0114305

Mochida, N., Akatani-Hasegawa, A., Saka, K., Ogino, M., Hosoda, Y., Wada, R., et al. (2013). Live births from isolated primary/early secondary follicles following a multistep culture without organ culture in mice. *Reproduction* 146, 37–47. doi: 10.1530/rep-13-0020

Montoro, D. T., Haber, A. L., Biton, M., Vinarsky, V., Lin, B., Birket, S. E., et al. (2018). A revised airway epithelial hierarchy includes CFTR-expressing ionocytes. *Nature* 560, 319–324. doi: 10.1038/s41586-018-0393-7

Moore, F. L., Jaruzelska, J., Fox, M. S., Urano, J., Firpo, M. T., Turek, P. J., et al. (2003). Human Pumilio-2 is expressed in embryonic stem cells and germ cells and interacts with DAZ (Deleted in AZoospermia) and DAZ-like proteins. *Proc. Natl. Acad. Sci. U.S.A.* 100, 538–543. doi: 10.1073/pnas.0234478100

Morohaku, K., Tanimoto, R., Sasaki, K., Kawahara-Miki, R., Kono, T., Hayashi, K., et al. (2016). Complete in vitro generation of fertile oocytes from mouse primordial germ cells. *Proc. Natl. Acad. Sci. U.S.A.* 113, 9021–9026. doi: 10.1073/pnas.1603817113

Nagano, M., Avarbock, M. R., Leonida, E. B., Brinster, C. J., and Brinster, R. L. (1998). Culture of mouse spermatogonial stem cells. *Tissue Cell.* 30, 389–397.

Nichols, J., and Smith, A. (2009). Naive and primed pluripotent states. *Cell Stem Cell.* 4, 487–492. doi: 10.1016/j.stem.2009.05.015

Niikura, Y., Niikura, T., and Tilly, J. L. (2009). Aged mouse ovaries possess rare premeiotic germ cells that can generate oocytes following transplantation into a young host environment. *Aging* 1, 971–978. doi: 10.18632/aging.100105

Nishikawa, S. I., Nishikawa, S., Hirashima, M., Matsuyoshi, N., and Kodama, H. (1998). Progressive lineage analysis by cell sorting and culture identifies $FLK1^{+}VE\text{-}cadherin^{+}$ cells at a diverging point of endothelial and hemopoietic lineages. *Development* 125, 1747–1757.

Nishioka, N., Inoue, K., Adachi, K., Kiyonari, H., Ota, M., Ralston, A., et al. (2009). The Hippo signaling pathway components Lats and Yap pattern Tead4 activity to distinguish mouse trophectoderm from inner cell mass. *Dev. Cell.* 16, 398–410. doi: 10.1016/j.devcel.2009.02.003

Norwitz, E. R., Schust, D. J., and Fisher, S. J. (2001). Implantation and the survival of early pregnancy. *N. Engl. J. Med.* 345, 1400–1408. doi: 10.1056/nejmra000763

O'Brien, M. J., Pendola, J. K., and Eppig, J. J. (2003). A revised protocol for in vitro development of mouse oocytes from primordial follicles dramatically improves their developmental competence1. *Biol. Reprod.* 68, 1682–1686. doi: 10.1095/biolreprod.102.013029

Ohta, H., Kurimoto, K., Okamoto, I., Nakamura, T., Yabuta, Y., Miyauchi, H., et al. (2017). In vitro expansion of mouse primordial germ cell-like cells recapitulates an epigenetic blank slate. *EMBO J.* 36, 1888–1907. doi: 10.15252/embj.201695862

Oliveira, P. F., Martins, A. D., Moreira, A. C., Cheng, C. Y., and Alves, M. G. (2015). The warburg effect revisited-lesson from the sertoli cell. *Med. Res. Rev.* 35, 126–151.

Paquet, D., Kwart, D., Chen, A., Sproul, A., Jacob, S., Teo, S., et al. (2016). Efficient introduction of specific homozygous and heterozygous mutations using CRISPR/Cas9. *Nature* 533, 125–129. doi: 10.1038/nature17664

Parte, S., Bhartiya, D., Telang, J., Daithankar, V., Salvi, V., Zaveri, K., et al. (2011). Detection, characterization, and spontaneous differentiation in vitro of very small embryonic-like putative stem cells in adult mammalian ovary. *Stem Cells Dev.* 20, 1451–1464. doi: 10.1089/scd.2010.0461

Picton, H. M., Wyns, C., Anderson, R. A., Goossens, E., Jahnukainen, K., Kliesch, S., et al. (2015). A European perspective on testicular tissue cryopreservation for fertility preservation in prepubertal and adolescent boys. *Hum. Reprod.* 30, 2463–2475. doi: 10.1093/humrep/dev190

Plusa, B., Piliszek, A., Frankenberg, S., Artus, J., and Hadjantonakis, A. K. (2008). Distinct sequential cell behaviours direct primitive endoderm formation in the mouse blastocyst. *Development* 135, 3081–3091. doi: 10.1242/dev.021519

Poh, Y., Chen, J., Hong, Y., Yi, H., Zhang, S., Chen, J., et al. (2014). Generation of organized germ layers from a single mouse embryonic stem cell. *Nat. Commun.* 5:4000. doi: 10.1038/ncomms5000

Pour, M., and Nachman, I. (2019). Building blastocysts from stem cells. *Stem Cell Rep.* 13, 437–439. doi: 10.1016/j.stemcr.2019.08.009

Qian, X., Nguyen, H. N., Song, M. M., Hadiono, C., Ogden, S. C., Hammack, C., et al. (2016). Brain-region-specific organoids using mini-bioreactors for modeling ZIKV exposure. *Cell* 165, 1238–1254. doi: 10.1016/j.cell.2016.04.032

Rathjen, P. D., Lake, J., Whyatt, L. M., Bettess, M. D., and Rathjen, J. (1998). Properties and uses of embryonic stem cells: prospects for application to human biology and gene therapy. *Reprod. Fertil. Dev.* 10, 31–47. doi: 10.1071/r98041

Rebourcet, D., O'Shaughnessy, P. J., Monteiro, A., Milne, L., Cruickshanks, L., Jeffrey, N., et al. (2014). Sertoli cells maintain Leydig cell number and peritubular myoid cell activity in the adult mouse testis. *PLoS One* 9:e105687. doi: 10.1371/journal.pone.0105687

Rivron, N. C., Frias-Aldeguer, J., Vrij, E. J., Boisset, J., Korving, J., Vivié, J., et al. (2018). Blastocyst-like structures generated solely from stem cells. *Nature* 557, 106–111. doi: 10.1038/s41586-018-0051-0

Saiz, N., and Plusa, B. (2013). Early cell fate decisions in the mouse embryo. *Reproduction* 145, R65–R80. doi: 10.1530/REP-12-0381

Sakai, Y., Nakamura, T., Okamoto, I., Gyobu-Motani, S., Ohta, H., Yabuta, Y., et al. (2019). Induction of the germ cell fate from pluripotent stem cells in cynomolgus monkeys. *Biol. Reprod.* 102, 620–638. doi: 10.1093/biolre/ioz205

Schlatt, S., and Ehmcke, J. (2014). Regulation of spermatogenesis: an evolutionary biologist's perspective. *Semin. Cell Dev. Biol.* 29, 2–16. doi: 10.1016/j.semcdb.2014.03.007

Schlatt, S., Foppiani, L., Rolf, C., Weinbauer, G. F., and Nieschlag, E. (2002). Germ cell transplantation into X-irradiated monkey testes. *Hum. Reprod.* 17, 55–62. doi: 10.1093/humrep/17.1.55

Seboun, E., Barbaux, S., Bourgeron, T., Nishi, S., Agulnik, A., Egashira, M., et al. (1997). Gene sequence, localization, and evolutionary conservation of DAZLA, a candidate male sterility gene. *Genomics* 41, 227–235. doi: 10.1006/geno.1997.4635

Shahbazi, M. N., Jedrusik, A., Vuoristo, S., Recher, G., Hupalowska, A., Bolton, V., et al. (2016). Self-organization of the human embryo in the absence of maternal tissues. *Nat. Cell Biol.* 18, 700–708. doi: 10.1038/ncb3347

Shinohara, T., Avarbock, M. R., and Brinster, R. L. (1999). 1- and 6-integrin are surface markers on mouse spermatogonial stem cells. *Proc. Natl. Acad. Sci. U.S.A.* 96, 5504–5509. doi: 10.1073/pnas.96.10.5504

Silvestris, E., Cafforio, P., De Oronzo, S., Felici, C., Silvestris, F., and Loverro, G. (2018). In vitro differentiation of human oocyte-like cells from oogonial stem cells: single-cell isolation and molecular characterization. *Hum. Reprod.* 33, 464–473. doi: 10.1093/humrep/dex377

Sozen, B., Amadei, G., Cox, A., Wang, R., Na, E., Czukiewska, S., et al. (2018). Self-assembly of embryonic and two extra-embryonic stem cell types into gastrulating embryo-like structures. *Nat. Cell Biol.* 20, 979–989. doi: 10.1038/s41556-018-0187-z

Stephenson, R. O., Yamanaka, Y., and Rossant, J. (2010). Disorganized epithelial polarity and excess trophectoderm cell fate in preimplantation embryos lacking E-cadherin. *Development* 137, 3383–3391. doi: 10.1242/dev.050195

Stimpfel, M., Skutella, T., Cvjeticanin, B., Meznaric, M., Dovc, P., Novakovic, S., et al. (2013). Isolation, characterization and differentiation of cells expressing pluripotent/multipotent markers from adult human ovaries. *Cell Tissue Res.* 354, 593–607. doi: 10.1007/s00441-013-1677-8

Sugawa, F., Arauzo-Bravo, M. J., Yoon, J., Kim, K. P., Aramaki, S., Wu, G., et al. (2015). Human primordial germ cell commitmentin vitro associates with a unique PRDM14 expression profile. *EMBO J.* 34, 1009–1024. doi: 10.15252/embj.201488049

Tachibana, M., Amato, P., Sparman, M., Gutierrez, N. M., Tippner-Hedges, R., Ma, H., et al. (2013). Human embryonic stem cells derived by somatic cell nuclear transfer. *Cell* 153, 1228–1238. doi: 10.1016/j.cell.2013.05.006

Tagelenbosch, R. A. J., and de Rooij, D. G. (1993). A quantitative study of spermatogonial multiplication and stem cell renewal in the C3H/101 F1 hybrid mouse. *Mutat. Res.* 290, 193–200. doi: 10.1016/0027-5107(93)90159-d

Takahashi, K., Tanabe, K., Ohnuki, M., Narita, M., Ichisaka, T., Tomoda, K., et al. (2007). Induction of pluripotent stem cells from adult human fibroblasts by defined factors. *Cell* 131, 861–872. doi: 10.1016/j.cell.2007.11.019

Takahashi, K., and Yamanaka, S. (2006). Induction of pluripotent stem cells from mouse embryonic and adult fibroblast cultures by defined factors. *Cell* 126, 663–676. doi: 10.1016/j.cell.2006.07.024

Tang, F., Barbacioru, C., Wang, Y., Nordman, E., Lee, C., Xu, N., et al. (2009). mRNA-Seq whole-transcriptome analysis of a single cell. *Nat. Methods*. 6, 377–382. doi: 10.1038/nmeth.1315

Tesarik, J., Mendoza, C., and Greco, E. (2000). In-vitro maturation of immature human male germ cells. *Mol. Cell Endocrinol.* 166, 45–50. doi: 10.1016/s0303-7207(00)00296-3

Toyooka, Y., Tsunekawa, N., Akasu, R., and Noce, T. (2003). Embryonic stem cells can form germ cells in vitro. *Proc. Natl. Acad. Sci. U.S.A.* 100, 11457–11462. doi: 10.1073/pnas.1932826100

Virant-Klun, I., Leicht, S., Hughes, C., and Krijgsveld, J. (2016). Identification of maturation-specific proteins by single-cell proteomics of human oocytes. *Mol. Cell. Proteom.* 15, 2616–2627. doi: 10.1074/mcp.m115.056887

Virant-Klun, I., Rožman, P., Cvjeticanin, B., Vrtacnik-Bokal, E., Novakovic, S., Rülicke, T., et al. (2009). Parthenogenetic embryo-like structures in the human ovarian surface epithelium cell culture in postmenopausal women with no naturally present follicles and oocytes. *Stem Cells Dev.* 18, 137–150. doi: 10.1089/scd.2007.0238.cxn

Virant-Klun, I., Stimpfel, M., Cvjeticanin, B., Vrtacnik-Bokal, E., and Skutella, T. (2013). Small SSEA-4-positive cells from human ovarian cell cultures: related to embryonic stem cells and germinal lineage? *J. Ovarian Res.* 6:24. doi: 10.1186/1757-2215-6-24

Virant-Klun, I., Zech, N., Rožman, P., Vogler, A., Cvjetičanin, B., Klemenc, P., et al. (2008). Putative stem cells with an embryonic character isolated from the ovarian surface epithelium of women with no naturally present follicles and oocytes. *Differentiation* 76, 843–856. doi: 10.1111/j.1432-0436.2008.00268.x

von Kopylow, K., Schulze, W., Salzbrunn, A., and Spiess, A. N. (2016). Isolation and gene expression analysis of single potential human spermatogonial stem cells. *Mol. Hum. Reprod.* 22, 229–239. doi: 10.1093/molehr/gaw006

Wang, M., Liu, X., Chang, G., Chen, Y., An, G., Yan, L., et al. (2018). Single-cell RNA sequencing analysis reveals sequential cell fate transition during human spermatogenesis. *Cell Stem Cell* 23, 599–614. doi: 10.1016/j.stem.2018.08.007

Wang, P. J., McCarrey, J. R., Yang, F., and Page, D. C. (2001). An abundance of X-linked genes expressed in spermatogonia. *Nat. Genet.* 27, 422–426. doi: 10.1038/86927

Warmflash, A., Sorre, B., Etoc, F., Siggia, E. D., and Brivanlou, A. H. (2014). A method to recapitulate early embryonic spatial patterning in human embryonic stem cells. *Nat. Methods* 11, 847–854. doi: 10.1038/nmeth.3016

Weber, S., Eckert, D., Nettersheim, D., Gillis, A. J. M., Schäfer, S., Kuckenberg, P., et al. (2010). Critical function of AP-2gamma/TCFAP2C in mouse embryonic germ cell maintenance1. *Biol. Reprod.* 82, 214–223. doi: 10.1095/biolreprod.109.078717

White, Y. A. R., Woods, D. C., Takai, Y., Ishihara, O., Seki, H., and Tilly, J. L. (2012). Oocyte formation by mitotically active germ cells purified from ovaries of reproductive-age women. *Nat. Med.* 18, 413–421. doi: 10.1038/nm.2669

Woods, D. C., and Tilly, J. L. (2012). The next (re)generation of ovarian biology and fertility in women: is current science tomorrow's practice? *Fertil. Steril.* 98, 3–10. doi: 10.1016/j.fertnstert.2012.05.005

Xie, L., Lin, L., Tang, Q., Li, W., Huang, T., Huo, X., et al. (2015). Sertoli cell-mediated differentiation of male germ cell-like cells from human umbilical cord Wharton's jelly-derived mesenchymal stem cells in an in vitro co-culture system. *Eur. J. Med. Res.* 20:9. doi: 10.1186/s40001-014-0080-6

Yamashiro, C., Sasaki, K., Yabuta, Y., Kojima, Y., Nakamura, T., Okamoto, I., et al. (2018). Generation of human oogonia from induced pluripotent stem cells in vitro. *Science* 362, 356–360. doi: 10.1126/science.aat1674

Yang, J., Ryan, D. J., Wang, W., Tsang, J. C., Lan, G., Masaki, H., et al. (2017). Establishment of mouse expanded potential stem cells. *Nature* 550, 393–397. doi: 10.1038/nature24052

Yang, Y., Liu, B., Xu, J., Wang, J., Wu, J., Shi, C., et al. (2017). Derivation of pluripotent stem cells with in vivo embryonic and extraembryonic potency. *Cell* 169, 243–257. doi: 10.1016/j.cell.2017.02.005

Ying, Y., Liu, X. M., Marble, A., Lawson, K. A., and Zhao, G. Q. (2000). Requirement of Bmp8b for the generation of primordial germ cells in the mouse. *Mol. Endocrinol.* 14, 1053–1063. doi: 10.1210/mend.14.7.0479

Yoshida, S., Sukeno, M., and Nabeshima, Y. (2007). A vasculature-associated niche for undifferentiated spermatogonia in the mouse testis. *Science* 317, 1722–1726. doi: 10.1126/science.1144885

Yu, C., Ji, S. Y., Dang, Y. J., Sha, Q. Q., Yuan, Y. F., Zhou, J. J., et al. (2016). Oocyte-expressed yes-associated protein is a key activator of the early zygotic genome in mouse. *Cell Res.* 26, 275–287. doi: 10.1038/cr.2016.20

Yu, J., Vodyanik, M. A., Smuga-Otto, K., Antosiewicz-Bourget, J., Frane, J. L., Tian, S., et al. (2007). Induced pluripotent stem cell lines derived from human somatic cells. *Science* 318, 1917–1920. doi: 10.1126/science.1151526

Zanganeh, B. M., Rastegar, T., Roudkenar, M. H., Kashani, I. R., Amidi, F., Abolhasani, F., et al. (2013). Co-culture of spermatogonial stem cells with Sertoli cells in the presence of testosterone and FSH improved differentiation via up-regulation of post meiotic genes. *Acta Med. Iran.* 51, 1–11.

Zhang, H., Panula, S., Petropoulos, S., Edsgard, D., Busayavalasa, K., Liu, L., et al. (2015). Adult human and mouse ovaries lack DDX4-expressing functional oogonial stem cells. *Nat. Med.* 21, 1116–1118. doi: 10.1038/nm.3775

Zhang, S., Chen, T., Chen, N., Gao, D., Shi, B., Kong, S., et al. (2019). Implantation initiation of self-assembled embryo-like structures generated using three types of mouse blastocyst-derived stem cells. *Nat. Commun.* 10:496. doi: 10.1038/s41467-019-08378-9

Zheng, Y., Thomas, A., Schmidt, C. M., and Dann, C. T. (2014). Quantitative detection of human spermatogonia for optimization of spermatogonial stem cell culture. *Hum. Reprod.* 29, 2497–2511. doi: 10.1093/humrep/deu232

Zhou, Q., Wang, M., Yuan, Y., Wang, X., Fu, R., Wan, H., et al. (2016). Complete meiosis from embryonic stem cell-derived germ cells in vitro. *Cell Stem Cell.* 18, 330–340. doi: 10.1016/j.stem.2016.01.017

Zou, K., Yuan, Z., Yang, Z., Luo, H., Sun, K., Zhou, L., et al. (2009). Production of offspring from a germline stem cell line derived from neonatal ovaries. *Nat. Cell Biol.* 11, 631–636. doi: 10.1038/ncb1869

Zuckerman, S. (1951). The number of oocytes in the mature ovary. *Rec. Prog. Horm. Res.* 6, 63–108.

Conflict of Interest: The authors declare that the research was conducted in the absence of any commercial or financial relationships that could be construed as a potential conflict of interest.

frontiers in Bioengineering and Biotechnology

ORIGINAL RESEARCH
published: 23 July 2020
doi: 10.3389/fbioe.2020.00851

Prediction of Human Induced Pluripotent Stem Cell Cardiac Differentiation Outcome by Multifactorial Process Modeling

Bianca Williams[1†], Wiebke Löbel[2†], Ferdous Finklea[1], Caroline Halloin[2], Katharina Ritzenhoff[2], Felix Manstein[2], Samira Mohammadi[1], Mohammadjafar Hashemi[1], Robert Zweigerdt[2], Elizabeth Lipke[1] and Selen Cremaschi[1]**

[1] Department of Chemical Engineering, Auburn University, Auburn, AL, United States, [2] Leibniz Research Laboratories for Biotechnology and Artificial Organs (LEBAO), Department of Cardiothoracic, Transplantation and Vascular Surgery, Hannover Medical School, Hanover, Germany

OPEN ACCESS

Edited by:
Tiago G. Fernandes,
University of Lisbon, Portugal

Reviewed by:
Steve Oh,
Bioprocessing Technology Institute (A*STAR), Singapore
Carlos Rodrigues,
University of Lisbon, Portugal

***Correspondence:**
Robert Zweigerdt
zweigerdt.robert@mh-hannover.de
Selen Cremaschi
selen-cremaschi@auburn.edu;
szc0113@auburn.edu

[†] These authors have contributed equally to this work

Specialty section:
This article was submitted to Bioprocess Engineering, a section of the journal Frontiers in Bioengineering and Biotechnology

Received: 30 April 2020
Accepted: 02 July 2020
Published: 23 July 2020

Citation:
Williams B, Löbel W, Finklea F, Halloin C, Ritzenhoff K, Manstein F, Mohammadi S, Hashemi M, Zweigerdt R, Lipke E and Cremaschi S (2020) Prediction of Human Induced Pluripotent Stem Cell Cardiac Differentiation Outcome by Multifactorial Process Modeling. Front. Bioeng. Biotechnol. 8:851. doi: 10.3389/fbioe.2020.00851

Human cardiomyocytes (CMs) have potential for use in therapeutic cell therapy and high-throughput drug screening. Because of the inability to expand adult CMs, their large-scale production from human pluripotent stem cells (hPSC) has been suggested. Significant improvements have been made in understanding directed differentiation processes of CMs from hPSCs and their suspension culture-based production at chemically defined conditions. However, optimization experiments are costly, time-consuming, and highly variable, leading to challenges in developing reliable and consistent protocols for the generation of large CM numbers at high purity. This study examined the ability of data-driven modeling with machine learning for identifying key experimental conditions and predicting final CM content using data collected during hPSC-cardiac differentiation in advanced stirred tank bioreactors (STBRs). Through feature selection, we identified process conditions, features, and patterns that are the most influential on and predictive of the CM content at the process endpoint, on differentiation day 10 (dd10). Process-related features were extracted from experimental data collected from 58 differentiation experiments by feature engineering. These features included data continuously collected online by the bioreactor system, such as dissolved oxygen concentration and pH patterns, as well as offline determined data, including the cell density, cell aggregate size, and nutrient concentrations. The selected features were used as inputs to construct models to classify the resulting CM content as being "*sufficient*" or "*insufficient*" regarding pre-defined thresholds. The models built using random forests and Gaussian process modeling predicted *insufficient* CM content for a differentiation process with 90% accuracy and precision on dd7 of the protocol and with 85% accuracy and 82% precision at a substantially earlier stage: dd5. These models provide insight into potential key factors affecting hPSC cardiac differentiation to aid in selecting future experimental conditions and can predict the final CM content at earlier

process timepoints, providing cost and time savings. This study suggests that data-driven models and machine learning techniques can be employed using existing data for understanding and improving production of a specific cell type, which is potentially applicable to other lineages and critical for realization of their therapeutic applications.

Keywords: machine learning, classification, feature selection, human induced pluripotent stem cells, cardiomyocytes, directed differentiation, bioreactor, cell production

INTRODUCTION

The heart is one of the least regenerative organs in the body; therefore, when disease or damage occurs to the myocardium, native cardiac muscle cells, cardiomyocytes (CMs), are replaced with fibrotic scar tissue. Recent work has shown that CMs can be derived from human pluripotent stem cells (hPSCs; including embryonic and induced pluripotent stem cells hESC and hiPSC, respectively) at more chemically defined conditions (Lian et al., 2012; Burridge et al., 2014) and that these cells have immense therapeutic potential (Chong et al., 2014). However, due to the large number of patients that suffer from cardiovascular disease along with the vast number of cells presumably needed for a therapeutic effect, scalable production of CMs in a consistent and reproducible manner is critical for the clinical translation and success of these treatments. Proof-of-concept for the production and directed cardiac differentiation of hPSCs in industry-compatible stirred tank bioreactors (STBRs) has been demonstrated (Kempf et al., 2014, 2015; Kropp et al., 2016; Halloin et al., 2019). However, the experimental development, optimization and upscaling of this complex, multifactorial process is time consuming, costly, and despite the recent success, still highly variable. The multifaceted interplay of numerous cellular, physiological, and mechanical parameters including hPSC expansion at the pluripotent state, impacts their directed differentiation, leading to challenges in establishing robust protocols for their efficient lineage-specific, i.e., cardiac, differentiation in bioreactors. The resulting variability in endpoint cell purity, or CM content, together with time constraints, CMs' phenotype and maturity impede commercial production and progress to clinical translation. This also precludes the use of hPSC-CMs for other mass applications, including high-throughput screenings for drug development and safety pharmacology (Fonoudi et al., 2015; Sun and Nunes, 2017; Machiraju and Greenway, 2019) and faster progress in cardiac tissue engineering (Kensah et al., 2013).

The potential of hPSCs for unlimited proliferation *in vitro* and their ability to differentiate into derivatives of the three germ layers (endo-, ecto-, and mesoderm) paved the way toward clinically relevant mass production of specific progenies required for disease-specific therapies, including CMs (Hazeltine et al., 2013). Cardiomyocyte differentiation is inherently complex; cardiac differentiation from hPSCs occurs through specific stages, including early primitive-streak-like priming, mesendoderm specification, and cardiac progenitor induction, followed by their expansion, terminal differentiation, and maturation (Kempf et al., 2016). Previously, a cardiac differentiation protocol to modulate the WNT signaling pathway in a heart development-like fashion using small molecules was reported; this included early upregulation of the WNT pathway for primitive streak-like mesendoderm priming followed by latter suppression for cardiac progeny specification (Lian et al., 2012). The glycogen synthase kinase 3 (GSK3β) inhibitor CHIR99021 (CHIR) was used to activate the WNT pathway, which inhibits the destruction complex of β-catenin and results in its accumulation. The differentiation outcome is therefore strongly dependent on the β-catenin concentration, which is sensitive to CHIR concentration, the timing of CHIR supplementation, and the timing of subsequent WNT pathway suppression by chemical factors such as IWP2, IWR1, or Wnt-C59 (Lian et al., 2012). Downstream of the chemical WNT pathway modulation, other autocrine and paracrine pathways are activated, in particular, TGF and NODAL, which occur in a cell density-dependent manner previously termed the bulk cell density (BCD; Kempf et al., 2016). Therefore, the process outcome is also influenced by the inoculation and proliferation-dependent BCD, particularly during the first 24 h of differentiation induction, which ultimately impacts the CM yield and content. Even in tightly controlled systems, the inherent complexity of these differentiation steps and the high number of molecular, cellular, environmental and physical parameters makes it challenging to consistently obtain uniform results, which is highly desirable for industrial and clinical applications. Notably, in reply to WNT pathway modulation, differentiation can result not only in the formation of CMs but also in multiple non-CM lineages of endodermal and/or mesodermal origin including, for example, endothelial cells (ECs) and fibroblasts (FBs) (Kempf and Zweigerdt, 2018). Moreover, hPSC-derived CMs may represent a subtype-specific mixture, including cardiac pacemaker-, atrial- and ventricular-like phenotypes, as suggested by their electrophysiological features (Zhang et al., 2009).

Establishing robust and scalable CM production processes from hPSCs is critical for obtaining clinically relevant cell numbers. In contrast to conventional cell culture in a dish, instrumented STBRs have the advantage of enabling continuous monitoring of numerous process parameters. For example, online measurements of pH and dissolved oxygen (DO) provide uninterrupted information on the cellular environment. Furthermore, bioreactor-based suspension culture enables continuous collection of process samples in adequate quantities for offline monitoring of additional parameters such as time-resolved changes in the aggregate size, cell-density (growth kinetics), and glucose and lactate levels, all of which provide valuable information on cell viability, proliferation, differentiation, and their metabolic status. The cultivation of

hPSCs as cell-only aggregates in STBRs enabled the production of millions of cells within one batch (Kropp et al., 2016). A scalable method utilizing spinner flasks for differentiating high purity CMs from hPSCs with scales up to 1 L has been reported with CM content of >96% (Chen et al., 2015). In that study, the impact of several parameters such as small molecule concentration, aggregate size, agitation rate, glucose and lactate concentrations, DO concentration, pH, and induction timing on cardiac differentiation was evaluated. Furthermore, STBR-based suspension culture in relatively large scales (100 mL up to 1 L) has been carried out for the production of CMs from hPSC aggregates (Kempf et al., 2014; Chen et al., 2015; Fonoudi et al., 2015; Halloin et al., 2019). In all these studies, successful CM induction was reported typically yielding >85% CM content. However, it was also highlighted that large inter-process variability exists, which may lead to >96% CM content in some processes but <60% CM content in independent process repeats. In the context of this study, a yield of >90% CM content is considered *sufficient*, i.e., a process success, whereas <90% CM content is considered *insufficient*, i.e., process failure. Given the above indicated multifactorial complexity along the transition of hPSCs into contractile CMs, it is currently not apparent which individual parameter(s) or their combinations are directly involved in causing the undesired process heterogeneity. This fact is a key challenge for the future envisioned CM production at GMP-compliant, industry compatible conditions in multi-liter scales.

Machine learning techniques have been used in bioprocess development for the identification of critical experimental factors, for example, to aid in the optimization of the production of several proteins and cell lines. Du et al. (2016) presented a method for identifying essential model parameters of computer models of cardiac sodium channels using Gaussian process modeling, and for reducing the complexity of the models. Charaniya et al. (2010) identified several process parameters with strong associations to outcomes for the manufacturing of recombinant proteins using support vector machines. Caschera et al. (2011) successfully increased the yield of their cell-free protein synthesis process by 350% via designing experimental conditions using artificial neural networks (ANNs), which were recently also applied to find the optimal harvest time for xylitol production by Pappu and Gummadi (2016). Others have looked at maximizing protein production by identifying and optimizing key factors in the fermentation process, also using ANNs (Sinha et al., 2014; Amiri et al., 2015).

Metabolic pathways are another target for manipulation to maximize protein production. The pathways have been modeled using both principal component analysis (PCA) (Alonso-Gutierrez et al., 2015) and an ensemble of ANNs (Zhou et al., 2018). Sokolov et al. (2017) used regression techniques to achieve improved monoclonal antibody quality, which was measured with 14 quality attributes, including the quantities of charge variants, aggregates, and glycoforms. These attribute values were optimized by changing experimental conditions such as the cell culture media formulations and conditions (pH, temperature) using PCA and partial least squares regression models. Kotidis et al. (2019) determined ranges of process inputs that would consistently meet several protein product quality indicators using global sensitivity analysis.

Although cardiac differentiation from hPSCs in suspension culture has recently become more efficient and robust (Halloin et al., 2019), there still exist opportunities for further understanding and improvement of these processes. For example, limited knowledge exists on how perturbations in bioreactor parameters and culture conditions affect cell yield and CM content. Utilizing data-driven modeling and machine learning techniques to understand mesendoderm differentiation, in particular cardiac priming, is an advantageous initial model. Notably, cardiac differentiation is a somewhat easier and better-studied model of lineage differentiation (Matsa et al., 2014; Kempf and Zweigerdt, 2018; Mummery, 2018) compared to more complex cell types such as hematopoietic lineages (Ackermann et al., 2018). Moreover, the *in vitro* cardiac differentiation process can be controlled by a low number of chemical factors such as the WNT modulators CHIR and IWP and can be completed in 10–14 days from hPSC seeding. Furthermore, there is substantial knowledge and existing data for hPSC-CM differentiation in STBRs due to the large interest in this cell type, including the first mathematical model to understand the controlling factors for cardiac mesoderm specification (Gaspari et al., 2018).

Based on our recent experience in a STBR-based hPSC-CM differentiation process (Halloin et al., 2019), we have here defined the induction of 90% CM content or higher as a "process success"; in contrast, induction of less than a 90% CM content is defined *insufficient* or a "process failure." Using machine learning techniques like classification for the interpretation of existing experimental data sets, the goal of this paper was to identify the most informative parameters predictive of the CM differentiation efficiency in a bioreactor platform. As a result, we here report predictive parameters and algorithms for this process (**Figure 1**). The study supports both the early interruption of failing processes (providing cost and time savings) and the rationale for further process modifications that may ultimately avoid future process failures.

MATERIALS AND METHODS

Basic hiPSC Culture and Directed Differentiation in a Stirred Tank Bioreactor System

The hiPSC line Phoenix (Haase et al., 2017) was cultured in E8 medium as described (Kempf et al., 2015; Halloin et al., 2019). In brief, cells were seeded at 0.5×10^4 cells/ml on Geltrex-coated cell culture flasks in E8 medium supplemented with 10 μM Y-27632 and passaged every 3.5 days.

For process "pre-culture expansion and aggregate formation" (**Figure 2A**), a STBR system (DASbox, Eppendorf) was inoculated with 5×10^5 hiPSCs/ml in E8 supplemented with 10 μM Y-27632 at a final volume of 150 ml per reactor vessel. Approximately 24 h after inoculation, perfusion was initiated with 4.2 ml/h fresh medium, as described in Kropp et al. (2016).

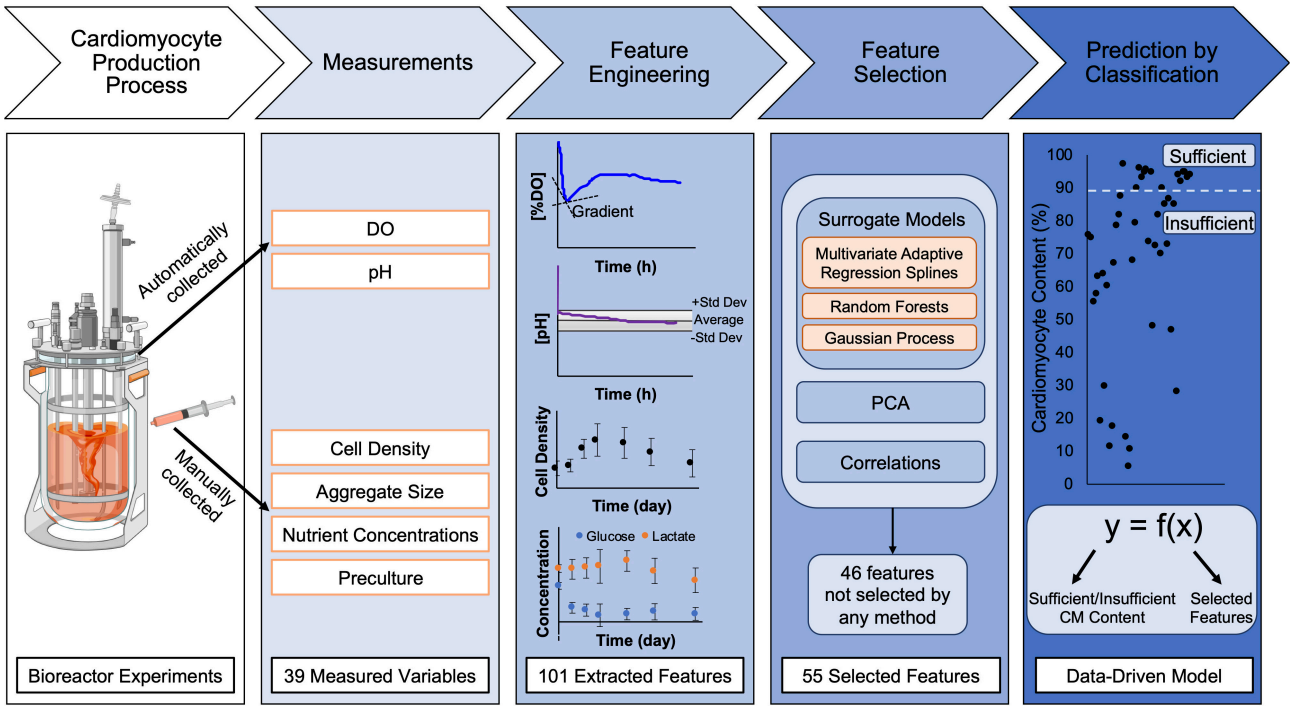

FIGURE 1 | Schematic of process to generate data-driven models for prediction of final CM content from bioreactor experiments. Human pluripotent stem cells (hPSCs) were seeded in bioreactors for expansion for 48 h prior to initiation of cardiac differentiation. To initiate cardiac differentiation, a WNT amplifier, CHIR, was added for 24 h followed by 48 h of WNT inhibition using IWP2. Differentiation experiments lasted 10 days and endpoint analysis for final CM content in bioreactors was performed on differentiation day 10. During the time course of differentiation, the dissolved oxygen (DO) and pH were continually monitored. Samples were collected from the bioreactor during differentiation to analyze cell density, aggregate size, nutrient concentrations, and preculture conditions. From the 39 measured variables throughout differentiation, feature engineering was performed to extract 101 features; for example, the continuous data was separated by differentiation day to obtain averages, gradients, and second derivatives for each day. Feature selection was performed using surrogate models, principal component analysis, and correlations to determine which of the extracted features impacted the variance in the data and outcome of differentiation. After feature selection was performed, data-driven models were developed using surrogate models (MARS, RF, and GP) to predict final CM content by classification of the data in two categories (created with Biorender.com).

For inducing chemically defined, directed differentiation, the cell density of the pre-culture was adjusted at 48 h after single cell inoculation to achieve 5 × 10^5 cells/ml in differentiation medium CDM3 with 5 μM CHIR and 5 μM Y-27632. After 24 h (dd1) the medium was replaced by CDM3 (Burridge et al., 2014) with 5 μM IWP-2; at 72 h (dd3; and every 2–3 days thereafter) 100 ml consumed medium was collected from the bioreactor and replaced with fresh CDM3 (Halloin et al., 2019).

Data Collection, Cell Sampling, Analysis, and Process Grouping Based on CMs Content

Over the course of the cultivation/differentiation process, data was collected as schematically shown in **Figure 2**. DO and pH were constantly measured online, whereas data on the cell density, aggregate diameter, nutrient concentration and CM content were evaluated offline. Bioreactor-derived sampling of cell aggregates in 2 ml medium was performed as previously described (Kempf et al., 2014; Kropp et al., 2016; Halloin et al., 2019). For aggregate analysis, microscopic images were taken (Axiovert A1; Zeiss); on these images, a minimum of 100 aggregates for each sample were assessed by an ImageJ macro to automatically define the mean diameter.

For cell density assessment and flow cytometry analysis, aggregates were dissociated and automatically counted (Vi-CELL XR; Beckman Coulter); in the remaining supernatant, glucose and lactate concentration was measured (BIOSEN C-line; EKF Diagnostic). For flow cytometry, 2.0 × 10^5 cells were fixed, permeabilized and incubated with the following CMs-specific primary antibodies: anti-cardiac Troponin T (1:200, clone 13-11, Thermo Scientific), anti-sarcomeric α-actinin (1:800, EA53, Sigma-Aldrich or 1:20, REA402, Miltenyi Biotec), anti-myosin heavy chain (1:20, MF20, Hybridoma Bank); after incubation with appropriate Cy5-conjugated antibodies (1:200, Jackson ImmunoResearch) data were acquired on an Accuri C6 flow cytometer (BD Biosciences) or MACSQuant Analyzer 10 (Miltenyi Biotec) and analyzed using FlowJo software (Flowjo, LLC).

By flow cytometry analysis of dd10 derived samples using the 3x CMs-specific antibodies outlined above, the average CMs content for each differentiation process was assessed; processes were consequently grouped into those with either *sufficient* or

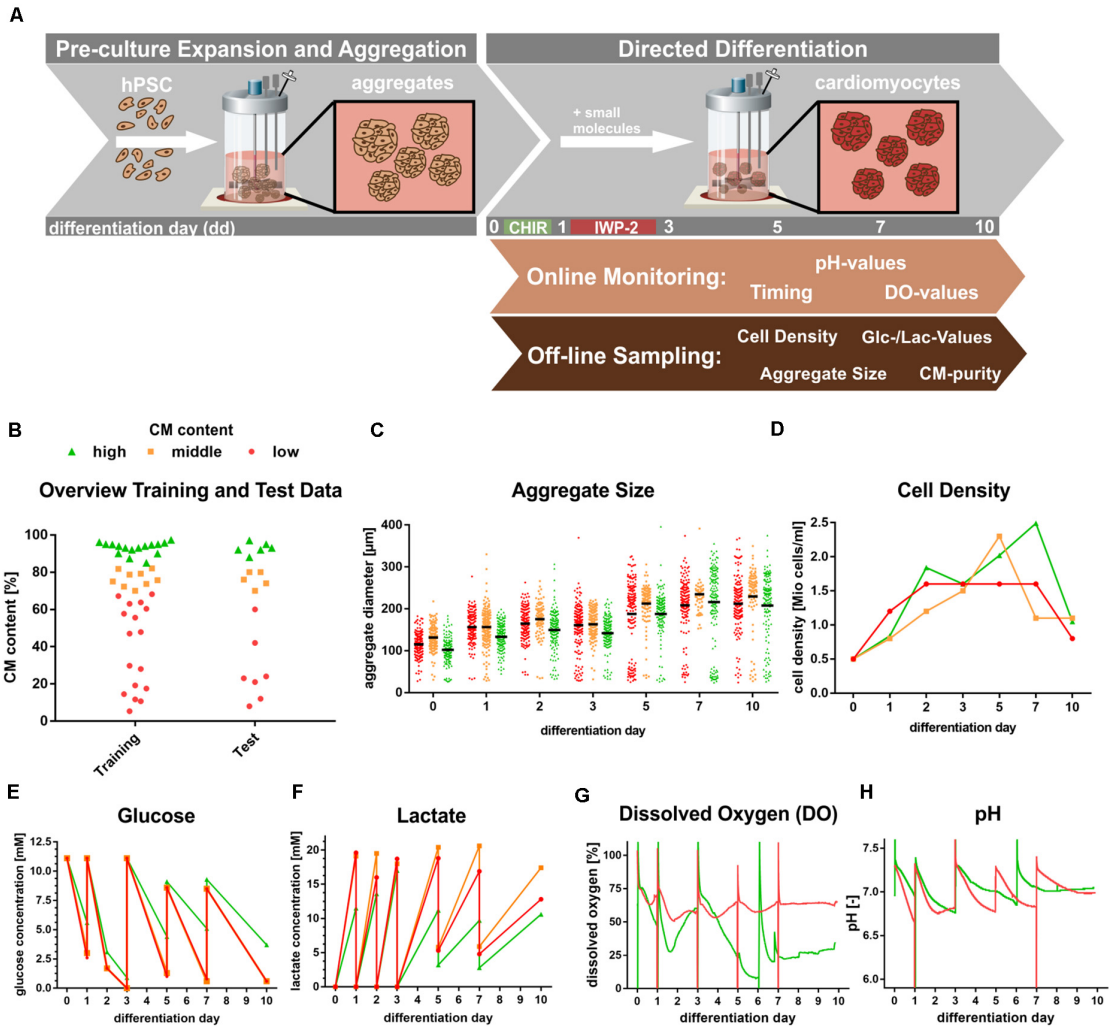

FIGURE 2 | Generation of experimental data. **(A)** Schematic bioreactor set-up of hPSCs expansion in suspension culture followed by directed cardiac differentiation by chemical WNT pathway modulation over 10 days. **(B)** Overview of Training and Test data spreads based on flow cytometry analysis of CM-specific MHC-expression. Definition: Endpoint analysis of processes resulting High ≥85% (green), middle 70–85% CM (orange) and low ≤70% CM content (red). **(C–H)** Representative patterns of process parameters, exemplifying processes typical for high (green), middle (orange), and low (red) CM content at process endpoint (day 10). **(C)** Aggregate size distribution at respective days of differentiation. **(D)** Representative cell density kinetics. **(E,F)** Glucose and lactate values over the course of differentiation. **(G,H)** Representative dissolved oxygen and pH patterns monitored via online analysis over the course of differentiation. Please note that the orange Glucose pattern in **(E)** is hardly visible due to the close overlay of the red pattern. In **(G,H)** only representative DO and pH patterns for respective high (green) and low (red) CM content processes are displayed to avoid loss of clarity by overlapping patterns.

insufficient CM content, with *insufficient* content being defined as a process with a CM content of <90% (**Figure 2B**).

COMPUTATIONAL METHODS AND THEORY

Employing Experimental Data for Feature Engineering

Experimental data used in computational analysis and model development were collected from 58 cardiac differentiation processes in bioreactors; notably, all processes performed in the relevant experimental setup were included in the study without any type of pre-selection procedure to explicitly exclude any investigator-dependent bias. Each of the differentiation process represents a single experimental datapoint to be used for model construction. In a first step, data sets from 42 of these processes were randomly chosen and used for constructing predictive models, while data sets from the remaining 16 processes were reserved for testing the models' performance.

From the data, a set of potential input variables, which we refer to as "bioprocess features," for use in predictive models was generated with the goal of this set fully describing the experimental conditions over the entire differentiation process. For model construction using machine learning, a feature is an

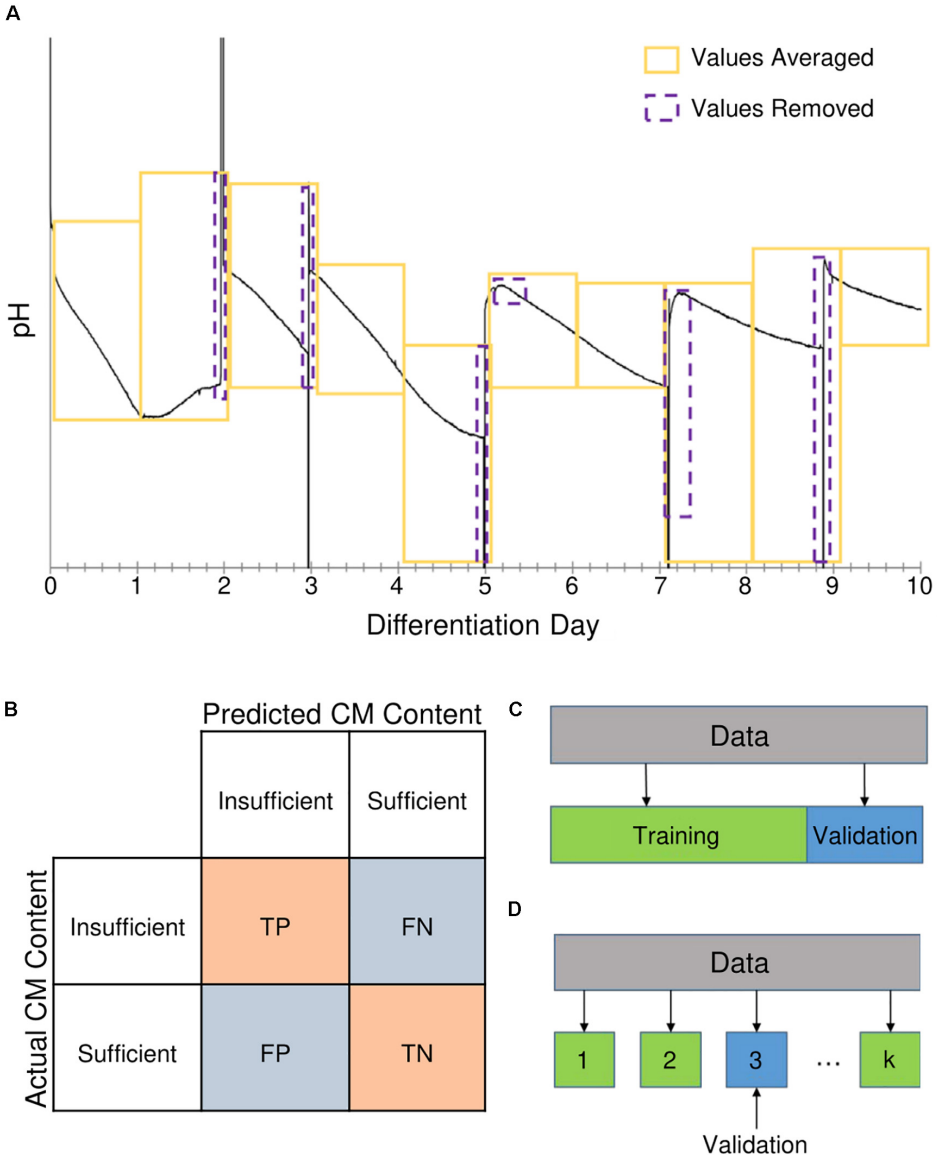

FIGURE 3 | Methods used for generation of features and evaluation of model performance. **(A)** Continuous measurements for pH and dissolved oxygen (DO) concentration were averaged by differentiation day. Yellow boxes represent time periods measurements were averaged over (i.e., differentiation days). Purple boxes represent measurements taken during media changes that were removed from the averaging. **(B)** Model performance was evaluated based on metrics from the classification confusion matrix. When the model correctly identified the result as "insufficient" or "sufficient," it was labeled as a true positive (TP) or true negative (TN) result, respectively. A "sufficient" result incorrectly identified as "insufficient" was considered a false positive (FP), whereas an "insufficient" result incorrectly identified as "sufficient" was a false negative (FN). **(C)** During model training, the performance was validated using leave one out (LOO) cross-validation and Monte Carlo (MC) cross-validation. In LOO cross-validation, a single data point was set aside while the model was built with the remaining data points; a prediction is then obtained for the data point that was left out. This process was repeated for each data point, resulting in a prediction for each data point that were used in calculating performance metrics. **(D)** For MC cross-validation, a set of data was randomly selected to be excluded for validation, and the model was built using the remaining data.

individual measurable or derived properties (using measured) of the system that is being modeled. Available experimental conditions included the rotation speed in the bioreactor and measurements such as differentiation day (dd) dependent cell densities, aggregate sizes, and nutrient concentrations, and measurements of DO concentration and pH over the course of the experiment. Examples of bioprocess features and how the data was collected are summarized in **Figures 1**, **2**.

The DO concentration and pH measurements were included as features by averaging their values over each day of the differentiation, illustrated in **Figure 3A**. Additional features were engineered from this data, as well as other time-dependent measurements, to capture how the conditions in the bioreactor were changing over time. These additional features were generated by estimating gradients and second derivatives for the cell density, aggregate size, DO concentration, and pH

measurements, resulting in a final set of 101 potential bioprocess features. The full list of bioprocess features is provided in **Supplementary Table 1**. Gradients and second derivatives were estimated using Eqs. (1) and (2),

$$g_{t_i} = \frac{y_{t_i} - y_{t_{i-1}}}{t_i - t_{i-1}} \quad (1)$$

$$h_{t_i} = \frac{g_{t_i} - g_{t_{i-1}}}{t_i - t_{i-1}} \quad (2)$$

where g_{t_i} and h_{t_i} are the gradient and second derivative, respectively, of bioreactor condition y at timepoint t_i .

Feature Selection Methods

Because of the large number of features (101) compared to the number of experimental data points (58), feature selection was performed on the available data to discover which of the bioprocess features were most influential and predictive of the cardiomyocyte content on dd10. The feature selection methods employed include correlation coefficients, PCA, and the built-in feature selection capabilities of the machine learning techniques investigated for predictive modeling. Two sets of features, Feature Set 1 and Feature Set 2, were considered, each with bioprocess features measured at earlier points in the differentiation process. Feature Set 1 consists of all the collected bioprocess features measured up until the seventh differentiation day 7 (dd7). Feature Set 2 consists of bioprocess features measured up until the fifth differentiation day 5 (dd5).

The dd7 and dd5 timepoints were chosen in order to use as much data as possible without using any data near the endpoint of the differentiation, such as dd9. Preliminary proof-of-concept studies revealed that classification was possible using data collected up to and including dd7, initiating analysis investigating the possibility of earlier predictions. Based on this analysis, dd5 was chosen as the earliest possible timepoint, as classification using data from earlier points in the differentiation did not yield satisfactory predictive capabilities.

Correlations

Pearson correlation coefficient

The Pearson correlation coefficient measures the linear relationship between two variables. Its value ranges from −1 to 1. A value of −1 corresponds to a perfect negative linear relationship between the variables, while a value of 1 indicates a positive linear relationship. A value of 0 demonstrates no linear correlation between the variables (Soper et al., 1915).

Spearman correlation coefficient

The Spearman correlation coefficient measures the strength and direction of a monotonic relationship between two variables. Its value ranges from −1 to 1. A value of 0 indicates no correlation between the variables. Values of −1 or 1 indicate a perfect negative or positive correlation, respectively (Spearman, 1904).

Principal Component Analysis (PCA)

Principal component analysis is a statistical dimension reduction tool. The method transforms a set of possibly correlated variables to uncorrelated principal components (PCs). It identifies a new set of orthogonal axes in the direction of the highest variance of the data. Each of the axes, which is a linear combination of original axes, represents a PC. Principal components are assigned in ordinal format with the first PC explaining the highest percentage of the variance and the last PC the least. The PCs with the lower ranks are generally not considered in further analysis reducing the number of dimensions while preserving much of the original variance (Hotelling, 1933).

Machine Learning Techniques

Multivariate Adaptive Regression Splines

Multivariate adaptive regression splines (MARS) models are non-parametric statistical models that consist of a linear summation of basis functions (Friedman, 1991). In general, basis functions are either a constant, a hinge function, or the product of two or more hinge functions. For the MARS models trained in this study, the Sci-Kit Learn pyEarth software package was used (Pedregosa et al., 2011). Detailed information MARS models and the other machine learning techniques described in this section are provided in the **Supplementary Material** (see section "Extended Machine Learning Technique Descriptions").

Random Forests

Random forests (RFs) are a machine learning method that utilizes a set of decision trees for predicting an output based on input data. Each tree is built independently based on a random subspace of the training data. The final output of a random forest model is determined by averaging the output value of every tree in the forest (Breiman, 2001). The features are selected according to the importance level calculated by the random forest model. The importance level is based on the impact of a feature on improving the separation of the data in each decision node of the tree. For the RF models trained in this study, the Sci-Kit Learn RandomForestRegressor software package was used to train forests with 5 trees (Pedregosa et al., 2011).

Gaussian Process Regression

Gaussian process regression (GPR) is a non-parametric machine learning method where the prediction of the output corresponding to an unknown input is calculated based on a weighted average of outputs for known inputs using a similarity metric: the kernel function (Rasmussen and Williams, 2005). The kernel function used for all GPR models in this paper is a radial basis function.

Gaussian process regression can be used for feature selection with its built-in automatic relevance determination (ARD) method. Further sensitivity analysis (Eq. 4) on the ARD results (Blix and Eltoft, 2018) provides an even greater separation of the features for selection. For the GPR models trained in this study, the Sci-Kit Learn GaussianProcessRegressor software package was used (Pedregosa et al., 2011).

Cardiomyocyte Content Classification

A binary process classification based on the CM content (%) at process endpoint (dd10) was applied, and the two classes defined were: "*sufficient*" for: CM content equal to and above 90%, and "*insufficient*" for CM content below 90%. A binary classification

model was chosen after an initial analysis with a multiclass model revealed that the available bioprocess data was not rich enough to train a multiclass model at this time.

To enable CM content prediction based on early process data, two regression models using MARS and GPR were built, and the data points were assigned to their classes (i.e., *sufficient* or *insufficient*) based on this predicted CM content value. For RFs, the classification is conducted directly using the classifier models, constructed by the RF.

To evaluate and compare the performances of the classification models, four metrics were considered: accuracy, precision, recall, and the Matthews correlation coefficient (MCC). The range for the first three metrics is zero to one, and MCC is between −1 and 1. These metrics are calculated based on the confusion matrix (Sokolova and Lapalme, 2009), which is illustrated in **Figure 3B**. The confusion matrix describes the performance of a classification model (algorithm). In this paper, we assign the *insufficient* CM content class as the positive class (**Figure 3B**) and the *sufficient* class as the negative one (**Figure 3B**). The error of the predictions is broken down for each class using the confusion matrix. The four cells of the confusion matrix correspond to true positive, false negative, false positive, and true negative. The values associated with each of the components give information about how many of the positive/negative classification results were correctly predicted by the model.

Classification Model Performance Metrics

Accuracy

Accuracy calculates the proportion of correct classifications (Sokolova and Lapalme, 2009). According to Eq. (5), accuracy is the number of all true positives and negatives compared to all prediction results. Accuracy of one indicates that the classification has been conducted accurately and that all the points with *sufficient* or *insufficient* CM content have been included in the right class ($FP + FN = 0$). Zero accuracy defines a totally wrong classification model, which is not able to predict the label of the points correctly.

$$Accuracy = \frac{(TP + TN)}{(TP + TN + FP + FN)} \tag{5}$$

Precision

Precision (Eq. 6) gives information about the proportion of the times the points identified as positive were truly positive (Sokolova and Lapalme, 2009). Precision of one means that all the positive results are actually positive outcomes. When a classifier model with precision of one predicts *insufficient* CM content for a point, it is supposed to have *insufficient* CM content in practice. Value of zero for precision indicates that all the identified positive outcomes are false.

$$Precision = \frac{TP}{(TP + FP)} \tag{6}$$

Recall

Recall, Eq. (7), is the proportion of actual positive results which were identified as positives (Sokolova and Lapalme, 2009). The value of one for recall demonstrated that the model is able to classify all the actual positive results as positive. In CM content case, all the *insufficient* points would be identified as *insufficient* using a model with recall equal to one. When all the positive classes are falsely identified negative, the value of recall equals to zero.

$$Recall = \frac{TP}{(TP + FN)} \tag{7}$$

Matthews's correlation coefficient (MCC)

Matthews's correlation coefficient (Eq. 8) defines the correlation between the predicted and actual classifications for all data points (Matthews, 1975). Value of one for MCC means there is a strong correlation between the predicted results and the actual values, indicating that the predicted label is correct for all the points. Value of −1 for MCC metric demonstrates a strong inverse correlation. Values of zero for MCC corresponds to no correlation between the predicted and actual results.

$$MCC = \frac{(TP \times TN) - (FP \times FN)}{\sqrt{(TP + FP)(TP + FN)(TN + FP)(TN + FN)}} \tag{8}$$

The classification model performance metrics, accuracy, precision, recall, and MCC, were calculated using two different cross-validation techniques: (1) leave one out (LOO) cross-validation (**Figure 3C**), and (2) Monte Carlo (MC) cross-validation (**Figure 3D**). Cross-validation is a tool for assessing how well a model can be generalized to new data, which the model has never seen. In MC cross-validation, a set of data is selected randomly to be excluded for validation, and this data set is called the validation set. The model is built using the remaining data, and the model is used to predict the classes for the validation set (Burman, 1989). These predictions are used to calculate performance metrics. In LOO cross-validation, a single data point is set aside (i.e., left out) for validation. The model is built using the remaining data points, and a prediction is obtained for the data point that was left out. This process is repeated for each data point, resulting in a prediction for each. **Figures 3C,D** illustrates how these cross-validation methods were used for evaluating the performance metrics (Wong, 2015).

RESULTS AND DISCUSSION

Feature Selection

Two different sets of features were considered for building the classification models. Feature Set 1 contained all potential bioprocess features measured through dd7. Feature Set 2 contained all features measured through dd5. Feature selection was performed on each feature set separately to identify potential features for predicting CM content class on dd10. Classification models were then built using these potential feature sets. We employed PCA, and built-in capabilities of MARS, RFs, and GPR for feature selection. Feature selection resulted in eight potential feature sets for classifying the CM content on dd10. A visual summary of the feature selection results is provided in **Figure 4**.

Principal component analysis yielded five principal components (FS1-PCA) that explained 94% of the variance

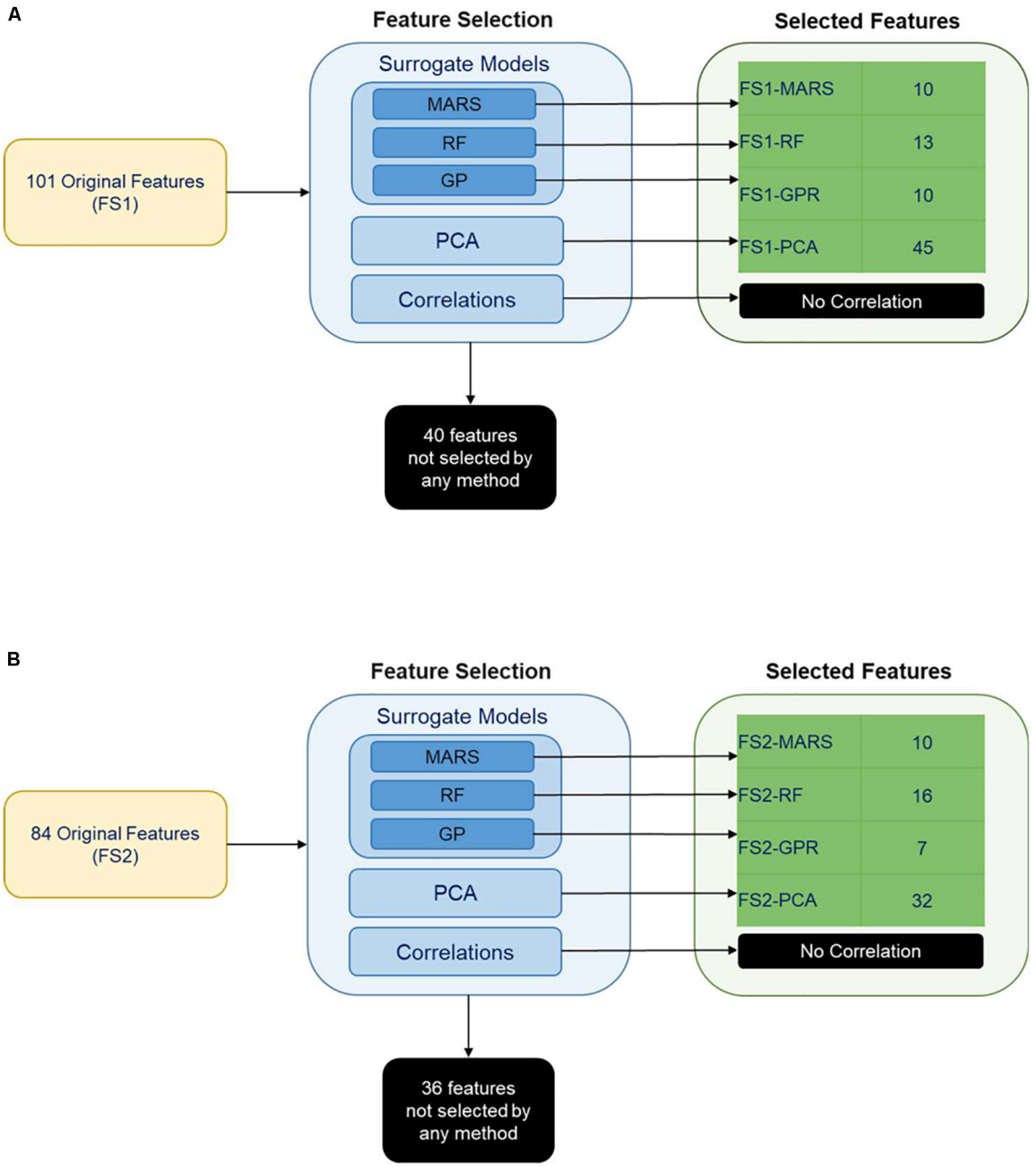

FIGURE 4 | Feature selection results for features selected from **(A)** feature set 1 and **(B)** feature set 2. MARS (Multi-adaptive regression splines), RF (Random Forest), GPR (Gaussian process regression) were the surrogate models implemented for the selection of the features that have a significant impact on classification. The other feature selection methods were PCA (Principal component analysis) and correlations between the variables.

in the input data for Feature Set 1 (**Figure 4A**) and yielded four principal components (FS2-PCA) that explained 94% of the variance for Feature Set 2 (**Figure 4B**). None of the principal components or bioprocess features strongly correlated with the CM content. The strongest linear correlation between a feature and the CM content was −0.51, and that feature was the time that the differentiation media was supplemented with WNT inhibitor IWP2. This lack of correlation indicates that none of the individual bioprocess features alone suffices to make a prediction on the CM content and that other means, such as machine learning techniques, are necessary to investigate the relationship. The number of features selected by each machine learning technique is provided in **Figure 4**. A list of features selected by each method is available in **Supplementary Tables 1**, **2**. **Tables 1**, **2** give a listing of the bioprocess features selected by each modeling technique for Feature Sets 1 and 2, respectively.

TABLE 1 | Bioprocess features selected by each surrogate modeling technique from Feature Set 1 (X = selected).

Feature	FS1-RF	FS1-GPR	FS1-MARS
Average DO concentration dd0	X		
Average DO concentration gradient d0	X		X
Average DO concentration gradient dd2		X	
Average DO concentration gradient dd6	X		
Average DO concentration gradient dd7		X	
d0 average pH gradient	X		
dd0 average pH gradient		X	
dd0 average acceleration of cell density normalized DO gradient	X		
dd0–dd1 cell density gradient		X	X
dd1 aggregate size			X
dd1 cell density	X		
dd2 average pH	X		
dd7 average pH		X	
dd3 aggregate size			X
dd3 average acceleration of DO gradient			X
dd3 average pH gradient	X		
dd3 average acceleration of cell density normalized DO gradient			X
dd5 average pH gradient			
dd5–dd7 aggregate size gradient	X		
dd5–dd7 cell density gradient			X
dd7 cell density	X	X	
Cell density normalized DO concentration dd2			X
Cell density normalized DO concentration dd3		X	X
Cell density normalized DO concentration dd7	X		
Average cell density normalized DO concentration gradient dd2	X	X	
Average cell density normalized DO concentration gradient dd5		X	
Average cell density normalized DO concentration gradient dd7	X		
IWP2 treatment time [h]			X
Preculture time [h]		X	

TABLE 2 | Bioprocess features selected by each surrogate modeling technique from Feature Set 2 (X = selected).

Feature	FS2-RF	FS2-GPR	FS2-MARS
Average DO concentration d0	X		
Average DO concentration dd0	X		
Average DO concentration dd2			X
Average DO concentration dd4	X		
Average DO concentration gradient d0	X		
Average DO concentration gradient dd2	X	X	
Average DO concentration gradient dd4	X		X
Average DO concentration gradient dd5	X		
d1 average pH gradient			X
dd0 aggregate size			X
dd0 cell density			X
dd0–dd1 cell density gradient		X	
dd1 average pH	X		X
dd1 average acceleration of cell density normalized DO gradient	X		
dd2 aggregate size	X		
dd2 average acceleration of DO gradient		X	
dd2 average pH			X
dd2 average pH gradient	X		
dd2 average acceleration of cell density normalized DO gradient	X		
dd2–dd3 aggregate size gradient	X		
dd3–dd5 cell density gradient			X
dd4 average pH gradient		X	
dd5 average acceleration of cell density normalized DO gradient	X	X	
Cell density normalized DO concentration dd1	X		
Average cell density normalized DO concentration gradient dd5		X	
IWP2 treatment time [h]		X	X
Overall aggregate size gradient	X		
Overall density gradient			X

The features selected by MARS, RF, and GPR encompassed features with known biological implications as well as potential mechanistic explanations, although the impacts of the features in combination have not been previously investigated. It is well established in developmental biology, that a bi-phasic WNT pathway modulation is essential for cardiac mesoderm specification and subsequent CM formation. As outlined in **Figure 2A**, cardiac differentiation in this study was controlled by chemical WNT modulators added in a temporal pattern. hPSC differentiation was initiated by the addition of the chemical WNT pathway accelerator CHIR on dd0 for 24 h followed by 48 h of WNT attenuation through addition of IWP2. The small molecule, CHIR, is solely sufficient to induce early primitive streak (PS)-like priming in hPSCs in a concentration-dependent manner (Lian et al., 2012; Kempf et al., 2016; Gaspari et al., 2018). The higher the CHIR dose, the faster hPSC differentiation will progress from an (anterior) endoderm-like fate toward cardiac mesoderm specification and subsequently toward more posterior fates such as somatic mesoderm-like PS priming. The dynamics of the CHIR induced differentiation processes, particularly during the first 24 h of differentiation, play an important role regarding the degree of heterogeneity of the cardiac differentiation process, of which identifying the underlying factors is one of the objectives of this study. However, our recent work revealed that the accelerating effect of CHIR on differentiation progression is

counteracted by cell-secreted factors such as the transforming growth factor beta (TGFb) family members, Nodal signaling antagonists left-right determination factor 1 (LEFTY1) and CERBERUS (CER1) (Kempf et al., 2016). The cell density directly impacts the accumulation of such secreted factors, particularly during the first 24 h of differentiation (dd0–dd1) and plays a key role in the subsequent specification of cell fates and subsequently the CM content (assessed on dd10 in this study); this suggests that the selected features "*dd0–dd1 cell density gradient*" and "*dd1 cell density*" identified by our modeling approach, have known mechanistic impacts on CM differentiation.

It is of biological relevance that the "*IWP2 treatment time*" was also selected as an important feature for model development, given the importance of temporal WNT signaling for proper lineage differentiation in embryogenesis and *in vitro* as well (Ueno et al., 2007; Burridge et al., 2014; Halloin et al., 2019). However, the feature selections "*dd1 average acceleration of DO gradient*" and "*dd3 cell density normalized DO concentration*" are non-obvious, interesting new observations. These model-extracted features strongly suggest that an acceleration/deceleration of the (cell density-normalized) DO gradient at a specific process interval impacts the final CM content. This may relate to process-dependent changes in the overall density of (oxygen-consuming) cells, as well as differentiation stage-dependent changes in cells' metabolism. During the differentiation process, the metabolism switches from predominantly glycolysis typical of undifferentiated hPSCs (Kropp et al., 2016), toward oxidative phosphorylation as a result of CM specification and maturation (Hu et al., 2018). Thus, our modeling approach suggests a concrete novel hypothesis requiring future experimental validation. Example values for these DO related features are illustrated in **Supplementary Figure 1**.

After mesoderm priming and cardiac progeny specification during the first ∼72–96 h of our differentiation protocol, progressive differentiation into functional, sarcomere protein expressing CMs occurs in the period between dd5 and dd10 (Halloin et al., 2019). It is thus interesting to note the MARS model selection of the features "*dd5–dd7 cell density gradient*" and "*dd5 average DO concentration gradient*" as being important for the CM content. A possible interpretation of this result is that the dd5–dd7 cell density/DO patterns may impact (i.e., inhibit or promote) the maturation of cardiac progenies into functional CMs. The cell density-dependent secretion of factors during this differentiation stage may impact the sarcomere protein expression including isotype switches resulting in CM maturation (Hu et al., 2018) equivalent to cell density-dependent mechanisms of primitive streak-like priming during the first 24 h of differentiation. Furthermore, since the DO gradient correlates to the cell density gradient, the "*dd5 average DO concentration gradient*" feature may relate to the "*dd5–dd7 cell density gradient*" feature.

Using the feature selection components of these data-driven models provides the possibility of examining bioprocess features in combination and in more detail. Some of the identified features presumably have known mechanistic impacts on the outcome of cardiac differentiation, as outlined above, thereby indicating the validity of our approach. However, there are several features identified by the feature selection but have not been previously examined or identified as important for predicting the CM content, including the dd5–dd7 cell density and DO gradients.

On the other hand, it is worth noting that, for example, supraphysiological glucose concentration has been found to impact the cardiac differentiation of hESC (Crespo et al., 2010; Yang et al., 2016). In our model, the glucose and the related lactate concentration patterns were not classified as important features, i.e., were not identified as being predictive of the CM content in our differentiation process. But this finding is not excluding, *per se*, that the glucose concentration is important for the cardiomyogenesis of hPSCs.

This in mind, it is important to note, that the impact of a selected feature on the differentiation outcome does not presumptively indicate a mechanistic relationship. This impact may be correlative only (rather than causative), potentially a result of processes not captured by the input data or through feature engineering. However, the identified features are informative for guiding future validation experiments; these can then be used to build more mechanistic models for understanding and potentially reducing variability in cardiac differentiation.

Classification Results

Classification models were constructed for predicting the outcome of the bioreactor experiments on dd10 using features measured up to dd7 and up to dd5, using each of the machine learning techniques described in Sections "Multivariate Adaptive Regression Splines," "Random Forests," and "Gaussian Process Regression." The models were built using the bioprocess features selected from Feature Set 1 (for predicting using features measured until dd7) and Feature Set 2 (for predicting using features measured until dd5). Results for classification model performance for each of the eight feature sets from the feature selection are summarized in **Tables 3**, **4**. Results were obtained using LOO cross-validation and are presented for both the bioprocess features selected by the built-in feature selection for each model, as well as for the PCs obtained from PCA. Both feature sets contained 42 data points chosen from the original set of 58 experiments for training. A visual summary of the results for each classification method with its associated feature sets is depicted in **Figure 5**. For all of the feature sets generated from Feature Set 1, for all of the techniques investigated, classification using the model-selected features always had a better performance than the principal components from PCA. Only two classification model-feature set combinations achieved favorable results for all four of the performance metrics, which is illustrated in **Figure 5**. RFs trained with feature set FS1-RF and GPR trained with FS1-GPR perform similarly for predicting if CM content will be *insufficient* for continuing the experiment. Both methods obtained accuracies of 90% and precisions around 90%, meaning that if a model predicts the CM content will be *insufficient*, there is a 90% probability that it is *insufficient*.

Similar to those generated from Feature Set 1, the model-selected feature sets for Feature Set 2 resulted in a better performance than the PCs. This indicates that while the PCs successfully explain the variance in the data, they fail to accurately

TABLE 3 | Classification model performance (calculated with LOO cross-validation) for models trained with features from Feature Set 1.

	MARS		RFs		GPR	
	FS1-MARS	**FS1-PCA**	**FS1-RF**	**FS1-PCA**	**FS1-GPR**	**FS1-PCA**
Accuracy	0.74	0.64	**0.90**	0.74	**0.87**	0.67
Precision	0.81	0.66	**0.90**	0.74	**0.89**	0.67
Recall	0.93	0.96	**0.96**	0.93	**0.96**	1.0
MCC	0.55	−0.11	**0.78**	0.36	**0.74**	0

Bold values indicate performance metrics for recommended, best-performing models.

TABLE 4 | Classification model performance (calculated with LOO cross-validation) for models trained with features from Feature Set 2.

	MARS		RFs		GPR	
	FS2-MARS	**FS2-PCA**	**FS2-RF**	**FS2-PCA**	**FS2-GPR**	**FS2-PCA**
Accuracy	0.62	0.67	**0.84**	0.67	0.69	0.67
Precision	0.68	0.68	**0.82**	0.73	0.70	0.67
Recall	0.82	0.93	**0.96**	0.79	0.93	1.0
MCC	0.04	0.11	**0.62**	0.22	0.23	0

Bold values indicate performance metrics for recommended, best-performing models.

characterize the relationship between the features and the cardiomyocyte content. When only the features up to dd5 are considered, RFs most successfully predict if the CM content will be *sufficient*. The decrease in the performance for GPR models is possibly due to the removal of the dd7 average value of the DO concentration gradient. This dd7 feature was identified as relevant for predicting dd10 CM content using a GPR and could be an indicator of levels of cell metabolism.

Table 5 contains examples of bioreactor experiments and the predictions for those experiments given by GPR models using FS1-GPR, as well as the values of the bioprocess features indicated by the GPR model to be relevant. For some of the experiments with different prediction types, the feature values are quite similar, for example, the *"preculture time"* of experiments 36 and 26. However, for some experiments with the same prediction, the features have a wide range of values, for example, the *"dd2 cell density normalized DO gradient"* of experiments 16 and 26. These disparities indicate that the individual features alone are not sufficient to determine what will make a good or bad prediction and that all the selected features need to be considered as a whole.

For model selection purposes, the MCC gives the most important information about how the models perform, as it gives a measure of the correlation between the predicted and actual classes, similar to an R^2 coefficient for a regression model. The other performance metrics should be assessed for their importance based on what the experimental goal of the bioprocess is. For example, if the differentiation process is being studied primarily for data collection and evaluating the outcomes, then maximizing the number of experimental datapoints being retained becomes more important, meaning that the precision of the model needs to be prioritized. However, for another application, such as an *in vivo* study, it would be more beneficial to stop unsuccessful experiments and start over, meaning that recall and accuracy of the model in identifying which experiments would not produce high CM contents would be prioritized. RF and GPR models were confirmed to be the most predictive of the

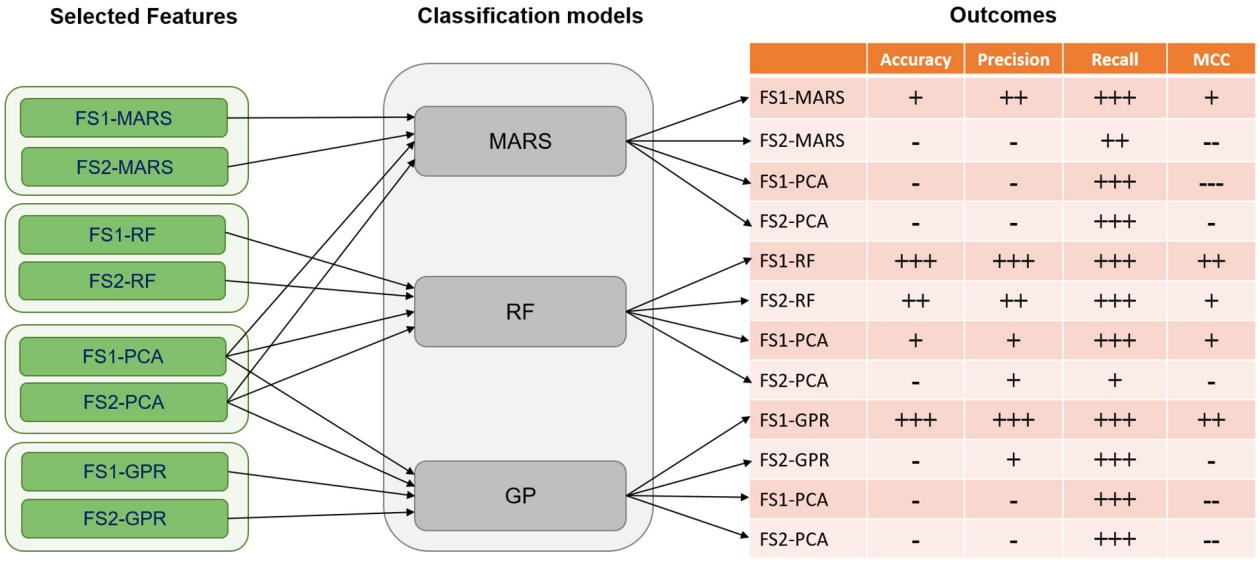

FIGURE 5 | Classification results were based on four metrics including accuracy, precision, recall, and MCC (Matthews correlation coefficient) for selected features of FS1 and FS2. The classification models of MARS (Multi-adaptive regression splines), RF (Random Forest), and GPR (Gaussian process regression) were implemented. For accuracy, precision, and recall the values are categorized as follows: (---) for values < 0.3, (--) for $0.3 \leq$ values < 0.6, (-) for $0.6 \leq$ values < 0.7, (+) for $0.7 \leq$ values < 0.8, (++) for $0.8 \leq$ values < 0.9, and (+++) for value ≥ 0.9. Moreover, for the MCC metric, the categorization was done as: (---) for values < 0, (--) for $0 \leq$ values < 0.1, (-) for $0.1 \leq$ values < 0.3, (+) for $0.3 \leq$ values < 0.7, (++) for $0.7 \leq$ values < 0.9, and (+++) for value ≥ 0.9.

TABLE 5 | Examples of selected features from GPR-FS1.

Exp. No.	Prediction	Average DO concentration gradient dd2	Average cell density normalized DO concentration gradient dd2	Preculture Time [h]	Average DO concentration gradient dd7	dd0–dd1 cell density gradient	dd0 average pH gradient	Average cell density normalized DO concentration gradient dd5
3	TP	2.06	1.96	53	−3.23	0.02	−0.22	−6.06
40	TP	−1.01	−0.49	48	−1.71	1.34	−0.18	−3.08
16	FP	1.08	0.58	46	0.63	0.41	−0.21	−1.54
26	FP	−3.07	−1.83	48	−0.34	0.34	−0.03	−1.77
21	TN	−1.40	−1.06	47	0.17	0.29	−0.03	−1.75
42	TN	−1.13	−0.60	48	−0.22	0.62	−0.01	−2.03
36	FN	−0.76	−0.61	48	−6.51	1.60	−0.05	−3.48
	Minimum	−80.07	−47.24	45	−6.51	−0.76	−0.23	−17.33
	Maximum	14.37	7.00	56	9.61	2.63	0.08	3.73

TABLE 6 | Model performance on test data.

	RFs		GPR	
	FS1-RF	**FS2-RF**	**FS1-GPR**	**FS2-GPR**
Accuracy	**0.89**	**0.83**	0.83	0.72
Precision	**0.92**	**0.81**	0.92	0.72
Recall	**0.92**	**1.0**	0.85	1
MCC	**0.72**	**0.57**	0.61	0.11

Bold values indicate performance metrics for recommended, best-performing models.

TABLE 7 | Model performance with constant IWP2 time.

	FS1-RF		FS2-RF	
	LOO	**Monte Carlo**	**LOO**	**Monte Carlo**
Accuracy	0.90	0.90	0.92	0.85
Precision	0.91	0.90	0.91	0.86
Recall	1.0	0.93	0.95	0.93
MCC	0.90	0.82	0.84	0.75

dd10 cardiomyocyte content because their MCC values (around 0.80) and their accuracy and precisions of about 90% were higher than the other models investigated.

After testing how the models performed on the original dataset, their performance was evaluated using the test data. The test data consisted of data from the 16 processes that were not used for feature selection and model construction. The values of the selected features from those 16 "control processes" were used as inputs to make predictions of the final CM classification employing the trained models (**Figure 1** Prediction by Classification), and those predictions were compared to the actual classifications from the process data. Since MARS had the worst performance for both feature sets, it was excluded from the analysis. The results are presented in **Table 6**. RFs and GPR had a similar performance for the test data for feature set FS1-GPR, both with an accuracy of 89%, precision and recall near 90%, and MCC values of 0.72. However, for the sets selected from feature set 2, RFs outperformed GPR. The results obtained for the test data are comparable to those for the data the models were trained on with LOO cross-validation, indicating that the models accurately captured the relationship between the features and the CM content necessary to make the classifications, while avoiding overfitting.

The "*IWP2 treatment time*" feature was consistently chosen as having high importance for the prediction of the CM content. This feature describes the amount of time that the IWP2 molecule was allowed to remain in the bioreactor system, i.e., impact the differentiation process. However, this feature was only modulated for a fraction of the process runs and held constant at exactly 48 h for the rest. To evaluate if our models were able to classify the CM content without using that feature, an additional dataset was constructed. This data set was thus exclusively derived from the original set of 58 processes using only those process runs where the time of IWP2 presence was held constant at 48 h, and the "*IWP2 treatment time*" feature was excluded in the analysis. Since RFs performed well for all the previously considered feature sets, the performance was only evaluated using this model. LOO cross-validation and Monte Carlo cross-validation were used to calculate the performance metrics. The Monte Carlo cross-validation used a test set size of 5 and 40 Monte Carlo trials. The results are summarized in **Table 7**. It is thus worth highlighting that, when the IWP2 feature is removed, RFs still successfully predict *insufficient* CM content with comparable performances for both LOO and Monte Carlo cross-validation for all the feature sets.

CONCLUSION

In this paper, we have constructed data-driven models for prediction of the CM content on dd10 of hPSC differentiation processes, using existing data sets from bioreactor-based experiments. Using features up to dd7, we were able to identify if an experiment would have an *insufficient* final CM content

of less than 90% with 90% accuracy and >90% precision with both RF and GPR models. Furthermore, we were able to identify if an experiment would have an *insufficient* final CM content on dd5 with 84% accuracy with a RF model. Through feature selection methods, these predictions used less than 16% of the collected data, potentially reducing the amount of resource-intense manual collection of data. Although these models can accurately and precisely predict final CM content, they do not provide any insight into the overall quantity of CMs produced or the resulting functionality and maturity of these cells. In addition, the prediction models were only constructed for small set of data with limited ranges of all the features. However, the ability to model the outcome of differentiation experiments at an early stage of differentiation, enables the timely interruption of failing experiments, providing savings in both time and resources. More importantly, results from the study provide valuable hypotheses for further experiments to improve robustness and reproducibility of cardiac differentiation processes, and have the potential to be leveraged for a broad variety of hPSC-derived cell and tissue production experiments.

DATA AVAILABILITY STATEMENT

The datasets generated for this study can be found in the online repositories. The names of the repository/repositories and accession number(s) can be found below: The datasets will be made available in the Cremaschi Group Github repository (https://github.com/CremaschiLab/Cardiac_Differentiation_Modeling).

AUTHOR CONTRIBUTIONS

BW performed all of the computational analysis and model development tasks, including the construction of the feature sets, feature selection, classification model construction, and wrote the related sections of the manuscript. CH and WL performed the experimental work, with assistance from FM. KR, CH, and WL collected and organized the experimental data into an appropriate database. RZ, CH, WL, EL, and FF gave input on biological implications of the results from the computational analysis. The study was conceptualized by SC, EL, RZ, and CH. SC, EL, and RZ provided supervision and guidance for the work. All authors contributed to manuscript drafting, revisions, and read and approved the submitted version.

FUNDING

This work was funded from the following sources: Department of Education GAANN grant #P200A150075, NSF grant #1743445, NSF GRFP (FBF). This work was supported by grants to RZ from: Deutsche Forschungsgemeinschaft (DFG: ZW64/4-1 and the Cluster of Excellence REBIRTH DFG EXC62/2, EXC62/3, and KFO311 ZW64/7-1), the German Ministry for Education and Science (grants: 13N14086, 01EK1601A, 01EK1602A, and 13XP5092B), and the European Union H2020 program (TECHNOBEAT grant 66724).

ACKNOWLEDGMENTS

The authors would like to acknowledge the funding sources for support on this work.

SUPPLEMENTARY MATERIAL

The Supplementary Material for this article can be found online at: https://www.frontiersin.org/articles/10.3389/fbioe.2020.00851/full#supplementary-material

REFERENCES

Ackermann, M., Kempf, H., Hetzel, M., Hesse, C., Hashtchin, A. R., Brinkert, K., et al. (2018). Bioreactor-based mass production of human iPSC-derived macrophages enables immunotherapies against bacterial airway infections. *Nat. Commun.* 9:5088. doi: 10.1038/s41467-018-07570-7

Alonso-Gutierrez, J., Kim, E. M., Batth, T. S., Cho, N., Hu, Q. J., Chan, L. J. G., et al. (2015). Principal component analysis of proteomics (PCAP) as a tool to direct metabolic engineering. *Metab. Eng.* 28, 123–133. doi: 10.1016/j.ymben.2014.11.011

Amiri, A., Mohamad, R., Rahim, R. A., Illias, R. M., Namvar, F., Tan, J. S., et al. (2015). Cyclodextrin glycosyltransferase biosynthesis improvement by recombinant Lactococcus lactis NZ:NSP:CGT: medium formulation and culture condition optimization. *Biotechnol. Biotechnol. Eq.* 29, 555–563. doi: 10.1080/13102818.2015.1009713

Blix, K., and Eltoft, T. (2018). Machine learning automatic model selection algorithm for oceanic chlorophyll-a content retrieval. *Remote Sens.* 10, 775–796. doi: 10.3390/rs10050775

Breiman, L. (2001). Random forests. *Mach. Learn.* 45, 5–32. doi: 10.1023/A:1010933404324

Burman, P. (1989). A comparative-study of ordinary cross-validation, nu-fold cross-validation and the repeated learning-testing methods. *Biometrika* 76, 503–514. doi: 10.2307/2336116

Burridge, P. W., Matsa, E., Shukla, P., Lin, Z. C., Churko, J. M., Ebert, A. D., et al. (2014). Chemically defined generation of human cardiomyocytes. *Nat. Methods* 11, 855–860. doi: 10.1038/nmeth.2999

Caschera, F., Bedau, M. A., Buchanan, A., Cawse, J., de Lucrezia, D., Gazzola, G., et al. (2011). Coping with complexity: machine learning optimization of cell-free protein synthesis. *Biotechnol. Bioeng.* 108, 2218–2228. doi: 10.1002/bit.23178

Charaniya, S., Le, H. O., Rangwala, H., Mills, K., Johnson, K., Karypis, G., et al. (2010). Mining manufacturing data for discovery of high productivity process characteristics. *J. Biotechnol.* 147, 186–197. doi: 10.1016/j.jbiotec.2010.04.005

Chen, V. C., Ye, J., Shukla, P., Hua, G., Chen, D., Lin, Z., et al. (2015). Development of a scalable suspension culture for cardiac differentiation from human pluripotent stem cells. *Stem Cell Res.* 15, 365–375. doi: 10.1016/j.scr.2015.08.002

Chong, J. J., Yang, X., Don, C. W., Minami, E., Liu, Y. W., Weyers, J. J., et al. (2014). Human embryonic-stem-cell-derived cardiomyocytes regenerate non-human primate hearts. *Nature* 510, 273–277. doi: 10.1038/nature13233

Crespo, F. L., Sobrado, V. R., Gomez, L., Cervera, A. M., and McCreath, K. J. (2010). Mitochondrial reactive oxygen species mediate cardiomyocyte formation from embryonic stem cells in high glucose. *Stem Cells* 28, 1132–1142. doi: 10.1002/stem.441

Du, D., Yang, H., Ednie, A. R., and Bennett, E. S. (2016). Statistical metamodeling and sequential design of computer experiments to model glyco-altered gating

of sodium channels in cardiac myocytes. *IEEE J. Biomed. Health Inform.* 20, 1439–1452. doi: 10.1109/JBHI.2015.2458791

Fonoudi, H., Ansari, H., Abbasalizadeh, S., Larijani, M. R., Kiani, S., Hashemizadeh, S., et al. (2015). A universal and robust integrated platform for the scalable production of human cardiomyocytes from pluripotent stem cells. *Stem Cells Transl. Med.* 4, 1482–1494. doi: 10.5966/sctm.2014-0275

Friedman, J. H. (1991). Multivariate adaptive regression splines - rejoinder. *Ann. Stat.* 19, 123–141. doi: 10.1214/aos/1176347973

Gaspari, E., Franke, A., Robles-Diaz, D., Zweigerdt, R., Roeder, I., Zerjatke, T., et al. (2018). Paracrine mechanisms in early differentiation of human pluripotent stem cells: insights from a mathematical model. *Stem Cell Res.* 32, 1–7. doi: 10.1016/j.scr.2018.07.025

Haase, A., Gohring, G., and Martin, U. (2017). Generation of non-transgenic iPS cells from human cord blood CD34(+) cells under animal component-free conditions. *Stem Cell Res.* 21, 71–73. doi: 10.1016/j.scr.2017.03.022

Halloin, C., Schwanke, K., Lobel, W., Franke, A., Szepes, M., Biswanath, S., et al. (2019). Continuous WNT control enables advanced hPSC cardiac processing and prognostic surface marker identification in chemically defined suspension culture. *Stem Cell Rep.* 13:775. doi: 10.1016/j.stemcr.2019.09.001

Hazeltine, L. B., Selekman, J. A., and Palecek, S. P. (2013). Engineering the human pluripotent stem cell microenvironment to direct cell fate. *Biotechnol. Adv.* 31, 1002–1019. doi: 10.1016/j.biotechadv.2013.03.002

Hotelling, H. (1933). Analysis of a complex of statistical variables into principal components. *J. Educ. Psychol.* 24, 417–441. doi: 10.1037/h0071325

Hu, D., Linders, A., Yamak, A., Correia, C., Kijlstra, J. D., Garakani, A., et al. (2018). Metabolic maturation of human pluripotent stem cell-derived cardiomyocytes by inhibition of HIF1alpha and LDHA. *Circ. Res.* 123, 1066–1079. doi: 10.1161/CIRCRESAHA.118.313249

Kempf, H., Andree, B., and Zweigerdt, R. (2016). Large-scale production of human pluripotent stem cell derived cardiomyocytes. *Adv. Drug Deliv. Rev.* 96, 18–30. doi: 10.1016/j.addr.2015.11.016

Kempf, H., Kropp, C., Olmer-, R., Martin, U., and Zweigerdt, R. (2015). Cardiac differentiation of human pluripotent stem cells in scalable suspension culture. *Nat. Protoc.* 10, 1345–1361. doi: 10.1038/nprot.2015.089

Kempf, H., Olmer, R., Kropp, C., Ruckert, M., Jara-Avaca, M., Robles-Diaz, D., et al. (2014). Controlling expansion and cardiomyogenic differentiation of human pluripotent stem cells in scalable suspension culture. *Stem Cell Rep.* 3, 1132–1146. doi: 10.1016/j.stemcr.2014.09.017

Kempf, H., and Zweigerdt, R. (2018). Scalable cardiac differentiation of pluripotent stem cells using specific growth factors and small molecules. *Eng. Appl. Pluripot. Stem Cell* 163, 39–69. doi: 10.1007/10_2017_30

Kensah, G., Lara, A. R., Dahlmann, J., Zweigerdt, R., Schwanke, K., Hegermann, J., et al. (2013). Murine and human pluripotent stem cell-derived cardiac bodies form contractile myocardial tissue in vitro. *Euro. Heart J.* 34, 1134–1146. doi: 10.1093/eurheartj/ehs349

Kotidis, P., Demis, P., Goey, C. H., Correa, E., McIntosh, C., Trepekli, S., et al. (2019). Constrained global sensitivity analysis for bioprocess design space identification. *Comput. Chem. Eng.* 125, 558–568. doi: 10.1016/j.compchemeng.2019.01.022

Kropp, C., Kempf, H., Halloin, C., Robles-Diaz, D., Franke, A., Scheper, T., et al. (2016). Impact of feeding strategies on the scalable expansion of human pluripotent stem cells in single-use stirred tank bioreactors. *Stem Cells Transl. Med.* 5, 1289–1301. doi: 10.5966/sctm.2015-0253

Lian, X., Hsiao, C., Wilson, G., Zhu, K., Hazeltine, L. B., Azarin, S. M., et al. (2012). Robust cardiomyocyte differentiation from human pluripotent stem cells via temporal modulation of canonical Wnt signaling. *Proc. Natl. Acad. Sci. U.S.A.* 109, E1848–E1857. doi: 10.1073/pnas.1200250109

Machiraju, P., and Greenway, S. C. (2019). Current methods for the maturation of induced pluripotent stem cell-derived cardiomyocytes. *World J. Stem Cells* 11, 33–43. doi: 10.4252/wjsc.v11.i1.33

Matsa, E., Burridge, P. W., and Wu, J. C. (2014). Human stem cells for modeling heart disease and for drug discovery. *Sci. Transl. Med.* 6:239s6. doi: 10.1126/scitranslmed.3008921

Matthews, B. W. (1975). Comparison of predicted and observed secondary structure of T4 phage lysozyme. *Biochim. Biophys. Acta* 405, 442–451. doi: 10.1016/0005-2795(75)90109-9

Mummery, C. L. (2018). Perspectives on the use of human induced pluripotent stem cell-derived cardiomyocytes in biomedical research. *Stem Cell Rep.* 11, 1306–1311. doi: 10.1016/j.stemcr.2018.11.011

Pappu, J. S. M., and Gummadi, S. N. (2016). Modeling and simulation of xylitol production in bioreactor by Debaryomyces nepalensis NCYC 3413 using unstructured and artificial neural network models. *Bioresour. Technol.* 220, 490–499. doi: 10.1016/j.biortech.2016.08.097

Pedregosa, F., Varoquaux, G., Gramfort, A., Michel, V., Thirion, B., Grisel, O., et al. (2011). Scikit-learn: machine learning in python. *J. Mach. Learn. Res.* 12, 2825–2830.

Rasmussen, C. E., and Williams, C. K. I. (2005). Gaussian processes for machine learning. *Adapt. Comput. Mach. Learn.* 1, 1–247.

Sinha, R., Singh, S., and Srivastava, P. (2014). Studies on process optimization methods for rapamycin production using *Streptomyces hygroscopicus* ATCC 29253. *Bioprocess Biosyst. Eng.* 37, 829–840. doi: 10.1007/s00449-013-1051-y

Sokolov, M., Ritscher, J., MacKinnon, N., Souquet, J., Broly, H., Morbidelli, M., et al. (2017). Enhanced process understanding and multivariate prediction of the relationship between cell culture process and monoclonal antibody quality. *Biotechnol. Prog.* 33, 1368–1380. doi: 10.1002/btpr.2502

Sokolova, M., and Lapalme, G. (2009). A systematic analysis of performance measures for classification tasks. *Inform. Process. Manag.* 45, 427–437. doi: 10.1016/j.ipm.2009.03.002

Soper, H. E., Young, A. W., Cave, B. M., Lee, A., and Pearson, K. (1915). On the distribution of the correlation coefficient in small samples - Appendix II to the papers of "student" and R A Fisher. A cooperative study. *Biometrika* 11, 328–413. doi: 10.1093/biomet/11.4.328

Spearman, C. (1904). The proof and measurement of association between two things. *Am. J. Psychol.* 15, 72–101. doi: 10.2307/1412159

Sun, X. T., and Nunes, S. S. (2017). Bioengineering approaches to mature human pluripotent stem cell-derived cardiomyocytes. *Front. Cell Dev. Biol.* 5:19. doi: 10.3389/fcell.2017.00019

Ueno, S., Weidinger, G., Osugi, T., Kohn, A. D., Golob, J. L., Pabon, L., et al. (2007). Biphasic role for Wnt/beta-catenin signaling in cardiac specification in zebrafish and embryonic stem cells. *Proc. Natl. Acad. Sci. U.S.A.* 104, 9685–9690. doi: 10.1073/pnas.0702859104

Wong, T. T. (2015). Performance evaluation of classification algorithms by k-fold and leave-one-out cross validation. *Pattern Recognit.* 48, 2839–2846. doi: 10.1016/j.patcog.2015.03.009

Yang, P., Chen, X., Kaushal, S., Reece, E. A., and Yang, P. (2016). High glucose suppresses embryonic stem cell differentiation into cardiomyocytes : high glucose inhibits ES cell cardiogenesis. *Stem Cell Res. Ther.* 7:187. doi: 10.1186/s13287-016-0446-5

Zhang, J., Wilson, G. F., Soerens, A. G., Koonce, C. H., Yu, J., Palecek, S. P., et al. (2009). Functional cardiomyocytes derived from human induced pluripotent stem cells. *Circ. Res.* 104, e30–e41. doi: 10.1161/CIRCRESAHA.108.192237

Zhou, Y., Li, G., Dong, J., Xing, X. H., Dai, J., and Zhang, C. (2018). MiYA, an efficient machine-learning workflow in conjunction with the YeastFab assembly strategy for combinatorial optimization of heterologous metabolic pathways in Saccharomyces cerevisiae. *Metab. Eng.* 47, 294–302. doi: 10.1016/j.ymben.2018.03.020

Conflict of Interest: The authors declare that the research was conducted in the absence of any commercial or financial relationships that could be construed as a potential conflict of interest.

frontiers in Bioengineering and Biotechnology

ORIGINAL RESEARCH
published: 25 September 2020
doi: 10.3389/fbioe.2020.573282

Tailored Cytokine Optimization for *ex vivo* Culture Platforms Targeting the Expansion of Human Hematopoietic Stem/Progenitor Cells

André Branco[1], Sara Bucar[1], Jorge Moura-Sampaio[1], Carla Lilaia[2], Joaquim M. S. Cabral[1], Ana Fernandes-Platzgummer[1] and Cláudia Lobato da Silva[1]*

[1] Department of Bioengineering, Institute for Bioengineering and Biosciences, Instituto Superior Técnico, Universidade de Lisboa, Lisbon, Portugal, [2] Hospital São Francisco Xavier, Centro Hospitalar de Lisboa Ocidental, Lisbon, Portugal

Umbilical cord blood (UCB) has been established as an alternative source for hematopoietic stem/progenitor cells (HSPC) for cell and gene therapies. Limited cell yields of UCB units have been tackled with the development of cytokine-based *ex vivo* expansion platforms. To improve the effectiveness of these platforms, namely targeting clinical approval, in this study, we optimized the cytokine cocktails in two clinically relevant expansion platforms for HSPC, a liquid suspension culture system (CS_HSPC) and a co-culture system with bone marrow derived mesenchymal stromal cells (BM MSC) (CS_HSPC/MSC). Using a methodology based on experimental design, three different cytokines [stem cell factor (SCF), fms-like tyrosine kinase 3 ligand (Flt-3L), and thrombopoietin (TPO)] were studied in both systems during a 7-day culture under serum-free conditions. Proliferation and colony-forming unit assays, as well as immunophenotypic analysis were performed. Five experimental outputs [fold increase (FI) of total nucleated cells (FI TNC), FI of $CD34^+$ cells, FI of erythroid burst-forming unit (BFU-E), FI of colony-forming unit granulocyte-monocyte (CFU-GM), and FI of multilineage colony-forming unit (CFU-Mix)] were followed as target outputs of the optimization model. The novel optimized cocktails determined herein comprised concentrations of 64, 61, and 80 ng/mL (CS_HSPC) and 90, 82, and 77 ng/mL (CS_HSPC/MSC) for SCF, Flt-3L, and TPO, respectively. After cytokine optimization, CS_HSPC and CS_HSPC/MSC were directly compared as platforms. CS_HSPC/MSC outperformed the feeder-free system in 6 of 8 tested experimental measures, displaying superior capability toward increasing the number of hematopoietic cells while maintaining the expression of HSPC markers (i.e., $CD34^+$ and $CD34^+CD90^+$) and multilineage differentiation potential. A tailored approach toward optimization has made it possible to individually maximize cytokine contribution in both studied platforms. Consequently, cocktail optimization has successfully led to an increase in the expansion platform performance, while allowing a rational side-by-side comparison among different platforms and enhancing our knowledge on the impact of cytokine supplementation on the HSPC expansion process.

Keywords: *ex vivo* expansion, umbilical cord blood, human hematopoietic stem/progenitor cells, cytokines, process optimization

OPEN ACCESS

Edited by:
Stephanie Michelle Willerth, University of Victoria, Canada

Reviewed by:
Omar Aljitawi, University of Rochester, United States
Pau Loke Show, University of Nottingham Malaysia Campus, Malaysia

****Correspondence:***
Ana Fernandes-Platzgummer
ana.fernandes@tecnico.ulisboa.pt

Specialty section:
This article was submitted to Bioprocess Engineering, a section of the journal Frontiers in Bioengineering and Biotechnology

Received: *16 June 2020*
Accepted: *09 September 2020*
Published: *25 September 2020*

Citation:
Branco A, Bucar S, Moura-Sampaio J, Lilaia C, Cabral JMS, Fernandes-Platzgummer A and Lobato da Silva C (2020) Tailored Cytokine Optimization for ex vivo Culture Platforms Targeting the Expansion of Human Hematopoietic Stem/Progenitor Cells. Front. Bioeng. Biotechnol. 8:573282. doi: 10.3389/fbioe.2020.573282

INTRODUCTION

Hematopoietic cell transplantation (HCT) continues to be the leading cell therapy for malignant and non-malignant blood-based disorders and advances in this field have expanded the options available for patients concerning graft source. Umbilical cord blood (UCB) is an accepted and appealing alternative source of hematopoietic stem/progenitor cells (HSPC) for HCT (Hough et al., 2016; Woolfrey et al., 2016). Compared with bone marrow (BM) or mobilized peripheral blood, UCB transplants have shown similar survival outcomes with lower chances of developing graft vs. host disease (GVHD) and lesser compatibility issues concerning human leukocyte antigen (HLA) matching (Rocha et al., 2001, 2004). However, low UCB volume recovered from births results in an unsatisfactory cell dose for transplants in adults, having initially limited transplants of a single UCB unit to pediatric patients (Wagner et al., 2014). In order to address this problem, *ex vivo* expansion of HSPC has been pursued. By manipulating UCB units to increase their cell yield, the drawbacks of single unit transplants (such as increased graft failure and delayed immune reconstitution) can potentially be surpassed (Kelly et al., 2009). Multiple strategies have been developed toward achieving a successful expansion, with several reaching phase III clinical trial level (Maung and Horwitz, 2019). Approaches have varied from promoting HSPC expansion with novel small molecules including StemRegenin-1 (Wagner et al., 2016), UM171 (Fares et al., 2014), and nicotinamide (Horwitz et al., 2014), co-culture with mesenchymal stromal cells (de Lima et al., 2012) and induction of Notch signaling pathways (Delaney et al., 2010).

Although different strategies have been explored, HSPC *ex vivo* expansion has always been largely based on the addition of exogenous cytokines (Lund et al., 2015). Numerous cytokines have been employed to promote HSPC expansion *ex vivo*, including fms-like tyrosine kinase 3 ligand (Flt-3L), granulocyte colony-stimulating factor (G-CSF), interleukin-3 (IL-3), interleukin-6 (IL-6), stem cell factor (SCF), and thrombopoietin (TPO) (Conneally et al., 1997; Ohmizono et al., 1997; Levac et al., 2005) (reviewed in Costa et al., 2018). However, selection of individual cytokines and their concentrations for an expansion cocktail has differed between existing strategies. Disparity of concentrations can reach 30-fold among similar cytokines included in different expansion protocols (Delaney et al., 2010; Çelebi et al., 2012). Whereas cytokine dosage may vary due to the nature of the expansion approach (e.g., targeted expansion of more primitive self-renewing hematopoietic stem cells compared to expansion of both hematopoietic stem cells and early committed progenitors), a defined and clear optimization rationale concerning cytokine supplementation has been lacking. Ignoring or underestimating optimization opportunities can have a negative impact on existing culture protocols, especially concerning cytokine supplementation. Suboptimal cytokine concentrations can cause underperformance of cell expansion driving misleading conclusions, especially when carrying out comparisons with other competitive strategies. On the other hand, overuse of cytokine supplementation has shown to interfere with HSPC self-renewal and promote unwanted differentiation (Zandstra et al., 1997a; Audet et al., 2002). Moreover, considering their significant cost, these abnormally high cytokine concentrations can also compromise process viability, cost-effectiveness and potential for clinical translation (Yoshida and Takagi, 2004; Aijaz et al., 2018). Thus, there is a clear gap in protocol standardization and optimization for current HSPC *ex vivo* expansion platforms.

With the lack of optimized platforms, current evaluation of the performance of various expansion approaches based on their published results might be inaccurate, since these platforms are most likely not performing at their peak production potential. Therefore, improper optimization of cytokine usage can affect decision-making and eventually be responsible for negligent or premature withdrawal of certain expansion approaches from the clinical approval pipeline. While improving existing expansion platforms, cytokine cocktail optimization will also enable a fair side-by-side comparison of current strategies.

Systematic studies on cytokine use in *ex vivo* expansion of HSPC will also support platforms toward an effective protocol for clinical applications based on good manufacturing practices (GMP). Besides highlighting the abovementioned cost reduction opportunities, cytokine optimization will also elucidate on important biological interactions between cytokines and cultured HSPC. The knowledge gathered from this relationship will benefit bioprocess engineering from a future manufacturing line perspective. The understanding of these cytokine requirements will have a direct impact on the feasibility of such a GMP-based expansion protocol, which is a priority for platforms at a clinical trial level (Kirouac and Zandstra, 2008). Although an initial focus on the cytokine cocktail existed during the early development of *ex vivo* HSPC expansion protocols, previous attempts to study cytokine influence are mostly based on simple dose-response studies and are outdated (Petzer et al., 1996; Ohmizono et al., 1997; Zandstra et al., 1997a,b, 1998; Ueda et al., 2000). Furthermore, due to major advances in *in vitro* culture of HSPC (e.g., development of serum-free medium formulations), tested culture conditions are inconsistent with expansion strategies presently in clinical trials, making the application of previous optimizations inadequate. With a considerable amount of HSPC expansion strategies in late-stage development, where major changes in the experimental procedure are rare, any cytokine optimization performed at this stage could endure. Thus, existing cytokine variation throughout current UCB-based expansion strategies was surveyed (reviewed in Kiernan et al., 2017; Costa et al., 2018). Despite some expected variants between strategies, we identified the trio of cytokines SCF, Flt-3L and TPO as the most used cytokine combination in the majority of expansion studies (reviewed in Costa et al., 2018), including those which have progressed to Phase I/II clinical trials (reviewed in Kiernan et al., 2017). By specifically selecting these three cytokines, we expect to boost the relevance of our study, turning its application more widespread.

Over the last years, we have gathered significant expertise in what concerns the *ex vivo* cultivation of human HSPC by

establishing a co-culture system with BM MSC, in order to improve our understanding of the mechanisms underlying the hematopoietic supportive capacity of human MSC (da Silva et al., 2005, 2009, 2010; Gonçalves et al., 2006; Andrade et al., 2011, 2015). Having identified the aforementioned gap in the field, we tackled the issue with initial efforts focused on pursuing optimization of our established co-culture platform with BM MSC using statistical tools, such as design of experiments (Andrade et al., 2010). Unable to perform feeder-free HSPC expansion with the selected culture conditions, in particular for UCB cells (da Silva et al., 2005), our previous optimization study was restricted to a single expansion platform, exclusively performed in a co-culture system with BM MSC.

Using the same statistical approach based on experimental design, in the present study, we have determined unique optimal cytokine cocktails for two different HSPC expansions systems (i.e., HSPC expanded alone in a liquid culture system or co-cultured with a BM MSC feeder layer) currently exploited in clinical trials. By enhancing the cytokine contribution for each platform, we were able to level the field and perform a rational and pragmatic comparative study between both systems (liquid suspension culture vs. co-culture). By optimizing the established expansion platforms, we have reached a durable optimal cytokine cocktail to hopefully endure and facilitate the road to regulatory approval of a viable cell product based on expanded UCB-derived HSPC. Furthermore, by expanding HSPC from cryopreserved UCB MNC, we have made our optimization more reliable and applicable to the manufacturing scenario. Indeed, upon collection, UCB units are routinely kept cryopreserved in public/private banks worldwide. Also, we have shown that tailored cytokine optimization should be used as a tool to enable unbiased evaluation of existing strategies, rationally impacting the highly competitive field of *ex vivo* expansion of HSPC, namely (but not limited to) UCB-derived.

MATERIALS AND METHODS

Human Tissues

Originally, UCB units and BM samples were obtained from healthy donors, upon informed consent, with the approval of the ethics committee of Hospital São Francisco Xavier, Centro Hospitalar de Lisboa Ocidental and of Instituto Português de Oncologia Francisco Gentil, Lisbon, Portugal, respectively (Directive 2004/23/EC of the European Parliament and of the Council of March 31st, 2004 regarding standards of quality and safety for the donation, procurement, testing, processing, preservation, storage and distribution of human tissues and cells, represented by the corresponding Portuguese Law 22/2007).

Cell Isolation

Mononuclear cells (MNC) were isolated from UCB using a Ficoll [GE Healthcare, United States of America (United States), **Supplementary Table 2**] density gradient and washed with Phosphate Buffered Saline (PBS) (Sigma-Aldrich, United States) supplemented with 2 mM ethylenediamine tetraacetic acid (EDTA) (Sigma-Aldrich). MNC were incubated with an ammonium chloride solution (155 mM) (Sigma-Aldrich) to remove any possible contamination with erythrocytes. Purified MNC were cryopreserved in Recovery^{TM} Cell Culture Freezing Medium (Thermo Fisher Scientific, United States) and stored in a liquid/vapor phase nitrogen tank.

CD34$^+$ Cell Enrichment From UCB MNC

Cryopreserved UCB MNC were thawed in low glucose Dulbecco's Modified Eagle's Medium (DMEM) (Thermo Fisher Scientific) containing 20% fetal bovine serum (FBS) (Thermo Fisher Scientific) and 1% Antibiotic-Antimycotic (Thermo Fisher Scientific) (DMEM-20%FBS) supplemented with 10 μg/mL DNase I (Sigma-Aldrich). Cells were washed with MACS buffer and CD34$^+$ cell selection was performed using a Human CD34 MicroBead Kit UltraPure (Miltenyi Biotec, Germany), following manufacturer's instructions.

Preparation of a BM MSC Feeder Layer

Bone marrow derived mesenchymal stromal cells were obtained from the Stem Cell Engineering Research Group (SCERG) cell bank, at the Institute for Bioengineering and Biosciences, Instituto Superior Técnico, Lisboa, Portugal. Cell isolation, expansion, characterization and preservation were done using previously established protocols (dos Santos et al., 2010). Cells from a single BM donor were used to establish feeder layers, mimicking an allogeneic universal donor. To establish the feeder layer, cryopreserved BM MSC, between passages P2-P5, were thawed in DMEM-20% FBS and plated at a cell density of 3000 cells/cm^2 with low glucose DMEM supplemented with 10% FBS MSC-qualified (Thermo Fisher Scientific) and 1% Antibiotic-Antimycotic (DMEM-10%FBS). After cells reached confluency, growth arrest was promoted by treating cells during 2.5−3 h at 37°C and 5% CO_2 with low glucose DMEM-10% FBS supplemented with 0.5 μg/mL of Mitomycin C (Sigma-Aldrich). Growth-arrested feeder layers were carefully washed twice with DMEM-10% FBS and incubated with the same medium until further use in co-culture experiments.

Ex vivo Expansion of HSPC

Umbilical cord blood-derived CD34$^+$ enriched cells were seeded on a 12-well plate at 30 000 cells/mL, using 2 mL of StemSpan^{TM} Serum-free Expansion Medium II (StemCell Technologies, Canada) per well (60 000 cells/well) supplemented with 1% Antibiotic-Antimycotic and defined cytokine cocktails composed of SCF, Flt-3L, and TPO (PeproTech, United States), with concentrations ranging between 0 and 100 ng/mL. Basic fibroblast growth factor (bFGF) (PeproTech) was additionally used in all conditions at a concentration of 5 ng/mL to support BM feeder layer cells during the co-culture experiments (Andrade et al., 2010). HSPC expansion was performed during 7 days at 37°C and 5% CO_2. For co-culture with BM MSC, DMEM-10% FBS culture medium was removed from the growth arrested feeder layers and CD34$^+$ enriched cells were carefully seeded on top as described above.

Proliferative and *in vitro* Clonogenic Assays

Proliferation Assay

At day 7 of expansion, suspended and adhered HSPC (in the case of co-cultures) were harvested through forced pipetting. Cell number was determined using the Trypan Blue (Thermo Fisher Scientific) exclusion method. Fold increase in total nucleated cell number (FI TNC) was calculated by dividing the cell number at day 7 by the initial seeding cell number (day 0).

Colony-Forming Unit (CFU) Assay

Cells were characterized according to their capacity, as progenitor cells, to proliferate and differentiate into several hematopoietic lineages. Cells were resuspended in MethoCult™ methylcellulose-based medium (STEMCELL Technologies) and seeded on a 24-well plate in triplicates. Colony formation was allowed for 14 days at 37°C and 5% CO_2. Formed colonies [erythroid burst-forming unit (BFU-E), colony forming unit granulocyte-monocyte (CFU-GM), and multilineage colony forming unit (CFU-Mix)] were classified and counted by visual inspection using bright-field microscopy (Olympus CK40, Japan). Colony number was normalized by the number of seeded cells and multiplied by the TNC number. FI in the number of colonies was calculated by dividing the total colony number at day 7 by the respective of day 0.

Cobblestone Area Forming-Cells (CAFC)

A growth-arrested feeder layer of a murine stromal cell line (MS-5) was prepared similarly as previously described for BM MSC (Andrade et al., 2010). To further characterize their stemness, expanded and non-expanded HSPC were resuspended in MyeloCult™ medium (STEMCELL Technologies) supplemented with 350 ng/mL of hydrocortisone (STEMCELL Technologies). Cells were seeded on a 24 well-plate in duplicates at 2000 cells/well and incubated for 14 days at 37°C and 5% CO_2. Wells were visually inspected using a phase-contrast microscope (Leica DMI3000 B, Germany) for the presence of colonies of more than 5 cells with cobblestone-like morphology (phase-dim, compact grouped, angular shaped cells, Denning-Kendall et al., 2003) that were able to migrate beneath the murine feeder layer. Colony number was normalized by the number of seeded cells and multiplied by the TNC number. FI values relative to the number of CAFC colonies were obtained by dividing the CAFC colonies at day 7 by initial CAFC colony population at day 0.

Cell Immunophenotype

Hematopoietic stem/progenitor cells phenotype was characterized by flow cytometry on a FACSCalibur™ flow cytometer (BD Biosciences, United States). Briefly, harvested cells were washed with PBS, viability was assessed through a Far Red LIVE/DEAD™ Fixable Dead Cell Stain Kit (Thermo Fisher Scientific), and cells were surface stained with previously titrated CD34 FITC (BioLegend, United States), CD34 PE (BioLegend), CD34 PerCP-Cy5.5 (BD Biosciences), and CD90 PE (BioLegend) at room temperature (RT) for 15 min. After PBS washing, cells were fixed in 1% formaldehyde (Sigma-Aldrich) at RT for 15 min. Data was analyzed using FlowJo v10 software (FlowJo LLC, United States).

Cytokine Experimental Design

Response surface methodology was applied to optimize cytokine concentrations for the *ex vivo* expansion of HSPC (Box et al., 1978). A face-centered central composite (CCF) design was used to select concentrations for three different cytokines (SCF, Flt-3L, and TPO), resulting in 17 experimental points. The tested observational window was limited by a minimum concentration of 0 ng/mL and a maximum of 100 ng/mL, for every cytokine. With defined limits, concentrations were coded to simplify listing of experimental points [lower level (−1) − 0 ng/mL; center level (0) − 50 ng/mL; higher level (1) − 100 ng/mL]. The experimental points included three center points in order to gain an estimation of the experimental error. Effect on cytokine variation on FI TNC, FI $CD34^+$ cells, FI BFU-E, FI CFU-GM, and FI CFU-Mix was investigated. These outputs were termed response variables (Y_n). Every response variable was measured in a blinded manner, eliminating experimental bias. A second-order polynomial function was suggested to describe and model the experimental data.

$$Y_n = K + \beta_1 [X_1] + \beta_2 [X_2] + \beta_3 [X_3] + \beta_{12} [X_1] [X_2] + \beta_{13} [X_1] [X_3] + \beta_{23} [X_2] [X_3] + \beta_{11} [X_1]^2 + \beta_{22} [X_2]^2 + \beta_{33} [X_3]^2 \quad (1)$$

Proposed second-order polynomial function as a behavior function for a specific response variable (Y_n), considering three cytokines (X_1, X_2, and X_3). This model includes an intercept (K), responsible for describing the response variable when no cytokines are present, and three different types of cytokine effects. These include main individual cytokine impact (β_i parameters), interaction between the different cytokines ($\beta_{i\,j}$ parameters), and molecular effects within the same cytokine ($\beta_{i\,i}$ parameters).

Validation

Determined regressions were validated by comparing predicted values for each response variable with corresponding experimental values of cytokine combinations not included in the original concentration panel. Two different cytokine combinations, the optimized cytokine cocktail and a previously established cocktail (Z9; [SCF] = 60 ng/mL; [Flt-3L] = 55 ng/mL; [TPO] = 50 ng/mL) from our previous study (Andrade et al., 2010) were chosen to test the applicability of the regressions in its defined experimental design space.

Statistical Analysis

Function fitting was performed using a backward stepwise regression. Briefly, all terms were considered in the regression. An iterative *F*-test on the overall regression was applied. In each step, when the respective *p*-Value was above the stipulated threshold (0.05), the least significant parameter was eliminated from the model. This was done repeatedly until the regression itself gained significance. Goodness of fit variables R-squared, Adjusted R-squared, and root mean squared error (RMSE) were

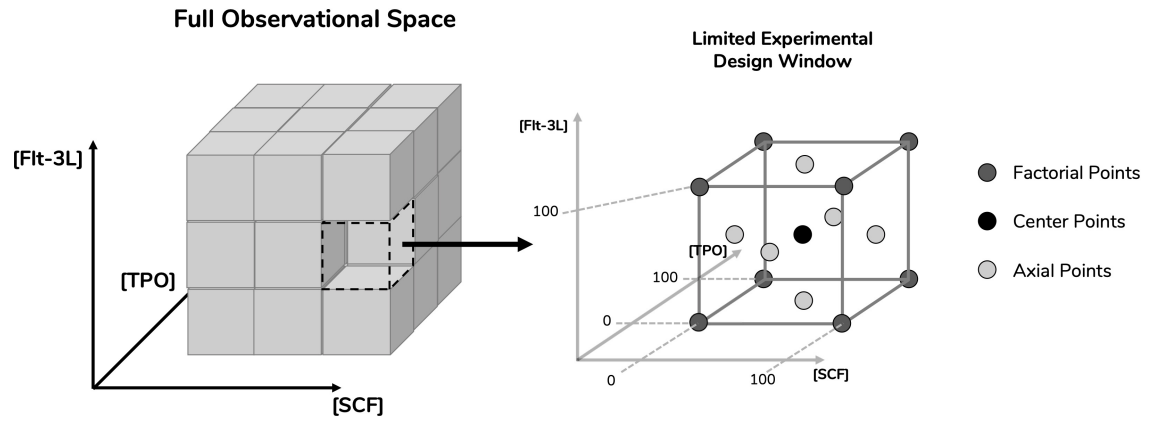

FIGURE 1 | Definition of experimental design space for the optimization studies. Surface response methodology requires limitation of parameters in order to study response variables. Concentrations of the cytokines stem cell factor (SCF), fms-related tyrosine kinase 3 ligand (Flt-3L) and thrombopoietin (TPO) were selected as parameters. A limited experimental design window was selected from their full observational space with respective concentration ranges between 0 and 100 ng/mL. By incorporating three levels of dimensionality, the design space gained a cubic geometry. Having defined the design space, a face-centered central composite design was applied, which provided the experimental points necessary in order to reach the response surface. These include center points, axial points (located in the center of the cubic planes) and factorial points (located in the cubic vertices).

TABLE 1 | List of cytokine combinations derived from the face-centered central composite (CCF) design.

Cytokine	Factorial points								Center points					Axial points			
SCF	+	+	+	+	–	–	–	–	0	0	0	0	0	+	–	0	0
Flt-3L	+	+	–	–	+	+	–	–	0	0	0	0	0	0	0	+	–
TPO	+	–	+	–	+	–	+	–	0	0	0	+	–	0	0	0	0
Combination	*1*	*2*	*3*	*4*	*5*	*6*	*7*	*8*	*9*	*10*	*11*	*12*	*13*	*14*	*15*	*16*	*17*

Concentrations values were symbol coded to facilitate identification and combinations were numbered to aid with cocktail recognition. In total, 17 combinations were defined, consisting of 8 factorial points, three repeated center points and 6 axial points. (+) 100 ng/mL; (0) 50 ng/mL; (–) 0 ng/mL.

determined to assess regression quality. Unless stated otherwise, plotted error bars and error intervals represent the standard error of the mean (SEM).

RESULTS

Combinations of selected cytokines (SCF, Flt-3L, and TPO) were defined using an experimental design approach (**Figure 1**). A CCF design delineated a panel of 17 cytokine combinations, which included three repeated center points to assess intra-donor variability of UCB cells (**Table 1**). Cytokine concentrations were limited to an experimental design window between 0 and 100 ng/mL. FI TNC, FI $CD34^+$, FI BFU-E, FI CFU-GM, and FI CFU-Mix were chosen as response variables for this optimization study, acting as measures of cytokine performance. Two different expansion platforms were studied, with HSPC being expanded alone in a liquid culture system (*CS_HSCP*) or co-cultured with a BM MSC feeder layer (*CS_HSPC/MSC*). Response variables were modeled and corresponding regression surfaces were maximized in order to uncover optimized cytokine cocktails for both expansion systems (**Figure 2**). Three independent donors of UCB cells were studied to include biological variability in the model. UCB $CD34^+$-enriched cells (purity: [82–98%]) were expanded in serum-free conditions for 7 days using both expansion strategies.

Response Variable Measurement

Selected response variables were successfully measured for three independent UCB unit donors. FI TNC number fluctuated considerably when expanding cells with the different cytokine combinations of the established panel in both expansion culture systems (coefficient of variation $CV_{CS\_HSPC/MSC} = 60 \pm 3\%$; $CV_{CS\_HSPC} = 76 \pm 1\%$; **Figure 3**). Taking into account every center point replicate, their low deviation ($CV_{Center} = 13 \pm 5\%$) demonstrated reproducibility of the expansion performance, discarding possible experimental error interference. Combinations with an absence of a certain cytokine caused a significant decrease in expansion capabilities, demonstrating the individual importance of the tested cytokines (**Figure 3**). Overall, cell expansion capacity varied to a higher extent at a lower range (0–50 ng/mL), while displaying similar culture performance for combinations with concentrations in the higher testing range (50–100 ng/ml). Nevertheless, cytokine panel screening resulted in a FI TNC reaction fingerprint that was coherent between donors. Although biological variability was present and the absolute values of measured variables were different, the overall pattern was very coincident. Additionally, this fingerprint was uniquely distinctive between expansion approaches.

The CFU assay contributed with three response variables (**Figure 3** and **Supplementary Table 1**). Since BFU-E formation

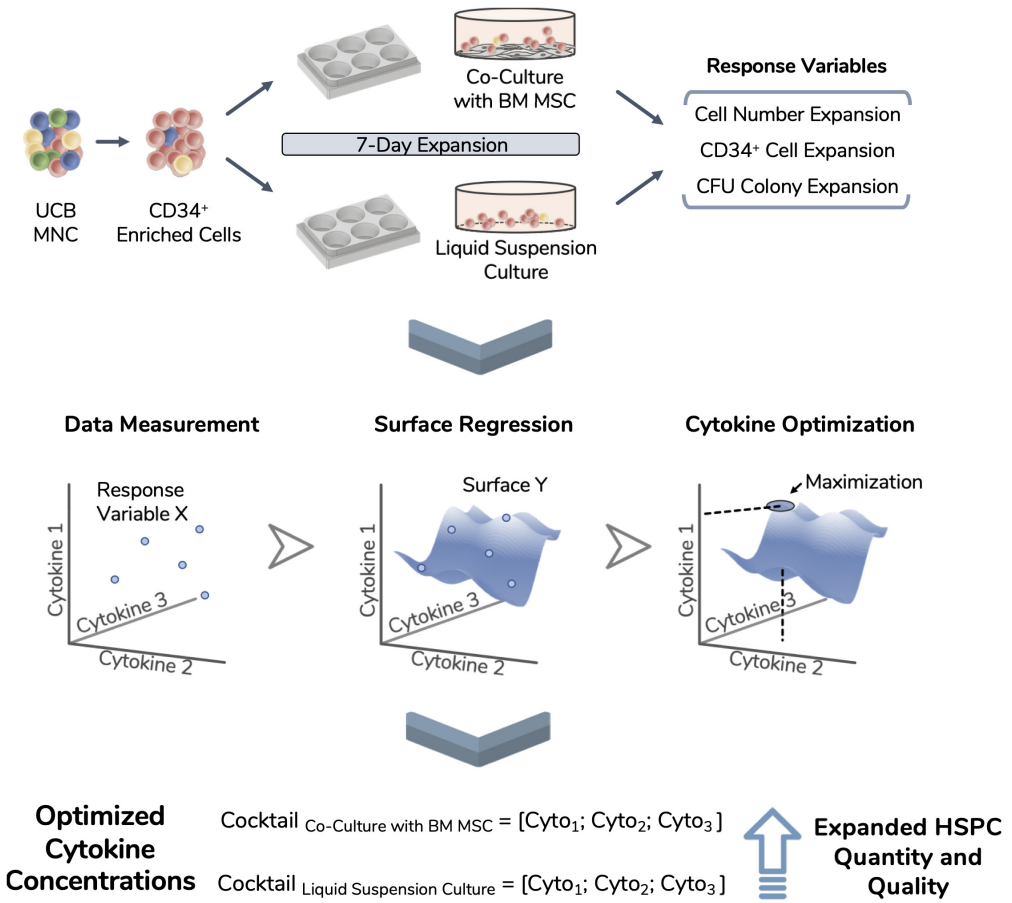

FIGURE 2 | Experimental workflow of the performed optimization. Umbilical cord blood (UCB) mononuclear cells (MNC) were thawed and enriched for CD34 expression. These isolated cells were used as the starting population in two different expansion systems (i.e., liquid suspension culture and co-culture with bone marrow-derived mesenchymal stromal cells) and expanded during 7 days. Total nucleated cell number, CD34 expressing cell number and CFU readouts were selected for optimization and termed as response variables. Using an experimental design approach, 17 different cytokine combinations were used during expansion runs and response variables were tracked. Experimental data points were modeled, giving rise to unique response surfaces for each expansion system. By locating the surface maximum, each response variable originated an optimized cytokine cocktail, improving the quantity and quality of the expanded cell product.

was always neglectable, it was not possible to progress with the variable FI BFU-E to the regression modeling phase. Without quantifiable BFU-E populations, CFU-GM and CFU-Mix were mirrored in their population percentage in each assay. FI CFU-GM and FI CFU-Mix demonstrated similar sensitivity to cytokine concentration variation as with FI TNC, but they developed their own cytokine fingerprint.

In contrast with the remaining response variables, CD34 expression did not show the same sensitivity toward different cytokine concentrations (not shown). Since CD34 expression exhibited minor influences by the cytokine panel, its respective response variable (FI $CD34^+$ cells) revealed the same response pattern as the FI TNC number (**Figure 3**).

Regression Determination and Analysis

Several steps were taken to prepare and polish the response variables for regression modeling. Data from each donor was normalized to remove the biological variability on cell expansion intensity, highlighting the effects driven by the cytokine panel (**Figure 4A** and **Supplementary Figures 1A, 2A, 3A**). Prior to regression determination, outliers were detected through a Z-score method and eliminated (**Figure 4B** and **Supplementary Figures 1B, 2B, 3B**). Regressions for each response variable were calculated, reaching significance in every case (**Table 2**).

For both expansion systems, the hypothesized model was able to describe cytokine influence on the values of FI TNC to a considerable extent. For CS_HSPC/MSC, every projected term was significantly present, except for interaction effects between Flt-3L and TPO (**Table 2**). Negative quadratic effects were determined, leading to the existence of a concavity in the response surface and the existence of a local maximum in the tested range. On the other hand, for CS_HSPC, there were no interaction terms between cytokines. Also, regression fitting determined a negative intercept ($K = -0.165$), which has no biological translation and was disregarded.

Colony-forming unit assay response was modeled by a lesser number of significant parameters. FI CFU-GM and FI CFU-Mix had regressions with two particular characteristics. Unlike

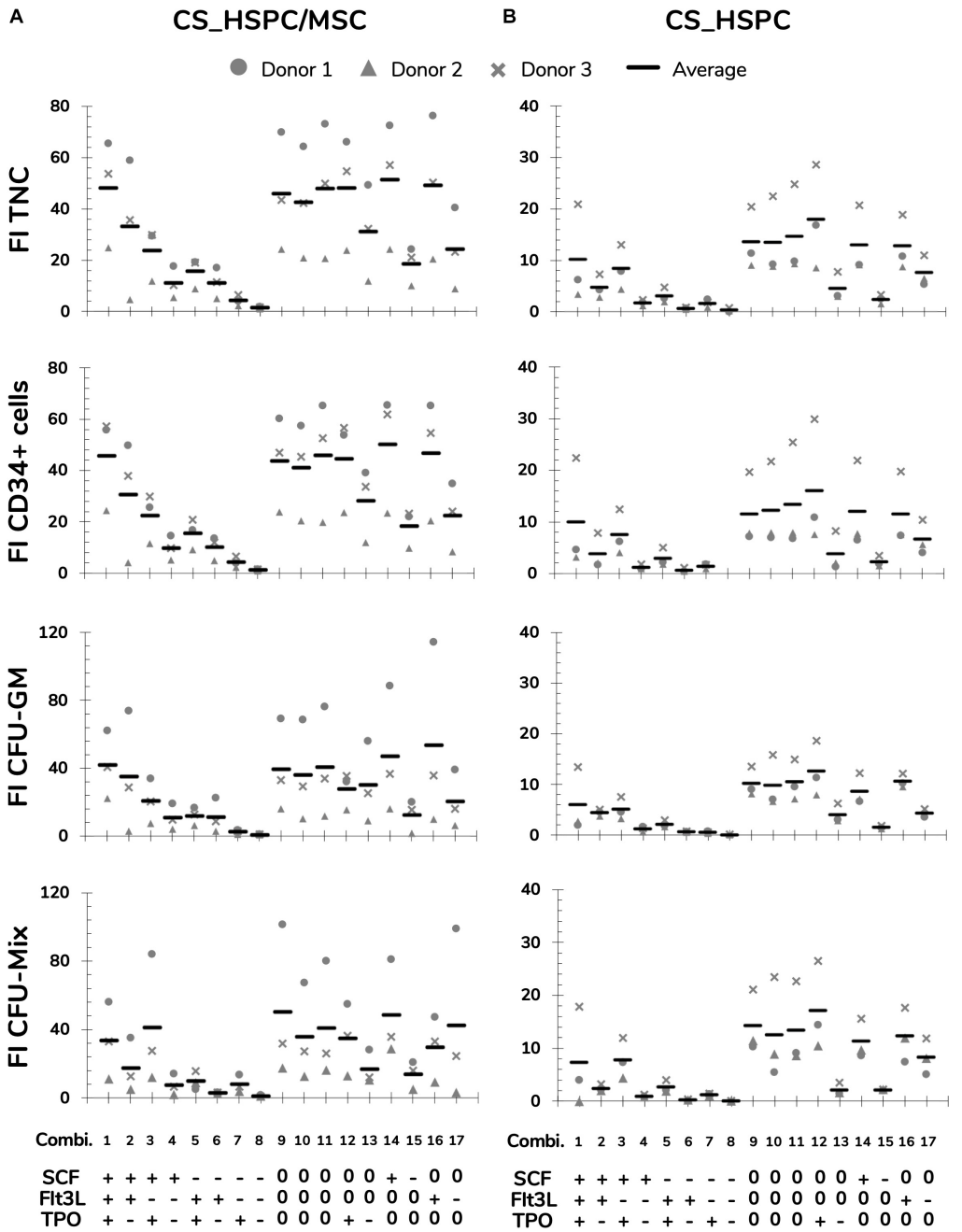

FIGURE 3 | Measurements of response variables for two different expansions systems, HSPC suspension culture (CS_HSPC) and co-culture with bone marrow mesenchymal stromal cells (CS_HSPC/MSC). Throughout the entire cytokine panel of 17 combinations, values of fold increase (FI) of total nucleated cells (TNC), FI of $CD34^+$ expressing cells, FI of colony-forming unit granulocyte-monocyte (CFU-GM) and FI of multilineage colony-forming unit (CFU-Mix) were followed. Cells isolated from three different donors were used for testing the response variables for CS_HSPC/MSC **(A)** and CS_HSPC **(B)**. (+) 100 ng/mL; (0) 50 ng/mL; (–) 0 ng/mL.

FI TNC number, some cytokines did not have a negative quadratic effect. Additionally, FI CFU-Mix for CS_HSPC showed total independence toward Flt-3L, lacking every type of cytokine effect considered in the model. In terms of overall regression quality, CFU-Mix originated fittings with lower quality ($R^2_{CS\_HSPC/MSC}$ = 0.65; $R^2_{CS\_HSPC}$ = 0.71) compared to the remaining response variables.

As previously observed, FI $CD34^+$ cells had similar behavior as the FI TNC number. Consequently, parameter estimation led to the same significant parameters and resembling values.

Regression performance was quantitatively assessed by the chosen quality measures. Although the regression quality varied, adjusted correlation coefficients maintained above 0.6 and were able to describe the experimental data significantly.

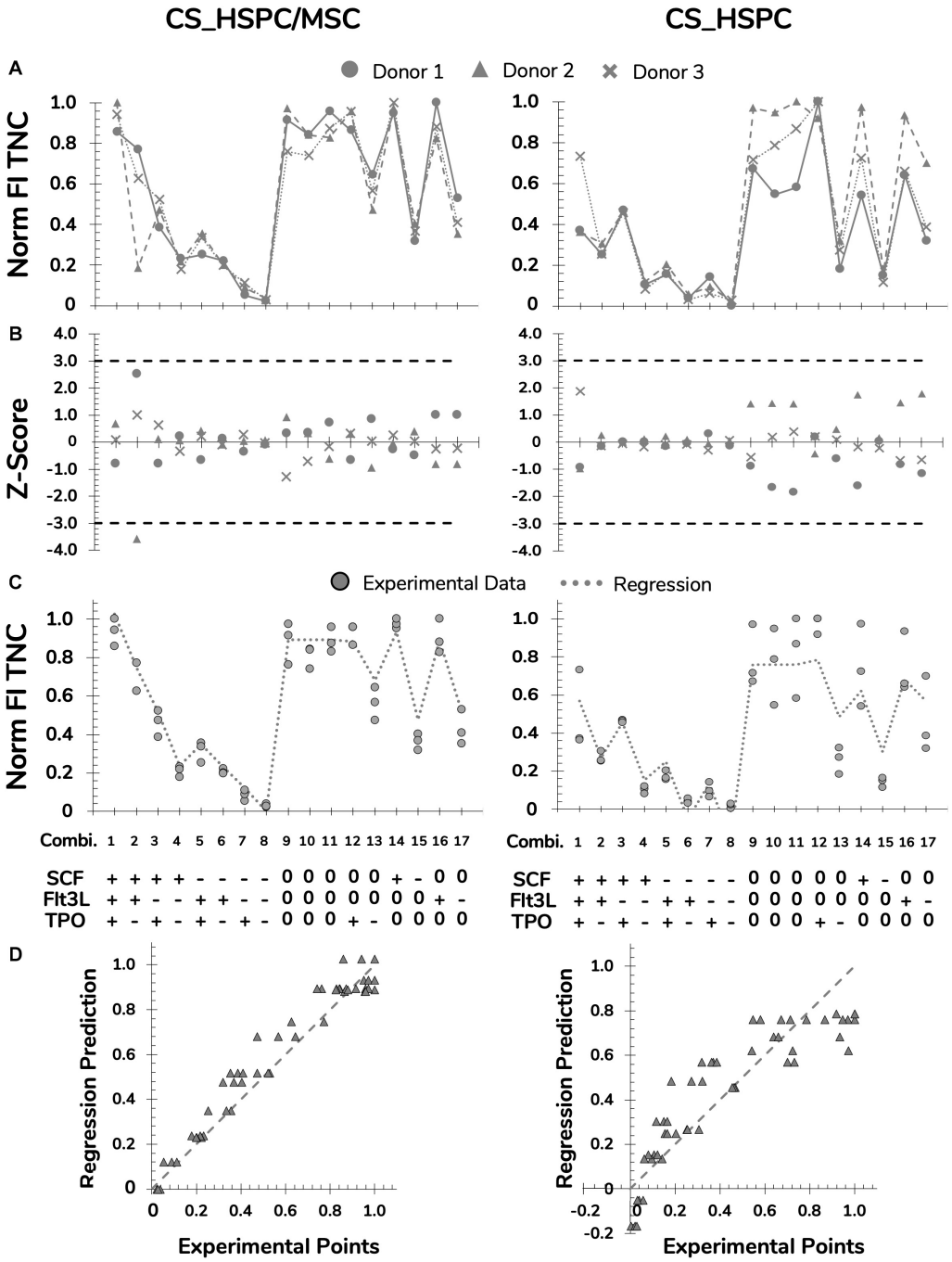

FIGURE 4 | Preparation and polishing of experimental data with assessment of regression quality for FI TNC for both expansion systems, HSPC suspension culture (CS_HSPC) and HSPC co-cultured with BM MSC (CS_HSPC/MSC). **(A)** Data from cells retrieved from every UCB donor was normalized revealing coinciding reaction patterns, highlighting variability exclusively due to different cytokine combinations. **(B)** Outlier screening was performed through Z-score determination. Data points with absolute score values higher than 3 were labeled outliers and were consequently removed from their data set before proceeding to the regression determination. **(C)** After regression determination, experimental data points were compared with calculated regression. **(D)** Deviations between data points and regressions were visualized. Norm, normalized.

Quantitative variables (FI TNC number and FI $CD34^+$ cells) consistently produced higher quality regressions when compared to the semi-quantitative variables (FI CFU-GM and FI CFU-Mix) of the same expansion system. Quality assured regressions were then used to predict responses for the cytokine panel and were compared with experimental data points (**Figure 4C** and **Supplementary Figures 1C, 2C, 3C**). Residual determination was performed to visualize and quantify

TABLE 2 | Parameter estimations after regression determination and quality measures for each response variables and expansion system.

	Normalized FI TNC		Normalized FI CD34$^+$ Cells		Normalized FI CFU-GM		Normalized FI CFU-Mix	
Parameter	**Estimate**	***p*-Value**	**Estimate**	***p*-Value**	**Estimate**	***p*-Value**	**Estimate**	***p*-Value**
CS_HSPC/MSC								
K	–	–	–	–	–	–	–	–
SCF	9.90×10^{-3}	1.05×10^{-9}	9.27×10^{-3}	1.04×10^{-8}	1.00×10^{-2}	2.02×10^{-5}	3.82×10^{-3}	6.09×10^{-6}
Flt-3L	9.89×10^{-3}	4.62×10^{-10}	9.95×10^{-3}	8.47×10^{-10}	6.88×10^{-3}	2.05×10^{-3}	6.70×10^{-3}	1.90×10^{-2}
TPO	5.67×10^{-3}	3.35×10^{-5}	6.66×10^{-3}	4.18×10^{-6}	1.09×10^{-3}	4.98×10^{-2}	1.24×10^{-2}	5.40×10^{-5}
SCF × Flt-3L	2.80×10^{-5}	1.60×10^{-4}	2.82×10^{-5}	2.15×10^{-4}	3.10×10^{-5}	1.48×10^{-2}	–	–
Flt-3L × TPO	–	–	–	–	–	–	–	–
SCF × TPO	1.60×10^{-5}	2.23×10^{-2}	1.51×10^{5}	3.49×10^{-2}	–	–	–	–
SCF^2	$-7.53 \times 10^{(5}$	5.49×10^{-8}	-6.95×10^{-5}	5.23×10^{-7}	-7.16×10^{-5}	6.17×10^{-4}	–	–
Flt-3L^2	-7.60×10^{-5}	4.53×10^{-8}	-7.62×10^{-5}	8.10×10^{-8}	-4.89×10^{-5}	1.53×10^{-2}	-6.08×10^{-5}	2.70×10^{-2}
TPO^2	-4.46×10^{-5}	3.19×10^{-4}	-5.35×10^{-5}	4.35×10^{-5}	–	–	-9.48×10^{-5}	8.89×10^{-4}
Regression quality								
R-squared (R^2)	0.95		0.95		0.79		0.65	
Root Mean Squared Error (RMSE)	0.08		0.08		0.15		0.20	
Adjusted R-squared	0.94		0.94		0.76		0.60	
F-statistic vs. constant model	97.8		92.8		26.8		16.0	
p-Value	3.23×10^{-24}		8.77×10^{-24}		4.89×10^{-13}		5.87×10^{-9}	
CS_HSPC								
K	-1.65×10^{-1}	9.90×10^{-3}	-1.86×10^{-1}	4.06×10^{-3}	-1.84×10^{-1}	5.52×10^{-3}	-1.38×10^{-1}	3.66×10^{-2}
SCF	1.51×10^{-2}	1.10×10^{-7}	1.47×10^{-2}	1.98×10^{-7}	1.80×10^{-2}	1.75×10^{-10}	1.63×10^{-2}	1.11×10^{-7}
Flt-3L	6.55×10^{-3}	8.85×10^{-3}	6.30×10^{-3}	1.14×10^{-2}	8.56×10^{-3}	3.05×10^{-4}	–	–
TPO	8.02×10^{-3}	1.65×10^{-3}	9.31×10^{-3}	3.26×10^{-4}	2.37×10^{-3}	2.09×10^{-4}	1.15×10^{-2}	5.53×10^{-5}
SCF × Flt-3L	–	–	–	–	–	–	–	–
Flt-3L × TPO	–	–	–	–	–	–	–	–
SCF × TPO	–	–	–	–	–	–	–	–
SCF^2	-1.19×10^{-4}	5.67×10^{-6}	-1.15×10^{-4}	1.02×10^{-5}	-1.49×10^{-4}	7.78×10^{-9}	-1.38×10^{-4}	1.55×10^{-6}
Flt-3L^2	-5.41×10^{-5}	2.40×10^{-2}	-5.12×10^{-5}	3.21×10^{-2}	-6.57×10^{-5}	3.04×10^{-3}	–	–
TPO^2	-5.01×10^{-5}	3.59×10^{-2}	-5.85×10^{-5}	1.50×10^{-2}	–	–	-8.22×10^{-5}	1.86×10^{-3}
Regression quality								
R-squared (R^2)	0.78		0.79		0.78		0.71	
Root Mean Squared Error (RMSE)	0.16		0.16		0.16		0.19	
Adjusted R-squared	0.75		0.76		0.76		0.69	
F-statistic vs. constant model	26.4		27.9		31.5		28.1	
p-Value	4.51×10^{-13}		1.77×10^{-13}		1.68×10^{-13}		9.96×10^{-12}	

Linear, interaction, and quadratic effects were included in an initial full quadratic model. A backward stepwise regression algorithm was used to correlate the experimental data with the proposed model. Significant estimations and their p-Values display the relationship between studied cytokines and the respective response variable. Quality of determined regressions and degree of correlations was expressed by the coefficient of determination (R^2), root mean squared error (RMSE), adjusted coefficient of determination and statistic regression test and associated p-Value. Every regression and quality measures were determined for CS_HSPC/MSC and CS_HSPC.

deviation between the model and data points (**Figure 4D** and **Supplementary Figures 1D, 2D, 3D**). With an average residual of 0.10 ± 0.02, CS_HSPC/MSC consistently showed increased correlation between the experimental data and the determined regressions for every response variable compared to the CS_HSPC with an average residual of 0.13 ± 0.01.

Cytokine Concentration Optimization

Each calculated regression gave rise to a distinct response surface, limited by the design space. As predicted by the estimated parameters, every response variable produced a response surface with some degree of concavity, being a direct consequence of negative quadratic effects (**Figure 5**). Maximization of each surface inside the design window was performed. Concentrations corresponding to the maximum were defined as the optimal cytokine combination for that specific response variable (**Table 3**). Since the values of FI TNC and FI CD34$^+$ cells possessed coinciding reaction fingerprints, their respective optimal combinations were very similar, which was observed for both expansion systems (**Figure 6**). Variables that did not possess negative quadratic effects for a certain cytokine in their regression caused their optimal concentration to reach the limit of the design space (100 ng/mL). Optimization was done for every response variable, which resulted in 4 optimized cytokine concentrations in each expansion approach. Due to their higher quality regressions and more quantitative nature, optimal concentrations of FI TNC number and FI CD34$^+$ cells were given priority over the CFU output variables. Equal importance

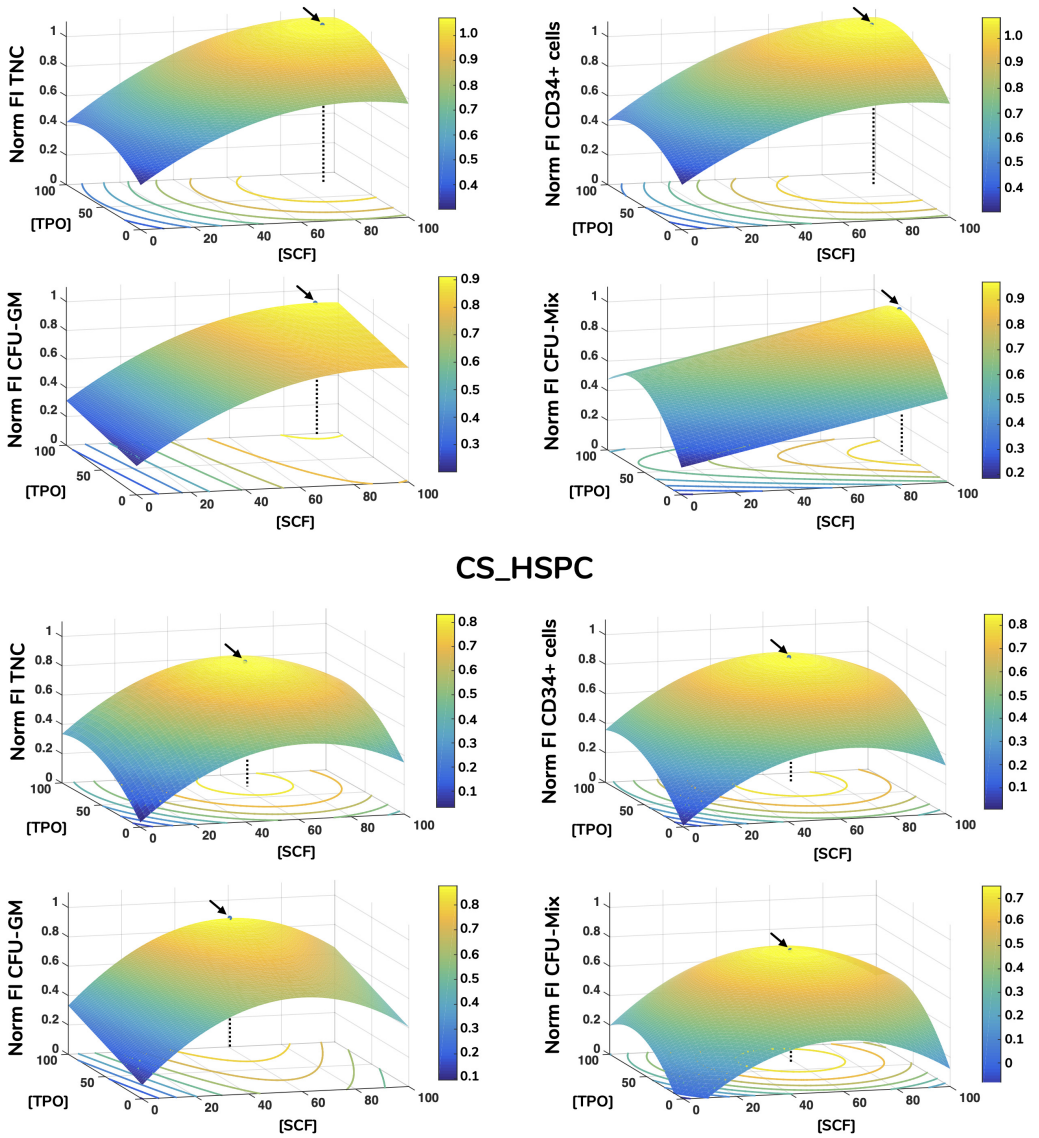

FIGURE 5 | Response surface plots of every response variable with localization of optimal cytokine concentrations for HSPC suspension culture (CS_HSPC) and HSPC co-cultured with BM MSC (CS_HSPC/MSC). Calculated regressions were extrapolated to the whole design window, originating response surfaces. Surface plots containing the response surfaces were observed for the identification of a local optimal response. Regressions were maximized inside the limited design window, giving rise to the optimized cytokine cocktail. These are represented by a black arrow, while a dotted line highlights the corresponding cytokine concentrations that led to the maximum response. Flt-3L concentration was maintained constant at their respective optimal concentration. Norm – normalized.

was given to the chosen variables and an average of their optimal combinations was performed to reach the final optimal combination (coined as AB20) for each expansion type.

Validation

In order to validate the determined response surfaces for each response variable, their range of applicability was evaluated. Cocktails with concentrations not included in the initial experimental design panel are excellent candidates to assess predictive capabilities of calculated regressions. Besides the optimized cocktails (AB20), the combination of cytokines from our previous study (Z9) (Andrade et al., 2010), determined exclusively for the co-culture expansion system and using a different serum-free culture medium formulation, was also selected for validation studies ([SCF] = 60 ng/mL; [Flt-3L] = 55 ng/mL; [TPO] = 50 ng/mL).

Respective regressions were applied to determine predicted responses of each variable. Also, confidence intervals were determined to define the expected range of prediction variation. HSPC expansion using the selected conditions was performed

TABLE 3 | List of every optimized cocktail with respective denomination and selection of the final selected combination (ng/mL).

		CS_HSPC/MSC				CS_HSPC		
Response variable	**Cocktail**	**[SCF]**	**[Ftl-3L]**	**[TPO]**	**Cocktail**	**[SCF]**	**[Flt-3L]**	**[TPO]**
FI TNC	**HM1**	88	82	80	**H1**	63	60	80
FI CD34 + cells	**HM2**	92	82	75	**H2**	64	62	80
FI CFU-GM	**HM3**	92	99	100	**H3**	61	65	100
FI CFU-Mix	**HM4**	100	55	75	**H4**	59	–	70
Selected cocktail	**AB20**	90	82	77	**AB20**	64	61	80

A total of 8 different optimal combinations were obtained. Prioritization for FI TNC and FI CD34$^+$ cells with an average of their optimal concentrations, originated the selected cocktail for both expansion systems (AB20).

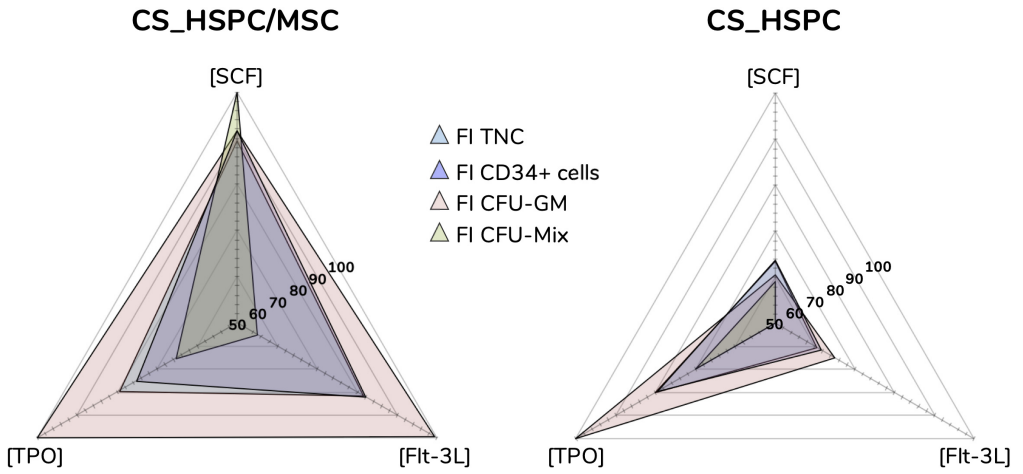

FIGURE 6 | Optimal cytokine concentrations for every response variable and expansion system (ng/mL). Maximization of regressions led to optimal cytokine concentrations. Concentration plots displaying the different optimal cocktails observed for each response variable. Sharp differences were detected between both expansion systems, evidencing that cytokine influence is majorly dependent on the expansion approach.

and resulting experimental data compared. Only 2 out of 32 experimental points (6.25%) were outside the predicted range, FI CFU-GM expanded with Z9 in CS_HSPC/MSC and FI CFU-GM expanded with AB20 in CS_HSPC (**Figure 7A**).

If regressions were to be used as a comparison tool and AB20 and Z9 considered as competitors, every regression would able to successfully predict the outcome between them. FI TNC number and FI CD34$^+$ cells using a AB20 combination in CS_HSPC/MSC were considerably higher when compared to the Z9 cocktail (FI $TNC_{CS\_HSPC/MSC}$: 1.00 ± 0.00 vs. 0.89 ± 0.03; FI TNC_{CS_HSPC}: 0.95 ± 0.05 vs. 0.97 ± 0.03) (FI $CD34^+_{CS\_HSPC/MSC}$: 1.00 ± 0.00 vs. 0.87 ± 0.03; FI $CD34^+_{CS\_HSPC}$: 0.97 ± 0.03 vs. 0.93 ± 0.07) (**Figure 7B**). The remaining comparisons resulted in no substantial difference between tested cytokine cocktails, as predicted by their respective regressions. CD34 median intensity fluorescence (MFI), CAFC assays and levels of expansion of cells with a more primitive phenotype (%CD34$^+$CD90$^+$) were also analyzed to discern the effects of the AB20 combination on other relevant clinical variables (**Figures 7C–E**). Coherent increases of CD34 MFI in both culture systems using the AB20 cocktail were observed when compared to the Z9 cocktail (CD34 $MFI_{CS\_HSPC/MSC}$: 1.00 ± 0.00 vs. 0.88 ± 0.06; CD34 MFI_{CS_HSPC}: 1.00 ± 0.00 vs. 0.80 ± 0.03). In terms of FI CAFC, AB20 cocktails in both expansion systems originated more colonies. Optimized cocktails were responsible for an increase of 2.5 ± 0.3 in CAFC compared to Z9 in the CS_HSPC/MSC, while AB20 also produced 4.7 ± 1.1 more colonies than Z9 in the CS_HSPC. On the other hand, AB20 cocktails had mixed performance concerning expansion of primitive progenitors. Both cocktails maintained a residual population percentage of CD34$^+$CD90$^+$ cells regardless of the culture system, with AB20 resulting in an average of 2.59 ± 0.68% and Z9 in an average of 2.65 ± 0.74%.

Differential Cytokine Influence

This systematic method of achieving optimization provided considerable insight into the relationship between cytokines and cells in both expansion systems (i.e., HSPC culture with/without a BM MSC feeder layer). Cytokine reaction fingerprints were previously mentioned and were compared to highlight differences in cytokine influence (**Figure 8**).

Normalized FI TNC number (**Figure 8A**) displayed significative differences in several specific combinations, leading to three main observations. Firstly, the total fingerprint area for this variable for CS_HSPC/MSC was higher compared to the CS_HSPC ($Area_{CS\_HSPC/MSC}$ = 1.02 vs. $Area_{CS\_HSPC}$ = 0.59). Thus, the presence of a feeder layer appears to synergize with

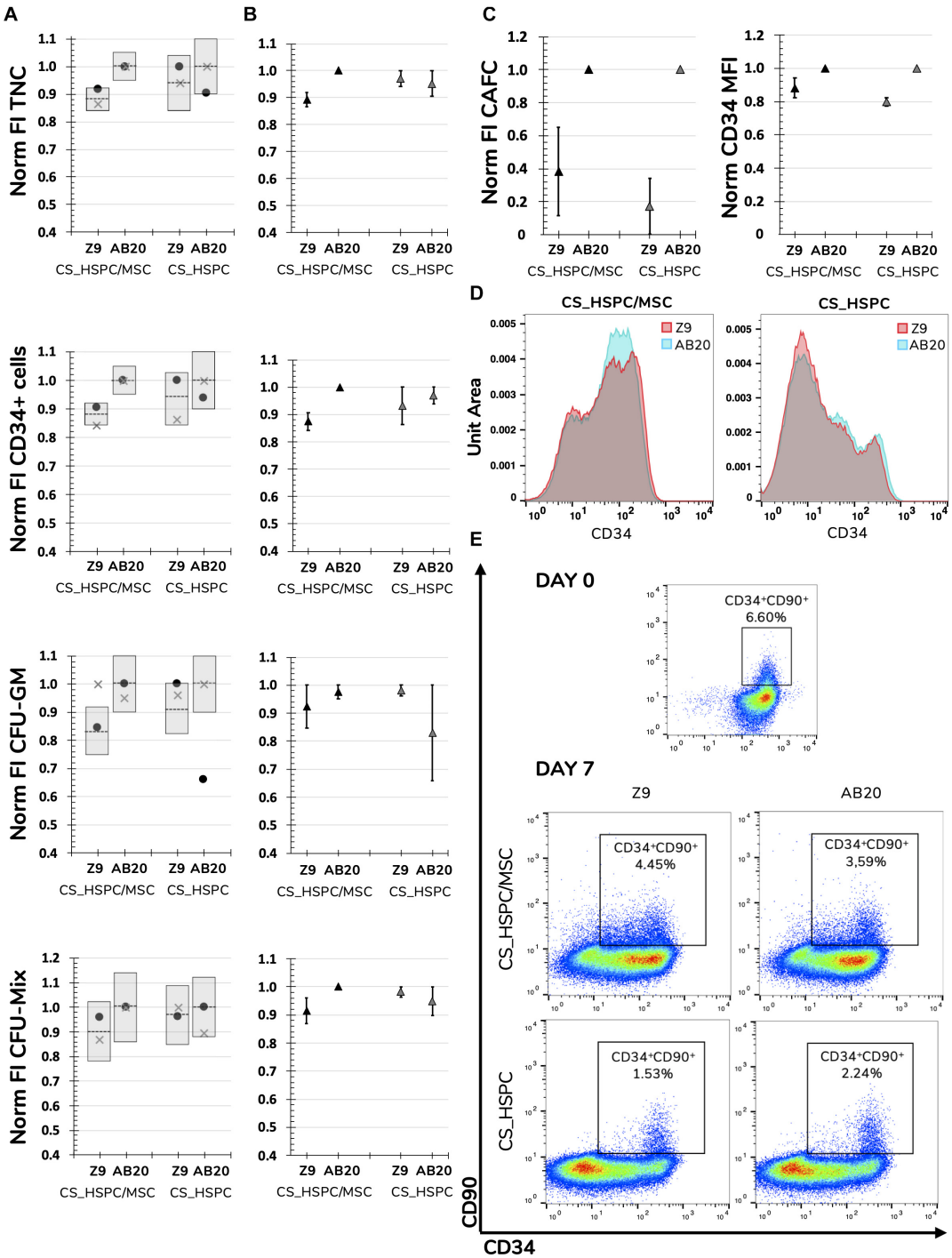

FIGURE 7 | Validation of determined response surfaces and in-depth analysis of AB20 cocktails. **(A)** AB20 and Z9 cocktails were used as validation tests for calculated regressions. Predictability of regressions was analyzed by comparing function predictions and respective confidence intervals with experimental confirmation for every response variable and expansion system. Prediction represented by dashed line and confidence intervals by gray columns. **(B)** Average of two different donors showed that biological variability did not affect the predicted outcomes of comparison between Z9 and AB20. AB20 performed better or similar to Z9 cocktails as anticipated by the prediction and respective 95% confidence intervals. **(C)** Further comparison highlighted that benefits of AB20 cocktail determination went beyond selected response variables. Expansion using AB20 cocktails led to higher fold increase in CAFC and higher CD34 median fluorescence intensity. **(D)** Representative histogram of CD34 expression demonstrating that AB20 cocktails are able to delay loss of this marker during expansion. **(E)** Representative dot plots of CD34 and CD90 expression before and after expansion using both culture systems and cocktails. Initial $CD34^{+}CD90^{+}$ population is mostly lost during expansion, although a residual population percentage is observable in every condition. Mixed results were visible concerning maintenance of the more primitive population. Populations were previously gated for live cells using a viability assay. Data is represented by the mean ± standard error of the mean.

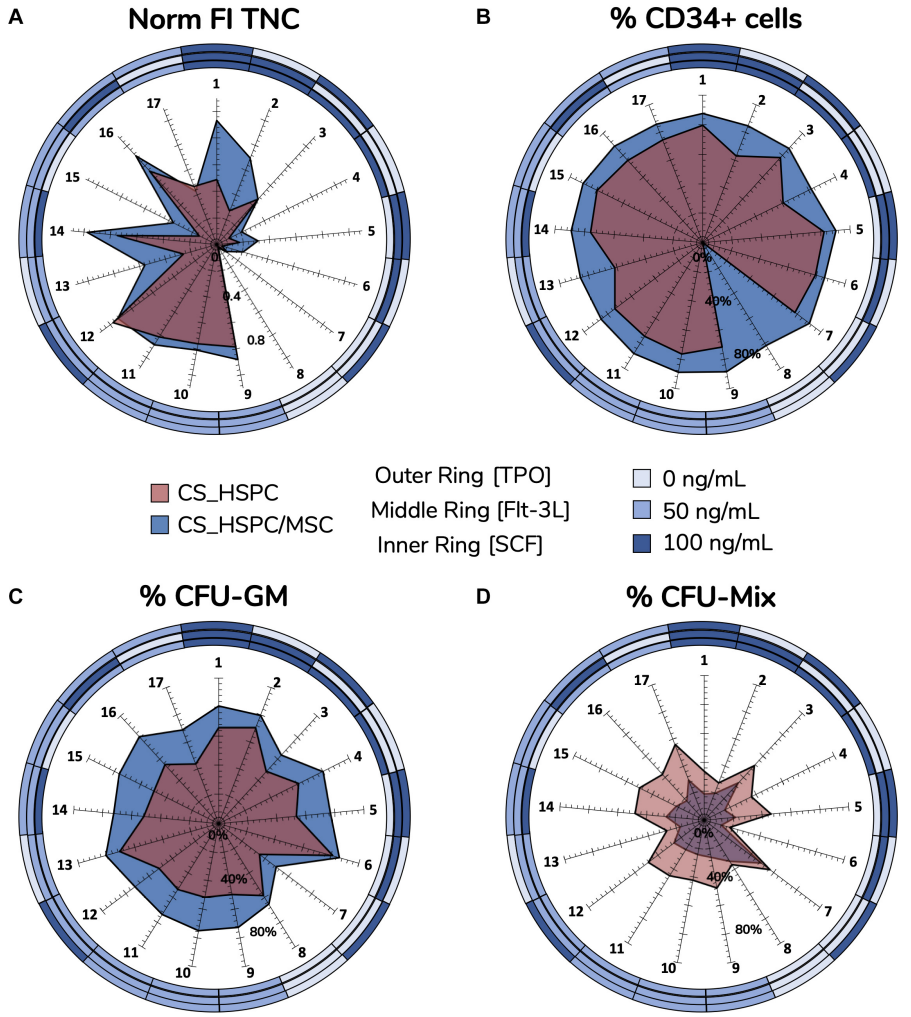

FIGURE 8 | Reaction fingerprints obtained out of the 17 cytokine combinations. Information obtained from creating response surfaces can be exploited to further assess the relationship between an expansion system and cytokine use. Unique reaction fingerprints were determined for normalized FI TNC **(A)**, percentage of $CD34^+$ cells **(B)**, percentage of CFU-GM **(C)**, and percentage of CFU-Mix **(D)**. Circular rings around plots display respective cytokine concentrations associated with each data point. CS_HSPC/MSC appear to synergize better with cytokines, except for CFU-Mix. Percentage of CD34 expression for cytokine combination 8 in the CS_HSPC was not quantified due to insufficient cell number.

cytokine benefit during culture, boosting expansion levels closer toward their maximum performance. Moreover, the reaction fingerprints show that CS_HSPC is more vulnerable to the lack of an individual cytokine than CS_HSPC/MSC. Cells expanded in co-culture display an alleviated negative response whenever a combination without the presence of a cytokine was used. Lastly, adverse effects in cell expansion performance due to excess of cytokines are evident in CS_HSPC, shown by the transition between center points (combination 9, 10, and 11) and the combination with highest concentration of each cytokine (combination 1).

Lack of sensitivity of CD34 expression (**Figure 8B**) to the cytokine panel led to a circular-shaped reaction fingerprint. Over the entire cytokine panel, CS_HSPC/MSC displayed a reduced CV of 4.5 ± 3.9% for $CD34^+$ cell percentage, while CS_HSPC exhibited a CV of 12.4 ± 8.8%. Nevertheless, CS_HSPC showed some dependence on TPO, since combinations without TPO had some negative impact on CD34 expression. **Figure 8B** evidences the impact of losing TPO for CS_HSPC. A decrease in $CD34^+$ cell percentage of 16.4% was observed between combination 1 to 2, 17.3% from combination 3 to 4 and 12.5% from combination 12 to 13.

Colony-forming unit outputs (**Figures 8C,D** and **Supplementary Table 1**) had complementary reaction fingerprints, due to insignificant BFU-E quantification. Percentage of CFU-GM had low variation due to the cytokine panel, although some differences were visible. Fingerprint area was ubiquitously larger for co-culture system ($Area_{CS\_HSPC/MSC}$ = 17 142 vs. $Area_{CS\_HSPC}$ = 9838), demonstrating that its priming toward the granulocyte-macrophage lineage did not change with different cytokine cocktails. Clear benefits were apparent from Flt-3L

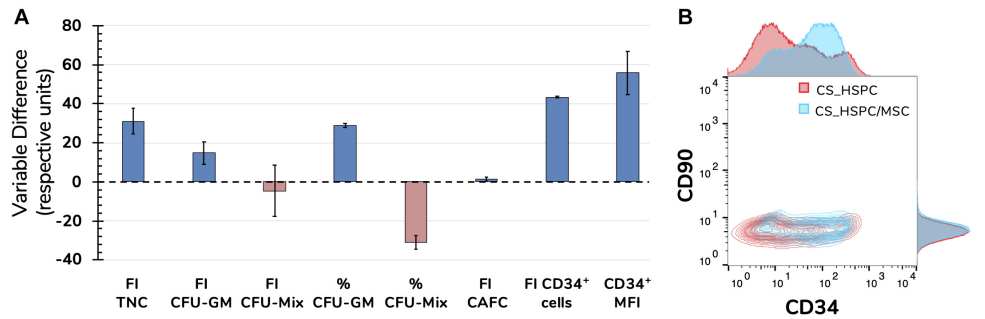

FIGURE 9 | Side-by-side comparison between expansion systems with respective optimal cytokine concentrations (n = 2). **(A)** A number of significant variables concerning HSPC expansion were chosen as comparison criteria between CS_HSPC (red) and CS_HSPC/MSC (blue). Co-culture displayed superior performance in most variables, with the exception of FI CFU-Mix and percentage of CFU-Mix. **(B)** Contour plot of CD34 and CD90 expression after 7 days expansion with AB20 cocktail. At day 7, CS_HSPC/MSC demonstrated a substantially different CD34 expression profile, being able to retain expression of CD34 more effectively when compared to CS_HSPC. Data is represented by the mean ± standard error of the mean.

supplementation, whereas TPO seemed to influence against CFU-GM development. This was more obvious in CS_HSPC, where combinations with those features (combination 2, 6, and 13) caused the differences in CFU-GM percentage between fingerprints of both systems to narrow.

Comparison of Expansion Strategies

Upon completion of the optimization approach, cytokine contribution in each HSPC expansion system was maximized allowing a fair side-by-side comparison of the two studied expansion platforms. Several variables were followed during cell expansion at their maximum cytokine strength. The overall scale was clearly favorable toward the co-culture system, with six out of eight measures (75%) evidencing a better performance (**Figure 9A**). However, CS_HSPC demonstrated more capability toward promoting mixed colonies in the CFU assay in detriment to granulocyte-macrophage colonies. Although none were able to maintain the initial CD34 phenotype of UCB cells after 7 days, CS_HSPC/MSC showed it was able to significantly reduce the loss of this surface marker in cultured cells with a positive CD34 MFI difference compared to the CS_HSPC of 55.8 ± 7.8. When compared, the respective CD34 expression histograms appear almost mirrored (**Figure 9B**). Thus, with their cytokine cocktails optimized, expansion using a co-culture system demonstrated an overall superior potential in generating an expanded a HSPC product with higher retention of CD34 expression and primed for originating more CFU-GM.

DISCUSSION

With cell therapy manufacturing gaining traction as more advanced cell-based therapies get approved and reach the commercialization stage, efforts have been made in promoting the adoption of "Quality by Design" (QbD) guidelines, including process optimization and experimental design, while encouraging their implementation early on during the research and development phase (Rathore and Winkle, 2009; Lipsitz et al., 2016).

Experimental design of cytokine cocktails has been previously pursued, especially during initial studies on UCB-derived HSPC *ex vivo* expansion (Andrade et al., 2010; Pineault et al., 2011). However, applicability of the aforementioned studies to current expansion strategies is restricted. Whether due to having been performed in non-human cells (Audet et al., 2002), used to study *ex vivo* hematopoietic differentiation rather than HSPC expansion (Cortin et al., 2005; Lim et al., 2011) or to the lack of surface response models and optimization (Petzer et al., 1996; Tursky et al., 2012), previous attempts struggle in being transposed to present expansion protocols. This can be justified by a gradual improvement of HSPC expansion protocols, where innovation has eventually led to inconsistencies between culture conditions in current strategies and in abovementioned optimizations. Basal culture media have had their own dynamic evolution over time. Earlier culture media used in *ex vivo* HSPC expansion protocols were typically composed of basic formulations, having been developed for more generic cell culture applications. These usually required supplementation with FBS in order to enrich the formulation to allow for cell expansion, with such basal media varying between Minimum Essential Medium Eagle – Alpha Modification (α-MEM) (Amsellem et al., 2003; de Lima et al., 2008; Horwitz et al., 2014), Iscove's modified Dulbecco's Medium (IMDM) (Gilmore et al., 2000; Çelebi et al., 2012) and others (reviewed in Costa et al., 2018). With the development of culture media specifically for human HSPC expansion, aligned with growing concerns with the use of FBS as an undefined supplement, formulations were developed to be serum-free, with protocols implementing specialized culture media such as X-VIVO™ 10 medium (Kögler et al., 1999), QBSF-60 serum-free medium (Qiu et al., 1999; Gonçalves et al., 2006), StemLine® stem cell expansion medium (Tiwari et al., 2013) and StemSpan™ serum-free expansion medium (Delaney et al., 2010; Fares et al., 2014; Wagner et al., 2016; Bari et al., 2018). This has benefited cell expansion results but ultimately compromised the applicability of previous optimizations described in the literature. Although we have contributed toward the resurgence of optimization of culture conditions targeting the expansion of human HSPC, our

own initial study on cytokine supplementation optimization was performed with QBSF-60 medium as the established expansion medium (Andrade et al., 2010). This proprietary serum-free medium was originally designed to support human $CD34^+$ cells (Qiu et al., 1999).

With StemSpan^{TM} (STEMCELL Technologies) medium being more prevalent in latest studies on HSPC *ex vivo* expansion and in most advanced clinical trials testing expanded HSPC (Wagner et al., 2016; Zonari et al., 2017; Bari et al., 2018; Calvanese et al., 2019; Cohen et al., 2019), we have seized this opportunity to achieve an enduring optimization with direct impact on ongoing late-stage development of cell therapies based on *ex vivo* expanded HSPC from UCB. However, the formulation StemSpan^{TM} serum-free medium used herein still has undisclosed supplements and some animal-derived components in its formulation (i.e., bovine albumin). In the absence of a clearly defined and disclosed formulation, possible extrapolation of our results to different media is limited and any animal-derived components increase the risks of contamination. Nevertheless, with the cell therapy manufacturing field pressing for animal-component free and chemically defined formulations, StemSpan^{TM} medium has currently adapted to those needs. If existing or novel strategies decide to transfer to such formulations through regulatory pressure or due to new GMP guidelines, our optimization study with StemSpan^{TM} stands a considerable chance in maintaining its applicability on clinical-grade *ex vivo* HSPC expansion.

In our work, we have aimed at achieving an enduring optimization of cytokine supplementation for two clinically relevant *ex vivo* HSPC expansion platforms, CS_HSCP and CS_HSPC/MSC (i.e., HSPC being expanded alone in a liquid culture system or co-cultured with a BM MSC feeder layer, respectively). With cytokines maintaining a significant role in protocols of *ex vivo* expansion of human HSPC (Lund et al., 2015), namely those from UCB, optimization of the used concentrations through experimental design is crucial. When attempted, optimization applied to biological issues with inherent variability is largely determined by the existence of a donor-independent pattern. Once approved as a therapy, UCB-derived expanded HSPC will hope to be produced from a single cord unit. Therefore, donor variability is a central issue and must be considered when performing such studies and thus selected response variables were followed for three different donors to increase the robustness of the optimized cocktail (Csaszar et al., 2013). As expected, biological variability was present and may be partly related to differences observed in the initial CD34 expression after enrichment (Andrade et al., 2011). Interestingly, this variability did not prevent the appearance of a recurring pattern in every response variable (**Figure 4** and **Supplementary Figures 1–3**). Although different donors of UCB cells originated different absolute values for the selected response variables, cell-cytokine relationship did not change and cytokine optimization was carried out.

Early on, we observed that our response variables displayed greater fluctuations with lower concentrations of the defined cytokine panel (SCF, Flt-3L, and TPO). A certain degree of cytokine saturation was apparent from the center points (concentrations of 50 ng/mL) onward (**Figure 3**). With many expansion platforms being employed in clinical trials using concentrations of 100 ng/mL or higher (Boitano et al., 2010; Delaney et al., 2010; de Lima et al., 2012; Fares et al., 2014), there is an observable overuse of cytokine supplementation without a rational justification. Excess amount of these molecules will be responsible for unnecessary costs, which might jeopardize the implementation of the respective potential cell therapies (Csaszar et al., 2013). Eventually, this overload of cytokine molecules can also have a negative impact on the cells themselves, since it largely differs from the levels of cytokines that HSPC experience *in vivo*. With concentrations of cytokines in the BM ranging in the picomolar (Wodnar-Filipowicz et al., 1993; Huchet et al., 2003; Zhang et al., 2016), several groups may be crippling their expansions with HSPC overstimulation. Interestingly, in contrast to the four main response variables (FI TNC, FI $CD34^+$ cells, FI CFU-GM, and FI CFU-Mix), CD34 expression observed post-expansion was an exception to the previously described behavior. This surface marker expressed by HSPC did not display any significant variation to the cytokine panel but did vary with other factors, such as cell expansion platform (CS_HSPC vs. CS_HSPC/MSC) and culture duration (**Figure 8B**). In general, selected response variables met optimization requirements, such as pattern emergence and fluctuation inside the design space.

As mentioned beforehand, modeling biological behavior with precision can be a challenge, depending on the nature of the selected response variables. Naturally, better quality regressions arose from more quantitative measures, such as FI TNC number (**Table 2**). Both CFU and CAFC outputs suffer from some subjectivity, inherent to these specific assays, requiring a significant dependence on experimental technique to originate results that make modeling possible (Purton and Scadden, 2007; Powell et al., 2016). The existence of a single outlier proves the quality of the response variable measurements.

Taking each of these regressions into account, CS_HSPC/MSC was able to produce more consistent results than its counterpart system (i.e., without a feeder layer). The presence of a BM MSC feeder layer (originally anticipated to better recreate the HSPC niche *ex vivo*) appears to create a buffer zone environment which is capable of making responses and expansion performance more uniform. This may be related with the specific cell expansion dynamics of a co-culture setting. During this type of culture, HSPC that adhere directly to the stromal feeder layer and are phase-bright (i.e., do not migrate underneath the feeder layer) become responsible for most of the cell division observed over the culture duration (Alakel et al., 2009). Although the fraction of non-adherent or suspended cells typically has the highest fold increase in cell number, these cells themselves do not seem to be proliferatively active. Only phase-bright adherent cells were observed to have an active cell cycle with a considerable cell number in the G2/M phase (Jing et al., 2010). Thus, attached HSPC, which saturate the entire stromal layer, are responsible for the increase in the non-adherent cell fraction observed by releasing their progeny into suspension (Jing et al., 2010). This behavior may justify lower cell expansion variation, since contact area saturation of the stromal layer appears to become the main regulator of proliferation, creating a stable cell expansion

mechanism. Although co-culture introduces more biological factors, the results obtained for this platform have displayed reduced experimental deviation. Despite this, every response variable in both systems originated a good degree of correlation in their respective regressions, despite the existence of some expected variability.

Regression manipulation gave origin to a total of 8 optimal combinations, resulting from the selection of four response variables (FI TNC, FI $CD34^+$ cells, FI CFU-GM, and FI CFU-Mix) for two different expansion systems (**Figure 6**). Prioritization of variables was required to appoint a single and representative optimal cytokine combination for each expansion platform. For most clinical trials related with *ex vivo* expansion of HSPC, TNC and number of $CD34^+$ cells are selected as critical parameters (Wagner et al., 2016; Cohen et al., 2019). Considering their significant clinical relevance allied to their higher regression quality, these two measures (i.e., FI TNC and FI $CD34^+$ cells) were chosen to define the optimal cocktails for each culture system. Following the described rationale, prioritization of variables led to determination of optimal cocktails (AB20) for the CS_HSPC ([SCF] = 90 g/mL; [Flt-3L] = 82 ng/mL; [TPO] = 77 ng/mL) and for the CS_HSPC/MSC ([SCF] = 64 ng/mL; [Flt-3L] = 61 ng/mL; [TPO] = 80 ng/mL) (**Table 3**). These cocktails were responsible for expansion results up to 49 FI TNC and 33 FI $CD34^+$ cells for the CS_HSPC and 75 FI TNC and 70 FI $CD34^+$ cells for the CS_HSPC/MSC from a single UCB unit. When comparing with clinical trial data using these types of platforms (Median FI TNC = 56, Median FI $CD34^+$ cells = 4 for cytokine-based expansion, i.e., feeder free) and Median FI TNC = 12, Median FI $CD34^+$ cells = 30 for co-culture expansion (Lund et al., 2015), cell expansions obtained herein with optimized cocktails demonstrated competitive outcomes, surpassing the performance of most reports of *ex vivo* HSPC expansion in similar platforms. Additionally, with the optimized cytokine cocktails displaying concentrations lower than many current protocols (e.g., Boitano et al., 2010; Delaney et al., 2010), we have highlighted avoidable costs and uncovered an opportunity for a cost-effectiveness measure. These results demonstrate the need for tailored optimization in improving the viability and financial feasibility of UCB-derived HSPC expansion platforms.

Following optimization, regression-derived response surfaces required validation in order to confirm their donor-independent applicability. Validation was successfully completed using two different cocktails, the determined optimal cocktails (AB20) and a previously established optimized cocktail by our group (Z9) (Andrade et al., 2010). Expansion outcome and behavior using these cocktails performed as projected by their respective regressions (**Figure 7A**). The few out-of-bounds experimental points were associated with the semi-quantitative nature of the CFU assay. When compared, AB20 cocktails outperformed or matched Z9 performance concerning the four response variables. Interestingly, AB20 cocktails were able to overtake Z9 in other important measures that were not included in the initial experimental design, including CD34 mean fluorescence intensity and CAFC formation (**Figures 7C,D**). However, since AB20 and Z9 cocktails were located in the higher concentration range, their comparison was challenging, since lower variations of response variables were previously highlighted for that range. As expected, with concentrations differences lower than 30 ng/mL, determined regressions predicted only slight differences between AB20 and Z9 for some response variables. Nevertheless, solid predictive capacity was demonstrated and optimized cocktails still showed superior expansion performance.

Throughout this study, we have once more confirmed the important role cytokines play in promoting HSPC expansion. Taking advantage of this optimization, we also focused on the cell-cytokine relationship to further complement our comparison between CS_HSPC and CS_HSPC/MSC. By identifying the existence of unique reaction fingerprints, we were able to shed light on the different impact cytokines have on both studied expansion platforms. These fingerprints showed obvious distinctions in cytokine reaction behavior. In agreement with previous observations, the BM MSC feeder layer seems to develop a protective microenvironment around the HSPCs, resembling their role in the BM niche. In fact, FI TNC reaction fingerprint from CS_HSPC evidenced its higher vulnerability to early culture saturation by excess quantities of cytokines (**Figure 8A**). Indeed, the presence of a BM MSC feeder layer was able to ameliorate negative cytokine inhibition. When adding an interactive feeder layer, the network of individual and synergistic cytokine effects changes and gains complexity (Kirouac and Zandstra, 2006). While the exogenous cytokines added to the culture medium in both systems are the same, the environment of endogenous cytokines and their respective quantities change due to feeder cell presence. With a very dynamic secretome, MSC are known to produce other cytokines that promote HSPC expansion (Lund et al., 2015). By better mimicking the hematopoietic niche with this stromal component, the microenvironment is able to reach a higher number and level of synergies which can potentially lead to higher cell expansion yields (Wagner et al., 2007; Méndez-Ferrer et al., 2010).

Knowledge from these reaction fingerprints and their regressions may be used for purposes other than the expansion of UCB-derived HSPC for HCT. Revived interest in autologous gene therapy has consolidated the application of expanded adult HSPC for treatment of genetic hematological diseases (Naldini, 2015; Dunbar et al., 2018). Approval of Strimvelis, a gene therapy product of transduced autologous BM-derived $CD34^+$ cells for treatment of severe combined immunodeficiency due to adenosine deaminase deficiency, was a milestone in the field and represents the considerable potential that expanded HSPC have in gene therapy (Hoggatt, 2016). Other areas within the hematological field can also potentially take advantage of these regression strategies to tailor HSPC culture for their own needs. There has been interest in using UCB-derived HSPC culture platforms for the differentiation of cells toward the lymphoid lineage for use in immunotherapy (e.g., donor lymphocyte infusions, tumor-infiltrating lymphocytes, etc., Singh and Zúñiga-Pflücker, 2018). Both culture systems included in this study have been explored for such purposes. CS_HSPC/MSC has been shown to have potential as a system to maintain early lymphoid progenitors (i.e., $CD34^+CD7^+$ cells) (da Silva et al., 2010) and support the generation of functional natural killer and

dendritic cells (Frias et al., 2008). On the other hand, CS_HSPC in combination with the small molecule StemRegenin-1 has been recently used for generation of progenitor T cells (Singh et al., 2019). Exploitation of these expansion systems for such different applications can also largely benefit from the cytokine optimization strategy established in the present study and the information gathered on the effects of cytokines on cultured cells.

To our knowledge, cytokine optimization has not been used as a tool to enable a correct side-by-side comparison of different strategies. This evaluation is critical for decision-making over which platform should be supported for clinical trial progression or apply for regulatory approval. Criteria for the selection of cytokine concentrations have roughly been the same throughout different types of expansion culture systems, ignoring high specificity of each strategy. Without determining unique cytokine cocktails for each one, direct comparison of published results in an unstandardized manner may cause unrealistic conclusions. By pursuing a tailored cytokine optimization in two expansion approaches, these may be rightfully compared at their full cytokine potential, making their critical steps and parameters more easily identifiable (Lipsitz et al., 2016).

In the optimized conditions of our study, CS_HSPC/MSC undoubtedly showed better capabilities in promoting HSPC expansion, which explains the progression of *ex vivo* mesenchymal-cell coculture through the clinical trial pipeline (de Lima et al., 2012). In our assessment, CS_HSPC/MSC proved to have a superior production capacity as a platform concerning every studied variable except for FI CFU-Mix (**Figure 9**). Notably, CD34 expression, which displayed reduced variability due to cytokine effects, was observed to be consistently higher in an HSPC/MSC co-culture setting. This difference was originally observed by comparing cytokine reaction fingerprints of the percentage of $CD34^+$ cells (**Figure 8B**) and was quantitively confirmed in optimal conditions by comparison of CD34 median intensity fluorescence (**Figures 9A,B**). Indeed, enhanced expansion of HSPC through a co-culture setting with MSC has also been observed in other studies. Beneficial impact compared to traditional liquid suspension has been described concerning cell expansion levels (da Silva et al., 2010; Fajardo-Orduña et al., 2017; Darvish et al., 2019), but also in what concerns the biological features of the cultured cells, for instances, contributing toward an enhanced migration capability of HSPC (Alakel et al., 2009; Perdomo-Arciniegas and Vernot, 2011). Overall, our evaluation of each expansion system after cytokine optimization has provided a more reliable and unbiased view over their genuine production capabilities of a potential expanded HSPC product.

To fully assess the viability of these systems as potential cell therapy platforms, the entire manufacturing process needs to be considered. Importantly, we have used cryopreserved UCB HSPC to mimic the UCB unit processing in current clinical trials, as these pioneering trials normally lay the groundwork for the manufacturing process of the respective approved product. With source cryopreservation being an important bioprocess step that can have an impact on the characteristics of the cell product (e.g., need for cell revitalization), disregarding it can also affect optimization applicability. Additionally, acquired process knowledge of cytokine interactions will also prove to be very useful in building such a manufacturing pipeline for an expanded HSPC product (Lipsitz et al., 2016). Determined regressions will provide critical information on expansion reaction and a degree of predictability if unavoidable changes in cytokine concentration should happen during production. However, expansion yield by itself is not the only priority in cell therapy development and an overall balance among operational parameters is needed (de Fuzeta et al., 2019). Although CS_HSPC/MSC was shown to produce a higher number of expanded HSPC with superior quality measures necessary for HCT, it also holds a higher level of complexity as a culture system. Normally, a trade-off between complexity and feasibility has existed in the manufacturing of cell therapies, hindering their translation (Dodson and Levine, 2015). In this case, the presence of a feeder layer in the expansion system will require add-ons or modifications to its manufacturing process when compared to the simpler CS_HSPC. An additional upstream source collection and isolation procedure for MSC will be needed, while downstream units will have to be able to separate MSC from expanded HSPC to assure end product purity. Also, preparation of MSC feeder layers inevitably increases the total culture duration and requires culture formats compatible with adherent cell culture. All these issues, which might prove challenging or costly, need to be considered and counterbalanced with the performance increase shown by CS_HSPC/MSC in product quantity and quality. Therefore, bioprocessing studies with economic modeling must accompany this co-culture system to determine if this more complex platform is worthwhile (Csaszar et al., 2013; Chilima et al., 2018; Mizukami et al., 2018; de Pinto et al., 2019).

Strategies similar to our experimental design should become widespread, as they represent a statistically sound and efficient way to reach optimal experimental conditions (Lipsitz et al., 2016; Toms et al., 2017). The methodology applied in our study, targeting the use of cytokines for *ex vivo* HSPC expansion, can be translated to other culture parameters and applications. Stem cell fate studies (self-renewal vs. differentiation) (Barbosa et al., 2012; Dias et al., 2019), as well as biomaterial development for tissue engineering (Levin et al., 2018), are fields that are centered on continuous improvement and optimization of experimental conditions in order to reach a defined differentiated cell type or scaffold, respectively. Filled with possible optimization parameters (e.g., differentiation media, oxygen tension, cell aggregate size, scaffold porosity, stirring speed in bioreactor systems, etc.), studies benefit immensely by using experimental design as they avoid unnecessary iterations of dose-response experiments, reduce reagent and material costs and become more time-efficient (Levin et al., 2018; Branco et al., 2019).

With our study, we had aimed at addressing three different goals. Initially, with expansion strategies reaching or advancing through the clinical trial pipeline, we recognized a window of opportunity where performed optimizations could be implemented without losing their applicability and sharing the same fate as previous studies. We were successful in optimizing each of the studied expansion systems, leading to improved expanded HSPC products with higher expansion yields while potentially maintaining the quality necessary for

expanded HSPC to produce their expected therapeutic value (i.e., reconstitute the entire hematopoietic system), characterized herein by their $CD34^+$ expression and multilineage-potential. Thus, we have produced enduring optimizations that directly influence clinically important HSPC expansion platforms or may even guide novel HSPC expansion strategies in the future. Secondly, as these strategies are simultaneously progressing toward regulatory approval, we had also ambitioned establishing optimization as a tool to perform a rational and comprehensive evaluation between different approaches. By doing so, differences between CS_HSPC and CS_HSPC/MSC were emphasized in an unbiased manner. Our study can influence decision-making and risk analysis of both systems as expansion platforms undergoing regulatory funneling to reach commercial approval. Finally, by increasing process knowledge on cytokine supplementation, we have contributed toward the implementation of an approved UCB-derived *ex vivo* expanded HSPC therapy concerning its manufacturing and production process. Moreover, we have promoted the framework behind our study and its results to be used for other potential stem cell-based products outside its original scope, in terms of development, manufacturing and economic perspectives.

The optimization performed herein will allow further work to build on improved expansion platforms. Having ascertained the necessary cytokine requirements for CS_HSPC/MSC and CS_HSPC systems, we expect to explore the scalability of these platforms. With a seeding density of 30 000 cells/mL, the validation of larger expansion volumes with optimized culture conditions will provide an opportunity to reach clinically relevant cell numbers and contribute toward the establishment of expanded HSPC as a clinically viable cell therapy. Also, recognizing the limitations of relying on immunophenotypic characterization as a predictor of therapeutic potential for expanded HSPC performed in clinical trials (e.g., expression of CD34), we anticipate an increased relevance of an omics-approach. With more thorough techniques in characterizing cell function, we anticipate that a possible cellular signature linked to therapeutic action in expanded HSPC may be unraveled, allowing the establishment of robust potency and functional assays for such cell-based products which are currently lacking (Kirouac and Zandstra, 2008).

DATA AVAILABILITY STATEMENT

All datasets generated for this study are included in the article/**Supplementary Material**.

ETHICS STATEMENT

UCB units and BM samples were obtained from healthy donors, upon informed consent, with the approval of the ethics committee of Hospital São Francisco Xavier, Centro Hospitalar de Lisboa Ocidental and of Instituto Português de Oncologia Francisco Gentil, Lisboa, Portugal, respectively.

AUTHOR CONTRIBUTIONS

AB, AF-P, and CLdS designed the research study and wrote the manuscript. AB conducted the experiments and modeled the data. SB and JM-S conducted the experiments. CL performed the umbilical cord blood collection, as well as donor screening and evaluation of donor suitability for our study. All authors critically revised and approved the final manuscript.

FUNDING

This work was funded by the iBB – Institute for Bioengineering and Biosciences through the FCT – Portuguese Foundation for Science and Technology (UID/BIO/04565/2019) and by the Programa Operacional Regional de Lisboa (POR) 2020 (Project No. 007317). We also acknowledge the funding received from POR de Lisboa 2020 through the projects PRECISE – Accelerating progress toward the new era of precision medicine (Project No. 16394) and from FCT through the project PTDC/QEQ-EPR/6623/2014. AB and SB acknowledge FCT for their Ph.D. fellowships SFRH/BD/132665/2017 and SFRH/BD/128379/2017, respectively.

ACKNOWLEDGMENTS

We would like to acknowledge the Hospital São Francisco Xavier – Centro Hospitalar Lisboa Ocidental and the Instituto Português de Oncologia de Lisboa Francisco Gentil for their collaboration concerning the donation of UCB units and BM samples, respectively. Current affiliation of JM-S is iBET, Instituto de Biologia Experimental e Tecnológica, and Instituto de Tecnologia Química e Biológica António Xavier, Universidade Nova de Lisboa.

GLOSSARY

UCB, umbilical cord blood; HSPC, hematopoietic stem/progenitor cells; CS_HSPC, HSPC culture system; BM MSC, bone marrow derived mesenchymal stromal cells; CS_HSPC/MSC, co-culture system with BM MSC; SCF, stem cell factor; Flt-3L, fms-like tyrosine kinase 3 ligand; TPO, thrombopoietin; FI, fold increase; FI TNC, fold increase in total nucleated cells; BFU-E, erythroid burst-forming unit; CFU-GM, colony-forming unit granulocyte-monocyte; CFU-Mix, multilineage colony-forming unit; HCT, hematopoietic cell transplantation; BM, bone marrow; GVHD, graft vs. host disease; HLA, human leukocyte antigen; G-CSF, granulocyte colony-stimulating factor; IL-3, interleukin-3; IL-6, Interleukin-6; GMP, good manufacturing practices; MNC, mononuclear cells; USA, United States of America; PBS, phosphate buffered saline; EDTA, ethylenediamine tetraacetic acid; DMEM, Dulbecco's Modified Eagle's medium; FBS, fetal bovine serum; SCERG, Stem Cell Engineering Research Group; bFGF, basic fibroblast growth factor; CAFC, cobblestone area forming-cells; RT, room temperature; CCF, face-centered central composite; RMSE, root

mean squared error; SEM, standard error of the mean; CV, coefficient of variation; R^2, coefficient of determination; MFI, median fluorescence intensity; QbD, quality by design; α-MEM, Minimum Essential Medium Eagle-Alpha Modification; IMDM, Iscove's Modified Dulbecco's Medium.

SUPPLEMENTARY MATERIAL

The Supplementary Material for this article can be found online at: https://www.frontiersin.org/articles/10.3389/fbioe.2020.573282/full#supplementary-material

REFERENCES

Aijaz, A., Li, M., Smith, D., Khong, D., LeBlon, C., Fenton, O. S., et al. (2018). Biomanufacturing for clinically advanced cell therapies. *Nat. Biomed. Eng.* 2, 362–376. doi: 10.1038/s41551-018-0246-6

Alakel, N., Jing, D., Muller, K., Bornhauser, M., Ehninger, G., and Ordemann, R. (2009). Direct contact with mesenchymal stromal cells affects migratory behavior and gene expression profile of CD133+ Hematopoietic stem cells during ex vivo expansion. *Exp. Hematol.* 37, 504–513. doi: 10.1016/j.exphem.2008.12.005

Amsellem, S., Pflumio, F., Bardinet, D., Izac, B., Charneau, P., Romeo, P. H., et al. (2003). Ex vivo expansion of human hematopoietic stem cells by direct delivery of the HOXB4 homeoprotein. *Nat. Med.* 9, 1423–1427. doi: 10.1038/nm953

Andrade, P. Z., da Silva, C. L., dos Santos, F., Almeida-Porada, G., and Cabral, J. M. S. (2011). Initial CD34 + cell-enrichment of cord blood determines hematopoietic stem/progenitor cell yield upon ex vivo expansion. *J. Cell. Biochem.* 112, 1822–1831. doi: 10.1002/jcb.23099

Andrade, P. Z., dos Santos, F., Almeida-Porada, G., da Silva, C. L., and Cabral, J. M. S. (2010). Systematic delineation of optimal cytokine concentrations to expand hematopoietic stem/progenitor cells in co-culture with mesenchymal stem cells. *Mol. BioSyst.* 6, 1207–1215. doi: 10.1039/b922637k

Andrade, P. Z., Soure, A. M., de Santos, F., dos Paiva, A., Cabral, J. M. S., and da Silva, C. L. (2015). Ex vivo expansion of cord blood haematopoietic stem/progenitor cells under physiological oxygen tensions: clear-cut effects on cell proliferation, differentiation and metabolism. *J. Tissue Eng. Regen. Med.* 9, 1172–1181. doi: 10.1002/term.1731

Audet, J., Miller, C. L., Eaves, C. J., and Piret, J. M. (2002). Common and distinct features of cytokine effects on hematopoietic stem and progenitor cells revealed by dose-response surface analysis. *Biotechnol. Bioeng.* 80, 393–404. doi: 10.1002/bit.10399

Barbosa, H. S. C., Fernandes, T. G., Dias, T. P., Diogo, M. M., and Cabral, J. M. S. (2012). New insights into the mechanisms of embryonic stem cell self-renewal under hypoxia: a multifactorial analysis approach. *PLoS One* 7:e38963. doi: 10.1371/journal.pone.0038963

Bari, S., Zhong, Q., Fan, X., Poon, Z., Lim, A. S. T., Lim, T. H., et al. (2018). Ex vivo expansion of CD34+CD90+CD49f+ hematopoietic stem and progenitor cells from non-enriched umbilical cord blood with Azole compounds. *Stem Cell. Transl. Med.* 7, 376–393. doi: 10.1002/sctm.17-0251

Boitano, A. E., Wang, J., Romeo, R., Bouchez, L. C., Parker, A. E., Sutton, S. E., et al. (2010). Aryl hydrocarbon receptor antagonists promote the expansion of human hematopoietic stem cells. *Science* 329, 1345–1348. doi: 10.1126/science.1191536

Box, G. E. P., Hunter, J. S., and Hunter, W. J. (1978). *Statistics for Experimenters: Design, Innovation, and Discovery*. Hoboken. NJ: John Wiley & Sons.

Branco, M. A., Cotovio, J. P., Rodrigues, C. A. V., Vaz, S. H., Fernandes, T. G., Moreira, L. M., et al. (2019). Transcriptomic analysis of 3D cardiac differentiation of human induced pluripotent stem cells reveals faster cardiomyocyte maturation compared to 2D culture. *Sci. Rep.* 9:9229. doi: 10.1038/s41598-019-45047-9

Calvanese, V., Nguyen, A. T., Bolan, T. J., Vavilina, A., Su, T., Lee, L. K., et al. (2019). MLLT3 governs human haematopoietic stem-cell self-renewal and engraftment. *Nature* 576, 281–286. doi: 10.1038/s41586-019-1790-2

Çelebi, B., Mantovani, D., and Pineault, N. (2012). Insulin-like growth factor binding protein-2 and neurotrophin 3 synergize together to promote the expansion of Hematopoietic Cells ex vivo. *Cytokine* 58, 327–331. doi: 10.1016/j.cyto.2012.02.011

Chilima, T. D. P., Moncaubeig, F., and Farid, S. S. (2018). Impact of allogeneic stem cell manufacturing decisions on cost of goods, process robustness and reimbursement. *Biochem. Eng. J.* 137, 132–151. doi: 10.1016/j.bej.2018.04.017

Cohen, S., Roy, J., Lachance, S., Delisle, J.-S., Marinier, A., Busque, L., et al. (2019). Hematopoietic stem cell transplantation using single UM171-expanded cord blood: a single-arm, phase 1-2 safety and feasibility study. *Lancet Haematol.* 7, e134–e145. doi: 10.1016/S2352-3026(19)30202-9

Conneally, E., Cashman, J., Petzer, A., and Eaves, C. (1997). Expansion in vitro of transplantable human cord blood stem cells demonstrated using a quantitative assay of their lympho-myeloid repopulating activity in nonobese diabetic-scid/scid mice. *Proc. Natl. Acad. Sci. U.S.A.* 94, 9836–9841. doi: 10.1073/pnas.94.18.9836

Cortin, V., Garnier, A., Pineault, N., Lemieux, R., Boyer, L., and Proulx, C. (2005). Efficient in vitro megakaryocyte maturation using cytokine cocktails optimized by statistical experimental design. *Exp. Hematol.* 33, 1182–1191. doi: 10.1016/j.exphem.2005.06.020

Costa, M. H. G., de Soure, A. M., Cabral, J. M. S., Ferreira, F. C., and da Silva, C. L., (2018). Hematopoietic niche – exploring biomimetic cues to improve the functionality of hematopoietic Stem/Progenitor cells. *Biotechnol. J.* 13:1700088. doi: 10.1002/biot.201700088

Csaszar, E., Cohen, S., and Zandstra, P. W. (2013). Blood stem cell products: toward sustainable benchmarks for clinical translation. *Bioessays* 35, 201–210. doi: 10.1002/bies.201200118

da Silva, C. L., Gonçalves, R., Crapnell, K. B., Cabral, J. M. S., Zanjani, E. D., and Almeida-Porada, G. (2005). A human stromal-based serum-free culture system supports the ex vivo expansion/maintenance of bone marrow and cord blood hematopoietic stem/progenitor cells. *Exp. Hematol.* 33, 828–835. doi: 10.1016/j.exphem.2005.03.017

da Silva, C. L., Gonçalves, R., dos Santos, F., Andrade, P. Z., Almeida-Porada, G., and Cabral, J. M. S. (2010). Dynamic cell-cell interactions between cord blood haematopoietic progenitors and the cellular niche are essential for the expansion of CD34+, CD34+CD38- and Early Lymphoid CD7+ Cells. *J. Tissue Eng. Regen. Med.* 4, 149–158. doi: 10.1002/term.226

da Silva, C. L., Gonçalves, R., Porada, C. D., Ascensão, J. L., Zanjani, E. D., Cabral, J. M. S., et al. (2009). Differences amid bone marrow and cord blood hematopoietic stem/progenitor cell division kinetics. *J. Cell. Physiol.* 220, 102–111. doi: 10.1002/jcp.21736

Darvish, M., Payandeh, Z., Soleimanifar, F., Taheri, B., Soleimani, M., and Islami, M. (2019). Umbilical cord blood mesenchymal stem cells application in hematopoietic stem cells expansion on nanofiber three-dimensional scaffold. *J. Cell. Biochem.* 120, 12018–12026. doi: 10.1002/jcb.28487

de Fuzeta, M. A., de Branco, A. D. M., Fernandes-Platzgummer, A., da Silva, C. L., and Cabral, J. M. S. (2019). Addressing the manufacturing challenges of cell-based therapies. *Adv. Biochem. Eng.* 171, 225–278. doi: 10.1007/10_2019_118

de Lima, M., McMannis, J., Gee, A., Komanduri, K., Couriel, D., Andersson, B. S., et al. (2008). Transplantation of ex vivo expanded cord blood cells using the copper chelator tetraethylenepentamine: a phase I/II Clinical Trial. *Bone Mar. Transpl.* 41, 771–778. doi: 10.1038/sj.bmt.1705979

de Lima, M., McNiece, I., Robinson, S. N., Munsell, M., Eapen, M., Horowitz, M., et al. (2012). Cord-blood engraftment with ex vivo mesenchymal-cell coculture. *New Engl. J. Med.* 367, 2305–2315. doi: 10.1056/NEJMoa1207285

de Pinto, D. S., Bandeiras, C., Fuzeta, M., de, A., Rodrigues, C. A. V., Jung, S., et al. (2019). Scalable manufacturing of human mesenchymal stromal cells in the vertical-wheel bioreactor system: an experimental and economic approach. *Biotechnol. J.* 14, 1–9. doi: 10.1002/biot.201800716

Delaney, C., Heimfeld, S., Brashem-Stein, C., Voorhies, H., Manger, R. L., and Bernstein, I. D. (2010). Notch-mediated expansion of human cord blood progenitor cells capable of rapid myeloid reconstitution. *Nat. Med.* 16, 232–236. doi: 10.1038/nm.2080

Denning-Kendall, P., Singha, S., Bradley, B., and Hows, J. (2003). Cobblestone area-forming cells in human cord blood are heterogeneous and differ from long-term culture-initiating cells. *Stem Cells* 21, 694–701. doi: 10.1634/stemcells.21-6-694

Dias, T. P., Fernandes, T. G., Diogo, M. M., and Cabral, J. M. S. (2019). Multifactorial modeling reveals a dominant role of wnt signaling in lineage commitment of human pluripotent stem cells. *Bioengineering* 6:71. doi: 10.3390/bioengineering6030071

Dodson, B. P., and Levine, A. D. (2015). Challenges in the translation and commercialization of cell therapies. *BMC Biotechnol.* 15:70. doi: 10.1186/s12896-015-0190-4

dos Santos, F., Andrade, P. Z., Boura, J. S., Abecasis, M. M., da Silva, C. L., and Cabral, J. M. S. (2010). Ex vivo expansion of human mesenchymal stem cells: a more effective cell proliferation kinetics and metabolism under hypoxia. *J. Cell. Physiol.* 223, 27–35. doi: 10.1002/jcp.21987

Dunbar, C. E., High, K. A., Joung, J. K., Kohn, D. B., Ozawa, K., and Sadelain, M. (2018). Gene therapy comes of age. *Science* 359:eaan4672. doi: 10.1126/science.aan4672

Fajardo-Orduña, G. R., Mayani, H., Flores-Guzmán, P., Flores-Figueroa, E., Hernández-Estévez, E., Castro-Manrreza, M., et al. (2017). Human mesenchymal stem/stromal cells from umbilical cord blood and placenta exhibit similar capacities to promote expansion of hematopoietic progenitor cells in vitro. *Stem Cells Int.* 2017, 6061729. doi: 10.1155/2017/6061729

Fares, I., Chagraoui, J., Gareau, Y., Gingras, S., Ruel, R., Mayotte, N., et al. (2014). Pyrimidoindole derivatives are agonists of human hematopoietic stem cell self-renewal. *Science* 345, 1509–1512. doi: 10.1126/science.1256337

Frias, A. M., Porada, C. D., Crapnell, K. B., Cabral, J. M. S., Zanjani, E. D., and Almeida-Porada, G. (2008). Generation of functional natural killer and dendritic cells in a human stromal-based serum-free culture system designed for cord blood expansion. *Exp. Hematol.* 36, 61–68. doi: 10.1016/j.exphem.2007.08.031

Gilmore, G. L., DePasquale, D. K., Lister, J., and Shadduck, R. K. (2000). Ex vivo expansion of human umbilical cord blood and peripheral blood CD34+ hematopoietic stem cells. *Exp. Hematol.* 28, 1297–1305. doi: 10.1016/S0301-472X(00)00531-2

Gonçalves, R., da Silva, C. L., Cabral, J. M. S., Zanjani, E. D., and Almeida-Porada, G. (2006). A stro-1+ human universal stromal feeder layer to expand/maintain human bone marrow hematopoietic stem/progenitor cells in a serum-free culture system. *Exp. Hematol.* 34, 1353–1359. doi: 10.1016/j.exphem.2006.05.024

Hoggatt, J. (2016). Gene therapy for "bubble boy". *Dis. Cell* 166:263. doi: 10.1016/j.cell.2016.06.049

Horwitz, M. E., Chao, N. J., Rizzieri, D. A., Long, G. D., Sullivan, K. M., Gasparetto, C., et al. (2014). Umbilical cord blood expansion with nicotinamide provides long-term multilineage engraftment. *J. Clin. Invest.* 124, 3121–3128. doi: 10.1172/JCI74556.transplantation

Hough, R., Danby, R., Russell, N., Marks, D., Veys, P., Shaw, B., et al. (2016). Recommendations for a standard UK approach to incorporating umbilical cord blood into clinical transplantation practice: an update on cord blood unit selection, donor selection algorithms and conditioning protocols. *Br. J. Haematol.* 172, 360–370. doi: 10.1111/bjh.13802

Huchet, A., Belkacémi, Y., Frick, J., Prat, M., Muresan-Kloos, I., Altan, D., et al. (2003). Plasma Flt-3 ligand concentration correlated with radiation-induced bone marrow damage during local fractionated radiotherapy. *Int. J. Radiat. Oncol. Biol. Phys.* 57, 508–515. doi: 10.1016/S0360-3016(03)00584-4

Jing, D., Fonseca, A. V., Alakel, N., Fierro, F. A., Muller, K., Bornhauser, M., et al. (2010). Hematopoietic stem cells in co-culture with mesenchymal stromal cells-modeling the niche compartments in vitro. *Haematologica* 95, 542–550. doi: 10.3324/haematol.2009.010736

Kelly, S. S., Sola, C. B. S., de Lima, M., and Shpall, E. J. (2009). Ex vivo expansion of cord blood. *Bone Marrow Transpl.* 44, 673–681. doi: 10.1007/978-1-84800-167-1_4

Kiernan, J., Damien, P., Monaghan, M., Shorr, R., McIntyre, L., Fergusson, D., et al. (2017). Clinical studies of ex vivo expansion to accelerate engraftment after umbilical cord blood transplantation: a systematic review. *Trans. Med. Rev.*31, 173–182. doi: 10.1016/j.tmrv.2016.12.004

Kirouac, D. C., and Zandstra, P. W. (2006). Understanding cellular networks to improve hematopoietic stem cell expansion cultures. *Curr. Opin. Biotechnol.* 17, 538–547. doi: 10.1016/j.copbio.2006.07.003

Kirouac, D. C., and Zandstra, P. W. (2008). The systematic production of cells for cell therapies. *Cell. Stem Cell* 3, 369–381. doi: 10.1016/j.stem.2008.09.001

Kögler, G., Nürnberger, W., Fischer, J., Niehues, T., Somville, T., Göbel, U., et al. (1999). Simultaneous cord blood transplantation of ex vivo expanded together with non-expanded cells for high risk leukemia. *Bone Marrow Transpl.* 24, 397–403. doi: 10.1038/sj.bmt.1701916

Levac, K., Karanu, F., and Bhatia, M. (2005). Identification of growth factor conditions that reduce ex vivo cord blood progenitor expansion but do not alter human repopulating cell function in vivo. *Haematologica* 90, 166–172.

Levin, A., Sharma, V., Hook, L., and García-Gareta, E. (2018). the importance of factorial design in tissue engineering and biomaterials science: optimisation of cell seeding efficiency on dermal scaffolds as a case study. *J. Tissue Eng.* 9:2041731418781696. doi: 10.1177/2041731418781696

Lim, M., Panoskaltsis, N., Ye, H., and Mantalaris, A. (2011). Optimization of in vitro erythropoiesis from cd34+ cord blood cells using design of experiments (DOE). *Biochem. Eng. J.* 55, 154–161. doi: 10.1016/j.bej.2011.03.014

Lipsitz, Y. Y., Timmins, N. E., and Zandstra, P. W. (2016). Quality cell therapy manufacturing by design. *Nat. Biotechnol.* 34, 393–400. doi: 10.1038/nbt.3525

Lund, T. C., Boitano, A. E., Delaney, C. S., Shpall, E. J., and Wagner, J. E. (2015). Advances in umbilical cord blood manipulation-from niche to bedside. *Nat. Rev. Clin. Oncol.* 12, 163–174. doi: 10.1038/nrclinonc.2014.215

Maung, K. K., and Horwitz, M. E. (2019). Current and future perspectives on allogeneic transplantation using ex vivo expansion or manipulation of umbilical cord blood cells. *Int. J. Hematol.* 110, 50–58. doi: 10.1007/s12185-019-02670-6

Méndez-Ferrer, S., Michurina, T. V., Ferraro, F., Mazloom, A. R., MacArthur, B. D., Lira, S. A., et al. (2010). Mesenchymal and haematopoietic stem cells form a unique bone marrow niche. *Nature* 466, 829–834. doi: 10.1038/nature09262

Mizukami, A., Pereira Chilima, T. D., Orellana, M. D., Neto, M. A., Covas, D. T., Farid, S. S., et al. (2018). Technologies for large-scale umbilical cord-derived msc expansion: experimental performance and cost of goods analysis. *Biochem. Eng. J.* 135, 36–48. doi: 10.1016/j.bej.2018.02.018

Naldini, L. (2015). Gene therapy returns to centre stage. *Nature* 526, 351–360. doi: 10.1038/nature15818

Ohmizono, Y., Sakabe, H., Kimura, T., Tanimukai, S., Matsumura, T., Miyazaki, H., et al. (1997). Thrombopoietin augments ex vivo expansion of human cord blood-derived heamatopoietic progenitors in combination with stem cell factor and Flt3 ligand. *Leukemia* 11, 524–530. doi: 10.1038/sj.leu.2400588

Perdomo-Arciniegas, A. M., and Vernot, J. P. (2011). Co-culture of hematopoietic stem cells with mesenchymal stem cells increases VCAM-1-dependent migration of primitive hematopoietic stem cells. *Int. J. Hematol.* 94, 525–532. doi: 10.1007/s12185-011-0970-0

Petzer, A. L., Zandstra, P. W., Piret, J. M., and Eaves, C. J. (1996). differential cytokine effects on primitive (CD34+CD38-) human hematopoietic cells: novel responses to Flt3-Ligand and Thrombopoietin. *J. Exp. Med.* 183, 2551–2558. doi: 10.1084/jem.183.6.2551

Pineault, N., Cortin, V., Boyer, L., Garnier, A., Robert, A., Thérien, C., et al. (2011). Individual and synergistic cytokine effects controlling the expansion of cord blood CD34+ cells and megakaryocyte progenitors in culture. *Cytotherapy* 13, 467–480. doi: 10.3109/14653249.2010.530651

Powell, K., Kwee, E., Nutter, B., Herderick, E., Paul, P., Thut, D., et al. (2016). variability in subjective review of umbilical cord blood colony forming unit assay. *Cytom. B Clin. Cytom.* 90, 517–524. doi: 10.1002/cyto.b.21376

Purton, L. E., and Scadden, D. T. (2007). Limiting factors in murine hematopoietic stem cell assays. *Cell Stem Cell* 1, 263–270. doi: 10.1016/j.stem.2007.08.016

Qiu, L., Meagher, R., Welhausen, S., Heye, M., Brown, R., and Herzig, R. H. (1999). Ex vivo expansion of CD34+ umbilical cord blood cells in a defined serum-free medium (QBSF-60) with early effect cytokines. *J. Hematother. Stem Cell Res.* 8, 609–618. doi: 10.1089/152581699319777

Rathore, A. S., and Winkle, H. (2009). Quality by design for biopharmaceuticals. *Nat. Biotechnol.* 27, 26–34.

Rocha, V., Cornish, C., Sievers, E. L., Filipovich, A., Locatelli, F., Peters, C., et al. (2001). Comparison of outcomes of unrelated bone marrow and umbilical cord blood transplants in children with acute leukemia. *Blood* 97, 2962–2971.

Rocha, V., Labopin, M., Sanz, G., Arcese, W., Schwerdtfeger, R., Bosi, A., et al. (2004). Transplants of umbilical-cord blood or bone marrow from unrelated donors in adults with acute leukemia. *New Engl. J. Med.* 351, 2276–2285. doi: 10.1056/NEJMoa041469

Singh, J., Chen, E. L. Y., Xing, Y., Stefanski, H. E., Blazar, B. R., and Zúñiga-Pflücker, J. C. (2019). Generation and function of progenitor t cells from

stemregenin-1-expanded CD34+ human hematopoietic progenitor cells. *Blood Adv.* 3, 2934–2948. doi: 10.1182/bloodadvances.2018026575

Singh, J., and Zúñiga-Pflücker, J. C. (2018). Producing ProT cells to promote immunotherapies. edited by intergovernmental panel on climate change. *Int. Immunol.* 53, 1–30. doi: 10.1093/intimm/dxy051

Tiwari, A., Tursky, M. L., Mushahary, D., Wasnik, S., Collier, F. M., Suma, K., et al. (2013). Ex vivo expansion of haematopoietic stem/progenitor cells from human umbilical cord blood on acellular scaffolds prepared from MS-5 stromal cell line. *J. Tissue Eng. Regen. Med.* 7, 871–883. doi: 10.1002/term.1479

Toms, D., Deardon, R., and Ungrin, M. (2017). Climbing the mountain: experimental design for the efficient optimization of stem cell bioprocessing. *J. Biol. Eng.* 11, 1–10. doi: 10.1186/s13036-017-0078-z

Tursky, M. L., Collier, F. M., Ward, A. C., and Kirkland, M. A. (2012). Systematic investigation of oxygen and growth factors in clinically valid ex vivo expansion of cord blood CD34+ hematopoietic progenitor cells. *Cytotherapy* 14, 679–685. doi: 10.3109/14653249.2012.666851

Ueda, T., Yasukawa, K., and Nakahata, T. (2000). Expansion of human NOD/SCID-repopulating cells by stem cell factor, Flk2/Flt3 Ligand, Thrombopoietin, IL-6, and Soluble IL-6 Receptor. *J. Clin. Invest.* 105, 1013–1021. doi: 10.1172/JCI8583

Wagner, J. E., Brunstein, C. G., Boitano, A. E., DeFor, T. E., McKenna, D., Sumstad, D., et al. (2016). Phase I/II trial of stemregenin-1 expanded umbilical cord blood hematopoietic stem cells supports testing as a stand-alone graft. *Cell Stem Cell* 18, 144–155. doi: 10.1016/j.stem.2015.10.004

Wagner, J. E., Verneris, M. R., Eapen, M., Margolis, D., Horowitz, M. M., Carter, S., et al. (2014). One-unit versus two-unit cord-blood transplantation for hematologic cancers. *New Engl. J. Med.* 371, 1685–1694. doi: 10.1056/NEJMoa1405584

Wagner, W., Roderburg, C., Wein, F., Diehlmann, A., Frankhauser, M., Schubert, R., et al. (2007). Molecular and secretory profiles of human mesenchymal stromal cells and their abilities to maintain primitive hematopoietic progenitors. *Stem Cells* 25, 2638–2647. doi: 10.1634/stemcells.2007-0280

Wodnar-Filipowicz, A., Yancik, S., Moser, Y., Dalle Carbonare, V., Gratwohl, A., Tichelli, A., et al. (1993). Levels of soluble stem cell factor in serum of patients with aplastic anemia. *Blood* 81, 3259–3264. doi: 10.1182/blood.v81.12.3259.bloodjournal81123259

Woolfrey, A., Flowers, M. E., Doney, K., Witherspoon, R., Mielcarek, M., Deeg, J. H., et al. (2016). Cord-blood transplantation in patients with minimal residual disease. *New Engl. J. Med.* 375, 944–953. doi: 10.1056/NEJMoa1602074

Yoshida, T., and Takagi, M. (2004). Cell processing engineering for ex vivo expansion of hematopoietic cells: a review. *Biochem. Eng. J.* 20, 99–106. doi: 10.1016/j.bej.2003.10.004

Zandstra, P. W., Conneally, E., Petzer, A. L., Piret, J. M., and Eaves, C. J. (1997a). Cytokine manipulation of primitive human hematopoietic cell self-renewal. *Proc. Natl. Acad. Sci. U.S.A.* 94, 4698–4703. doi: 10.1073/pnas.94.9.4698

Zandstra, P. W., Conneally, E., Piret, J. M., and Eaves, C. J. (1998). Ontogeny-associated changes in the cytokine responses of primitive human haemopoietic cells. *Br. J. Haematol.* 101, 770–778. doi: 10.1046/j.1365-2141.1998.00777.x

Zandstra, P. W., Petzer, A. L., Eaves, C. J., and Piret, J. M. (1997b). Cellular determinants affecting the rate of cytokine depletion in cultures of human hematopoietic cells. *Biotechnol. Bioeng.* 54, 58–66.

Zhang, J., Wu, Q., and Zheng, Y. (2016). Persistent elevated bone marrow plasma levels of thrombopoietin in patients with aplastic anemia. *Cytokine* 85, 11–13. doi: 10.1016/j.cyto.2016.05.020

Zonari, E., Desantis, G., Petrillo, C., Boccalatte, F. E., Lidonnici, M. R., Kajaste-Rudnitski, A., et al. (2017). Efficient ex vivo engineering and expansion of highly purified human hematopoietic stem and progenitor cell populations for gene therapy. *Stem Cell Rep.* 8, 977–990. doi: 10.1016/j.stemcr.2017.02.010

Conflict of Interest: The authors declare that the research was conducted in the absence of any commercial or financial relationships that could be construed as a potential conflict of interest.

frontiers in Bioengineering and Biotechnology

ORIGINAL RESEARCH
published: 20 October 2020
doi: 10.3389/fbioe.2020.557447

A General Theoretical Framework to Study the Influence of Electrical Fields on Mesenchymal Stem Cells

Jonathan Dawson[1]*, *Poh Soo Lee*[2], *Ursula van Rienen*[1,3,4] and *Revathi Appali*[1,3]*

[1] Department of Computer Science and Electrical Engineering, Institute of General Electrical Engineering, University of Rostock, Rostock, Germany, [2] Max Bergmann Center for Biomaterials, Institute for Materials Science, Technical University of Dresden, Dresden, Germany, [3] Department of Ageing of Individuals and Society, Interdisciplinary Faculty, University of Rostock, Rostock, Germany, [4] Department of Life, Light and Matter, Interdisciplinary Faculty, University of Rostock, Rostock, Germany

Mesenchymal stem cell dynamics involve cell proliferation and cell differentiation into cells of distinct functional type, such as osteoblasts, adipocytes, or chondrocytes. Electrically active implants influence these dynamics for the regeneration of the cells in damaged tissues. How applied electric field influences processes of individual stem cells is a problem mostly unaddressed. The mathematical approaches to study stem cell dynamics have focused on the stem cell population as a whole, without resolving individual cells and intracellular processes. In this paper, we present a theoretical framework to describe the dynamics of a population of stem cells, taking into account the processes of the individual cells. We study the influence of the applied electric field on the cellular processes. We test our mean-field theory with the experiments from the literature, involving *in vitro* electrical stimulation of stem cells. We show that a simple model can quantitatively describe the experimentally observed time-course behavior of the total number of cells and the total alkaline phosphate activity in a population of mesenchymal stem cells. Our results show that the stem cell differentiation rate is dependent on the applied electrical field, confirming published experimental findings. Moreover, our analysis supports the cell density-dependent proliferation rate. Since the experimental results are averaged over many cells, our theoretical framework presents a robust and sensitive method for determining the effect of applied electric fields at the scale of the individual cell. These results indicate that the electric field stimulation may be effective in promoting bone regeneration by accelerating osteogenic differentiation.

Keywords: mathematical modeling, mean-field approach, data-driven modeling, stem cell differentiation, electrical stimulation, human mesenchymal cells

OPEN ACCESS

Edited by:
Yuguo Lei,
University of Nebraska-Lincoln, United States

Reviewed by:
Allen L. Garner,
Purdue University, United States
Zigang Ge,
Peking University, China

***Correspondence:**
Jonathan Dawson
jonathan.dawson2@uni-rostock.de
Revathi Appali
revathi.appali@uni-rostock.de

Specialty section:
This article was submitted to Bioprocess Engineering, a section of the journal Frontiers in Bioengineering and Biotechnology

Received: *30 April 2020*
Accepted: *08 September 2020*
Published: *20 October 2020*

Citation:
Dawson J, Lee PS, van Rienen U and Appali R (2020) A General Theoretical Framework to Study the Influence of Electrical Fields on Mesenchymal Stem Cells. Front. Bioeng. Biotechnol. 8:557447. doi: 10.3389/fbioe.2020.557447

1. INTRODUCTION

Human mesenchymal stem cells (hMSCs) possess a unique capability of self-renewal and differentiation into cells of various types of tissues, such as bone, cartilage, and adipose. Thus, the hMSCs are the promising cell types for regenerative medicine and tissue engineering. The gene expression levels of an hMSC are known to be the decisive regulators of hMSCs differentiation. These gene expression levels might be influenced by both cell internal cues (De-Leon and Davidson, 2007; Ralston, 2008) and external cues (Engler et al., 2006; Eyckmans et al., 2012; Hess et al., 2012a; Dingal et al., 2014; Najafabadi et al., 2016). Experimental studies (Mousavi and Hamdy Doweidar, 2015) have shown that the *in vitro* differentiation of hMSC into cells of distinct functional types can

be controlled by external factors. Therefore, stem cell differentiation mediated by external factors is a compelling approach that has led to the development of bio-implants, for clinical applications in regenerative medicine.

The applied electric field (EF) is one of the proven external factors known to influence hMSCs dynamics such as migration (Ciombor and Aaron, 1993; Schemitsch and Kuzyk, 2009; Banks et al., 2015; Funk, 2015), elongation (Rajnicek et al., 2008; Tandon et al., 2009), proliferation (Hartig et al., 2000; Lohmann et al., 2000; Kim et al., 2009; Sun et al., 2009), and differentiation (Jansen et al., 2010; Hess et al., 2012b; Petecchia et al., 2015; Miyamoto et al., 2019; Rohde et al., 2019). Comparing these studies, it is evident that the results are inconsistent and show the disparity. While several works have demonstrated an increase in proliferation after exposing cells to EF or electromagnetic field (EMF) (Hartig et al., 2000; Chang et al., 2004; Kim et al., 2009; Sun et al., 2009), others did not detect significant differences or had recorded reduced cell number following EMF exposure (Lohmann et al., 2000; Schwartz et al., 2008; Jansen et al., 2010). Similarly, stimulation effects on osteogenic differentiation are also controversial, ranging from no effects (Chang et al., 2004; Lin and Lin, 2011) to a high increase in the expression of bone-related gene markers (Hartig et al., 2000; Schwartz et al., 2008; Jansen et al., 2010). Due to the complex parameters and the different experimental approaches used, it is difficult to compare these results among each other. In addition, the choice of stimulation method can also influence cellular behavior.

These methods consist of direct or indirect electrical stimulation of the tissue (Schemitsch and Kuzyk, 2009). In the direct stimulation method, the electrodes are placed in contact with the targeted tissue. Some of the disadvantages of direct stimulation are the damage caused to tissues by invasive electrodes and the corrosion of the electrodes due to electrochemical processes (Ciombor and Aaron, 1993). The indirect stimulation method includes capacitive coupling and inductive coupling of electromagnetic fields (EMF). The capacitive coupling is slightly invasive and provides electrical stimulation to the tissue, whereas non-invasive inductive coupling involves both magnetic and electrical stimulation.

To study the stand-alone effects of the EF on the biological tissue, an *in vitro* setup, which is non-invasive and free from the magnetic fields, is necessary. In this context, Hess et al., have developed a novel *in vitro* transformer-like coupling (TC) setup (Hess et al., 2012a). This approach enables a non-invasive electrical stimulation of *in-vitro* culture of hMSCs with homogeneous EF in the cell culture chamber. The TC setup exerts pure EFs to the cell culture, with negligible magnetic field strength (see section 2.1). Thus allowing direct correlation of observed results solely to EF stimulation.

Besides the experimental evaluations, there is a great interest in mathematical modeling and simulation to (i) further gather an in-depth understanding of the cellular mechanism underlying the stem cell response to EMFs, and (ii) to predict optimal stimulation parameters. Fricke (1953) was the first to introduce an empirical equation for the electric potential induced in an ellipsoidal cell in suspension when exposed to an external EF. The first theoretical description (analytical solution of Laplace equation) for the induced potential in a spherical cell in suspension exposed to external EF was given by Schwan (1994) where a spherical shell representing the membrane approximates the cell. This Schwan model treats the cell as a non-conducting membrane subjected to both constant and alternating external EF (Grosse and Schwan, 1992). Schwan's theory has been extended by Kotnik et al. (1997) by considering the conductivity using constant, oscillating, and pulsed EF. Later other geometries such as cylindrical, spheroidal, and ellipsoidal cells suspended in the medium were investigated (Gimsa and Wachner, 2001a,b; Valic et al., 2003; Maswiwat et al., 2008). To determine the induced EF in the internal membranes of the cells, the cells were modeled as multiple concentric shells (Kotnik and Miklavčič, 2006; Vajrala et al., 2008). Several techniques were also employed to examine different cells of complex shapes suspended in an electrolyte, for example, Finite Element Models (FEM) (Miller and Henriquez, 1988; Sebastián et al., 2004; Meny et al., 2007; Ying and Henriquez, 2007), Transport Lattice Models (TLM) (Gowrishankar and Weaver, 2003; Stewart et al., 2004; Gowrishankar et al., 2013) and equivalent circuit models (Ramos et al., 2003; Schoenbach et al., 2004). The effect of surface charge and membrane conductivity was studied on the induced potential in spherical and non-spherical cell geometries by Kotnik and Miklavčič (2006) and Mezeme and Brosseau (2010).

In little over a decade, the theoretical approaches to study stem cell dynamics have begun (Tabatabai et al., 2011; Pisu et al., 2012; Paździorek, 2014; Sun and Komarova, 2015). Although experiments have shown that the external EF affects cellular processes, the theoretical approaches have mainly focused on the collective dynamics of stem cells (Tonge et al., 2010; Lei et al., 2014; MacArthur, 2014; Paździorek, 2014; Renardy et al., 2018; Farooqi et al., 2019; Sarkar et al., 2019). Such approaches consider the stem cell population as a compartment (Tabatabai et al., 2011; Sun and Komarova, 2012, 2015; Yang et al., 2015) and do not resolve the dependency of processes of individual cells on the external factors (Pisu et al., 2012). To the best of our knowledge, the existing mathematical models have not incorporated the cellular responses of interaction with EF distribution in the cell compartments (Pisu et al., 2012).

In this context, we investigate the influence of applied EFs on the dynamics of an *in vitro* culture of hMSCs in a TC setup (see sections 2.2, 2.3). Our mean-field theoretical framework takes into account processes at the scale of an individual stem cell and describes the dynamics of a stem cell population (see sections 3.1 and 3.2). We compare our theory with experimental results reported by Hess et al., and provide a quantitative explanation for the observed behavior of the total number of cells and the total alkaline phosphatase (ALP) activity over time.

2. PREVIOUS EXPERIMENTAL RESULTS

Our data-driven modeling is based on previous experiments by Hess et al. We use the time dependent experimental data from Hess et al., to study the effect of EFs on hMSC proliferation and differentiation. In the following subsections we recapitulate the experimental TC setup and quantification procedure introduced

in Hess et al. We then discuss the corresponding experimental results of the total number of cells and the total ALP activity in the stimulation chamber, which forms the basis for our general theoretical framework.

2.1. Electrical Stimulation With TC-Induced Electrical Field

The hMSCs were isolated from bone marrow aspirates of 3 healthy male donors between the age of 20 to 40 years old (for more details on isolation and expansion of cells in Hess et al., 2012a). In a spinner flask containing expansion medium (exm, Dulbecco's modified Eagle's medium with 10% fetal bovine serum and 100 I.U./mL penicillin-streptomycin), about 50,000 hMSCs were seeded on a collagen-coated polycaprolactone (PCL) disc-shaped scaffold at 37 °C with 7% CO_2 for 24 h (Hess et al., 2012a).

Subsequently, the PCL-scaffolds with hMSCs were transferred to a cultivation chamber of the transformer-like coupling (TC) system previously described (Hess et al., 2012a) and prepared for electrical stimulation (**Figure 1B**). In each cultivation chamber, only PCL-scaffolds seeded with the same donor were allowed, so as to avoid side-effects induced by endocrine signaling between hMSC from different donors. Next, 100 ml osteogenic differentiation medium (osm) composed of exm supplemented with 10 nM dexamethasone, 0.2 μM ascorbic acid and 10 mM β-glycerophosphate (all Sigma Aldrich); was added to each cultivation chamber and incubated at 37 °C, 7% CO_2. Further, medium change was performed every 4 days over the entire course of cultivation. An electrical stimulation regime with rectangular pulses (7 ms, 3.6 mV/cm, 10 Hz) was applied intermittently (4 h stimulation, 4 h pause) over 28 days (Hess et al., 2012a,b). To ensure a homogeneous EF for the cell culture, the cells are seeded on the long arms of the chamber where the electrical field was uniform. Our FEM simulation of the chamber confirms the same (see **Figure 1A**). Corresponding negative controls without electrical stimulation were set up in identical cultivation chambers, but were not connected to the transformer core.

2.2. Total Number of Cells and Total ALP Activity in the TC Apparatus

To study the influence of EFs on stem cell dynamics, cell proliferation and cell differentiation were quantified using standard colorimetric measurement protocol. hMSC proliferation and differentiation were determined via lactate dehydrogenase (LDH) and ALP assay, respectively. Experimental data was recorded on 7, 14, 21, and 28 d after the electrical stimulation regime was applied. Four samples from each condition (control and electrically stimulated) were collected and stored in −80 °C for analyses later as a whole. To prepare the samples for analysis, they were thawed on ice for 30 min, followed by cell lysis for 50 min in cold lysis buffer consist of 1% w/v Triton X-100 / Phosphate buffer saline (PBS). To determine ALP activity at each time point, 25 μl cell lysate was added to 125 μl ALP substrate consisting 1 mg/ml p-nitorphenyl phosphate (Sigma Aldrich), 0.1 M diethanolamine, 1 mM $MgCl_2$ and 0.1% w/v Triton X-100/PBS, pH 9.8. The reaction was prepared in 96-well microplate, incubated at 37 °C for 30 min and stopped with 73 μl NaOH. This was followed by centrifugation at 16,000 g for 10 min and 170 μl of supernatant from individual well was transferred to a new 96-well microplate. The absorbance was measured on TECAN microplate reader at 405 nm and corresponding negative controls had used lysis buffer instead of cell lysate. ALP activity was interpreted as μmol para-nitrophenol (pNP) per 10^6 cells. To determine the cell number present in each scaffold over time,

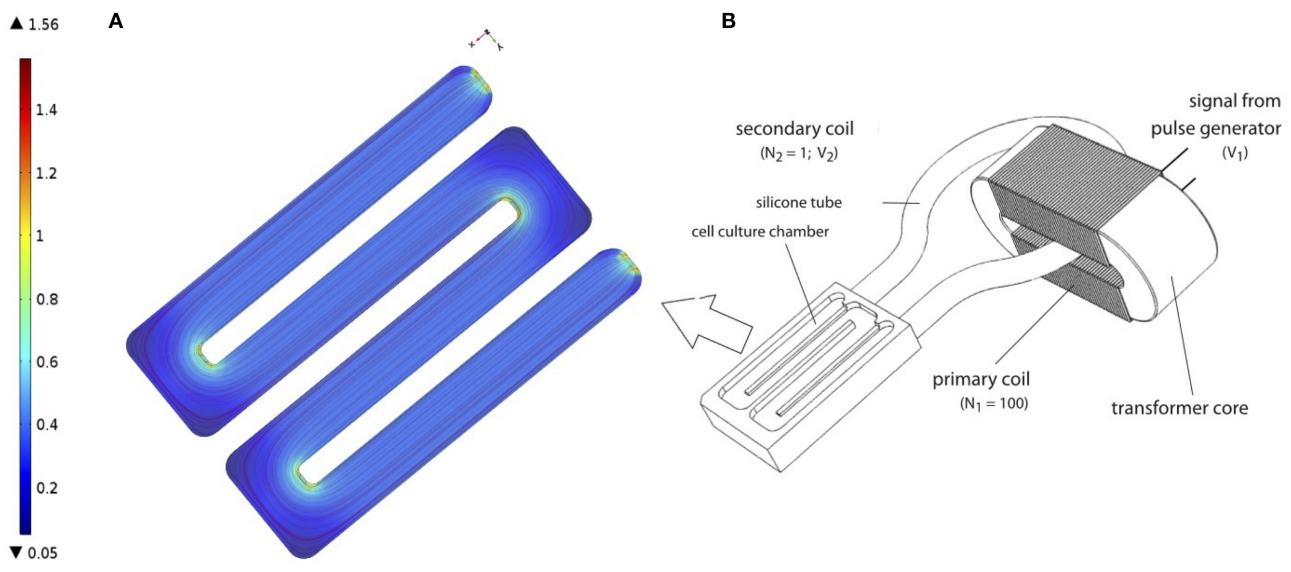

FIGURE 1 | (A) Finite Element Model (FEM) of cell culture chamber with the electrical field as described in Hess et al. (2012a). FEM model was performed using COMSOL Multiphysics 4.2a® **(B)** Schematic representation of TC, as described in Hess et al. (2012a). Figure obtained with permission from Hess et al. (2012a).

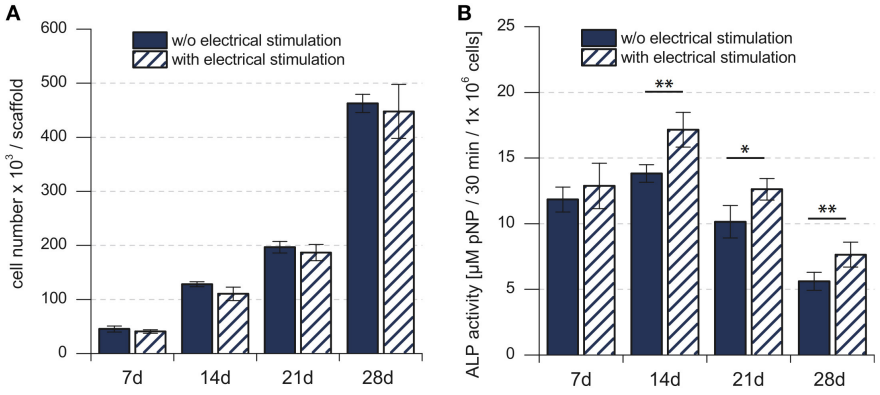

FIGURE 2 | (A) Total number of mesenchymal stem cells in the cell culture. **(B)** Biochemical analysis of the total ALP activity in the cell culture. Total number of hMSCs indicated stem cell proliferation, whereas the total ALP activity indicated the stem cell differentiation. *$p < 0.05$, **$p < 0.01$. Figure obtained with permission from Hess et al. (2012a).

50 μl of cell lysate was added to equal volume of LDH substrate (Takara, France) in a 96-well microplate and incubated at room temperature for 5 min. The reaction was stopped by adding 50 μl 0.5 M HCl to each well and the absorbance was measured on TECAN microplate reader at 492 nm. The cell numbers were determined by correlating the measured values against a calibration curve derived with defined number of hMSCs. For both assays, the measurements were done in triplicates to increase the accuracy.

2.3. Experimental Results

Cell proliferation, indicated by the change in the total number of cells over time, showed continuous increase for 28 days, in both the electrically stimulated samples and the non-stimulated control samples (**Figure 2A**). Statistical analysis showed no detectable differences in the total number of cells between stimulated and non-stimulated samples (Hess et al., 2012a). The total ALP activity increased over time and reached the peak after 14 days, followed by a decrease until 28 days. The statistical analysis showed significant difference between the electrically stimulated and non-stimulated control samples. The ALP activity in the electrically stimulated samples was 30% higher than the non-stimulated control samples. This indicated a role of applied EFs in the differentiation process.

3. MATHEMATICAL MODELING

Based on the experimental data, discussed in the previous section, we made the following observations. First, the non-stimulated control samples show different time-dependent behaviors for the total number of cells and the total ALP activity. Second, the applied EF significantly influences only the time-dependent behavior of the total ALP activity. In order to provide a quantitative explanation for these observations, we formulated a general theoretical description of stem cell dynamics.

3.1. General Theoretical Framework for Stem Cell Dynamics

In our mean-field model, the time-dependent behavior of the stem cell population augments from the processes at the scale of a single stem cell (**Figure 3**). An individual stem cell undergoes division, giving rise to new cells and thus sustaining the stem cell population. The ALP activity of a stem cell is maintained by the intracellular biochemical processes. Subsequently, a stem cell leaves the stem cell population due to terminal differentiation. Taking these processes into account at the scale of an individual cell, we describe the state of the mesenchymal stem cell population by $n(a, t)$, where a is the ALP activity of a cell in the stem cell population at time t. Precisely, $n(a, t)\Delta a$ is the total number of cells with ALP activity in the range a and $a + \Delta a$ at the time t. Generally, n can depend on multiple variables besides intracellular ALP activity, such as the cell size, the ALP gene expression of the cell, the EF strength experienced by the cell, the orientation of the cell with respect to the applied EF etc. The change in n over time reflects the dynamics of individual stem cells.

$$\begin{aligned}\frac{\partial n(a,t)}{\partial t} &= -\frac{1}{2}\int_0^a n(a,t)k_d(a-a',a')da' \\ &+ \int_0^\infty n(a+a',t)k_d(a,a')da' - \frac{\partial(n(a,t)s_i(a))}{\partial a} \\ &+ \frac{\partial(n(a,t)d_o(a))}{\partial a} - k_f(a)n(a,t) \quad . \end{aligned} \tag{1}$$

Equation (1) is based on the Smoluchowski equation describing coagulation phenomena (Smoluchowski, 1916). Similar equations have been studied in a variety of other problems (Baskaran and Marchetti, 2008; Foret et al., 2012; Lade et al., 2015). The first two terms on the right hand side of Equation (1) represent cell divisions in the stem cell population. These cell divisions result in stem cell proliferation. Such cell divisions occur at the rate $k_d(a, a')$, and replace a cell having ALP activity $a + a'$, with two daughter cells having ALP activities a and a', respectively. These cell divisions described in Equation (1)

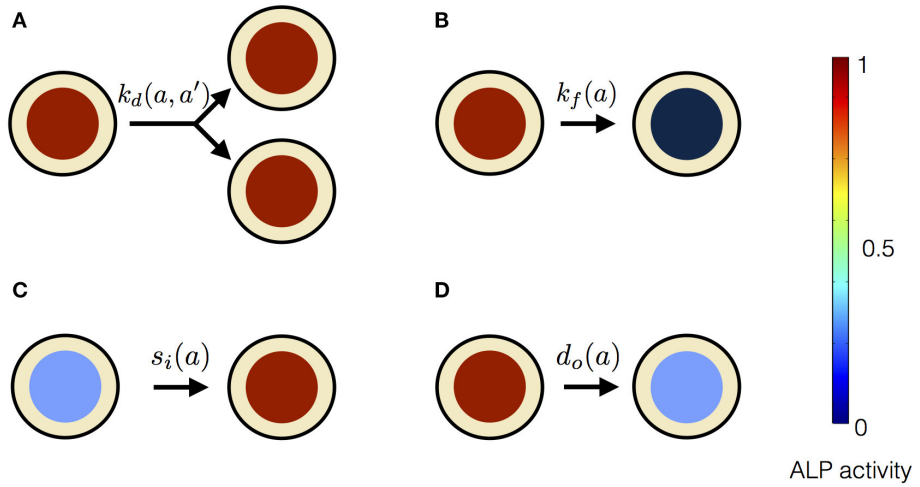

FIGURE 3 | Processes affecting the distribution of ALP activity $n(a, t)$ in the population of hMSCs. **(A)** When a cell with ALP activity $a + a'$ divides, it is replaced by two new cells with ALP activity a and a'. The colored circles represent the level of the ALP activity of the cell, according to the color scale. High level of the ALP activity is represented by red color, whereas no ALP activity is represented by black color. Such divisions occur at the rate $k_d(a, a')$ and result in the stem cell proliferation. **(B)** A cell can instantaneously lose detectable ALP activity because of terminal osteogenic differentiation into an osteoblast. Such processes occur at the rate $k_f(a)$. **(C)** ALP activity in a cell can increase due to intracellular ALP synthesis, denoted by influx $s_i(a)$. **(D)** ALP activity in a cell can decrease due to intracellular ALP degradation, denoted by out-flux $d_o(a)$.

conserve the ALP activity. In the case of non-conserved cell divisions, both daughter cells have the same measure of ALP activity as the dividing parent cell. Such cell divisions will be described by only one term, namely, $\int_0^\infty da' n(a, t) k_d(a, a')$ instead of two terms as in Equation (1). The third and the fourth term on the right hand side of Equation (1) represent the flux of ALP activity in the cell due to the intracellular biosynthesis and degradation of ALP, respectively. In our theoretical description we assume the ALP activity of a stem cell to be regulated by the intracellular ALP biosynthesis and degradation processes. For a cell with ALP activity a, $s_i(a)$ is the average ALP activity gained per unit time due to ALP biosynthesis and $d_o(a)$ is the average ALP activity lost per unit time due to ALP degradation. The last term on the right hand side of Equation (1) represents the loss of a cell with ALP activity a from the population. Such losses occur at the rate $k_f(a)$ due to instantaneous differentiation of a hMSC into a fully differentiated osteoblast cell. Our theoretical framework describes the dynamics of a population of undifferentiated hMSCs, and does not include osteoblasts, i.e., terminally differentiated hMSCs. In our description, cells with measurable ALP activity are classified as undifferentiated mesenchymal stem cells. We assume the osteoblasts to have lower ALP activity, compared to the undifferentiated mesenchymal stem cells. We also assume that the intracellular ALP activity reaches its maximum in the mesenchymal stem cells undergoing differentiation. Now, we introduce two quantities $N(t)$ and $\Phi(t)$ as follows,

$$N(t) = \int_0^\infty n(a, t) da, \ \Phi(t) = \int_0^\infty a n(a, t) da, \tag{2}$$

where, $N(t)$ represents the total number of cells, and $\Phi(t)$ represents the total ALP activity in the hMSC population at time t. The time-dependent behavior of N and Φ describe the dynamics of hMSC population as whole. Using Equation (2) and Equation (1), we can write down the balance relations for N and Φ, in the case of cell divisions that conserve ALP activity, as follows,

$$\begin{aligned} \frac{dN}{dt} &= \frac{1}{2} \int_0^\infty \int_0^\infty k_d(a, a') n(a + a', t) da da' \\ &\quad - \int_0^\infty k_f(a) n(a, t) da \end{aligned} \tag{3}$$

$$\begin{aligned} \frac{d\Phi}{dt} &= \int_0^\infty s_i(a) n(a, t) da - \int_0^\infty d_o(a) n(a, t) da \\ &\quad - \int_0^\infty a k_f(a) n(a, t) da. \end{aligned} \tag{4}$$

From Equations (3) and (4) we see that the macroscopic quantities N and Φ result from the dynamics of individual cells, such as cell division, ALP biosynthesis and degradation governing cellular ALP activity and cell differentiation. The details of the calculation involved in the derivation of Equations (3) and (4) are presented in the **Supplementary Material** (section 2).

4. RESULTS

The experimentally observed time-dependent behavior of N and Φ can be explained by a model that includes stem cell proliferation due to cell divisions and osteogenic differentiation. Mesenchymal stem cell differentiation into an osteoblast could either occur instantaneously or proceed gradually giving rise to intermediate pre-osteoblasts with detectable ALP activity. Our

theoretical framework distinguishes between these two subtly different processes, which will be discussed in the following.

4.1. Progressive Stem Cell Differentiation Model

In this model, stem cell proliferation occurs due to symmetric non-conserved cell divisions. The osteogenic differentiation in this model is due to a gradual decrease in ALP activity via intracellular ALP degradation. The parameter choice for this model is given in **Table 1**. The cell division in this model occurs at the rate of k_d and results in two daughter cells with the same magnitude of the ALP activity as the parent cell. The stem cell differentiation in this model occurs gradually at the rate of d_o, i.e., ALP out-flux due to intracellular ALP degradation is proportional to the cell's ALP activity (**Figure 4**). The dynamic equation for $n(a,t)$ using the parameter choice listed in **Table 1** is given by,

$$\frac{\partial n(a,t)}{\partial t} = k_d n(a,t) \int_0^\infty \delta(a-a')da' - d_o \frac{\partial n(a,t)}{\partial a} \quad . \quad (5)$$

Equation (5) is solved by using the Laplace transformation technique (**Supplementary Material**) to obtain the balance relations for N and Φ. The time rate of change of N is,

$$\frac{dN}{dt} = k_d N \quad . \quad (6)$$

To fit Equation (6) to the experimental data of the total number of stem cells at each time point in the stimulation chamber, we used $k_d = 2/t$. The solution of Equation (6) with this choice of k_d is given by,

$$N(t) = \bar{N}_0 t^2, \quad (7)$$

where $\bar{N}_0 = \frac{N_0}{t_0^2}$ and N_0 is the total number of cells showing ALP activity in the hMSC population at the initial time t_0. The fitting was performed using the least squares fitting method, giving an estimate for $\bar{N}_0 = 535 \pm 40$ (**Figure 5A**). The χ^2 value is equal to 36.789 for the fit shown in **Figure 5A**. The dynamic equation for Φ, obtained from Equation (5), is

$$\frac{d\Phi}{dt} = k_d \Phi - d_o \Phi \quad . \quad (8)$$

The solution of Equation (8), with our choice of $k_d = 2/t$, is

$$\Phi(t) = \bar{\Phi}_0 t^2 e^{-d_o t}, \quad (9)$$

where $\bar{\Phi}_0 = \frac{\Phi_0 e^{d_o t_o}}{t_0^2}$ and Φ_0 is the total ALP activity in all the cells in the hMSC population at the initial time t_0. Equation (9) was fit to the experimental data of the total ALP activity at each time point in the stimulation chamber (**Figure 5B**). Since the statistical analysis showed a significant difference between the non-stimulated control and electrically stimulated samples (**Figure 2B**), we performed data fitting of each sample separately (**Figure 5B**). The parameter values of the function, given by Equation (9), obtained as a result of the fit to the experimental data are given in **Table 2**. The χ^2 value is equal to 0.972 for the fit shown in **Figure 5B** to the unstimulated experimental data, and the χ^2 value is equal to 0.626 for the fit to the electrically stimulated experimental data.

The comparison of the PSCD model with the experimental data suggests that the stem cell division rate decreases with time $k_d \sim 1/t$, whereas the total number of cells grows quadratically $N(t) \sim t^2$. Using these two results we analytically derived the dependence of the stem cell division rate on the stem cell density. Our analysis reveals a negative correlation between the divison rate of the stem cells and the stem cell number density, $k_d \sim 1/\sqrt{\rho}$ (**Figure 5C**). The stem cell number density is given by

TABLE 1 | Choice of parameters for progressive stem cell differentiation model.

$k_d(a,a')$	$k_d\delta(a-a')$
$k_f(a)$	0
$s_i(a)$	0
$d_o(a)$	$d_o a$

This model includes cell proliferation due to symmetric non-conserved cell divisions and gradual differentiation of a hMSC into an osteoblast cell due to out-flux of ALP activity.

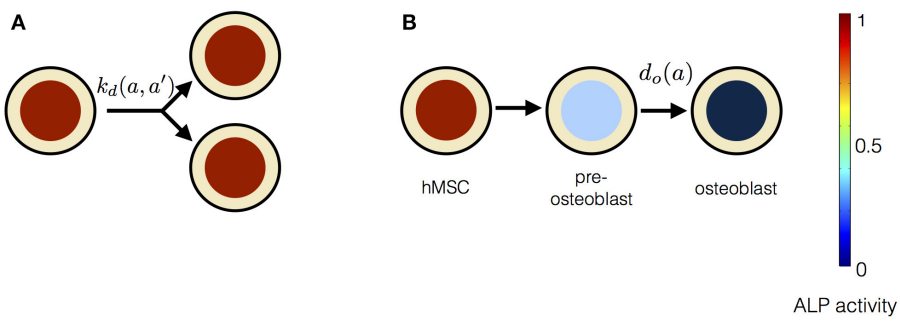

FIGURE 4 | The constituents of progressive stem cell differentiation model are **(A)** Symmetric non-conserved cell division. The division of a stem cell with ALP activity *a* results in two daughter stem cells, each with ALP activity *a*. **(B)** Osteogenic differentiation. The osteogenic differentiation in Model 1 proceeds via gradual loss of ALP activity. Such a process gives rise to temporary states of intermediate pre-osteoblasts.

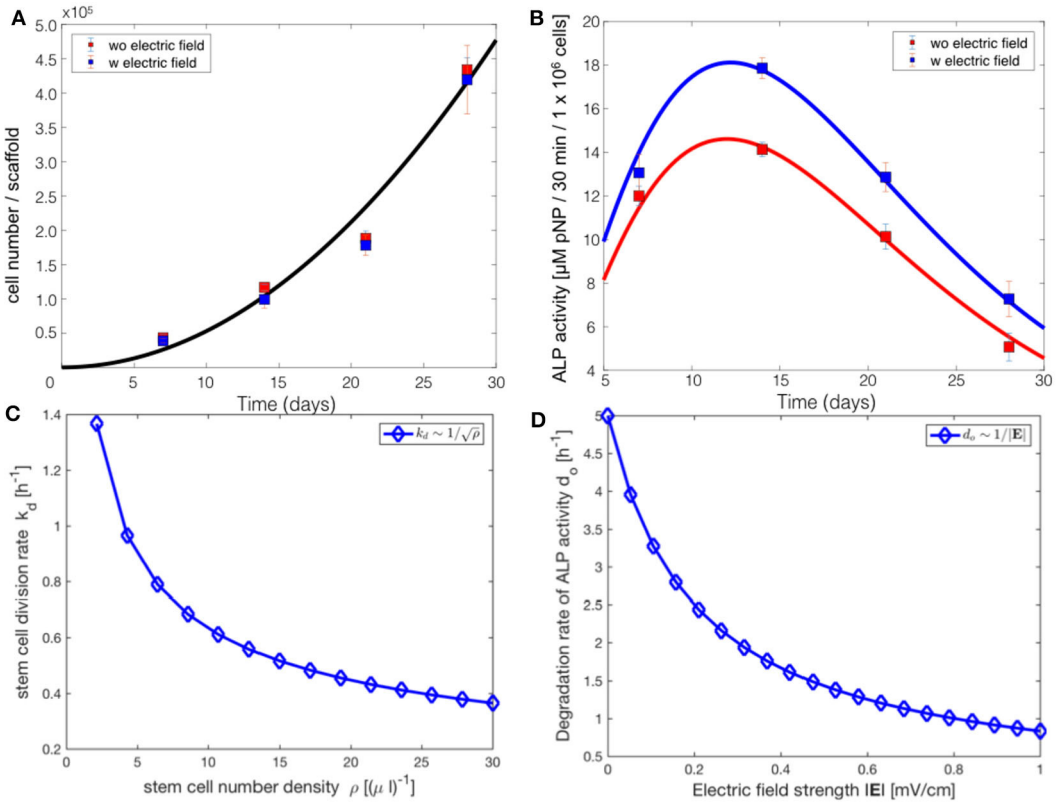

FIGURE 5 | Comparsion of the progressive stem cell differentiation (PSCD) model with experimental results for electrically stimulated (blue box) and non-stimulated (red box) cell culture samples after 7, 14, 21 and 28 days. **(A)** The total number of cells in a scaffold over time. The solid curve is the fit of the analytical solution of PSCD model, given by Equation (7), to the experimental data. **(B)** The total ALP activity of cells in a scaffold cultivated in the stimulation chamber. The solid curve is the fit of the analytical solution of the PSCD model, given by Equation (9), to the experimental data. Error-bars show the standard deviation in the experimental data. **(C)** The result of the fit of the PSCD model to the experimental data for the total number of cells suggests that the divison rate k_d of the stem cells in the hMSC population is inversely proportional to the stem cell number density ρ. **(D)** The result of the fit of the PSCD model to the experimental data for the total ALP activity suggests that the degradation rate of the ALP activity of a cell is inversely proportional to the strength of the applied EF. d_o indicates the rate of osteogenic differentiation.

TABLE 2 | Parameter values obtained as a result of the fit of Equation (9) to the experimental total ALP activity of stem cells in the stimulation chamber.

	Control (without ES)	With ES
Φ_0	0.8007 ± 0.03	0.84 ± 0.034
d_o^{-1}	5.84 ± 0.09	6.2 ± 0.1

the relation $\rho = N/V$, where N is the total number of stem cells in the scaffold of the stimuation chamber at time t, and V is the volume of the scaffold. The volume of the scaffold V is fixed. Fitting the PSCD model to the experimental data (see **Table 2**), reveals an inverse dependence of the degradation rate of the ALP activity d_o on the strength of the applied EF, i.e., $d_o \sim 1/|\mathbf{E}|$ (**Figure 5D**).

4.2. Instantaneous Stem Cell Differentiation Model

Instantaneous stem cell differentiation model (ISCD) includes stem cell proliferation due to symmetric non-conserved cell divisions, similar to PSCD model. However, the difference between the two models lies in the precise mechanism of osteogenic differentiation. In ISCD model, the differentiation of a stem cell into an osteoblast cell occurs instantaneously, resulting in the total loss of ALP activity in the differentiated osteoblast cell (**Figure 6**). In this model, such a sudden loss of a cell with ALP activity might also imply apoptosis. The parameter choice for ISCD model is given in **Table 3**. The dynamic equation for $n(a,t)$ using the parameter choice listed in **Table 3** is given by,

$$\frac{\partial n(a,t)}{\partial t} = k_d n(a,t) \int_0^\infty \delta(a-a')da' - k_f n(a,t) \quad . \quad (10)$$

The change of N and Φ over time is,

$$\frac{dN}{dt} = \bar{k}N, \quad (11)$$

and,

$$\frac{d\Phi}{dt} = \bar{k}\Phi, \quad (12)$$

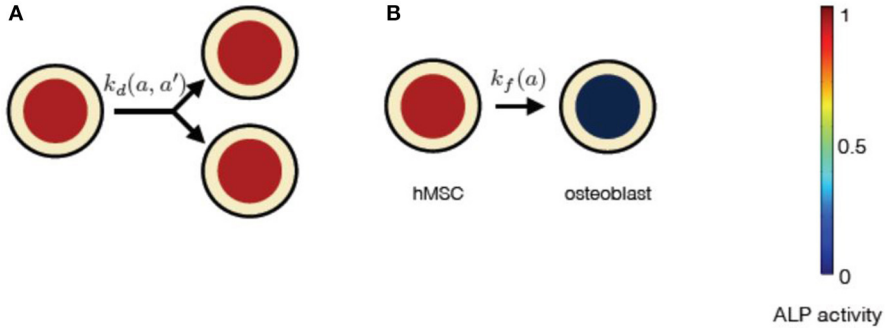

FIGURE 6 | The constituents of progressive stem cell differentiation model are **(A)** Symmetric non-conserved cell division. The division of a stem cell with ALP activity *a* results in two daughter stem cells, each with ALP activity *a*. **(B)**The osteogenic differentiation in instantaneous stem cell differentiation model occurs instantaneously via sudden loss of a cell's ALP activity. Such a process instantaneously gives rise to an osteoblast cell with no ALP activity.

TABLE 3 | Choice of parameters for instantaneous stem cell differentiation model.

$k_d(a, a')$	$k_d\delta(a - a')$
$k_f(a)$	k_f
$s_i(a)$	0
$d_o(a)$	0

This model includes cell proliferation due to symmetric non-conserved cell divisions and instantaneous differentiation of a hMSC into osteoblast cell.

respectively, where $\bar{k} = k_d - k_f$.

Since Equation (11) and Equation (12) have exactly the same form, their solutions also have exactly the same functional form. The solution of Equation (11) and Equation (12), by choosing $\bar{k} = k = 2/t$ as in Model 1, we get,

$$N(t) = \bar{N}_0 t^2, \tag{13}$$

$$\Phi(t) = \bar{\Phi}_0 t^2, \tag{14}$$

where, $\bar{N}_0 = \frac{N_0}{t_0^2}$ and $\bar{\Phi}_0 = \frac{\Phi_0}{t_0^2}$. N_0 and Φ_0 are as defined in Model 1. The ISCD model describes the experimental data for the total number of cells, but it fails to capture the non-monotonic time dependent behavior of the experimental data for the total ALP activity. Equation (14) shows a continuous increase of the total ALP activity for all time points, whereas experimental data, for both the control and stimulated samples, show an increase in the total ALP activity only up to 14 days (**Figure 2B**). After 14 days, the total ALP activity shows a continuous decrease till 28 days in both control and stimulated samples which is not captured by this model (**Figure 2B**).

5. DISCUSSION

In this study we developed a general theoretical framework to describe how applied EFs influence the stem cell dynamics. Our mean-field description of stem cell dynamics augments from elementary processes such as stem cell division, differentiation and intracellular regulation of ALP activity. Current theoretical approaches to the study of stem cell dynamics are based on biochemical assays that consider stem cell population as a whole and do not resolve processes at the scale of individual cells. Although the approaches accounting for the discrete nature of the stem cell population, consisting of many individual cells, are scarce, these do not consider dependencies of the cellular processes on the external EF (Tabatabai et al., 2011; Pisu et al., 2012). Our theoretical framework takes into account processes governing the dynamics of individual cells in the stem cell population. The advantage of our general theory is that it allows for studying the influence of various factors, such as the external EF, on the rates of cellular processes. In addition, our theoretical framework can serve as a useful tool to distinguish between different mechanisms through which cellular processes occur. We tested our theory with *in vitro* electrical stimulation experiments by Hess et al. (2012a). We show that our first model, PSCD model, derived from our general theory, can fully describe the time dependent behaviors of the total number of ALP expressing hMSCs and the total ALP activity in the scaffold cultivated in the stimulation chamber. In this model, stem cell proliferation is due to symmetric non-conserved cell divisions and stem cell differentiation occurs via gradual loss of the ALP activity in the stem cells. The rate of stem cell differentiation in this model depend on the ALP activity of the stem cell. In the second model, referred to as the instantaneous stem cell differentiation model, we studied the cell differentiation due to the sudden loss of ALP activity, and its effect on the stem cell dynamics. The rate at which the stem cell differentiation occur, in this model, is independent of the ALP activity of the stem cell. A comparison of our two precisive models with the experiments suggests that the stem cell differentiation occurs gradually, as described in the progressive stem cell differentiation model. This mechanism of osteogenic differentiation gives rise to pre-osteoblast cells, which confirms the experimental results of Rutkovskiy et al. (2016).

Our analysis reveals a negative correlation between the stem cell proliferation rate and the cell number density. The coupling between the cell proliferation rate and the cell density

could either be due to density-dependent inter-cellular signaling or mechanical compression, or both (Eyckmans et al., 2012; Najafabadi et al., 2016). Recent experiments have shown that the *in vitro* osteogenic differentiation is associated with the processing of type-1 collagen and progressive deposition of the extracellular collagen matrix (Hanna et al., 2018). The deposition of the extracellular matrix over time might restrict cells from growing and dividing. This could explain the dependence of cell proliferation rate on the cell density, as our analysis suggests. The density-dependent cell division rate has been explored in other context of cellular systems as well (Hoffmann et al., 2011; Recho et al., 2016).

Our results show that the applied EF influences stem cell differentiation rather than stem cell proliferation, which confirms the experimental result of Hess et al. (2012a). We found that the rate of degradation of the ALP activity is inversely proportional to the applied EF strength. In order to precisely quantify the dependency of the stem cell differentiation on the applied EF, further studies of stimulation of hMSCs with varying field strengths are needed.

Our theoretical framework serves as a first step toward developing a more comprehensive model to study the influence of other electric field parameters, such as mode of electric stimulation (AC or DC), the pulse duration, and the frequency on hMSC proliferation and differentiation. Since our framework includes biological rates that are defined as functions of multiple parameters, it allows for studying the dependence of these rates on various biological and physical factors. This can be done by performing a parametric study that involves extending the functional dependence of the kinetic rates to multiple parameters. Cell migration also plays an important role in tissue regeneration. Our theoretical framework, presented in this study, does not contain spatial information of the cells necessary for studying cell migration. By introducing spatial dimensions into our framework, we will be able to study the influence of electric field parameters on stem cell polarization and, thereby, cell migration.

6. CONCLUSION

We draw the following conclusions from our analysis presented in this study. First, despite the complexity of the process, reflected in the multiplicity in its regulatory steps, we show that the stem cell dynamics can be understood by a simple description that captures vital processes. Secondly, our analysis shows that the applied EFs predominantly influence stem cell differentiation. Thirdly, we show that the progressive stem cell differentiation model thoroughly describes the experimental results of Hess et al. (2012a). This model suggests that the osteogenic differentiation of hMSCs progresses gradually, giving rise to pre-osteoblast cells. Fourthly, our analysis shows that the stem cell division rate is cell density-dependant. Finally, our framework allows us to measure the rates of cellular processes and estimates their dependency on external EF. This method is robust and sensitive since the time dependent macroscopic quantities result from an average over many individual cells and multiple experimental repetitions. This framework could serve as a tool to study the influence of external factors on stem cell dynamics through genetic and chemical perturbation of various cellular processes.

DATA AVAILABILITY STATEMENT

All datasets generated for this study are included in the article/**Supplementary Material**.

AUTHOR CONTRIBUTIONS

RA and UR have conceptualized the study. RA has designed the project, supervised the work including data analysis, and model development. JD developed the mean-field model and derived analytical results. JD and RA worked on the simple model for dynamics of MSCs. JD performed data fitting. RA has performed the FEM simulations. JD, PL, UR, and RA wrote sections of the manuscript. RA critically revised the manuscript and took the responsibility for the integrity of the study as a whole. All authors contributed to manuscript revision, read, and approved the submitted version.

FUNDING

Funded by the Deutsche Forschungsgemeinschaft (DFG, German Research Foundation) SFB 1270/1 - 299150580.

ACKNOWLEDGMENTS

We are grateful to Dr. Ricarda Hess and Prof. Dieter Scharnweber for providing the experimental data for this mathematical modeling. We thank Prof. Hans-Peter Wiesmann for permitting PL to work on our analysis and acknowledge the financial support from the DFG Transregio 67 (Project A3). We acknowledge Dr. Kiran Sriperumbudur for his help in revising the paper.

SUPPLEMENTARY MATERIAL

The Supplementary Material for this article can be found online at: https://www.frontiersin.org/articles/10.3389/fbioe.2020.557447/full#supplementary-material

REFERENCES

Banks, T. A., Luckman, P. S. B., Frith, J. E., and Cooper-White, J. J. (2015). Effects of electric fields on human mesenchymal stem cell behaviour and morphology using a novel multichannel device. *Integr. Biol.* 7, 693–712. doi: 10.1039/c4ib00297k

Baskaran, A., and Marchetti, M. C. (2008). Enhanced diffusion and ordering of self-propelled rods. *Phys. Rev. Lett.* 101:268101. doi: 10.1103/PhysRevLett.101.268101

Chang, W. H.-S., Chen, L.-T., Sun, J.-S., and Lin, F.-H. (2004). Effect of pulse-burst electromagnetic field stimulation on osteoblast cell activities. *Bioelectromagnetics* 25, 457–465. doi: 10.1002/bem.20016

Ciombor, D. M., and Aaron, R. K. (1993). Influence of electromagnetic fields on endochondral bone formation. *J. Cell. Biochem.* 52, 37–41. doi: 10.1002/jcb.240520106

De-Leon, S. B.-T., and Davidson, E. H. (2007). Gene regulation: gene control network in development. *Annu. Rev. Biophys. Biomol. Struct.* 36, 191–212. doi: 10.1146/annurev.biophys.35.040405.102002

Dingal, P. C. D. P., Wells, R. G., and Discher, D. E. (2014). Simple insoluble cues specify stem cell differentiation. *Proc. Natl. Acad. Sci. U.S.A.* 111, 18104–18105. doi: 10.1073/pnas.1421562112

Engler, A. J., Sen, S., Sweeney, H. L., and Discher, D. E. (2006). Matrix elasticity directs stem cell lineage specification. *Cell* 126, 677–689. doi: 10.1016/j.cell.2006.06.044

Eyckmans, J., Lin, G. L., and Chen, C. S. (2012). Adhesive and mechanical regulation of mesenchymal stem cell differentiation in human bone marrow and periosteum-derived progenitor cells. *Biol. Open* 1, 1058–1068. doi: 10.1242/bio.20122162

Farooqi, A. R., Bader, R., and Van Rienen, U. (2019). Numerical study on electromechanics in cartilage tissue with respect to its electrical properties. *Tissue Eng. B* 25, 152–166. doi: 10.1089/ten.teb.2018.0214

Foret, L., Dawson, J. E., Villasenor, R., Collinet, C., Deutsch, A., Brusch, L., et al. (2012). A general theoretical framework to infer endosomal network dynamics from quantitative image analysis. *Curr. Biol.* 22, 1381–1390. doi: 10.1016/j.cub.2012.06.021

Fricke, H. (1953). The electric permittivity of a dilute suspension of membrane-covered ellipsoids. *J. Appl. Phys.* 24, 644–646. doi: 10.1063/1.1721343

Funk, R. H. W. (2015). Endogenous electric fields as guiding cue for cell migration. *Front. Physiol.* 6:143. doi: 10.3389/fphys.2015.00143

Gimsa, J., and Wachner, D. (2001a). Analytical description of the transmembrane voltage induced on arbitrarily oriented ellipsoidal and cylindrical cells. *Biophys. J.* 81, 1888–1896. doi: 10.1016/S0006-3495(01)75840-7

Gimsa, J., and Wachner, D. (2001b). On the analytical description of transmembrane voltage induced on spheroidal cells with zero membrane conductance. *Eur. Biophys. J.* 30, 463–466. doi: 10.1007/s002490100162

Gowrishankar, T. R., Smith, K. C., and Weaver, J. C. (2013). "Transport-based biophysical system models of cells for quantitatively describing responses to electric fields," in *Proceedings of the IEEE (Institute of Electrical and Electronics Engineers Inc.)*. doi: 10.1109/JPROC.2012.2200289

Gowrishankar, T. R., and Weaver, J. C. (2003). An approach to electrical modeling of single and multiple cells. *Proc. Natl. Acad. Sci. U.S.A.* 100, 3203–3208. doi: 10.1073/pnas.0636434100

Grosse, C., and Schwan, H. P. (1992). Cellular membrane potentials induced by alternating fields. *Biophys. J.* 63, 1632–1642. doi: 10.1016/S0006-3495(92)81740-X

Hanna, H., Mir, L. M., and Andre, F. M. (2018). *In vitro* osteoblastic differentiation of mesenchymal stem cells generates cell layers with distinct properties. *Stem Cell Res. Ther.* 9, 203. doi: 10.1186/s13287-018-0942-x

Hartig, M., Joos, U., and Wiesmann, H.-P. (2000). Capacitively coupled electric fields accelerate proliferation of osteoblast-like primary cells and increase bone extracellular matrix formation *in vitro*. *Eur. Biophys. J.* 29, 499–506. doi: 10.1007/s002490000100

Hess, R., Jaeschke, A., Neubert, H., Hintze, V., Moeller, S., Schnabelrauch, M., et al. (2012a). Synergistic effect of defined artificial extracellular matrices and pulsed electric fields on osteogenic differentiation of human MSCs. *Biomaterials* 33, 8975–8985. doi: 10.1016/j.biomaterials.2012.08.056

Hess, R., Neubert, H., Seifert, A., Bierbaum, S., Hart, D. A., and Scharnweber, D. (2012b). A novel approach for *in vitro* studies applying electrical fields to cell cultures by transformer-like coupling. *Cell Biochem. Biophys.* 64, 223–232. doi: 10.1007/s12013-012-9388-4

Hoffmann, M., Kuska, J. P., Zscharnack, M., Loeffler, M., and Galle, J. (2011). Spatial organization of mesenchymal stem cells *in vitro*-results from a new individual cell-based model with podia. *PLoS ONE* 6:e21960. doi: 10.1371/journal.pone.0021960

Jansen, J. H., van der Jagt, O. P., Punt, B. J., Verhaar, J. A., van Leeuwen, J. P., Weinans, H., et al. (2010). Stimulation of osteogenic differentiation in human osteoprogenitor cells by pulsed electromagnetic fields: an *in vitro* study. *BMC Musculoskelet. Disord.* 11:188. doi: 10.1186/1471-2474-11-188

Kim, I. S., Song, J. K., Song, Y. M., Cho, T. H., Lee, T. H., Lim, S. S., et al. (2009). Novel effect of biphasic electric current on *in vitro* osteogenesis and cytokine production in human mesenchymal stromal cells. *Tissue Eng. A* 15, 2411–2422. doi: 10.1089/ten.tea.2008.0554

Kotnik, T., Bobanović, F., and Miklavčič, D. (1997). Sensitivity of transmembrane voltage induced by applied electric fields - A theoretical analysis. *Bioelectrochem. Bioenerg.* 43, 285–291. doi: 10.1016/S0302-4598(97)00023-8

Kotnik, T., and Miklavčič, D. (2006). Theoretical evaluation of voltage inducement on internal membranes of biological cells exposed to electric fields. *Biophysical J.* 90, 480–491. doi: 10.1529/biophysj.105.070771

Lade, S. J., Coelho, M., Tolić, I. M., and Gross, T. (2015). Fusion leads to effective segregation of damage during cell division: an analytical treatment. *J. Theor. Biol.* 378, 47–55. doi: 10.1016/j.jtbi.2015.04.022

Lei, J., Levin, S. A., and Nie, Q. (2014). Mathematical model of adult stem cell regeneration with cross-talk between genetic and epigenetic regulation. *Proc. Natl. Acad. Sci. U.S.A.* 111, E880–E887. doi: 10.1073/pnas.1324267111

Lin, H.-Y., and Lin, Y.-J. (2011). *In vitro* effects of low frequency electromagnetic fields on osteoblast proliferation and maturation in an inflammatory environment. *Bioelectromagnetics* 32, 552–560. doi: 10.1002/bem.20668

Lohmann, C. H., Schwartz, Z., Liu, Y., Guerkov, H., Dean, D. D., Simon, B., et al. (2000). Pulsed electromagnetic field stimulation of MG63 osteoblast-like cells affects differentiation and local factor production. *J. Orthop. Res.* 18, 637–646. doi: 10.1002/jor.1100180417

MacArthur, B. D. (2014). Collective dynamics of stem cell populations. *Proc. Natl. Acad. Sci. U.S.A.* 111, 3653–3654. doi: 10.1073/pnas.1401030111

Maswiwat, K., Wachner, D., and Gimsa, J. (2008). Effects of cell orientation and electric field frequency on the transmembrane potential induced in ellipsoidal cells. *Bioelectrochemistry* 74, 130–141. doi: 10.1016/j.bioelechem.2008.06.001

Meny, I., Burais, N., Buret, F., and Nicolas, L. (2007). Finite-element modeling of cell exposed to harmonic and transient electric fields. *IEEE Trans. Magn.* 43, 1773–1776. doi: 10.1109/TMAG.2007.892517

Mezeme, M. E., and Brosseau, C. (2010). Time-varying electric field induced transmembrane potential of a core-shell model of biological cells. *J. Appl. Phys.* 108, 014701. doi: 10.1063/1.3456163

Miller, C., and Henriquez, C. (1988). Three-dimensional finite element solution for biopotentials: erythrocyte in an applied field. *IEEE Trans. Biomed. Eng.* 35, 712–718. doi: 10.1109/10.7272

Miyamoto, H., Sawaji, Y., Iwaki, T., Masaoka, T., Fukada, E., Date, M., et al. (2019). Intermittent pulsed electromagnetic field stimulation activates the mTOR pathway and stimulates the proliferation of osteoblast-like cells. *Bioelectromagnetics* 40, 412–421. doi: 10.1002/bem.22207

Mousavi, S. J., and Doweidar, M. H. (2015). Role of mechanical cues in cell differentiation and proliferation: a 3D numerical model. *PLoS ONE* 10:e0124529. doi: 10.1371/journal.pone.0124529

Najafabadi, M. M., Bayati, V., Orazizadeh, M., Hashemitabar, M., and Absalan, F. (2016). Impact of cell density on differentiation efficiency of rat adipose-derived stem cells into schwann-like cells. *Int. J. Stem Cells* 9, 213–220. doi: 10.15283/ijsc16031

Październiorek, P. R. (2014). Mathematical model of stem cell differentiation and tissue regeneration with stochastic noise. *Bull. Math. Biol.* 76, 1642–1669. doi: 10.1007/s11538-014-9971-5

Petecchia, L., Sbrana, F., Utzeri, R., Vercellino, M., Usai, C., Visai, L., et al. (2015). Electro-magnetic field promotes osteogenic differentiation of BM-hMSCs through a selective action on Ca2+-related mechanisms. *Sci. Rep.* 5, 13856. doi: 10.1038/srep13856

Pisu, M., Concas, A., and Cao, G. (2012). Simulation models for stem cells differentiation. *Chem. Biochem. Eng. Q.* 26, 435–446. doi: 10.1016/j.compbiolchem.2008.06.001

Rajnicek, A. M., Foubister, L. E., and McCaig, C. D. (2008). Alignment of corneal and lens epithelial cells by co-operative effects of substratum topography and DC electric fields. *Biomaterials* 29, 2082–2095. doi: 10.1016/j.biomaterials.2008.01.015

Ralston, A. (2008). *Gene Expression Regulates Cell Differentiation*. Nature Education.

Ramos, A., Raizer, A., and Marques, J. L. (2003). A new computational approach for electrical analysis of biological tissues. *Bioelectrochemistry* 59, 73–84. doi: 10.1016/S1567-5394(03)00004-5

Recho, P., Ranft, J., and Marcq, P. (2016). One-dimensional collective migration of a proliferating cell monolayer. *Soft Matter* 12, 2381–2391. doi: 10.1039/C5SM02857D

Renardy, M., Jilkine, A., Shahriyari, L., and Chou, C. S. (2018). Control of cell fraction and population recovery during tissue regeneration in stem cell lineages. *J. Theor. Biol.* 445, 33–50. doi: 10.1016/j.jtbi.2018.02.017

Rohde, M., Ziebart, J., Kirschstein, T., Sellmann, T., Porath, K., Kühl, F., et al. (2019). Human osteoblast migration in DC electrical fields depends on store operated ca2+-release and is correlated to upregulation of stretch-activated TRPM7 channels. *Front. Bioeng. Biotechnol.* 7:422. doi: 10.3389/fbioe.2019.00422

Rutkovskiy, A., Stenslokken, K.-O., and Vaage, I. J. (2016). Osteoblast differentiation at a glance. *Med. Sci. Monit. Basic Res.* 22, 95–106. doi: 10.12659/MSMBR.901142

Sarkar, N., Prost, J., and Jülicher, F. (2019). Field induced cell proliferation and death in a model epithelium. *New J. Phys.* 21. doi: 10.1101/467159

Schemitsch, E., and Kuzyk, P. (2009). The science of electrical stimulation therapy for fracture healing. *Indian J. Orthop.* 43, 127. doi: 10.4103/0019-5413.50846

Schoenbach, K. H., Joshi, R. P., Kolb, J. F., Chen, N., Stacey, M., Blackmore, P. F., et al. (2004). Ultrashort electrical pulses open a new gateway into biological cells. *Proc. IEEE* 92, 1122–1136. doi: 10.1109/JPROC.2004.829009

Schwan, H. (1994). "Electrical properties of tissues and cell suspensions: mechanisms and models," in *Proceedings of 16th Annual International Conference of the IEEE Engineering in Medicine and Biology Society* (Maryland: IEEE), A70–A71.

Schwartz, Z., Simon, B. J., Duran, M. A., Barabino, G., Chaudhri, R., and Boyan, B. D. (2008). Pulsed electromagnetic fields enhance BMP-2 dependent osteoblastic differentiation of human mesenchymal stem cells. *J. Orthop. Res.* 26, 1250–1255. doi: 10.1002/jor.20591

Sebastián, J. L., Munoz San Martin, S., Sancho, M., and Miranda, J. M. (2004). Modelling the internal field distribution in human erythrocytes exposed to MW radiation. *Bioelectrochemistry* 64, 39–45. doi: 10.1016/j.bioelechem.2004.02.003

Smoluchowski, M. (1916). Drei Vortrage uber Diffusion, Brownsche Bewegung und Koagulation von Kolloidteilchen. *Z. Phys.* 17, 557–585.

Stewart, D. A., Gowrishankar, T. R., and Weaver, J. C. (2004). Transport lattice approach to describing cell electroporation: use of a local asymptotic model. *IEEE Trans. Plasma Sci.* 32, 1696–1708. doi: 10.1109/TPS.2004.832639

Sun, L.-Y., Hsieh, D.-K., Lin, P.-C., Chiu, H.-T., and Chiou, T.-W. (2009). Pulsed electromagnetic fields accelerate proliferation and osteogenic gene expression in human bone marrow mesenchymal stem cells during osteogenic differentiation. *Bioelectromagnetics.* 31, 209–219. doi: 10.1002/bem.20550

Sun, Z., and Komarova, N. L. (2012). Stochastic modeling of stem-cell dynamics with control. *Math. Biosci.* 240, 231–240. doi: 10.1016/j.mbs.2012.08.004

Sun, Z., and Komarova, N. L. (2015). Stochastic control of proliferation and differentiation in stem cell dynamics. *J. Math. Biol.* 71, 883–901. doi: 10.1007/s00285-014-0835-2

Tabatabai, M. A., Bursac, Z., Eby, W. M., and Singh, K. P. (2011). Mathematical modeling of stem cell proliferation. *Med. Biol. Eng. Comput.* 49, 253–262. doi: 10.1007/s11517-010-0686-y

Tandon, N., Goh, B., Marsano, A., Chao, P.-H., Montouri-Sorrentino, C., Gimble, J., et al. (2009). "Alignment and elongation of human adipose-derived stem cells in response to direct-current electrical stimulation," in *2009 Annual International Conference of the IEEE Engineering in Medicine and Biology Society* (Minneapolis, MN: IEEE), 6517–6521. doi: 10.1109/IEMBS.2009.5333142

Tonge, P. D., Olariu, V., Coca, D., Kadirkamanathan, V., Burrell, K. E., Billings, S. A., et al. (2010). Prepatterning in the stem cell compartment. *PLoS ONE* 5:e10901. doi: 10.1371/journal.pone.0010901

Vajrala, V., Claycomb, J. R., Sanabria, H., and Miller, J. H. (2008). Effects of oscillatory electric fields on internal membranes: an analytical model. *Biophys. J.* 94, 2043–2052. doi: 10.1529/biophysj.107.114611

Valic, B., Golzio, M., Pavlin, M., Schatz, A., Faurie, C., Gabriel, B., et al. (2003). Effect of electric field induced transmembrane potential on spheroidal cells: theory and experiment. *Eur. Biophys. J.* 32, 519–528. doi: 10.1007/s00249-003-0296-9

Yang, J., Sun, Z., and Komarova, N. L. (2015). Analysis of stochastic stem cell models with control. *Math. Biosci.* 266, 93–107. doi: 10.1016/j.mbs.2015.06.001

Ying, W., and Henriquez, C. S. (2007). Hybrid finite element method for describing the electrical response of biological cells to applied fields. *IEEE Trans. Biomed. Eng.* 54, 611–620. doi: 10.1109/TBME.2006.889172

Conflict of Interest: The authors declare that the research was conducted in the absence of any commercial or financial relationships that could be construed as a potential conflict of interest.

frontiers in Bioengineering and Biotechnology

ORIGINAL RESEARCH
published: 26 October 2020
doi: 10.3389/fbioe.2020.580135

Functionalization of Electrospun Nanofibers and Fiber Alignment Enhance Neural Stem Cell Proliferation and Neuronal Differentiation

*Miriam C. Amores de Sousa[1], Carlos A. V. Rodrigues[1], Inês A. F. Ferreira[1], Maria Margarida Diogo[1], Robert J. Linhardt[2], Joaquim M. S. Cabral[1] and Frederico Castelo Ferreira[1]**

[1] Institute for Bioengineering and Biosciences, Department of Bioengineering, Instituto Superior Técnico, Universidade de Lisboa, Lisbon, Portugal, [2] Center for Biotechnology and Interdisciplinary Studies, Department of Chemistry and Chemical Biology, Rensselaer Polytechnic Institute, Troy, NY, United States

OPEN ACCESS

Edited by:
Yuguo Lei,
University of Nebraska-Lincoln,
United States

Reviewed by:
Jingwei Xie,
University of Nebraska Medical Center, United States
Oscar Castano,
University of Barcelona, Spain
Carlos Aleman,
Universitat Politecnica de Catalunya, Spain

***Correspondence:**
Frederico Castelo Ferreira
frederico.ferreira@tecnico.ulisboa.pt

Specialty section:
This article was submitted to Biomaterials, a section of the journal Frontiers in Bioengineering and Biotechnology

Received: 04 July 2020
Accepted: 24 September 2020
Published: 26 October 2020

Citation:
Amores de Sousa MC, Rodrigues CAV, Ferreira IAF, Diogo MM, Linhardt RJ, Cabral JMS and Ferreira FC (2020) Functionalization of Electrospun Nanofibers and Fiber Alignment Enhance Neural Stem Cell Proliferation and Neuronal Differentiation. Front. Bioeng. Biotechnol. 8:580135. doi: 10.3389/fbioe.2020.580135

Neural stem cells (NSCs) have the potential to generate the cells of the nervous system and, when cultured on nanofiber scaffolds, constitute a promising approach for neural tissue engineering. In this work, the impact of combining nanofiber alignment with functionalization of the electrospun poly-ε-caprolactone (PCL) nanofibers with biological adhesion motifs on the culture of an NSC line (CGR8-NS) is evaluated. A five-rank scale for fiber density was introduced, and a 4.5 level, corresponding to 70–80% fiber density, was selected for NSC *in vitro* culture. Aligned nanofibers directed NSC distribution and, especially in the presence of laminin (PCL-LN) and the RGD-containing peptide GRGDSP (PCL-RGD), promoted higher cell elongation, quantified by the eccentricity and axis ratio. *In situ* differentiation resulted in relatively higher percentage of cells expressing Tuj1 in PCL-LN, as well as significantly longer neurite development (41.1 ± 1.0 μm) than PCL-RGD (32.0 ± 1.0 μm), pristine PCL (25.1 ± 1.2 μm), or PCL-RGD randomly oriented fibers (26.5 ± 1.4 μm), suggesting that the presence of LN enhances neuronal differentiation. This study demonstrates that aligned nanofibers, functionalized with RGD, perform as well as PCL-LN fibers in terms of cell adhesion and proliferation. The presence of the full LN protein improves neuronal differentiation outcomes, which may be important for the use of this system in tissue engineering applications.

Keywords: PCL, functionalization, nanofibers, electrospinning, neural stem cells, laminin, GRGDSP, alignment

INTRODUCTION

Neural stem cells (NSCs) are self-renewing multipotent cells with the capacity to differentiate into neurons and glial cells (astrocytes and oligodendrocytes) (Pollard et al., 2006b; Conti and Cattaneo, 2010). The use of NSCs combined with engineered biomaterials has the potential to provide new therapeutic routes, including the regeneration of the central nervous system (CNS) when impaired by neurodegenerative diseases, such as Alzheimer or Parkinson diseases, or traumatic injuries such

as spinal cord injury (Grochowski et al., 2018; Pereira et al., 2019). Moreover, NSCs can be used to generate *in vitro* disease models (Jakel et al., 2004; Zhao and Moore, 2018), which may be important tools to provide new insights into disease mechanisms, as well as to discover and test new drugs (Gorba and Conti, 2013).

Neural stem cell-based therapeutic strategies may involve the stimulation of endogenous stem cells or on the transplantation of exogenous stem cells previously expanded *in vitro*. The use of biomaterial scaffolds provides an adequate surface for cell adhesion, enabling efficient cell proliferation, differentiation, and organization into a mature and functional engineered tissue (Kim et al., 2012). The role of the biomaterial scaffold also provides appropriate mechanical and physicochemical properties to the new tissue, as well as a geometry that contributes to cell organization (e.g., cell alignment) (Schaub et al., 2016).

The NSC niche is a complex structure, with a specific extracellular matrix (ECM) composition, able to support NSC maintenance and differentiation *in vivo*. The components of the ECM interact with cells through transmembrane proteins, called integrins, which trigger intracellular signaling pathways, influencing cell function and cell fate (Flanagan et al., 2006; Wang et al., 2011). Culture substrates processed from natural and synthetic materials have been developed to mimic the role of the native ECM on the support of NSCs (Ciardelli et al., 2005; Kim and Park, 2006; Hiraoka et al., 2009; Ananthanarayanan et al., 2010; Hackett et al., 2010; Cooper et al., 2011; Nakaji-Hirabayashi et al., 2012). Among the latter, polyesters such as poly-ε-caprolactone (PCL), polylactic acid, polyglycolic acid, and their copolymers are of particular interest in regenerative medicine as scaffolds. Such polymers are biocompatible and biodegradable and have been approved by the regulatory entities for medical applications (Schaub et al., 2016). However, the use of these synthetic biomaterials as substrates for cell culture often requires functionalization with specific biological motifs, namely, ECM proteins such as laminin" (LN), which is a protein found in the basement membrane and described to support NSC adhesion, migration, and differentiation (Hall et al., 2008; Koh et al., 2008; Hiraoka et al., 2009; Klinkhammer et al., 2010). The use of synthetic peptides, with cell adhesion motifs recognizable by integrins, for biomaterial functionalization has also been described and circumvents the issues raised by use of proteins of animal origin (batch to batch variability, pathogen, and immunogenic contamination), also being more cost-effective (Hersel et al., 2003; Hall et al., 2008; Ananthanarayanan et al., 2010). The arginine–glycine–aspartate peptide, or RGD, is a small amino acid sequence, which is conserved in nature and is present in many ECM proteins, including fibronectin and LN (Hersel et al., 2003; Causa et al., 2010; Gloria et al., 2012).

Nanofiber matrices, which can be produced by electrospinning, are promising structural substrates for NSC culture because this configuration can provide specific geometries at the cell scale, capable of reproducing the native tissue architecture (Xue et al., 2020). The nanofiber mesh affords a high surface-to-volume ratio while providing high porosity and permeability, permitting suitable diffusion of nutrients, metabolites, and gases. The substrate morphology and the presence of specific biochemical cues (adhesion molecules and growth factors) are critical to control cellular fate *in vitro*, impacting, for instance, cellular adhesion and morphology (elongation, spreading) (Beachley and Wen, 2009; Ghasemi-Mobarakeh et al., 2010; Hackett et al., 2010; Gloria et al., 2012). Previous studies have shown the importance of using electrospun fibers to culture NSCs from different sources, using fiber geometry to promote tissue organization. Aligned PLLA nanofibers promoted NSC alignment and neurite extension according to fiber alignment direction (Yang et al., 2005). Neural precursors, derived from human embryonic stem cells (ESCs), were cultured on aligned LN-coated PCL fibers, showing a more accentuated polar morphology, increased neuronal differentiation, and neurite extension along the fiber direction (Mahairaki et al., 2011). LN-coated aligned PCL nanofibers were used to culture adult rat NSCs, promoting accentuated cellular alignment, neurite extension along the fiber alignment axis, and also a higher number of differentiated $Tuj1^+$ cells (Lim et al., 2010). NSCs with more polarized and elongated morphology were also obtained in LN-coated aligned polystyrene nanofibers, together with high neuronal lineage differentiation (Bakhru et al., 2011). Different peptides containing biological motifs have been incorporated into synthetic materials to improve cell adhesion to the nanofibers, as well as differentiation outcomes, with higher reproducibility and manufacture standardization. Examples of these studies include the culture of mouse ESCs in aligned and functionalized fibers with YIGSR, a peptide derived from LN, which leads to increased expression of neuronal markers (Tuj1) and neurite extensions when compared to random and non-functionalized fibers (Smith Callahan et al., 2013). Aligned fibers, functionalized with epidermal growth factor (EGF) (Lam et al., 2010), were used to culture human ESC-derived NSCs, leading also to higher expression of glial and neuronal markers and axon extension. Cortical NSCs had higher proliferation and preferentially differentiate into oligodendrocytes and neurons in both randomly oriented and aligned brain-derived neurotrophic factor (BDNF)–functionalized PCL nanofibers (Horne et al., 2009). Glial cell-derived neurotrophic factor–functionalized PCL fibrous scaffolds (Wang T.Y. et al., 2012) were also successfully used to culture neural stem/progenitor cells with increased cell viability, proliferation and neurite outgrowth, upon transplantation. PCL nanofibers were also functionalized with the GYIGSR or RGD peptides and used to study the impact of these peptides and fiber morphology on mouse ESC neural differentiation (Silantyeva et al., 2018; Philip et al., 2019). PCL fibers functionalized with GYIGSR accelerated neural differentiation, whereas the use of RGD nanofibers promoted enhanced GFAP expression. Guidance of neurites parallel to the fiber direction was observed in both cases, when aligned fibers were used.

In this work, a detailed comparative study was performed, to understand the importance of combining fiber organization and selected biological motifs on NSC proliferation, differentiation, and morphology. PCL was selected because of its slow biodegradability (in the range of 1–2 years), which ensures support of cells during slow tissue regeneration *in vivo*. PCL nanofibers with different morphologies, random and aligned,

were functionalized with adhesion factors that promote NSC elongation, namely, LN, a complete protein widely used to promote cell adhesion and neural differentiation, or GRGDSP, one of the most active RGD-containing peptides for recognition by cell adhesion molecules (Hautanen et al., 1989; Hersel et al., 2003). The functionalized nanofibers were used to study the impact of the selected ECM motif over NSC proliferation, differentiation, and cellular morphology. The CGR8-NS cell line, derived from the mouse embryonic cell line CGR8, was selected as NSC model. This robust cellular model can be stably expanded *in vitro* and maintain neuronal and glial differentiation even after long-term passaging (Conti et al., 2005; Pollard et al., 2006a). Moreover, these cells proliferate adherent to physical supports as a cell monolayer (Rodrigues et al., 2010, 2011), which is of particular interest to easily assess the effect of fibers with different morphologies on cell populations including their orientation and shape. The results obtained show, in a comparative manner, the impact of the different biological motifs in combination with fiber geometry, on cell attachment, proliferation, and differentiation, as well as on cell alignment and morphology. This study demonstrates that despite small peptide motifs (GRDGSP) can provide equivalent results to LN in terms of cell adhesion and proliferation, the use of the full LN protein has advantages in terms of neuronal differentiation. The current work also presents for the first time a five-rank scale for fiber density, which allows us to standardize the nanofiber scaffolds prepared and improves the reproducibility of the experiments.

MATERIALS AND METHODS

PCL Nanofiber Preparation by Electrospinning

Aligned and randomly distributed PCL nanofibers were prepared using an electrospinning apparatus, as described elsewhere (Canadas et al., 2014). The equipment setup (**Figure 1A**), assembled inside a fume hood, was composed of a high-voltage power supply (Model PS/EL40P0, Series EL 1; Glassman High Voltage Inc., High Bridge, NJ, United States), a syringe pump (Model KDS Legato 210; KDS Scientific, Holliston, MA, United States), and a tube connecting a syringe (Henke Sass Wolf, Germany) to a needle (Needle Valve Dispense Tip Kit; EFD International Inc., United Kingdom) with an inner diameter of 0.84 mm. Two types of collectors were used: two parallel steel plates with a 2-cm gap collector (**Figures 1B,C**) and a flat copper plate (**Figure 1D**), positioned below and perpendicular to the needle, as reported in the literature (Li et al., 2003; Teo and Ramakrishna, 2006; Beachley and Wen, 2009). Operational parameters applied on the electrospinning process were previously optimized in-house (data not shown). The nanofibers were prepared with 6% wt/wt solution of PCL (70,000–90,000 MW; Sigma–Aldrich, St. Louis, MO, United States) in 1,1,1,3,3,3-hexafluoro-2-propanol (HFP; Sigma–Aldrich) at a flow rate of 1 mL h^{-1}, with an applied electrical potential and working distance (tip of the needle to the nanofiber deposition target) of 26 kV and 20 cm or 30 kV and 35 cm to produce aligned or randomly distributed nanofibers.

The fibers were carefully collected from the supports and fixed onto glass coverslips (13-mm diameter; VWR, Radnor, PA, United States) with medical-grade biocompatible silicone glue (Silastic Medical Adhesive Silicone type A; Dow Corning, Midland, MI, United States), ensuring that the mesh maintained structure integrity throughout the experiments (**Figure 1E**). The ranges for humidity and temperature working conditions were 30–40% and 22–25°C, respectively.

The fiber alignment was estimated by measuring the angle of each fiber relative to a horizontal reference line. The angle values were normalized and represented in a histogram within a range of −90° and +90°.

We used both optical microscopy images and higher-resolution scanning electron microscopy (SEM) images of different fiber series to establish the "five-scale fiber-density ranking." The images were analyzed using ImageJ, being converted in bimodal images (with only black and white pixels) to estimate the ratio between empty space and fibers (Wang et al., 2010).

Functionalization of the PCL Nanofibers

Aminolysis Reaction

The nanofibers were washed with a 50% vol/vol solution of ethanol (Thermo Fisher Scientific, Waltham, MA, United States) in water for 1 h and rinsed with deionized water under gentle agitation, at room temperature. The aminolysis reaction took place immersing the samples in 10% wt/vol 1,6-hexanediamine (HDA, Fluka, Germany) in isopropanol (Thermo Fisher Scientific) for 40 min at 37°C, as described elsewhere (Zhu et al., 2002). After aminolysis, the nanofibers were rinsed with deionized water five times.

Protein Immobilization

Solutions of Laminin (LN, 20 μg mL^{-1}; Sigma–Aldrich) and of the peptide glycine–arginine–glycine-aspartic acid–serine–proline (GRGDSP, 50 μg mL^{-1}; Sigma–Aldrich) were prepared in phosphate-buffered saline (PBS; Life Technologies, Waltham, MA, United States). Protein or peptide crosslinking to the amine group, previously introduced in the PCL fibers by aminolysis, was performed by reaction over 24 h in glutaraldehyde atmosphere (Migneault et al., 2004), using a solution of 2.5% vol/vol glutaraldehyde (GA; Sigma–Aldrich). Afterward, the samples were washed with PBS five times and immersed in a solution of glycine (100 mg mL^{-1} in PBS; Sigma–Aldrich) for 1 h at room temperature, to quench free aldehyde groups. Finally, the samples were washed again five times with PBS at room temperature.

Quantification of Immobilized Protein

The quantity of protein or peptide attached to the scaffold surface was estimated using the colorimetric ninhydrin assay, which quantifies the total amine groups (Zhu et al., 2002; Friedman, 2004). This method is based on the reaction of the amine groups with ninhydrin, resulting in the formation of a blue compound measurable by absorbance spectroscopy. Nanofiber samples of equivalent dimensions (nanofiber mesh covering approximately 0.8 cm^2 of surface area) were removed from the glass slides, immersed in 0.5 mL of 1.0 mol L^{-1} ninhydrin (Merck, Germany)

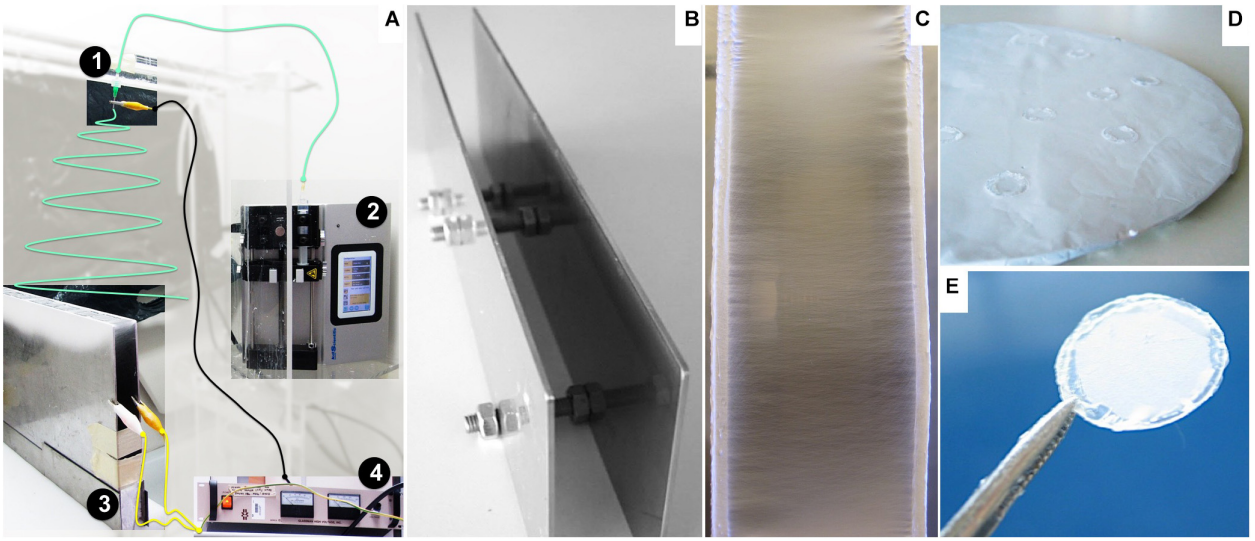

FIGURE 1 | Nanofiber preparation and assembly: **(A)** Adapted view of the electrospinner apparatus: 1: needle, 2: syringe pump, 3: parallel plate collector, 4: power source. The polymer solution contained in the syringe is loaded at a constant flow by the pump (2) along a tube (green line) to the needle (1) positioned above and perpendicular to the grounded collector (3). The power source equipment (4) provides the electric potential to charge the polymer solution, wired to the stainless steel tip of the needle by the black cable, while permitting grounding the collector connected by the yellow wires. **(B)** Parallel plates used as a collector for aligned nanofibers. **(C)** Detailed view of deposited aligned nanofibers oriented perpendicular to the edges of the plates. **(D)** Round flat collector covered with a random fiber mesh. **(E)** Nanofiber sample fixed on a glass slide.

in ethanol for 1 min at room temperature and heated at 80°C for 20 min, until complete ethanol evaporation. To dissolve the PCL mesh sample, 0.5 mL of 1,4-dioxane (Thermo Fisher Scientific) was added, followed by 0.5 mL of isopropanol, to stabilize the blue compound formed. Pristine PCL fibers, without any chemical treatment, were used as control for any non-specific residual chromophore response, and PCL fibers submitted to aminolysis, but without protein functionalization, were used as an additional control. The absorbance of the reaction product was measured at 538 nm using a microplate reader (Infinite M200 Pro, Tecan, Switzerland). A reference calibration curve was obtained measuring the absorbance of ninhydrin–NH_2 product as a function of graded concentrations of HDA in 1:1 vol/vol of 1,4-dioxane/isopropanol solutions (**Supplementary Figure 1D**).

NSC Culture

The cell model used was the NSC line CGR8-NS, derived from the mouse ESC line CGR8 (Conti et al., 2005) and provided by the laboratory of Professor Austin Smith (Welcome Trust Centre for Stem Cell Research, Cambridge, United Kingdom).

CGR8-NS Culture in Standard Polystyrene Surface

The NSC culture was performed as previously described (Conti et al., 2005; Rodrigues et al., 2010). Cryopreserved CGR8-NS cells, upon thawing, were expanded on uncoated tissue culture T-flasks or 24-well plates (Falcon; BD Biosciences, San Jose, CA, United States), in serum-free NSC expansion medium composed of Dulbecco modified eagle medium (DMEM)/F12 + Glutamax (Thermo Fisher Scientific) supplemented with 1% vol/vol N2 (Thermo Fisher Scientific), 20 ng mL^{-1} of both FGF-2 and EGF (PeproTech, Rocky Hill, NJ, United States), 0.1% vol/vol B27 (Life Technologies), 1% vol/vol penicillin–streptomycin (10,000 U mL^{-1}, Thermo Fisher Scientific), 1.6 g L^{-1} glucose (Sigma–Aldrich), and 20 mg L^{-1} insulin (Sigma–Aldrich). The cells were cultured at 37°C under 5% CO_2 humidified atmosphere and maintained at passages between 45 and 54. Each passage was performed at 80–90% confluence. Cells were harvested using Accutase (Sigma–Aldrich), and cell viability was evaluated using the trypan blue (Thermo Fisher Scientific) exclusion method (Strober, 2001) by direct counting of viable cells in a hemacytometer, under an optical microscope (Olympus, Germany). Cell viability remained greater than 90%.

CGR8-NS Culture on the PCL Nanofibers

The nanofibers were placed in sterile 24-well ultralow attachment cell culture plates (Corning, NY, United States) and sterilized with antibiotic–antimycotic (Thermo Fisher Scientific) solution overnight. After sterilization, the nanofibers were washed with sterile PBS and rinsed with culture medium before cell seeding. A suspension of 100 μL with 2.0×10^5 CGR8-NS cells in fresh supplemented medium was deposited carefully on top of each nanofiber and incubated for 1 to 2 h to promote initial cell deposition and adhesion to the material.

The seeding density was defined considering a previously optimized value of 1.0×10^4 cells cm^{-2} (Rodrigues et al., 2010) and also the surface available for cells to adhere to the nanofibers as being at least three times higher than the flat surface of the well of the tissue culture plate. Reported in *Functionalization of the Nanofiber Surface*, a ratio 6:1 of fibers per flat surface was estimated, so the cell density was increased accordingly. After cell adhesion to the nanofibers, culture medium was added up to final volume of 0.5 mL. CGR8-NS cells (2.5×10^4 cells cm^{-2}) were

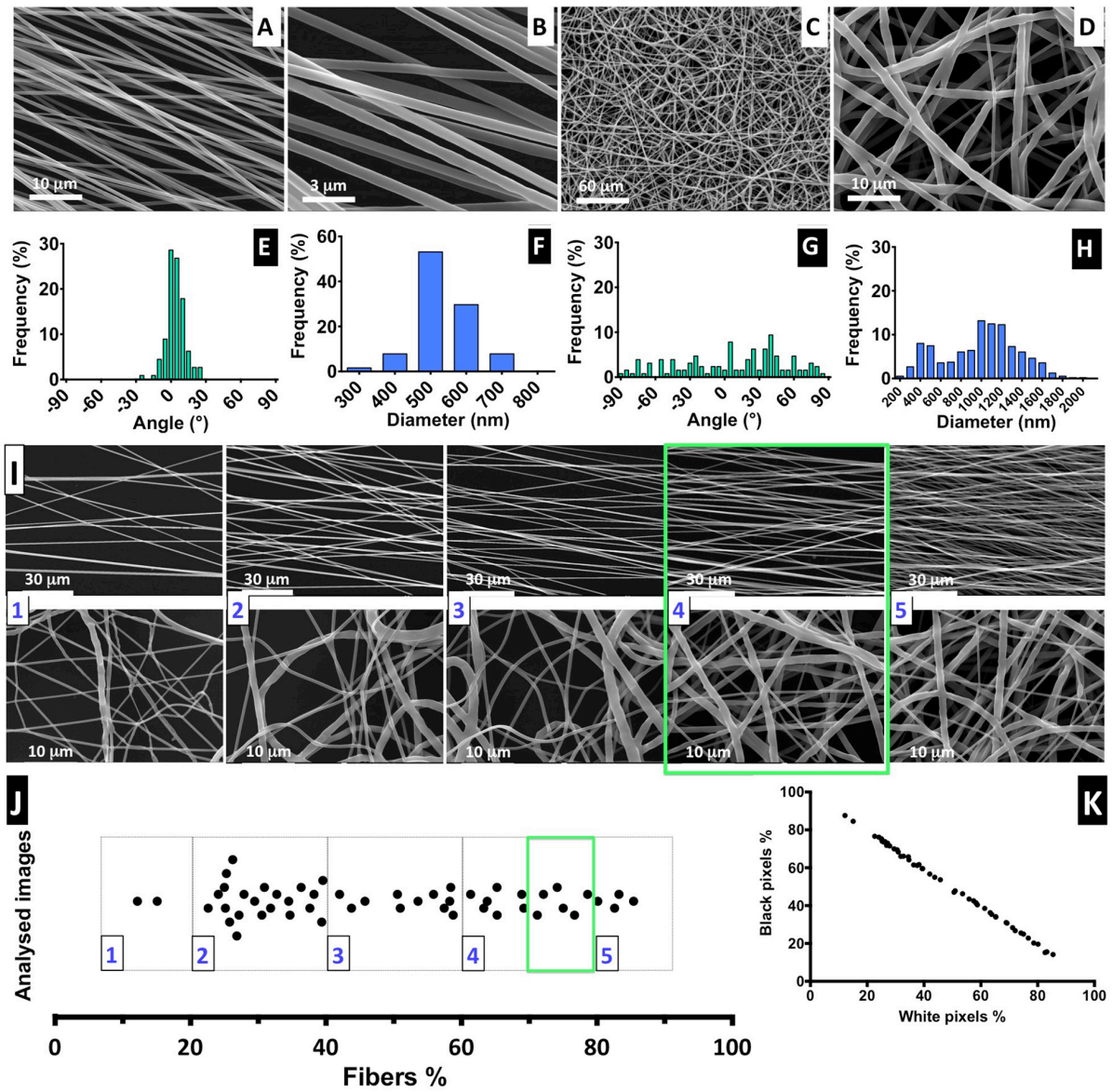

FIGURE 2 | Fiber characterization: **(A–D)** SEM images of aligned and randomly distributed fibers (fiber density 70–80%). **(E–H)** Histograms of alignment profile and fiber diameter distribution. At least 100 fibers were measured in each case. **(I)** SEM images for aligned and random fibers, ordered from low- to high-density mesh; scale bars: 30 and 1 µm for the aligned and random meshes, respectively. **(J)** Distribution of analyzed images with correspondent percentage of fiber mesh, divided into five degrees of density percentage; highlighted with a green square is the interval of fiber density of the samples selected for the cell culture experiments. **(K)** Proportion of the black and white pixels that compose the bimodal images.

also cultured in standard uncoated 24-well tissue culture plates as a control (**Supplementary Figure 2**).

Evaluation of Cell Growth

Viability and estimation of CGR8-NS cell number were monitored indirectly over time using Alamar Blue (Thermo Fisher Scientific) according to the manufacturer instructions and through a calibration curve (**Supplementary Figure 3**) relating the fluorescence intensity with the number of CGR8-NS cells, counted using a hemocytometer. Fluorescence was measured using a microplate reader at excitation and emission wavelengths of 560 and 590 nm, respectively.

The cell growth rate (μ) was determined using an "Ln X versus time" plot, as the slope of a linear regression line, according to the following (1):

$$\mathrm{Ln}\,(X) = \mathrm{Ln}\,(X_0) + \mu t \quad (1)$$

where X is the cell number and X_0 the initial cell number. The doubling time was obtained by (2):

$$t_{1/2} = \mathrm{Ln}\,2/\mu \quad (2)$$

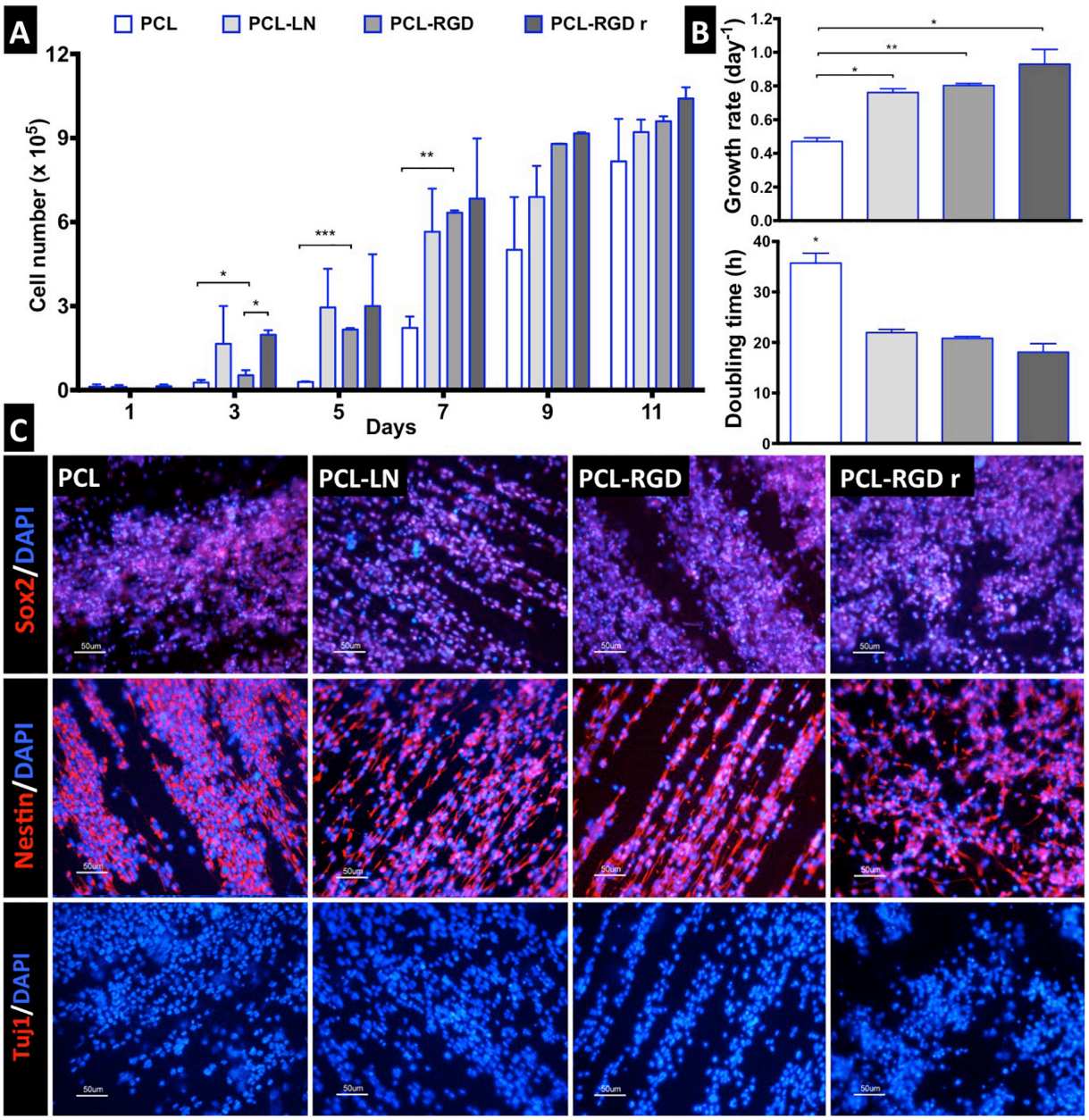

FIGURE 3 | CGR8-NS growth profile on aligned PCL, PCL-LN, PCL-RGD, and random PCL-RGD nanofibers: **(A)** Cell number variation over 11 days of culture ($n = 2$); values correspond to initial cell seeding of 2.0×10^5 cells per scaffold. **(B)** Growth rates (day^{-1}) and doubling times (h) for each condition; error bars are standard error of the mean; $^*p < 0.05$, $^{**}p < 0.01$, $^{***}p < 0.001$. **(C)** Fluorescence microscopy images of immunocytochemistry for Nestin, Sox2, and βIII–tubulin/Tuj1. Nuclei counterstained with DAPI; scale bar = 50 μm.

CGR8-NS Differentiation

After 11 days of NSC expansion on the nanofibers, a neuronal differentiation protocol was adapted (Pollard et al., 2006a) and performed *in situ*. At day 1 of differentiation, NSC medium (as described in *CGR8-NS Culture in Standard Polystyrene Surface*) was refreshed. On the next day, medium was replaced, this time without EGF, and with 5 ng · mL^{-1} of FGF-2 and 2% vol/vol B27. Half the medium was replaced after 4 days. At day 9, culture medium was replaced by a 1:1 mixture of DMEM/F12 and neurobasal medium (1×) (Thermo Fisher Scientific) without EGF or FGF-2 and with 2% vol/vol B27. Half the medium was replaced after 4 days, and culture was maintained until day 15 of differentiation. **Supplementary Figure 4** summarizes the applied protocol.

Cell Staining and Immunocytochemistry

The spatial distribution and morphology of CGR8-NS cells on the nanofibers were qualitatively assessed by labeling the

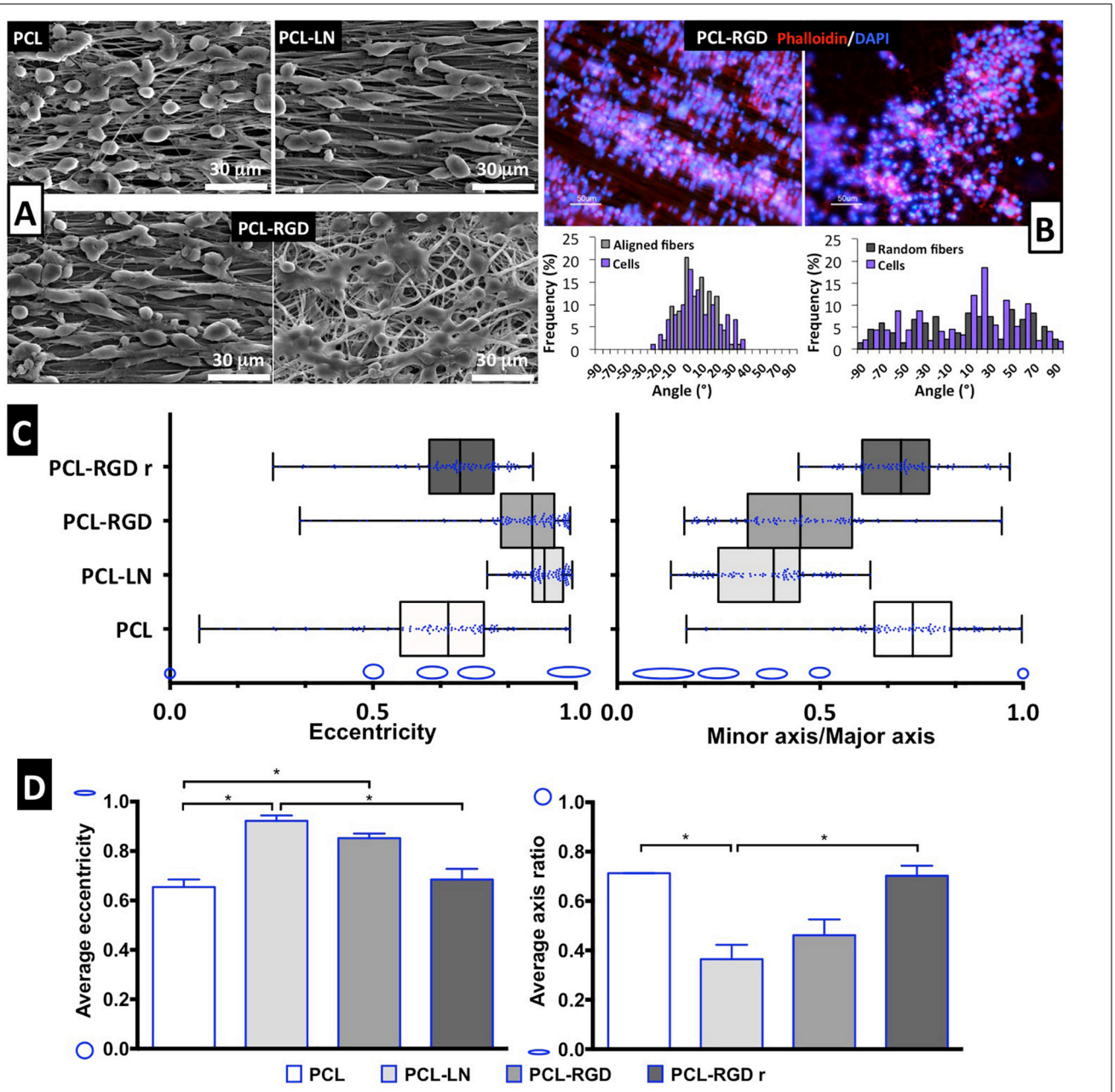

FIGURE 4 | Evaluation of cell morphology and organization after CGR8-NS cell expansion on the PCL nanofibers. **(A)** SEM images after 3 days of expansion; scale bar 30 µm. **(B)** Image of cellular cytoskeleton staining with rhodamine phalloidin in PCL-RGD and PCL-RGDr, with respective histograms of cell alignment versus fiber arrangement; scale bar 50 µm. **(C)** Box-and-whisker plot for eccentricity (E = 0, perfect circle; E = 1, elongated shape) and aspect ratio (AR = 1, perfect circle; AR = 0, elongated shape) for cellular elongation quantification. The box boundaries represent the 25th and the 75th percentile; the straight line inside is the median. A minimum of 50 cells were measured. **(D)** Average values for eccentricity and aspect ratio. The shape corresponding to discrete eccentricity and axis ratio values is illustrated on the y axis. Error bars represent standard error of the mean; $^*p < 0.05$ (n = 2).

nuclei with 4',6-diamino-2-phenylindole (DAPI; Sigma–Aldrich) and F-actin filaments of the cytoskeleton with the fluorescent dye rhodamine phalloidin (Thermo Fisher Scientific). CGR8-NS cells were fixed with 4% paraformaldehyde (PFA; Sigma–Aldrich) for 10 min at room temperature, washed once with PBS, and permeabilized with 0.1% vol/vol Triton X-100 (Sigma–Aldrich) and 5% vol/vol normal goat serum (NGS; Sigma–Aldrich) in PBS for 15 min. The cells were stained with 300 µL of rhodamine phalloidin probe (0.2 µg mL^{-1} in PBS) for 45 min at room temperature. After washing once with PBS, the cells were incubated with 300 µL of DAPI (1.5 µg mL^{-1} in PBS) for 5 min. Finally, the cells were washed two times in PBS. Cells were visualized under a fluorescence optical microscope (DMI 3000B; Leica, Germany).

Digital images were taken with a digital camera (DXM 1200F; Nikon, Japan).

Immunophenotype analysis was performed for Sox2, Nestin, Tuj1, and GFAP antibodies. The cells were fixed in 4% PFA for 10 min at room temperature, washed once with PBS, and permeabilized with 0.1% vol/vol Triton X-100 and 10% vol/vol NGS in PBS for 1 h at room temperature. Primary antibodies were incubated overnight at 4°C in 0.1% vol/vol Triton X-100 and 5% vol/vol NGS in PBS. The following primary antibodies were used: anti-Sox2 (1:100, R&D Systems, MN, United States), anti-Nestin mouse monoclonal antibody (1:200, Millipore, Germany), anti–βIII-tubulin (Tuj1,1:2000, Covance, Princeton, NJ, United States), and anti–glial fibrillary acidic protein GFAP (1:100, GFAP; Millipore). After primary antibody incubation, the cells were washed once with PBS and incubated with the proper secondary antibody conjugated with Alexa Fluor 546 (1:500; Life Technologies) for 1 h at room temperature, protected from light. Next, the cells were washed with PBS and nuclei stained with DAPI (1.5 $\mu g\ mL^{-1}$ in PBS) for 5 min at room temperature. Finally, the cells were washed two times in PBS and visualized under a fluorescence optical microscope.

Scanning Electron Microscopy

The nanofibers and cell morphology were examined by SEM. Scaffold samples containing cells were fixed with 4% PFA for 15 min, washed once with PBS, and dried by immersion in graded concentrations of ethanol solutions in water (25, 50, 75, and 100% vol/vol). The samples were kept in an aseptic environment until complete drying. Prior to SEM visualization, the samples were coated with a 45-nm gold/palladium layer by a sputter coater (model E5100, ex-Polaron; Quorum Technologies, ON, Canada) and observed under a conventional SEM (model S2400; Hitachi, Japan) with an electron beam with 20 kV of accelerating voltage. SEM images were analyzed with ImageJ (National Institutes of Health, United States) to estimate both orientation and fiber diameter profiles. At least 50 samples were individually measured for each condition.

Cell Shape Analysis

The eccentricity is a parameter that can be used to describe the cellular shape (Xie et al., 2009a,b). The NSC bipolar shape obtained from SEM images was fitted using ImageJ to an elliptical geometric form, to determine the major and minor axis. The eccentricity was calculated with Equation (1),

$$Eccentricity = \frac{\sqrt{\left(a^2 - b^2\right)}}{a} \quad (3)$$

where a and b are the semimajor and semiminor axis of the ellipse, respectively. Eccentricity values vary between 0 (which corresponds to a circle) and 1 (in this limit closest to a line segment).

Additionally, the elongation of the elliptical form measured was evaluated by the ratio between the minor and the major axis that, inversely, when equal to 1 corresponds to a perfect circle and when closest to 0 describes a shape approaching a line segment.

Statistical Analysis

The results are expressed as mean ± standard error of the mean. Statistical analysis was performed with ordinary one-way analysis of variance for multiple group comparison tests. Statistical comparison between two groups was performed with an unpaired t test. Statistically significant results were considered for $p < 0.05$.

RESULTS

Nanofiber Alignment, Diameter, and Density

The electrospinning conditions were optimized for a solution of 6% PCL to produce constant, uniform, and reproducible deposition of aligned and random defect-free nanofibers with smooth surface morphology. In **Figure 2**, SEM images of the prepared nanofibers are shown, as well as the distribution of diameters and relative orientation angles. **Figures 2A,B** show images of aligned fibers at low and high magnification, respectively. Representative images of randomly organized fibers at low (**Figure 2C**) and high magnification (**Figure 2D**) are also presented. **Figures 2A,D** are shown at the same magnification. The estimated average diameter of the aligned nanofibers was 0.54 ± 0.08 μm, with more than 90% of the fibers oriented within a range of ±30° angle to a reference axis, evidencing a clear uniaxial disposition (**Figure 2E**). The random fibers obtained present a wide dispersion, with the fiber angles relative to the reference axis (**Figure 2G**) covering all the angle range and with approximately only 35% fibers oriented within the narrower range of ± 30°; this feature highly contrasts the tight distribution found for the aligned fibers. Also, the random fibers have more heterogeneous diameters, in a range of 0.32 to 1.55 μm (average = 0.99 ± 0.37 μm) (**Figure 2H**). The difference between aligned and random fiber diameters and dispersion profile can be explained by the use of different collectors (**Figure 1**). The two-parallel-steel-plates electrode collector promotes the formation of fibers stretched on the 2-cm gap between the two narrow edges of the plates. Such process promotes not only fiber alignment, but also more uniform and smaller fiber diameters. The flat copper plate electrode provides a wide surface for fiber deposition promoting a broader electrical field shape and dispersion of fiber formation paths, thus leading to a wider range of diameter sizes. The flat copper plate is much less effective than the parallel-plate collector on stretching the fibers upon their formation and on promoting solvent evaporation from the deposited fibers. These factors can contribute to the existence of larger diameter fibers on randomly organized fiber scaffolds.

The electrospinning setup used for producing the nanofibers is non-automatic and performed manually, but it is challenging to control the density of the deposited fiber mesh produced. Therefore, to ensure the fiber meshes used in cell culture have a similar density, we implemented a post-manufacturing step of fiber mesh sorting, in which we suggest the introduction of a "five-scale fiber-density ranking" method. Representative SEM images to illustrate each level of density are shown in **Figure 2I**,

for both aligned and randomly distributed fiber meshes, and the respective images obtained by optical microscopy are presented in **Supplementary Figure 5**.

The quantification of fiber percentage (from approximately 10–90%) and the number of analyzed nanofiber SEM images, distributed by the five levels, is shown in **Figure 2I**. In **Figure 2K**, the proportion of both black and white pixels that compose the bimodal images is presented. For the NSC culture work performed in this study, the nanofiber meshes used were sorted based on optical microscopy examination to fall into 4.5 level of the "five-scale fiber-density ranking." This level, highlighted in the green square of **Figures 2I,J**, corresponds to a 70–80% fiber density and was selected because the nanofiber mesh was not too dense, allowing us to visualize the cells and fibers, while avoiding cell growth on the underlying glass coverslip.

Functionalization of the Nanofiber Surface

The next step for the preparation of the nanofibers for cell culture was to bind LN and the GRGDSP peptide on the material surface. The aligned PCL nanofiber meshes were identified as "PCL," for non-modified pristine PCL nanofibers, "PCL-NH_2" for aminolysed PCL nanofibers, and "PCL-LN" or "PCL-RGD" for LN and GRGDSP functionalized nanofibers, respectively. The random PCL fibers functionalized with GRGDSP were identified as PCL-RGDr. Examples of SEM images of the PCL nanofibers after aminolysis show structural integrity with no alteration on morphology, and the reaction schemes for the formation of the treated material PCL-NH_2 are presented in **Supplementary Figures 1A,B**, respectively.

The overall surface area of the scaffolds fiber mesh was estimated to be 5 cm^2 from SEM imaging covering 0.8 cm^2 of glass slide, which corresponds to a ratio of approximately 6:1 cm^2 of fiber surface per slide. The engrafted NH_2 groups on the polymer surface and the immobilized LN and GRGDSP peptide were both evaluated by the ninhydrin method (Zhu et al., 2002; Kim and Park, 2006), which quantifies the equivalent free amine groups (**Supplementary Figure 1**). This method quantifies amines without discriminating whether peptide or protein is immobilized to the fibers surface covalently or through weak physiochemical interactions (adsorption). In this work, to minimize the contribution of adsorption, the samples were extensively washed before the ninhydrin assay. However, the chemical strategy carried out herein (i.e., ester aminolysis followed by reaction with glutaraldehyde for the functionalization of PCL nanofibers with the protein/peptide) follows the methodology reported in previous studies (Zhu et al., 2002) for immobilization of gelatin, and collagen, where PCL functionalization was demonstrated by *x*-ray photoelectron spectroscopy and contact angle measurements.

Regardless of the limitations on the ninhydrin method, the amount of NH_2 groups per mesh surface area was estimated at a value of (7.1 ± 0.8) nmol cm^{-2} for PCL-NH_2 samples (not quenched with glycine), assuming insertion of functional amine groups onto the nanofibers (**Supplementary Figure 1C**). Estimated equivalent amine densities for the PCL-LN and PCL-RGD samples, at values of (28.1 ± 0.8) and (277.2 ± 61.2) nmol cm^{-2}, respectively, were higher than for PCL-NH_2 samples. In pristine PCL fibers, a background misreading absorbance was estimated as 2.4 ± 0.5 nmol cm^{-2}. By comparing the ninhydrin assay results for the initial solutions used in the crosslinking reaction and for the respective nanofiber meshes (**Supplementary Figure 1C**), an efficiency of nanofiber functionalization was estimated as 22.1 ± 1.5% and 83.8 ± 16.8% for PCL-LN and PCL-RGD, respectively.

NSC Proliferation on the Nanofiber Scaffolds

The NSC proliferation profile on the nanofiber scaffolds is represented in **Figure 3A**. In general, the number of cells increased over time in all the conditions. Analyzing in details of the 11 days of the cell culture, an initial drop in cell number is observed in the beginning of the culture (day 1). The initial cell number (2.0×10^5 cells) was achieved after only 3 days, in the case of PCL-LN and PCL-RGDr; after 5 days, for cultures in PCL-RGD aligned; and after 7 days, for pristine PCL fibers. Significantly higher cell numbers were observed on functionalized PCL-RGD fibers, relative to pristine PCL, at days 7 and 9.

However, these differences decreased and turned out fairly reduced by day 11. The scaffold area is similar for all the conditions, and when its maximum capacity for cell support is used, cell proliferation becomes reduced, indicating that cell confluence may have been reached, and therefore, differences between cell numbers are dissipated in the functionalized scaffolds by day 11.

The cell numbers at the end of the culture were $(8.2 \pm 1.5) \times 10^5$, $(9.2 \pm 0.4) \times 10^5$, $(9.6 \pm 0.2) \times 10^5$, and $(1.0 \pm 0.4) \times 10^6$ cells for PCL, PCL-LN, PCL-RGD and PCL-RGDr, respectively. The lower growth rate and higher doubling time were determined (**Figure 3B**) for cultures on pristine PCL (0.47 ± 0.02 day^{-1} and 35.7 ± 1.9 h). In contrast, higher cell growth rates and lower doubling times were observed in PCL-LN (0.76 ± 0.02 day^{-1}; 21.9 ± 0.6 h), PCL-RGD (0.80 ± 0.01 day^{-1}; 20.8 ± 0.4 h), and PCL-RGDr (0.92 ± 0.09 day^{-1}; 18.1 ± 1.7 h). No major differences in terms of growth kinetics were observed between aligned and random matrices (PCL-RGD).

The cell quality after 11 days of culture on the PCL nanofiber scaffolds was evaluated by immunocytochemistry analysis for specific NSC markers (Nestin, Sox2) and for a neuronal differentiation marker (Tuj1/βIII–tubulin), as shown in **Figure 3C**. It was observed that Sox2 and Nestin are expressed in all the conditions, whereas βIII–tubulin expression was never detected. Moreover, the immunostaining images provide evidence of the impact of the aligned structure of the substrate on the cellular organization on the nanofibers, being clear that cellular distribution follows the nanofiber arrangement.

Evaluation of NSC Organization and Morphology

Scanning electron microscopy images were obtained for each of the conditions to better characterize the

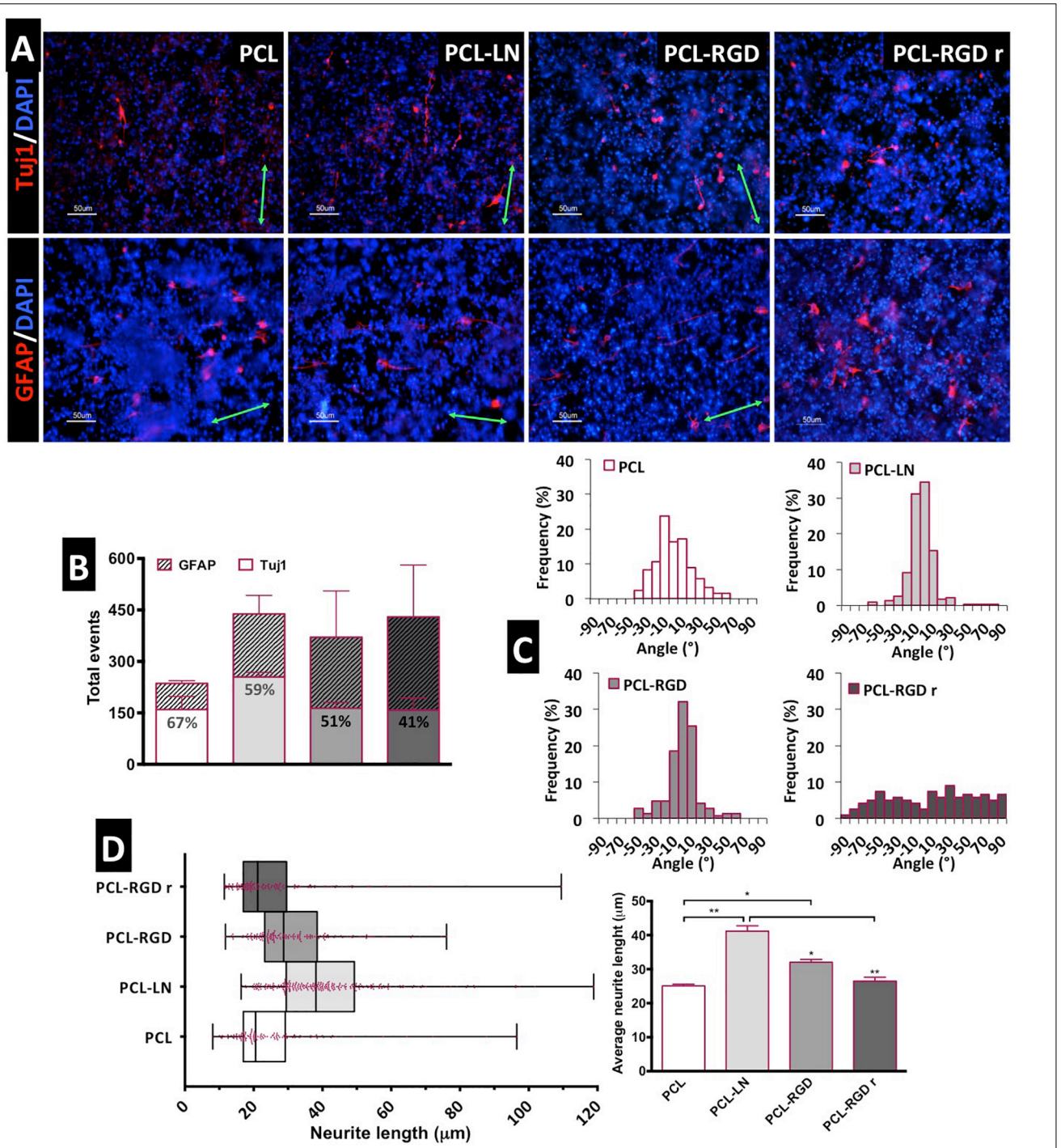

FIGURE 5 | Evaluation of *in situ* CGR8-NS differentiation: **(A)** Immunofluorescence images of the expression of the neuronal marker βIII-tubulin (Tuj1) and astrocyte marker GFAP (green arrows indicate the fiber direction). **(B)** Total differentiated cells (events) counted. **(C)** Histograms of neuron alignment distribution. **(D)** Representation of the neurite length distribution (on the left). The box boundaries represent the 25th and the 75th percentile; the straight line inside the box is the median. On the right, average neurite lengths; a minimum of 50 cells were measured; $^{*}p < 0.05$; $^{**}p < 0.01$ ($n = 2$).

morphology of the NSCs cultured on the different nanofibers (**Figure 4A**). It is possible to observe that NSCs are spread and round-shaped when cultivated on PCL-RGD random and pristine PCL–aligned nanofibers. In contrast, cells cultured on PCL-LN– and PCL-RGD–aligned nanofibers had an elongated shape, following the nanofiber axis orientation. Fluorescence microscopy images obtained with rhodamine phalloidin, which stains the F-actin fibers of the

cellular cytoskeleton, on PCL-RGD and PCL-RGDr fibers (**Figure 4B**) also reveal an ordered distribution of the cells, aligned in the direction of the PCL-RGD nanofibers and a more dispersed and spread cellular distribution in the random nanofibers. The quantification of these differences is represented in **Figure 4B**, with histograms showing the measured angles of the stained F-actin fibers with reference to the direction of the nanofibers. The cells in the aligned fibers are distributed across a narrower angle range of ±30°, while in the non-aligned nanofibers the angle distribution to which cells occupy is wider over the interval of ±90°.

Cell shape analysis results are shown in **Figure 4C**. The box-and-whisker distributions profiles are identical between both shape parameters, with both PCL-LN and PCL-RGD boxes located in values that correspond to an elongated cell shape. Tighter population distributions in terms of eccentricity are found for PCL-LN and aligned PCL-RGD. The estimated averages of both shape parameters (**Figure 4D**) are also in agreement with the previous observations and differ identically for each nanofiber condition. The average cell eccentricities in PCL-LN reached a value of 0.92 ± 0.03 (very close to 1), being significantly different to PCL and PCL-RGDr, with average eccentricities of 0.65 ± 0.04 and 0.72 ± 0.13, respectively. In PCL-RGD scaffolds, the NSCs show also higher elongation with average eccentricity of 0.85 ± 0.09, comparable to PCL-LN. Eccentricity of PCL-NH2 fibers was also estimated (**Supplementary Figure 6**) at a value of 0.62 ± 0.03 (and aspect ratio of 0.73 ± 0.03), values similar to the pristine PCL fibers. This result suggests that the adhesion peptide/protein biological motifs on the scaffolds establish important interactions with the cells.

NSC Differentiation in the Nanofibers

After 11 days of NSC expansion on the nanofiber scaffolds, neuronal differentiation was induced for 15 days. In **Figure 5A**, immunofluorescence images show the expression of Tuj1 and GFAP, indicating the presence of neurons and astrocytes, respectively, in all the nanofibers conditions.

The evaluation of the number of differentiated cells in each of the nanofibers was performed based on the immunofluorescence images, taken at day 15 of the differentiation protocol. The cells expressing Tuj1 or GFAP were counted and considered as "differentiated cells," cells expressing neither of these two markers are most likely non-differentiated immature neural progenitors. The relative percentage of neurons and astrocytes for each condition was estimated (**Figure 5B**). Overall, the results suggest a higher number of differentiated cells on PCL-LN and PCL-RGD nanofibers and a lower number of differentiated cells in pristine PCL nanofibers (**Figure 5B**). Regarding the relative percentage of neurons/astrocytes, higher percentages of neurons (values indicated in the Tuj1 bars) were estimated in pristine PCL (67%) and PCL-LN (59%), similar percentages of neurons and astrocytes were estimated for aligned PCL-RGD (∼50%), and a higher percentage of astrocytes was found for PCL-RGDr (59%).

The number of differentiated cells (differentiation events) was normalized with the total number of cells, assessed by the number of DAPI-stained nuclei to give an approximate overview of the differentiated cells relative to the total number of cells in culture (**Supplementary Figure 7**). In general, a low percentage of differentiated cells relative to the total number of cells in culture was obtained (**Supplementary Figure 7**) ranging from the highest, obtained in PCL-LN (7% of neurons and 3% of astrocytes), to the lowest, in pristine PCL (3.4% of neurons and 1.4% of astrocytes), with the percentage of Tuj1 expressing cells higher for all the conditions.

The alignment histograms (**Figure 5C**) show the influence of the nanofiber organization on the differentiated cell orientation. In aligned pristine PCL matrices, cells were distributed along a ±50° orientation angle range, evidencing a well-defined peak of cell alignment. Regarding PCL-LN and PCL-RGD, sharper histogram peaks are obtained, indicating that a higher percentage of the cell population follows the fiber alignment, approximately within a narrower range of ±30° orientation angles, for both conditions. Cells cultured in PCL-RGDr present a wide distribution of alignment angles within the broad interval of ±90° orientation distribution, highly in contrast with the alignment peaks in the histograms determined for the aligned nanofiber conditions.

The neurite lengths profile distribution, displayed in the box-and-whisker plot, and the corresponding average neurite lengths are represented in **Figure 5D**, left and right, respectively. Tight length distribution (narrower boxes) was observed in PCL-RGDr and in non-functionalized PCL nanofibers, where shorter neurites developed (26.5 ± 1.4 and 25.1 ± 1.2 μm, respectively). A broader length distribution (wider box) was found in PCL-LN nanofibers with the longest average cellular extensions determined (41.07 ± 1 μm). The higher neurite lengths found in PCL-LN differ significantly from the remaining conditions, especially with pristine PCL and PCL-RGDr. The lowest neurite extensions found in pristine PCL also differed significantly from the PCL-RGD condition.

DISCUSSION

In the current study, four types of electrospun nanofibers were produced, and the NSC response and interaction with the scaffolds were assessed. Aligned pristine PCL scaffolds, i.e., aligned PCL nanofibers without any biological functionalization, were used to evaluate the effects of fiber alignment on the NSCs; aligned PCL fibers functionalized with LN (PCL-LN) and GRGDSP (PCL-RGD) were used to evaluate the synergistic effects of nanofiber alignment and the biological cell adhesion motifs; randomly oriented nanofibers functionalized with GRGDSP (PCL-RGDr), with a dispersion of diameters and fiber alignments, were also used to assess the effect of a fibrous disordered structure on NSCs. The effect of each of the four scaffolds in cell culture was analyzed according to (i) cell organization, through estimation of cell alignment after 11 days of expansion and at the end of the differentiation stage; (ii) cell morphology, estimated by cell eccentricity or axis ratio at the end of the expansion stage; and (iii) cell differentiation, determined at the end of differentiation by the relative percentage of Tuj1

(neurons) and GFAP (astrocytes)–positive cells, as well as the length of the neurites developed.

The PCL Nanofiber Scaffolds

The distributions of diameters and relative orientation angles of the prepared aligned and random nanofibers are in agreement with other examples reported in literature (Wang et al., 2009, 2010; Cooper et al., 2011). For this particular study, heterogeneity in the random fiber meshes is desirable, as we were interested in producing a random matrix structure contrasting with the uniformity of the aligned nanofiber samples, to obtain two distinct types of morphologies with impact on NSC proliferation and differentiation (Yang et al., 2005; Nisbet et al., 2008; Christopherson et al., 2009; Horne et al., 2009; Hackett et al., 2010). The highest average diameter was obtained for random fibers when compared with aligned fibers, which can be attributed to the different collector material and configurations, because the other main conditions for the electrospinning process, polymer concentration/solution viscosity, applied potential, flow rate, and solvent (Teo and Ramakrishna, 2006; Nezarati et al., 2013) were kept the same.

The fiber mesh density is also an important feature as a parameter for cell culture. The use of scaffolds with similar fiber densities is important for the consistency of the cell culture experimental results. The fiber density should be high enough to permit cell–cell and cell–material contact but should also provide enough porosity to ensure good culture media infiltration. Highly compact meshes may perform, at the cell length scale ($\sim$30 μm), as a membrane or film, with less pronounced three-dimensional (3D) structure (Stevens and George, 2005; Agarwal et al., 2008), and microscopic visualization and characterization of cultured cells may be difficult. However, the fiber density should facilitate the covering of the glass surface of the slide, avoiding cell adhesion to the glass, and inaccurate estimation of cell proliferation on the nanofibers. To avoid the effects mentioned above, a fiber density of 70–80% (i.e., a "surface porosity" of 20–30%) was selected for this study. This fiber density corresponds to a rank of 4.5 on the "five-scale fiber-density ranking" here established by collecting and testing a series of nanofibers with different mesh densities. The selected nanofiber samples, with a uniformly dense mesh, show evidence of a porous structure. While pore size and volumetric porosity were not estimated, fiber density (and "surface porosity") provides a semiquantitative metric for scaffold porosity. Therefore, the two types of scaffolds selected for this study provide high surface areas and similar fiber densities, but very different morphologies, in terms of fiber diameter and alignment, allowing us to compare cell responses (e.g., organization and shape) to these geometries.

The next step for the preparation of the nanofibers for cell culture was to covalently bind LN and the GRGDSP peptide on the material surface. Covalent attachment of biological motifs has been shown to be advantageous for tissue engineering applications, especially for long-term cell culture, providing a more stable layer of proteins on the culture surface, in comparison with physical adsorption (Yoo et al., 2009; Ghasemi-Mobarakeh et al., 2010; Zander et al., 2010). Therefore, a protocol for covalent immobilization of LN and GRGDSP onto the PCL was applied in this study. The biological factors were immobilized successfully, with higher efficiency of immobilization for the GRGDSP peptide (83.8 $\pm$ 16.8%) when compared with LN (22.1 $\pm$ 1.5%). Considering the amine content for LN and GRGDSP and orthogonal even distribution of these species at the fiber scaffold surface, estimated equivalent amine immobilization densities would translate on molecules densities of 7.2 nmol cm^{-2} and 0.60 pmol cm^{-2} for GRGDSP and LN, respectively. Such molecular density would imply that LN molecules would be at 18.2 nm from each other (assuming LN size and shape as a cross-like structure with 8 nm for 70- to 90-nm size). Regardless of the potential inaccuracy of these estimations, they provide an order of magnitude estimation of peptide and protein coverage of the fiber surface.

In fact, the large 810-kDa multidomain glycoprotein of LN and the small 587-Da synthetic linear peptide GRGDSP differ greatly in size and structure (Beck et al., 1990; Hersel et al., 2003). The size of GRGDSP might be advantageous in terms of reactivity (easy diffusion and chemical lability), making a more effective use of the NH_2 groups available at the PCL-NH_2 fiber network and resulting in higher functionalization efficiency. It is important to note that during the glutaraldehyde reaction step, in addition to the crosslink between biomolecule and amine groups in the PCL-NH_2 fibers, interbiomolecule crosslinking can occur, implying several layers of linked biomolecules. Overall, it can be said that it was possible to successfully immobilize LN and RGD in the nanofibers, providing biological motives for cell adhesion in the functionalized nanofibers.

NSC Culture on the PCL Nanofibers

The nanofiber scaffolds prepared were demonstrated to be appropriate substrates for the proliferation of CGR8-NS cells. The cells retained expression of NSC markers, as well as the differentiation potential, and in the PCL-LN and PCL-RGD nanofibers improved cell adhesion; higher growth rates and final cell numbers were observed, in relation to pristine PCL. Studies report variable tendencies in cell proliferation in aligned and random matrices. Increased proliferation of neural progenitor cells (NPs) was found in aligned collagen nanofibers (Wang et al., 2011), of Schwann cells in PCL-PLGA (Subramanian et al., 2012), of human NPs in PCL nanofibers (Mahairaki et al., 2011), and mouse NSCs in PCL/collagen nanofibers (Hackett et al., 2010). Others report no statistically significant differences between aligned and random matrices as with PC-12 cells in PCL functionalized with LN and collagen (Zander et al., 2010), with cortical NSCs in PCL-BDNF nanofibers (Horne et al., 2009) or with Schwann cells in PCL–chitosan nanofibers (Cooper et al., 2011). An enhanced cellular expansion is associated with a geometry and biochemistry of the substrate that offers more accessible contact points for cells to adhere and a degree of porosity that facilitates increased diffusion, better biochemical enrichment of the substrate, and cell infiltration (He et al., 2010; Wang et al., 2011; Wheeldon et al., 2011). The highest final cell numbers were obtained with the PCL-RGD and PCL-RGDr. The random nanofiber structure (PCL-RGDr) permits the

cells to efficiently adhere and to proliferate, even if the cells are organized in several directions, without the unidirectional structure observed in aligned nanofibers. Comparable levels of cell expansion were observed with PCL-LN. Although LN has the potential to provide more specific interaction with NSC integrins, the unpredictable orientation of the biomolecule after immobilization in the fibers as well as the interactions with the substrate (water affinity, morphology, charge) might restrict the access of the cellular integrin receptors to LN (Hersel et al., 2003; Nakaji-Hirabayashi et al., 2012). Moreover, protein crosslinking by glutaraldehyde may lead to some extent of protein denaturation, which can also impair cell adhesion and proliferation (Migneault et al., 2004). The surface of the pristine PCL nanofibers facilitated cellular attachment, possibly mediated by adsorption of proteins present in the culture media, permitting NSCs to proliferate but to a lower extent. PCL has a relatively high hydrophobic character, described by high contact angles ($\theta > 90°$) on solid surfaces (Fang et al., 2011; Yuan and Lee, 2013), and therefore, cell adhesion is more difficult to occur. Nevertheless, cellular survival and proliferation in untreated PCL random nanofibers have been previously reported (Schnell et al., 2007; Chew et al., 2008; Nisbet et al., 2008).

NSC Organization and Morphology

Stem cell morphology and differentiation potential are influenced by the physical substrate, and in particular, for highly polarized cells, such as NSCs, substrate morphology is often determinant (Ingber, 2003; Bettinger et al., 2009; Qi et al., 2013). The parameters here analyzed, cell alignment and shape (eccentricity and axis ratio), demonstrated the influence of nanofiber morphology on cell orientation and shape. As expected, NSCs were able to align and elongate, extensively exhibiting a highly bipolar morphology, especially in the presence of adhesion factors in PCL-LN and PCL-RGD. Aligned but less elongated cell populations were found in pristine PCL fibers, and cells with a round and spread shape morphology were found in PCL-RGDr. Note that it was reported that contact angle dropped from about 80° in pristine PCL films to the range 59–68°, both for PCL films aminolysed or further functionalized with proteins (Zhu et al., 2002). In the current study, similar NSC eccentricity and aspect ratio were obtained for cultures on pristine or aminolysed PCL fibers, suggesting that the adhesion peptide/protein biological motifs on the scaffolds establish important interactions with the cells.

Similar illustrative examples regarding the effect of the morphology were also described with adult NSCs in LN-coated PCL nanofibers (Lim et al., 2010) and with NPs after 3 days of culture in PCL poly-ornithine/LN–coated nanofibers, where cells in the random substrate show a spread and less polar morphology (Mahairaki et al., 2011).

NSC *in situ* Differentiation and Cell Morphology

The NSCs used in this work were able to differentiate into neurons and astrocytes, in all nanofiber conditions tested. However, a relatively low percentage of differentiated cells was obtained, taking into account an average of 10–40% differentiated neurons reported in the literature (Pollard et al., 2006a). The differentiation protocol used was optimized for culture in tissue culture plates, and the conditions described may require further optimization when adapted to culture on nanofiber scaffolds. In this study, the differentiation stage was initiated from cell cultures at very high density, over a relatively short period (2 weeks compared to 5–6 weeks in other studies) and without the use of specific factors to direct differentiation or support survival of differentiated cells. Therefore, further improvement on differentiation efficiency may be attained by optimization of initial cell density before inducing differentiation, by adjusting the concentration of growth factors and/or the length of the differentiation steps, permitting a longer differentiation time and by supplementing the culture with specific molecules, such as neurotrophic factors (e.g., BDNF), to enhance neuronal differentiation (Pollard et al., 2006a). Other strategies to enhance differentiation include the application of physical stimuli using electroconductive materials (Garrudo et al., 2019a,b) and/or applying electrical stimulation (Pires et al., 2015).

In relation to the total cells in culture, the relative percentage of neurons was higher under all the conditions. When considering the percentage of neurons in relation to the number of differentiated cells, neurons were in higher proportion in aligned PCL and PCL-LN, in even percentage with astrocytes in PCL-RGD, and in lower percentage in PCL-RGDr. This tendency suggests that the alignment of the fibers promotes neuronal differentiation, but RGD functionalization favored differentiation toward astrocytes. Still, it is difficult to draw strong conclusions, because the overall differences (**Figure 5B**) were found not to be statistically meaningful and were associated with a considerable error.

Previous studies reported that substrate dimensions and alignment has an influence on directing neuronal differentiation of adult NSCs (Lim et al., 2010) and alignment of neurites parallel to nanofiber direction (Silantyeva et al., 2018; Philip et al., 2019). It was suggested that aligned substrates favored the survival of neural progenitors in detriment with non-neuronal progenitors, and nanofiber dimensions influenced cell–substrate interactions (Lim et al., 2010). Other studies showed that neuronal lineage differentiation was favored in aligned nanofibers with negligible expression of astrocytes and oligodendrocytes markers (Mahairaki et al., 2011), and a greater extent of neuronal differentiation (80%) (Bakhru et al., 2011) or accelerated neural differentiation (Silantyeva et al., 2018) was observed when NSCs were cultivated on fiber substrates. In the current study, the apparent prevalence of astrocytes in the random nanofibers can be explained by the physical cues provided by the random distribution of fiber diameters and fiber alignments in the PCL-RGDr. Such morphology presents discrete scattered surface contact points for cell adhesion, that can promote broader spread morphology, and hence the astrocyte lineage can be favored under these conditions. In non-functionalized PCL nanofibers, although the number of differentiated cells was smaller, an increased number of neurons were observed. Based on previous reports, aligned fiber

morphology is able to promote neuronal lineage differentiation, and the high percentage of neuronal cells within the detected differentiated cells could be explained by the effect of the alignment of the matrix itself.

The neuron alignment and neurite extension are in agreement with previous observations for NSCs, illustrating the effect of the functionalized material in cell organization and morphology (Yang et al., 2005; Zander et al., 2010; Wang J. et al., 2012; Smith Callahan et al., 2013). The higher cell adhesion to the nanofibers provided by the LN or GRGDSP motifs and the unidirectional organization of the substrate contributed to guide the cellular distribution and to a more extensive neuronal elongation. The shorter neurite length found in PCL-RGDr is likely due to the disordered disposition of the nanofibers, where the cells developed a more spread and multidirectional morphology. The neurite extension of Tuj1-positive neuronal cells was clearly improved by the nanofiber alignment and in the presence of adhesion factors, in particular LN.

CONCLUSION

The nanofiber scaffolds prepared were found to be suitable for the proliferation and differentiation of mouse ESC-derived NSCs. This NSC population was able to proliferate in adherent monolayer and to maintain the multipotent potential. Under differentiation conditions, the morphology of the substrate was shown to have a role in cell fate. The results obtained show the existence of a synergistic effect of substrate morphology and specific cell adhesion motifs on NSC morphology, proliferation, and differentiation. The functionalization with biological motifs promoted cellular adhesion to the fibers, leading also to increased NSC proliferation. Non-functionalized aligned PCL nanofibers were able to promote cell alignment but performed poorly in promoting NSC elongation. In contrast, cellular elongation was improved in aligned scaffolds functionalized with GRGDSP or LN, which promote specific adhesion points according to the uniaxial matrix structure. Randomly distributed GRGDSP functionalized fibers also improve cell adhesion, but because of the lack of a single direction axis, the cellular orientation follows a distribution in arbitrary directions. These observations are valid for undifferentiated NSCs after 11 days of proliferation and for cells after the differentiation step.

The nanofiber morphology directed neuronal lineage and neurite elongation in the aligned matrices especially in the presence of the adhesion motifs. PCL-LN fibers led to the highest percentage of neurons within the differentiated cells, as well as to the longer average neurite length. In contrast, random GRGDSP matrices were found to be relatively preferential for astrocyte maturation. PCL-GRGDSP–aligned substrate was found to promote cellular adhesion, elongation, and proliferation, also permitting neuronal lineage differentiation, although to a lower extent than PCL-LN.

The prepared scaffolds, in particular when LN is used, can be considered promising for NSC culture and may, in the future, be applied in therapies for regeneration of CNS injuries. Moreover, cellular alignment is an interesting property that can be beneficial to tissues requiring such geometry, such as in spinal cord injury repair. One of the major problems of biomaterial scaffolds is the ability to maintain cellular viability when applied *in vivo*. However, as *in vivo* studies were out of the scope of the current study, additional improvements and scaffold development may need to be explored. Depending on the type of CNS tissue (spinal cord or brain), a deep assessment of the *in vivo* conditions is important in order to design and develop the most compatible material for *in situ* cellular delivery complemented with trophic factors and/or drugs to provide an environment suitable for cellular survival and function. Blends of polymers to optimize the biomaterial stiffness, combination of the fibers with a hydrogel to gradually release of biochemical cues or assemblies of microstructures and nanostructures to provide specific architecture and 3D environment, are interesting concepts for future scaffold design.

DATA AVAILABILITY STATEMENT

The raw data supporting the conclusions of this article will be made available by the authors, without undue reservation.

AUTHOR CONTRIBUTIONS

FF, MA, and CR contributed to original idea, experimental plan, and manuscript writing. MA, CR, and IF contributed to preliminary results. MA and IF assisted by CR and FF contributed to electrospun and cell work experiments. MA with guidance by CR and FF contributed to data analysis and figures preparation. CR, MD, RL, JC, and FF contributed to scientific guidance and discussions, laboratory space, and funding. All authors revised the manuscript.

FUNDING

The authors acknowledge funding from FCT—Portuguese Funding for Science and Technology, NEURON grant (PTDC/CTM-CTM/30237/2017), iBB grant (UID/BIO/045 65/2020), Post-Doc grant SFRH/BPD/82056/2011 and Ph.D. scholarship (SFRH/BD/73560/2010), from POR Lisboa 2020 grant PRECISE (Project No. 16394) and from United States National Institutes of Health, grant # DK111958 and New York State grant # SCRIB DOH01-PART2-2017.

ACKNOWLEDGMENTS

Thanks to Isabel Nogueira for technical support on SEM images acquisition at MicroLab facilities at IST Lisbon.

SUPPLEMENTARY MATERIAL

The Supplementary Material for this article can be found online at: https://www.frontiersin.org/articles/10.3389/fbioe.2020.580135/full#supplementary-material

REFERENCES

Agarwal, S., Wendorff, J. H., and Greiner, A. (2008). Use of electrospinning technique for biomedical applications. *Polymer* 49, 5603–5621. doi: 10.1016/j.polymer.2008.09.014

Ananthanarayanan, B., Little, L., Schaffer, D. V., Healy, K. E., and Tirrell, M. (2010). Neural stem cell adhesion and proliferation on phospholipid bilayers functionalized with RGD peptides. *Biomaterials* 31, 8706–8715. doi: 10.1016/j.biomaterials.2010.07.104

Bakhru, S., Nain, A. S., Highley, C., Wang, J., Campbell, P., Amon, C., et al. (2011). Direct and cell signaling-based, geometry-induced neuronal differentiation of neural stem cells. *Integr. Biol. Quant. Biosci. Nano Macro* 3, 1207–1214. doi: 10.1039/c1ib00098e

Beachley, V., and Wen, X. (2009). Effect of electrospinning parameters on the nanofiber diameter and length. *Mater. Sci. Eng. C Mater. Biol. Appl.* 29, 663–668. doi: 10.1016/j.msec.2008.10.037

Beck, K., Hunter, I., and Engel, J. (1990). Structure and function of laminin: anatomy of a multidomain glycoprotein. *FASEB J.* 4, 148–160.

Bettinger, C. J., Langer, R., and Borenstein, J. T. (2009). Engineering substrate topography at the micro- and nanoscale to control cell function. *Angew. Chem. Int. Ed.* 48, 5406–5415. doi: 10.1002/anie.200805179

Canadas, R. F., Cavalheiro, J. M. B. T., Guerreiro, J. D. T., de Almeida, M. C. M. D., Pollet, E., da Silva, C. L., et al. (2014). Polyhydroxyalkanoates: waste glycerol upgrade into electrospun fibrous scaffolds for stem cells culture. *Int. J. Biol. Macromol.* 71, 131–140. doi: 10.1016/j.ijbiomac.2014.05.008

Causa, F., Battista, E., Della Moglie, R., Guarnieri, D., Iannone, M., and Netti, P. A. (2010). Surface investigation on biomimetic materials to control cell adhesion: the case of RGD conjugation on PCL. *Langmuir ACS J. Surf. Colloids* 26, 9875–9884. doi: 10.1021/la100207q

Chew, S. Y., Mi, R., Hoke, A., and Leong, K. W. (2008). The effect of the alignment of electrospun fibrous scaffolds on Schwann cell maturation. *Biomaterials* 29, 653–661. doi: 10.1016/j.biomaterials.2007.10.025

Christopherson, G. T., Song, H., and Mao, H.-Q. (2009). The influence of fiber diameter of electrospun substrates on neural stem cell differentiation and proliferation. *Biomaterials* 30, 556–564. doi: 10.1016/j.biomaterials.2008.10.004

Ciardelli, G., Chiono, V., Vozzi, G., Pracella, M., Ahluwalia, A., Barbani, N., et al. (2005). Blends of Poly-(ε-caprolactone) and polysaccharides in tissue engineering applications. *Biomacromolecules* 6, 1961–1976. doi: 10.1021/bm0500805

Conti, L., and Cattaneo, E. (2010). Neural stem cell systems: physiological players or in vitro entities? *Nat. Rev. Neurosci.* 11, 176–187. doi: 10.1038/nrn2761

Conti, L., Pollard, S. M., Gorba, T., Reitano, E., Toselli, M., Biella, G., et al. (2005). Niche-independent symmetrical self-renewal of a mammalian tissue stem cell. *PLoS Biol.* 3:e283. doi: 10.1371/journal.pbio.0030283

Cooper, A., Bhattarai, N., and Zhang, M. (2011). Fabrication and cellular compatibility of aligned chitosan-PCL fibers for nerve tissue regeneration. *Carbohydr. Polym.* 85, 149–156. doi: 10.1016/j.carbpol.2011.02.008

Fang, Z., Fu, W., Dong, Z., Zhang, X., Gao, B., Guo, D., et al. (2011). Preparation and biocompatibility of electrospun poly(l-lactide-co-ε-caprolactone)/fibrinogen blended nanofibrous scaffolds. *Appl. Surf. Sci.* 257, 4133–4138. doi: 10.1016/j.apsusc.2010.12.011

Flanagan, L. A., Rebaza, L. M., Derzic, S., Schwartz, P. H., and Monuki, E. S. (2006). Regulation of human neural precursor cells by laminin and integrins. *J. Neurosci. Res.* 83, 845–856. doi: 10.1002/jnr.20778

Friedman, M. (2004). Applications of the ninhydrin reaction for analysis of amino acids, peptides, and proteins to agricultural and biomedical sciences. *J. Agric. Food Chem.* 52, 385–406. doi: 10.1021/jf030490p

Garrudo, F. F., Chapman, C. A., Hoffman, P., Udangawa, R. W., Silva, J. C., Mikael, P. E., et al. (2019a). Polyaniline-polycaprolactone blended nanofibers for neural cell culture. *Eur. Polym. J.* 117, 28–37. doi: 10.1016/j.eurpolymj.2019.04.048

Garrudo, F. F., Udangawa, R. W., Hoffman, P., Sordini, L., Chapman, C. A., Mikael, P. E., et al. (2019b). Polybenzimidazole nanofibers for neural stem cell culture. *Mater. Today Chem.* 14:100185. doi: 10.1016/j.mtchem.2019.08.004

Ghasemi-Mobarakeh, L., Prabhakaran, M. P., Morshed, M., Nasr-Esfahani, M. H., and Ramakrishna, S. (2010). Bio-functionalized PCL nanofibrous scaffolds for nerve tissue engineering. *Mater. Sci. Eng. C* 30, 1129–1136. doi: 10.1016/j.msec.2010.06.004

Gloria, A., Causa, F., Russo, T., Battista, E., Della Moglie, R., Zeppetelli, S., et al. (2012). Three-dimensional poly(ε-caprolactone) bioactive scaffolds with controlled structural and surface properties. *Biomacromolecules* 13, 3510–3521. doi: 10.1021/bm300818y

Gorba, T., and Conti, L. (2013). Neural stem cells as tools for drug discovery: novel platforms and approaches. *Expert Opin. Drug Discov.* 8, 1083–1094. doi: 10.1517/17460441.2013.805199

Grochowski, C., Radzikowska, E., and Maciejewski, R. (2018). Neural stem cell therapy—Brief review. *Clin. Neurol. Neurosurg.* 173, 8–14. doi: 10.1016/j.clineuro.2018.07.013

Hackett, J. M., Dang, T. T., Tsai, E. C., and Cao, X. (2010). Electrospun biocomposite polycaprolactone/collagen tubes as scaffolds for neural stem cell differentiation. *Materials* 3, 3714–3728. doi: 10.3390/ma3063714

Hall, P. E., Lathia, J. D., Caldwell, M. A., and ffrench-Constant, C. (2008). Laminin enhances the growth of human neural stem cells in defined culture media. *BMC Neurosci.* 9:71. doi: 10.1186/1471-2202-9-71

Hautanen, A., Gailit, J., Mann, D. M., and Ruoslahti, E. (1989). Effects of modifications of the RGD sequence and its context on recognition by the fibronectin receptor. *J. Biol. Chem.* 264, 1437–1442.

He, L., Liao, S., Quan, D., Ma, K., Chan, C., Ramakrishna, S., et al. (2010). Synergistic effects of electrospun PLLA fiber dimension and pattern on neonatal mouse cerebellum C17.2 stem cells. *Acta Biomater.* 6, 2960–2969. doi: 10.1016/j.actbio.2010.02.039

Hersel, U., Dahmen, C., and Kessler, H. (2003). RGD modified polymers: biomaterials for stimulated cell adhesion and beyond. *Biomaterials* 24, 4385–4415.

Hiraoka, M., Kato, K., Nakaji-Hirabayashi, T., and Iwata, H. (2009). Enhanced survival of neural cells embedded in hydrogels composed of collagen and laminin-derived cell adhesive peptide. *Bioconjug. Chem.* 20, 976–983. doi: 10.1021/bc9000068

Horne, M. K., Nisbet, D. R., Forsythe, J. S., and Parish, C. L. (2009). Three-dimensional nanofibrous scaffolds incorporating immobilized BDNF Promote proliferation and differentiation of cortical neural stem cells. *Stem Cells Dev.* 19, 843–852. doi: 10.1089/scd.2009.0158

Ingber, D. E. (2003). Tensegrity I. Cell structure and hierarchical systems biology. *J. Cell Sci.* 116, 1157–1173.

Jakel, R. J., Schneider, B. L., and Svendsen, C. N. (2004). Using human neural stem cells to model neurological disease. *Nat. Rev. Genet.* 5, 136–144.

Kim, H., Cooke, M. J., and Shoichet, M. S. (2012). Creating permissive microenvironments for stem cell transplantation into the central nervous system. *Trends Biotechnol.* 30, 55–63. doi: 10.1016/j.tibtech.2011.07.002

Kim, T. G., and Park, T. G. (2006). Biomimicking extracellular matrix: cell adhesive RGD peptide modified electrospun poly(D,L-lactic-co-glycolic acid) nanofiber mesh. *Tissue Eng.* 12, 221–233. doi: 10.1089/ten.2006.12.221

Klinkhammer, K., Bockelmann, J., Simitzis, C., Brook, G. A., Grafahrend, D., Groll, J., et al. (2010). Functionalization of electrospun fibers of poly(epsilon-caprolactone) with star shaped NCO-poly(ethylene glycol)-stat-poly(propylene glycol) for neuronal cell guidance. *J. Mater. Sci. Mater. Med.* 21, 2637–2651. doi: 10.1007/s10856-010-4112-7

Koh, H. S., Yong, T., Chan, C. K., and Ramakrishna, S. (2008). Enhancement of neurite outgrowth using nano-structured scaffolds coupled with laminin. *Biomaterials* 29, 3574–3582. doi: 10.1016/j.biomaterials.2008.05.014

Lam, H. J., Patel, S., Wang, A., Chu, J., and Li, S. (2010). In vitro regulation of neural differentiation and axon growth by growth factors and bioactive nanofibers. *Tissue Eng. Part A* 16, 2641–2648. doi: 10.1089/ten.TEA.2009.0414

Li, D., Wang, Y., and Xia, Y. (2003). Electrospinning of polymeric and ceramic nanofibers as uniaxially aligned arrays. *Nano Lett.* 3, 1167–1171. doi: 10.1021/nl0344256

Lim, S. H., Liu, X. Y., Song, H., Yarema, K. J., and Mao, H.-Q. (2010). The effect of nanofiber-guided cell alignment on the preferential differentiation of neural stem cells. *Biomaterials* 31, 9031–9039. doi: 10.1016/j.biomaterials.2010.08.021

Mahairaki, V., Lim, S. H., Christopherson, G. T., Xu, L., Nasonkin, I., Yu, C., et al. (2011). Nanofiber matrices promote the neuronal differentiation of human embryonic stem cell-derived neural precursors in vitro. *Tissue Eng. Part A* 17, 855–863. doi: 10.1089/ten.TEA.2010.0377

Migneault, I., Dartiguenave, C., Bertrand, M. J., and Waldron, K. C. (2004). Glutaraldehyde: behavior in aqueous solution, reaction with proteins, and application to enzyme crosslinking. *BioTechniques* 37, 790–796, 798–802.

Nakaji-Hirabayashi, T., Kato, K., and Iwata, H. (2012). Improvement of neural stem cell survival in collagen hydrogels by incorporating laminin-derived cell adhesive polypeptides. *Bioconjug. Chem.* 23, 212–221. doi: 10.1021/bc200481v

Nezarati, R. M., Eifert, M. B., and Cosgriff-Hernandez, E. (2013). Effects of humidity and solution viscosity on electrospun fiber morphology. *Tissue Eng. Part C Methods* 19, 810–819. doi: 10.1089/ten.TEC.2012.0671

Nisbet, D. R., Yu, L. M. Y., Zahir, T., Forsythe, J. S., and Shoichet, M. S. (2008). Characterization of neural stem cells on electrospun poly(ε-caprolactone) submicron scaffolds: evaluating their potential in neural tissue engineering. *J. Biomater. Sci. Polym. Ed.* 19, 623–634. doi: 10.1163/156856208784089652

Pereira, I. M., Marote, A., Salgado, A. J., and Silva, N. A. (2019). Filling the gap: neural stem cells as A promising therapy for spinal cord injury. *Pharmaceuticals* 12:65. doi: 10.3390/ph12020065

Philip, D. L., Silantyeva, E. A., Becker, M. L., and Willits, R. K. (2019). RGD-functionalized nanofibers increase early GFAP expression during neural differentiation of mouse embryonic stem cells. *Biomacromolecules* 20, 1443–1454. doi: 10.1021/acs.biomac.9b00018

Pires, F., Ferreira, Q., Rodrigues, C. A. V., Morgado, J., and Ferreira, F. C. (2015). Neural stem cells differentiation by electrical stimulation using a cross-linked PEDOT substrate: expanding the use of biocompatible conjugated conductive polymers for neural tissue engineering. *BBA Gen Subjects* 1850, 1158–1168. doi: 10.1016/j.bbagen.2015.01.020

Pollard, S. M., Benchoua, A., and Lowell, S. (2006a). Neural stem cells, neurons, and glia. *Methods Enzymol.* 418, 151–169. doi: 10.1016/S0076-6879(06)18010-6

Pollard, S. M., Conti, L., Sun, Y., Goffredo, D., and Smith, A. (2006b). Adherent neural stem (NS) cells from fetal and adult forebrain. *Cereb. Cortex N. Y. N.* 1991(16 Suppl. 1), i112–i120. doi: 10.1093/cercor/bhj167

Qi, L., Li, N., Huang, R., Song, Q., Wang, L., Zhang, Q., et al. (2013). The effects of topographical patterns and sizes on neural stem cell behavior. *PLoS One* 8:e59022. doi: 10.1371/journal.pone.0059022

Rodrigues, C. A. V., Diogo, M. M., da Silva, C. L., and Cabral, J. M. S. (2010). Hypoxia enhances proliferation of mouse embryonic stem cell-derived neural stem cells. *Biotechnol. Bioeng.* 106, 260–270. doi: 10.1002/bit.22648

Rodrigues, C. A. V., Diogo, M. M., da Silva, C. L., and Cabral, J. M. S. (2011). Microcarrier expansion of mouse embryonic stem cell-derived neural stem cells in stirred bioreactors. *Biotechnol. Appl. Biochem.* 58, 231–242. doi: 10.1002/bab.37

Schaub, N. J., Johnson, C. D., Cooper, B., and Gilbert, R. J. (2016). Electrospun fibers for spinal cord injury research and regeneration. *J. Neurotrauma* 33, 1405–1415. doi: 10.1089/neu.2015.4165

Schnell, E., Klinkhammer, K., Balzer, S., Brook, G., Klee, D., Dalton, P., et al. (2007). Guidance of glial cell migration and axonal growth on electrospun nanofibers of poly-epsilon-caprolactone and a collagen/poly-epsilon-caprolactone blend. *Biomaterials* 28, 3012–3025. doi: 10.1016/j.biomaterials.2007.03.009

Silantyeva, E. A., Nasir, W., Carpenter, J., Manahan, O., Becker, M. L., and Willits, R. K. (2018). Accelerated neural differentiation of mouse embryonic stem cells on aligned GYIGSR-functionalized nanofibers. *Acta Biomater.* 75, 129–139. doi: 10.1016/j.actbio.2018.05.052

Smith Callahan, L. A., Xie, S., Barker, I. A., Zheng, J., Reneker, D. H., Dove, A. P., et al. (2013). Directed differentiation and neurite extension of mouse embryonic stem cell on aligned poly(lactide) nanofibers functionalized with YIGSR peptide. *Biomaterials* 34, 9089–9095. doi: 10.1016/j.biomaterials.2013.08.028

Stevens, M. M., and George, J. H. (2005). Exploring and engineering the cell surface interface. *Science* 310, 1135–1138. doi: 10.1126/science.1106587

Strober, W. (2001). Trypan blue exclusion test of cell viability. *Curr. Protoc. Immunol.* Appendix 3:Aendix3B. doi: 10.1002/0471142735.ima03bs21

Subramanian, A., Krishnan, U. M., and Sethuraman, S. (2012). Fabrication, characterization and in vitro evaluation of aligned PLGA-PCL nanofibers for neural regeneration. *Ann. Biomed. Eng.* 40, 2098–2110. doi: 10.1007/s10439-012-0592-6

Teo, W. E., and Ramakrishna, S. (2006). A review on electrospinning design and nanofibre assemblies. *Nanotechnology* 17, R89–R106. doi: 10.1088/0957-4484/17/14/R01

Wang, H. B., Mullins, M. E., Cregg, J. M., Hurtado, A., Oudega, M., Trombley, M. T., et al. (2009). Creation of highly aligned electrospun poly-L-lactic acid fibers for nerve regeneration applications. *J. Neural Eng.* 6:016001. doi: 10.1088/1741-2560/6/1/016001

Wang, H. B., Mullins, M. E., Cregg, J. M., McCarthy, C. W., and Gilbert, R. J. (2010). Varying the diameter of aligned electrospun fibers alters neurite outgrowth and Schwann cell migration. *Acta Biomater.* 6, 2970–2978. doi: 10.1016/j.actbio.2010.02.020

Wang, J., Ye, R., Wei, Y., Wang, H., Xu, X., Zhang, F., et al. (2012). The effects of electrospun TSF nanofiber diameter and alignment on neuronal differentiation of human embryonic stem cells. *J. Biomed. Mater. Res. A* 100A, 632–645. doi: 10.1002/jbm.a.33291

Wang, T. Y., Forsythe, J. S., Nisbet, D. R., and Parish, C. L. (2012). Promoting engraftment of transplanted neural stem cells/progenitors using biofunctionalised electrospun scaffolds. *Biomaterials* 33, 9188–9197. doi: 10.1016/j.biomaterials.2012.09.013

Wang, Y., Yao, M., Zhou, J., Zheng, W., Zhou, C., Dong, D., et al. (2011). The promotion of neural progenitor cells proliferation by aligned and randomly oriented collagen nanofibers through β1 integrin/MAPK signaling pathway. *Biomaterials* 32, 6737–6744. doi: 10.1016/j.biomaterials.2011.05.075

Wheeldon, I., Farhadi, A., Bick, A. G., Jabbari, E., and Khademhosseini, A. (2011). Nanoscale tissue engineering: spatial control over cell-materials interactions. *Nanotechnology* 22:212001. doi: 10.1088/0957-4484/22/21/212001

Xie, J., MacEwan, M. R., Li, X., Sakiyama-Elbert, S. E., and Xia, Y. (2009a). Neurite outgrowth on nanofiber scaffolds with different orders, structures, and surface properties. *ACS Nano* 3, 1151–1159. doi: 10.1021/nn900070z

Xie, J., Willerth, S. M., Li, X., Macewan, M. R., Rader, A., Sakiyama-Elbert, S. E., et al. (2009b). The differentiation of embryonic stem cells seeded on electrospun nanofibers into neural lineages. *Biomaterials* 30, 354–362. doi: 10.1016/j.biomaterials.2008.09.046

Xue, J., Pisignano, D., and Xia, Y. (2020). Maneuvering the migration and differentiation of stem cells with electrospun nanofibers. *Adv. Sci.* 7:2000735. doi: 10.1002/advs.202000735

Yang, F., Murugan, R., Wang, S., and Ramakrishna, S. (2005). Electrospinning of nano/micro scale poly(l-lactic acid) aligned fibers and their potential in neural tissue engineering. *Biomaterials* 26, 2603–2610. doi: 10.1016/j.biomaterials.2004.06.051

Yoo, H. S., Kim, T. G., and Park, T. G. (2009). Surface-functionalized electrospun nanofibers for tissue engineering and drug delivery. *Adv. Drug Deliv. Rev.* 61, 1033–1042. doi: 10.1016/j.addr.2009.07.007

Yuan, Y., and Lee, T. R. (2013). "Contact angle and wetting properties," in *Surface Science Techniques Springer Series in Surface Sciences*, eds G. Bracco and B. Holst (Berlin: Springer), 3–34. doi: 10.1007/978-3-642-34243-1_1

Zander, N. E., Orlicki, J. A., Rawlett, A. M., and Beebe, T. P. (2010). Surface-modified nanofibrous biomaterial bridge for the enhancement and control of neurite outgrowth. *Biointerphases* 5, 149–158. doi: 10.1116/1.3526140

Zhao, X., and Moore, D. L. (2018). Neural stem cells: developmental mechanisms and disease modeling. *Cell Tissue Res.* 371, 1–6. doi: 10.1007/s00441-017-2738-1

Zhu, Y., Gao, C., Liu, X., and Shen, J. (2002). Surface modification of polycaprolactone membrane via aminolysis and biomacromolecule immobilization for promoting cytocompatibility of human endothelial cells. *Biomacromolecules* 3, 1312–1319. doi: 10.1021/bm020074y

Conflict of Interest: The authors declare that the research was conducted in the absence of any commercial or financial relationships that could be construed as a potential conflict of interest.

frontiers in Bioengineering and Biotechnology

ORIGINAL RESEARCH
published: 05 November 2020
doi: 10.3389/fbioe.2020.580744

Toward a Microencapsulated 3D hiPSC-Derived *in vitro* Cardiac Microtissue for Recapitulation of Human Heart Microenvironment Features

*Bernardo Abecasis[1,2], Pedro G.M. Canhão[1,2], Henrique V. Almeida[1,2], Tomás Calmeiro[3], Elvira Fortunato[3], Patrícia Gomes-Alves[1,2], Margarida Serra[1,2] and Paula M. Alves[1,2]**

[1] iBET, Instituto de Biologia Experimental e Tecnológica, Oeiras, Portugal, [2] Instituto de Tecnologia Química e Biológica António Xavier, Universidade Nova de Lisboa, Oeiras, Portugal, [3] CENIMAT| i3N, Departamento de Ciência dos Materiais, Faculdade de Ciências e Tecnologia, Universidade NOVA de Lisboa, Caparica, Portugal

OPEN ACCESS

Edited by:
Tiago G. Fernandes,
University of Lisbon, Portugal

Reviewed by:
Robert Zweigerdt,
Hannover Medical School, Germany
Luca Sala,
Istituto Auxologico Italiano (IRCCS), Italy

***Correspondence:**
Paula M. Alves
marques@ibet.pt

Specialty section:
This article was submitted to Biomaterials, a section of the journal Frontiers in Bioengineering and Biotechnology

Received: 06 July 2020
Accepted: 14 September 2020
Published: 05 November 2020

Citation:
Abecasis B, Canhão PGM, Almeida HV, Calmeiro T, Fortunato E, Gomes-Alves P, Serra M and Alves PM (2020) Toward a Microencapsulated 3D hiPSC-Derived in vitro Cardiac Microtissue for Recapitulation of Human Heart Microenvironment Features. Front. Bioeng. Biotechnol. 8:580744. doi: 10.3389/fbioe.2020.580744

The combination of cardiomyocytes (CM) and non-myocyte cardiac populations, such as endothelial cells (EC), and mesenchymal cells (MC), has been shown to be critical for recapitulation of the human heart tissue for *in vitro* cell-based modeling. However, most of the current engineered cardiac microtissues still rely on either (i) murine/human limited primary cell sources, (ii) animal-derived and undefined hydrogels/matrices with batch-to-batch variability, or (iii) culture systems with low compliance with pharmacological high-throughput screenings. In this work, we explored a culture platform based on alginate microencapsulation and suspension culture systems to develop three-dimensional (3D) human cardiac microtissues, which entails the co-culture of human induced pluripotent stem cell (hiPSC) cardiac derivatives including aggregates of hiPSC–CM and single cells of hiPSC–derived EC and MC (hiPSC–EC+MC). We demonstrate that the 3D human cardiac microtissues can be cultured for 15 days in dynamic conditions while maintaining the viability and phenotype of all cell populations. Noteworthy, we show that hiPSC–EC+MC survival was promoted by the co-culture with hiPSC–CM as compared to the control single-cell culture. Additionally, the presence of the hiPSC–EC+MC induced changes in the physical properties of the biomaterial, as observed by an increase in the elastic modulus of the cardiac microtissue when compared to the hiPSC–CM control culture. Detailed characterization of the 3D cardiac microtissues revealed that the crosstalk between hiPSC–CM, hiPSC–EC+MC, and extracellular matrix induced the maturation of hiPSC–CM. The cardiac microtissues displayed functional calcium signaling and respond to known cardiotoxins in a dose-dependent manner. This study is a step forward on the development of novel 3D cardiac microtissues that recapitulate features of the human cardiac microenvironment and is compliant with the larger numbers needed in preclinical research for toxicity assessment and disease modeling.

Keywords: hiPSC, cardiomyocytes, endothelial cells, fibroblasts, engineered cardiac tissues, microencapsulation, 3D culture

INTRODUCTION

The development of reliable human *in vitro* cardiac tissues that better mimic the physiology of the human heart is critical to bridge the gap between the animal models currently used in preclinical research and the human clinical setting. Human induced pluripotent stem cells (hiPSCs) have emerged as a relevant tool for human *in vitro* cardiac cell-based modeling, mainly due to (i) the human origin, (ii) the unlimited proliferative capacity, (iii) the ability to differentiate into different cardiac cell lineages, and (iv) the potential for personalized (patient-specific) medicine.

Recapitulation of the human heart microenvironment in physiological or pathophysiological context for *in vitro* cell-based modeling requires the utilization of the different cellular populations that compose the human heart, namely, cardiomyocytes (CM), endothelial cells (EC), and mesenchymal cells (MC; which comprise mainly cardiac fibroblasts, pericytes, and smooth muscle cells). Although there is a general consensus that CM constitute approximately 30% of the mammalian heart, estimated frequencies of the other populations have been involved in some controversy (Zhou and Pu, 2016). One of the reasons for this controversy is not only the interspecies or intertissue variations but also the dynamic turnover of the human heart during aging (Zhou and Pu, 2016). For example, in the postnatal period, CM represent the majority of the cardiac cells (66%), as opposed to the 30% in the adult mammalian heart (Bergmann et al., 2015). Another reason for this controversy is that divergent results have been obtained using different analytical tools. Nevertheless, the proximity between these different cell populations enables for intercellular communication mediated by paracrine factors, cell–cell interactions, and/or extracellular matrix (ECM) deposition (Kofron and Mende, 2017). Thus, the derivation of these cellular components from hiPSC has been pursued by our group and others. Nevertheless, current protocols for generation of CM from hiPSC (hiPSC–CM) result in cells with an immature phenotype, showing metabolic, structural, and functional characteristics that more closely resemble fetal CM rather than adult CM (Correia et al., 2017). Studies with three-dimensional (3D) hiPSC–derived engineered cardiac tissues have shown a positive impact of cardiac non-myocyte populations (EC and MC) on hiPSC–CM structural and functional maturation (Burridge et al., 2014; Masumoto et al., 2016; Ravenscroft et al., 2016; Giacomelli et al., 2017, 2020). However, most of these studies have either used simplistic 3D spheroid configurations (Ravenscroft et al., 2016; Giacomelli et al., 2017, 2020) and/or hydrogels composed of undefined matrix components, such as Matrigel™ (Thavandiran et al., 2013; Burridge et al., 2014; Masumoto et al., 2016; Nakane et al., 2017). Moreover, the current methodologies for production of such cardiac tissue models are still limited due to (i) low throughput of aggregation protocols dependent of 96-well plate forced aggregation (Ravenscroft et al., 2016; Giacomelli et al., 2017, 2020); (ii) dependence on microfabrication tools (Thavandiran et al., 2013; Nakane et al., 2017); and (iii) low-throughput hydrogel encapsulation techniques (Burridge et al., 2014; Masumoto et al., 2016). Thus, further effort should be performed to develop protocols that enable the scalable production of a biologically relevant hiPSC-derived cardiac tissue model in defined conditions for further implementation of large pharmacological screenings.

In this work, we aim to recapitulate human heart microenvironment features through the design of a 3D human cardiac microtissue by exploring a culture platform based on xeno-free alginate microencapsulation of hiPSC–CM aggregates and single cells of hiPSC–derived EC and MC (hiPSC–EC+MC). We characterize the 3D hiPSC–derived cardiac microtissue at the phenotypic, structural, and functional levels and performed a proof-of-concept toxicological analysis.

MATERIALS AND METHODS

hiPSC Culture and Differentiation Into Cardiovascular Lineages

hiPSC Expansion

In this study, hiPSC line DF19-9-11T.H from WiCell was used. hiPSCs were cultured on Matrigel® (Corning)–coated plates in mTESR1 medium (STEMCELL Technologies, hereafter designated as expansion medium) at 37°C, in a humidified atmosphere of 5% CO_2 (vol/vol) in air. Cells were routinely subcultured when reaching 80% confluence using Versene (Thermo Fisher Scientific) as described by our group (Correia et al., 2016).

hiPSC–CM Differentiation

Differentiation of hiPSCs into CM was performed using the 3D protocol described before by our group (Correia et al., 2018). Briefly, hiPSCs were cultured as monolayers as described in section "*hiPSC Expansion*," and differentiation into CM was initiated when cell confluence reached 80 to 90%. At this timepoint (day 0), expansion medium was replaced by RPMI medium (Thermo Fisher Scientific) supplemented with B27 without insulin (RPMI/B27, Thermo Fisher Scientific), 12 μM CHIR99021 (Tocris), 80 ng/mL activin A (PeproTech), and 50 μg/mL ascorbic acid (Sigma–Aldrich). After 24 h, the medium was replaced by RPMI/B27 supplemented with 5 μM IWR-1 (Sigma–Aldrich) and 50 μg/mL ascorbic acid (Sigma–Aldrich). At day 3 (72 h after differentiation induction), medium was exchanged for RPMI/B27 supplemented with 5 μM IWR-1. At day 7, cell monolayers were dissociated by incubation with TrypLE Select (Thermo Fisher Scientific) for 5 min at 37°C, followed by addition of culture medium (RPMI/B27) and centrifugation at 220 × *g* for 5 min at room temperature (RT, 18°C–20°C). Single cells were then inoculated in AggreWell™400Ex plates (Stem Cell Technologies) at 1,500 cells/microwell, centrifuged at 100 × *g* for 3 min at RT, and cultured in RPMI/B27 medium. 2 days after seeding, the generated cell aggregates were transferred to shake flasks (i.e., Erlenmeyer) and cultured in RPMI/B27 medium at an agitation rate of 90 rpm for additional 6 days (total culture time, 15 days). Medium was replaced every 2 days. During differentiation period, cells were cultured at 37°C, in a humidified atmosphere of 5% CO_2 (vol/vol) in air. At day 15, hiPSC–CM

aggregates were dissociated, counted by trypan blue exclusion assay (see section "*Cell Counting, Viability, and Metabolic Activity*"), and characterized by flow cytometry (see section "*Flow Cytometry of hiPSC–CM*"). These hiPSC–CM aggregates were then encapsulated in alginate as described below (see section "*3D hiPSC–Derived Cardiac Microtissue Culture*").

hiPSC–EC+MC Differentiation

Human iPSCs were propagated as described in section "*hiPSC expansion*" and endothelial/mesenchymal differentiation was induced according to the protocol published by Giacomelli et al., 2017. Briefly, hiPSCs were seeded at 12.5×10^3 cells/cm^2 on the day before starting the differentiation (day -1). At day 0, cardiac mesoderm was induced by changing the medium to APEL-LI medium (Thermo Fisher Scientific), supplemented with a mixture of cytokines (20 ng/mL BMP4, PeproTech; 20 ng/mL activin A, PeproTech; and 1.5 μM GSK3 inhibitor CHIR99021, Tocris). At day 3, cytokines were removed, and vascular endothelial growth factor (VEGF; 50 ng/mL, PeproTech) was added. APEL-LI medium supplemented with VEGF was refreshed every 3 days until day 10. During differentiation cells were cultured at 37°C, in a humidified atmosphere of 5% CO_2 (vol/vol) in air. At day 10, hiPSC–EC+MC were harvested using TrypLE Select, counted by trypan blue exclusion assay (see section "*Cell Counting, Viability, and Metabolic Activity*"), and characterized by flow cytometry (see section "*Flow Cytometry of hiPSC–CM*"). These cells were then encapsulated in alginate as described below (see section "*3D hiPSC–Derived Cardiac Microtissue Culture*").

3D hiPSC–Derived Cardiac Microtissue Culture

The 3D hiPSC–derived cardiac microtissues were developed using microencapsulation technology. Alginate microencapsulation of cells/aggregates was performed as described previously (Rebelo et al., 2015, 2018; Estrada et al., 2016). More specifically, hiPSC–CM aggregates [total of 1.2×10^4 aggregates corresponding to approximately 5×10^6 cells, counted by trypan blue exclusion assay (see section "*Cell Counting, Viability, and Metabolic Activity*")], were collected from suspension cultures and mixed with single cells of hiPSC–EC+MC (10×10^6 cells, harvested from adherent cultures and counted by trypan blue exclusion method) for a ratio of 1:2 (hiPSC–CM:hiPSC–EC+MC). The suspension of hiPSC–CM aggregates and hiPSC–EC+MC single cells was centrifuged at $300 \times g$, for 5 min at RT, and resuspended in 1 mL of 1.1% (wt/vol) of 1:1 mixture of Ultrapure MVG alginate (NovaMatrix, Pronova Biomedical) and NOVATACH MVG GRGDSP peptide-coupled alginate (NovaMatrix, Pronova Biomedical) dissolved in NaCl 0.9% (wt/vol) solution. Cell microencapsulation was performed using an electrostatic bead generator (VarV1, Nisco), to produce beads of approximately 1,500 μm in diameter. The alginate droplets were cross-linked in a 100 mM $CaCl_2$/10 mM HEPES (pH 7.4) solution for 7 min, washed three times in a 0.9% (wt/vol) NaCl solution and then equilibrated in culture medium [1:1 mixture of RPMI medium supplemented with B27 without insulin and Endothelial Cell Growth Medium 2 (Promocell)]. The microencapsulated microtissues were then transferred to shake flasks (50 mL of culture, approximately 14 capsules/mL) and cultured in suspension at 90 rpm in a humidified incubator with 5% (vol/vol) CO_2 in air at 37°C for 15 days. Medium exchange was performed every 2 to 3 days (three times a week). Monocultures of hiPSC–CM (5×10^6 cell/mL of alginate) and co-cultures of hiPSC–EC+MC (10×10^6 cell/mL of alginate) were also microencapsulated and used as controls.

Cell Culture Characterization

Flow Cytometry of hiPSC–CM

Human iPSC–CM aggregates were harvested from culture and dissociated with TypLE™ Select for 5 min at 37°C with agitation. Afterward, single cells were washed twice with Dulbecco's phosphate-buffered saline (DPBS) (Thermo Fisher Scientific), and 5×10^5 cells were incubated in the dark with one of the following conjugated antibodies for 1 h at 4°C: SIRPα/β (CD172a/b-PE, BioLegend, diluted 1:20 in DPBS), VCAM (CD106-PE, BD Biosciences, diluted 1:5 in DPBS), or isotype control immunoglobulin G1 (IgG1),κ-PE (BD Biosciences, diluted 1:5 in DPBS). For detection of intracellular marker (Troponin T, Thermo Fisher Scientific), cells were fixed and permeabilized with Inside Stain Kit (Miltenyi Biotec) according to the manufacturer's instructions. Cells were incubated with primary antibody (diluted 1:200 in InsidePerm) for 10 min at RT, washed with InsidePerm, and incubated with secondary antibody anti–mouse IgG Alexa Fluor 488 (diluted 1:200 in InsidePerm) for 10 min at RT. Cells were washed with InsidePerm and analyzed by a CyFlow® space (Partec GmbH). Ten thousand events were analyzed per sample.

Flow Cytometry of hiPSC–EC+MC

Human iPSC–EC+MC were harvested from culture by dissociation with TypLE™ Select for 5 min at 37°C. Afterward, single cells were washed twice with DPBS, and 5×10^5 cells were processed as described in section "*Flow Cytometry of hiPSC–CM*." Primary antibodies used were CD31 (Agilent, diluted 1:50 in DPBS), VE-cadherin (R&D Systems, diluted 1:13 in DPBS), vimentin (Abcam, diluted 1:100 in InsidePerm), or α-smooth muscle actin (α-SMA; Agilent, diluted 1:100 in InsidePerm). Secondary antibody used was anti–mouse IgG Alexa Fluor 488 (diluted 1:200 in InsidePerm). Cells were analyzed by a CyFlow® space (Partec GmbH). Ten thousand events were analyzed per sample.

Cell Counting, Viability, and Metabolic Activity

Viable cells were quantified by trypan blue exclusion, as described elsewhere (Abecasis et al., 2017). For viability assessment, the enzyme substrate fluorescein diacetate (FDA, Sigma–Aldrich) and the DNA dye propidium iodide (PI, Sigma–Aldrich) were used (Serra et al., 2011; Silva et al., 2015). In this method, direct staining of the live aggregates was performed followed by observation at the fluorescence microscope (DMI6000, Leica, Wetzlar, Germany), as described elsewhere (Serra et al., 2011). Cells that accumulated the metabolized product of FDA were considered live, and cells stained with PI were considered dead.

For evaluation of metabolic activity, the reduction capacity of the cultures was measured by PrestoBlue® Viability Reagent reduction assay (Life Technologies), according to the manufacturer's instruction. PrestoBlue® reagent is reduced by viable cells and becomes highly fluorescent. This color change can be detected using fluorescence measurements. Samples of 2 to 5 capsules were taken from suspension agitated cultures into a 96-well plate. The microencapsulated cells were incubated with PrestoBlue® reagent for 3 h at 37°C. After this period, the supernatant was collected, and the fluorescence was read at 560-nm excitation and 590-nm emission in the microplate reader Infinite®200 PRO (NanoQuant, Tecan Trading AG).

Gene Expression Analysis

Alginate microcapsules of cardiac microtissues were dissolved with a chelating solution (sodium citrate 50 mM, sodium chloride 100 mM) and centrifuged at 300 × *g* for 5 min at RT. Pellets were snap-frozen and kept at -80°C until RNA isolation. Total RNA was isolated with the High Pure RNA Isolation Kit (Roche). The RNA was quantified, and purity checked by Nanodrop 2000c (Thermo Scientific). RNA reverse transcription to double-stranded cDNA was performed with the Transcriptor High Fidelity cDNA Synthesis Kit (Roche). Real-time quantitative polymerase chain reaction (RT-qPCR) was conducted with the LightCycler 480 Probes Master system (Roche) using TaqMan Gene Expression Assays (Thermo Fisher Scientific). The performed cycles were as follows: preincubation at 95°C for 10 min, 45 cycles of amplification with denaturation at 95°C for 15 s, and annealing at 60°C for 1 min; extension at 72°C for 5 min. Threshold cycles (Ct) were automatically determined by the LightCycler 480 Software (Roche). All data were analyzed using the $2^{-\Delta\Delta Ct}$ method for relative gene expression analysis (Livak and Schmittgen, 2001). Changes in gene expression were normalized using the Ct geometric mean of housekeeping genes *RPLP0* and *GAPDH*.

Immunofluorescence Microscopy

Cryosectioning

Microencapsulated cells were collected from culture and fixed in 4% (wt/vol) formaldehyde with 4% (wt/vol) sucrose in phosphate-buffered saline (PBS) for 20 min at RT. For cryosectioning preparation, samples were dehydrated in 30% (wt/vol) sucrose overnight at 4°C, embedded in Tissue-Tek® O.C.T. (Sakura) and frozen at -80°C. The frozen samples were sliced with a thickness of 10 µm in a cryostat (Cryostat CM 3050 S, Leica). The cryosections were permeabilized for 10 min with 0.1% (vol/vol) Triton X- 100 (Sigma–Aldrich) and blocked with 0.2% (wt/vol) fish-skin gelatin (FSG; Sigma–Aldrich) in PBS for 30 min. Primary and secondary antibodies were prepared in 0.125% (wt/vol) of FSG in PBS and incubated for 2 h. The primary antibodies used were as follows: cardiac troponin T (cTnT, Thermo Fisher Scientific, 1:200), sarcomeric α-actinin (Sigma–Aldrich, 1:200), collagen I (Abcam, 1:100), and collagen IV (Abcam, 1:100). Secondary antibodies used were as follows: anti–mouse IgG Alexa Fluor 594, anti–rabbit IgG Alexa Fluor 594, anti–mouse IgG Alexa Fluor 488, anti–rabbit IgG Alexa Fluor 488, and anti–mouse IgG Alexa Fluor 594 (all from Thermo Fisher Scientific, 1:500). The samples were mounted in Prolong® Gold reagent containing DAPI (Life Technologies). Samples were visualized using a confocal fluorescence microscope (SP5, Leica).

Whole mount

Microencapsulated cells were collected from culture and fixed in 4% (wt/vol) formaldehyde with 4% (wt/vol) sucrose in PBS for 20 min at RT. Samples were permeabilized and blocked with 1% (wt/vol) Triton X-100 solution/0.2% FSG for 2 h at RT and subsequently incubated overnight at RT with primary antibodies (CD31, Agilent; vimentin, Abcam) diluted in 0.1% (wt/vol) TX-100 and 0.125% (wt/vol) FSG. Samples were then washed three times with DPBS and incubated with secondary antibodies (AlexaFluor 488 goat anti–mouse IgG, AlexaFluor 549 goat anti–rabbit IgG, Thermo Fisher Scientific) diluted in 0.125% (wt/vol) FSG, for 5 h at RT. After three washes with DPBS, cell nuclei were counterstained with DRAQ5 (Thermo Fisher Scientific). Samples were visualized using light-sheet fluorescence microscopy (LSFM) or multiphoton immunofluorescence microscopy (IFM) as described previously (Estrada et al., 2016).

Transmission Electron Microscopy

Microencapsulated cells were fixed in 4% (wt/vol) paraformaldehyde with 4% (wt/vol) sucrose in DPBS for 20 min at RT. Fixed samples were washed twice with DPBS and stored at 4°C. Second fixation was performed using 2% (vol/vol) formaldehyde (EMS) and 2.5% (vol/vol) glutaraldehyde (Polysciences) in 0.1 M phosphate buffer (PB), for 1 h at 4°C. Cells were washed with PB and embedded in 2% low melting point agarose (OmniPur) for further processing. Postfixation was performed with 1% (wt/vol) osmium tetroxide (EMS) in 0.1 M PB for 30 min on ice in the dark. After two washes with 0.1 M PB and two washes with water, samples were incubated with 1% aqueous tannic acid (wt/vol; EMS) for 20 min on ice. After five washes with water, samples were contrasted with 0.5% aqueous uranyl acetate (wt/vol), 1 h on ice in the dark. Dehydration was performed using a graded series of ethanol (30, 50, 75, 90, and 100%), and samples were embedded in Embed-812 epoxy resin (EMS). Ultrathin sections were cut on a Leica UC7 ultramicrotome. Sections were collected on grids coated with 1% (wt/vol) formvar (Agar Scientific) in chloroform (VWR) and stained with 1% (wt/vol) uranyl acetate and Reynolds lead citrate, for 5 min each. Images were taken on a Hitachi H-7650 at 100 keV equipped with a XR41M mid mount AMT digital camera.

Calcium Imaging

Calcium imaging was performed using the Fluo-4 Direct™ Calcium Assay Kit (Thermo Fisher Scientific) according to the manufacturer's instructions. Briefly, microencapsulated cells were transferred onto four-well µslides (Ibidi). The samples were loaded with the calcium indicator dye Fluo-4 (diluted 1:2 in culture medium) for 45 min at 37°C plus 15 min at RT and washed twice with culture media. Analysis was performed under temperature control (37°C), and spontaneous calcium activity was recorded. Cells were analyzed alone or exposed

to norepinephrine (60 μM, norepinephrine bitartrate, Sigma–Aldrich). Alginate microcapsules were imaged using a spinning disk confocal microscope (Revolution XD, Andor), and 30-s videos were acquired using Micro-Manager 1.4 software. Fluorescence videos were analyzed by manually selecting each individual aggregate within the alginate microcapsule using ImageJ open source software (Rasband, WS, ImageJ, United States National Institutes of Health, Bethesda, MD, United States, http://imagej.nih.gov/ij/, 1997–2018). Extracted data were treated using a developed in-house script in MATLAB (MathWorks). Briefly, data were normalized to baseline fluorescence (ΔF/F0), and each peak was analyzed for the following parameters: amplitude, rise time, maximal upstroke velocity, time to 50 and 80% decay, maximal decay velocity, and time between peaks, as previously described (Abecasis et al., 2019).

Cardiotoxic Drug Exposure

After 15 days of culture, microencapsulated cardiac microtissues and hiPSC–CM controls were harvested from suspension culture and transferred to 96-well plate (two to five capsules were inoculated per well). Cells were first evaluated for metabolic activity and cell viability as explained in section "*Cell Counting, Viability, and Metabolic Activity*." Then, the cultures were washed twice with DPBS and incubated with doxorubicin or paclitaxel (0.1, 0.5, 1, 5, 10, 50, and 100 μM, MedChemExpress) for 72 h in a humidified incubator with 5% (vol/vol) CO_2 in air at 37°C under agitation (90 rpm). After this period, cells were assessed again for metabolic activity and cell viability (see section "*Cell Counting, Viability, and Metabolic Activity*").

Atomic Force Microscopy

Atomic force microscopy (AFM) characterization was performed to compare surface topography and mechanobiological behavior of alginate capsules and the cardiac microtissues 15 days after microencapsulation. Samples were collected and fixed as indicated previously (see section "*Whole Mount*"). Fixed samples were washed twice with DPBS and stored at 4°C until AFM characterization. Alginate microcapsules were embedded in 2% (wt/vol) high-melting-temperature agarose (Lonza), forming a thin film, which was kept hydrated up to AFM analysis. All measurements were performed in an Asylum Research MFP-3D Stand Alone system, whereas samples were immersed in PBS buffer. Surface topography measurements were acquired in alternate contact mode using commercially available AFM probes (Olympus BL-AC40-TS; $f_0 = 110$ kHz; $k = 0.09$ N/m). Acquisition of load–unload force curves (force spectroscopy) was performed with the same probes, after previous calibration through thermal tuning (Green et al., 2004). Asylum Research's analysis software packages loaded in IGOR Pro software (WaveMetrics) were used to generate low-order plane-fitted topography images and determine average pore diameter. Load–unload curves were analyzed in the same software, being considered curves from, at least, three capsules per condition. Apparent elastic moduli of the samples were determined by fitting the elastic Sneddon contact model for conical indenters (Sneddon, 1965) to the unload curves.

Statistical Analysis

Statistical analysis was performed with GraphPad Prism6 (GraphPad Software Inc.). Values are represented as mean ± standard error of the mean (SEM) of measurements or assays in independent alginate microcapsules from one or two independent differentiation batches, as stated in the respective results figures. Statistical significance was determined by Student *t* test. $p < 0.05$ was considered as statistically significant.

RESULTS

Establishment of a 3D hiPSC–Derived Cardiac Microtissue Model

In this work, we developed a 3D cardiac microtissue model using CM, EC, and MC derived from hiPSC microencapsulated in alginate. Differentiation of hiPSC into CM lineage was performed as previously described by our group (Correia et al., 2018), yielding 3D aggregates of hiPSC–CM with uniform size distribution (average size: 142 ± 26 μm) and high cell viability (**Supplementary Figure 1A**). Noteworthy, the hiPSC–CM aggregates showed high CM purity by the end of the differentiation protocol, with majority of the cells expressing SIRPα/β (81% ± 1%), VCAM-1 (73% ± 5%) and cTnT (77%) at day 15 of differentiation (**Supplementary Figure 1B**). In parallel, hiPSC were also differentiated into EC and MC, using a monolayer-based differentiation protocol developed by other authors (Giacomelli et al., 2017). This protocol generated a mixed population of cells expressing CD31 (27% ± 4%), VE-Cad (21% ± 3%), vimentin (90% ± 1%), and α-SMA (35% ± 12%), which are markers for EC (CD31 and VE-Cad) and fibroblasts and/or vascular smooth muscle cells (vimentin and α-SMA; hereafter designated as hiPSC–EC+MC, **Supplementary Figure 1C**). After 10 days of differentiation, hiPSC–EC+MC were harvested and co-cultured with hiPSC–CM aggregates, collected at day 15, within alginate microcapsules.

Cell/aggregate microencapsulation in alginate (1:1 mixture of Ultrapure MVG alginate and NOVATACH MVG GRGDSP peptide-coupled alginate; see section "*3D hiPSC–Derived Cardiac Microtissue Culture*") was carried out using the methodology already reported by our group (Rebelo et al., 2015, 2018; Estrada et al., 2016). A preliminary study was performed to evaluate the impact of aggregate concentration [hiPSC–CM aggregates/mL of 1.1% (wt/vol) alginate solution] on the percentage of empty capsules generated. Results showed that the percentage of empty capsules was reduced when using a concentration of at least 12,000 aggregates/mL of alginate (**Supplementary Figure 1D**), and thus this condition was selected to perform the microencapsulation of cell aggregates. For the generation of 3D microencapsulated cardiac microtissues, hiPSC–CM aggregates were mixed with hiPSC–EC+MC single cells in a 1:2 cellular ratio in order to obtain a cell composition similar to what has been reported for human adult heart: approximately 33% CM, 17% EC, and 50% MC (Bergmann et al., 2015). The cell/aggregate suspension was then microencapsulated in alginate mixture (hereafter designated as cardiac microtissues; **Figure 1A**).

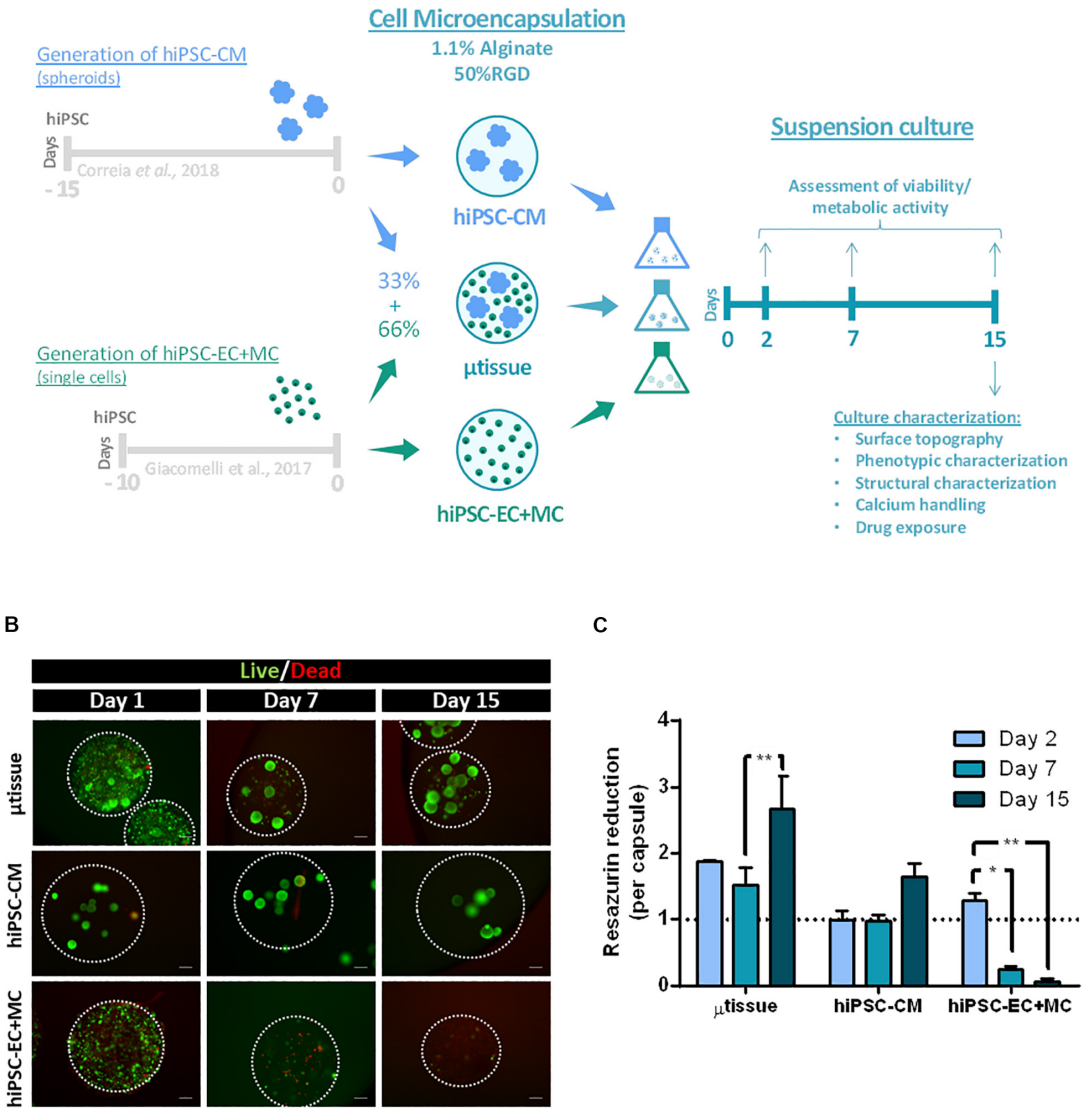

FIGURE 1 | (A) Schematic representation of the alginate microencapsulation protocol for cardiac microtissue (µtissue) formation and respective control cultures hiPSC–CM and hiPSC–EC+MC. Capsules were maintained in dynamic suspension culture until day 15 post-microencapsulation for further microtissue characterization. **(B,C)** Evaluation of cell viability and metabolic activity for the cardiac microtissue (µtissue) and control cultures (hiPSC–CM and hiPSC–EC+MC). **(B)** Viability analysis of the three microencapsulated cell cultures throughout time (days 1, 7, and 15), stained with fluorescein diacetate (FDA—live cells, green) and propidium iodide (PI—dead cells, red). Microcapsules are marked with white dashed line. Scale bar: 200 µm. **(C)** Metabolic activity of the three microencapsulated cell cultures during time (days 2, 7, and 15), measured by the capacity of reduction of Presto-Blue™ Viability Reagent, normalized by capsule and to hiPSC–CM culture condition on day 2. Data represented as mean ± SEM; $n = 3$ independent measurements from one differentiation batch; $^{*}p < 0.05$, $^{**}p < 0.005$.

Microencapsulation of hiPSC–CM aggregates alone and hiPSC–EC+MC single cells was also performed and used as controls (**Figure 1A**). All cell microencapsulated conditions (cardiac microtissues, hiPSC–CM aggregates, and hiPSC–EC+MC) were cultured in agitated suspension conditions for additional 15 days.

Cell viability and metabolic activity of all cultures were evaluated after 1, 7, and 15 days of microencapsulation by live/dead staining and PrestoBlue™ assay (**Figures 1B,C**). The results showed that cardiac microtissues maintained high cell viability throughout culture time, displaying significantly higher metabolic activities than both control cultures (**Figures 1B,C**; at day 15 µtissue vs. hiPSC–CM $p = 0.0074$ and µtissue vs. hiPSC–EC+MC $p < 0.001$). This result is also related with the higher number of cells inoculated within the cardiac microtissues microcapsules when compared to the values used in control cultures. Noteworthy, our data also show evidence of the protective effect of hiPSC–CM on hiPSC–EC+MC survival. In particular, we observed a significant drop in viability

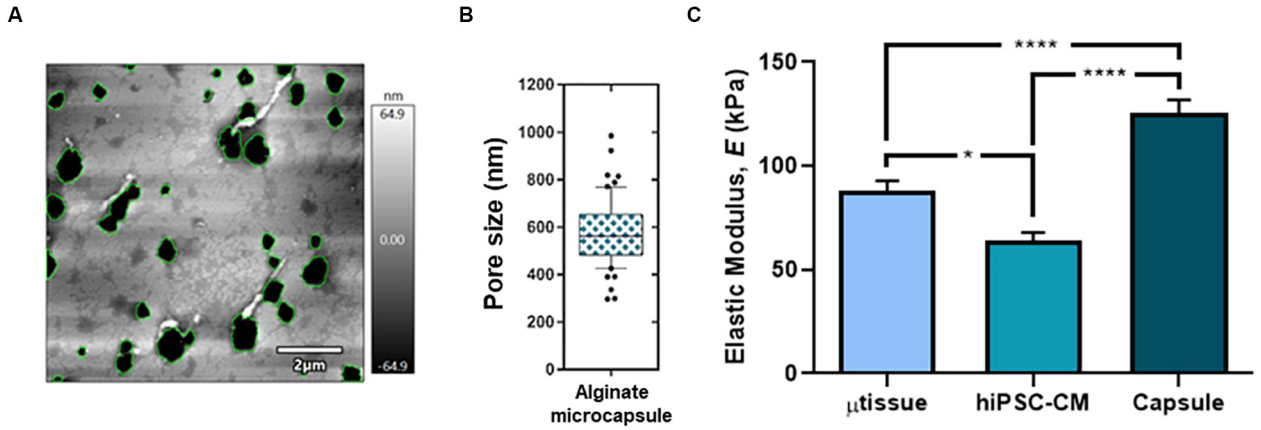

FIGURE 2 | Topographical characterization of the cardiac microtissue and the alginate microcapsule at day 15 post-microencapsulation. Surface topography **(A)** and pore size (**B**; $n = 61$ independent measurements from two differentiation batches) of the alginate capsule by atomic force microscopy (AFM). **(C)** Mechanical characterization (elastic modulus, E) for the microtissue (µtissue; triculture), hiPSC–CM and the empty alginate capsule via AFM. Data represented as mean ± SEM; $n > 40$ independent measurements from two differentiation batches; $^{*}p < 0.05$, $^{****}p < 0.0001$.

and metabolic activity from day 7 onward in hiPSC–EC+MC cultures, contrasting with cardiac microtissues and hiPSC–CM monocultures that maintained high cell viability and metabolic activity through time (**Figures 1B,C**). The significant increase in metabolic activity of cardiac microtissues from days 7 to 15 may indicate either an increase in cell numbers due to cell proliferation of non-myocyte cells or an increase in metabolic capacity of hiPSC–CM aggregates, as previously described by our group (Correia et al., 2018). In fact, a similar profile was observed in hiPSC–CM control culture that showed a peak in metabolic activity at day 15.

In addition, characterization of mechanical and topographical properties was performed via AFM in empty alginate capsules and encapsulated cultures (hiPSC–CM aggregates and cardiac microtissue). AFM topographical imaging evidenced an alginate porous surface structure (**Figure 2A**), with heterogeneity, particularly in the microcapsule constructs containing hiPSC–CM aggregates and cardiac microtissue when compared with cell-free capsules (data not shown), demonstrating cell–biomaterial interaction and its impact on morphology and topography. Additionally, analysis of the AFM images showed that the microcapsule average pore diameter was 579.6 ± 137.0 nm (**Figures 2A,B**), enabling effective diffusion of nutrients, metabolites, and drugs into the microcapsule. Furthermore, characterization was performed via load–unload force curves (force spectroscopy) for the empty alginate capsules and encapsulated at the last day of culture (**Figure 2C**). The calcium RGD-alginate microcapsule biomaterial alone denoted an elastic modulus of 132.3 ± 53.7 kPa, significantly superior to the cellularized constructs (**Figure 2C**). This seems to indicate that the microenvironment in the presence of the cells is less stiff, when compared to the biomaterial alone. In addition, in comparison to the encapsulated hiPSC–CM aggregates, the cardiac microtissue's elastic modulus is significantly higher (**Figure 2C**), exhibiting a stiffer microenvironment more resistant to deformation, which may be consistent with a remodeling of the cardiac microenvironment resulting from the presence of the non-myocyte cells.

Phenotypic, Structural, and Functional Characterization of the 3D hiPSC-Derived Cardiac Microtissue

Cardiac microtissues were characterized at phenotypic, structural, and functional level and compared with hiPSC–CM. LSFM was used to confirm the presence of the non-myocyte cellular populations, namely, EC (stained for CD31 and VE-cadherin) and MC (stained for vimentin and α-SMA), as single cells within alginate microcapsules after 15 days of culture (**Figure 3A**). Vimentin and α-SMA staining was also observed within the aggregates of the cardiac microtissues either by LSFM (**Figure 3A**) and IFM of the cryosections (**Figure 3B**). These MC most likely originate from the percentage of cells in the CM differentiation protocol that do not express cardiac specific markers (**Supplementary Figure 1B**), because these stainings were also observed in the hiPSC–CM aggregates control culture (**Figures 3A,B**). Cardiac microtissues showed expression and organization of sarcomeric structural proteins (cTnT and α-actinin) after 15 days of culture (**Figure 3C**). In addition, f-actin counterstaining clearly illustrates assembly and organization of myofibrils (**Figure 3C**). Staining for collagen I, collagen IV, and fibronectin confirmed expression of these ECM components in cardiac microtissues by imaging through whole-mount multiphoton microscopy (**Figure 4A**) and cryosections' confocal microscopy (**Figure 4B**). Noteworthy, collagen IV staining was more noticeable inside the cardiac microtissue alginate capsule (and outside the hiPSC–CM aggregates; **Figure 4A**), when compared to hiPSC–CM control, likely originated from the non-myocyte cells.

Gene expression analysis of cardiac microtissues by RT-qPCR revealed an increase in expression of gene isoforms

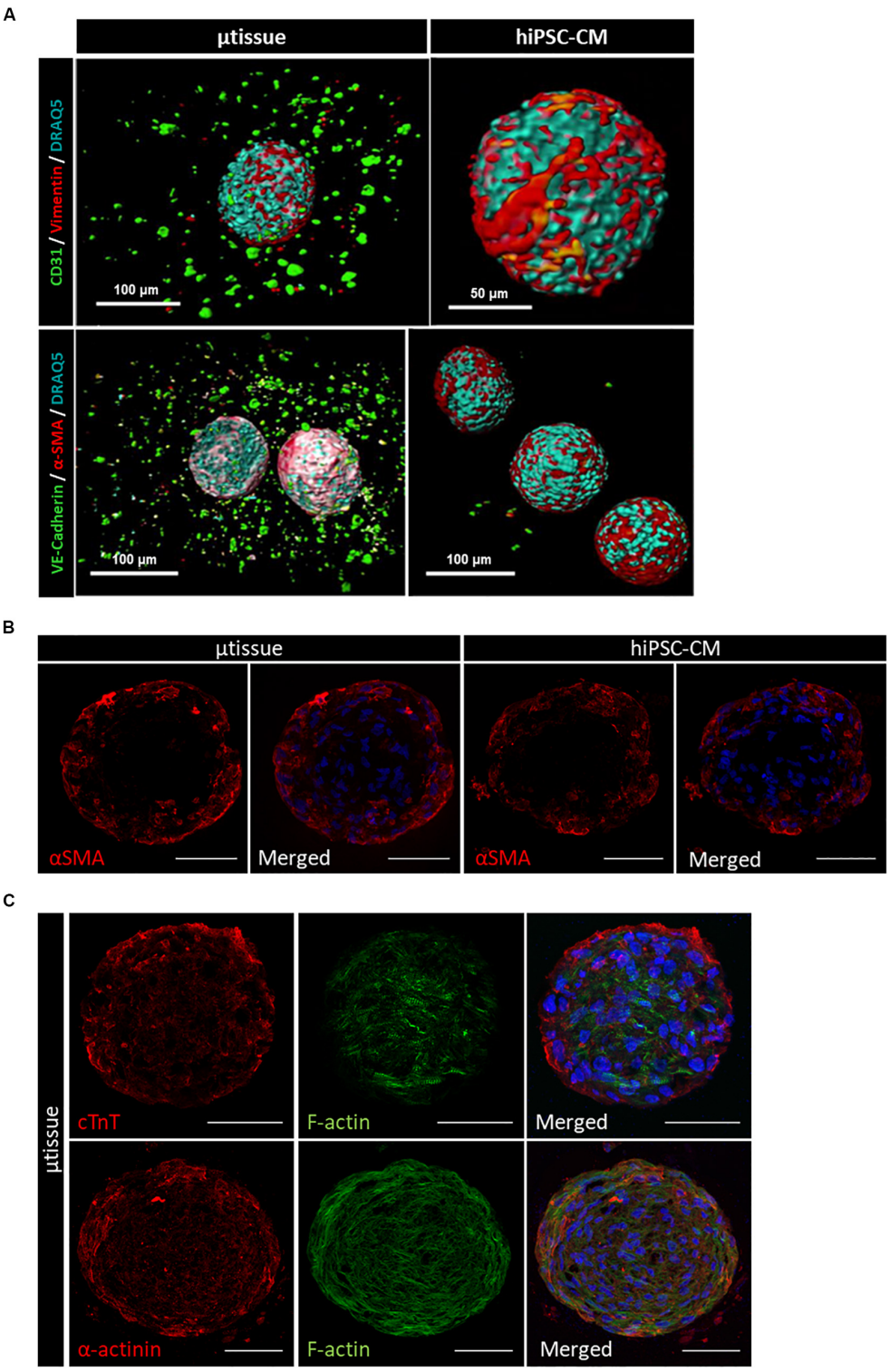

FIGURE 3 | Phenotypic characterization of cardiac microtissue (µtissue) and hiPSC–CM control culture by immunofluorescence microscopy at day 15. **(A)** Light-sheet immunofluorescence microscopy of the whole-mount microencapsulated cardiac microtissue and hiPSC–CM. Cells were stained for endothelial cell markers (CD31 and VE-cadherin, green) and MC markers (vimentin and α-SMA, red). Images were counterstained with DRAQ5 (nuclei, cyan). Scale bar = 100 µm. **(B,C)** Immunofluorescence microscopy of cryosections of cardiac microtissue and hiPSC–CM aggregates. **(B)** Cells were stained for α-smooth muscle actin (α-SMA, red). Images were counterstained with and DAPI (nuclei, blue). Scale bar = 50 µm. **(C)** Cells from cardiac microtissue (µtissue) were stained for sarcomeric structural proteins (cTnT and α-actinin, red). Images were counterstained with phalloidin (f-actin, green) and DAPI (nuclei, blue). Scale bar = 50 µm.

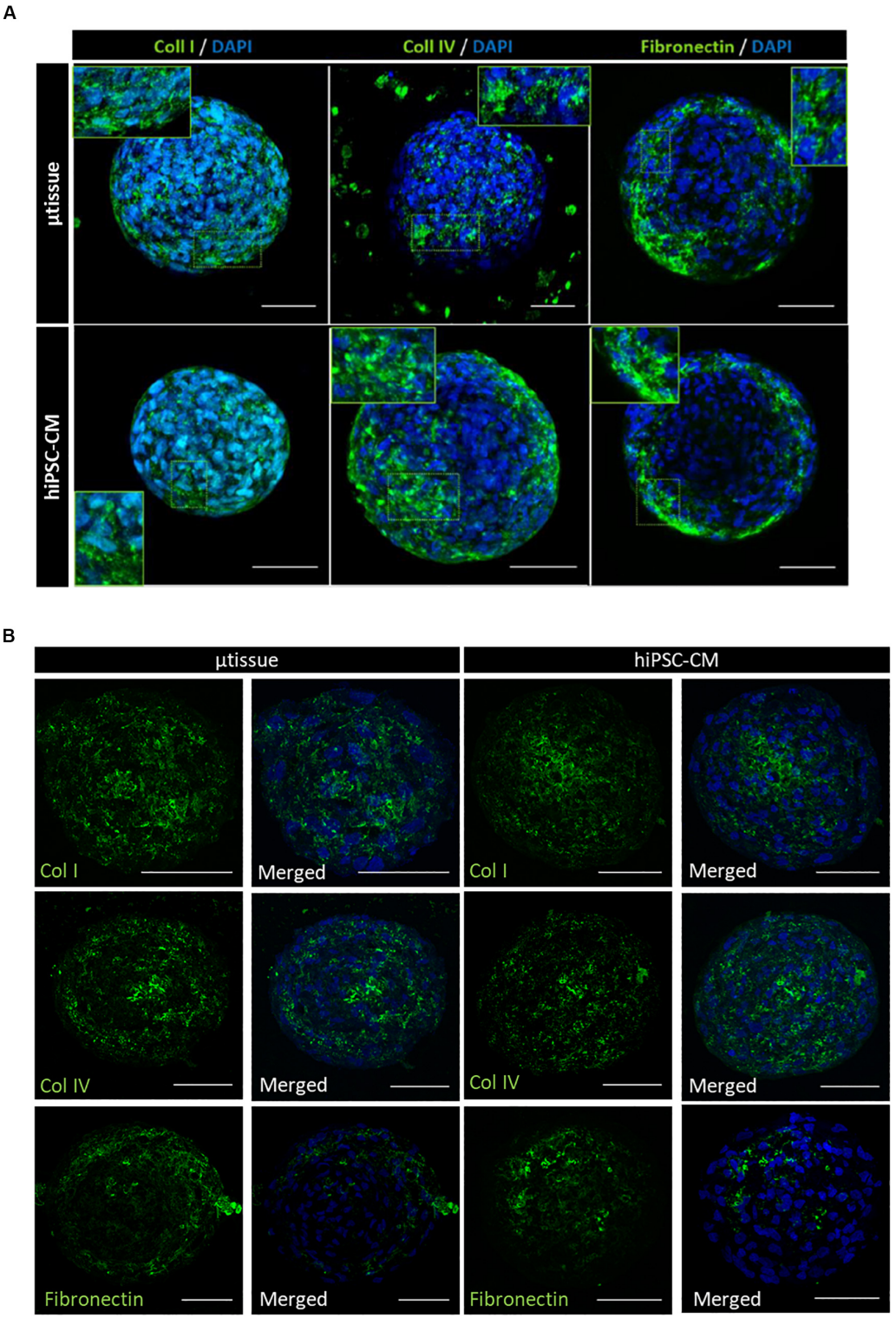

FIGURE 4 | Phenotypic characterization of cardiac microtissue (µtissue) and hiPSC–CM by immunofluorescence microscopy after 15 days' culture. Cells were stained for ECM proteins (collagen I, collagen IV, and fibronectin). Images are counterstained with DAPI. **(A)** Multiphoton immunofluorescence microscopy of the whole-mount microencapsulated cardiac microtissue and control hiPSC–CM. Scale bar = 50 µm. **(B)** Immunofluorescence microscopy of the cryosections of cardiac microtissue and control hiPSC–CM monoculture for characterization of the hiPSC–CM aggregates. Scale bar = 50 µm.

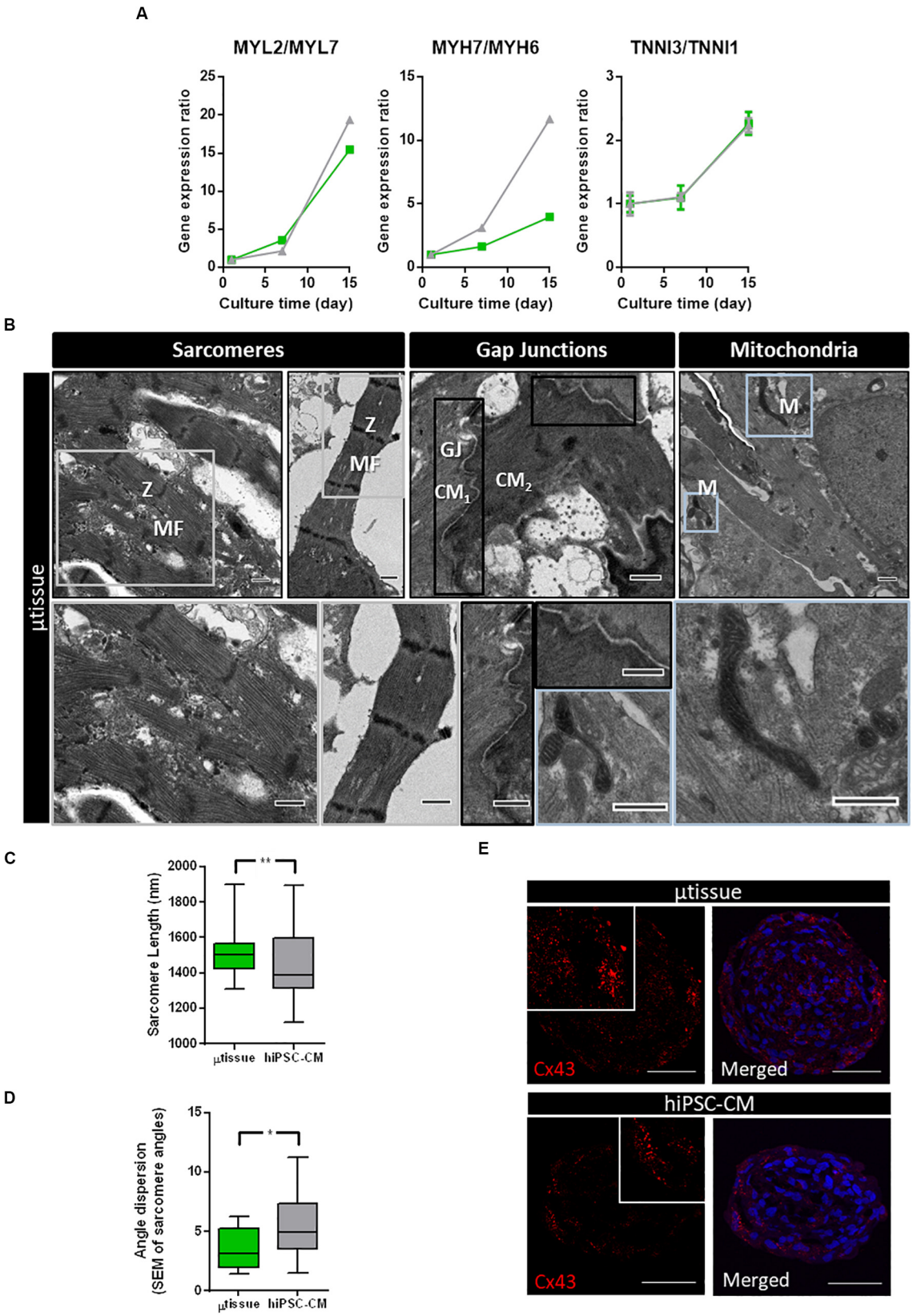

FIGURE 5 | Continued

FIGURE 5 | Characterization of structural maturation of the cardiac microtissues after 15 days of culture. **(A)** Analysis of gene expression by RT-qPCR of specific genes associated with cardiomyocyte structure and organization in cardiac microtissue (green) and hiPSC–CM (gray) throughout the culture time. Expression ratios for cardiac isoforms of mature (MYL2, MYH7, and TNNI3) and immature (MYL7, MYH6, and TNNI1) phenotypes were displayed. Gene expression was normalized to day 1. Data represented as mean ± SEM; $n = 3$ independent measurements from one differentiation batch. **(B)** Transmission electron microscopy images of cardiac microtissue (μtissue) and hiPSC–CM culture: (i) aligned myofibrils, composed by sarcomeres with organized Z-disks, A-bands, and I-bands; (ii) cell junctions (gap junctions, GJ) between adjacent hiPSC–CM; and (iii) abundant mitochondria (M). Scale bar: 2 μm. **(C)** Analysis of sarcomere length of cardiac microtissue (μtissue, green) and hiPSC–CM culture (gray). Data represented as mean ± SEM; $n > 40$ independent measurements from one differentiation batch; $^{**}p < 0.01$. **(D)** Analysis of myofibril alignment (as shown by myofibril angle dispersion) of cardiac microtissue (μtissue, green) and hiPSC–CM control (gray). Data represented as mean ± SEM; $n > 8$ independent measurements from one differentiation batch; $^{*}p < 0.05$. **(E)** Phenotypic characterization of cardiac microtissue (μtissue) and hiPSC–CM culture by immunofluorescence after 15 days' culture. Cells were stained for connexin 43 (Cx43, red). Images are counterstained with DAPI (blue). Scale bar = 50 μm.

associated with mature sarcomeric structures when compared to more immature isoforms (MYL2/MYL7, MYH7/MYH6, and TNNI3/TNNI1 ratios) along culture time (**Figure 5A**). Although similar profiles were observed in terms of sarcomeric gene expression for cardiac microtissue and hiPSC–CM, ultrastructural analysis showed differences in terms of sarcomeric length and alignment, indicative of hiPSC–CM maturation. Ultrastructure analyses of the cardiac microtissues show the presence of sarcomeres with organized *Z*-disks, A-bands, and I-bands by day 15 of culture (**Figure 5B**), which were not observed by the beginning of the culture (data not shown). Intercalated disks between adjacent hiPSC–CM and abundant mitochondria were also identified (**Figure 5A**). Analysis of sarcomere length and alignment from images obtained by transmission electron microscopy (TEM) suggested improved structural maturation of hiPSC–CM in the cardiac microtissues compared to the control hiPSC–CM aggregates. In particular, sarcomere length and myofibril alignment were significantly higher in cardiac microtissues when compared to hiPSC–CM aggregates (**Figures 5C,D**). In agreement, IFM of aggregate cryosections indicated evidences of increased expression of Cx43 in cardiac microtissues than in hiPSC–CM aggregates (**Figure 5E**), which could also be indicative of improved structural maturation of the formers, as previously described by other studies (Hussain et al., 2013; Giacomelli et al., 2020).

Calcium imaging was performed using a fluorescent calcium indicator (**Figures 6A–F**, **Supplementary Figure 2** and **Supplementary Video 1**), enabling the evaluation of the functionality of generated cardiac microtissues and estimation of different calcium kinetics' parameters. Spontaneous calcium transients were observed in the cardiac microtissues, indicating the presence of functional calcium handling machinery (**Figure 6B**). Exposure to an adrenergic agonist (norepinephrine, 60 μM) resulted in a positive chronotropic response (**Figure 6B**). Analysis of the calcium kinetics' parameters revealed that exposure to norepinephrine resulted in decrease in rise and decay time (**Figures 6C–F**) and decrease in cycle length (**Figure 6G**), demonstrating functional β-adrenergic response. Moreover, increased expression of the L-type calcium-channel subunit α-1C (CACNA1C) was also observed over time in the cardiac microtissue (**Figure 6H**), which could be indicative of increased calcium handling functionality in the cardiac microtissue.

To evaluate the feasibility of this cardiac microtissue for application in toxicology, a proof-of-concept study was performed by exposing cell microcapsules to two chemotherapy anticancer drugs with known cardiotoxicity effects (**Figures 6H–J**): doxorubicin and paclitaxel (Bovelli et al., 2010). Our results indicate that cardiac microtissues were sensitive to both drugs. A decrease in cell viability and metabolic activity after exposure to doxorubicin and paclitaxel in a concentration-dependent manner was observed (**Figures 6H,I**). Noteworthy, hiPSC–CM seem to have an increased sensitivity to doxorubicin when compared to the cardiac microtissue showing lower metabolic activities (**Figure 6H**). No major differences in sensitivity were observed between hiPSC–CM and the cardiac microtissue for the paclitaxel exposure (**Figure 6I**), both displaying low metabolic activities for concentrations greater than 10 μM. Representative images of live/dead staining after exposure to doxorubicin and paclitaxel are shown in **Figure 6J**.

DISCUSSION

Drug development is a long and costly process with low success rates, in which cardiotoxicity is one of the major reasons for failure (Eder et al., 2016). Current preclinical testing relies mainly on (i) *in vitro* systems that have low compliance with high-throughput screenings; or (ii) cost- and labor-intensive animal models that differ from human physiology and should be restricted to a minimum use from an ethical point of view (Eder et al., 2016). The development of biologically relevant and reliable human *in vitro* cardiac tissue models using hiPSC derivatives may circumvent some of these limitations, allowing better understanding of human cardiac diseases and improvement of the assessment of cardiotoxicity of new drugs in a human setting. In this study, we developed a novel *in vitro* 3D human cardiac microtissue by combining hiPSC–CM aggregates and hiPSC–EC+MC single cells inside alginate microcapsules.

Cell microencapsulation technology has been thoroughly explored by our group for different applications in (stem) cell bioprocessing, such as expansion/cryopreservation of hESC (Serra et al., 2011), culture of hepatocyte spheroids (Tostões et al., 2011; Rebelo et al., 2015), and tumor *in vitro* modeling (Estrada et al., 2016; Rebelo et al., 2018), showing positive impact on cell viability, phenotype and functionality. The small spherical capsules (approximately 1,500 μm in diameter) confer protection to shear stress, while creating an extracellular environment that enables diffusion of nutrients and soluble factors through the hydrogel structure and prevents the

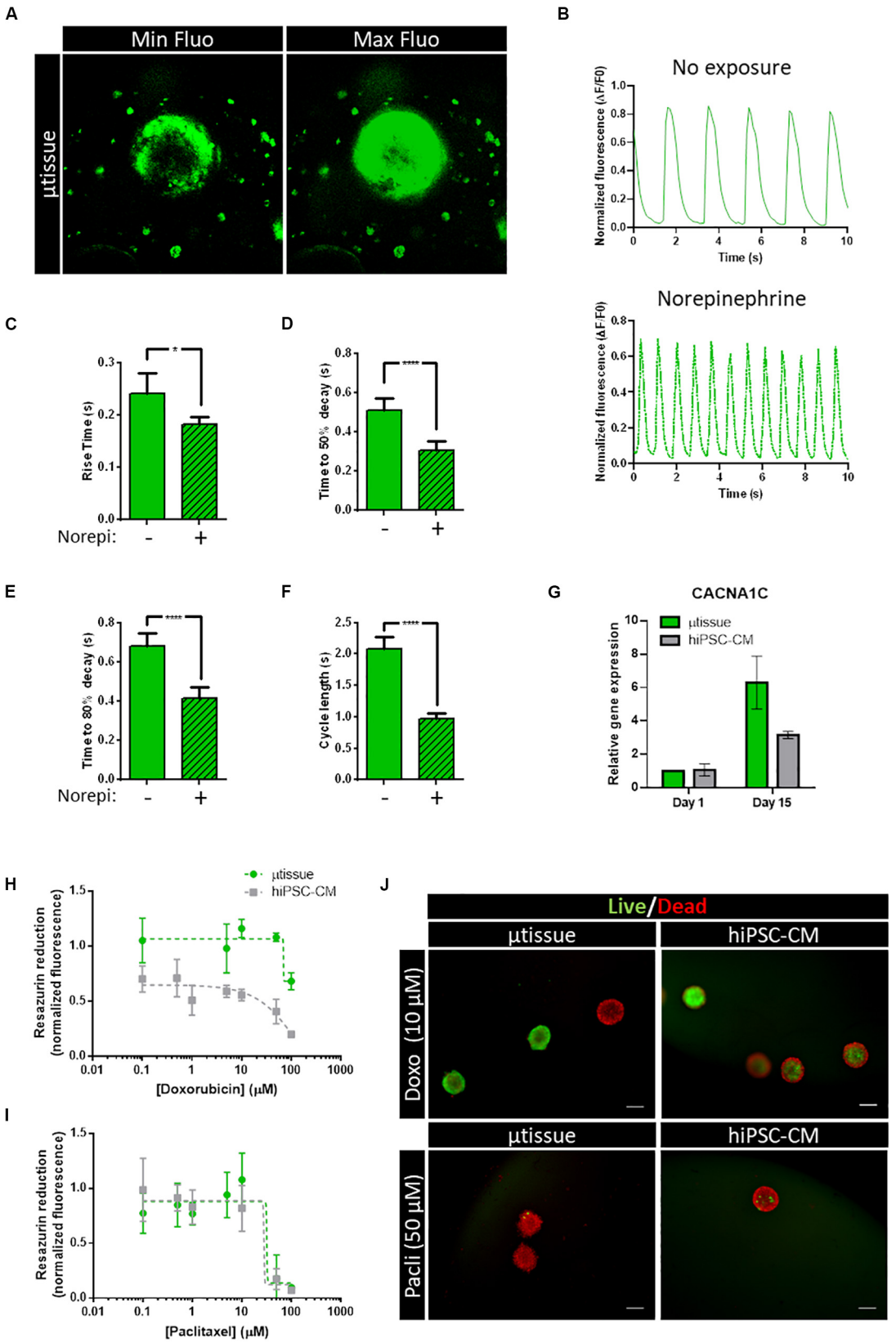

FIGURE 6 | Continued

FIGURE 6 | (A–F) Characterization of calcium handling kinetics of cardiac microtissue by fluorescent calcium imaging at day 15 post-microencapsulation. **(A)** Representative images of the maximum and minimum fluorescence of the videos analyzed. **(B)** Representative profile of spontaneous calcium transients in the cardiac microtissue: without drug exposure and with exposure to 60 μM of norepinephrine. **(C–F)** Calcium kinetics parameters obtained from the analysis of the transients: **(C)** rise time, **(D)** time to 50% decay, **(E)** time to 80% decay, and **(F)** cycle length. Data represented as mean ± SEM; $n > 8$ independent measurements from one differentiation batch; $^{*}p < 0.05$, $^{****}p < 0.0001$. **(G)** Analysis of gene expression by RT-qPCR of voltage-dependent L-type calcium channel subunit α-1C (CACNA1C). Data represented as mean ± SEM; $n = 3$ independent measurements from one differentiation batch. **(H–J)** Evaluation of metabolic activity and cell viability of the cardiac microtissue (μtissue) after 72-h exposure to doxorubicin or paclitaxel. **(H,I)** Dose–response curve showing the effect of **(H)** doxorubicin and **(I)** paclitaxel on cell metabolic activity measured by the capacity of reduction of Presto-Blue™ Viability Reagent. Values were normalized to metabolic activity of cardiac microtissue before exposure. Data represented as mean ± SEM; $n = 3$ independent measurements from one differentiation batch. **(J)** Representative images of cell viability analysis of cardiac microtissues and hiPSC–CM after 72-h exposure to 10 μM of doxorubicin (Doxo) and 50 μM of paclitaxel (Pacli), stained with fluorescein diacetate (FDA—live cells, green) and propidium iodide (PI—dead cells, red). Scale bar: 200 μm.

washout of ECM and soluble factors (Tostões et al., 2011; Serra et al., 2012; Rebelo et al., 2015, 2018; Estrada et al., 2016); therefore, a microenvironment is generated in which the effect of paracrine interactions between the different cardiac cell types (hiPSC–CM and hiPSC–EC+MC) can be studied. The pore size estimated by AFM (579.6 ± 137.0 nm) seem to support that appropriate diffusion of nutrients and oxygen has occurred, as well as the proper diffusion of the cardiotoxic drugs in the proof-of-concept toxicology study. Additionally, alginate is biomaterial with no animal-derived components, and the combination of AggreWell technology and alginate microencapsulation is compatible with agitated suspension cultures (e.g., shake flasks and bioreactors) and high-throughput screening studies. Furthermore, if required, separation of both cell types (aggregates and single cells) is facilitated by the end of the co-culture period, enabling the study and characterization (e.g., flow cytometry, mass spectrometry, and functional characterization, etc.) of each population individually without the need of adding extra cell dissociation steps that usually compromise cells' viability and quality attributes.

Another main benefit of cell microencapsulation technology is the possibility of designing the scaffold environment with specific biomaterials and/or hydrogels that can be further functionalized to create tailored microenvironments that regulate cell fate decisions, i.e., improved cell viability, expansion/differentiation, and/or functionality. In this study, a mixture of peptide-coupled alginate containing RGD motifs (arginine–glycine–aspartic acid) was used to promote attachment and survival of anchorage-dependent single cells (hiPSC–EC+MC), as previously described for *in vitro* cardiac cell-based models (Shachar et al., 2011). Our designed hydrogel showed to be suitable for the preservation of cell viability and phenotype of all cardiac populations within 15 days of culture. Noteworthy, we showed for the first time evidences of the protective effect of hiPSC–CM on hiPSC–EC+MC survival, similarly to what has been described for *in vivo* cardiac development conditions (Hsieh et al., 2006). Our findings may be related with paracrine factors produced by CM known to be responsible for maintenance of non-myocyte cells viability during *in vivo* cardiac development, namely, VEGF-A, or angiopoietin (Hsieh et al., 2006). In fact, a previous study from our group has identified expression of angiogenic factors (including VEGF) in the secretome hiPSC–CM aggregates (Sebastião et al., 2020). A deeper understanding of how hiPSC–CM communicate with hiPSC–EC+MC will be important not only to develop more physiologically relevant cardiac tissue models but also to design advanced therapies for cardiac regeneration.

The use of a combination of different bioimaging techniques confirmed the organization of sarcomeric structure in hiPSC–CM aggregates as well as the presence of the non-myocyte cellular populations within the alginate capsule of cardiac microtissues at day 15 of culture. Noteworthy, gene expression analysis and ultrastructure characterization of the cardiac microtissues showed that hiPSC–CM displayed improved structural maturation with culture time. This result is aligned with other studies reporting the importance of EC and CF in enhancing the maturation of hiPSC–CM at the structural, functional, and metabolic level. In a recent work, Giacomelli and coworkers identified key mechanisms in the tricellular interactions, involving cAMP/β-adrenergic and cell junction assembly pathways (Giacomelli et al., 2020). In fact, the microencapsulated cardiac microtissues developed herein also showed increased expression of the gap junction protein Cx43.

Other heterotypic communication mechanisms, such as cell–ECM interactions or paracrine effects, have also been shown to impact on the maturation of hiPSC–CM (Fong et al., 2016; Abecasis et al., 2019). Indeed, the alginate microencapsulation supported the remodeling of the cells' microenvironment, namely, the deposition of ECM components, such as collagen IV. However, the observed ECM deposition may have impacted the hiPSC–CM maturation not only directly through cell–ECM communication but also through the changes in the physical properties of the supporting biomaterial. The results from AFM indicated an increase in the elastic modulus when comparing the cardiac microtissue with the hiPSC–CM; which may be related to the observed ECM deposition, concordantly to previous studies with multicellular cardiac patches (Stevens et al., 2009). Overall, the elastic modulus estimated for the cardiac microtissue is within the range of values reported for the human cardiac muscle (10–15 kPa; Mathur et al., 2016; Kofron and Mende, 2017; Dunn and Palecek, 2018). Further optimization of this cardiac microtissue can be evaluated by extending the time in culture to increase microtissue maturation or by improving the complexity/functionalization of the biomaterial used for microencapsulation (Dalheim et al., 2019), as previously studied in other cellular models (Almeida et al., 2017). In the future, a time-resolved analysis of the topographical and physical changes of the cardiac

microtissue would be beneficial for the characterization of the profiles along time and identification of the culture timepoint where a better recapitulation of the human cardiac microenvironment would occur.

The microencapsulated hiPSC–based cardiac microtissues displayed functional calcium signaling, as well as positive response to known cardiotoxins. A recent study using 3D hiPSC–derived cardiac microtissues has reported an IC_{50} 16 μM for doxorubicin (Archer et al., 2018), which is the same magnitude but lower when compared to our results for the hiPSC–CM control (approximately 56 μM). More importantly, our results show that there seems to be a significant difference in the doxorubicin resistance comparing the hiPSC–CM and the cardiac microtissue, because the cardiac microtissue viability was maintained up to 50 μM and only demonstrated a drop at 100 μM (not reaching the IC_{50}). This result might suggest that the co-culture of the different cell types in this configuration contributed to drug resistance, to some extent, although further testing should be performed with additional hiPSC lines. Indeed, a study from Burridge and coauthors showed that patient-specific hiPSC–CM can recapitulate the predilection to doxorubicin-induced cardiotoxicity of individual patients at the cellular level (Burridge et al., 2016), strengthening the importance of genetically diverse hiPSC–derivatives for cardiotoxic studies in future studies. In contrast, the same difference was not observed in paclitaxel exposure, indicating a drug-dependent response. A study from the same group has also generated a "cardiac safety index" to reflect the cardiotoxicities of existing tyrosine kinase inhibitors, using individual populations of hiPSC–CM, hiPSC–EC, and hiPSC–CF (Sharma et al., 2017). Our designed cardiac microtissue may be used to complement these toxicological screenings, enabling the inclusion of the effect of paracrine interaction between the different cellular compartments and may also be applied for pathophysiological studies, similarly to recently published reports incorporating diseased cells (Giacomelli et al., 2020).

In this study, we demonstrated the application of alginate microencapsulation technology for cardiac tissue modeling where the cardiac cell populations were generated using protocols that were reported to ensure high differentiation efficiency and robustness across different hiPSC lines (Giacomelli et al., 2017; Correia et al., 2018). Although we performed two independent differentiation runs with one hiPSC line, additional studies with replicate differentiation batches of multiple hiPSC lines are needed to validate the robustness of the cardiac microtissue model. We believe that this very flexible system can be combined with several other reported hiPSC–CM maturation techniques, such as medium supplementation or biomaterial functionalization (or even by using starting material, which is already in advanced state of maturation) to achieve higher hiPSC–CM functional maturation and recapitulation of cardiac microenvironment. Because our microtissue model focused mainly on the paracrine interaction between the different cardiac cell populations, further studies are needed to understand if direct cell–cell communication would have an impact in the phenotypic and functional features of the cardiac microtissue model. In particular, the extension of the culture time, functionalization of the alginate microcapsule, and/or screening of different hiPSC lines might be evaluated and optimized to promote cell migration and physical interaction between CM and stromal cell. Nevertheless, this study is a step forward on the development of a biologically relevant hiPSC–derived cardiac microtissue that recapitulates features of the human cardiac microenvironment and is compliant with the larger numbers needed for pharmacological screenings.

DATA AVAILABILITY STATEMENT

The raw data supporting the conclusions of this article will be made available by the authors, without undue reservation.

AUTHOR CONTRIBUTIONS

BA, MS, and PA: conception and design. BA, PC, HA, and TC: experimental work. All authors contributed to data analysis and interpretation. BA and HA: manuscript writing. All authors contributed to manuscript revision. MS and PA coordinated the study and approved the final manuscript. All authors contributed to the article and approved the submitted version.

FUNDING

This work was supported by Fundação para a Ciência e Tecnologia (FCT)-funded projects NETDIAMOND (SAICTPAC/0047/2015), MetaCardio (PTDC/BTMSAL/32566/2017), and Neocoronary (PTDC/MEC-CAR/29590/2017); iNOVA4Health, ref. UIDB/04462/2020 and UIDP/04462/2020, a program financially supported by Fundação para a Ciência e Tecnologia/Ministério da Educação e Ciência, through national funds; and EU-funded project BRAV3 (H2020, ID:874827). BA and HVA were supported by FCT Grants SFRH/BD/52475/2013 and SFRH/BPD/120595/2016, respectively.

ACKNOWLEDGMENTS

The authors acknowledge A.L. Sousa and E.M. Tranfield from the Electron Microscopy Facility at the Instituto Gulbenkian de Ciência (IGC) for the technical support in TEM; and G. Martins from the Advanced Imaging Facility at IGC for the technical support in immunofluorescence microscopy.

SUPPLEMENTARY MATERIAL

The Supplementary Material for this article can be found online at: https://www.frontiersin.org/articles/10.3389/fbioe.2020.580744/full#supplementary-material

REFERENCES

Abecasis, B., Aguiar, T., Arnault, É, Costa, R., Gomes-Alves, P., Aspegren, A., et al. (2017). Expansion of 3D human induced pluripotent stem cell aggregates in bioreactors: bioprocess intensification and scaling-up approaches. *J. Biotechnol.* 246, 81–93. doi: 10.1016/j.jbiotec.2017.01.004

Abecasis, B., Gomes-Alves, P., Rosa, S., Gouveia, P. J., Ferreira, L., Serra, M., et al. (2019). Unveiling the molecular crosstalk in a human induced pluripotent stem cell−derived cardiac model. *Biotechnol. Bioeng.* 116, 1245–1252. doi: 10.1002/bit.26929

Almeida, H. V., Sathy, B. N., Dudurych, I., Buckley, C. T., O'Brien, F. J., and Kelly, D. J. (2017). Anisotropic shape-memory alginate scaffolds functionalized with either Type I or Type II collagen for cartilage tissue engineering. *Tissue Eng. Part A* 23, 55–68. doi: 10.1089/ten.TEA.2016.0055

Archer, C. R., Sargeant, R., Basak, J., Pilling, J., Barnes, J. R., and Pointon, A. (2018). Characterization and validation of a human 3D cardiac microtissue for the assessment of changes in cardiac pathology. *Sci. Rep.* 8:10160. doi: 10.1038/s41598-018-28393-y

Bergmann, O., Zdunek, S., Felker, A., Salehpour, M., Alkass, K., Bernard, S., et al. (2015). Dynamics of cell generation and turnover in the human heart. *Cell* 161, 1566–1575. doi: 10.1016/j.cell.2015.05.026

Bovelli, D., Plataniotis, G., and Roila, F. (2010). Cardiotoxicity of chemotherapeutic agents and radiotherapy-related heart disease: ESMO clinical practice guidelines. *Ann. Oncol.* 21(Suppl. 5), v277–v282. doi: 10.1093/annonc/mdq200

Burridge, P. W., Li, Y. F., Matsa, E., Wu, H., Ong, S. G., Sharma, A., et al. (2016). Human induced pluripotent stem cell-derived cardiomyocytes recapitulate the predilection of breast cancer patients to doxorubicin-induced cardiotoxicity. *Nat. Med.* 22, 547–556. doi: 10.1038/nm.4087

Burridge, P. W., Metzler, S. A., Nakayama, K. H., Abilez, O. J., Simmons, C. S., Bruce, M. A., et al. (2014). Multi-cellular interactions sustain long-term contractility of human pluripotent stem cell-derived cardiomyocytes. *Am. J. Transl. Res.* 6, 724–735.

Correia, C., Koshkin, A., Carido, M., Espinha, N., Šariæ, T., Lima, P. A., et al. (2016). Effective hypothermic storage of human pluripotent stem cell-derived cardiomyocytes compatible with global distribution of cells for clinical applications and toxicology testing. *STEM CELLS Transl. Med.* 5, 658–669. doi: 10.5966/sctm.2015-0238

Correia, C., Koshkin, A., Duarte, P., Hu, D., Carido, M., Sebastião, M. J., et al. (2018). 3D aggregate culture improves metabolic maturation of human pluripotent stem cell derived cardiomyocytes. *Biotechnol. Bioeng.* 115, 630–644. doi: 10.1002/bit.26504

Correia, C., Koshkin, A., Duarte, P., Hu, D., Teixeira, A., Domian, I., et al. (2017). Distinct carbon sources affect structural and functional maturation of cardiomyocytes derived from human pluripotent stem cells. *Sci. Rep.* 7:8590. doi: 10.1038/s41598-017-08713-4

Dalheim, M., Omtvedt, L. A., Bjørge, I. M., Akbarzadeh, A., Mano, J. F., Aachmann, F. L., et al. (2019). Mechanical properties of ca-saturated hydrogels with functionalized alginate. *Gels* 5:23. doi: 10.3390/gels5020023

Dunn, K. K., and Palecek, S. P. (2018). Engineering scalable manufacturing of high-quality stem cell-derived cardiomyocytes for cardiac tissue repair. *Front. Med.* 5:110. doi: 10.3389/fmed.2018.00110

Eder, A., Vollert, I., Hansen, A., and Eschenhagen, T. (2016). Human engineered heart tissue as a model system for drug testing. *Adv. Drug Delivery Rev.* 96, 214–224. doi: 10.1016/j.addr.2015.05.010

Estrada, M. F., Rebelo, S. P., Davies, E. J., Pinto, M. T., Pereira, H., Santo, V. E., et al. (2016). Modelling the tumour microenvironment in long-term microencapsulated 3D co-cultures recapitulates phenotypic features of disease progression. *Biomaterials* 78, 50–61. doi: 10.1016/j.biomaterials.2015.11.030

Fong, A. H., Romero-López, M., Heylman, C. M., Keating, M., Tran, D., Sobrino, A., et al. (2016). Three-dimensional adult cardiac extracellular matrix promotes maturation of human induced pluripotent stem cell-derived cardiomyocytes. *Tissue Eng. Part A* 22, 1016–1025. doi: 10.1089/ten.tea.2016.0027

Giacomelli, E., Bellin, M., Sala, L., van Meer, B. J., Tertoolen, L. G. J., Orlova, V. V., et al. (2017). Three-dimensional cardiac microtissues composed of cardiomyocytes and endothelial cells co-differentiated from human pluripotent stem cells. *Development* 144:dev.143438. doi: 10.1242/dev.143438

Giacomelli, E., Meraviglia, V., Campostrini, G., Cochrane, A., Cao, X., van Helden, R. W. J., et al. (2020). Human-iPSC-Derived cardiac stromal cells enhance maturation in 3D cardiac microtissues and reveal non-cardiomyocyte contributions to heart disease. *Cell Stem Cell* 26, 862–879.e11. doi: 10.1016/j.stem.2020.05.004

Green, C. P., Lioe, H., Cleveland, J. P., Proksch, R., Mulvaney, P., and Sader, J. E. (2004). Normal and torsional spring constants of atomic force microscope cantilevers. *Rev. Sci. Instrum.* 75:1988. doi: 10.1063/1.1753100

Hsieh, P. C. H., Davis, M. E., Lisowski, L. K., and Lee, R. T. (2006). Endothelial-cardiomyocyte interactions in cardiac development and repair. *Annu. Rev. Physiol.* 68, 51–66. doi: 10.1146/annurev.physiol.68.040104.124629

Hussain, A., Collins, G., Yip, D., and Cho, C. H. (2013). Functional 3-D cardiac co-culture model using bioactive chitosan nanofiber scaffolds. *Biotechnol. Bioeng.* 110, 637–647. doi: 10.1002/bit.24727

Kofron, C. M., and Mende, U. (2017). *In Vitro* models of the cardiac microenvironment to study myocyte and non-myocyte crosstalk: bioinspired approaches beyond the polystyrene dish. *J. Physiol.* 595, 3891–3905. doi: 10.1113/JP273100

Livak, K. J., and Schmittgen, T. D. (2001). Analysis of relative gene expression data using real-time quantitative PCR and the $2-\Delta\Delta CT$ method. *Methods* 25, 402–408. doi: 10.1006/meth.2001.1262

Masumoto, H., Nakane, T., Tinney, J. P., Yuan, F., Ye, F., Kowalski, W. J., et al. (2016). The myocardial regenerative potential of three-dimensional engineered cardiac tissues composed of multiple human iPS cell-derived cardiovascular cell lineages. *Sci. Rep.* 6:29933. doi: 10.1038/srep29933

Mathur, A., Ma, Z., Loskill, P., Jeeawoody, S., and Healy, K. E. (2016). In vitro cardiac tissue models: current status and future prospects. *Adv. Drug Delivery Rev.* 96, 203–213. doi: 10.1016/j.addr.2015.09.011

Nakane, T., Masumoto, H., Tinney, J. P., Yuan, F., Kowalski, W. J., Ye, F., et al. (2017). Impact of cell composition and geometry on human induced pluripotent stem cells-derived engineered cardiac tissue. *Sci. Rep.* 7:45641. doi: 10.1038/srep45641

Ravenscroft, S. M., Pointon, A., Williams, A. W., Cross, M. J., and Sidaway, J. E. (2016). Cardiac non-myocyte cells show enhanced pharmacological function suggestive of contractile maturity in stem cell derived cardiomyocyte microtissues. *Toxicol. Sci.* 152, 99–112. doi: 10.1093/toxsci/kfw069

Rebelo, S. P., Costa, R., Estrada, M., Shevchenko, V., Brito, C., and Alves, P. M. (2015). HepaRG microencapsulated spheroids in DMSO-free culture: novel culturing approaches for enhanced xenobiotic and biosynthetic metabolism. *Arch. Toxicol.* 89, 1347–1358. doi: 10.1007/s00204-014-1320-9

Rebelo, S. P., Pinto, C., Martins, T. R., Harrer, N., Estrada, M. F., Loza-Alvarez, P., et al. (2018). 3D-3-culture: a tool to unveil macrophage plasticity in the tumour microenvironment. *Biomaterials* 163, 185–197. doi: 10.1016/j.biomaterials.2018.02.030

Sebastião, M. J., Gomes-Alves, P., Reis, I., Sanchez, B., Palacios, I., Serra, M., et al. (2020). Bioreactor-based 3D human myocardial ischemia/reperfusion in vitro model: a novel tool to unveil key paracrine factors upon acute myocardial infarction. *Transl. Res.* 215, 57–74. doi: 10.1016/j.trsl.2019.09.001

Serra, M., Brito, C., Correia, C., and Alves, P. M. (2012). Process engineering of human pluripotent stem cells for clinical application. *Trends Biotechnol.* 30, 350–359. doi: 10.1016/j.tibtech.2012.03.003

Serra, M., Correia, C., Malpique, R., Brito, C., Jensen, J., Bjorquist, P., et al. (2011). Microencapsulation technology: a powerful tool for integrating expansion and cryopreservation of human embryonic stem cells." edited by christina chan. *PLoS One* 6:e23212. doi: 10.1371/journal.pone.0023212

Shachar, M., Tsur-Gang, O., Dvir, T., Leor, J., and Cohen, S. (2011). The effect of immobilized RGD peptide in alginate scaffolds on cardiac tissue engineering. *Acta Biomater.* 7, 152–162. doi: 10.1016/j.actbio.2010.07.034

Sharma, A., Burridge, P. W., McKeithan, W. L., Serrano, R., Shukla, P., Sayed, N., et al. (2017). High-throughput screening of tyrosine kinase inhibitor cardiotoxicity with human induced pluripotent stem cells. *Sci. Transl. Med.* 9:eaaf2584. doi: 10.1126/scitranslmed.aaf2584

Silva, M. M., Rodrigues, A. F., Correia, C., Sousa, M. F. Q., Brito, C., Coroadinha, A. S., et al. (2015). Robust expansion of human pluripotent stem cells: integration of bioprocess design with transcriptomic and metabolomic characterization. *Stem Cells Transl. Med.* 4, 731–742. doi: 10.5966/sctm.2014-0270

Sneddon, I. N. (1965). The relation between load and penetration in the axisymmetric boussinesq problem for a punch of arbitrary profile. *Int. J. Eng. Sci.* 3, 47–57. doi: 10.1016/0020-7225(65)90019-4

Stevens, K. R., Kreutziger, K. L., Dupras, S. K., Korte, F. S., Regnier, M., Muskheli, V., et al. (2009). Physiological function and transplantation of scaffold-free and vascularized human cardiac muscle tissue. *Proc. Natl. Acad. Sci. U.S.A.* 106, 16568–16573. doi: 10.1073/pnas.0908381106

Thavandiran, N., Dubois, N., Mikryukov, A., Massé, S., Beca, B., Simmons, C. A., et al. (2013). Design and formulation of functional pluripotent stem cell-derived cardiac microtissues. *Proc. Natl. Acad. Sci. U.S.A.* 110, E4698–E4707. doi: 10.1073/pnas.1311120110

Tostões, R. M., Leite, S. B., Miranda, J. P., Sousa, M., Wang, D. I. C., Carrondo, M. J. T., et al. (2011). Perfusion of 3D encapsulated hepatocytes–a synergistic effect enhancing long-term functionality in bioreactors. *Biotechnol. Bioeng.* 108, 41–49. doi: 10.1002/bit.22920

Zhou, P., and Pu, W. T. (2016). Recounting cardiac cellular composition. *Circulat. Res.* 118, 368–370. doi: 10.1161/CIRCRESAHA.116.308139

Conflict of Interest: The authors declare that the research was conducted in the absence of any commercial or financial relationships that could be construed as a potential conflict of interest.

frontiers in Bioengineering and Biotechnology

ORIGINAL RESEARCH
published: 09 November 2020
doi: 10.3389/fbioe.2020.580352

The StemCellFactory: A Modular System Integration for Automated Generation and Expansion of Human Induced Pluripotent Stem Cells

*Andreas Elanzew[1,2], Bastian Nießing[3], Daniel Langendoerfer[2], Oliver Rippel[2,3], Tobias Piotrowski[3], Friedrich Schenk[3], Michael Kulik[3], Michael Peitz[1,4], Yannik Breitkreuz[1,2], Sven Jung[3], Paul Wanek[5,6], Laura Stappert[2], Robert H. Schmitt[3,7], Simone Haupt[1,2], Martin Zenke[5,6], Niels König[3] and Oliver Brüstle[1,2]**

[1] Institute of Reconstructive Neurobiology, University of Bonn Medical Faculty and University Hospital Bonn, Bonn, Germany, [2] LIFE&BRAIN GmbH, Cellomics Unit, Bonn, Germany, [3] Fraunhofer Institute for Production Technology, Aachen, Germany, [4] Cell Programming Core Facility, University of Bonn Medical Faculty, Bonn, Germany, [5] Institute for Biomedical Engineering, Cell Biology, Faculty of Medicine, RWTH Aachen University, Aachen, Germany, [6] Helmholtz Institute for Biomedical Engineering, RWTH Aachen University, Aachen, Germany, [7] Laboratory for Machine Tools and Production, RWTH Aachen University, Aachen, Germany

OPEN ACCESS

Edited by:
Tiago G. Fernandes,
University of Lisbon, Portugal

Reviewed by:
Claudia Canelas Miranda,
University of Lisbon, Portugal
Carmel O'Brien,
Commonwealth Scientific and Industrial Research Organisation (CSIRO), Australia

***Correspondence:**
Oliver Brüstle
brustle@uni-bonn.de

Specialty section:
This article was submitted to Bioprocess Engineering, a section of the journal Frontiers in Bioengineering and Biotechnology

Received: 05 July 2020
Accepted: 09 September 2020
Published: 09 November 2020

Citation:
Elanzew A, Nießing B, Langendoerfer D, Rippel O, Piotrowski T, Schenk F, Kulik M, Peitz M, Breitkreuz Y, Jung S, Wanek P, Stappert L, Schmitt RH, Haupt S, Zenke M, König N and Brüstle O (2020) The StemCellFactory: A Modular System Integration for Automated Generation and Expansion of Human Induced Pluripotent Stem Cells. Front. Bioeng. Biotechnol. 8:580352. doi: 10.3389/fbioe.2020.580352

While human induced pluripotent stem cells (hiPSCs) provide novel prospects for disease-modeling, the high phenotypic variability seen across different lines demands usage of large hiPSC cohorts to decipher the impact of individual genetic variants. Thus, a much higher grade of parallelization, and throughput in the production of hiPSCs is needed, which can only be achieved by implementing automated solutions for cell reprogramming, and hiPSC expansion. Here, we describe the StemCellFactory, an automated, modular platform covering the entire process of hiPSC production, ranging from adult human fibroblast expansion, Sendai virus-based reprogramming to automated isolation, and parallel expansion of hiPSC clones. We have developed a feeder-free, Sendai virus-mediated reprogramming protocol suitable for cell culture processing via a robotic liquid handling unit that delivers footprint-free hiPSCs within 3 weeks with state-of-the-art efficiencies. Evolving hiPSC colonies are automatically detected, harvested, and clonally propagated in 24-well plates. In order to ensure high fidelity performance, we have implemented a high-speed microscope for in-process quality control, and image-based confluence measurements for automated dilution ratio calculation. This confluence-based splitting approach enables parallel, and individual expansion of hiPSCs in 24-well plates or scale-up in 6-well plates across at least 10 passages. Automatically expanded hiPSCs exhibit normal growth characteristics, and show sustained expression of the pluripotency associated stem cell marker TRA-1-60 over at least 5 weeks (10 passages). Our set-up enables automated, user-independent expansion of hiPSCs under fully defined conditions, and could be exploited to generate a large number of hiPSC lines for disease modeling, and drug screening at industrial scale, and quality.

Keywords: automation, cell culture, reprogramming, induced pluripotent stem cells, cell production

INTRODUCTION

The advent of the human induced pluripotent stem cells (hiPSCs) technology offers unprecedented opportunities for disease modeling, personalized medicine, and the development of new therapeutic interventions. In particular, hiPSC-based models provide a powerful tool to identify genetic risk factors, and to study cellular and molecular mechanisms that contribute to the pathogenesis of a disease. Driven by the huge potential ascribed to hiPSCs, the field has seen important investment in optimizing the procedures for hiPSC generation, including integration-free approaches for reprogramming factor delivery (Schlaeger et al., 2015) such as mRNAs (Warren et al., 2010) or Sendai virus (Fusaki et al., 2009), to defined adhesion matrices (Brafman et al., 2010; Miyazaki et al., 2012; Rodin et al., 2014) and serum-free cell culture medium formulations (Ludwig et al., 2006; Chen et al., 2011). However, to realize the full potential of hiPSCs for disease modeling and drug screening, several challenges still need to be overcome, as there is the high variability between hiPSC lines, the risk of accumulating genetic aberrations when culturing hiPSCs, and the lack of standardized procedures for hiPSC generation as such (reviewed by Volpato and Webber, 2020). Human iPSCs from different donors are inevitably different, and this inter-individual variability was reported to account for 5–46% of the variation in hiPSCs phenotypes (Carcamo-Orive et al., 2017; Kilpinen et al., 2017). Furthermore, there is also some variability among clones derived from the same donor background (intra-individual variability). This might be due to a number of reasons, including genetic mosaicism of source cells, culture-derived de novo mutations, epigenetic differences caused by erosion of X chromosome inactivation or modulated Polycomb transcriptional repressors (Ji et al., 2012; Young et al., 2012; Carcamo-Orive et al., 2017; Kilpinen et al., 2017; Merkle et al., 2017; D'Antonio et al., 2018; Bar and Benvenisty, 2019). At the same time, the effect size of many genetic disease variants is very small, and a considerable number of hiPSC lines might be required to detect statistically significant and relevant differences between mutant and control lines. Finally, recent advances in genetic studies have led to the discovery of an increasing number of genetic loci that might contribute to the pathogenesis of a single clinical disorder, as has been shown for complex psychiatric or neurodegenerative disorders (Falk et al., 2016; Sullivan and Geschwind, 2019; Diaz-Ortiz and Chen-Plotkin, 2020). In order to be able to assess the functional impact of hundreds of risk variants in human stem cell-based models, the throughput of hiPSCs generation has to be improved. Furthermore, process-related issues such as primary hiPSC clone drop-out (e.g., due to spontaneous differentiation), lack of transgene silencing and acquisition of chromosomal aberrations make it necessary to pre-screen several primary hiPSC clones from the same donor to obtain a high-quality clone suitable for follow-up studies (Shutova et al., 2016). This holds even more true when it comes to generating genetically modified hiPSCs, e.g., in order to establish isogenic mutation-corrected hiPSCs as controls, which demands hiPSC sub-cloning, extensive clonal selection and quality control. The lack of standard protocols for hiPSC generation further adds to the variability among hiPSC lines.

All these challenges create an enormous need for a high degree of parallelization in hiPSC generation, and processing (Falk et al., 2016; Germain and Testa, 2017), a need that can be met by automated cell culture solutions. Indeed, a number of studies have been initiated to develop automated systems for hiPSC generation and cultivation (Conway et al., 2015; Konagaya et al., 2015; Paull et al., 2015; Archibald et al., 2016; Crombie et al., 2017; Daniszewski et al., 2017). Most of these systems focus on distinct cell culture steps, while comprehensive solutions covering all relevant processes for cell culturing are still scarce. This may also be due to the fact that integration of diverse devices into one integrated system and their adaptation to the demands, requires combined expertise from different fields including liquid handling, imaging, hardware and software integration, controlling and – after all – stem cell biology. This especially true for demands, which come with handling highly sensitive stem cell preparations.

Here, we report the development of the StemCellFactory, a modular platform, which automates the reprogramming process and enables parallel derivation and expansion of hiPSCs lines. The current setting employs state-of-the-art cell culture techniques for optimal automated reprogramming of human fibroblasts (HF), clonal isolation and deposition of the emerging hiPSCs as well as parallel, multiclonal expansion in 24-well-multititerplates (24-well plates) and expansion of hiPSCs in 6-well-multititerplates (6-well plates) over 10 passages to generate seed stocks of hiPSC lines. A key advantage of our system is that the hardware and software required for each module (**Figure 1**) can be controlled via a single lead software. In addition, we have implemented high-speed microscopy and deep learning algorithms for in-process control of the hiPSCs.

MATERIALS AND METHODS

Human Pluripotent Stem Cell Culture

Human iPSC expansion experiments were performed using either newly generated hiPSC lines derived from HF cells or prior established hiPSC lines iLB-108bf-s3, and iLB-199-bf-s1, $LRRK2^{GS/GS}$ and a gene-corrected counterpart derived thereof (C-$LRRK2^{neo/+}$, Liu et al., 2012). All hiPSCs were maintained under normoxic conditions (37°C, 21% O_2, 5% CO_2) on Geltrex (0.4 mg/ml in DMEM/F12) in modified E8 medium (Chen et al., 2011): 500 ml DMEM/F-12 HEPES (Thermo Fisher), 50 μg bFGF (PeproTec), 2 μg TGFβ1 (PeproTec), 50 μg heparin, 5.4 mg transferrin, 271.5 mg sodium bicarbonate, 7 μg sodium selenite, 32 mg L-ascorbic acid 2-phosphate, 9.7 mg insulin (all from Sigma-Aldrich). Human iPSCs were cultured in NUNC 6-well plates and daily media changes were performed (2 ml/well). Cultures were passaged as small cell clumps in the presence of 10 μM ROCK inhibitor (RI; Y-27632, Merck) using 0.5 μM EDTA in PBS for cell detachment.

Human Fibroblast Culture

Human fibroblasts were grown in T75 flask in 12 ml MEF medium (DMEM high glucose, FBS 10%, sodium pyruvate 1%, none essential amino acid 1%, L-glutamine 1%, all from Thermo

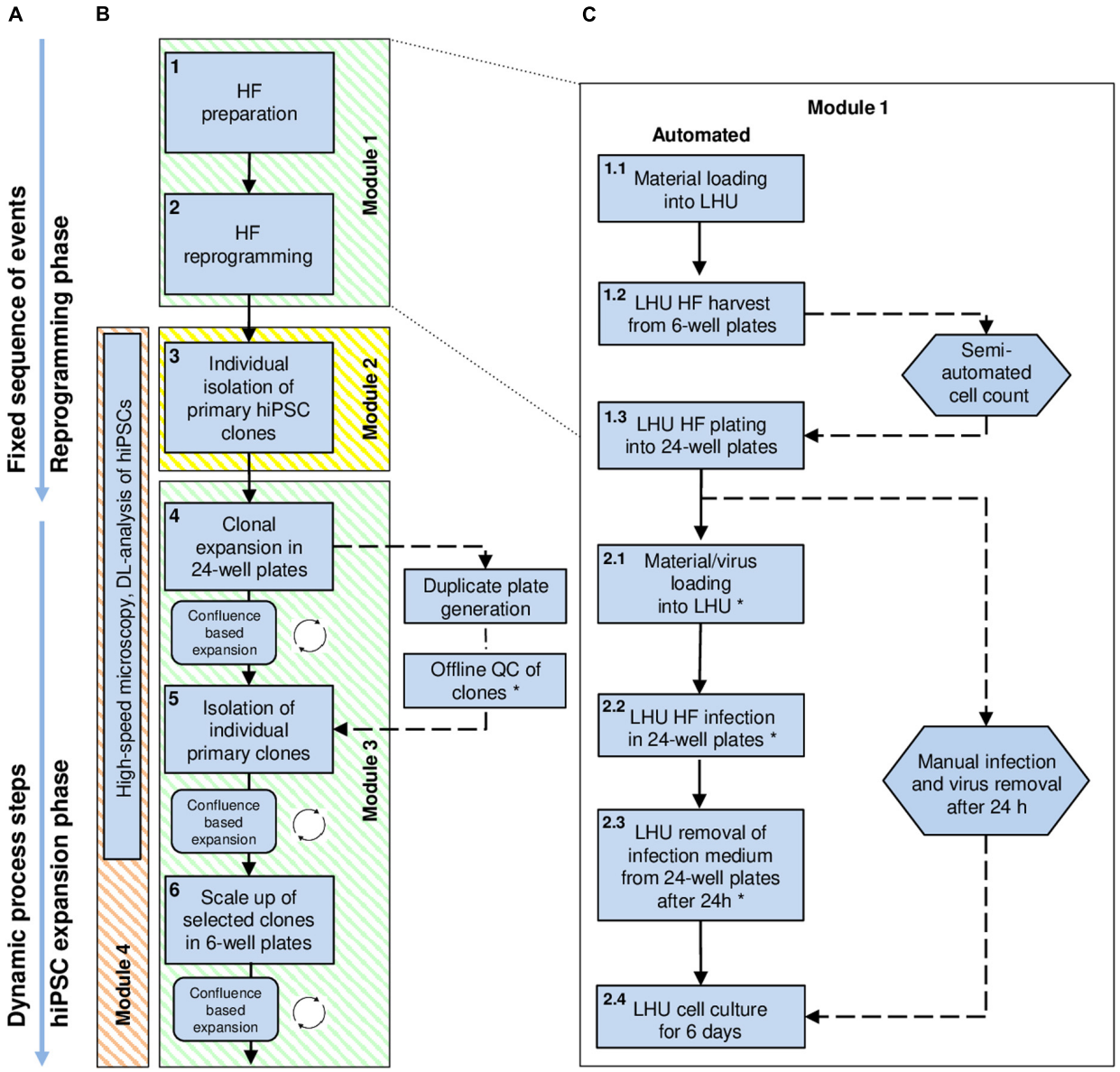

FIGURE 1 | High-level workflow chart for automated reprogramming of human skin fibroblasts (HF) into hiPSCs using the StemCellFactory. **(A)** The process of hiPSC generation can be divided into two phases: (i) the initial reprogramming phase following a fixed sequence and (ii) the dynamic phase of hiPSC expansion. **(B)** Blue square boxes represent individual protocol steps embedded in the automation process. They are numbered, arranged in consecutive order, and grouped into distinct modules. Modules 1 and 3 (green) are running on the LHU. Module 2 (yellow) is performed using the CellCelector, and Module 4 (orange) by the upgraded high-speed microscope (Nikon). **(C)** Detailed protocol steps developed for the reprogramming of HF (Module 1, protocol steps 1 and 2). Straight arrows: consecutively executed steps; circular arrows: repetitive steps; dashed arrows: steps performed manually outside the StemCellFactory; Hexagon shapes indicate steps involving manual handling. Steps marked with an asterisk are automated but can also be performed manually, depending on the biosafety classification of the laboratory environment. DL, Deep-learning; HF, Human fibroblasts; LHU, Liquid handling unit.

Fisher) medium under normoxic conditions (37°C, 21% O_2, 5% CO_2). HF cells were harvested by removing the medium, washing with 10 ml of PBS, adding 6 ml trypsin 1× (Trypsin EDTA Solution, Thermo Fisher) followed by incubation for 5 min at 37°C. Following neutralization with 10 ml MEF medium, cells were centrifuged at 285 *g* for 5 min. The supernatant was removed, cells were resuspended in 5 ml MEF medium and a desired fraction of cells was plated on a new T75 flask or for later transfer onto the StemCellFactory on 6-well plates. In either case the medium was changed every other day.

Automated Geltrex Coating

To prepare the Geltrex coating, the stock solution of Geltrex (12–18 mg/ml, (Thermo Fisher)) was gently thawed on ice at 4°C overnight. Geltrex working solution of 0.4 mg/ml in 4°C cold DMEM/F12 (Thermo Fisher) was prepared in a 50 ml tube

and introduced into the StemCellFactory. 6- or 24-well plates were automatically coated by adding 1000 or 300 µl of the Geltrex solution, respectively. Coated plates were incubated at RT for 1 h before use.

Technical Set-Up of the Automated hiPSC Cultivation Platform "StemCellFactory"

We developed a system integration consisting of more than 30 active instruments, to provide automation solutions for hiPSC generation and expansion (**Figure 2A**). Cultured cells are maintained under normoxic conditions (37°C, 21% O_2, 5% CO_2) in two automated incubators featuring automated plate loading/unloading, 440 multititerplate (MTP) storage positions and user defined environmental control options (STX500-SA and STX44 (for optional O_2 control), LiCONiC Services). A robotic unit (KR 5 sixx 850 CR, KUKA AG) is used for material transport. All hardware was assigned with defined designators and material specific storage capacity numbers. A digital material tracing/storage communication framework was implemented to control and document material flow through the different hardware designations. The liquid handling unit (LHU) used for all media operations is a MicroLAB STAR (Star line, Hamilton Robotics) equipped with four 1000 µl channels and four 5 ml channels, 2 carriers with 10 rags for tip storage (6 rags for 1 ml pipet tips (1 rag = 96 tips) and 4 rags for 5 ml pipet tips (1 rag = 48 tips)), 4 separate/individual MTP tilt modules, 8 lid parking positions, 3 media lines, 1 active waste station, 1 heating or cooling station for 12 50 ml tubes, 1 heater shaker for MTPs and 1 plate presenter (switching between portrait to landscape orientation for the LHU deck layout operations). Protocols for individual cell culture operations were designed in Hamilton's own VENUS software (Version 3). Additional integrated devices include a plate reader for absorption-based detection of contaminations (BMG FLUOstar OPTIMA, BMG Labtech), a centrifuge (Sigma 4-16K, Sigma), a clone picker for automated clonal isolation and deposition of primary hiPSC clones (AVISO CellCelector, ALS GmbH), an in-house developed high-speed microscope for daily image acquisition and cell confluence determination (Nikon, TI-E, Märzhäuser TANGO 4 plus Aux I/O option, SCANplus IM 130 × 85, Gardasoft RT220F-20, Märzhäuser LED 100, PCO pco.edge 5.5, nPoint Z300 with LC.400, interferometric focus measurement device, Nikon and Fraunhofer IPT), a decapper station for opening and closing of 50 ml tubes (proprietary technology of Fraunhofer IPT) and a material gate for introduction and storage of 50 ml tubes, 6- and 24-well plates, 1 and 5 ml tips and other consumables (proprietary technology of Fraunhofer IPT). The entire set-up is encased in a custom-made laminar flow system equipped with pre- and exhaust filters (HEPA-H14) operating at an airflow of 1440 m^3/h (Goller Reinraumtechnik GmbH), (**Figure 2B** and **Supplementary Movie 1**). The overall control level software is proprietary technology developed by the Fraunhofer IPT and customized for controlling, monitoring, tracking and operating the StemCellFactory.

Automated Communication Interface and Data/Material Management

To manage the system integration platform, Fraunhofer IPT developed a control software, which enables execution of commands, creation of process flows, data handling and visualization of collected data (**Figure 3**). The measurement data and the material data are written into a specific SQL database, which permanently saves the current situation as well any historical data. The required hardware devices use heterogeneous protocols like open platform communication unified architectures (OPC-UA), different programmable logic controller (PLC) software (like Beckhoff or Siemens), associated software developments kits (SDK) or other protocols to communicate with external programs. To embed all these different communication protocols, a middleware or so-called software agent was developed for every device. These software agents communicate to the control software via a standardized interface (TCP/IP-based) and translate the commands from the control software to the specific protocols of the devices. This agent-based architecture makes it possible to add a new device to the StemCellFactory just by changing or reprogramming a software agent. A change or extension of the hardware does not affect the control software. By using this adaptive system of individual software agents, it is possible to homogenize a heterogeneous device landscape with many different interfaces in a single control software. This way the user has to operate only one single software, and the extension of the hardware is possible with little programming effort.

Reprogramming of Human Fibroblasts

Reprogramming experiments were performed using HF derived from three male donors with age 4, 30, and 34. To initiate the reprogramming process, HF cells were first automatically harvested from 6-well plates using the LHU for all pipetting steps including medium removal, 2× washing with 4 ml of PBS per well of a 6-well plate and addition of 1 ml trypsin 1× (Trypsin EDTA Solution, Thermo Fisher), followed by incubation for 5 min at 37°C. Subsequently, cells were recovered by adding 5 ml of MEF medium (DMEM high glucose, FBS 10%, sodium pyruvate 1%, none essential amino acid 1%, L-glutamine 1%, all from Thermo Fisher), aspirated and transferred to an empty 50 ml centrifuge tube. Additional 4 ml of MEF medium was added to the well and pooled into the same tube to wash-off any remaining cells. The tube was automatically retrieved from the LHU, closed, transferred to the centrifuge and spun for 3 min at 1200 rpm (Sigma 4-16K) at RT. Subsequently, the tube was retrieved, opened, transported back to the LHU to aspirate and discard the supernatant. Then, the cell pellet was resuspended, a sample taken manually, and the cells were semi-automatically counted using the Cedex analyzer (Roche). The cell suspension was adjusted to a concentration of 80,000 cells/ml in 1 ml MEF medium, and cells were automatically seeded in individual wells of a 24-well plates. The next day, Sendai virus infection was conducted outside the StemCellFactory by adding 250 µl of the infection medium, i.e., advanced 94% DMEM/F-12, 5% FCS, 1% L-glutamine, and CytoTune-iPS 2.0

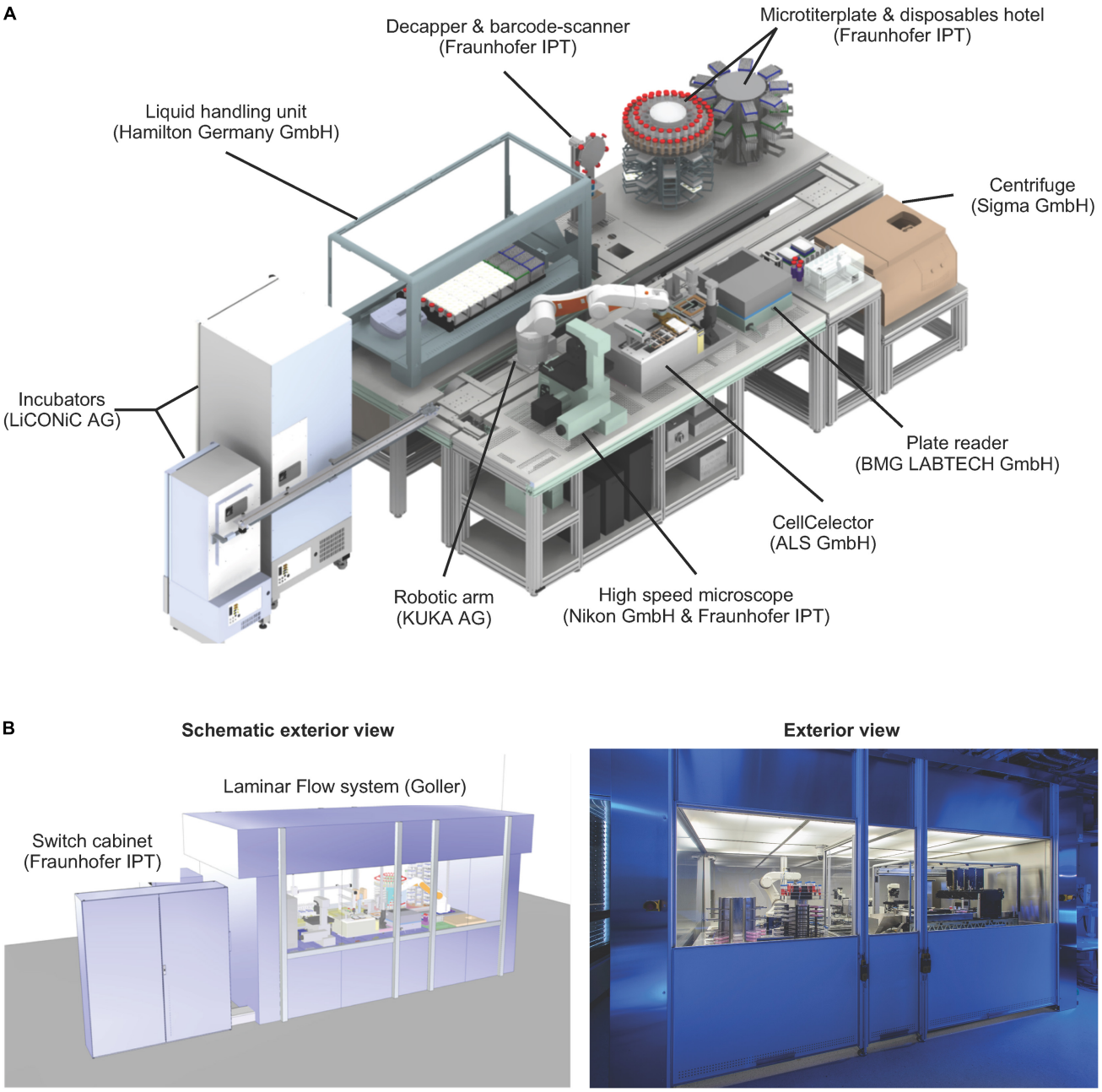

FIGURE 2 | Technical set-up of the StemCellFactory. **(A)** The platform includes a liquid handling unit, automated incubators, a robotic arm, a microscope, a clone picker, a plate reader, a centrifuge and a microtiter plate & disposable hotel. All units are functionally joined for culturing/reprogramming of human fibroblasts, selection of primary hiPSC clones and expansion of hiPSC lines. The manufacturer of each instrument is indicated in brackets. **(B)** The entire unit is encased in a clean room cabinet.

vectors (Thermo Fisher): polycistronic KLF4-OCT4-SOX2, MOI: 5; MYC, MOI: 5 and KLF4, MOI:1. In some cases, virus was diluted to titrate the optimal virus concentration per number of plated HF cells. The following day, cells were washed 2× with 1 ml of PBS, followed by addition of reprogramming medium (94% Advanced DMEM/F-12, 5% FCS 5% and 1% L-glutamine, all from Thermo Fisher), after which the cells were transported back to the StemCellFactory. From here on all steps are performed automatically. During the next 5 days, daily media changes with 500 µl of medium were performed. At day 7 after infection, wells were re-seeded into 6-well plates coated with Geltrex (Thermo Fisher) at a density of 20,000 cells per well. The detachment of cells is similar to the steps described above, however, a 0.5× trypsin solution was used. From this point on, cells were incubated using E7 medium (E8 medium lacking TGFβ1) with daily media changes until primary hiPSC colonies

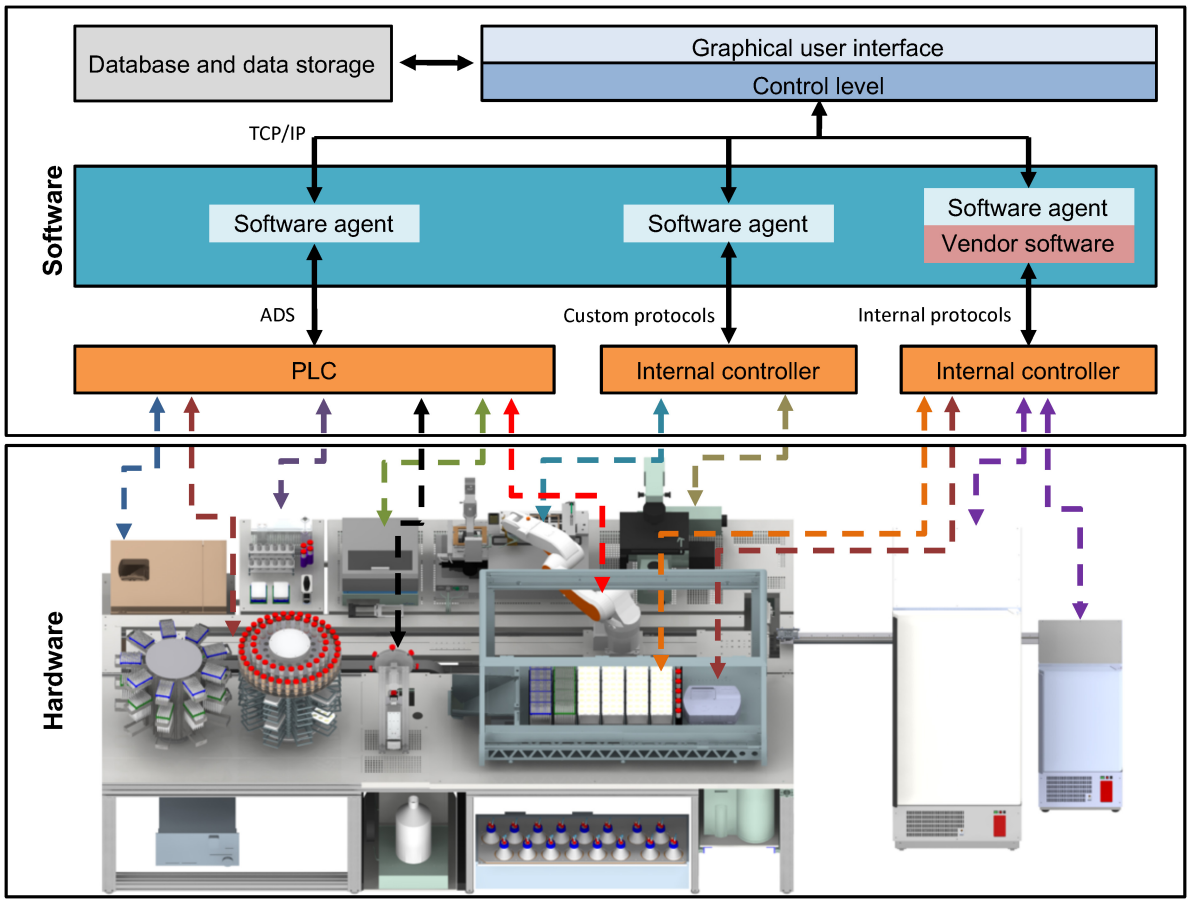

FIGURE 3 | Functional interconnection of hard- and software. All hardware devices of the StemCellFactory are functionally embedded in a control software system (upper box). The lower box displays the diverse hardware, which is controlled by a variety of different controllers and interfaces. The centrifuge, the robotic arm and the plate reader communicate using PLC/ADS systems. Other hardware such as the LHU, incubators or the microscope use other internal control systems. The software system comprises an integration framework, which serves as middleware and employs software agents to link in the different hardware components. Consequently, all connections merge in one control system by using standard TCP/IP protocols. The control system is linked to a database. PLC, Programmable Logic Controller, ADS, Accelerator Driven System, TCP/IP, Transmission Control Protocol/Internet Protocol, LHU, Liquid handling unit.

emerged. Around day 21, automated picking of primary hiPSCs clones was performed using the CellCelector system (see below).

Automated Clonal Isolation of Primary hiPSC Clones

Source 6-well plate, target 24-well plate, CellCelector (CC) tray, and CC empty tray were automatically loaded onto the CellCelector. The CC generates automated whole well overview images by applying the autofocus function at 12 evenly distributed points inside the source well, moving at a speed of 6% of max speed using a horizontal-comb traversing pathway and a pausing interval of 500 ms before image acquisition. Primary clones were either automatically identified by adjusting a specific threshold gray value range of 85–285 of the CCD camera or manually selected by the user. In either case, a picking list was generated. The pick-up position of the source plate was at 40.27 mm (6-well plates from NUNC). Primary hiPSC clones were first detached by scraping using individual 500 µm diameter scrape capillaries (with a crosswise movement at a speed of 2% of max speed and a distance of 550 µm), and then aspirated into the scrape capillaries (with an aspiration volume of 28 µl and using 27% aspiration speed of max speed during an upward movement of 900 µm distance). The process cycle was concluded with the dispensing of the isolated cell fragment into the target 24-well plate well. The target wells were coated with Geltrex and prefilled with 0.5 ml of E8 medium as previously described. Images were acquired automatically before and after cell isolation. Only wells loaded with cells were further processed. Medium was replaced daily by automatically exchanging 0.5 ml, and hiPSCs were passaged on day 5 (see **Supplementary Movie 2**).

Automated Confluence-Based Passaging of hiPSCs

For cell detachment, source wells were washed 2× with 4 ml of PBS per well of a 6-well plate followed by the addition of 1000 µl of 0.5 µm EDTA and incubation for 10 min at RT. Subsequently,

cells were detached by shaking the 6-well plate at 2000 rpm for 10 s on the heat shaker module of the LHU. Next, cells were washed down by addition of 4 ml of E8 medium in order to inactivate the EDTA. The whole suspension was transferred to an empty 50 ml tube and the respective wells were once more washed with 2 ml E8 medium, followed by pooling of both harvests. Geltrex was aspirated from the target wells and replaced by E8 media minus the calculated cell suspension volume (final volume 1.5 ml). All media were supplemented with 10 μM RI. The medium was replaced daily by automatically exchanging 1.5 ml, and the hiPSCs were passaged regularly every 3–4 days.

Confluence-based expansion of hiPSCs in 6-well plates employs measured confluence values for the subsequent expansion. Confluence values were acquired using the CellaVista (see below) and saved in the MTP specific barcoded folder as respective CSV files. The CSV file was read by the LHU program (Venus 3) and internally used to calculate the maximally possible dilution ratio, which was translated into respective liquid volumes (cell suspension volume and media volume) used for transferring the cell suspension to the target MTP wells.

The confluence-based passaging in 24-well plates follows the same workflow as described above with adapted suspension volumes to account for the maximum allowed volume of 1 ml per well. If the confluence was ≤10%, a 1:1 passaging was performed transferring the entire volume of the source well to one mirror target well. In such a case no duplicate plates were generated.

Automated High-Speed, Deep-Learning Microscopy

The basic Nikon Ti-E microscope was further upgraded with additional hardware in order to provide a fast acquisition mode for high speed imaging of MTPs (Schenk et al., 2015). In short, imaging of the CMOS high speed camera (pco.edge, Germany) was synchronized with stroboscopic LED flashing and the continuous movement of the stage (Märzhäuser Wetzlar, Germany). The images are evaluated (confluence and/or colony morphology, topology) by a trained deep learning algorithm, based on the Caffe deep-learning framework (Berkeley AI Research, Berkley, CA, United States) and the U-Net architecture, for the various predefined classes (hiPSCs, background, differentiated cells and dead cells), (Rippel et al., Unpublished).

Confluence Measurement Using a Reference Device

Cell culture confluence was measured by bright field imaging using the Cellavista® system (SynenTec) outside the StemCellFactory. This was done by measuring the area covered by cell bodies in relation to whole well area using the manufacturers pre-set cell confluence 4× magnification protocol.

Flow Cytometry

For quality check, hiPSCs were harvested using Accutase (Thermo Fisher, 1 mg/ml). In short, medium was removed and cells were incubated with Accutase for 10 min at 37°C and 5% CO_2. Cells were washed down and resuspended with an appropriate volume of PBS, pelleted for 3 min at 1200 rpm (Centrifuge 5702) at RT and resuspended in PBS. Samples were stained with monoclonal mouse IgM TRA-1-60 (Merck Millipore, Billerica, MA, United States, 1:1000) antibody and goat anti-mouse IgG Alexa 488 (Thermo Fisher; 1:1000) as secondary antibody. Analysis was performed on a FACS Calibur™ analytic flow cytometer (BD Bioscience). Data were analyzed and arranged using FlowJo Analysis Software (Tree Star Inc.).

Sendai Virus Detection

Total RNA was extracted using the semiautomated Maxwell® RSC System (Promega) and transcribed into cDNA using the qScript cDNA synthesis kit following manufacturer's instructions. 1 μg of cDNA was used for PCR analysis. The PCR conditions were as follows: 1 min at 95°C, 30 s at 95°C, 30 s at 60°C, 1 min at 72°C (40 cycles), 5 min at 72°C using Pan Sendai virus Primers (For: GGATCACTAGGTGATATCGAGC, Rev: ACCAGACAAGAGTTTAAGAGATATGTATC). Agarose gel electrophoresis was used to detect PCR products.

Epi-Pluri-Score Analysis

This epigenetic pluripotency biomarker assay was performed by Cygenia[1] and is based on DNA methylation (DNAm) levels at three specific CpG sites: The Epi-Pluri-Score combines genomic DNA methylation levels at the two CpG sites ANKRD46 and C14orf115, defined as: β-value [ANKRD46] – β-value [C14orf115]. A positive Epi-Pluri-Score indicates pluripotency (Lenz et al., 2015). The third CpG site is located within the pluripotency gene POU5F1 (OCT4) and demarcates early differentiation events.

SNP Analysis

SNP analyses were performed at the Institute of Human Genetics, University Hospital Bonn, Germany, using the PsychArray-24 v1.1 BeadChip (Illumina) and GenomeStudio (Illumina) for the analysis.

RESULTS

Modular Design for Automated hiPSC Production

The StemCellFactory concept aims at providing an automated, modular platform for automated generation and expansion of hiPSCs (**Supplementary Movie 1**). We decided to use HF cells as source cells, Sendai virus technology (Fusaki et al., 2009) for integration-free delivery of the reprogramming factors (OCT4, SOX2, KLF4, c-MYC; Takahashi et al., 2007) and conventional MTPs for adherent cell culturing. The hiPSC generation process can be divided into two phases and further subdivided into three series-connected modules (**Figure 1**). First is the reprogramming phase, which includes HF preparation and Sendai virus infection as well as the derivation of primary hiPSC clones (Module 1). This phase is characterized by a linear

[1]http://www.cygenia.com/

execution of each protocol at its distinct time point. The second phase comprises isolation and deposition of nascent hiPSC clones (Module 2) as well as expansion of hiPSCs to generate seed stocks (Module 3). This phase is defined by a dynamic growth characteristic of hiPSCs, which requires a situative cell culture passaging method (**Figure 1A**). We have also included an optional module for in-process control via image analysis (Module 4). For each of the modules, we have devised automated processes. The robotic instruments required for each module were integrated in one platform, which we have designated as StemCellFactory (**Figure 2**).

A central component of the StemCellFactory is the Microlab STAR LHU from Hamilton, which was coupled to two automated incubators from LiCONiC (STX400 and STX44) and a centrifuge (4-16K centrifuge from Sigma) to perform all necessary cell culture steps. For automated primary hiPSC isolation and deposition, a cell isolation system was implemented (CellCelector, ALS). For daily image acquisition, an automated high-speed microscopy system was implemented. This set-up is based on stroboscopic flash image acquisition, capturing entire MTPs at 4× and 10× magnification in less than 3 min (Nikon and Fraunhofer IPT; Schenk et al., 2015). Moreover, a plate reader (BMG Labtech) for regular turbidity measurements to detect bacterial contamination was installed. The entire set-up is encased in a custom-made laminar flow system measuring 6.4 m in length, 2.6 m in width and 2.75 m in height to provide sterile working conditions. The robotic KR 5 sixx arm (KUKA AG) is arranged on a horizontal axis for material transportation across the entire platform and connects individual modules. Each protocol used on the respective device was developed in stand-alone mode using the device-specific software. All hardware devices are functionally joined and integrated into a control system, which orchestrates process execution and data handling (**Figure 3**). Each device has its local software agent, which serves as middleware and abstracts the hardware heterogeneity. The local information and functionality from the individual devices are processed through the middleware up to the higher-level of the control system, and the user only operates one software executing control over the entire system.

Module 1: Automated Cultivation and Reprogramming of Human Fibroblasts

The initial quality of source cell material is key for obtaining high-quality hiPSCs. Therefore, we first invested in establishing protocols for automatic HF cell expansion (Module 1, process step 1, **Figure 1**) by comparing the performance of automated versus manual handling. To that end, HF cells were propagated in 6-well plates using either our automatic set-up or manual processing with daily media changes and cell growth monitoring. Automatically expanded HF cells showed no deviation in cell numbers from their manually processed counterparts (**Figures 4A,B**). The second process step encompasses preparation of HF cells for automated reprogramming. This involves transfer of HF cells from 6-well plates to 24-well plates, delivery of Sendai virus for reprogramming, aspiration of viral particle containing supernatant and culturing of HF cells for 6 days (**Figure 1C**). For automated HF cell passaging a standard enzymatic reaction was used resulting in an average detachment of 96.6 ± 1.6% of HF cells from a 6-well plate and 90.3 ± 50% from a 24-well plate (**Figures 4C,D**). Replating for subsequent viral infection was adjusted to 80,000 HF. The viability remained at a high level with 89 ± 3.90% in 6-well plates and 96.9 ± 2.7% in 24-well plates (**Figure 4E**). Plating cell density is a crucial parameter for several protocol steps including, e.g., preparation for viral infection and post-infection clone selection. Indeed, more accurate and precise pipetting of defined cell numbers is achieved using the employed LHU as compared to manual processing (**Supplementary Figure 1**).

To develop a protocol suitable for efficient reprogramming of HF cells into hiPSCs (Module 1, process step 2, **Figure 1B**), we first tested different culture parameters, which we expected to be critical for derivation of primary reprogrammed clones, e.g., cell adhesion matrix, Sendai virus titer and the initial number of plated HFs to allow clonal expansion of emerging hiPSCs. We used a commercially available Sendai virus system consisting of a combination of poly- and monocistronic vectors (CytoTune-iPS 2.0 Reprogramming Kit, Thermo Fisher). All experiments were done using Geltrex as the adhesion matrix. We found that re-plating HF cells at day 6 after Sendai virus infection at a density of 20,000 cells per well of a 6-well plate provided optimal conditions for hiPSC clone formation. Employing this scheme, primary clones from three different HF lines from three independent donors could be derived within 21 days (**Figure 5A**) with an average yield of 40 clones per well of a 6-well plate and a reprogramming efficiency ranging between 0.6 and 0.8% (**Figures 5B,C**). The efficiency of our automated reprogramming process is comparable to reprogramming efficiencies reported by the manufacturer (≈1% for CytoTune-iPS 2.0 Reprogramming Kit, Thermo Fisher) and sufficient for subsequent automated isolation of primary hiPSC clones.

Module 2: Clonal Isolation of Primary hiPSC Clones

We next focused on setting-up a procedure for the automated, individual isolation of primary hiPSCs clones from 6-well plates and their clonal deposition into 24-well plates (Module 2, process step 3, **Figure 1B**). To that end, we integrated the CellCelector system from ALS into our StemCellFactory and established protocols for automated detachment of cell colonies, their transfer/deposition, and imaging-based quality control (**Supplementary Movie 2**).

For each clone an individual capillary is used for detachment and transfer in order to eliminate cross contamination. Moreover, each clone is automatically imaged before and after the isolation to validate successful detachment of the selected clone (**Figures 6A,B**). We thoroughly analyzed the efficiency of each step (detachment, transfer to target well and attachment of the retrieved colonies). While mean detachment and transfer rates were >95% for both manual and automated handling, the re-attachment of harvested clones was higher in the automated mode (automated: 94.8 ± 0.2% vs. manual: 65.0 ± 2.1%), indicating that the automated process is highly efficient

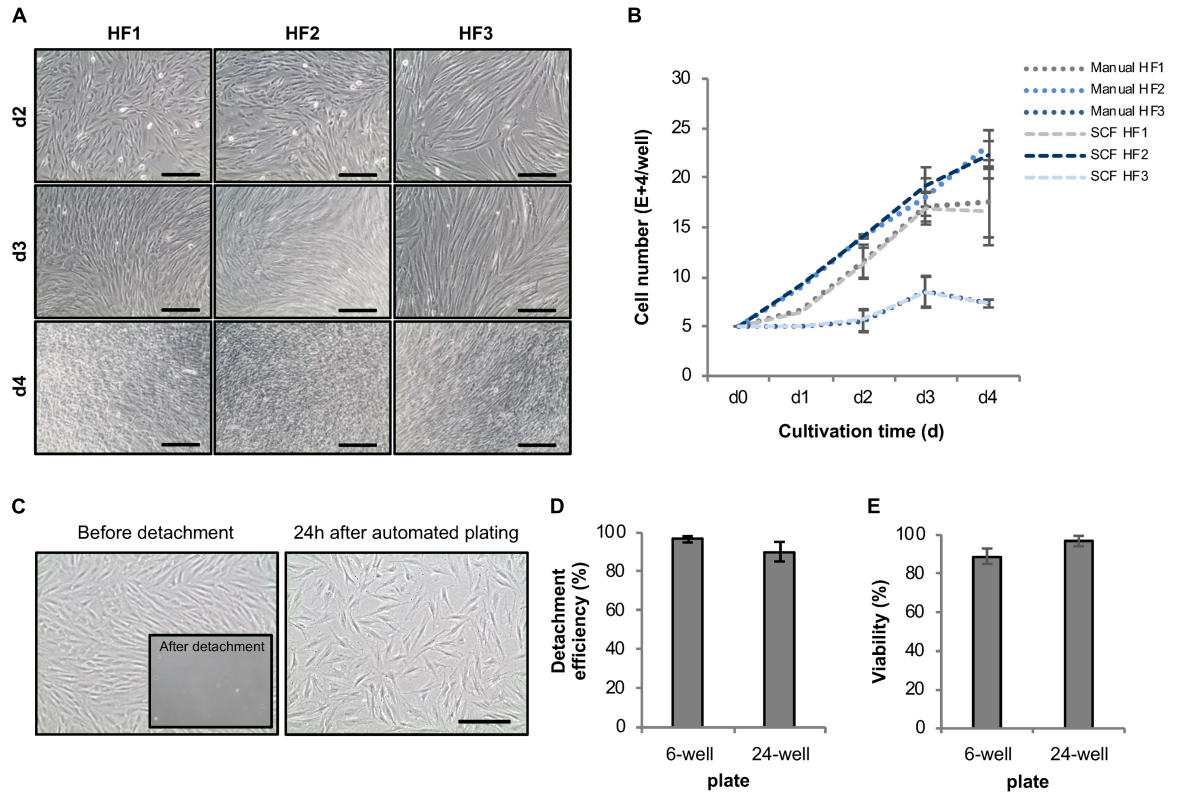

FIGURE 4 | Development of an automated expansion and plating protocol for human fibroblasts. **(A)** Representative phase-contrast images of different HF lines automatically cultivated in 6-well plates using the StemCellFactory. **(B)** Average cell number of automatically vs. manually cultivated human fibroblast lines over the duration of 4 days (mean ± SD; *n* = 3). **(C)** Representative phase-contrast images of HF cells before and after enzyme-based, automated detachment and one day after automated re-plating of 80,000 HF (sub-confluence density) cells into a well of a 24-well plate. **(D)** Mean detachment efficiency was determined by quantifying the amount of cell retrieved by automated detachment versus the number of cells remaining on the plate and collected by subsequent manual detachment [6-well plates, mean ± SD (*n* = 4); 24-well plates, mean ± SD (*n* = 5)]. **(E)** Cell viability of detached cells was determined via trypan blue staining [6-well plates, mean ± SD (*n* = 6); 24-well plates, mean ± SD (*n* = 5)]. SD, standard deviation; SCF, StemCellFactory; HF, human fibroblasts. Scale bar = 200 μm.

(**Figure 6C**). Using this process, clones for stocking a full 24-well plate were automatically processed in less than 10 min without any user interference (**Figure 6D**). First passaging of the retrieved clones was performed at day 5 after plating using EDTA-based splitting at a 1:1 ratio.

Module 3: Parallel Expansion of Primary hiPSC Clones and Establishment of Transgene-Free hiPSC Lines

In order to eliminate Sendai viral vectors, hiPSCs have to be propagated across several passages. Commonly, hiPSCs are split every third or fourth day whereby the experimenter usually decides based on cell layer confluence or cell counting at what ratio the cells are re-plated into daughter wells. On the one hand, hiPSC cultures should only be propagated until 80% confluency to avoid spontaneous differentiation. On the other hand, unnecessary splitting and too low cell density should be avoided not only for economic reasons, but also to avoid undue selection pressure. We aimed at implementing an unbiased method to automatically determine the dilution ratio based on easy measurable cell confluence values as a proxy for the total cell number per well (**Figure 7A**). At the envisaged day of splitting, cell densities are never completely identical. In order to enable parallel splitting of wells containing different cell numbers, we employed an imaging-based determination of well-specific splitting ratios. Specifically, the system acquires whole-well images via a CellaVista microscopy system (SynenTec, Elmshorn, Germany) and calculates the splitting ratio, with the target re-plating cell density set to 10%. Using this method, we were able to clonally expand primary hiPSC clones in 24-well plates in individual wells for at least 10 passages with only few clones being lost across time (**Figure 7B**). Our data indicate that well-specific confluence-based splitting increases clone survival compared to fixed splitting ratios based e.g., on the highest measured confluence value measured in the entire plate (**Supplementary Figure 2**).

Quality Control of Newly Generated hiPSC Clones

A number of assays were implemented for the quality control of automatically generated hiPSC clones. RT-PCR was employed to confirm Sendai virus elimination. A representative series of RT-PCR analyses conducted at passage 9 revealed successful Sendai virus elimination in 72% of the clones (*n* = 18;

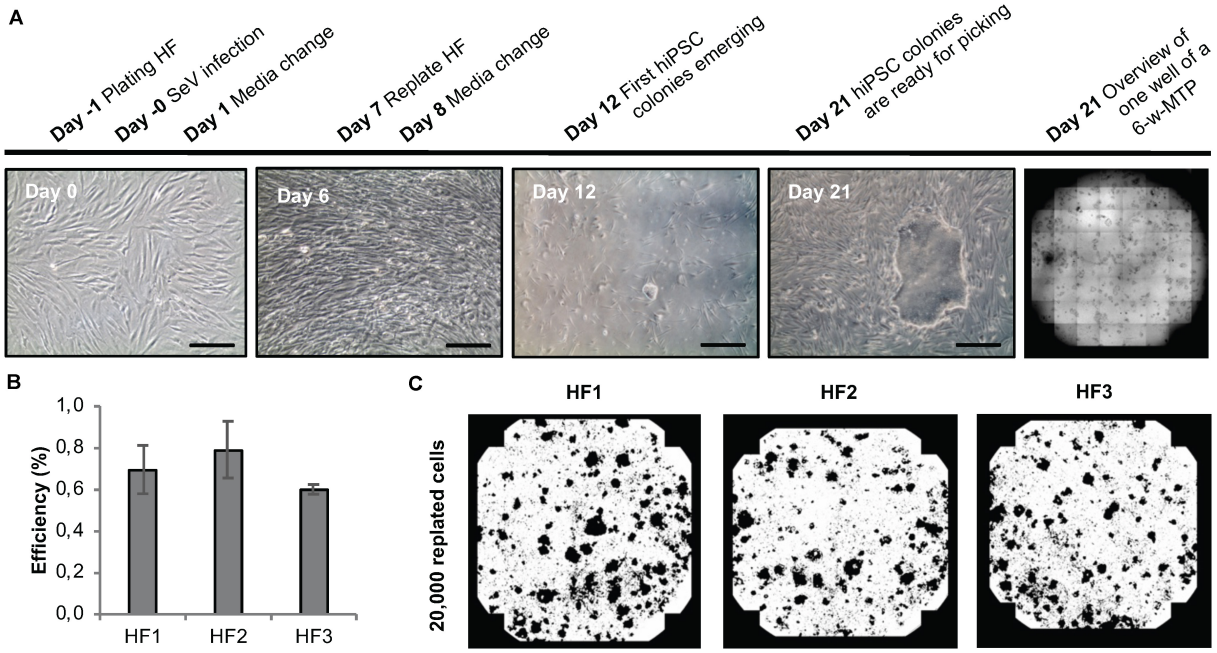

FIGURE 5 | Sendai virus-based reprogramming protocol suitable for automation. **(A)** Reprogramming scheme and emergence of clones. Key time points and processing steps are indicated. **(B)** Reprogramming efficiency assessed 21 days after infection of three different human fibroblast populations. Shown are mean values ± SD (n = 9). **(C)** Representative whole-well binary images of single wells of a 6-well plate at day 21 post infection show cell colonies in black and cell-free areas in white. Scale bars: 100 μm. HF, human fibroblasts.

Figure 7C). Genetic integrity was assessed via high resolution SNP analysis; typically, we use CNV sizes of >0.5 Mb as exclusion criterium. This approach suffices not only to detect stable genomic aberrations but also emergence of de novo alterations due to mosaicism in the starting cell population or reprogramming-associated mutagenesis (see examples in **Supplementary Figure 3A**).

Flow cytometric assessment of TRA-1-60 expression was used for routine analysis of pluripotency; this pluripotency-associated marker was found robustly expressed in newly generated hiPSC clones (**Figure 7D**). As additional option we also used the commercially available epigenetic biomarker assay Epi-Pluri-Score, which enables reliable allocation of tested clones to a pluripotency space defined by differentially methylated CpG sites (Lenz et al., 2015). In a representative series of 5 clones reprogrammed from 2 genetic backgrounds all clones showed beta-values compatible with pluripotency (**Supplementary Figure 3B**).

Confluence-Based Splitting for Scale-Up of hiPSCs

Well-specific confluence-based splitting was not only used for clonal expansion in 24-well plates but also for further upscaling of hiPSCs in 6-well plates (Module 3 process step 6, **Figure 1B**) and evaluated using hiPSC lines from different genetic backgrounds (**Figure 8**). Human iPSCs expanded well across at least 10 consecutive passages and showed continuous and linear growth with only subtle cell line-specific variations (**Figure 8A**). ExpandedhiPSC lines further maintained TRA-1-60 positivity (>90% of the cells; **Figure 8B**) and a typical growth pattern with prominent colony formation (**Figure 8C**). Thus, the established well-specific confluence-based passaging scheme is most suitable for automated expansion of both, newly generated hiPSC clones and established hiPSC lines.

Module 4: Automated High-Speed Microscopy and Deep Learning-Based Image Analysis

For fast image acquisition and analysis of hiPSCs, we integrated a high-speed microscope as optional feature (**Figure 1**, Module 4). This set-up was developed by Schenk et al. (2015) and is based on the acquisition of whole well images during continuous movement of the plate, thereby avoiding the lengthy stop-and-go motion that is typically used for serial images. This is achieved by stroboscopic illumination, which is synchronized with the movement of the microscope table. The focus is maintained by a piezo Z stage, which online synchronizes the Z position with a prior acquired topological focus map of the imaged well (**Supplementary Figure 4** and **Supplementary Movie 3**). A full MTP was scanned in less than 3 min, enabling rapid quality control of the cultured cells (**Supplementary Figure 4D**; for details see Schenk et al., 2015). Furthermore, we established a trained deep learning algorithm for the analysis of the acquired images (**Supplementary Figures 4B,C**). As a training data set, images of hiPSC cultures were used and manually annotated for the respective criteria. The algorithm enables unbiased detection of dead or differentiated cells and other cell culture parameters such as cell free areas and hiPSC colony size (Rippel et al.,

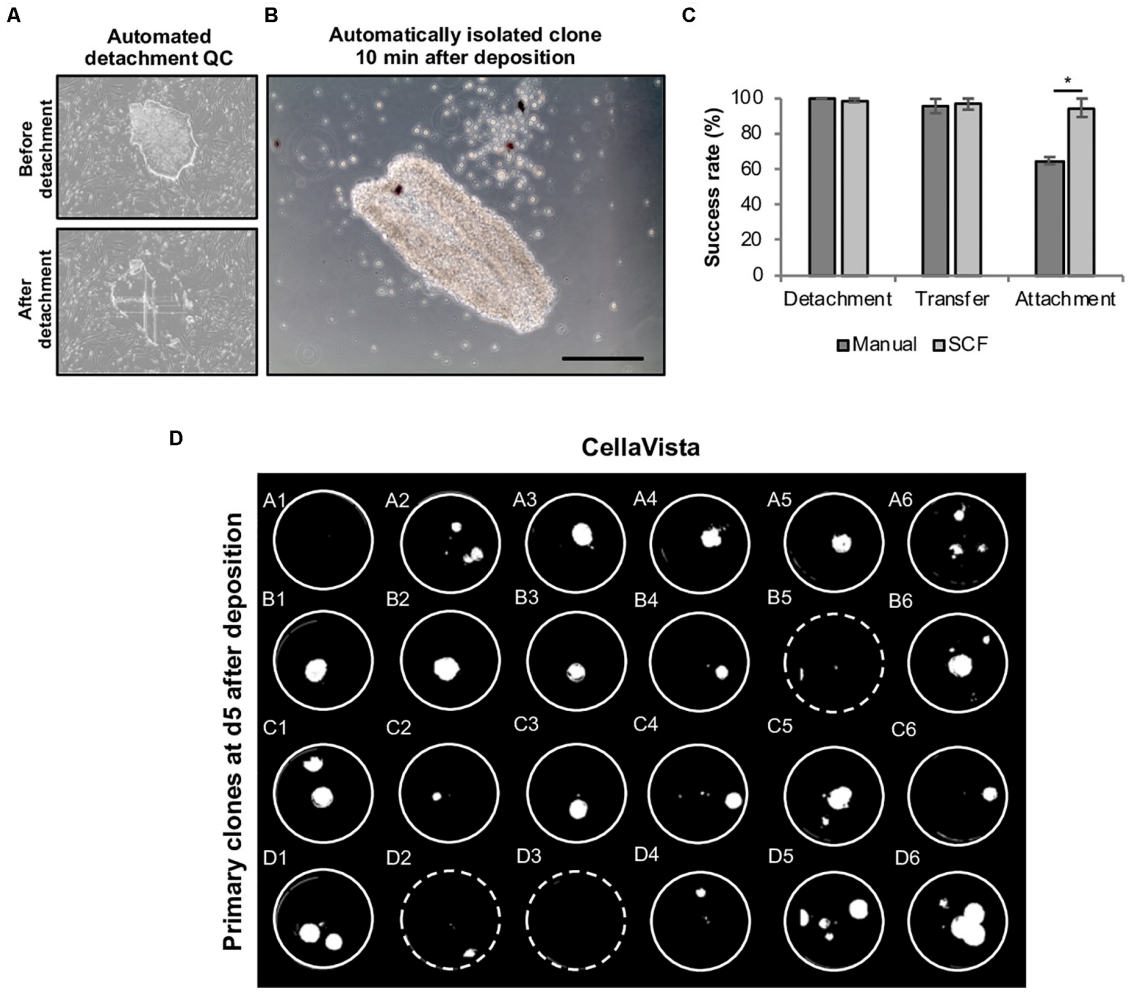

FIGURE 6 | Automated harvesting of primary hiPSC clones using the CellCelector system. Primary colonies were automatically detached and clonally deposited in a 24-well plate. **(A)** Representative images (automatically taken by the CellCelector as a quality control parameter) of primary hiPSC clones before and after automated detachment. **(B)** Representative image of a primary hiPSC clone 10 min after automated clonal deposition. **(C)** Comparative analysis of detachment, transfer and attachment efficiency in manual versus automated processing. Shown are mean values ± SD, $n = 48$ (manual), $n = 96$ (SCF). **(D)** Whole 24-well plate detection of primary clones at day 5 after clonal deposition. Dashed wells contain clones located close to the wall of the wells are thus difficult to visualize. Scale bar: 100 μm. SCF, StemCellFactory. *$p \leq 0.005$ (Unpaired Students *T*-test).

Unpublished). The combination of high-speed live microscopy with automated image analysis facilitates in-process monitoring and sophisticated morphological quality control of automatically processed hiPSCs.

DISCUSSION

While it is commonly accepted that automated cell culture solutions can increase standardization and throughput, to date only a few fully automated facilities exist, and even the mere use of robotic LHUs for culturing hiPSCs, embryonic stem cells and somatic stem cells is still sparse (Marx et al., 2013; Schenk et al., 2015; Moutsatsou et al., 2019). The systems described so far employ different liquid handling systems and global control software resulting in different levels of automation and modularity. For example, Paull et al. (2015) and Crombie et al. (2017), automated the MTP-compliant reprogramming of fibroblasts without clonal expansion of primary clones. While both systems adopted cell culture protocols to automation-friendly MTP formats for the generation of polyclonal hiPSCs, they lack automated isolation and deposition of clones and subsequent clonal expansion. Konagaya et al. (2015) and Archibald et al. (2016), showed automated maintenance of hPSCs for a prolonged period of time, but their systems employ non MTP-compliant 10 cm and T175 cell culture formats requiring specialized robotic handling. Conway and colleagues described a semi-automated MTP-compliant system, which was used for propagating established hiPSC cultures in 96-well plates (Conway et al., 2015).

While these automation regimens are largely based on static protocols covering a defined set of processes, our key

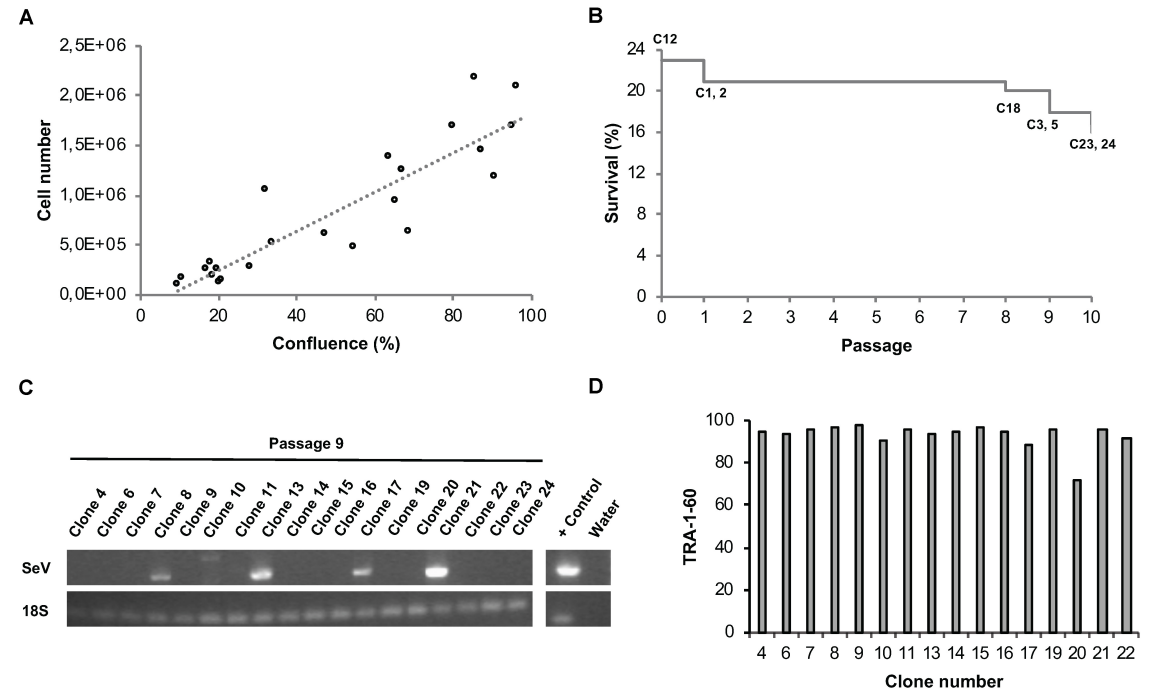

FIGURE 7 | Automated parallel expansion of hiPSC clones. Human iPSC clones were automatically expanded in parallel in a single 24-well plate based on well-specific confluence values. **(A)** To establish a confluence-based readout method for automatic determination of the dilution ratio, the measured confluence values were correlated with the cell number using two exemplar hiPSC control lines. hiPSCs were plated at low density in 6-well plates, confluence values as well as cell numbers were determined daily. Linear regression; $R^2 = 0.81$). **(B)** Survival plot of automatically expanded clones after 10 consecutive passages. Non-surviving clones are indicated. Passage 0 refers to the automated isolation of 24 primary clones using the CellCelector system (clone 12 was lost before passage 1). **(C)** RT-PCR analysis for detection of residual Sendai virus at passage 9. **(D)** TRA-1-60 flow cytometry analysis of expanded hiPSC clones at passage 10 after picking.

interest was to establish a system stretching across the entire reprogramming workflow including fibroblast culture, selection of reprogrammed clones and their expansion. Most importantly, the system was set up to support parallelized hiPSC generation with a capacity to house and propagate up 44 reprogramming batches. Additionally, the system is designed in a modular fashion, thereby enabling individual or combined use of several functional components. Given the fast development in the fields of stem cell technology and automation, it is to be expected that both, cell handling protocols and available hardware evolve rapidly. Thus, modular platforms are advantageous with respect to flexibility and implementation of novel processes, workflows and technologies.

Despite the modularity of the StemCellFactory, all its automation devices are integrated into a single sterile unit and controlled by one lead software. All protocols were adapted to MTP formats in order to facilitate standardized robotic handling. Although non-MTP-conform formats have been used in several robotic systems (Konagaya et al., 2015; Archibald et al., 2016), such formats pose limitations in particular with respect to the extent of parallelization. As for the mode of transgene delivery, we have opted for Sendai virus-based reprogramming as one of the most robust and efficient non-integrating approaches for generating iPSCs from both fibroblasts and blood cells (Schlaeger et al., 2015). Here we show that standard reprogramming efficiencies (0.7%) can be achieved for automated reprogramming through optimization of plating cell densities for viral infection, coating and Sendai virus concentration. This allows avoiding further purification steps including e.g., MACS sorting (Paull et al., 2015; Crombie et al., 2017; Daniszewski et al., 2017) for the enrichment of successfully reprogrammed cells. We found the vast majority of clones to be transgene-free already at passage 9, although a prolonged expansion phase might further increase the fraction of transgene-free clones. TRA-1-60 flow cytometry and the optional Epi-Pluri-Score analysis further confirmed pluripotency of newly generated hiPSC clones on a marker level. Most importantly, the implemented SNP analysis enabled reliable identification of CNVs, which might be due to de novo acquisition or selective expansion of clones from a low-grade mosaic starting population. Such *in vitro* selection events are known to be driven by various parameters such as e.g., cell culture media, splitting procedures, cell densities and others (Liang and Zhang, 2013).

While our current data suggest that the quality of hiPSCs generated with the StemCellFactory is equivalent to hiPSC lines generated manually in an experienced laboratory environment, future comparative studies involving a larger number of isogenic hiPSC clones should allow even deeper quality assessment of genomic integrity and pluripotency scores in automatically vs. manually generated clones.

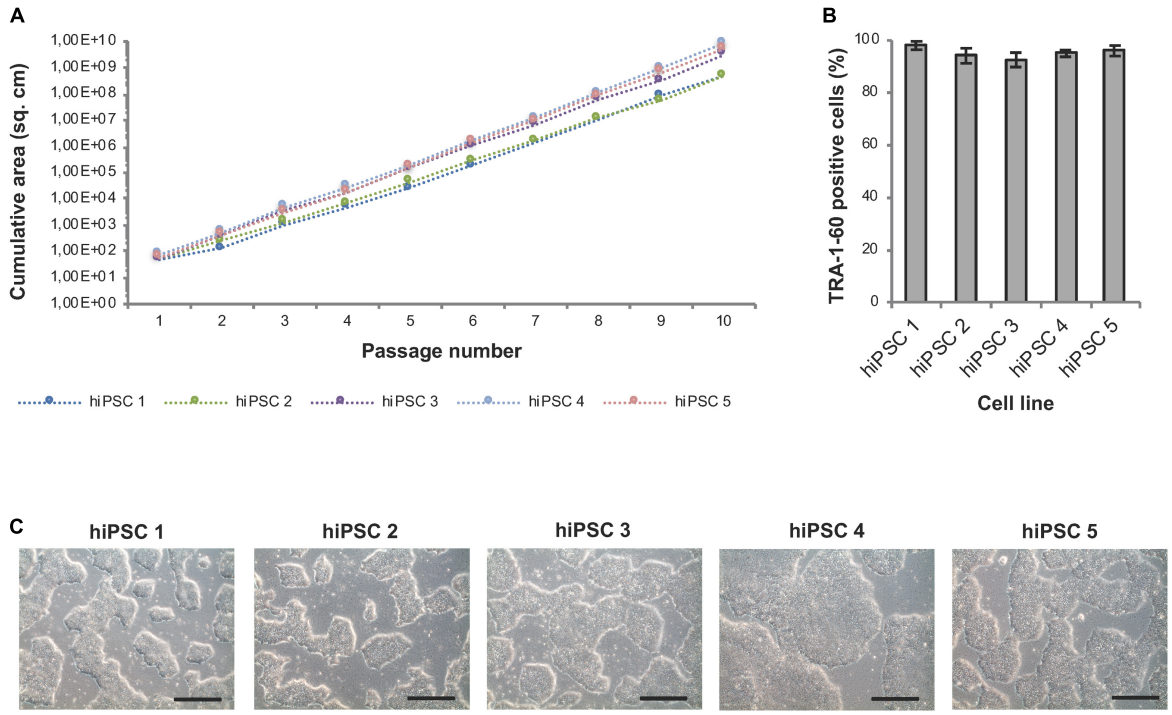

FIGURE 8 | Automated expansion of hiPSCs in 6-well plates. Five distinct hiPSC lines were automatically expanded in 6-well plates using Geltrex coating and E8 medium. Dilution ratios were determined via well-specific confluence measurements. **(A)** HiPSC lines expanded via the StemCellFactory show constant and exponential cell growth over 10 passages. Passaging was performed every 3–4 days. **(B)** Flow cytometry analysis was performed after each passage and showed a high expression of TRA-1-60 in all evaluated cell lines. Data are taken from every passage and shown as mean ± SD (n = 10). **(C)** Representative phase contrast images of hiPSC lines at passage 10. Scale bars: 100 μm.

A key challenge associated with parallelization of cell culture workflows is the fact that different cell populations typically exhibit subtle variations in growth. This also applies to newly generated hiPSCs, where inter-clone variability is a broadly recognized issue. Rigid passaging routines are typically not capable of dealing with variations in clonal growth and can thus lead to overgrown cultures or extremely low densities. Since cell–cell interactions and non-cell autonomous effects among cultured cells can be important for self-renewal and survival, low densities might result in loss of cultures, whereas overconfluent cultures might drift towards unwanted spontaneous differentiation. Taking this into consideration, we used automated determination of confluence values as a proxy for cell numbers and implemented a confluence-based automated splitting procedure. Our data show that this user-independent and thus unbiased system is highly suitable for parallel expansion of clones and cell populations with different growth kinetics while maintaining pluripotency marker expression. In addition to the automated confluence-based splitting paradigm, our system integration features a number of other unique properties. These include automated isolation and deposition of hiPSC clones, parallel clonal expansion of 24 primary hiPSC clones in 24-well plates in an adaptive, confluence-based manner, long-term expansion of hiPSCs in 6-well plates with well-specific confluence-based splitting and high-speed stroboscopic phase-contrast image acquisition.

To our knowledge, automated clonal selection is not part of the existing automated hiPSC systems, which instead work with pooled, polyclonal hiPSC lines (Paull et al., 2015; Crombie et al., 2017). It is a matter of current debates whether clonal or polyclonal hiPSC lines might be better suited for probing the impact of genetic variants to certain diseases (Willmann et al., 2013). Independent of that discussion, there are numerous scientific questions and translational applications where clonal derivation of hiPSCs is required. Implementation of automated clone selection is also an important prerequisite for CRISPR/Cas9-mediated genome editing, for which the StemCellFactory, in principle, features all necessary automation steps (see section "Future Perspectives"). In addition, automated clonal selection can decrease variability in cell handling observed during manual operation. Indeed, manual handling of hiPSCs has been shown to result in greater variation in the expression of germ layer-specific and pluripotency markers (Paull et al., 2015). Interestingly, we found that automated clone retrieval results in significantly higher re-attachment of harvested colonies compared to standard manual clone picking. This might be due to more gentle scratching and aspiration achieved with the scratch capillary compared to the user-dependent manual picking procedure.

For the cultivation of hiPSCs, we used an in-house developed control level software. In addition to controlling the hardware of the StemCellFactory, the control level software covers image

and data storage and as well as graphical data visualization. These data are used by the operator for decision making on the next module to be activated (**Supplementary Figure 5**). The functionalities of each device (microscope, LHU, robotic arm, etc.) can be combined into complex sequences and saved as executable templates (logics). In the future, the data collected by the control level software may be also used for automated, operator-independent data-driven process decisions (Jung et al., 2018).

Future Perspectives

Cell culture automation systems such as the one described here will be essential to cover the foreseeable future need of human pluripotent stem cell lines for fundamental biomedical research, disease modeling, drug development and eventually cell therapy. In this context, disease modeling comes with a particular need for high parallelization: Over the last decade, a wealth of genetic variants contributing to the pathogenesis of numerous diseases have been identified. In most cases, the effect size of these variants is very small, and a reliable association with a given disease may require hundreds or even thousands of samples. For such a scenario, the phenotypic differences resulting from a specific genetic variant in an hiPSC-based model will be too small to exceed the noise level and thus remain undetectable (Germain and Testa, 2017; Hoffman et al., 2017; Popp et al., 2018). In order to link the results of the vast number of genome-wide association studies with phenotypes detectable in a hiPSC model, large numbers of variant and control hiPSC cell lines would have to be compared. This in turn necessitates a very high level of parallelization of hiPSC production under ideally fully standardized conditions (Paull et al., 2015; Archibald et al., 2016; Daniszewski et al., 2017). Systems such as the StemCellFactory are a first step in this direction, although it is likely that blood cells will replace skin-derived fibroblasts as starting population for reprogramming in such a large-scale context. Indeed, preliminary feasibility studies suggest that the existing infrastructure can be adapted to accommodate the automated generation of peripheral blood mononuclear cells for subsequent reprogramming using the StemCellFactory (Elanzew, Breitkreuz, unpublished observations).

Strong interest in parallelization is further fueled by the advent of genome editing. On the one hand, the ease of CRISPR-Cas9-based genome editing and their numerous modifications has been leading to a surge of studies requiring hPSC lines with one or even several modified genetic loci. On the other hand, disease modeling based on editing of genetic disease variants, too, is complicated by the small effect sizes of many variants and might thus require larger numbers of control and disease-associated samples in order to delineate a statistically relevant effect. This need can most likely not be met by manual culture but requires automated systems – ideally in a configuration that also covers the editing process itself. Indeed, many of the modules implemented in the StemCellFactory, including generation and harvesting of clones, high-speed imaging-based quality control and long-term expansion provide key prerequisites for expanding the platform towards this application.

In general, standardization of the cell production is also a key prerequisite for therapeutic applications involving hiPSC-derived cells. In such scenarios, cell production units have to work under GMP-compliant conditions (De Sousa et al., 2016; Huang et al., 2019). Automated cell culture platforms with a built-in tracking system of incoming and outgoing material and the possibility of constant in-process control will facilitate the implementation of GMP-compliant automated process, although further changes will be required to adapt the StemCellFactory to GMP standards.

Recent progress in machine learning and artificial intelligence (AI) might enable further refinement of cell culture automation towards smart technologies (Göppert et al., 2018; Jung et al., 2019). Such systems may exploit in-process-data such as automatically assessed confluency values and machine learning-based image analysis (Schenk et al., 2015; Rippel et al., Unpublished) for adaptive cell processing involving autonomous decision making and prioritization of process scheduling (**Supplementary Figure 5**; Jung et al., 2018).

CONCLUSION

Standardization and parallelization of hiPSC production are prerequisites for setting up large-scale studies that enable a correlation of the vast number of disease-relevant genetic variants with phenotypic differences in hiPSC-based in vitro models. Modular cell culture automation platforms such as the StemCellFactory facilitate this process. Encompassing the entire reprogramming workflow from preparation of source cells via generation and harvesting of individual hiPSC clones to subsequent expansion and maintenance culture, this system combines newly designed and off-the-shelf hardware components in a sterile housing and under a central control software. Novel tools such as confluence-based, well-specific splitting and stroboscope illumination-based high-speed imaging can adapt to slight differences in the growth kinetics of individual cell populations. In concert with the implemented systems for continuous quality control and documentation, the automation modules of the StemCellFactory may also provide a basis for implementing automated solutions for genome editing and eventually GMP-based cell production.

DATA AVAILABILITY STATEMENT

The raw data supporting the conclusions of this article will be made available by the authors, without undue reservation.

ETHICS STATEMENT

The generation and experimental use of hiPSC lines was approved by the Ethics Committee of the Medical Faculty of the University of Bonn (approval 275/08). Informed written consent was obtained from the donors. No potentially identifiable human data are presented in this study. All experiments were performed in accordance with German guidelines and regulations.

AUTHOR CONTRIBUTIONS

AE, BN, DL, OR, TP, FS, MK, SJ, RS, and NK conceived the overall technical infrastructure of the StemCellFactory, including computational framework and hardware design. AE, DL, BN, SJ, and MK implemented the technical set-up. FS and TP implemented the high-speed imaging system. AE, MP, YB, PW, LS, SH, MZ, and OB conceived the biological studies for validating the automation system, which were conducted by AE and OR. AE, LS, BN, MP, YB, and OB wrote the manuscript. All authors contributed to the article and approved the submitted version.

FUNDING

This work was co-funded by the Ministry of Culture and Science of the State of North Rhine-Westphalia and the European Regional Development Fund (EFRE) (StemCellFactory I), the Ministry of Culture and Science of the State of North Rhine-Westphalia (StemCellFactory II), and the European Regional Development Fund (EFRE) (Stem Cell Factory III).

ACKNOWLEDGMENTS

We thank Keiichiro Suzuki and Juan Carlos Izpisua Belmonte (The Salk Institute for Biological Studies, La Jolla California, US) for providing hiPSC lines, and Sybille Krauss (DZNE, Bonn, Germany) and Wolfram S. Kunz (Institute of Experimental Epileptology and Cognition Research, University of Bonn Medical Faculty & University Hospital Bonn, Bonn, Germany) for providing human fibroblasts.

SUPPLEMENTARY MATERIAL

The Supplementary Material for this article can be found online at: https://www.frontiersin.org/articles/10.3389/fbioe.2020.580352/full#supplementary-material

Supplementary Figure 1 | Comparison between automated and manual plating of human fibroblasts. Assessment of successfully plated cells after automated vs. manual seeding of 80,000 HF into wells of a 24-well plate (mean ± SD; n = 9). Plated cells were directly recovered after distribution and counted.
CV = Coefficient of variation (%); SCF = StemCellFactory.

Supplementary Figure 2 | Automated splitting based on well-specific confluency vs. plate-specific confluency. Survival plot based on 24 hiPSC clones propagated for 10 consecutive passages in the StemCellFactory using either well-specific or plate-specific dilution ratios for passaging. Well-specific dilution ratios were calculated based on the confluence of each individual well; the plate-specific dilution ratio based on the confluence of the most confluent well of the 24-well plate.

Supplementary Figure 3 | Pluripotency and SNP analysis of automatically reprogrammed hiPSCs. Shown are 5 distinct hiPSC clones generated from 2 independent donors. HiPSCs were analyzed at passages 10-12 upon confirmation of transgene elimination. **(A)** Genetic integrity was assessed by SNP genotyping. For each chromosome the B allele frequency (upper row) and the log R ratio (lower row) are shown. The SNP analysis of two clones from donor 1 depicts copy number variations (CNVs) in chromosomes 1q and 18q (clone 1) as well as 20q (clone 2) highlighted with red boxes, which were not present in the parental fibroblast population (data not shown) and might be caused by a low-grade mosaicism in the fibroblast source cells or by an in vitro selection of mutations acquired during the reprogramming and cell culture process. **(B)** Pluripotency was assessed using the Epi-Pluri-Score (Cygenia GmbH, Aachen), which is an epigenetic pluripotency biomarker assay based on DNA methylation (DNAm) levels at three specific CpG sites: The Epi-Pluri-Score combines genomic DNA methylation levels at the two CpG sites ANKRD46 and C14orf115, defined as: β-value [ANKRD46] – β-value [C14orf115]. A positive Epi-Pluri-Score indicates pluripotency (Lenz et al., 2015). The third CpG site is located within the pluripotency gene POU5F1 (OCT4) and shows a DNA methylation level of > 0.4 in non-pluripotent cells.

Supplementary Figure 4 | High-speed microscopy and deep learning algorithm-based morphological analysis of hiPSCs (Module 4). High-speed microscope for image acquisition and morphological assessment of the hiPSCs in 6-well plates. Image acquisition is performed by stroboscopic flashing directly from a moving microscopic stage. **(A)** Nikon, TI-E microscope upgraded by the Fraunhofer IPT for high-speed, whole well imaging acquisition. **(B,C)** Exemplary classification of the acquired images (hiPSC classification: black = cell free area, gray = hiPSCs, red = differentiated cells, purple = dead cells (examples are encircled), green circumference = open border of a colony, blue circumference = enclosed border of a colony.

Supplementary Figure 5 | Data-driven workflow for automated cultivation and quality control of hiPSCs in the StemCellFactory. Microscopic data and turbidity measurements for quality control assessed during the on-going expansion of hiPSCs are used for decision making on whether cells (1) are incubated further, (2) need a medium change, (3) need to be passaged at a certain ratio or (4) should be discarded due to contamination or bad cell quality. Transport steps to the concerning modules are indicated in green boxes. Decision steps are indicated in light blue diamond-shaped boxes (comparator evaluation).

Supplementary Movie 1 | StemCellFactory (overview).

Supplementary Movie 2 | Automated isolation and deposition of primary hiPSC clones using the integrated CellCelector system (Module 2).

Supplementary Movie 3 | High-speed microscopy of hiPSCs (Module 4).

REFERENCES

Archibald, P. R. T., Chandra, A., Thomas, D., Chose, O., Massouridès, E., Laâbi, Y., et al. (2016). Comparability of automated human induced pluripotent stem cell culture: a pilot study. *Bioprocess Biosyst. Eng.* 39, 1847–1858. doi: 10.1007/s00449-016-1659-9

Bar, S., and Benvenisty, N. (2019). Epigenetic aberrations in human pluripotent stem cells. *EMBO J.* 38:e101033. doi: 10.15252/embj.2018101033

Brafman, D. A., Chang, C. W., Fernandez, A., Willert, K., Varghese, S., and Chien, S. (2010). Long-term human pluripotent stem cell self-renewal on synthetic polymer surfaces. *Biomaterials* 31, 9135–9144. doi: 10.1016/j.biomaterials.2010.08.007

Carcamo-Orive, I., Hoffman, G. E., Cundiff, P., Beckmann, N. D., D'Souza, S., Knowles, J. W., et al. (2017). Analysis of transcriptional variability in a large human iPSC library reveals genetic and non-genetic determinants of heterogeneity. *Cell Stem Cell* 20, 518.e9–532.e9. doi: 10.1016/j.stem.2016.11.005

Chen, G., Gulbranson, D. R., Hou, Z., Bolin, J. M., Ruotti, V., Probasco, M. D., et al. (2011). Chemically defined conditions for human iPS cell derivation and culture. *Nat. Methods* 8, 424–429. doi: 10.1038/nmeth.1593

Conway, M. K., Gerger, M. J., Balay, E. E., O'Connell, R., Hanson, S., Daily, N. J., et al. (2015). Scalable 96-well plate based iPSC culture and production using a robotic liquid chen handling system. *J. Vis. Exp* 99:52755. doi: 10.3791/52755

Crombie, D. E., Daniszewski, M., Liang, H. H., Kulkarni, T., Li, F., Lidgerwood, G. E., et al. (2017). Development of a modular automated system for

maintenance and differentiation of adherent human pluripotent stem cells. *SLAS Discov. Adv. Sci. Drug Discov.* 22, 1016–1025. doi: 10.1177/2472555217696797

Daniszewski, M., Crombie, D. E., Henderson, R., Liang, H. H., Wong, R. C. B., Hewitt, A. W., et al. (2017). Automated cell culture systems and their applications to human pluripotent stem cell studies. *SLAS Technol. Transl. Life Sci. Innov.* 23, 315–325. doi: 10.1177/2472630317712220

D'Antonio, M., Benaglio, P., Jakubosky, D., Greenwald, W., Matsui, H., Donovan, M., et al. (2018). Insights into the mutational burden of human induced pluripotent stem cells from an integrative multi-omics approach. *Cell Rep.* 24, 883–894. doi: 10.1016/j.celrep.2018.06.091

De Sousa, P. A., Downie, J. M., Tye, B. J., Bruce, K., Dand, P., Dhanjal, S., et al. (2016). Development and production of good manufacturing practice grade human embryonic stem cell lines as source material for clinical application. *Stem Cell Res.* 17, 379–390.

Diaz-Ortiz, M. E., and Chen-Plotkin, A. S. (2020). Omics in neurodegenerative disease: hope or hype? *Trends Genet.* 36, 152–159. doi: 10.1016/j.tig.2019.12.002

Falk, A., Heine, V. M., Harwood, A. J., Sullivan, P. F., Peitz, M., Brüstle, O., et al. (2016). Modeling psychiatric disorders: from genomic findings to cellular phenotypes. *Mol. Psychiatry* 21, 1167–1179. doi: 10.1038/mp.2016.89

Fusaki, N., Ban, H., Nishiyama, A., Saeki, K., and Hasegawa, M. (2009). Efficient induction of transgene-free human pluripotent stem cells using a vector based on Sendai virus, an RNA virus that does not integrate into the host genome. *Proc. JPN Acad. Ser. B. Phys. Biol. Sci.* 85, 348–362. doi: 10.2183/pjab.85.348

Germain, P.-L., and Testa, G. (2017). Taming human genetic variability: transcriptomic meta-analysis guides the experimental design and interpretation of iPSC-based disease modeling. *Stem Cell Rep.* 8, 1784–1796. doi: 10.1016/j.stemcr.2017.05.012

Göppert, A., Huettemann, G., Jung, S., Grunert, D., and Schmitt, R. (2018). Frei verkettete Montagesysteme: ein Ausblick. *ZWF.* 113, 151–155. doi: 10.3139/104.111889

Hoffman, G. E., Hartley, B. J., Flaherty, E., Ladran, I., Gochman, P., Ruderfer, D. M., et al. (2017). Transcriptional signatures of schizophrenia in hiPSC-derived NPCs and neurons are concordant with post-mortem adult brains. *Nat. Commun.* 8:2225. doi: 10.1038/s41467-017-02330-5

Huang, C.-Y., Liu, C.-L., Ting, C.-Y., Chiu, Y.-T., Cheng, Y.-C., Nicholson, M. W., et al. (2019). Human iPSC banking: barriers and opportunities. *J. Biomed. Sci.* 26:87. doi: 10.1186/s12929-019-0578-x

Ji, J., Ng, S. H., Sharma, V., Neculai, D., Hussein, S., Sam, M., et al. (2012). Elevated Coding mutation rate during the reprogramming of human somatic cells into induced pluripotent stem cells. *Stem Cells* 30, 435–440. doi: 10.1002/stem.1011

Jung, S., Ochs, J., Kulik, M., König, N., and Schmitt, R. (2018). Highly modular and generic control software for adaptive cell processing on automated production platforms. *Procedia CIRP* 72, 1245–1250. doi: 10.1016/j.procir.2018.03.189

Jung, S., Schnichels, A., Schmitt, R., Kuhlenkötter, B., and Prinz, C. (2019). Leitsysteme 4.0: *Herausforderungen und Potenziale der Industrie* 4.0 für flexible Produktionsleitsysteme. *ZWF* 114, 154–157. doi: 10.3139/104.112045

Kilpinen, H., Goncalves, A., Leha, A., Afzal, V., Alasoo, K., Ashford, S., et al. (2017). Common genetic variation drives molecular heterogeneity in human iPSCs. *Nature* 546, 370–375. doi: 10.1038/nature22403

Konagaya, S., Ando, T., Yamauchi, T., Suemori, H., and Iwata, H. (2015). Long-term maintenance of human induced pluripotent stem cells by automated cell culture system. 5:16647. doi: 10.1038/srep16647

Lenz, M., Goetzke, R., Schenk, A., Schubert, C., Veeck, J., Hemeda, H., et al. (2015). Epigenetic biomarker to support classification into pluripotent and non-pluripotent cells. *Sci. Rep.* 5:8973. doi: 10.1038/srep08973

Liang, G., and Zhang, Y. (2013). Genetic and epigenetic variations in iPSCs: potential causes and implications for application. *Cell Stem Cell* 13, 149–159. doi: 10.1016/j.stem.2013.07.001

Liu, G.-H., Qu, J., Suzuki, K., Nivet, E., Li, M., Montserrat, N., et al. (2012). Progressive degeneration of human neural stem cells caused by pathogenic LRRK2. *Nature* 491, 603–607. doi: 10.1038/nature11557

Ludwig, T. E., Bergendahl, V., Levenstein, M. E., Yu, J., Probasco, M. D., and Thomson, J. A. (2006). Feeder-independent culture of human embryonic stem cells. *Nat. Methods* 3, 637–646. doi: 10.1038/nmeth902

Marx, U., Schenk, F., Behrens, J., Meyr, U., Wanek, P., Zang, W., et al. (2013). Automatic production of induced pluripotent stem cells. *Procedia CIRP* 5, 2–6. doi: 10.1016/j.procir.2013.01.001

Merkle, F. T., Ghosh, S., Kamitaki, N., Mitchell, J., Avior, Y., Mello, C., et al. (2017). Human pluripotent stem cells recurrently acquire and expand dominant negative P53 mutations. *Nature* 545, 229–233. doi: 10.1038/nature22312

Miyazaki, T., Futaki, S., Suemori, H., Taniguchi, Y., Yamada, M., Kawasaki, M., et al. (2012). Laminin E8 fragments support efficient adhesion and expansion of dissociated human pluripotent stem cells. *Nat. Commun* 3:1236. doi: 10.1038/ncomms2231

Moutsatsou, P., Ochs, J., Schmitt, R., Hewitt, C., and Hanga, M. (2019). Automation in cell and gene therapy manufacturing: from past to future. *Biotechnol. Lett.* 41, 1245–1253. doi: 10.1007/s10529-019-02732-z

Paull, D., Sevilla, A., Zhou, H., Hahn, A. K., Kim, H., Napolitano, C., et al. (2015). Automated, high-throughput derivation, characterization and differentiation of induced pluripotent stem cells. *Nat. Methods* 12, 885–892. doi: 10.1038/nmeth.3507

Popp, B., Krumbiegel, M., Grosch, J., Sommer, A., Uebe, S., Kohl, Z., et al. (2018). Need for high-resolution genetic analysis in iPSC: results and lessons from the ForIPS Consortium. *Sci. Rep.* 8:17201. doi: 10.1038/s41598-018-35506-0

Rodin, S., Antonsson, L., Niaudet, C., Simonson, O. E., Salmela, E., Hansson, E. M., et al. (2014). Clonal culturing of human embryonic stem cells on laminin-521/E-cadherin matrix in defined and xeno-free environment. *Nat. Commun.* 5:3195. doi: 10.1038/ncomms4195

Schenk, F., Kulik, M., and Schmitt, R. (2015). Metrology-based quality and process control in automated stem cell production. *Tm Tech. Mess.* 82, 309–316. doi: 10.1515/teme-2015-0036

Schlaeger, T. M., Daheron, L., Brickler, T. R., Entwisle, S., Chan, K., Cianci, A., et al. (2015). A comparison of non-integrating reprogramming methods. *Nat. Biotechnol.* 33, 58–63. doi: 10.1038/nbt.3070

Shutova, M., Surdina, A., Ischenko, D., Naumov, V., Bogomazova, A., Vassina, E., et al. (2016). An integrative analysis of reprogramming in human isogenic system identified a clone selection criterion. *Cell Cycle* 15, 986-997. doi: 10.1080/15384101.2016.1152425

Sullivan, P. F., and Geschwind, D. H. (2019). Defining the genetic, genomic, cellular, and diagnostic architectures of psychiatric disorders. *Cell* 177, 162–183. doi: 10.1016/j.cell.2019.01.015

Takahashi, K., Tanabe, K., Ohnuki, M., Narita, M., Ichisaka, T., Tomoda, K., et al. (2007). Induction of pluripotent stem cells from adult human fibroblasts by defined factors. *Cell* 131, 861–872. doi: 10.1016/j.cell.2007.11.019

Volpato, V., and Webber, C. (2020). Addressing variability in iPSC-derived models of human disease: guidelines to promote reproducibility. *Dis. Model. Mech.* 13:dmm042317. doi: 10.1242/dmm.042317

Warren, L., Manos, P. D., Ahfeldt, T., Loh, Y.-H., Li, H., Lau, F., et al. (2010). Highly efficient reprogramming to pluripotency and directed differentiation of human cells using synthetic modified mRNA. *Cell Stem Cell.* 7, 618–630. doi: 10.1016/j.stem.2010.08.012

Willmann, C. A., Hemeda, H., Pieper, L. A., Lenz, M., Qin, J., Joussen, S., et al. (2013). To clone or not to clone? Induced pluripotent stem cells can be generated in bulk culture. *PLoS One* 8:e65324. doi: 10.1371/journal.pone.0065324

Young, M., Larson, D., Sun, C.-W., George, D., Ding, L., Miller, C., et al. (2012). Background mutations in parental cells account for most of the genetic heterogeneity of induced pluripotent stem cells. *Cell Stem Cell* 10, 570–582. doi: 10.1016/j.stem.2012.03.002

Conflict of Interest: AE, YB, OR, LS, SH, and OB were employed by the company Life&Brain GmbH.

The remaining authors declare that the research was conducted in the absence of any commercial or financial relationships that could be construed as a potential conflict of interest.

frontiers in Bioengineering and Biotechnology

ORIGINAL RESEARCH
published: 12 February 2021
doi: 10.3389/fbioe.2021.591838

Effect of Electrical Stimulation Conditions on Neural Stem Cells Differentiation on Cross-Linked PEDOT:PSS Films

Laura Sordini[1,2], Fábio F. F. Garrudo[1,2,3], Carlos A. V. Rodrigues[1], Robert J. Linhardt[3], Joaquim M. S. Cabral[1], Frederico Castelo Ferreira[1] and Jorge Morgado[2]**

[1] Department of Bioengineering and iBB – Institute for Bioengineering and Biosciences, Instituto Superior Técnico, Universidade de Lisboa, Lisbon, Portugal, [2] Department of Bioengineering and Instituto de Telecomunicações, Instituto Superior Técnico, Universidade de Lisboa, Lisbon, Portugal, [3] Department of Chemistry and Chemical Biology, Center for Biotechnology and Interdisciplinary Studies, Rensselaer Polytechnic Institute, Troy, NY, United States

OPEN ACCESS

Edited by:
Stephanie Michelle Willerth,
University of Victoria, Canada

Reviewed by:
Daniele Mantione,
UMR5629 Laboratoire de Chimie des Polymères Organiques (LCPO), France
Shui Guan,
Dalian University of Technology, China

***Correspondence:**
Frederico Castelo Ferreira
frederico.ferreira@tecnico.ulisboa.pt
Jorge Morgado
jmfmorgado@tecnico.ulisboa.pt

Specialty section:
This article was submitted to Biomaterials, a section of the journal Frontiers in Bioengineering and Biotechnology

Received: 05 August 2020
Accepted: 21 January 2021
Published: 12 February 2021

Citation:
Sordini L, Garrudo FFF, Rodrigues CAV, Linhardt RJ, Cabral JMS, Ferreira FC and Morgado J (2021) Effect of Electrical Stimulation Conditions on Neural Stem Cells Differentiation on Cross-Linked PEDOT:PSS Films. Front. Bioeng. Biotechnol. 9:591838. doi: 10.3389/fbioe.2021.591838

The ability to culture and differentiate neural stem cells (NSCs) to generate functional neural populations is attracting increasing attention due to its potential to enable cell-therapies to treat neurodegenerative diseases. Recent studies have shown that electrical stimulation improves neuronal differentiation of stem cells populations, highlighting the importance of the development of electroconductive biocompatible materials for NSC culture and differentiation for tissue engineering and regenerative medicine. Here, we report the use of the conjugated polymer poly(3,4-ethylenedioxythiophene) doped with polystyrene sulfonate (PEDOT:PSS CLEVIOS P AI 4083) for the manufacture of conductive substrates. Two different protocols, using different cross-linkers (3-glycidyloxypropyl)trimethoxysilane (GOPS) and divinyl sulfone (DVS) were tested to enhance their stability in aqueous environments. Both cross-linking treatments influence PEDOT:PSS properties, namely conductivity and contact angle. However, only GOPS-cross-linked films demonstrated to maintain conductivity and thickness during their incubation in water for 15 days. GOPS-cross-linked films were used to culture ReNcell-VM under different electrical stimulation conditions (AC, DC, and pulsed DC electrical fields). The polymeric substrate exhibits adequate physicochemical properties to promote cell adhesion and growth, as assessed by Alamar Blue® assay, both with and without the application of electric fields. NSCs differentiation was studied by immunofluorescence and quantitative real-time polymerase chain reaction. This study demonstrates that the pulsed DC stimulation (1 V/cm for 12 days), is the most efficient at enhancing the differentiation of NSCs into neurons.

Keywords: electrical stimulation, neural stem cells, neuronal differentiation, ReNcell VM, conjugate polymer, electroconductive material, PEDOT:PSS, cross-linking

INTRODUCTION

The World Health Organization (WHO) predicted that by 2040 neurodegenerative diseases will be the second cause of death worldwide after cardiovascular diseases (Gammon, 2014). The steady increase in the number of diagnosed cases of neurodegenerative diseases accompanies the increase in life expectation. In the USA alone, between 2000 and 2017, the number of declared deaths attributed to Alzheimer's disease increased by 145% (8.5% a year) (Alzheimer's Association, 2019). A common pattern to all neurodegenerative diseases is a genetic, cellular, and/or neural circuit dysregulation that leads to progressive and yet massive neuronal death (Heemels, 2016). The conventional pharmacological and non-pharmacological approaches available are only palliative and cannot halt or reverse the disease. It is therefore pivotal to develop more effective treatments and/or new therapeutics able to tackle neurodegenerative diseases (Heemels, 2016; Erkkinen et al., 2018).

Tissue engineering strategies are promising for the definitive cure of neurodegenerative diseases through tissue regeneration. Orchestrating such strategies is no trivial task, as the complexity and the widespread of brain areas affected by these diseases calls for a multidisciplinary approach. As such cell-based approaches, including encapsulated cell technology, drugs and growth factor delivery, genetic manipulation, and also the use of bioactive materials must be integrated for success (Borlongan et al., 1999; Tresco, 2000).

Despite the difficulties in isolating, neural stem cells (NSCs) are attractive for cell-based therapies because of their potential ease of propagation and manipulation, their ability to migrate to disease affected sites and their capacity of differentiating into any neural cell type required (Harrower and Barker, 2004). However, the difficulty to isolate these cells from tissues has driven several researchers to study the development of effective protocols to differentiate induced pluripotent stem cells (iPSCs) into NSC (Galiakberova and Dashinimaev, 2020, Fernandes et al., 2015). NSC *in vitro* culture and survival under transplantation can be enhanced by the use of appropriate scaffolds, which can replicate the cues of the NSC niche and promote differentiation toward specific lineages. Some of these cues include topography (Qi et al., 2013), mechanical (Pathak et al., 2014), and electrical stimuli (Zhu et al., 2019).

The *in vivo* electrical stimulation of specific brain areas stands at the cutting edge of potential therapeutic approaches. For example, deep brain stimulation (DBS) is a powerful clinical therapeutic technique that can alleviate movement disorders in patients that no longer respond satisfactorily to pharmacological management (Kühn and Volkmann, 2017). It requires the implantation of an array of electrodes in specific areas of the brain for the delivery of electrical pulses. These can be used to block abnormal neural activity associated with Parkinson's disease and help to normalize cell homeostasis (Benabid, 2003).

Electrical stimulation can also be harnessed to enhance the neural differentiation of NSCs cultured *in vitro* (Ghasemi-Mobarakeh et al., 2009; Pires et al., 2015; Yang et al., 2017). Electroconductive scaffolds with good biocompatibility profile were needed to achieve such goals. Among the electroconductive materials available to produce such platforms, the most used are metals and organic materials, namely graphene, and conjugated polymers. Conjugated polymers present numerous advantages toward neural tissue engineering applications, namely: (1) they can be processed into any desired 3D-shape (Garrudo et al., 2019a,b; Kayser and Lipomi, 2019); (2) can be easily functionalized allowing the tailoring of their mechanical, chemical, and electrical properties; (3) can exhibit high electroconductivity values, approaching those of metals; and (4) combine ionic and electronic conductivity, improving the "quality" of the interfaces with biological tissues (Rivnay et al., 2014; Inal et al., 2018; Goel et al., 2019; Pace et al., 2019). While electronic conductivity promotes higher current flow across the material, ion conductivity may prove to be essential to interface with tissues, as electrical signals in the human body are predominantly associated to ion currents. Therefore, the use of the mixed ionic-electronic of these doped conjugated polymers systems, rather than metals, allows the creation of an interface with an ion "transduction" between external electronic devices/systems and the biological tissues, where electrical signaling occurs via ionic conduction. As an example, the work of Inácio et al. (2020) evidences improved electrical interfacing of neural probes with PEDOT:PSS, which allows the recording of cellular electrical signals with higher signal-to-noise ratio than metals.

The most studied conjugated polymers for neural tissue engineering applications include poly(pyrrole) (PPy), poly(aniline) (PANI), and poly(3,4-ethylenedioxythiophene):polystyrene sulfonate (PEDOT:PSS) (Du et al., 2020). All of these have been proven to be biocompatible for neural applications, with minimal inflammatory response (Guarino et al., 2016; Garrudo et al., 2019a). Upon charge-transfer doping, their electroconductivity can reach values up to 7.5×10^3 S cm^{-1} (Kaur et al., 2015). PEDOT:PSS offers significant advantages when compared to PPy and PANI, including superior thermal and electrochemical stability, charge capacity, low impedance at the interface with electrolytes and combined electronic and ionic conductivity (Collazos-Castro et al., 2010). This justifies the use of PEDOT:PSS in the development of coatings for electrodes capable of being used in deep brain stimulation (Balint et al., 2014). For example, coating metal electrodes with PEDOT:PSS can enhance the electrode's performance by decreasing the interfacial impedance and increasing the charge storage capacity (Bodart et al., 2019). The *in vivo* performance of neural signal recording electrodes coated with PEDOT and carbon nanotubes was tested and a consistent reading signal was found after 11 days of implantation (Alba et al., 2015). Moreover, PEDOT:PSS can also be employed in the design of electroactive scaffolds (Wang et al., 2017; Tomaskovic-Crook et al., 2019).

Cross-linking is the simplest approach to improve the structural stability of PEDOT:PSS-based substrates to support cell culture. Two main cross-linking agents have been reported: (3-glycidyloxypropyl)trimethoxysilane (GOPS) and divinylsulfone (DVS). Neural cells differentiated on PEDOT:PSS films cross-linked with GOPS were found to

elongate and exhibit longer neurites after electrical stimulation by pulsed direct current (pulsed DC) (Pires et al., 2015). Mantione et al. (2017) have demonstrated that the use of DVS as PEDOT:PSS cross-linker shows full biocompatibility and better support for neuro-regeneration when compared to GOPS cross-linked material.

The effects of electrical stimulation on NSCs have been widely investigated (Yamada et al., 2007; Chang et al., 2011; Huang et al., 2015; Du et al., 2018; Zhu et al., 2019). Several studies have reported that the application of an extracellular DC field can direct the migration of NSCs and promote neurite outgrowth cathodically (Feng et al., 2012; Meng et al., 2012; Li et al., 2014; Zhao et al., 2015; Hayashi et al., 2016; Yao and Li, 2016). Exposure of NSCs to 0.53 or 1.83 V m^{-1} is associated with increased cell elongation, longer neurites, mature neuronal morphology and increased *βIII-Tubulin* expression (Kobelt et al., 2014). Additionally, cells populations derived from stimulated NSCs showed an increase in intracellular Ca^{2+} concentration during stimulation, a signal for the presence of functional neurons. Pulsed electrical stimulation (0.25 mA cm^{-2}, biphasic waveform of 100 μs pulses) through laminin-coated PPy electroconductive films can promote the differentiation of NSCs to neurons (Stewart et al., 2015). Moreover, the neurons obtained exhibited clustering and increased neurite growth (longer neurites and greater branching). The application of an alternate current (AC) was shown to induce a morphological change of PC12 cells, promoting neurite growth even in the absence of nerve growth factor (NGF) (Kimura et al., 1998).

Although the reported literature shows the numerous benefits of electrical stimulation on promoting NSC differentiation into neurons, an optimized protocol has not yet been established. Therefore, the main aim of this study is to investigate the effects of applying different types of current flow (AC, DC, or pulsed DC) on NSCs growth and differentiation, when cultivated on electroconductive PEDOT:PSS films. To do this, PEDOT:PSS platforms were optimized and the effect of the cross-linkers GOPS and DVS on polymer properties was compared.

MATERIALS AND METHODS

Cross-Linked PEDOT:PSS Films

Cross-linked PEDOT:PSS films were prepared as follows: glass coverslips were cleaned with acetone and isopropanol under ultrasounds, followed by drying with a nitrogen stream. The surface was then treated with oxygen plasma (PlasmaPrep2, GaLa Instrument), to remove organic residues and increase the hydrophilicity of the surface. PEDOT:PSS dispersion (Heraeus, CLEVIOS P AI 4083, PEDOT:PSS weight ratio 1:6, solids content 1.3–1.7%) was filtered with a 0.45 μm filter before use. Two different solutions were prepared and used to make thin films by spin coating (Spin-Coater KW-4A, Chemat Technology) according to the following protocols:

(i) PEDOT:PSS + GOPS: This dispersion was prepared by adding the dopants ethylene glycol (EG) (added in a 1:4 volume parts, Sigma-Aldrich) and dodecylbenzenesulfonic acid (DBSA) (0.5 μL mL^{-1}, Sigma-Aldrich), and GOPS (10 μL.mL^{-1}, Sigma-Aldrich) to improve film formation and stability (Pires et al., 2015). The obtained aqueous dispersion was spun-coated at a spinning speed of 1,800 rpm for 60 s. Afterwards, the obtained film samples (PEDOT:GOPS) were annealed at 150°C for 2 min in air.

(ii) PEDOT:PSS + DVS: This dispersion was prepared by adding the dopants EG (1:4 volume parts, Sigma-Aldrich) and DBSA (1 μL mL^{-1}, Sigma-Aldrich), and DVS (30 μL mL^{-1}, Sigma-Aldrich) to improve film formation and stability (Mantione et al., 2017). The aqueous dispersion was spin coated onto cleaned glass coverslips at a spinning speed of 1,000 rpm for 40 s. Afterwards, the obtained film samples (PEDOT:DVS) were annealed at 50°C for 1 h in air.

PEDOT:PSS Film Characterization

Thickness and Morphology

Film thickness was measured with a Bruker's Dektak® 3.21 Profilometer: a cut in the film was made with a scalpel until reaching the glass substrate and the height of the cut (film thickness) was measured upon surface scanning perpendicularly to the cut. The morphology of the cross-linked PEDOT:PSS films was evaluated using scanning electron microscopy (SEM Hitachi S-2400, Hitachi) at 15 kV, after coating with a thin layer of gold/palladium. Elemental analysis was carried using an EDS Bruker SDD light elements detector.

Contact Angle Measurements

Contact angle measurements were performed through the sessile drop method using a Kruss DSA25B goniometer. A drop of distilled water was deposited on the surface of the various PEDOT cross-linked thin films ($n = 3$) and Drop Shape Analysis 4 software was used to take measurements every 5 s for 2 min.

Four-Point Probe Electroconductivity Measurement

Four stripes of gold were deposited on the cross-linked PEDOT films by physical vapor deposition (PVD) with an Edwards E306A thermal evaporator, across the entire film and with equal distance from each other. Silver paste (HAZ Electrodrag 1415, Agar) was used to connect the probes to the gold stripes to ease the measurements, performed in triplicate ($n = 3$) and averaged. Upon recording of the potential difference between the two inner contacts for every value of applied current (at the outer contacts), it is possible to derive the slope of the straight line (R = V/I) following Ohm's law. At a constant temperature, the resistance of the sample (R) is proportional to its resistivity (ρ) and to the separation between the two inner contacts (L), and inversely proportional to the cross-section (A) (product of the sample thickness by the sample width), as described by Equation (1):

$$R = \rho \times (L/A)\ [S^{-1}\ or\ \Omega] \quad (1)$$

Conversely, it is possible to calculate the conductivity of our sample (σ), as the reciprocal of the ρ value obtained using Equation (2):

$$\sigma = 1/\rho\ [S\ cm^{-1}] \quad (2)$$

Cross-Linked PEDOT:PSS Films Stability Assay

The assessment of cross-linked PEDOT:PSS stability was performed by immersing the obtained PEDOT:DVS and

PEDOT:GOPS films in MilliQ water for 7 and 15 days. At these time points, samples were dried with nitrogen stream and their thickness and conductivity were measured.

Cell Culture and Characterization

NSCs Culture Conditions

ReNcell-VM (Millipore®) is a human neural progenitor cell line derived from the ventral mesencephalon region of the fetal brain and immortalized by retroviral transduction with the v-myc oncogene. ReNcell-VM were first expanded in T-flasks (Falcon®, Corning) previously coated with poly-L-ornithine (PO) (20 μg mL^{-1}, Sigma-Aldrich) for 30 min and laminin (LN) (10 μg mL^{-1} in PBS, Sigma-Aldrich) for 4 h at 37°C and 5% CO_2. After seeding, cells were expanded in N2 medium, consisting of DMEM/F12 with glucose (1.6 g L^{-1}, Sigma-Aldrich), N2-supplement (1%, Thermo Fisher), penicillin/streptomycin (1%, Thermo Fisher) and insulin (20 μg mL^{-1}, Sigma-Aldrich), and supplemented with EGF (20 ng mL^{-1}, Peprotech), FGF-2 (20 ng mL^{-1}, Peprotech), and B27 supplement (20 μl mL^{-1}, Thermo Fisher).

Electrical Stimulation

Cell culture setups were prepared according to the following procedure. 3D-printed poly(lactic acid) chambers were glued to PEDOT:GOPS films using medical glue (Sylastic A Medical Adhesive, Dow Corning). Copper wires were glued to each end of the PEDOT films with silver paste (HAZ Electrodrag 1415, Agar) and outside the chamber to stimulate the PEDOT films only. An external power supply (Tektronix AFG 1022), connected to the electrodes, was used to apply an electric field across the PEDOT film (**Figure 1A**). An oscilloscope (Tektronix TBS 200 Digital Oscilloscope) was also connected to the circuit in order to record the applied voltage across the sample.

Setups were sterilized with Anti-anti solution (1%, Thermo Fisher) for 3 h and then coated with poly-L-ornithine and laminin before ReNcell-VM (passage between 20 and 30) seeding (140,000 cells cm^{-2}). Cells were let to attach at 37°C and 5% CO_2 for 1 h before initiating the electrical stimulation. The maximum stimulation threshold value was chosen to avoid the electrolysis of water, which occurs at 1.2 V and can lead to changes in the culture medium pH. The values of frequency and peak duration were set according to the protocols used by Pires et al. (2015). Three different types of electrical stimulation protocols were used in the experiments (**Figure 1A**):

(i) *Pulsed DC* voltage of +1 V, with a square wave of 1 V peak-to-peak amplitude (+1 V, 0 V), 100 Hz frequency, 10 ms period;
(ii) *AC voltage* of ± 1 V, applied with a square wave of 2V peak-to-peak amplitude (+1 V, −1 V), 100 Hz frequency, 10 ms period;
(iii) *DC voltage* +1 V, with a square wave of 2 mV peak-to-peak amplitude and an offset of +1 V (+999 mV, +1,001 mV), 12.5 MHz frequency, 0.08 μs period. For the DC voltage, the highest frequency reachable by the power supply and the smallest modulation amplitude of the wave were selected aiming to approximate the output to a DC stimulation.

Cross-linked PEDOT films with no applied electric field and polystyrene cell culture plates (Falcon®, Corning), both coated with poly-L-ornithine and laminin (PO/LN) as previously described, were used as control. Cells were expanded for 4 days under continuous stimulation (24 h), then differentiation was carried on with 12 h continuous stimulation per day for 8 days (**Figure 1B**).

Differentiation was induced by the withdrawal of growth factors EGF and FGF2 and switching the culture medium to N2B27 to induce neural differentiation. This medium is composed of a 1:1 mixture of N2 medium and B27 medium, this last composed of Neurobasal medium (Thermo Fisher) supplemented with B27 (20 μl mL^{-1}, Thermo Fisher), L-glutamine (2 mM, Thermo Fisher), and penicillin streptomycin (0.5%, Thermo Fisher). During the 8 days of the differentiation phase the medium was changed every 2 days.

Metabolic Activity Under Electrical Stimulation

Alamar Blue® cell viability reagent was used to study ReNcell-VM metabolic activity under different electrical stimulation conditions during the expansion phase ($n = 2$). Cells were incubated with Alamar Blue® (10% in N2 medium) for 2 h, before sample collection and fluorescence intensity analysis (excitation at 560 nm and emission collected at 590 nm) using Tecan Infinite M200 Pro plate reader.

Differentiation Under Electrical Stimulation

After following the different stimulation protocols for the proliferation and differentiation of ReNcells-VM (**Figure 1**), cell samples were collected for immunocytochemistry and quantitative real-time polymerase chain reaction (qRT-PCR).

qRT-PCR

qRT-PCR was performed using SYBR Green® gene expression assays. The genes for β3-tubullin (TUBB3—immature neurons), microtubule-associated protein 2 (MAP2—mature neurons), glial fibrillary acidic protein (GFAP—astrocytes), NESTIN (late NSCs), and (sex determining region Y)-box 2 (SOX2—NSCs) were chosen as the most relevant to be targeted at the end of the differentiation phase (Day 13). Gene expression for each condition was determined using the ΔΔCt method, normalized to the housekeeping gene GAPDH ($n = 3$). The primer sequences can be found in **Table 1**.

Immunocytochemistry

Cell samples were fixed with paraformaldehyde (PFA) 4% for 30 min at room temperature (RT), washed twice with PBS, and then incubated for 30 min at RT with blocking solution, consisting of Normal Goat Serum (10%, Sigma-Aldrich) and Triton-X-100 (0.2%, Thermo Fisher). The primary antibodies used, anti-TUJ1 (mouse, Biolegend) and anti-GFAP (rabbit, Millipore), were first diluted in staining solution, consisting of a 1:2 dilution of blocking solution in PBS, before incubation with the cells at 4°C, overnight. After this, cells were washed three times with PBS and incubated with the secondary antibodies, goat anti-mouse Alexa 488 (Thermo Fisher) and goat anti-rabbit Alexa 546 (Thermo Fisher), for 45 min at RT and protected from light. Finally, cells samples were washed

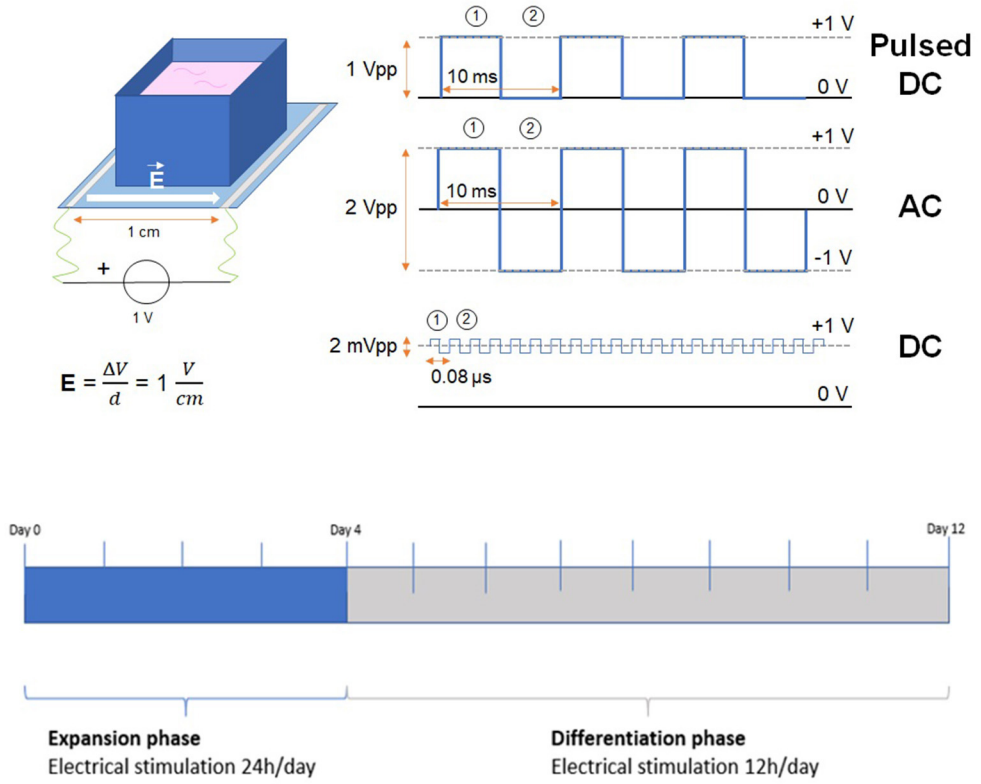

FIGURE 1 | (Top) Experimental scheme of the three different types of applied electrical stimulation (pulsed DC, AC, and DC) on cross-linked PEDOT films. **(Bottom)** Timeline of cell expansion and differentiation phases.

TABLE 1 | Primer sequences used for SYBR® Green chemistry-based qPCR.

Genes	Forward primer sequence (5′-3′)	Reverse primer sequence (5′-3′)
GAPDH	GAGTCAACGGATTTGGTCGT	TTGATTTTGGAGGGATCTCG
SOX2	GGGAAATGGGAGGGGTGCAAAAGAGG	TTGCGTGAGTGTGGATGGGATTGGTG
NESTIN	GAAACAGCCATAGAGGGCAAA	TGGTTTTCCAGAGTCTTCAGTGA
TUBB3	CTCAGGGGCCTTTGGACATC	CAGGCAGTCGCAGTTTTCAC
MAP2	GGCATTGAAGAATGGCAGAT	CCCTGTATGGGAATCCATTG
GFAP	CCGCCACTTGCAGGAGTACCAG	TTCTGCTCGGGCCCCTCATGAG

twice with PBS, the nuclei counterstained with DAPI (1 mg mL^{-1}, Sigma-Aldrich) for 5 min at RT and again washed twice with PBS. Immunostained cells were visualized using a fluorescence microscope (Leica DMI 3000B equipped with Nikon-AcT1 software). ImageJ software (National Institute of Health) was used to calculate the extent of expression of both differentiation markers. For every analyzed picture, the percentage of area characterized by TUJ1 staining was calculated and divided by the percentage of area characterized by GFAP expression, in order to obtain a quantitative value describing the neuronal/glial differentiation profile in different conditions. At least 7 pictures were analyzed for every condition. The details on the calculations of the ratios, as well as the results of the expression calculated for each biomarker alone, are presented in **Supplementary Information 4**. Statistical analysis was performed by one-way ANOVA followed by Tukey's HSD Test ($p < 0.05$ for statistical significance).

RESULTS

PEDOT:PSS Film Characterization

In this work, both GOPS and DVS cross-linking agents were used to prepare thin conductive PEDOT films, following protocols similar to the ones previously used, for evaluation of long-term stability and characterization of surface properties. Cross-linkers were added to the PEDOT:PSS dispersions before the spin-coating process and annealing of the films was carried to allow the clearance of residual traces of water improving

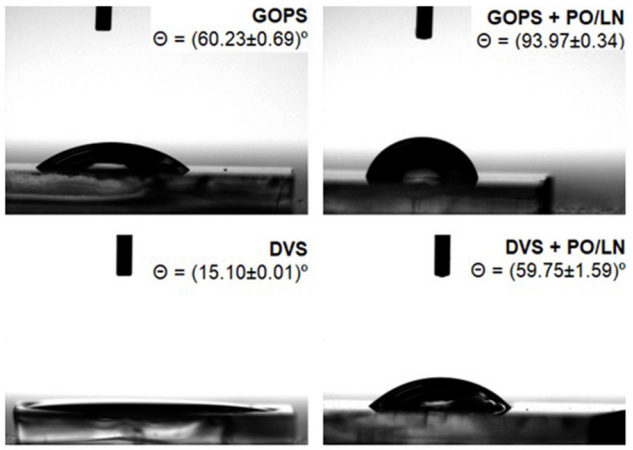

FIGURE 2 | Contact angle images of water droplets deposited on PEDOT:DVS and PEDOT:GOPS samples before and after coating with Poly-ornithine/Laminin (PO/LN); $n = 3$ samples for each condition (each measurement was performed in triplicates).

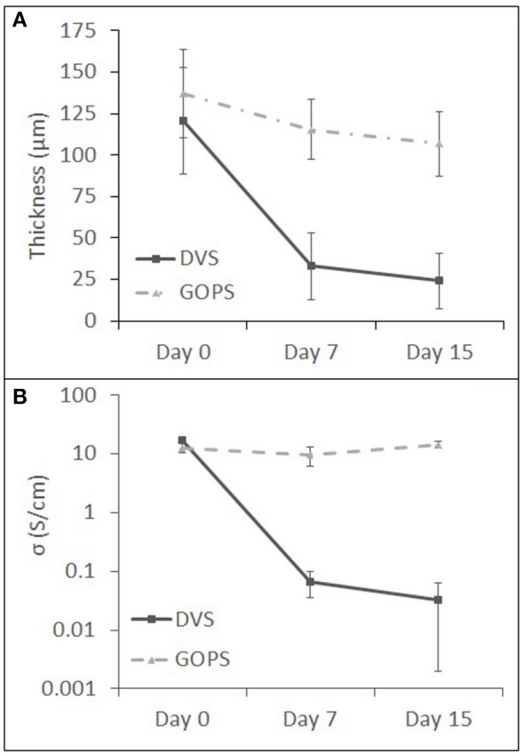

FIGURE 3 | Variation in thickness **(A)** and conductivity **(B)** of PEDOT:GOPS and PEDOT:DVS films upon immersion in MilliQ water; $n = 3$ samples for each time point (each measurement was performed in triplicates).

the electrical performance and progression of the cross-linking reactions. The surface of the samples appeared to be flat and homogeneous, as shown in **Supplementary Figure 1**. The samples were further characterized for surface wettability, thickness, electrical conductivity and long-term water stability (15 days).

Contact angle (Θ [°]) analysis allowed to evaluate the differences in surface wettability between GOPS- and DVS-cross-linked films, before and after PO/LN coating, being LN a ECM protein fundamental for NSCs adhesion. Wettability analysis allows us to establish whether a surface can be considered hydrophobic (Θ >90°) or hydrophilic (Θ <90°), which impacts initial cell adhesion and survival (Tamada and Ikada, 1993; Hornyak and Rao, 2016). PEDOT:DVS films obtained are more hydrophilic than PEDOT:GOPS ones, with contact angles of 15.10 ± 0.01° and 60.23 ± 0.69°, respectively (**Figure 2**). Moreover, surface coating with PO/LN leads to a decrease in hydrophilicity of both cross-linked films, but PEDOT:DVS film (59.75 ± 1.59°) continues to be more hydrophilic than PEDOT:GOPS (93.97 ± 0.34°).

Stability of Cross-Linked PEDOT Films

Structural stability of cross-linked PEDOT:PSS films upon immersion in water was studied in this work. The goal was to assess possible changes in the film's properties. PEDOT:DVS and PEDOT:GOPS film samples were left immersed in MilliQ water for 7 and 15 days (**Figure 3** and **Table 2**). Water immersion lead to changes in the thickness (**Figure 3A**) and electroconductivity (**Figure 3B**) of both films. PEDOT:DVS suffered an 80% thickness loss after 15 days, while PEDOT:GOPS shows only 22% loss. The conductivity followed a similar trend. A dramatic reduction of PEDOT:DVS conductivity occurs after 7 days (from an initial value of 17 to 0.07 S cm^{-1}), which was then maintained after 15 days of immersion (0.03 S cm^{-1}). The electroconductivity of PEDOT:GOPS films slightly decreases after 7 days (from 13 to 10 S cm^{-1}) and increased again after 15 days (15 S cm^{-1}). Despite the cross-linked nature of the PEDOT films, with the DVS-cross-linked ones evidencing a loser network, both films will probably swell upon prolonged contact with water or the culture medium electrolyte. In case of the loser network, material may by "re-suspended," leading to a material loss of the film, with the concomitant thickness decrease. The loss in conductivity suggests that also doped PEDOT will be released from the film. In addition, the material may also delaminate from the supporting glass substrate. We do not expect that the flow of current through the PEDOT film will induce a degradation. The results obtained for the PEDOT:PSS:GOPS films support this conclusion.

Therefore, we can assume that PEDOT:GOPS films show a constant conductivity trend during time in water, with an approximate value of 12 S cm^{-1}, contrary to PEDOT:DVS films. Moreover, the reduction in thickness in PEDOT:DVS samples suggests that material loss into the water occurs along the timeframe of our envisaged cell studies, contrary to what is observed for PEDOT:GOPS. In view of these results, PEDOT:GOPS was used as a substrate for the electrical stimulation of NSCs.

TABLE 2 | Thickness and conductivity values of PEDOT:PSS films cross-linked with GOPS and DVS measured after different immersion times in water (Day 0, Day 7, and Day 15) (mean ± std., $n = 3$).

	Thickness (μm)		Conductivity σ (S cm^{-1})	
	DVS	GOPS	DVS	GOPS
Day 0	121 ± 32	137 ± 27	17 ± 1	13 ± 2
Day 7	33 ± 20	115 ± 18	0.07	10 ± 3
Day 15	24 ± 16	107 ± 19	0.03	15 ± 2

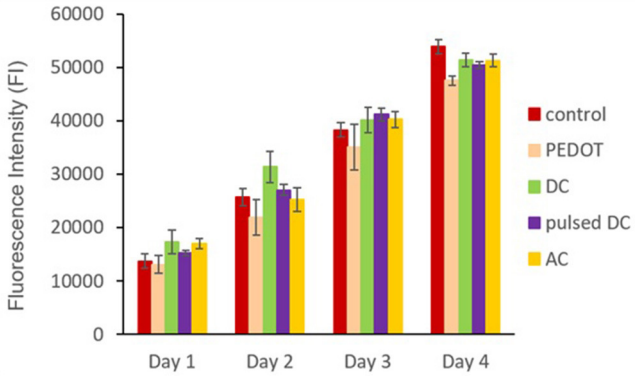

FIGURE 4 | Fluorescence intensity of Alamar Blue® bioassay from ReNcells-VM cultured on PEDOT:GOPS films under different electrical stimulation conditions (DC, pulsed DC, and AC). "Control" corresponds to tissue culture plates and "PEDOT" to PEDOT:GOPS setups with no application of electrical stimulation; $n = 2$ replicates of the experiment (each experiment performed in triplicates for each tested condition).

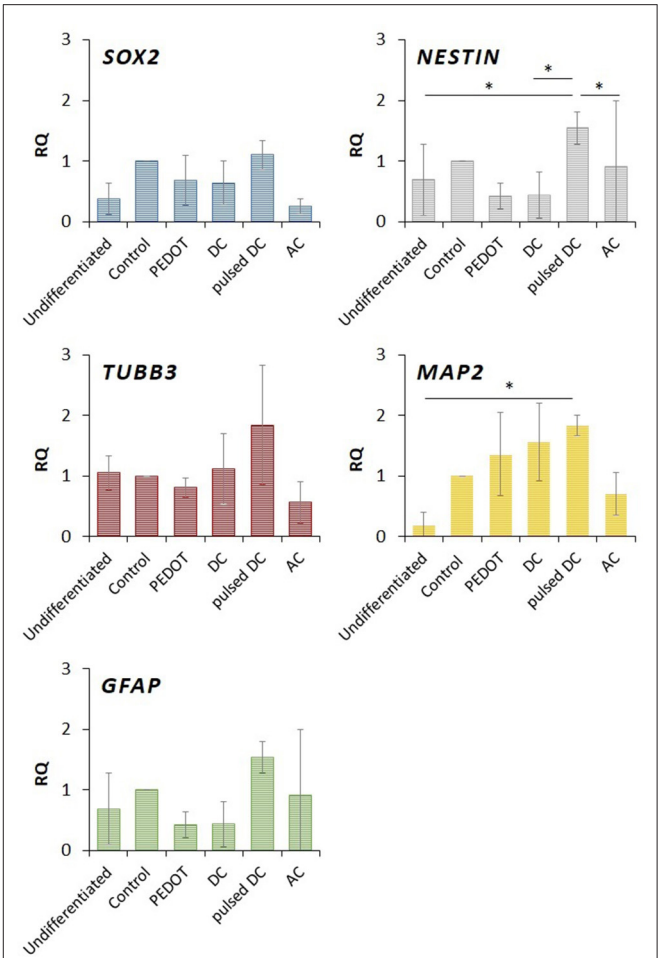

FIGURE 5 | Profiles of gene expression obtained with qRT-PCR on ReNcells-VM after 8 days of differentiation under various electrical stimulation conditions (DC, pulsed DC, and AC). The following genes were considered: SOX2 and NESTIN (stem/progenitor cells), TUBB3 (early neurons), MAP2 (mature neurons), GFAP (glial cells) (mean ± std., $n = 2$) replicates of the experiment (each experiment performed in triplicates for each tested condition), *p-value < 0.05.

Electrical Stimulation of ReNcell-VM—Metabolic Activity

After ReNcell-VM seeding onto the polymeric films, cell metabolic activity was assessed during the expansion phase (24 h stimulation per day, N2 expansion medium) by Alamar Blue® viability assay (**Figure 4**). ReNcell-VM cells on PEDOT:GOPS were exposed to different electrical stimulation conditions (DC, pulsed DC, and AC). Standard tissue culture plates and PEDOT:GOPS setups without electrical stimulation were used as controls.

Results show that the different electrical stimulation protocols used do not compromise ReNcells-VM metabolic activity throughout the time period assessed. All samples show a constant increase in fluorescence intensity, suggesting cell number increase. All samples with applied electrical stimulation show slightly higher values, but without statistically significant differences from the samples without electrical stimulation.

Electrical Stimulation of ReNcell-VM—Differentiation

The effect of electrical stimulation on ReNcell-VM differentiation (8 days) profile was evaluated using immunofluorescence and qRT-PCR. The ReNcells-VM differentiation into neuronal and glial lineages was promoted by growth factor removal and switching to N2B27 medium (Donato et al., 2007).

qRT-PCR was performed to analyze gene transcription activity at the end of the differentiation protocol under the various electrical stimulation patterns. The results of qRT-PCR for SOX2, NESTIN, TUBB3 (the gene encoding for TUJ1), GFAP, and MAP2 are depicted in **Figure 5**. It also includes the cells collected at the end of the expansion phase, and differentiated on the tissue culture plate and on PEDOT:GOPS setups without electrical stimulation. The expression of SOX2 is similar for all conditions, but slightly decreased for AC electrical stimulation. Considering NESTIN, pulsed DC stimulation shows a higher expression compared to the other electrical stimulation conditions and to undifferentiated ReNcells-VM, with statistical significance ($p < 0.05$). These results indicate that ReNcells-VM

still exhibit expression of neural progenitor genes after 8 days of differentiation.

Cells stimulated with pulsed DC showed increased expression of the differentiation genes tested (TUBB3, MAP2, and GFAP) in relation to the other conditions. The expression of mature neurons (MAP2), under pulsed DC, was significantly increased with respect to undifferentiated ReNcells-VM ($p < 0.05$). MAP2 also increased on DC stimulation and PEDOT:GOPS films without electrical stimulation. TUBB3 expression was enhanced by DC and pulsed DC stimulation.

Cells were immunostained for the markers TUJ1 and GFAP to evaluate the differentiation into specific neural phenotypes. Results for immunostaining are shown in **Figure 6.** All cultures show positive staining for both markers. The percentage of TUJ1 and GFAP was quantified using ImageJ and the ratio TUJ1/GFAP was calculated to compare neuronal against glial differentiation under the different electrical stimulation conditions. The results (**Figure 6**) show higher ratios for cultures under electric stimulation (DC, pulsed DC, or AC stimulation), with statistical significance ($p < 0.05$). TUJ1/GFAP ratio is higher than 1 for all electrical stimulation conditions, suggest that a slightly higher number of neurons is present in culture than astrocytes. For PEDOT:GOPS films without electrical stimulation the ratio is equal to 1, meaning equal quantities of neurons and astrocytes coexist in the non-stimulated setup, and for the tissue culture plate the ratio is <1, suggesting slightly higher number of astrocytes in the culture.

DISCUSSION

Preparation of Cross-Linked PEDOT:PSS Films

The preparation of electroconductive substrates is critical for neural tissue engineering applications using electrical stimulation (Luo et al., 2008; Balint et al., 2014; Guo and Ma, 2018). However, limited comparison exists between the electrical stimulation protocols available. For such study, a reliable electroconductive platform is required. PEDOT:PSS was our choice as it is one of the most stable, safe and versatile electroconductive polymers available (Luo et al., 2008; Shi et al., 2015; Heo et al., 2019). Commercially available PEDOT:PSS aqueous dispersions can be used as received to prepare PEDOT:PSS films with a wide range of electroconductivities. However, without further treatment, such films will re-suspend in water, which limits their use as scaffolds on aqueous environments, namely to support neural cell cultures. Such limitation can be addressed by the use of appropriate cross-linking protocols able to stabilize PEDOT:PSS films in aqueous environments, while retaining or improving their electroconductive and biocompatible properties (Shi et al., 2015). GOPS has been reported as a cross-linking agent able to yield a biocompatible and stable PEDOT:PSS film, but contributing also to reduce its conductivity (Balint et al., 2014; Håkansson et al., 2017). In this work, the performance of two different cross-linking protocols, based on distinct cross-linking agents (GOPS and DVS) was compared. Two different starting dispersions were prepared with the same amount of PEDOT:PSS (as received dispersion) and EG (1:4 by volume), adding a percentage of cross-linker and secondary dopant (DBSA) as described in literature, namely 1% (v/v) of GOPS and 0.05% (v/v) of DBSA for the first solution (Pires et al., 2015) and 3% (v/v) of DVS and 0.1% (v/v) of DBSA for the second one (Mantione et al., 2017). Annealing process was carried on following the same protocols described in literature (Pires et al., 2015; Mantione et al., 2017).

DVS was used as a cross-linking agent for PEDOT:PSS films, which can also act as a secondary dopant, to increase films electroconductivity (Mantione et al., 2017). The performance of GOPS and DVS cross-linked PEDOT:PSS was compared by Mantione et al. using a protocol slightly different from ours. In this previous study it was used a different PEDOT:PSS formulation, with lower PSS content and higher conductivity. Moreover, in such study, for the preparation of cross-linked PEDOT:PSS with GOPS, a 1:4 volume ratio of EG to PEDOT:PSS was also used, but a higher DBSA concentration (1.0 vs. 0.5 $\mu L\ mL^{-1}$), and various percentages of GOPS (from 1 to 5%) were studied. GOPS cross-linked PEDOT:PSS films were prepared by Mantione et al. at 1,000 rpm for 40 s and annealed at 140°C for 40 min for conductivity measurements, while for cell culture the films were annealed at 50°C for 60 min under vacuum. For the corresponding PEDOT:DVS samples, 1:16 volume parts of EG to PEDOT:PSS were used but with the same DBSA content as used in this study (1.0 $\mu L\ mL^{-1}$) and different percentages of DVS, from 0 to 8%, were studied using conductivity measurements. In the end, films were prepared at 1,000 rpm for 40 s and annealed at 140°C for 40 min for conductivity measurements, while for cell culture films were annealed at 50°C for 60 min under vacuum. In our study we used the same annealing conditions for the samples used in the conductivity studies and in the cell culture. Furthermore, the aqueous stability of PEDOT:GOPS and PEDOT:DVS films was not reported by Mantione et al. Therefore, we decided in our study to compare and further characterize the cross-linked films obtained with respect to the critical properties for NSC cell culture: hydrophilicity, electroconductivity, and stability in water.

Characterization of Cross-Linked PEDOT:PSS Films

The surface properties of a biomaterial are responsible for its interplay with cells, fluids, and components of the extracellular matrix (e.g., adhesion proteins; Menzies and Jones, 2010). Thus, biocompatibility can be highly influenced by material surface properties. In this study, PEDOT:GOPS films are more hydrophilic than PEDOT:DVS samples (**Figure 2**), being the contact angles reduced upon coating of the surfaces with PO/LN. We can, therefore, assume that the nature of the cross-linker used is the main determinant of the material surface properties. The contact angle values we obtained were previously described to be favorable to the adhesion of NSCs (Arima and Iwata, 2007; Tian et al., 2016), and therefore, considering also the stability upon contact with the culture medium, we pursued our studies with the PEDOT:GOPS substrates.

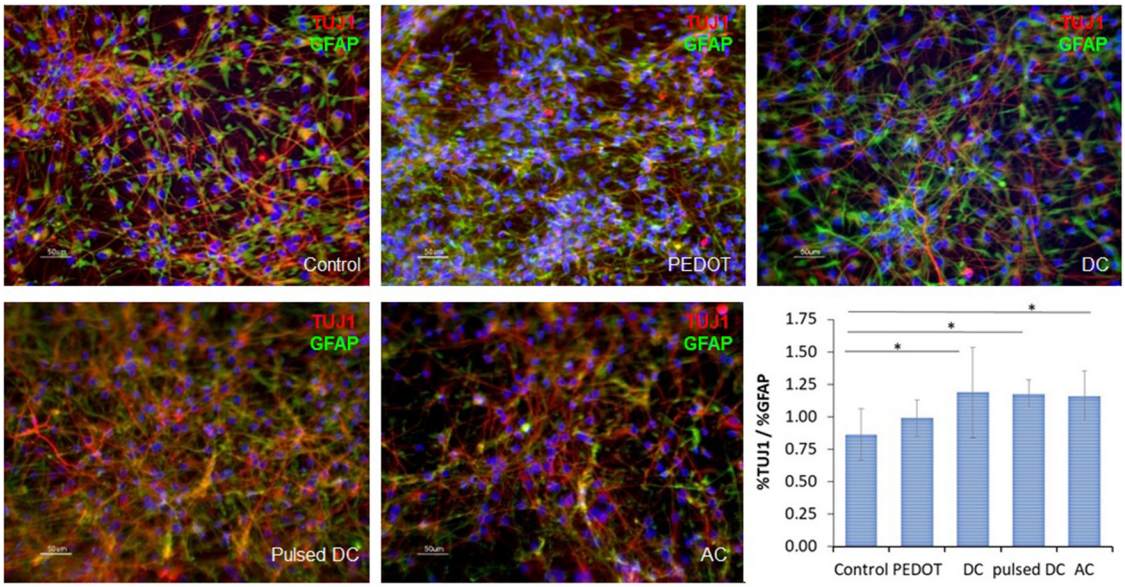

FIGURE 6 | Immunofluorescence of ReNcells-VM cultured under different electrical stimulation conditions (DC, pulsed DC, and AC), after 4 days of expansion and 8 days of differentiation, stained for TUJ1 (red), GFAP (green), DAPI (blue). Cultures on standard tissue culture plates ("Control") and on PEDOT:GOPS without electrical stimulation ("PEDOT") were used as controls. Ratio between TUJ1 % and GFAP % calculated using the total image area (bottom right panel); $n = 8$ ratios for each condition, $^*p$-value < 0.05, scale bar: 50 μm.

Electroconductive conjugated polymers such as PEDOT possess delocalized π orbitals that enable electrons mobility. Therefore, the more electroconductive materials enable a more efficient electrical stimulation of the cells. No threshold electroconductivity value exists in the literature for the application of conductive materials in cells electrical stimulation, but it is generally assumed that its value has to at least exceed that of the culture medium (0.01 S cm^{-1}) (Mazzoleni et al., 1986). We obtained high electroconductivity values (**Table 2**) for our PEDOT:GOPS (13 ± 2 S cm^{-1}) and PEDOT:DVS (17 ± 1 S cm^{-1}) samples, all of them above 0.01 S cm^{-1}.

The electroconductivity of the PEDOT:GOPS sample is higher than the value reported by Pires et al. (2015) for their films, and we hypothesize this is related to variations in the composition of the PEDOT:PSS water dispersion and/or details of the samples preparation. As for PEDOT:DVS, the electroconductivity obtained (17 ± 1 S cm^{-1}) is lower than that previously obtained by Mantione et al. (2017) (∼600 S cm^{-1}). This is explained by the use of different PEDOT:PSS dispersions: we used Clevios P VP Al 4083, with a PEDOT:PSS ratio of 1:6, while Mantione et al. used Clevios PH 1000, with a PEDOT:PSS ratio of 1:2.5, a more conductive formulation (Mantione et al., 2017).

The stability of PEDOT:GOPS and PEDOT:DVS films in water was determined to evaluate their suitability for cell culture applications. Our results indicate that, for the materials preparation conditions employed, GOPS maintained film integrity in wet environments for long incubation periods (15 days) in contrast to DVS. This is evidenced by the maintenance of film's electrical properties and average thickness. Supporting evidence of these findings has been reported (ElMahmoudy et al., 2017), demonstrating that a concentration of 1% wt of GOPS can promote high electrical conductivity, sufficient mechanical stability, and steady performance over 3 weeks.

We found that PEDOT:GOPS and PEDOT:DVS films have different stability profiles in water (**Table 2**). GOPS is a bifunctional organosilane with three methoxy groups on one side and an epoxy ring on the other, whereas DVS is a sulfone compound with two S-vinyl substituents. The differences observed might be explained by the different cross-linking mechanisms involved for GOPS and DVS, a matter that is still under debate. The cross-linking mechanism with PEDOT has been reported to be similar for both GOPS (Håkansson et al., 2017) and DVS (Jennings et al., 2018), where the epoxy and vinyl groups, respectively, react with the sulfonate group of PSS. This process allows the establishment of bridges across different PSS molecules, forming a network that is responsible to stabilize the obtained PEDOT film. The main difference between them is that GOPS can also establish Si-O-Si bonds with other GOPS molecules extending the network density, or even with the supporting glass to further anchor the film and reduce delamination (Håkansson et al., 2017; Solazzo et al., 2019), whereas DVS cannot (Mantione et al., 2017; Bora et al., 2019). In addition, the ethylene glycol used in the two cross-linkable formulations, may also undergo a condensation reaction with Si-OCH_3 group, further extending the network. Our results show that, under the conditions we have used, the network established in PEDOT:GOPS films is chemically more stable and resistant to erosion and delamination when compared to PEDOT:DVS, leading to an improved stability of PEDOT:GOPS in water. As such, PEDOT:GOPS films were used for our studies on electrical stimulation of NSCs.

Electrical Stimulation of ReNcell-VM

NSCs in their cell niche undergo asymmetric division generating two daughter cells, one that is identical to the original cell and one that is programmed to differentiate into a non-stem cell. When this mechanism is induced by external cues provided to the precursor cell, it is called extrinsic asymmetric cell division. Depending on their position in the stem cell niche, the daughter cells may acquire different fates owing to exposure to varying external signals (Morrison and Kimble, 2006). We hypothesize that the combination of chemical and pulsed electrical cues is able to better mimic the complexity of the neural stem cell niche *in vivo* and that plays a key role in the differentiation mechanism of NSCs.

PEDOT:GOPS films were used to study the effect of different electrical stimulation protocols on ReNcell-VM metabolic activity and differentiation. Results from Alamar Blue® Assay (**Figure 4**) demonstrate that all samples show a constant increase in fluorescence intensity, suggesting cell number increase. No differences were found regarding cell growth during the expansion phase, indicating the absence of toxic effects on the cells upon use of both PEDOT:GOPS platform and the electrical stimulation protocols. The positive effect of the electrical stimulation on NSCs growth and proliferation has been widely described in the literature (Yamada et al., 2007; Chang et al., 2011; Huang et al., 2015; Zhu et al., 2019). However, our results suggest that none of the protocols tested produced significant effects on ReNcell-VM metabolic activity during the first 4 days of stimulation.

At the end of the differentiation phase, qPCR and Immunofluorescence analysis were performed. qPCR analysis revealed a trend in gene expression: electrical stimulation by DC and pulsed DC was associated with higher expression of NESTIN, TUBB3, and MAP2. Among the electrical stimulation protocols tested, statistically significant increases in gene expression were found for NESTIN and MAP2 expression in pulsed DC. This indicates that pulsed DC positively influences ReNcell-VM expression of neuronal differentiation marker genes. Differences in TUBB3 and GFAP expression were found for the different various electrical stimulation protocols tested, but these were not statistically significant.

Immunofluorescence analysis was performed to evaluate ReNcell-VM morphology and neuron/astrocyte marker expression. In this study, we focused our analysis on the specific cell marker analysis for neurons (Tuj1) and astrocytes (GFAP). The images obtained (**Figure 6A**) show elongated cells with numerous projections, indicating that the differentiation of ReNcell-VM was successful. The relative quantification of the proteins TUJ11 and GFAP was then performed by immunostaining to investigate the effect of electrical stimulation on cell fate. The higher number of TUJ1 positive over GFAP positive staining in electrical stimulation samples suggests a greater prevalence of neuronal- over glial-committed cells. These results show that the electrical stimulation has a positive effect on NSCs phenotypic expression of markers of differentiation toward neuronal lineage. A similar trend has also been shown for MAP2 (neurons) and GFAP (astrocytes) expression cells when differentiated on flat titanium substrates under electrical stimulation (Yang et al., 2017). Other studies in the literature report similar trends (Chang et al., 2011; Kobelt et al., 2014; Pires et al., 2015; Stewart et al., 2015).

Immunofluorescence results were in accordance with the results of qRT-PCR. The analysis focused on the relative expression of SOX2 and NESTIN (neural stem/progenitor cells), and three genes that are expressed during cell differentiation: TUBB3 (early neurons), MAP2 (intermediate neurons), and GFAP (glial cells). Specifically, the transcription factor SOX2 is expressed in neural progenitor populations in the developing central nervous system and it is necessary to maintain their progenitor identity (Hutton and Pevny, 2011). NESTIN is an intermediate filament protein that is known as a neural stem/progenitor cell marker, expressed in undifferentiated central nervous system cells during development (Suzuki et al., 2010). During neuro- and glio-genesis, NESTIN is replaced by cell type-specific intermediate filaments, such as neurofilaments and GFAP. GFAP is the main intermediate filament protein in mature astrocytes, but also an important component of the cytoskeleton in astrocytes and immature neurons during development (Casper and McCarthy, 2006; Dráberová et al., 2008; Middeldorp and Hol, 2011). Finally, the expression of the genes TUBB3 and MAP2 are typical neuron-specific markers. TUJ1 (encoded by TUBB3 gene) is the protein that provides stability to microtubules in neuronal cell bodies and axons, and it is present in the early stages of neuron development (Huang et al., 2012). MAP2 belongs to a family of proteins responsible for stabilizing neuronal shape by promoting microtubule synthesis (Morrison et al., 1998). MAP2 expression is only observed in the middle to late stages of neuron development.

To summarize, ReNcells-VM are capable of differentiating into a higher number of neurons in a non-stimulated PEDOT:GOPS substrate then on standard tissue plate culture plates, but this effect is further enhanced when cultures on PEDOT:GOPS are electrically stimulated. DC and pulsed DC stimulation have a similar impact on ReNcell-VM differentiation toward neurons, as demonstrated by immunofluorescence. Moreover, AC stimulation failed to show significant impact in the expression of both neuronal and astrocytic markers. Pulsed DC electrical stimulation, as demonstrated also by immunofluorescence analysis, was the condition that led to higher efficiency of ReNcell-VM differentiation toward neuronal lineage. We hypothesize that this type of stimulus better suits the conditions for higher production of neural cells for tissue engineering applications, being even similar to the conditions observed *in vivo* (Mazaheri and Jensen, 2010).

CONCLUSION

In this study PEDOT:GOPS and PEDOT:DVS films were compared. PEDOT:GOPS films were found to have higher contact angle ($60.23 \pm 0.69^{\circ}$ vs. $15.1 \pm 0.01^{\circ}$), similar electroconductivity ($13 \pm 2\,S\ cm^{-1}$ vs. $17 \pm 1\,S\ cm^{-1}$) and increased stability for 15 days in water when compared to PEDOT:DVS. PEDOT:GOPS was used as a platform to study the effect of different electrical stimulation protocols

(AC, DC, and pulsed DC) on ReNcell-VM metabolic activity and differentiation (1 V cm^{-1}). qRT-PCR results suggest that pulsed DC stimulation enhances NSCs neuronal differentiation. The ratio of TUJ1/GFAP markers expression was significantly higher for all electrical stimulation conditions. With this study, we demonstrate that differences in electrical cues affect NSCs fate. PEDOT:PSS cross-linked substrates coupled with pulsed DC electrical stimulation are powerful candidates for mimicking stem cell niches for tissue engineering applications. We believe that these findings also have relevant implications for PEDOT-PSS coating of deep brain electrodes for application in neurodegenerative disorders.

DATA AVAILABILITY STATEMENT

The raw data supporting the conclusions of this article will be made available by the authors, without undue reservation.

AUTHOR CONTRIBUTIONS

LS, CR, FF, and JM: original idea. LS, FG, CR, FF, and JM: experimental plan. LS assisted by FF and JM: experimental work on materials. LS assisted by CR and FF: experimental work with cell culture. LS assisted by FG and CR: cell characterization. LS and FG: qRT-PCR. LS with guidance by CR, FG, JM, and FF: data analysis and figures preparation. CR, RL, JC, FF, and JM: scientific guidance and discussions, laboratory space, and funding. LS and FG: manuscript writing and original drafting. CR, RL, JC, JM, and FF: writing—review and editing. All authors revised the manuscript.

FUNDING

The authors acknowledge funding from FCT—Portuguese Foundation for Science and Technology, NEURON grant (PTDC/CTM-CTM/30237/2017), iBB grant (UID/BIO/04565/2020), FCT/MCTES funding to IT (UIDB/50008/2020), Post-Doc grant (SFRH/BPD/82056/2011) and Ph.D. scholarships (PD/BD/114045/2015, 2020.07979.BD), from POR Lisboa 2020 grant PRECISE (Project No. 16394).

ACKNOWLEDGMENTS

We thank Isabel Nogueira for technical support on SEM images acquisition at MicroLab facilities at IST Lisbon.

SUPPLEMENTARY MATERIAL

The Supplementary Material for this article can be found online at: https://www.frontiersin.org/articles/10.3389/fbioe.2021.591838/full#supplementary-material

REFERENCES

Alba, N. A., Du, Z. J., Catt, K. A., Kozai, T. D., and Cui, X. T. (2015). *In vivo* electrochemical analysis of a PEDOT/MWCNT neural electrode coating. *Biosens. Basel* 5, 618–646. doi: 10.3390/bios5040618

Alzheimer's Association (2019). 2019 Alzheimer's disease facts and figures. *Alzheimers Dement.* 15, 321–87. doi: 10.1016/j.jalz.2019.01.010

Arima, Y., and Iwata, H. (2007). Effect of wettability and surface functional groups on protein adsorption and cell adhesion using well-defined mixed self-assembled monolayers. *Biomaterials* 28, 3074–3082. doi: 10.1016/j.biomaterials.2007.03.013

Balint, R., Cassidy, N. J., and Cartmell, S. H. (2014). Conductive polymers: towards a smart biomaterial for tissue engineering. *Acta Biomater.* 10, 2341–2353. doi: 10.1016/j.actbio.2014.02.015

Benabid, A. L. (2003). Deep brain stimulation for Parkinson's disease. *Curr. Opin. Neurobiol.* 13, 696–706. doi: 10.1016/j.conb.2003.11.001

Bodart, C., Rossetti, N., Hagler, J., Chevreau, P., Chhin, D., Soavi, F., et al. (2019). Electropolymerized poly(3,4-ethylenedioxythiophene) (PEDOT) coatings for implantable deep-brain-stimulating microelectrodes. *ACS Appl. Mater. Interfaces* 11, 17226–17233. doi: 10.1021/acsami.9b03088

Bora, P. J., Anil, A. G., Vinoy, K. J., and Ramamurthy, P. C. (2019). Outstanding absolute electromagnetic interference shielding effectiveness of cross-linked PEDOT:PSS film. *Adv. Mater. Interfaces* 6:1901353. doi: 10.1002/admi.201901353

Borlongan, C. V., Sanberg, P. R., and Freeman, T. B. (1999). Neural transplantation for neurodegenerative disorders. *Lancet* 353(Suppl. 1), SI29–SI30. doi: 10.1016/s0140-6736(99)90229-5

Casper, K. B., and McCarthy, K. D. (2006). GFAP-positive progenitor cells produce neurons and oligodendrocytes throughout the CNS. *Mol. Cell. Neurosci.* 31, 676–684. doi: 10.1016/j.mcn.2005.12.006

Chang, K. A., Kim, J. W., Kim, J. A., Lee, S. E., Kim, S., Suh, W. H., et al. (2011). Biphasic electrical currents stimulation promotes both proliferation and differentiation of fetal neural stem cells. *PLoS ONE* 6:e18738. doi: 10.1371/journal.pone.0018738

Collazos-Castro, J. E., Polo, J. L., Hernández-Labrado, G. R., Padial-Cañete, V., and García-Rama, C. (2010). Bioelectrochemical control of neural cell development on conducting polymers. *Biomaterials* 31, 9244–9255. doi: 10.1016/j.biomaterials.2010.08.057

Donato, R., Miljan, E. A., Hines, S. J., Aouabdi, S., Pollock, K., Patel, S., et al. (2007). Differential development of neuronal physiological responsiveness in two human neural stem cell lines. *BMC Neurosci.* 8:36. doi: 10.1186/1471-2202-8-36

Dráberová, E., Del Valle, L., Gordon, J., Marková, V., Smejkalová, B., Bertrand, L., et al. (2008). Class III beta-tubulin is constitutively coexpressed with glial fibrillary acidic protein and nestin in midgestational human fetal astrocytes: implications for phenotypic identity. *J. Neuropathol. Exp. Neurol.* 67, 341–354. doi: 10.1097/NEN.0b013e31816a686d

Du, J., Zhen, G., Chen, H., Zhang, S., Qing, L., Yang, X., et al. (2018). Optimal electrical stimulation boosts stem cell therapy in nerve regeneration. *Biomaterials* 181, 347–359. doi: 10.1016/j.biomaterials.2018.07.015

Du, L., Li, T., Jin, F., Wang, Y., Li, R., Zheng, J., et al. (2020). Design of high conductive and piezoelectric poly (3,4-thylenedioxythiophene)/chitosan nanofibers for enhancing cellular electrical stimulation. *J. Colloid Interface Sci.* 559, 65–75. doi: 10.1016/j.jcis.2019.10.003

ElMahmoudy, M., Inal, S., Charrier, A., Uguz, I., Malliaras, G. G., and Sanaur, S. (2017). Tailoring the electrochemical and mechanical properties of PEDOT:PSS films for bioelectronics. *Macromol. Mater. Eng.* 302:1600497. doi: 10.1002/mame.201600497

Erkkinen, M. G., Kim, M. O., and Geschwind, M. D. (2018). Clinical neurology and epidemiology of the major neurodegenerative diseases. *C.S.H. Perspect. Biol.* 10:a033118. doi: 10.1101/cshperspect.a033118

Feng, J. F., Liu, J., Zhang, X. Z., Zhang, L., Jiang, J.-Y., Nolta, J., and Zhao, M. (2012). Guided migration of neural stem cells derived from human embryonic stem cells by an electric field. *Stem Cells* 30, 349–355. doi: 10.1002/stem.779

Fernandes, T. G., Duarte, S. T., Ghazvini, M., Gaspar, C., Santos, D. C., Porteira, A. R., et al. (2015). Neural commitment of human pluripotent stem cells under

defined conditions recapitulates neural development and generates patient-specific neural cells. *Biotechnol. J.* 10: 1578–1588. doi: 10.1002/biot.201400751

Galiakberova, A. A., Dashinimaev, E. B. (2020). Neural stem cells and methods for their generation from induced pluripotent stem cells *in vitro*. *Front. Cell Dev. Biol.* 8:815. doi: 10.3389/fcell.2020.00815

Gammon, K. (2014). Neurodegenerative disease: brain windfall. *Nature* 515, 299–300. doi: 10.1038/nj7526-299a

Garrudo, F., Chapman, C. A., Hoffman, P. R., Udangawa, R. N., Silva, J. C., Mikael, P. E., et al. (2019a). Polyaniline-polycaprolactone blended nanofibers for neural cell culture. *Eur. Polym. J.* 117, 28–37. doi: 10.1016/j.eurpolymj.2019.04.048

Garrudo, F., Udangawa, R. N., Hoffman, P. R., Sordini, L., Chapman, C. A., Mikael, P. E., et al. (2019b). Polybenzimidazole nanofibers for neural stem cell culture. *Mater. Today Chem.* 14:100185. doi: 10.1016/j.mtchem.2019.08.004

Ghasemi-Mobarakeh, L., Prabhakaran, M. P., Morshed, M., Nasr-Esfahani, M. H., and Ramakrishna, S. (2009). Electrical stimulation of nerve cells using conductive nanofibrous scaffolds for nerve tissue engineering. *Tissue Eng. Part A* 15, 3605–3619. doi: 10.1089/ten.TEA.2008.0689

Goel, M., David Heinrich, C., Krauss, G., and Thelakkat, M. (2019). Principles of structural design of conjugated polymers showing excellent charge transport toward thermoelectrics and bioelectronics applications. *Macromol. Rapid Commun.* 40:1800915. doi: 10.1002/marc.201800915

Guarino, V., Zuppolini, S., Borriello, A., and Ambrosio, L. (2016). Electro-active polymers (EAPs): a promising route to design bio-organic/bioinspired platforms with on demand functionalities. *Polymers* 8:185. doi: 10.3390/polym8050185

Guo, B., and Ma, P. X. (2018). Conducting polymers for tissue engineering. *Biomacromolecules* 19, 1764–1782. doi: 10.1021/acs.biomac.8b00276

Håkansson, A., Han, S., Wang, S., Lu, J., Braun, S., Fahlman, M., et al. (2017). Effect of (3-glycidyloxypropyl)trimethoxysilane (GOPS) on the electrical properties of PEDOT:PSS films. *J. Polym. Sci. Part B Polym. Phys.* 55, 814–820. doi: 10.1002/polb.24331

Harrower, T. P., and Barker, R. A. (2004). Is there a future for neural transplantation? *BioDrugs* 18, 141–153. doi: 10.2165/00063030-200418030-00001

Hayashi, H., Edin, F., Li, H., Liu, W., and Rask-Andersen, H. (2016). The effect of pulsed electric fields on the electrotactic migration of human neural progenitor cells through the involvement of intracellular calcium signaling. *Brain Res.* 1652, 195–203. doi: 10.1016/j.brainres.2016.09.043

Heemels, M. T. (2016). Neurodegenerative diseases. *Nature* 539:179. doi: 10.1038/539179a

Heo, D., Lee, S.-J., Timsina, R., Qiu, X., Castro, N., and Zhang, L. (2019). Development of 3D printable conductive hydrogel with crystallized PEDOT:PSS for neural tissue engineering. *Mater. Sci. Eng. C* 99, 582–590. doi: 10.1016/j.msec.2019.02.008

Hornyak, G. L., and Rao, A. K. (2016). "Chapter 2: Fundamentals of nanoscience (and nanotechnology)" in *Nanoscience in Dermatology*, eds M. R. Hamblin, P. Avci and T. W. Prow (London: Academic Press), 15–29. doi: 10.1016/B978-0-12-802926-8.00002-1

Huang, Y., Li, Y., Chen, J., Zhou, H., and Tan, S. (2015). Electrical stimulation elicits neural stem cells activation: new perspectives in CNS repair. *Front. Hum. Neurosci.* 9:586. doi: 10.3389/fnhum.2015.00586

Huang, Y. J., Wu, H. C., Tai, N. H., and Wang, T. W. (2012). Carbon nanotube rope with electrical stimulation promotes the differentiation and maturity of neural stem cells. *Small* 8, 2869–2877. doi: 10.1002/smll.201200715

Hutton, S. R., and Pevny, L. H. (2011). SOX2 expression levels distinguish between neural progenitor populations of the developing dorsal telencephalon. *Dev. Biol.* 352, 40–47. doi: 10.1016/j.ydbio.2011.01.015

Inácio, P. M. C., Medeiros, M. C. R., Carvalho, T., Félix, R. C., Mestre, A., Hubbard, P. C., et al. (2020). Ultra-low noise PEDOT:PSS electrodes on bacterial cellulose: a sensor to access bioelectrical signals in non-electrogenic cells. *Org. Electron.* 85:105882. doi: 10.1016/j.orgel.2020.105882

Inal, S., Rivnay, J., Suiu, A. O., Malliaras, G. G., and McCulloch, I. (2018). Conjugated polymers in bioelectronics. *Acc. Chem. Res.* 51, 1368–1376. doi: 10.1021/acs.accounts.7b00624

Jennings, M., Kendrick, I., Green, C., and Lustig, S. (2018). *PEDOT: PSS-DVS Crosslinking Reaction Monitored via ATR-FTIR for Air Cathode Application in Microbial Fuel Cells.* Boston, MA: RISE: Research, Innovation, and Scholarship Expo, Northeast University. Available online at: http://hdl.handle.net/2047/D20287676 (accessed January 31, 2021).

Kaur, G., Adhikari, R., Cass, P., Bown, M., and Gunatillake, P. (2015). Electrically conductive polymers and composites for biomedical applications. *RSC Adv.* 5, 37553–37567. doi: 10.1039/C5RA01851J

Kayser, L. V., and Lipomi, D. J. (2019). Stretchable conductive polymers and composites based on PEDOT and PEDOT:PSS. *Adv. Mater.* 31:1806133. doi: 10.1002/adma.201806133

Kimura, K., Yanagida, Y., Haruyama, T., Kobatake, E., and Aizawa, M. (1998). Gene expression in the electrically stimulated differentiation of PC12 cells. *J. Biotechnol.* 63, 55–65. doi: 10.1016/s0168-1656(98)00075-3

Kobelt, L. J., Wilkinson, A. E., McCormick, A. M., Willits, R. K., and Leipzig, N. D. (2014). Short duration electrical stimulation to enhance neurite outgrowth and maturation of adult neural stem progenitor cells. *Ann. Biomed. Eng.* 42, 2164–2176. doi: 10.1007/s10439-014-1058-9

Kühn, A. A., and Volkmann, J. (2017). Innovations in deep brain stimulation methodology. *Mov. Disord.* 32, 11–19. doi: 10.1002/mds.26703

Li, Y., Weiss, M., and Yao, L. (2014). Directed migration of embryonic stem cell-derived neural cells in an applied electric field. *Stem Cell Rev.* 10, 653–662. doi: 10.1007/s12015-014-9518-z

Luo, S.-C., Mohamed Ali, E., Tansil, N., Yu, H., Gao, S., and Kantchev, E. (2008). Poly(3,4-ethylenedioxythiophene) (PEDOT) nanobiointerfaces: thin, ultrasmooth, and functionalized PEDOT films with *in vitro* and *in vivo* biocompatibility. *Langmuir* 24, 8071–8077. doi: 10.1021/la800333g

Mantione, D., Del Agua, I., Schaafsma, W., ElMahmoudy, M., Uguz, I., Sanchez-Sanchez, A., et al. (2017). Low-Temperature cross-linking of PEDOT:PSS films using divinylsulfone. *ACS Appl. Mater. Interfaces* 9, 18254–18262. doi: 10.1021/acsami.7b02296

Mazaheri, A., and Jensen, O. (2010). Rhythmic pulsing: linking ongoing brain activity with evoked responses. *Front. Hum. Neurosci.* 4:177. doi: 10.3389/fnhum.2010.00177

Mazzoleni, A. P., Sisken, B. F., and Kahler, R. L. (1986). Conductivity values of tissue culture medium from 20 degrees C to 40 degrees C. *Bioelectromagnetics* 7, 95–99. doi: 10.1002/bem.2250070111

Meng, X., Li, W., Young, F., Gao, R., Chalmers, L., Zhao, M., and Song, B. (2012). Electric field-controlled directed migration of neural progenitor cells in 2D and 3D environments. *J. Vis. Exp.* 60:3453. doi: 10.3791/3453

Menzies, K. L., and Jones, L. (2010). The impact of contact angle on the biocompatibility of biomaterials. *Optom. Vis. Sci.* 87, 387–399. doi: 10.1097/OPX.0b013e3181da863e

Middeldorp, J., and Hol, E. M. (2011). GFAP in health and disease. *Prog. Neurobiol.* 93, 421–443. doi: 10.1016/j.pneurobio.2011.01.005

Morrison, J., Hof, P. R., and Huntley, G. W. (1998). "Chapter II - Neurochemical organization of the primate visual cortex" in *Handbook of Chemical Neuroanatomy*, *Vol. 14*, eds F. E. Bloom, A. Björklund, and T. Hökfelt (Amsterdam: Elsevier), 299–430. doi: 10.1016/S0924-8196(98)80004-3

Morrison, S., and Kimble, J. (2006). Asymmetric and symmetric stem-cell divisions in development and cancer. *Nature* 441, 1068–1074. doi: 10.1038/nature04956

Pace, G., Bargigia, I., Noh, Y., Silva, C., and Caironi, M. (2019). Intrinsically distinct hole and electron transport in conjugated polymers controlled by intra and intermolecular interactions. *Nat. Commun.* 10:5226. doi: 10.1038/s41467-019-13155-9

Pathak, M. M., Nourse, J. L., Tran, T., Hwe, J., and Arulmoli, J. (2014). Stretch-activated ion channel Piezo1 directs lineage choice in human neural stem cells. *Proc. Natl. Acad. Sci. U.S.A.* 111, 16148–16153. doi: 10.1073/pnas.1409802111

Pires, F., Ferreira, Q., Rodrigues, C. A., Morgado, J., and Ferreira, F. C. (2015). Neural stem cell differentiation by electrical stimulation using a cross-linked PEDOT substrate: Expanding the use of biocompatible conjugated conductive polymers for neural tissue engineering. *Biochim. Biophys. Acta* 1850, 1158–1168. doi: 10.1016/j.bbagen.2015.01.020

Qi, L., Li, N., Song, Q., Wang, L., and Zhang, Q. (2013). The effects of topographical patterns and sizes on neural stem cell behavior. *PLoS ONE* 8:e59022. doi: 10.1371/journal.pone.0059022

Rivnay, J., Owens, R. M., and Malliaras, G. G. (2014). The rise of organic bioelectronics. *Chem. Mater.* 26, 679–685. doi: 10.1021/cm4022003

Shi, H., Liu, C., Jiang, Q., and Xu, J. (2015). Effective approaches to improve the electrical conductivity of PEDOT:PSS: a review. *Adv. Electron. Mater.* 1:1500017. doi: 10.1002/aelm.201500017

Solazzo, M., Krukiewicz, K., Zhussupbekova, A., Fleischer, K., Biggs, M., and Monaghan, M. (2019). PEDOT:PSS interfaces stabilised using a PEGylated crosslinker yield improved conductivity and biocompatibility. *J. Mater. Chem. B* 7, 4811–4820. doi: 10.1039/C9TB01028A

Stewart, E., Kobayashi, N. R., Higgins, M. J., Quigley, A. R., Jamali, S., Moulton, S. E., et al. (2015). Electrical stimulation using conductive polymer polypyrrole promotes differentiation of human neural stem cells: a biocompatible platform for translational neural tissue engineering. *Tissue Eng Part C Methods* 21, 385–393. doi: 10.1089/ten.tec.2014.0338

Suzuki, S., Namiki, J., Shibata, S., Mastuzaki, Y., and Okano, H. (2010). The neural stem/progenitor cell marker nestin is expressed in proliferative endothelial cells, but not in mature vasculature. *J. Histochem. Cytochem*. 58, 721–730. doi: 10.1369/jhc.2010.955609

Tamada, Y., and Ikada, Y. (1993). Cell adhesion to plasma-treated polymer surfaces. *Polymer* 34, 2208–2212. doi: 10.1016/0032-3861(93)90752-V

Tian, L., Prabhakaran, M. P., Hu, J., Chen, M., Besenbacher, F., Ramakrishna, S. (2016). Synergistic effect of topography, surface chemistry and conductivity of the electrospun nanofibrous scaffold on cellular response of PC12 cells. *Colloids Surf. B Biointerfaces* 145, 420–429. doi: 10.1016/j.colsurfb.2016.05.032

Tomaskovic-Crook, E., Zhang, P., Ahtiainen, A., Kaisvuo, H., Lee, C.-Y., Beirne, S., et al. (2019). Human neural tissues from neural stem cells using conductive biogel and printed polymer microelectrode arrays for 3D electrical stimulation. *Adv. Healthc. Mater*. 8:e1900425. doi: 10.1002/adhm.201900425

Tresco, P. A. (2000). Tissue engineering strategies for nervous system repair. *Prog. Brain Res.* 128, 349–363. doi: 10.1016/S0079-6123(00)28031-X

Wang, S., Guan, S., Zhu, Z., Li, W., Liu, T., and Ma, X. (2017). Hyaluronic acid doped-poly(3,4-ethylenedioxythiophene)/chitosan/gelatin (PEDOT-HA/Cs/Gel) porous conductive scaffold for nerve regeneration. *Mater. Sci. Eng. C Mater. Biol. Appl.* 71, 308–316. doi: 10.1016/j.msec.2016.10.029

Yamada, M., Tanemura, K., Okada, S., Iwanami, A., Nakamura, M., Mizuno, H., et al. (2007). Electrical stimulation modulates fate determination of differentiating embryonic stem cells. *Stem Cells* 25, 562–570. doi: 10.1634/stemcells.2006-0011

Yang, K., Yu, S. J., Lee, J. S., Lee, H.-R., Chang, G.-E., Seo, J., et al. (2017). Electroconductive nanoscale topography for enhanced neuronal differentiation and electrophysiological maturation of human neural stem cells. *Nanoscale* 9, 18737–18752. doi: 10.1039/c7nr05446g

Yao, L., and Li, Y. (2016). The role of direct current electric field-guided stem cell migration in neural regeneration. *Stem Cell Rev. Rep*. 12, 365–375. doi: 10.1007/s12015-016-9654-8

Zhao, H., Steiger, A., Nohner, M., and Ye, H. (2015). Specific intensity direct current (DC) electric field improves neural stem cell migration and enhances differentiation towards βIII-tubulin+ neurons. *PLoS ONE* 10:e0129625. doi: 10.1371/journal.pone.0129625

Zhu, R., Sun, Z., Li, C., Ramakrishna, S., Chiu, K., and He, L. (2019). Electrical stimulation affects neural stem cell fate and function *in vitro*. *Exp. Neurol.* 319:112963. doi: 10.1016/j.expneurol.2019.112963

Conflict of Interest: The authors declare that the research was conducted in the absence of any commercial or financial relationships that could be construed as a potential conflict of interest.

Advantages of publishing in Frontiers

OPEN ACCESS
Articles are free to read for greatest visibility and readership

FAST PUBLICATION
Around 90 days from submission to decision

HIGH QUALITY PEER-REVIEW
Rigorous, collaborative, and constructive peer-review

TRANSPARENT PEER-REVIEW
Editors and reviewers acknowledged by name on published articles

Frontiers
Avenue du Tribunal-Fédéral 34
1005 Lausanne | Switzerland

Visit us: www.frontiersin.org
Contact us: frontiersin.org/about/contact

REPRODUCIBILITY OF RESEARCH
Support open data and methods to enhance research reproducibility

DIGITAL PUBLISHING
Articles designed for optimal readership across devices

FOLLOW US
@frontiersin

IMPACT METRICS
Advanced article metrics track visibility across digital media

EXTENSIVE PROMOTION
Marketing and promotion of impactful research

LOOP RESEARCH NETWORK
Our network increases your article's readership